gels

Special Issue Reprint

Hydrogelated Matrices

Structural, Functional and Applicative Aspects

Edited by
Enrico Gallo and Carlo Diaferia

mdpi.com/journal/gels

MDPI

Hydrogelated Matrices: Structural, Functional and Applicative Aspects

Hydrogelated Matrices: Structural, Functional and Applicative Aspects

Guest Editors

Enrico Gallo
Carlo Diaferia

MDPI

Basel • Beijing • Wuhan • Barcelona • Belgrade • Novi Sad • Cluj • Manchester

Guest Editors

Enrico Gallo IRCCS Synlab SDN Naples Italy	Carlo Diaferia Department of Pharmacy University of Naples "Federico II" Naples Italy

Editorial Office
MDPI AG
Grosspeteranlage 5
4052 Basel, Switzerland

This is a reprint of the Special Issue, published open access by the journal *Gels* (ISSN 2310-2861), freely accessible at: https://www.mdpi.com/journal/gels/special_issues/6TWD5K3GNT.

For citation purposes, cite each article independently as indicated on the article page online and as indicated below:

Lastname, A.A.; Lastname, B.B. Article Title. *Journal Name* **Year**, *Volume Number*, Page Range.

ISBN 978-3-7258-4359-6 (Hbk)
ISBN 978-3-7258-4360-2 (PDF)
https://doi.org/10.3390/books978-3-7258-4360-2

Contents

About the Editors

Enrico Gallo

Dr. Enrico Gallo obtained his PhD in Drug Science from the Department of Pharmacy at the University of Naples “Federico II.” He currently holds a permanent position as Pharmaceutical Researcher at IRCCS SYNLAB SDN in Naples. His research focuses on the solid-phase synthesis of peptides and the structural characterization of fibers and soft materials using spectroscopic and microscopy techniques, with applications in bioimaging and magnetic resonance imaging (MRI). Additionally, his research interests extend to the development of supramolecular diagnostic and therapeutic tools for applications in nanomedicine.

Carlo Diaferia

Dr. Diaferia completed his PhD in 2018 at the University of Naples “Federico II”, and his MD before that in 2014 at the same university. His research is related to the topics of peptide-based materials, supramolecular chemistry, self-assembling hydrogels, and nanostructured tools for the development of novel nanoplatforms for application in materials science, functional coatings, diagnostics, therapeutics, drug delivery, and optoelectronics. He is a member of the ItPS (Italian Peptide Society) and an Expose Researcher for the National Centre for Gene Therapy and Drugs based on RNA Technology.

Preface

This reprint, as part of the Special Issue *Hydrogelated Matrices: Structural, Functional and Applicative Aspects*, presents a comprehensive exploration of the latest developments in gel materials, their synthesis, and their expanding range of applications across diverse fields. Our aim is to highlight the transformative potential of gel-based matrices and technologies and how they are shaping new frontiers in industries and applications such as biomedical engineering, environmental sustainability, and supramolecular chemistry.

Examples of the cutting-edge advancements in gel materials presented here include self-healing and stimuli-responsive systems, the development of smart gels, and their promising applications in drug delivery, tissue engineering, water treatment, and energy storage. The motivation behind this collection derives from the growing importance of gelated systems in addressing complex, multifactorial and multidisciplinary challenges. By exploring the current advancements and future directions of gel technologies, we aim to provide the scientific community with valuable insights into how these materials can contribute to a more sustainable and innovative future.

This collection is primarily addressed to researchers, academics, and professionals in the fields of materials science, biotechnology, environmental engineering, and related disciplines. We hope that it serves as a resource for those seeking to understand the dynamic role of gel materials and to foster further research and collaboration in this exciting area.

We would like to express our sincere gratitude to the contributing authors, whose expertise and dedication have made this Special Issue possible. Their contributions have been invaluable in shaping this reprint and advancing the field of gel materials. We also acknowledge the assistance of our colleagues and peers, whose support has been instrumental in the successful compilation of this work.

We hope this reprint inspires further exploration and innovation in gel materials, and we look forward to seeing how these technologies will continue to evolve and impact a wide range of industries in the years to come.

Enrico Gallo and Carlo Diaferia
Guest Editors

gels

Editorial

Editorial for Special Issue "Hydrogelated Matrices: Structural, Functional and Applicative Aspects"

Enrico Gallo [1,†] and Carlo Diaferia [2,*,†]

[1] IRCCS SYNLAB SDN, Via G. Ferraris 144, 80146 Naples, Italy; enrico.gallo@synlab.it
[2] Department of Pharmacy, University of Naples "Federico II", Via D. Montesano 49, 80131 Naples, Italy
* Correspondence: carlo.diaferia@unina.it
† These authors contributed equally to this work.

1. Introduction and Summary

Gel-based materials have found important applications in fields such as food, healthcare, cosmetics, and bioanalysis [1–4]. Meanwhile, advances in our understanding of the functional, structural, and manufacturing processes of gels are expanding their potential as tunable elements in fields including energy, soft robotics, water treatment, chemistry, and pharmaceutical sciences [5–8]. Recent advances have shown that gels can function as dynamic systems with programmable properties, making them highly adaptable to specific requirements across diverse disciplines. For instance, their responsiveness to external stimuli—such as temperature, pH, and light—has expanded their use in the design of smart materials [9–11].

Multiscale analyses and the development of supramolecular low-molecular-weight gelators, including peptide-based ones, have broadened the range of soft-gel materials [12,13]. Notably, peptide-based gels have garnered significant attention due to their biocompatibility and potential for sustainable applications, particularly in drug delivery and tissue engineering. The growing interest in gels is also reflected in the expanding variety of gelation-triggering techniques and methods, along with enhancements in rheological properties and shapability. This progress underscores the potential of gels to serve as foundational materials for next-generation technologies, ranging from biomedical devices to environmental remediation systems [14–16].

In this context, this Special Issue, entitled "Hydrogelated Matrices: Structural, Functional, and Applicative Aspects" in *Gels*, aims to bring together and report on these complementary aspects of gels, showcasing examples of both polymeric and peptide self-assembling gels. In addition to this Editorial, we are pleased to highlight that the Special Issue features 15 articles in total, reflecting researchers' interest in the properties, formulations, application scenarios, and characterization of gels. These contributions collectively underscore the growing recognition of gels as versatile and transformative materials across multiple scientific domains, paving the way for Vol II.

The following content provides a brief overview of the diverse topics explored in this Special Issue, highlighting the innovative approaches and breakthroughs in the study and application of gels. These articles exemplify the stimulating interdisciplinary approaches facilitated by gelated matrices.

2. Overview

Polyvinyl alcohol (PVA), poloxamer 407 (P407), and vinylcaprolactam (VCL) are among the synthetic polymers evaluated for gel formulation and applicability.

Gels **2025**, *11*, 146 https://doi.org/10.3390/gels11020146

The study by Quispe-Siccha et al. [17] focuses on the development and characterization of PVA capsule-shaped matrices. Two types of PVA, differing in molecular weight, were used as starting materials in a two-step process involving gel preparation and hydrogel cryogelation. Additionally, various PVA concentrations were evaluated. Biocompatibility (tested on the SUP-B15 cell line), porosity, cell proliferation profiles, and diffusion rates were analyzed and correlated with the controlled release of glucose, which was incorporated into the matrices through a post-formulation injection step. By varying both PVA concentration and molecular weight, Ramírez-Chavarría et al. [18] analyzed the physical–mechanical properties and dynamic models of hydrogel matrices with tissue-mimicking profiles. Notably, the photoacoustic response signal was found to influence the hydrogel features, demonstrating a linear relationship between energy absorption capacity, energy transfer, and PVA concentration. The damping ratio and natural frequency were also shown to correlate with both density and elasticity modulus, with progressively increasing values as PVA concentration rose. Overall, the results highlight the potential application of hydrogels as biomimetic platforms for tissue simulation and imaging.

Poloxamer 407 (P407) facilitates gelation in an in situ thermo-gelling approach. To improve the formulation's adhesiveness and gel strength, P407 was combined with hydroxypropyl methylcellulose to create a vehicle for the nasal drug delivery of chlorhexidine–silver nanoparticle conjugates, as reported by Ivanova et al. [19]. Key functional parameters, such as sprayability, mucosal retention time, washout time, drug release, and antimicrobial activity, were also studied.

Raduly et al. [20] found that Ag^0–ginger nanocomposites exhibit antimicrobial activity when physically incorporated into hydrogels composed of natural polymers to form gelled matrices. These nanocomposites were integrated into three types of matrices based on rice flour, alginate, and carob flour. The resulting materials were then deposited onto cotton fabrics, producing hydrophilic films with antimicrobial properties, highlighting their potential applications in the textile industry.

Voycheva et al. [21] proposed hydrogels functionalized with mesoporous silica nanoparticles for thermosensitive and pH-dependent drug delivery of doxorubicin. The grafted matrix was synthesized by combining vinylcaprolactam (VCL) and agar using a free radical polymerization approach. Drug delivery efficiency was evaluated under tumor-simulating conditions (40 °C and pH 4.0), achieving complete release within 72 h.

Peptide-based hydrogels constitute an innovative class of biomaterials with tunable properties and excellent biocompatibility, making them highly suitable for applications in biomedicine, tissue engineering, and drug delivery. These hydrogels are formed through the self-assembly of peptides into highly ordered nanostructures, driven by non-covalent interactions such as hydrogen bonding, π-π stacking, and hydrophobic forces. The resulting networks exhibit unique viscoelastic properties and can respond to external stimuli such as pH, temperature, and ionic strength, further enhancing their versatility. The design of peptide hydrogels often involves ultrashort peptides or peptide amphiphiles that capitalize on minimalistic sequences to achieve functional properties.

The study by Jitaru et al. [22] presents the design and characterization of a novel pentapeptide, FEYNF-NH_2, derived from the hen egg-white lysozyme sequence FESNF-NH_2. This peptide demonstrated its ability to self-assemble into β-sheet-driven dendritic structures under physiological conditions, while fluorescence analysis identified a quenching phenomenon at two peptide concentrations. Microscopic techniques, including POM and TEM, revealed the complex framework of the self-assembled structures, indicating their potential to form gel-like materials. In silico studies confirmed the β-sheet arrangements and further revealed non-covalent interactions between the FEYNF peptide's protonated dimer and the Drew–Dickerson dodecamer DNA sequence, a widely used model in structural biology. This finding underscores the peptide's potential for DNA recognition, linking peptide self-assembly with nucleic acid interactions.

Gallo et al. [23] broadened the scope of Fmoc-FF-based hydrogels by incorporating a lysine (K) residue at the C-terminus of the peptide sequence, introducing a functional amino group with potential for derivatization with bioactive molecules. The study investigated the properties of the Fmoc-FFK tripeptide both individually and in combination with Fmoc-FF at various weight ratios (1:1, 1:5, 1:10, 1:20 *w*/*w*). The Fmoc-FFK monomer exhibited self-assembly and gelation above a concentration of 1.0 wt%, forming a soft hydrogel ($G' = 24$ Pa). The incorporation of Fmoc-FFK into Fmoc-FF significantly improved the mechanical properties of the multicomponent hydrogels while preserving the structural organization and morphology of the pure Fmoc-FF hydrogel. Biocompatibility tests, conducted in vitro on HaCaT and 3T3-L1 cell lines, yielded favourable results for all proposed systems.

Buzzaccaro et al. [24] demonstrated the production of homogeneous and transparent gels using $(LDLK)_3$-based SAPs at concentrations ranging from 1 to 10 g/L, controlled via a urea–urease hydrolysis reaction. The method allows independent regulation of the final pH (via urea concentration) and gelation rate (via urease concentration). At high SAP concentrations, rigid gels are formed, which immobilize nanoparticles, while lower concentrations produce flexible gels with partial nanoparticle mobility. These adaptable morphologies are promising for multi-drug release, tissue regeneration, and 3D cell culture applications. The slow gelation process enhances scaffold reproducibility, enables the inclusion of chemotactic agents, and provides insights into gelation mechanisms through light scattering. The approach can be extended to other gelators, offering promising applications in biomaterials and regenerative medicine.

Natural polymers offer numerous advantages for hydrogel formation, making them valuable across biomedical, environmental, and industrial fields. Key benefits include biocompatibility and biodegradability, ensuring safe interaction with biological systems and eco-friendly degradation. Moreover, as they are derived from renewable resources, these polymers are sustainable and cost-effective.

The manuscript of Machado et al. [25] demonstrates that encapsulation in calcium–alginate-based hydrogel is an effective strategy for delivering Akkermansia muciniphila. The technique produced high-loaded capsules that maintained probiotic viability at ~10^8 CFU/g during 28 days of refrigerated aerobic storage. The encapsulating hydrogels exhibited greater viability and stability under in vitro gastrointestinal conditions compared to free cells, suggesting that the method mitigates the adverse effects of prolonged storage and subsequent gastrointestinal transit. Furthermore, the encapsulation ensured delivery levels exceeding the probiotic threshold (10^6 CFU/g) even after storage and gastrointestinal passage.

Loi et al. [26] developed linear polycaprolactone substrates with microchannels, where a fibrinogen-based hydrogel containing C2C12 cells was deposited to examine the impact of the co-printing technique on cellular behavior. They assessed cell viability and differentiation over a 21-day culture period, reporting significant enhancement of differentiation at 14 days. The study also evaluated the viability and differentiation of C2C12 myoblasts on distinct geometries, demonstrating that the linear pattern outperformed the others in promoting C2C12 myotube differentiation. After 14 days in culture, C2C12 cells in the linear structure fused to form aligned myotubes, particularly at the edges of the structure, with elevated expression levels of skeletal muscle markers such as MyoD.

Enache et al. [27] used sodium carboxymethyl cellulose (CMC) to create ionically cross-linked hydrogels in the form of magnetic beads by incorporating $MnFe_2O_4$ nanoparticles and SDS surfactant to enhance adsorption capacity and stability. The beads were characterized and evaluated for their adsorption properties. The adsorption followed the PFO model and Langmuir isotherm, indicating spontaneous, exothermic adsorption. The beads demonstrated 93% desorption efficiency and could be reused. Molecular docking revealed that the interaction between the beads and MB dye was electrostatic. These CMC-based hydrogels are promising sorbents for environmental applications due to their biocompatibility, high adsorption capacity, and recyclability.

The study conducted by Materni et al. [28] examined the preventive effect of the sunflower oil-based ozone gel Ozosan® on dry sockets through a double-blind, split-mouth, randomized placebo-controlled clinical trial involving 200 patients. The results indicated that Ozosan® effectively reduces the incidence of dry sockets, following the extraction of an inferior third molar. Furthermore, no adverse effects or noticeable differences in the post-extraction wound healing process were reported. This promising result in preventing alveolitis encourages further randomized studies on treating periodontitis and other inflammatory oral diseases.

A cross-linked gel polymer electrolyte (C-GPE) based on epoxidized soybean oil (ESO) was synthesized by Zhang et al. [29] using an in situ thermal polymerization with lithium bis(fluorosulfonyl)imide (LiFSI) as an initiator. The macroscopical organization of the cross-linked structure was found able to increase the ionic conductivity and ion mobility. The wide electrochemical window (of up to 5.19 V vs. Li^+/Li), along with high ionic conductivity, super-low glass transition temperature, and good interfacial electrodes/electrolyte stability, demonstrated the potential of these matrices in improving anode stability by adjusting the distribution of electrolyte on electrode surfaces in lithium gel polymer batteries.

The effect of pressurization and extraction from natural acorns was evaluated by Castro et al. [30] Significant structural and property changes, in terms of span distribution and uniformity, were detected in relation to amylose/amylopectin ratios. However, no substantial differences were found in parameters including gelatinization temperatures, relative crystallinity, and polymorphism. Acorn starch matrices also exhibited lower gelatinization temperatures, enthalpies, in vitro digestibility, superior pseudoplastic behavior, and lower resistance to deformation with respect to commercial starch, thus suggesting the potential for the acorn starches as a novel food ingredient.

The study of Kim et al. [31] focused on the development of a gel-based drug delivery system aimed at improving colon cancer treatment by incorporating 6-mercaptopurine (6-MP), an anticancer drug, into a thiolated gelatin/polyethylene glycol diacrylate matrix (6MP-GPGel). The system demonstrated a controlled, sustained release of 6-MP, with enhanced release rates in acidic or glutathione-rich environments simulating a tumor pH. In vitro results showed that while pure 6-MP allowed for cancer cell proliferation after five days, the 6MP-GPGel formulation effectively suppressed cell survival continuously. The study concludes that the 6MP-GPGel system offers a promising, minimally invasive, and localized drug delivery approach for colon cancer therapy, potentially improving treatment outcomes.

Author Contributions: C.D. and E.G.; conceptualization, supervision, methodology, writing-original draft preparation, writing—review and editing. All authors have read and agreed to the published version of the manuscript.

Funding: This research received no external funding.

Acknowledgments: The Guest Editor is very grateful to all the authors for their appreciated contributions to this Special Issue.

Conflicts of Interest: The authors declare no conflicts of interest.

References

1. Moench, S.A.; Lemke, P.; Weisser, J.; Stoev, I.D.; Rabe, K.S.; Domínguez, C.M.; Niemeyer, C.M. Quantitative Characterization of RCA-Based DNA Hydrogels—Towards Rational Materials Design. *Chem. Eur. J.* **2024**, *30*, e202401788. [CrossRef] [PubMed]
2. Di Gregorio, E.; Rosa, E.; Ferrauto, G.; Diaferia, C.; Gallo, E.; Accardo, A.; Terreno, E. Development of cationic peptide-based hydrogels loaded with iopamidol for CEST-MRI detection. *J. Mater. Chem. B* **2023**, *11*, 7435–7441. [CrossRef] [PubMed]
3. Aswathy, S.H.; Narendrakumar, U.; Manjubala, I. Commercial hydrogels for biomedical applications. *Heliyon* **2020**, *6*, e03719. [CrossRef]
4. Ghosh, S.; Sepay, N.; Banerji, B. Crystal to Hydrogel Transformation in S-Benzyl-L-Cysteine-Containing Cyclic Dipeptides—Nanostructure Elucidation and Applications. *Chem. Eur. J.* **2024**, *30*, e202401874. [CrossRef]
5. Rosa, E.; Diaferia, C.; Gianolio, E.; Sibillano, T.; Gallo, E.; Smaldone, G.; Stornaiuolo, M.; Giannini, C.; Morelli, G.; Accardo, A. Multicomponent Hydrogel Matrices of Fmoc-FF and Cationic Peptides for Application in Tissue Engineering. *Macromol. Biosci.* **2022**, *22*, 2200128. [CrossRef] [PubMed]
6. López-Díaz, A.; Vázquez, A.S.; Vázquez, E. Hydrogels in Soft Robotics: Past, Present, and Future. *ACS Nano* **2024**, *18*, 20817–20826. [CrossRef] [PubMed]
7. Das, B.K.; Samanta, R.; Ahmed, S.; Pramanik, B. Cover Feature: Disulphide Cross-Linked Ultrashort Peptide Hydrogelator for Water Remediation. *Chem. Eur. J.* **2023**, *29*, e202301626. [CrossRef]
8. Liu, X.; Luo, Y.; Xu, F.; Wu, X.; Liu, D.; Wang, B. Design and characterization of high-performance energetic hydrogels with enhanced mechanical and explosive properties. *Sci. Rep.* **2024**, *14*, 30104. [CrossRef] [PubMed]
9. Neumann, M.; di Marco, G.; Iudin, D.; Viola, M.; van Nostrum, C.F.; van Ravensteijn, B.G.P.; Vermonden, T. Stimuli-Responsive Hydrogels: The Dynamic Smart Biomaterials of Tomorrow. *Macromolecules* **2023**, *56*, 8377–8392. [CrossRef]
10. Diaferia, C.; Rosa, E.; Gallo, E.; Smaldone, G.; Stornaiuolo, M.; Morelli, G.; Accardo, A. Self-supporting hydrogels based on fmoc-derivatized cationic hexapeptides for potential biomedical applications. *Biomedicine* **2021**, *6*, 678. [CrossRef]
11. Chen, Q.; Wu, S. Stimuli-Responsive Polymers for Tubal Actuators. *Chem. Eur. J.* **2025**, *31*, e202403429. [CrossRef]
12. Dasgupta, A.; Mondal, J.H.; Debapratim, D. Peptide hydrogels. *RSC Adv.* **2013**, *3*, 9117–9149. [CrossRef]
13. Rosa, E.; Gallo, E.; Sibillano, T.; Giannini, C.; Rizzuti, S.; Gianolio, E.; Scognamiglio, P.L.; Morelli, G.; Accardo, A.; Diaferia, C. Incorporation of PEG Diacrylates (PEGDA) Generates Hybrid Fmoc-FF Hydrogel Matrices. *Gels* **2022**, *8*, 831. [CrossRef]
14. Ginesi, R.E.; Murray, N.R.; Dalgliesh, R.M.; Doutch, J.; Draper, E.R. Using Solution History to Control Hydrogel Properties of a Perylene Bisimide. *Chem. Eur. J.* **2023**, *27*, e202301042. [CrossRef]
15. Rosa, E.; Di Gregorio, E.; Ferrauto, G.; Diaferia, C.; Gallo, E.; Terreno, E.; Accardo, A. Hybrid PNA-peptide hydrogels as injectable CEST-MRI agents. *J. Mater. Chem. B* **2024**, *12*, 6371–6383. [CrossRef]
16. Giuri, D.; D'Agostino, D.; Ravarino, P.; Faccio, D.; Falini, G.; Tomasini, C. Water Remediation from Pollutant Agents by the Use of an Environmentally Friendly Supramolecular Hydrogel. *ChemNanoMat* **2022**, *8*, e202200093. [CrossRef]
17. Quispe-Siccha, R.; Medina-Sandoval, O.; Estrada-Tinoco, A.; Pedroza-Pérez, J.; Martínez-Tovar, A.; Olarte-Carrillo, I.; Cerón-Maldonado, R.; Reding-Bernal, A.; López-Alvarenga, J. Development of Polyvinyl Alcohol Hydrogels for Controlled Glucose Release in Biomedical Applications. *Gels* **2024**, *10*, 668. [CrossRef] [PubMed]
18. Ramírez-Chavarría, R.; Pérez-Pacheco, A.; Terán, E.; Quispe-Siccha, R. Study of Polyvinyl Alcohol Hydrogels Applying Physical-Mechanical Methods and Dynamic Models of Photoacoustic Signals. *Gels* **2023**, *9*, 727. [CrossRef] [PubMed]
19. Ivanova, N.; Ermenlieva, N.; Simeonova, L.; Vilhelmova-Ilieva, N.; Bratoeva, K.; Stoyanov, G.; Andonova, V. In Situ Gelling Behavior and Biopharmaceutical Characterization of Nano-Silver-Loaded Poloxamer Matrices Designed for Nasal Drug Delivery. *Gels* **2024**, *10*, 385. [CrossRef] [PubMed]
20. Raduly, F.; Raditoiu, V.; Raditoiu, A.; Grapin, M.; Constantin, M.; Răut, I.; Nicolae, C.; Frone, A. Ag0–Ginger Nanocomposites Integrated into Natural Hydrogelated Matrices Used as Antimicrobial Delivery Systems Deposited on Cellulose Fabrics. *Gels* **2024**, *10*, 106. [CrossRef] [PubMed]
21. Voycheva, C.; Slavkova, M.; Popova, T.; Tzankova, D.; Stefanova, D.; Tzankova, V.; Ivanova, I.; Tzankov, S.; Spassova, I.; Kovacheva, D.; et al. Thermosensitive Hydrogel-Functionalized Mesoporous Silica Nanoparticles for Parenteral Application of Chemotherapeutics. *Gels* **2023**, *9*, 769. [CrossRef] [PubMed]
22. Jitaru, S.; Enache, A.; Cojocaru, C.; Drochioiu, G.; Petre, B.; Gradinaru, V. Self-Assembly of a Novel Pentapeptide into Hydrogelated Dendritic Architecture: Synthesis, Properties, Molecular Docking and Prospective Applications. *Gels* **2024**, *10*, 86. [CrossRef]
23. Gallo, E.; Diaferia, C.; Giordano, S.; Rosa, E.; Carrese, B.; Piccialli, G.; Borbone, N.; Morelli, G.; Oliviero, G.; Accardo, A. Ultrashort Cationic Peptide Fmoc-FFK as Hydrogel Building Block for Potential Biomedical Applications. *Gels* **2024**, *10*, 12. [CrossRef] [PubMed]
24. Buzzaccaro, S.; Ruzzi, V.; Gelain, F.; Piazza, R. A Light Scattering Investigation of Enzymatic Gelation in Self-Assembling Peptides. *Gels* **2023**, *9*, 347. [CrossRef]

25. Machado, D.; Fonseca, M.; Vedor, R.; Sousa, S.; Barbosa, J.; Gomes, A. Akkermansia muciniphila Encapsulated in Calcium-Alginate Hydrogelated Matrix: Viability and Stability over Aerobic Storage and Simulated Gastrointestinal Conditions. *Gels* **2023**, *9*, 869. [CrossRef]
26. Loi, G.; Scocozza, F.; Aliberti, F.; Rinvenuto, L.; Cidonio, G.; Marchesi, N.; Benedetti, L.; Ceccarelli, G.; Conti, M. 3D Co-Printing and Substrate Geometry Influence the Differentiation of C2C12 Skeletal Myoblasts. *Gels* **2023**, *9*, 595. [CrossRef] [PubMed]
27. Enache, A.; Grecu, I.; Samoila, P.; Cojocaru, C.; Harabagiu, V. Magnetic Ionotropic Hydrogels Based on Carboxymethyl Cellulose for Aqueous Pollution Mitigation. *Gels* **2023**, *9*, 358. [CrossRef] [PubMed]
28. Materni, A.; Pasquale, C.; Longo, E.; Frosecchi, M.; Benedicenti, S.; Bozzo, M.; Amaroli, A. Prevention of Dry Socket with Ozone Oil-Based Gel after Inferior Third Molar Extraction: A Double-Blind Split-Mouth Randomized Placebo-Controlled Clinical Trial. *Gels* **2023**, *9*, 289. [CrossRef] [PubMed]
29. Zhang, W.; Bae, W.; Jin, L.; Park, S.; Jeon, M.; Kim, W.; Jang, H. Cross-Linked Gel Polymer Electrolyte Based on Multiple Epoxy Groups Enabling Conductivity and High Performance of Li-Ion Batteries. *Gels* **2023**, *9*, 384. [CrossRef]
30. Castro, L.; Caço, A.; Pereira, C.; Sousa, S.; Brassesco, M.; Machado, M.; Ramos, Ó.; Alexandre, E.; Saraiva, J.; Pintado, M. Modification of Acorn Starch Structure and Properties by High Hydrostatic Pressure. *Gels* **2023**, *9*, 757. [CrossRef]
31. Kim, S.; Lee, W.; Park, H.; Kim, K. Tumor Microenvironment-Responsive 6-Mercaptopurine-Releasing Injectable Hydrogel for Colon Cancer Treatment. *Gels* **2023**, *9*, 319. [CrossRef] [PubMed]

gels

Article

Prevention of Dry Socket with Ozone Oil-Based Gel after Inferior Third Molar Extraction: A Double-Blind Split-Mouth Randomized Placebo-Controlled Clinical Trial

Alberto Materni [1,†], Claudio Pasquale [1,2,*,†], Eugenio Longo [1], Massimo Frosecchi [1], Stefano Benedicenti [1], Matteo Bozzo [3] and Andrea Amaroli [3,*]

[1] Department of Surgical and Diagnostic Sciences (DISC), University of Genoa, 16132 Genoa, Italy
[2] Department of Civil, Chemical and Environmental Engineering (DICCA), University of Genoa, 16100 Genoa, Italy
[3] Department of Earth, Environmental and Life Sciences (DISTAV), University of Genoa, 16132 Genoa, Italy
* Correspondence: clodent@gmail.com (C.P.); andrea.amaroli@unige.it (A.A.)
† These authors contributed to the manuscript equally.

Abstract: Tooth extraction is followed by a sequence of elaborate local changes affecting hard and soft tissues. Dry socket (DS) can occur as intense pain around and in the extraction site, with an incidence from 1–4% after generic tooth extraction to 45% for mandibular third molars. Ozone therapy has gained attention in the medical field because of its success in the treatment of various diseases, its biocompatible properties and its fewer side effects or discomfort than drugs. To investigate the preventive effect of the sunflower oil-based ozone gel Ozosan® (Sanipan srl, Clivio (VA), Italy) on DS, a double-blind split-mouth randomized placebo-controlled clinical trial was conducted according to the CONSORT guidelines. Ozosan® or the placebo gel were put in the socket, and the gels were washed off 2 min later. In total, 200 patients were included in our study. The patient population comprised 87 Caucasian males and 113 Caucasian females. The mean age of the included patients was 33.1 ± 12.4 years. Ozosan reduced the incidence of DS after inferior third molar extraction from 21.5% of the control to 2% ($p < 0.001$). Concerning the dry socket epidemiology, the incidence was not significantly correlated with gender, smoking or mesioangular, vertical or distoangular Winter's classification. Post hoc power calculation showed a power of 99.8% for this data, with alpha = 0.001.

Keywords: alveolar osteitis; alveolar periostitis; alveolar periostitides; alveolus; dental; wisdom tooth; mucositis; third molar; oral disease

1. Introduction

Tooth extraction is one of the main procedures for oral health management. However, despite being a routine surgical practice, its consequences have not always been accurately assessed. Tooth extraction induces a sequence of elaborate local changes affecting hard and soft tissues, and the healing of the extraction socket can, therefore, show complications that reduce the patient's quality of life. One possible complication is a dry socket (DS), a postoperative problem also referred to as alveolar osteitis, fibrinolytic alveolitis, septic socket, localized osteomyelitis or necrotic socket [1]. A DS manifests as intense pain around and in the extraction site, 1 to 3 days after tooth extraction. Its incidence depends on the tooth extracted, with an overall incidence of 1–4% after extraction, but a 10-fold higher incidence for lower teeth than for upper teeth, and an incidence of 45% for mandibular third molars [1,2].

A considerable number of aetiological factors such as dislodgement of the clot, oral micro-organisms, trauma during surgery, anaesthesia, drugs (oral contraceptives), smoking, age and gender appear to influence DS although a multifactorial origin is likely [3,4].

Because of the inconsistent identification of the main causative variables of DS, there is no consensus on the best prophylactic management for this disorder. The literature suggests the identification of risk factors associated with prevention, and both non-pharmacological and pharmacological measures can support DS aetiology and recovery [2,3,5,6].

However, despite the advice for DS prevention, including procedural details and surgical skills, no single method has achieved universal success or acceptance [2].

Past and recent reviews [2,3] have described the therapeutic interventions currently used in DS management, which can include antibacterial, antiseptic, antifibrinolytic and clot support agents, lavages and obtundent dressings. Management is generally directed primarily towards timely relief of the patient's pain during the healing process through palliative means (antibacterial or obtundent dressings, topical anaesthetic or combinations of these) [2,7,8].

Ozonated compounds have been employed in industries and have recently gained attention in the literature for clinical applications [9,10]. Indeed, ozone therapy has gained attention in the medical field because of its success in the treatment of various diseases, its biocompatible properties and its fewer side effects or discomfort than drugs [11]. In particular, its immunomodulation, analgesic, antihypnotic, detoxifying, antimicrobial, bioenergetic and biosynthetic properties could support many dentistry challenges [12].

It is worth noting that Scribante et al. [13] have recently highlighted the significance of tailoring minimally invasive protocols to manage the oral microbiota, clinically and microbiologically, with ozone playing a crucial role among other approaches. This can help integrate bacterial load, increase the proportion of commensal bacteria, prevent the resetting of the oral microbiota and avoid the use of chemical pharmacological substances.

The subject of ozone and its uses in medicine is still a surprising and controversial topic of discussion [14].

As reviewed by Saini [12], ozone therapy can be applied in three fundamental forms: ozonated water, ozonated olive oil in natural and gel formulations and oxygen/ozone gas. Although the properties of ozone may be similar in the different formulations, the gas's stability, release and effect vary with variations in the product's gaseous, aqueous, oily or gel condition [9]. Indeed, gaseous ozone can be toxic and unstable, and ozonated water decomposes more rapidly than gels [9,15,16]. Therefore, ozone in the form of an oil-based gel may be significantly more stable when in contact with the target surface for a more extended period [17].

Recently, a novel sunflower oil-based ozone gel (Ozosan®—Sanipan srl, Clivio (VA), Italy) showed the efficacy of ozone in the healing of osteoradionecrosis of the jaws [15] and as a dentin primer, to improve the microtensile bond strength and endogenous enzymatic activity of two adhesive systems [18].

In the current study, we investigated the preventive effect of this oil-based ozone gel on DS in a double-blind split-mouth randomized placebo-controlled clinical trial conducted according to the CONSORT guidelines.

The predictor variable was the property of ozone in the sunflower oil-based gel formula [12,14,17]. The primary endpoint was the reduction in DS incidence after an inferior third molar extraction. The secondary endpoint was the adverse effects of ozone.

2. Results

2.1. Patient and Baseline Characteristics

More than 200 patients (Figure 1) with two impacted lower third molars were assessed and treated. Eight patients were excluded due to the failure of the first procedure, which was followed by discomfort and infection risks as a consequence of the trapping of food by the gels.

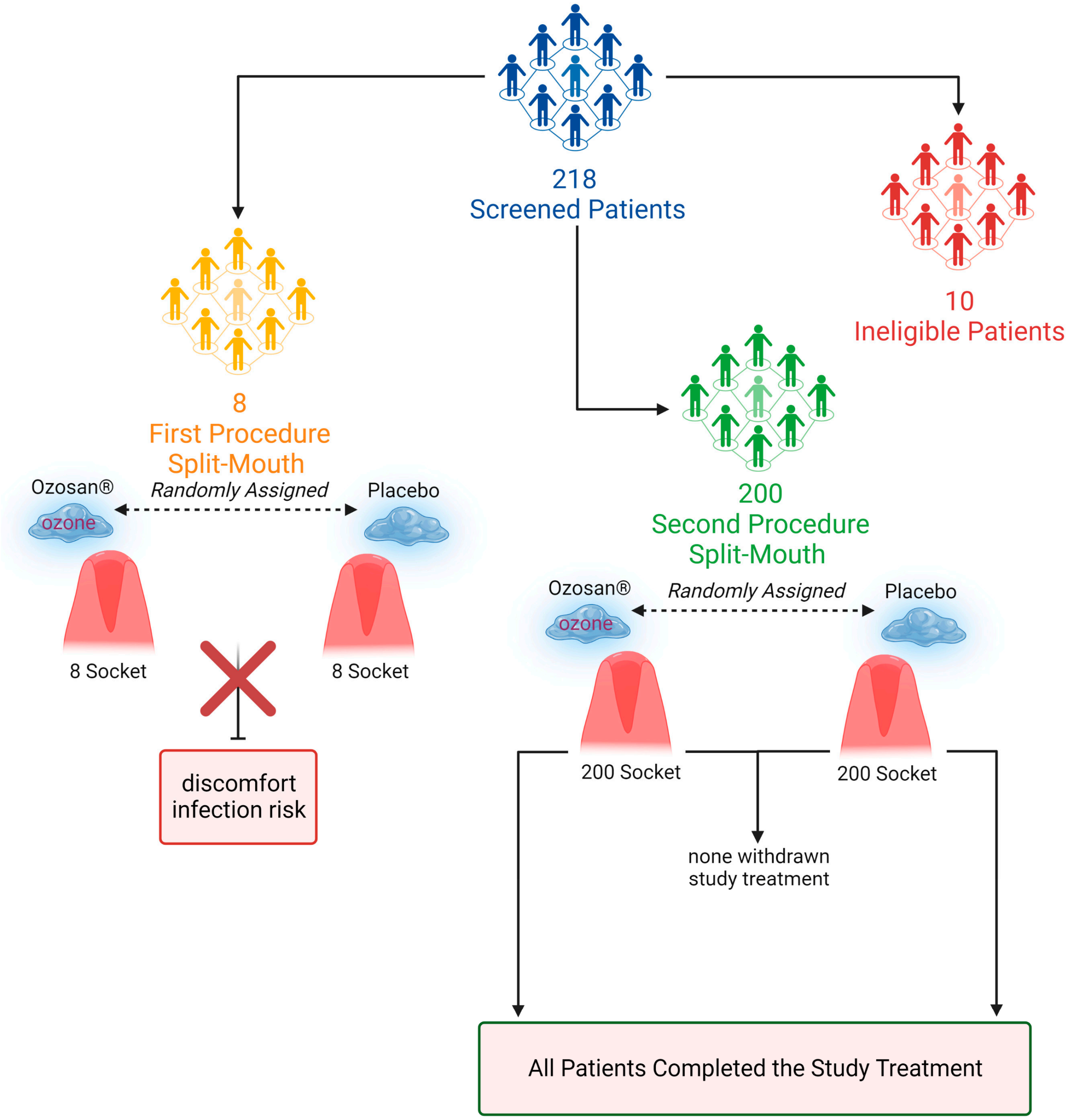

Figure 1. Design of experimental set-up according to CONSORT guidelines.

The 200 remaining patients received the second procedure and were followed to monitor the occurrence of DS and the side effects of ozone.

As shown in Table 1, the patient population comprised 87 Caucasian males and 113 Caucasian females. The mean age of the included patients was 33.1 ± 12.4 years (range: from 18 to 65 years). Partial inclusion of the third molar was observed in 72% of patients, while 28% showed total inclusion. Osteotomy and odontotomy were performed in all patients (100%). According to Winter's classification of impacted third molars, 42% of patients were classified as Mesio (M), 45% as Vertical (V) and 13% as Distally (D) tilted. Of the 200 patients, 36.6% smoked cigarettes.

Table 1. Baseline characteristics of the treated population.

Patients' Age	**(Mean ± Standard Deviation (Min-Max))**			
	33.1 ± 12.4 (18–64)			
Patients' gender	Male	Female		
	87	113		
Smoker	Yes	No		
	36.60%	63.40%		
Winter classification of the third molar	Vertical	Mesioangular	Distoangular	Horizontal
	45%	42%	13%	0%

Patient recruitment and follow-up were completed between June 2021 and October 2022.

2.2. *Effect of Ozonated Gel on Dry Socket Incidence*

A dry socket occurred in four patients in the Ozosan group and in 43 patients in the placebo group (Table 2). The incidence percentage of dry socket was 2% and 21.5%, respectively. Chi-square analysis revealed a highly significant difference ($p < 0.001$) between the Ozosan and placebo treatments regarding the occurrence of DS (Table 2).

Table 2. The table displays the number of diagnosed dry sockets after treatment with ozone in the form of sunflower oil-based gel (Ozosan) or placebo gel. The incidence percentage of dry sockets was calculated with respect to 200 inferior third molars extracted per treatment. The * symbol denotes a statistically significant difference ($p < 0.05$) between the two treatments, as calculated using the chi-square test.

Dry Sockets Diagnosis	**Ozosan**	**Placebo**
Presence of dry socket (number)	4	43
Absence of dry socket (number)	196	157
% of diagnosed dry sockets	2% *	21.5% *

The post hoc power calculation showed a power of 99.8% for our data, with alpha= 0.001. No bilateral alveolar osteitis was described and complete healing of the wound was observed on both sides of the mouth (Test and Placebo side), involving complete soft tissue wound closure with correct repair/neoformation of the attached gingiva and oral mucosa. Dry socket occurred in two males and two females in the Ozosan group and in 17 males and 26 females in the placebo group. No significant differences ($p > 0.05$) were observed in relation to gender in the Ozosan vs placebo treatment (Table 3). Inferior third inferior molar inclusion Winter's Classification (Table 4) and smoking (Table 5) were not correlated with the DS emergence ($p > 0.05$).

Table 3. The table displays the number of diagnosed dry sockets in female or male patients after treatment with ozone in the form of sunflower oil-based gel (Ozosan) or placebo gel. The incidence percentage of dry sockets was calculated with respect to the number of female patients (113) or male patients (87) with third molars extracted. The * symbol denotes a statistically significant difference ($p < 0.05$) between the two treatments, as calculated using the chi-square test.

Treatment with Ozone in the Form of Sunflower Oil-Based Gel (Ozosan)		
	Males	Females
Presence of dry socket (number)	2	2
Absence of dry socket (number)	85	111
% of diagnosed dry sockets	2.30%	1.80%

Table 3. *Cont.*

Treatment with Ozone in the Form of Sunflower Oil-Based Gel (Ozosan)		
Treatment with placebo gel		
	Males	Females
Presence of dry socket (number)	17	26
Absence of dry socket (number)	70	87
% of diagnosed dry sockets	19.50%	23.00%

Table 4. The table displays the number of diagnosed dry sockets with respect to the third molar Winter's Classification after treatment with ozone in the form of sunflower-oil-based gel (Ozosan) or placebo gel. The incidence percentage of dry sockets was calculated with respect to the number of mesioangular (84), vertical (88) or distoangular (28) classified third molars. The * symbol denotes a statistically significant difference ($p < 0.05$) between the two treatments, as calculated using the chi-square test.

Treatment with Ozone in the Form of Sunflower Oil-Based Gel (Ozosan)			
	Mesioangular	Vertical	Distoangular
Presence of dry socket (number)	2	1	1
Absence of dry socket (number)	82	87	27
% of diagnosed dry sockets	2.40%	1.10%	3.60%
Treatment with placebo gel			
	Mesioangular	Vertical	Distoangular
Presence of dry socket (number)	21	14	8
Absence of dry socket (number)	63	74	20
% of diagnosed dry sockets	25.00%	15.90%	28.60%

Table 5. The table displays the number of diagnosed dry sockets in smoker and non-smoker patients after treatment with ozone in the form of sunflower-oil-based gel (Ozosan) or placebo gel. The incidence percentage of dry sockets was calculated with respect to the number of female patients (113) or male patients (87) with third molars extracted. The * symbol denotes a statistically significant difference between the two treatments, as calculated using the chi-square test.

Treatment with Ozone in the Form of Sunflower-Oil-Based Gel (Ozosan)		
	Smokers	Non-Smokers
Presence of dry socket (number)	2	2
Absence of dry socket (number)	71	125
% of diagnosed dry sockets	2.70%	1.60%
Treatment with placebo gel		
	Males	Females
Presence of dry socket (number)	20	23
Absence of dry socket (number)	53	104
% of diagnosed dry sockets	27.40%	18.10%

2.3. Amount of Peroxide in Ozosan® Gel and Release

According to the UNI EN ISO 3960:2017 standards, the percentage of Ozosan's ozone release over time was evaluated. The total amount of peroxide in the gel was found to be 1320 meqO2/Kg (100%), which meets with the manufacturer's instructions. The time- and temperature-dependent release expressed in percentage is shown in Figure 2. Essentially, the % of oxidizing residues in the gel was, 100% (0 min), 91.10% (1 min), 80.10% (2 min), 67.70% (3 min); 60.70% (4 min), 43,70% (5 min), 33.50% (6 min), 18.20% (7 min), 11.40% (8 min), 8.70% (9 min), 3.50% (10 min), 1.6% (11 min), <1.5% 12 min. It is worth noting that, in our study, at the same 2 min exposure time, less than 20% of the peroxide had been released. These results highlight the significant difference in peroxide release between the 2 min exposure time and the 10 min exposure time. The lesser exposure time resulted in a lower peroxide release percentage, which could have important implications for the role and cellular responses to Ozosan in certain applications.

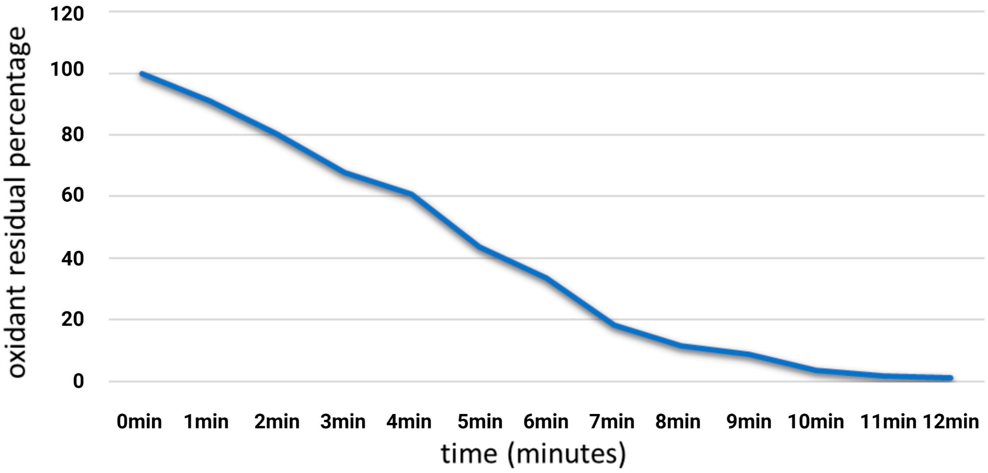

Figure 2. Percentage of Ozosan's ozone release over time. According to the UNI EN ISO 3960:2017 standards, the total amount of peroxide in the gel was evaluated at 1322.4 meqO2/Kg (100%). The time-temperature-dependent release expressed in % indicates that after 10 min, about 97% of the initial peroxide had been released. Of note, at the same 2 min exposure time employed in our study, less than 20% of the peroxide had been released.

3. Discussion

Epidemiological studies have revealed several contradictory risk factors in the development of post-extraction alveolitis: surgical trauma as a consequence of the difficulty in extraction and/or inexperience of the surgeon, inadequate intraoperative irrigation, use of oral contraceptives and/or immunosuppression, advanced age, female sex and smoking. However, the true causes of the condition are not known [2,7,19–21].

Our data showed a dry socket prevalence of 21.5%, consistent with its more frequent occurrence following inferior third molar extraction [2,19]. This incidence was lower than the 35–45% reported in the literature [1,7,8] but consistent with the data of Kaur et al. [20] from 150 patients.

While DS epidemiology was not prominent in our study, its incidence was not significantly correlated with gender, smoking or mesioangular, vertical or distoangular Winter's classification. As discussed by Pattanaik et al. [11] and Parthasarathi et al. [22], the smoking data were supported by recent research showing that smoking has no effect on the incidence of alveolar osteitis, particularly when the results were analyzed in a multivariate fashion [21]. The lack of any gender correlation is also consistent with Parthasarathi et al. [22], who found no difference in the incidence of alveolar osteitis between males and females, and no influence of the Winter classification, which can be attributed to the long-standing experience of the surgeons [23].

Conversely, the ozone in the sunflower oil-based gel formula (Ozosan) significantly reduced the occurrence of DS on the treated side of the mouth. Our double-blind split-mouth randomized placebo-controlled clinical trial showed a DS incidence after a third inferior molar extraction of 2% on the Ozosan-treated side and a more than tenfold higher incidence on the placebo side. Comparison with the results obtained by Haraji et al. [24] and Kaur et al. [20] when using chlorhexidine and a similar experimental setup (80 and 150 patients, respectively) revealed the significantly more efficient effect of Ozosan ($p < 0.05$); no significant differences were detected among the corresponding placebo groups. The use of chlorhexidine can result in discomforts such as mucosal irritation, altered taste sensation, tooth staining and possible impairment of wound healing, which have discouraged prolonged treatment for the irrigation of oral mucosa or the periodontal pockets [25,26]. Conversely, ozonated compounds show higher biocompatibility [27]. The evidence-based literature shows the undisputed disinfection power of ozone, which, at a concentration of 4 mg/L in water, effectively killed gram-positive and gram-negative oral bacteria and fungi [28]. However, according to the time-dependent release of ozone from the Ozosan gel shown in our results, a correlation between antimicrobial ozone properties and DS was only apparent following the first (aborted) procedure, which involved longer application times and, therefore, a higher gas release. Indeed, 10 min is required to release almost the entire amount of gas and induce a bactericidal effect. Conversely, after 2 min, less than 20% had been released. The few minutes of Ozosan application in the second (reliable) procedure was probably not sufficient to disinfect the surgery-impacted area. However, the results suggest a stimulating low-ozone-dose effect on tissues. Indeed, gases such as reactive oxygen species (ROS) and nitric oxide (NO) drastically improved healing recovery [29,30], and novel biomaterials that are able to release these gases have been developed [31,32].

Recently, Viebahn-Haensler and León Fernández [33] reviewed the low-dose ozone theory and its mechanisms of action on diseases. Essentially, they described the bioregulatory role of low-dose ozone in chronic inflammatory diseases and its direct mechanism of action in topical treatments via radical reactions.

Previous studies on stomatological challenges [34] have described the efficacy of ozonated compounds on osteoradionecrosis of the jaws [17], anti-inflammatory effects [35], and post-surgical pain [36,37], as well as ozonated water, which appeared to be effective adjuvant treatment to scaling and root planning for periodontal disease [13]. Based on the excellent clinical responses of several diseases and pain to ozone, the biological activity of this gas would be properly mediated by modulated responses to mild oxidative stress induced after its application [14]. Thus, as suggested by Re [14], according to the ancestral environment of our cells and its strictly metabolic binding to oxygen burn, the ubiquitous signalling pathway mediated by NF-E2–related factor 2 (Nrf2) could play a role in the low-dose ozone-mediated effects. Indeed, the Nrf2 pathway acts in the defence against oxidative stress, carcinogenesis, anti-inflammation, stem cell regulation, anti-ageing, protection against brain and skin injuries and so forth [38]. Overall, our data seem to suggest a lower prevalence of DS following Ozosan treatment, which may indicate the preventive effect of ozone on the signalling pathways that lead to osteoblast apoptosis, inflammation and tissue necrosis, factors that, as reported by Mamoun [8], appear strictly correlated with DS incidence.

4. Conclusions

In conclusion, our double-blind split-mouth randomized placebo-controlled clinical trial supported our primary and secondary endpoint. Indeed, Ozosan reduces the incidence of DS after an inferior third molar extraction. Additionally, no side effects or macroscopic differences in post-extraction wound recovery were observed. Focused in vitro and in vivo studies on the effect of Ozosan on the regeneration of tissues will be necessary to clarify the possibility of combining DS prevention with more rapid recovery from surgery. This promising preventive result on alveolitis paves the way for further randomized studies on the treatment of periodontitis and inflammatory oral diseases.

5. Materials and Methods

5.1. Study Design and Participants

Our double-blind split-mouth randomized placebo-controlled clinical trial followed the CONSORT guidelines (Figures 1 and S1) and was approved by the University of Genoa, Department of Surgical Sciences and Integrated Diagnostics (DISC) Ethics Committee (decision number: document No. 2021/55 of the University Research Ethics Committee). The study was conducted in accordance with the Declaration of Helsinki, Good Clinical Practice guidelines of 1975, as revised in 2013, and applicable local laws. The procedures were explained to participants who signed a consent form.

Eligible patients were females or males who required bilateral extraction of mandibular third molars. Patients were excluded if they presented acute swelling, infections, diabetes, cancer, genetic immunodeficiency, angiogenic disorders or any neurological or psychological diseases, and if they had taken anti-inflammatory, antibiotic, bisphosphonate, analgesics and/or blood pressure or angiogenic medications 3 months before enrolment. Pregnant and lactating women were also excluded. A full medical history of each subject was obtained, and a thorough oral examination was undertaken before participation in the study.

5.2. Randomization and Masking

Each patient's right and left inferior third molars were randomly allocated (1:1) to be treated with either novel sunflower oil-based ozone gel (Ozosan®, Sanipan srl, Clivio (VA), Italy) (O group) or placebo gel (P group). Randomization was based on a random–sequence software program (www.random.org/sequences (accessed on 20 February 2023)), which generates randomized sequences. The molar was added to the O group if it received an odd number, and to the P group if it received an even number.

5.3. Operative Technique

A traditional envelope flap approach was performed [39–41]. This classical technique consists of a first distal incision starting from the 2M distal surface in the attached gingiva and moving distobuccally 45° for around 10 mm. Then a second incision is made perpendicularly to the first incision around 3 or 4 mm distally from the 2M, directed towards the 2M buccal sulcus, going through it and finishing in the buccal papilla between the second and first molars. A triangle of soft tissue is defined just distal to the 2M, which is eliminated with a mini-Friedmann 90° rongeur (RMF90 rongeur Friedmann 90°, small cod RMF90, Hu-Friedy Mfg. Co., Chicago, IL, USA). A full-thickness flap is elevated using a Prichard periosteal elevator (3 Prichard periosteal PPR36, Hu-Friedy Mfg. Co., Chicago, IL, USA) exposing the buccal and the occlusal bone in the case of fully impacted teeth to the oblique mandibular line. The flap is protected on the buccal side with an 11 × 40 mm Langenbeck metal retractor (Stoma Dentalsysteme Dentalsysteme GmbH & Co KG, Emmingen-Liptingen, Germany). A buccal ostectomy is performed using a surgical steel bur (Komet H31LR316 016, Komet Dental Gebr. Brasseler GmbH & Co., Lemgo, Germany) in a 45° angle surgical hand-piece with a cooling water port and no air spray (NSK TI-MAX 45° Stand-Titan, NSK Dental, Kanuma, Japan). An odontotomy is made in order to extract the tooth more efficiently using a surgical hart-metal bur (Komet H31LR316 016, Komet Dental Gebr. Brasseler GmbH & Co., Lemgo, Germany) in a 45° angle surgical handpiece with a cooling water port and no air spray (NSK TI-MAX 45° Stand-Titan, NSK Dental, Kanuma, Japan). The tooth is extracted in sections to avoid a wider ostectomy. Friedman elevators 31F, 32F and 3C are used to assist extraction (Hu-Friedy Mfg. Co., Chicago, IL, USA). The extraction site is evaluated using a 3 mm Lucas bone curette, which is kept superficial to avoid any accidental damage to the inferior alveolar nerves. Care is taken to avoid placing the instrument too deeply into the apical portion of the alveolus. The surgical procedure concludes with the placement of a monofilament synthetic absorbable poliglecaprone 4/0 USP surgical PGCL suture, using a 16 mm 3/8 OMNIA reverse cutting needle (OMNIA S.p.A., Fidenza, Italy). This helps to maintain the flap in its original position, without tension, and to create a triangular open communication distal to the 2M for an open healing process. A knot is tied to hold the flap distal to the 2M in an apical position, and usually, two additional knots are tied to close the distal incision.

5.4. Ozone Gel or Placebo Treatment

To test the effect of ozone gel on the occurrence of DS, the Ozosan® Gel was employed. According to the manufacturer's description, the gel has a sunflower oil base that has undergone ozone saturation treatment and been gelled; the cold gel (5 °C) formulation prevents rapid ozone migration towards the surface. As the temperature of the gel increases due to body temperature, the capacity of the gel to hold the ozone molecules vanishes, thus generating their rapid dispersion in the air [17] (https://bioactiva.it/prodotti/ (accessed on 20 February 2023)). The placebo gel was a similar-looking sunflower oil without ozone. Therefore, the patients and study team members responsible for the administration of the treatment were masked in treatment allocation. The Ozosan and placebo gels were inserted in the socket before suturing. One millilitre of gel was necessary to fill the socket.

In the first round of procedures, the gels were left in the socket and suturing was performed. However, patients experienced discomfort (see results section) and the procedure was subsequently modified, such that the gels were added to the socket as described above, but then washed away after 2 min, before suturing (there was no gel in the socket after suturing). Two experienced clinicians, who were not involved in the surgery or treatment administration, assessed the outcomes and showed 100% intra-examiner agreement for all DS diagnosis criteria, following the advice given by Rakhshan et al. [4]. Calibration was performed before the study following an independent assessment of the experimental purposes. Patients were consulted daily and monitored for the first week post-extraction and at 8 weeks in order to evaluate the resolution of the soft tissue wound. The two examiners were blinded to the two experimental groups. The investigator responsible for statistical data analysis was also masked to treatment assignment. An anonymously numbered questionnaire was used to gather patients' screening information.

5.5. Outcomes

In accordance with the literature [12,14,17], the predictor variable was the property of ozone in the oil-based gel formula. The primary endpoint was the reduction of DS incidence after an inferior third molar extraction. The secondary endpoint was the adverse effects of ozone.

5.6. Determination of Peroxide Values in Ozosan® Gel

The peroxide amount was evaluated through iodometric determination in accordance with the UNI EN ISO 3960:2017 standards [42] and according to the classical procedure described by Radzimierska-Kaźmierczak et al. [43], modified. The release was evaluated to mimic the experimental conditions for 12 min. The release of peroxide was determined and expressed in milliequivalents of active oxygen per kilogram of gel, (methods error: ±0.2 mEq O2/kg).

5.7. Data Analysis

Outcome measures were statistically analyzed. The incidence (yes/no) of DS and the sample size's statistical power were considered. Calculations were performed using SPPS 25 (IBM Corp. Released in 2017. IBM SPSS Statistics for Windows, Version 25.0, Armonk, New York, NY, USA). Tests were considered significant if $p < 0.05$.

According to Rosner, the sample size was calculated to determine the minimum number of subjects for adequate study power using the ClinCalc Sample Size Calculator [44]. The previously published mean value of the primary endpoint and the work of Kaur et al. were taken into account. Therefore, based on an incidence of 22.6% in group 1 and 6.6% in group 2, a sample size of 150 patients was considered sufficient to have a power of 0.8 with an alpha of 0.5 and a beta of 0.2.

Supplementary Materials: The following supporting information can be downloaded at: https://www.mdpi.com/article/10.3390/gels9040289/s1, Figure S1: CONSORT checklist.

Author Contributions: Conceptualization, A.M., C.P. and A.A.; methodology, A.M., C.P., E.L., M.B. and M.F.; software, C.P. and A.A.; validation, A.A. and S.B.; formal analysis, A.A.; investigation, A.M., C.P., E.L., A.A., M.B. and M.F.; resources, S.B.; data curation, A.A.; writing—original draft preparation, A.M. and A.A.; writing—review and editing, C.P., E.L., M.F. and S.B.; supervision, A.A. All authors have read and agreed to the published version of the manuscript.

Funding: This research received no external funding.

Institutional Review Board Statement: The study was conducted in accordance with the Declaration of Helsinki, and approved by the Ethics Committee of the Department of Surgical and Diagnostic Sciences, University of Genoa (decision number: document No. 2021/55 of the University Research Ethics Committee).

Informed Consent Statement: Informed consent was obtained from all subjects involved in the study.

Data Availability Statement: All data generated or analyzed during this study are included in this published article (and its Supplementary Information files).

Conflicts of Interest: The authors declare no conflict of interest.

References

1. Cardoso, C.L.; Rodrigues, M.T.V.; Ferreira, O.; Garlet, G.P.; de Carvalho, P.S.P. Clinical Concepts of Dry Socket. *J. Oral Maxillofac. Surg.* **2010**, *68*, 1922–1932. [CrossRef] [PubMed]
2. Chow, O.; Wang, R.; Ku, D.; Huang, W. Alveolar Osteitis: A Review of Current Concepts. *J. Oral Maxillofac. Surg.* **2020**, *78*, 1288–1296. [CrossRef] [PubMed]
3. Blum, I.R. Contemporary Views on Dry Socket (Alveolar Osteitis): A Clinical Appraisal of Standardization, Aetiopathogenesis and Management: A Critical Review. *Int J. Oral Maxillofac. Surg.* **2002**, *31*, 309–317. [CrossRef] [PubMed]
4. Rakhshan, V. Common Risk Factors of Dry Socket (Alveolitis Osteitis) Following Dental Extraction: A Brief Narrative Review. *J. Stomatol. Oral Maxillofac. Surg.* **2018**, *119*, 407–411. [CrossRef]
5. Taberner-Vallverdú, M.; Nazir, M.; Sánchez-Garcés, M.Á.; Gay-Escoda, C. Efficacy of Different Methods Used for Dry Socket Management: A Systematic Review. *Med. Oral Patol. Oral Cir. Bucal* **2015**, *20*, e633–e639. [CrossRef]
6. Taberner-Vallverdú, M.; Camps-Font, O.; Gay-Escoda, C.; Sánchez-Garcés, M.A. Previous Dry Socket as a Risk Factor for Alveolar Osteitis: A Nested Case-Control Study in Primary Healthcare Services. *J. Clin. Exp. Dent.* **2022**, *14*, 479–485. [CrossRef]
7. Bowe House Officer, D.C.; Rogers, S.; Stassen, L.F. The Management of Dry Socket Alveolar Osteitis The Management of Dry Socket/ Alveolar Osteitis Introduction/Review of Literature. *J. Ir. Dent. Assoc.* **2011**, *57*, 305–310.
8. Mamoun, J. Dry Socket Etiology, Diagnosis, and Clinical Treatment Techniques. *J. Korean Assoc. Oral Maxillofac. Surg.* **2018**, *44*, 52. [CrossRef]
9. Leon, B.R.; Romary, D.J.; Landsberger, S.A.; Bradner, K.N.; Ramirez, M.; Lubitz, R.M. Risks of Ozonated Oil and Ozonated Water on Human Skin: A Systematic Review. *Int. Wound J.* **2022**, *19*, 1901–1910. [CrossRef]
10. Scribante, A.; Gallo, S.; Pascadopoli, M.; Soleo, R.; Di Fonso, F.; Politi, L.; Venugopal, A.; Marya, A.; Butera, A. Management of Periodontal Disease with Adjunctive Therapy with Ozone and Photobiomodulation (PBM): A Randomized Clinical Trial. *Photonics* **2022**, *9*, 138. [CrossRef]
11. Pattanaik, B.; Jetwa, D.; Pattanaik, S.; Manglekar, S.; Naitam, D.N.; Dani, A. Ozone Therapy in Dentistry: A Literature Review. *J. Interdiscip. Dent.* **2011**, *1*, 87. [CrossRef]
12. Saini, R. Ozone Therapy in Dentistry: A Strategic Review. *J. Nat. Sci. Biol. Med.* **2011**, *2*, 151. [CrossRef] [PubMed]
13. Scribante, A.; Butera, A.; Alovisi, M. Customized Minimally Invasive Protocols for the Clinical and Microbiological Management of the Oral Microbiota. *Microorganisms* **2022**, *10*, 675. [CrossRef] [PubMed]
14. Re, L. Ozone in Medicine: A Few Points of Reflections. *Front. Physiol.* **2022**, *13*, 842229. [CrossRef] [PubMed]
15. Li, X.; Ma, J.; He, H. Recent Advances in Catalytic Decomposition of Ozone. *J. Environ. Sci.* **2020**, *94*, 14–31. [CrossRef]
16. Batakliev, T.; Georgiev, V.; Anachkov, M.; Rakovsky, S.; Zaikov, G.E. Ozone Decomposition. *Interdiscip. Toxicol.* **2014**, *7*, 47–59. [CrossRef]
17. Bianco, E.; Maddalone, M.; Porcaro, G.; Amosso, E.; Baldoni, M. Treatment of Osteoradionecrosis of the Jaw with Ozone in the Form of Oil-Based Gel: 1-Year Follow-Up. *J. Contemp. Dent. Pract.* **2019**, *20*, 270–276. [CrossRef]
18. Abstracts of the 10th Virtual Conseuro 2021 Congress. *Clin. Oral Investig.* **2021**, *25*, 4185–4238. [CrossRef]

19. Houston, J.P.; McCollum, J.; Pietz, D.; Schneck, D. Alveolar Osteitis: A Review of Its Etiology, Prevention, and Treatment Modalities. *Gen. Dent.* **2002**, *50*, 457–463; quiz 464.
20. Kaur, J.; Raval, R.; Bansal, A.; Kumawat, V. Repercussions of Intraalveolar Placement of Combination of 0.2% Chlorhexidine & 10 Mg Metronidazole Gel on the Occurrence of Dry Sockets—A Randomized Control Trial. *J. Clin. Exp. Dent.* **2017**, *9*, e284–e288. [CrossRef]
21. Hermesch, C.B.; Hilton, T.J.; Biesbrock, A.R.; Baker, R.A.; Cain-Hamlin, J.; McClanahan, S.F.; Gerlach, R.W. Perioperative Use of 0.12% Chlorhexidine Gluconate for the Prevention of Alveolar Osteitis: Efficacy and Risk Factor Analysis. *Oral Surg. Oral Med. Oral Pathol. Oral Radiol. Endod.* **1998**, *85*, 381–387. [CrossRef] [PubMed]
22. Parthasarathi, K.; Smith, A.; Chandu, A. Factors Affecting Incidence of Dry Socket: A Prospective Community-Based Study. *J. Oral Maxillofac. Surg.* **2011**, *69*, 1880–1884. [CrossRef] [PubMed]
23. Torres-Lagares, D.; Serrera-Figallo, M.; Romero-Ruiz, M.-M.; Infante-Cossio, P.; García-Calderón, M.; Gutierrez-Perez, J. Update on Dry Socket: A Review of the Literature. *Med. Oral Patol. Oral Cir. Bucal* **2005**, *10*, 81–85.
24. Haraji, A.; Rakhshan, V.; Khamverdi, N.; Alishahi, H. Effects of Intra-Alveolar Placement of 0.2% Chlorhexidine Bioadhesive Gel on Dry Socket Incidence and Postsurgical Pain: A Double-Blind Split-Mouth Randomized Controlled Clinical Trial. *J. Orofac. Pain* **2013**, *27*, 256–262. [CrossRef] [PubMed]
25. Huth, K.C.; Quirling, M.; Lenzke, S.; Paschos, E.; Kamereck, K.; Brand, K.; Hickel, R.; Ilie, N. Effectiveness of Ozone against Periodontal Pathogenic Microorganisms. *Eur. J. Oral Sci.* **2011**, *119*, 204–210. [CrossRef] [PubMed]
26. Bassetti, C.; Kallenberger, A. Influence of Chlorhexidine Rinsing on the Healing of Oral Mucosa and Osseous Lesions. *J. Clin. Periodontol.* **1980**, *7*, 443–456. [CrossRef]
27. Küçük, F.; Yıldırım, S.; Çetiner, S. Cytotoxicity Assessment of Different Doses of Ozonated Water on Dental Pulp Cells. *BMC Oral Health* **2021**, *21*, 32. [CrossRef]
28. Srikanth, A.; Sathish, M.; Harsha, A.V.S. Application of Ozone in the Treatment of Periodontal Disease. *J. Pharm. Bioallied. Sci.* **2013**, *5*, S89. [CrossRef]
29. Rizk, M.; Witte, M.B.; Barbul, A. Nitric Oxide and Wound Healing. *World J. Surg.* **2004**, *28*, 301–306. [CrossRef]
30. Dunnill, C.; Patton, T.; Brennan, J.; Barrett, J.; Dryden, M.; Cooke, J.; Leaper, D.; Georgopoulos, N.T. Reactive Oxygen Species (ROS) and Wound Healing: The Functional Role of ROS and Emerging ROS-Modulating Technologies for Augmentation of the Healing Process. *Int. Wound J.* **2017**, *14*, 89–96. [CrossRef]
31. Liu, H.; Zhu, X.; Guo, H.; Huang, H.; Huang, S.; Huang, S.; Xue, W.; Zhu, P.; Guo, R. Nitric Oxide Released Injectable Hydrogel Combined with Synergistic Photothermal Therapy for Antibacterial and Accelerated Wound Healing. *Appl. Mater. Today* **2020**, *20*, 100781. [CrossRef]
32. Zhao, H.; Huang, J.; Li, Y.; Lv, X.; Zhou, H.; Wang, H.; Xu, Y.; Wang, C.; Wang, J.; Liu, Z. ROS-Scavenging Hydrogel to Promote Healing of Bacteria Infected Diabetic Wounds. *Biomaterials* **2020**, *258*, 120286. [CrossRef] [PubMed]
33. Viebahn-Haensler, R.; León Fernández, O.S.; Malatesta, M.; Cisterna, B.; Costanzo, M. Ozone in Medicine. The Low-Dose Ozone Concept and Its Basic Biochemical Mechanisms of Action in Chronic Inflammatory Diseases. *Int. J. Mol. Sci.* **2021**, *22*, 7890. [CrossRef] [PubMed]
34. Azarpazhooh, A.; Limeback, H. The Application of Ozone in Dentistry: A Systematic Review of Literature. *J. Dent.* **2008**, *36*, 104–116. [CrossRef] [PubMed]
35. Colombo, M.; Gallo, S.; Garofoli, A.; Poggio, C.; Arciola, C.R.; Scribante, A. Ozone Gel in Chronic Periodontal Disease: A Randomized Clinical Trial on the Anti-Inflammatory Effects of Ozone Application. *Biology* **2021**, *10*, 625. [CrossRef] [PubMed]
36. Hidalgo-Tallón, F.J.; Torres-Morera, L.M.; Baeza-Noci, J.; Carrillo-Izquierdo, M.D.; Pinto-Bonilla, R. Updated Review on Ozone Therapy in Pain Medicine. *Front. Physiol.* **2022**, *13*, 840623. [CrossRef]
37. Ghanem, W.M.A.; Al-Moudallal, Y.; Droubi, M.; Al-Nerabieah, Z. Effect of Intrasocket Application of Ozonized Olive Oil Gel on Postsurgical Pain and Soft Tissue Healing of Impacted Mandibular Third Molars Surgery: Split-Mouth Randomized Controlled Trial. *Int. J. Dent. Oral Sci.* **2021**, *8*, 1408–1414. [CrossRef]
38. Cores, Á.; Piquero, M.; Villacampa, M.; León, R.; Menéndez, J.C. NRF2 Regulation Processes as a Source of Potential Drug Targets against Neurodegenerative Diseases. *Biomolecules* **2020**, *10*, 904. [CrossRef]
39. Materni, A.; de Angelis, N.; di Tullio, N.; Colombo, E.; Benedicenti, S.; Amaroli, A. Flapless Surgical Approach to Extract Impacted Inferior Third Molars: A Retrospective Clinical Study. *J. Clin. Med.* **2021**, *10*, 593. [CrossRef]
40. Dolanmaz, D.; Esen, A.; Isik, K.; Candirli, C. Effect of 2 Flap Designs on Postoperative Pain and Swelling after Impacted Third Molar Surgery. *Oral Surg. Oral Med. Oral Pathol. Oral Radiol.* **2013**, *116*, e244–e246. [CrossRef]
41. Materni, A.; Pasquale, C.; Signore, A.; Benedicenti, S.; Amaroli, A. Comparison between the Flapless Surgical Approach and a Novel Single Incision Access in Terms of Recovery Time and Comfort after Extraction of Impacted Inferior Third Molars: A Randomised, Blinded, Split-Mouth Controlled Clinical Trial. *J Clin Med.* **2023**, *2*, 1995. [CrossRef]
42. Ghohestani, E.; Tashkhourian, J.; Hemmateenejad, B. Colorimetric Determination of Peroxide Value in Vegetable Oils Using a Paper Based Analytical Device. *Food Chem.* **2023**, *403*, 134345. [CrossRef] [PubMed]

43. Radzimierska-Kazmierczak, M.; Smigielski, K.; Sikora, M.; Nowak, A.; Plucinska, A.; Kunicka-Styczynska, A.; Czarnecka-Chrebelska, K.H. Olive Oil with Ozone-Modified Properties and Its Application. *Molecules* **2021**, *26*, 3074. [CrossRef] [PubMed]
44. Rosner, B. *Bernard Rosner Fundamentals of Biostatistics*, 8th ed.; Cengage Learning: Boston, MA, USA, 2015; p. 927; ISBN 978-1305268920.

gels

MDPI

Article

Tumor Microenvironment-Responsive 6-Mercaptopurine-Releasing Injectable Hydrogel for Colon Cancer Treatment

Sungjun Kim, Wonjeong Lee, Heewon Park and Kyobum Kim *

Department of Chemical & Biochemical Engineering, Dongguk University, 30, Pildong-ro 1-gil, Jung-gu, Seoul 22012, Republic of Korea; sungjun.kim@dgu.ac.kr (S.K.); jeong99@dgu.ac.kr (W.L.); hana4339@gmail.com (H.P.)
* Correspondence: kyobum.kim@dongguk.edu; Tel.: +82-2-2260-8597

Abstract: Colon cancer is a significant health concern. The development of effective drug delivery systems is critical for improving treatment outcomes. In this study, we developed a drug delivery system for colon cancer treatment by embedding 6-mercaptopurine (6-MP), an anticancer drug, in a thiolated gelatin/polyethylene glycol diacrylate hydrogel (6MP-GPGel). The 6MP-GPGel continuously released 6-MP, the anticancer drug. The release rate of 6-MP was further accelerated in an acidic or glutathione environment that mimicked a tumor microenvironment. In addition, when pure 6-MP was used for treatment, cancer cells proliferated again from day 5, whereas a continuous supply of 6-MP from the 6MP-GPGel continuously suppressed the survival rate of cancer cells. In conclusion, our study demonstrates that embedding 6-MP in a hydrogel formulation can improve the efficacy of colon cancer treatment and may serve as a promising minimally invasive and localized drug delivery system for future development.

Keywords: hydrogel; colon cancer; 6-mercaptopurine; drug delivery system; anticancer

1. Introduction

Colon cancer, also known as colorectal cancer, is a type of cancer that develops in the colon or rectum. It is the third most common cancer and the second leading cause of cancer-related deaths in the United States [1,2]. Treatment for colon cancer typically involves a combination of surgery, chemotherapy, and radiation therapy. However, these therapies have side effects and limited therapeutic efficacy [3]. For instance, depending on the location of the cancer, a partial colectomy might be performed to remove a portion of the colon, or a rectal resection is performed to remove the rectum. Radiation therapy can cause damage to healthy tissues surrounding the tumor, leading to side effects, such as fatigue, skin irritation, and damage to organs. Moreover, chemotherapy for colon cancer could cause significant side effects, including liver toxicities, gastrointestinal toxicities, and hematologic disorders [4,5].

A drug delivery system that responds to and localizes in the tumor microenvironment (TME) can be a technology that maximizes the efficacy of anticancer treatment while minimizing the side effects of existing anticancer drugs [6,7]. Recently, hydrogels have attracted a lot of interest in the field of anticancer therapy due to their ability to encapsulate drugs, peptides, and other therapeutic agents and deliver them to targeted sites in a controlled and sustained manner [8–11]. One of the key advantages of using hydrogels for cancer therapy is localized drug delivery to the tumor site, which can reduce the side effects associated with systemic drug administration. Additionally, hydrogels could be designed to respond to different stimuli, such as changes in pH, temperature, and enzyme activity, which allows for the targeted release of therapeutic agents in response to specific conditions in the TME. Among various chemical bonds, the disulfide bond is an attractive candidate that can be dissociated in response to GSH or an acidic pH [12–17].

In this study, we developed an anticancer drug (6-mercaptopurine, 6MP), an embedded composite hydrogel, consisting of thiolated gelatin (GelSH) and poly(ethylene glycol) diacrylate (PEGDA). Various natural and synthetic polymers have been utilized for hydrogel fabrication. Gelatin, a denatured biomacromolecule from collagen, possesses desirable physicochemical properties, such as biocompatibility, low antigenicity, biodegradability, and cell attachability [18,19]. Additionally, gelatin is recognized by the FDA as generally safe for consumption (GRAS) [20]. Despite its benefits, gelatin has limitations, such as low mechanical strength, low thermal stability, and rapid water degradation, which hinder its use in versatile tissue engineering applications [21,22]. To overcome these issues, gelatin molecules can be chemically modified to increase crosslinking density or incorporated into interpenetrating polymer networks (IPNs) with complementary substances. Thiolated polymers have been extensively employed for hydrogel design due to the high reactivity of the sulfhydryl moiety [23]. In the fabrication of IPN hydrogels, GelSH was combined with a synthetic PEGDA polymer, which offers excellent controllability. This GelSH/PEGDA hydrogel (GPGel) can be used as an implantable scaffold for various tissue engineering applications including bone and osteochondral tissues [18,24,25]. A series of studies have demonstrated, in vitro/in vivo, the long-term stability of GPGel. Moreover, GPGel exhibits non-immunogenicity and excellent biocompatibility. 6-MP is a well-known anticancer drug that can induce apoptosis by interfering with DNA replication and RNA transcription [26,27]. In this regard, 6-MP was conjugated with GelSH (6MP-GelSH) through a disulfide bond (Figure 1A) and then gelated with PEGDA (Figure 1B). Hence, our 6-MP-embedded GPGel (6MP-GPGel) could be used as an effective scaffold that is injectable, with high stability and the ability to release drugs in response to the TME.

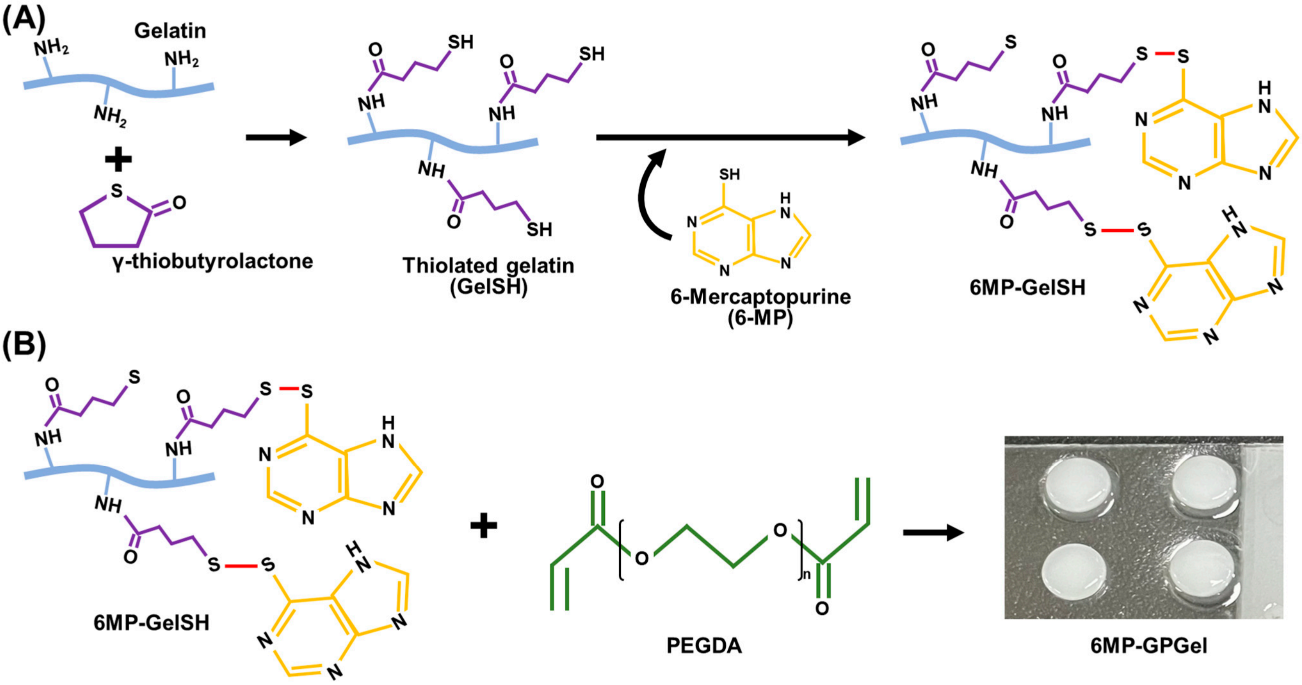

Figure 1. A schematic illustration of (**A**) the synthesis of thiolated gelatin and disulfide bond-mediated 6-MP conjugation, and (**B**), the fabrication of 6MP-GPGel.

Herein, we evaluated the anticancer function of 6MP-GPGel as an injectable and implantable composite hydrogel scaffold. It was found that 6-MP was highly released from 6MP-GPGel in response to the TME conditions, especially acidic pH and high GSH environments. Consequently, 6-MP released from 6MP-GPGel effectively inhibits colon cancer cells (i.e., HCT-116). The objectives of the current study were to investigate the (1) sensitivity of colon cancer cells to 6-MP, (2) TME-responsive 6-MP release, and (3) anticancer activity of 6MP-GPGel.

2. Results and Discussion

2.1. Sensitivity of Colon Cancer to 6-Mercaptopurine

TRAIL 6-MP is an analog of thiopurine and it is a well-known anticancer drug that can inhibit the growth of tumor cells by interfering with purine synthesis, which is closely related to DNA and RNA biosynthesis [28]. In this study, nine types of cancer cells including colon cancer, breast cancer, pancreatic cancer, liver cancer, and cervical cancer were treated with 6-MP to select cancer cell lines sensitive to 6-MP. As a result, colorectal cancer cells, HCT-116 and HT29, showed significantly lower cell viability compared to breast cancers (MCF-7 and MDA-MB-231), pancreatic cancers (PanC-1, MIA PaCa-2, and AsPC-1), liver cancer (HepG2), and cervical cancer (HeLa) (Figure 2). These results demonstrated that colon cancers are sensitive to 6-MP. In addition, slightly lower cell viability was found for HCT-116 (48.4%) compared to that of HT29 (51.3%). Therefore, we designated HCT-116 as a major target for cancer. The viability of HCT-116 cells was 6-MP concentration-dependent. The IC_{50} value of 6-MP for HCT-116 cells was 36.1 μg/mL (Figure 3). Notably, no toxicity was observed for fibroblasts in a normal cell model after treatment with 6-MP at concentrations of up to 200 μg/mL. Consequently, 6-MP could be used as an excellent anticancer drug candidate that can sensitively kill colon cancer without any toxicity to normal cells.

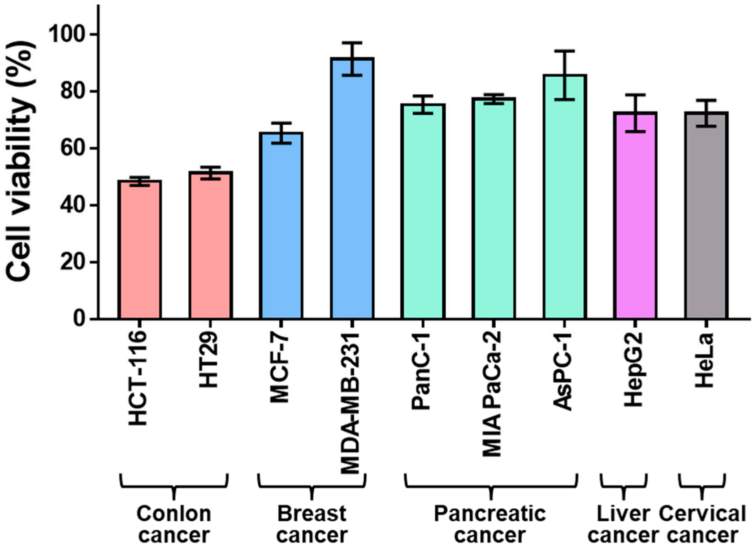

Figure 2. Anticancer efficacy of 6-MP (50 μg/mL) against various cancer cells including colon cancer, breast cancer, pancreatic cancer, liver cancer, and cervical cancer cells.

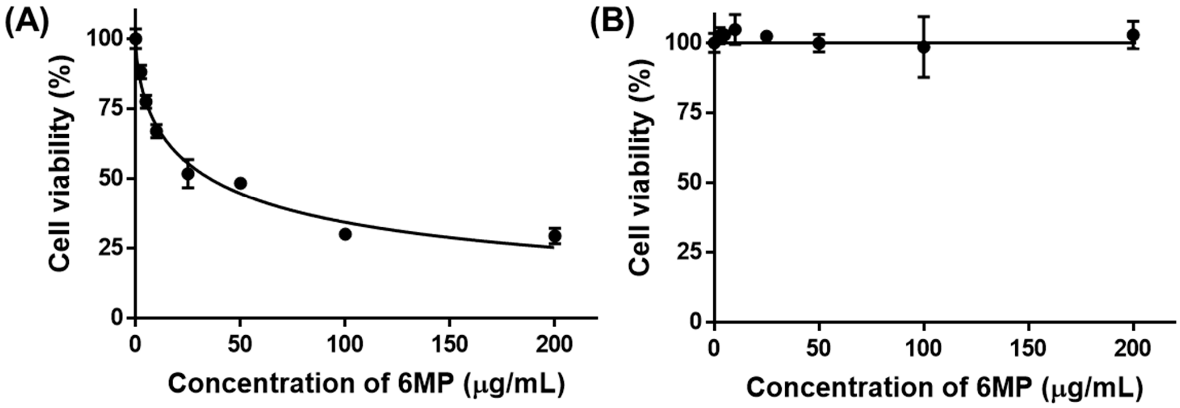

Figure 3. Viability of (**A**) HCT-116 cells and (**B**) fibroblasts after treatment with different concentrations of 6-MP.

2.2. Characterization of Hydrogel

In this study, we conjugated 6-MP to GelSH via disulfide bonds (Figure 1A), and the success of the conjugation was confirmed through UV spectroscopy. Specifically, GelSH did not exhibit a peak around 320 nm, whereas 6MP-GelSH showed a distinctive peak at that wavelength (Figure S1). These results demonstrated that 6-MP was effectively conjugated to GelSH. Then, hydrogels were fabricated by mixing 6MP-GelSH and PEGDA. Gelatin has desirable intrinsic physicochemical properties such as excellent biocompatibility, biodegradability, and low antigenicity. It is well known as a suitable hydrogel material [29,30]. However, hydrogels made only from gelatin often exhibit disadvantages, such as poor mechanical properties, low thermal stability, and instantaneous dissolution in water, which often cause failure in tissue engineering applications [21,22]. Fabricating hydrogels in combined use with PEGDA can be a way to overcome these problems. The resulting GPGel shows improved physical and chemical fragility of the component by increasing its mechanical strength through chain-wide polymerization [31,32]. Here, gelation by sol–gel phase transition of the 6MP-GPGel was evaluated using a vial tilting method (Figure 4A,B). The prepared sol solution was injectable. It could be cast into a desired shape according to the mold (Figure 4C). In addition, we used SEM to observe the 3D interconnected porous structure of 6MP-GPGel, which revealed a pore size of approximately 81.8 ± 30.2 μm (Figure S2). The porous architecture of hydrogels has a significant impact on various mechanical properties, including biodegradability and Young's modulus. In a previous study, we investigated the structural–physical relationship of GPGel and synthesized GPGels with various ratios of PEGDA and GelSH [18]. Our results showed that GPGel with a smaller pore size exhibited improved mechanical properties, such as slower degradation and higher Young's modulus. Therefore, by adjusting the content of GelSH and PEGDA, it is possible to achieve desired properties and customize GPGels for specific applications.

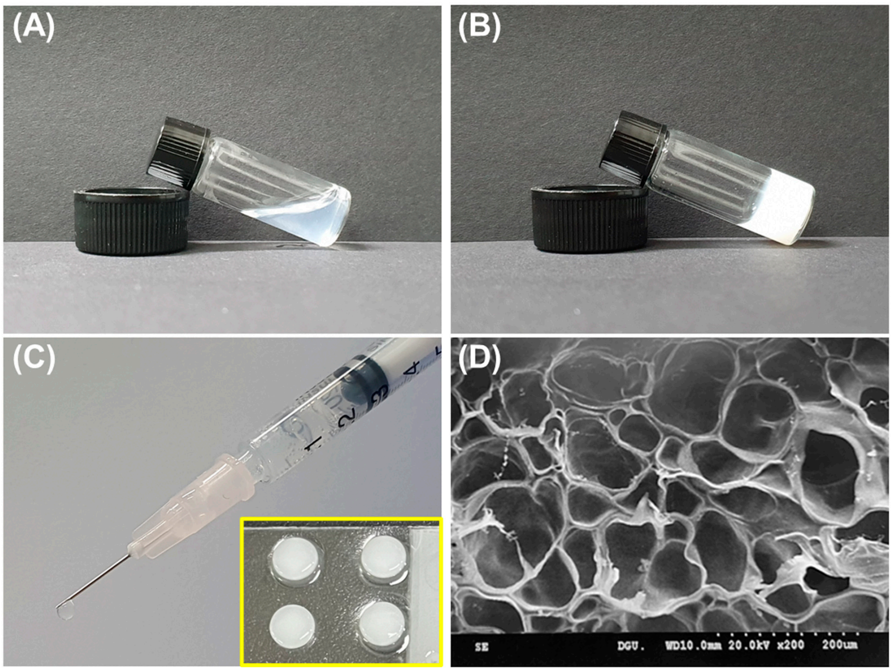

Figure 4. Characterization of 6MP-GPGel. (**A**,**B**) Sol–gel phase transition of hydrogels; (**C**) macroscopic image of hydrogel injection using a syringe. Yellow box showing hydrogels fabricated using a Teflon mold; and (**D**) SEM image of cross-sectioned 6MP-GPGel.

2.3. Release of 6-MP from 6MP-GPGel

6MP-GPGels containing 10 μg of 6-MP were fabricated, and the release profile of 6-MP was evaluated in TME-mimicking environments [33]. Under PBS conditions, a sustained

6-MP release profile was observed, and 3.9% of cumulative release was recorded over 7 days (Figure 5A,B). In contrast, a burst 6-MP release profile was observed in TME-mimicking conditions, such as an acidic pH (pH 5.5) (Figure 5A) and higher GSH concentration (10 mM) (Figure 5B). Specifically, we observed 11.7% and 16.0% of cumulative release for 7 days at pH 5.5 and 10 mM GSH conditions, respectively. These results might be caused by the acidic pH and various reducing activities of GSH. Tumor tissues exhibit exclusive cellular microenvironments (e.g., acidic, enzymatic, and reducing environments) due to their unique physiological properties [34,35]. In a GSH-reducing environment, polymeric materials with disulfide bonds can depolymerize at a faster rate than other types of redox-reactive carriers. Moreover, the pH of the TME ranges from 5.5–7.0 [36]. Therefore, in this study, we conducted a 6-MP release experiment in an environment with a pH of 5.5, which could significantly accelerate the release of 6-MP. Accordingly, a reducing environment by pH could also accelerate drug release [12,37]. In addition, HCT-116 cells were treated with 6-MP released from 6MP-GPGel to estimate the maintenance of the anticancer efficacy of 6-MP (Figure 6A). As a result, 6-MP released from 6MP-GPGel showed anticancer activity similar to that of pure 6-MP at the same concentration. These results demonstrated that the series of processes in which 6-MP was embedded and released in our hydrogel system did not affect the biochemical functionality of 6-MP. Additionally, in vitro biocompatibility tests were performed according to the International Organization for Standardization 10993-5 and previous related studies [18,38,39]. Treatment with 6-MP-free GpGel releasates showed no toxicity to HCT-116 cells (Figure 6A) or fibroblasts (Figure 6B). In addition, the 6MP-GPGel releasates failed to kill fibroblasts as 6-MP did not induce any toxicity in fibroblasts, as previously demonstrated (Figure 3B). The biosafety of GPGel-based hydrogel systems has been demonstrated in a series of in vitro and in vivo studies [18,24,25]. The cytocompatibility was assessed in vitro using two methods: (1) treatment of cell cultures with GPGel releasates [18], and (2) encapsulation of cells within the hydrogel [24]. No toxicity was observed when fibroblasts or HaCaT cells were treated with releasates of GPGel prepared using various combinations of GelSH, PEGDA, and initiator (APS or TEMED) [18]. Additionally, adipose-derived mesenchymal stem cells were encapsulated within GPGel and cultured for 14 days, with only green-stained cells (i.e., live cells) observed [24]. In vivo biocompatibility was confirmed by implanting GPGel subcutaneously in mice for 3, 7, and 15 days. Tissue sections harvested at each time point were stained with a CD68 macrophage marker for inflammation analysis, with the control PEGDA hydrogel group exhibiting a severe inflammatory response, while the GPGel-induced group only displayed a mild response [24]. Furthermore, when GPGel was implanted into mouse calvarial bone [25] and osteochondral defects [24], no necrosis or toxicity of surrounding tissue was observed. Therefore, our smart hydrogel system, 6MP-GPGel, could achieve effective anticancer activity by rapidly releasing drugs under pH and GSH conditions in the TME with excellent biocompatibility.

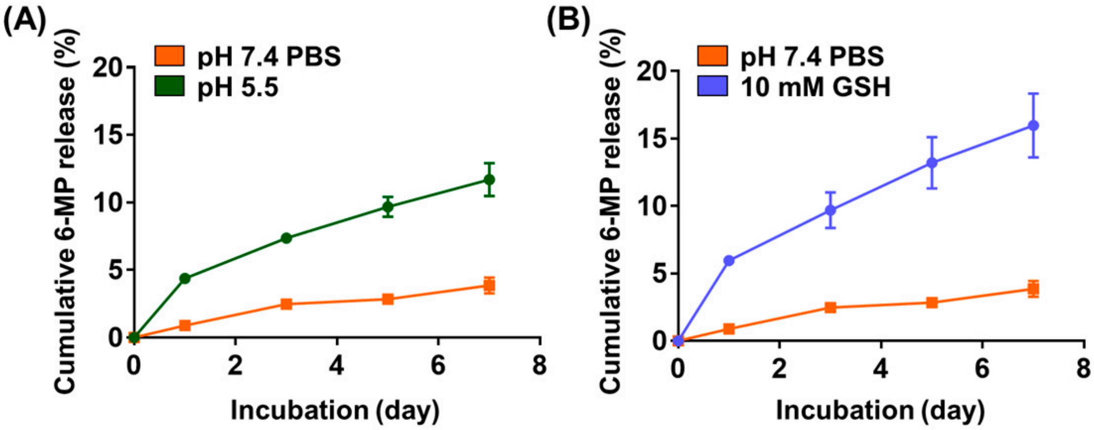

Figure 5. % cumulative 6-MP release profile at (**A**) different pH and (**B**) glutathione concentrations.

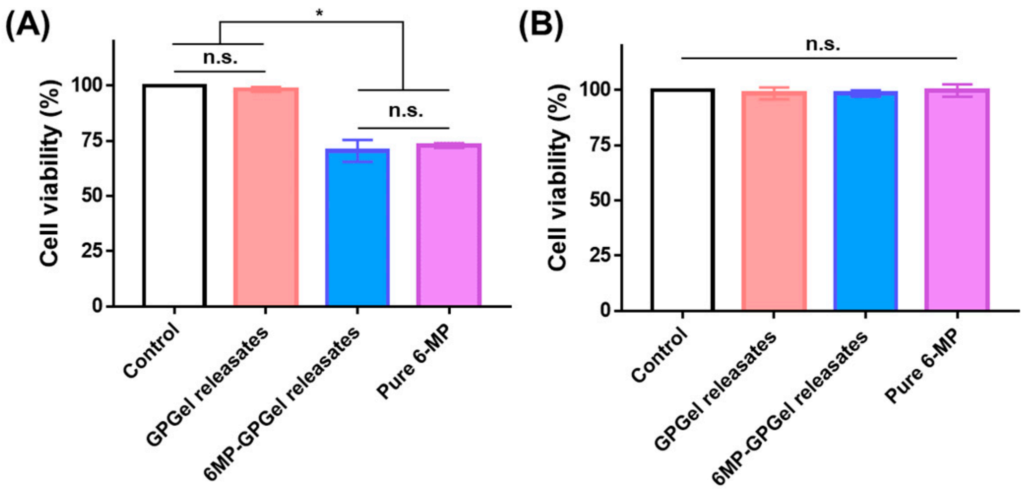

Figure 6. Biological anticancer activity and biocompatibility of 6-MP released from 6MP-GPGel to (**A**) HCT-116 cells and (**B**) fibroblasts. (*) indicates that experimental groups are statistically different from each other. (n.s.) indicates that experimental groups are not significantly different.

2.4. Anticancer Efficacy of 6MP-GPGel

Colon cancer recurrence is a risk factor that occurs in 30–50% of patients after standard chemotherapy [40]. Therefore, it is important to not only drastically reduce cancer at the beginning of treatment but also to continuously suppress colon cancer. In this study, the viability of HCT-116 cells was examined for 7 days (Figure 7). In the control HCT-116 group, cells continued to proliferate over time. The cell viability decreased to 66.9% on day 3, but increased to 76.1% and 115.5% on days 5 and 7, respectively, in the pure 6-MP-treated group. Inactivation of 6-MP often causes failure of continuous treatment. Thus, it is necessary to develop a delivery system capable of stably supplying the drug [41]. The viability of HCT-116 cells cultured with 6MP-GPGel decreased over time to 92.7%, 83.7%, and 72.3% at 3, 5, and 7 days, respectively. These results were attributed to the continuous supply of 6-MP in response to the TME (Figure 5) while maintaining the biochemical activity of 6-MP (Figure 6) in the 6MP-GPGel. Various carriers have been developed to deliver 6-MP in recent decades. For instance, Nezhad-Mokhtari et al. developed multi-stimuli-responsive polymeric nanogels [42]. These nanogels were linked to 6-MP through a disulfide bond and released 6-MP in response to GSH and an acidic environment (pH 5.3). The nanogels were effectively uptaken by MCF-7 cells and induced the apoptosis of cancer cells. Additionally, Jakubowski et al. developed zinc zeolite particles loaded with 6-MP, which demonstrated a significant improvement in anticancer efficacy compared to standard bolus 6-MP treatment [43]. This drug delivery system, based on particles, can effectively accumulate in tumor tissue through the enhanced permeability and retention effect and the binding of various targeting molecules. However, the challenge of overcoming their accumulation primarily in the liver and kidney upon intravenous injection still remains. In contrast, our hydrogel-based 6-MP delivery system can be injected and localized around the cancer, preventing accumulation in other organs in the body. To the best of our knowledge, this is the first study to develop a localized hydrogel-based 6-MP delivery system that is recognized by the tumor microenvironment. Additionally, in our previous studies, we demonstrated a significant increase in the therapeutic efficacy of GPGel by encapsulating coacervate, a protein drug delivery carrier, and/or therapeutic cells (ADSCs) into the hydrogel [24,25]. The encapsulation with coacervate was found to further improve long-term treatment efficiency compared to direct drug loading into GPGels. Coacervate is a self-assembling microdroplet that has been used as a versatile protein therapeutic drug delivery system [44–46]. When a protein therapeutic agent for anticancer treatment was loaded into coacervate, it protected the internal protein from the harsh external environment and released the therapeutic agent in response to the TME [6]. For instance, the rapid release of

TRAIL was observed when it was loaded into coacervate in the highly ionic environment of the TME. This allowed the TRAIL-loaded coacervate to effectively inhibit the recurrence of colon cancer [3]. Loading additional anticancer drugs into these coacervates and embedding them in 6MP-GPGel has the potential to further maximize their anticancer functionality. Taken together, these results suggest that the noninvasive local administration of 6MP-GPGel with excellent biocompatibility could effectively induce colon cancer cell death and suppress recurrence.

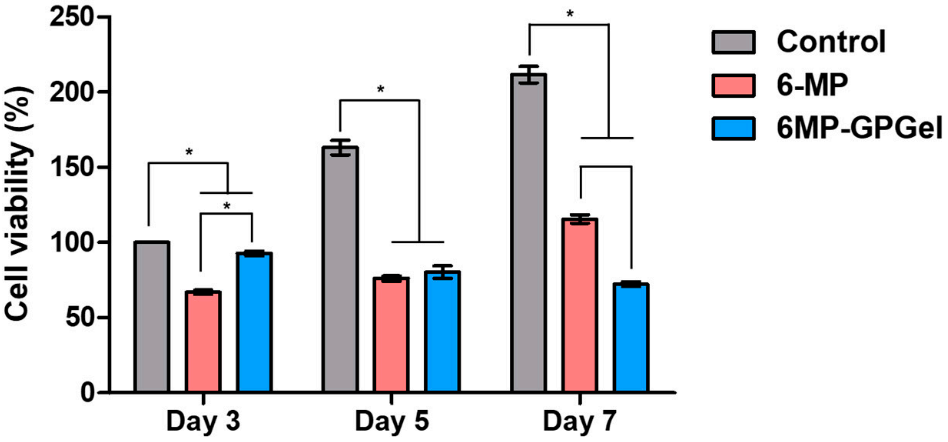

Figure 7. In vitro anticancer effects of 6MP-GPGel on colon cancer HCT-116 cells. (*) indicates that experimental groups are statistically different from each other.

3. Conclusions

In this study, the 6MP-GPGel was manufactured and the anticancer efficacy was evaluated. 6MP was more sensitive to colon cancer than breast cancer, pancreatic cancer, liver cancer, and uterine cancer. It induced colon cancer cell death. In particular, among two types of colon cancer cells, HCT-116 and HT29, HCT-116 showed slightly higher sensitivity. After that, 6-MP was conjugated with GelSH to produce an injectable composite IPN hydrogel. In addition, 6MP-GPGel exhibited (1) excellent biocompatibility, (2) a sustained 6-MP release profile, (3) a TME-responsive 6-MP release, and (4) retained anticancer functionality of the released 6-MP. The treatment of HCT-116 cells with 6-MP treatment resulted in early cancer cell death. However, inactivation over time led to the repopulation of cancer cells starting from day 5. In contrast, administering the 6MP-GPGel to HCT-116 cells inhibited cancer recurrence from day 5 and exhibited a more potent anticancer effect than 6-MP alone on day 7. The focus of developing anticancer drug delivery systems using 6-MP has mainly been on particle-based systems, which may accumulate not only in the target tumor tissue but also in various organs and tissues, resulting in potential toxicity and other problems. In contrast, the 6MP-GPGel developed in this study can induce the death of colon cancer by releasing 6-MP only in the localized area around the tumor tissue, thus minimizing the risk of unwanted tissue accumulation and associated toxicity. Therefore, our 6MP-GPGel system can serve as a novel protein drug delivery platform to inhibit the recurrence of residual cancer after cancer resection or chemotherapy by continuously supplying available 6-MP to the tumor.

4. Materials and Methods

4.1. Materials

Gelatin, ethylenediaminetetraacetic acid (EDTA), γ-thiobutyrolactone, β-mercaptoethanol, imidazole, PEGDA, ammonium persulfate (APS), N,N,N,N′-tetramethylethylenediamine (TEMED), 6-MP, and Ellman's reagent were purchased from Sigma–Aldrich. Dulbecco's modified Eagle's medium (DMEM), penicillin–streptomycin solution, and fetal bovine serum (FBS) were obtained from Corning. EZ-Cytox was bought from Daeil Lab Service.

4.2. Anticancer Efficacy of 6-Mercaptopurine

All types of cells were cultured in growth media consisting of DMEM (89% (*v*/*v*)), penicillin–streptomycin solution (1% (*v*/*v*)), and FBS (10% (*v*/*v*)). To evaluate the anticancer effect of 6-MP on colon cancer cells, various types of cancer cells including colon cancer (HCT-116 and HT29), breast cancer (MCF-7 and MDA-MB-231), pancreatic cancer (PANC-1, MIA PaCa-2, and AsPC-1), liver cancer (HepG2), and cervical cancer (HeLa) cells were treated with 6-MP. Cells were seeded at 10,000 cells/well into 96-well plates and incubated at 37 °C with 5% CO_2 and 95% humidity for 24 h. The old medium was discarded and replaced with a fresh growth medium containing 50 µg/mL 6-MP. After 24 h of incubation, WST-1 reagent was prepared by mixing EZ-Cytox and growth medium at a 1:10 (*v*/*v*) ratio and was added to each well. WST-1 reagent-treated cells were incubated at 37 °C for 3 h. The optical density was then measured at 440 nm using microplate spectrophotometry. To investigate the concentration-dependent anticancer efficacy against colon cancer cells and the biosafety of 6-MP, HCT-116 cells and human fibroblasts were seeded at 10,000 cells/well on 96-well plates and incubated at 37 °C with 5% CO_2 and 95% humidity for 24 h. Thereafter, the old medium was discarded and replaced with fresh growth medium containing 0–200 µg/mL 6-MP. After 24 h of incubation, the WST-1 assay was performed as described above.

4.3. Synthesis of Thiolated Gelatin

Gelatin was thiolated as described in our previous studies [18,24,25]. Briefly, 100 mL of 1% (*w*/*v*) gelatin solution was mixed with 1 mL of 1.85% (*w*/*v*) EDTA and 2 mL of 34% (*w*/*v*) imidazole. After 10 min of stirring, 840 µL of γ-thiobutyrolactone was added to the gelatin mixture and further reacted at 40 °C for 24 h. The reacted mixture was then dialyzed (molecular weight cutoff 14,000) against 0.2% (*v*/*v*) β-mercaptoethanol for 20 h and DW for the next 4 h. The produced GelSH was lyophilized and stored at −80 °C before use. The final thiol content determined by Ellman's assay was 190.2 µmol/g.

4.4. Conjugation of 6-Mercaptopurine to Thiolated Gelatin

To conjugate 6-MP to GelSH, 30 mg of GelSH was dissolved in 3 mL of DW, and 5 mg of 6-MP was dissolved in 1 mL of DMSO. Subsequently, 6-MP was dropped into GelSH solution under stirring at 40 °C. The reactant was stirred for 24 h and dialyzed (molecular weight cutoff 14,000) against DW for 72 h. The final product (i.e., 6MP-GelSH) was lyophilized and stored at −80 °C before use. The UV spectra of GelSH and 6MP-GelSH were measured in the wavelength range of 280–500 nm. To measure 6-MP content in 6MP-GelSH, 5 mg of 6MP-GelSH was dissolved in 30 mL of HCl solution, and the optical density was measured at 320 nm using microplate spectrophotometry [47]. Here, GelSH (without 6-MP) was used to determine the background signal, and pure 6-MP was used as a standard.

4.5. Fabrication of Drug-Embedded Composite Hydrogel

6MP-GelSH, APS, and TEMED were dissolved in DW at 5%, 4%, and 2% (*w*/*v*), respectively. PEGDA solutions were diluted to have a final concentration of 12.5% (*w*/*v*). 6MP-GelSH and PEGDA solutions were mixed first. Initiators (i.e., APS and TEMED) were added subsequently. For 2 mL of 6MP-GPGel, 1 mL of 6MP-GelSH, 0.8 mL of PEGDA, 0.1 mL of APS, and 0.1 mL of TEMED solutions were mixed. The mixed 6MP-GPGel was immediately transferred into a syringe and incubated at 37 °C for 30 min after injection.

4.6. Scanning Electron Microscopy

Three-dimensional porous structures of the 6MP-GPGel were observed with a scanning electron microscope (SEM). The prepared 6MP-GPGel solution was injected into a Teflon mold (8 mm in diameter and 2 mm in height) through a syringe and incubated at 37 °C for 30 min for gelation. Subsequently, the fabricated 6MP-GPGel was lyophilized until all solvents were completely removed. Dried hydrogels were coated in Pt by sputter

(E-1010, HITACHI, Tokyo, Japan). The surface morphologies of the composite hydrogels were obtained using an SEM (S-3000 N, HITACHI) at a 20 kV accelerating voltage. Pore size was analyzed using ImageJ software (http://rsbweb.nih.gov/ij/, accessed on 6 March 2023, National Institutes of Health, Bethesda, MD, USA).

4.7. In Vitro 6-Mercaptopurine Release Profile

Hydrogels containing 10 µg of 6-MP were fabricated to determine the kinetics of 6-MP release from composite 6MP-GPGel hydrogels. Fabricated hydrogels were subsequently incubated with 1 mL of PBS at pH 5.5, or GSH solution (10 mM) solution on a shaker table at 100 rpm and 37 °C, for mimicking the TME. On days 1, 3, 5, and 7, the supernatant was collected after centrifugation and resuspended with each fresh solution. Released 6-MP was measured, as previously and above, and GPGel was used to determine the background signal.

4.8. Anticancer Activity of Released 6-MP from Hydrogel

The bioactivity of the released 6-MP from 6MP-GPGel was estimated by comparison with same the amount of pure 6-MP. Briefly, 10,000 HCT-116 cells or fibroblasts were seeded onto 96-well plates and incubated at 37 °C with 5% CO_2 and 95% humidity for 24 h. The old medium was then discarded and replaced with fresh growth medium containing hydrogel releasates (2.3 µg/mL collected 6-MP) or pure 6-MP. After 24 h of incubation, cell viability was measured using the WST-1 assay.

4.9. Anticancer Effect of Composite Hydrogel

To determine the anticancer effect of 6MP-GPGel, 100,000 HCT-116 cells were seeded into 24-well plates and incubated at 37 °C with 5% CO_2 and 95% humidity for 24 h. The old medium was then changed to a fresh medium or 20 µM GSH-containing medium. The fabricated GPGel or 6MP-GPGel was deposited on the center of a Transwell® insert and incubated with the prepared HCT-116 cells for 5 days. Cell viability was measured using the WST-1 assay.

4.10. Statistical Analysis

For quantitative data, all statistical analyses were conducted with GraphPad Prism 7.0 (GraphPad Software Inc., San Diego, CA, USA). Quantitative experiments were performed in triplicate and analyzed using one-way analysis of variance (ANOVA) and Tukey's multiple-comparison test.

Supplementary Materials: The following supporting information can be downloaded at: https://www.mdpi.com/article/10.3390/gels9040319/s1, Figure S1: UV spectra of GelSH and 6MP-GelSH.; Figure S2: Pore size distribution of 6MP-GPGel. Pore size was obtained from SEM images.

Author Contributions: Conceptualization, S.K. and K.K.; data analysis and curation, S.K. and K.K.; methodology, S.K., W.L. and H.P.; writing—review and editing, S.K. and K.K.; funding acquisition, K.K. All authors have read and agreed to the published version of the manuscript.

Funding: This research was supported by the National Research Foundation of Korea (NRF) grant funded by the Korean government (MSIT) (2021R1A4A3024237) and the Korean Fund for Regenerative Medicine (KFRM) grant funded by the Korean government (the Ministry of Science and ICT, the Ministry of Health & Welfare) (RS-2022-00070304).

Institutional Review Board Statement: Not applicable.

Informed Consent Statement: Not applicable.

Data Availability Statement: Not applicable.

Conflicts of Interest: The authors declare no conflict of interest.

References

1. Sung, H.; Ferlay, J.; Siegel, R.L.; Laversanne, M.; Soerjomataram, I.; Jemal, A.; Bray, F. Global cancer statistics 2020: GLOBOCAN estimates of incidence and mortality worldwide for 36 cancers in 185 countries. *CA-Cancer J. Clin* **2021**, *71*, 209–249. [CrossRef]
2. Sawicki, T.; Ruszkowska, M.; Danielewicz, A.; Niedzwiedzka, E.; Arlukowicz, T.; Przybylowicz, K.E. A Review of Colorectal Cancer in Terms of Epidemiology, Risk Factors, Development, Symptoms and Diagnosis. *Cancers* **2021**, *13*, 2025. [CrossRef]
3. Kim, S.; Jwa, Y.; Hong, J.; Kim, K. Inhibition of Colon Cancer Recurrence via Exogenous TRAIL Delivery Using Gel-like Coacervate Microdroplets. *Gels* **2022**, *8*, 427. [CrossRef] [PubMed]
4. Banerjee, A.; Pathak, S.; Subramanium, V.D.; Dharanivasan, G.; Murugesan, R.; Verma, R.S. Strategies for targeted drug delivery in treatment of colon cancer: Current trends and future perspectives. *Drug Discov. Today* **2017**, *22*, 1224–1232. [CrossRef]
5. Khan, F.A.; Albalawi, R.; Pottoo, F.H. Trends in targeted delivery of nanomaterials in colon cancer diagnosis and treatment. *Med. Res. Rev.* **2022**, *42*, 227–258. [CrossRef]
6. Kim, S.; Choi, Y.; Kim, K. Coacervate-mediated novel pancreatic cancer drug Aleuria Aurantia lectin delivery for augmented anticancer therapy. *Biomater. Res.* **2022**, *26*, 35. [CrossRef]
7. Mani, G.; Kim, S.; Kim, K. Development of Folate-Thioglycolate-Gold Nanoconjugates by Using Citric Acid-PEG Branched Polymer for Inhibition of MCF-7 Cancer Cell Proliferation. *Biomacromolecules* **2018**, *19*, 3257–3267. [CrossRef]
8. Lali Raveendran, R.; Valsala, M.; Sreenivasan Anirudhan, T. Development of nanosilver embedded injectable liquid crystalline hydrogel from alginate and chitosan for potent antibacterial and anticancer applications. *J. Ind. Eng. Chem.* **2023**, *119*, 261–273. [CrossRef]
9. Sun, Z.Y.; Song, C.J.; Wang, C.; Hu, Y.Q.; Wu, J.H. Hydrogel-Based Controlled Drug Delivery for Cancer Treatment: A Review. *Mol. Pharm.* **2020**, *17*, 373–391. [CrossRef] [PubMed]
10. Fan, D.Y.; Tian, Y.; Liu, Z.J. Injectable Hydrogels for Localized Cancer Therapy. *Front. Chem.* **2019**, *7*, 675. [CrossRef]
11. Zolfagharian, S.; Zahedi, P.; Shafiee Ardestani, M.; Khatibi, A.; Jafarkhani, S. Sodium alginate/xanthan-based nanocomposite hydrogels containing 5-fluorouracil: Characterization and cancer cell death studies in presence of halloysite nanotube. *J. Ind. Eng. Chem.* **2023**, *120*, 374–386. [CrossRef]
12. Guo, X.S.; Cheng, Y.; Zhao, X.T.; Luo, Y.L.; Chen, J.J.; Yuan, W.E. Advances in redox-responsive drug delivery systems of tumor microenvironment. *J. Nanobiotechnol.* **2018**, *16*, 74. [CrossRef]
13. Li, M.; Yin, S.; Lin, M.; Chen, X.; Pan, Y.; Peng, Y.; Sun, J.; Kumar, A.; Liu, J. Current status and prospects of metal–organic frameworks for bone therapy and bone repair. *J. Mater. Chem. B* **2022**, *10*, 5105–5128. [CrossRef] [PubMed]
14. Ma, Z.M.; Gao, X.Z.; Raza, F.; Zafar, H.; Huang, G.H.; Yang, Y.Y.; Shi, F.; Wang, D.Q.; He, X. Design of GSH-Responsive Curcumin Nanomicelles for Oesophageal Cancer Therapy. *Pharmaceutics* **2022**, *14*, 1802. [CrossRef]
15. Wang, Q.; Guan, J.K.; Wan, J.L.; Li, Z.F. Disulfide based prodrugs for cancer therapy. *Rsc. Adv.* **2020**, *10*, 24397–24409. [CrossRef]
16. Xu, Z.; Wu, Z.; Huang, S.; Ye, K.; Jiang, Y.; Liu, J.; Liu, J.; Lu, X.; Li, B. A metal-organic framework-based immunomodulatory nanoplatform for anti-atherosclerosis treatment. *J. Control. Release* **2023**, *354*, 615–625. [CrossRef] [PubMed]
17. Liu, W.; Yan, Q.; Xia, C.; Wang, X.; Kumar, A.; Wang, Y.; Liu, Y.; Pan, Y.; Liu, J. Recent advances in cell membrane coated metal–organic frameworks (MOFs) for tumor therapy. *J. Mater. Chem. B* **2021**, *9*, 4459–4474. [CrossRef] [PubMed]
18. Kim, S.; Choi, Y.; Lee, W.; Kim, K. Fabrication Parameter-Dependent Physico-Chemical Properties of Thiolated Gelatin/PEGDA Interpenetrating Network Hydrogels. *Tissue Eng. Regen. Med.* **2022**, *19*, 309–319. [CrossRef]
19. Hathout, R.M.; Omran, M.K. Gelatin-based particulate systems in ocular drug delivery. *Pharm. Dev. Technol.* **2016**, *21*, 379–386. [CrossRef]
20. Abdelhedi, O.; Salem, A.; Nasri, R.; Nasri, M.; Jridi, M. Food applications of bioactive marine gelatin films. *Curr. Opin. Food Sci.* **2022**, *43*, 206–215. [CrossRef]
21. Han, L.; Xu, J.L.; Lu, X.; Gan, D.L.; Wang, Z.X.; Wang, K.F.; Zhang, H.P.; Yuan, H.P.; Weng, J. Biohybrid methacrylated gelatin/polyacrylamide hydrogels for cartilage repair. *J. Mater. Chem. B* **2017**, *5*, 731–741. [CrossRef] [PubMed]
22. Gyles, D.A.; Castro, L.D.; Silva, J.O.C.; Ribeiro-Costa, R.M. A review of the designs and prominent biomedical advances of natural and synthetic hydrogel formulations. *Eur. Polym. J.* **2017**, *88*, 373–392. [CrossRef]
23. Gajendiran, M.; Rhee, J.S.; Kim, K. Recent Developments in Thiolated Polymeric Hydrogels for Tissue Engineering Applications. *Tissue Eng. Part B Rev.* **2018**, *24*, 66–74. [CrossRef]
24. Cho, H.; Kim, J.; Kim, S.; Jung, Y.C.; Wang, Y.; Kang, B.J.; Kim, K. Dual delivery of stem cells and insulin-like growth factor-1 in coacervate-embedded composite hydrogels for enhanced cartilage regeneration in osteochondral defects. *J. Control. Release* **2020**, *327*, 284–295. [CrossRef]
25. Kim, S.; Kim, J.; Gajendiran, M.; Yoon, M.; Hwang, M.P.; Wang, Y.D.; Kang, B.J.; Kim, K. Enhanced Skull Bone Regeneration by Sustained Release of BMP-2 in Interpenetrating Composite Hydrogels. *Biomacromolecules* **2018**, *19*, 4239–4249. [CrossRef] [PubMed]
26. Fernandez-Ramos, A.A.; Marchetti-Laurent, C.; Poindessous, V.; Antonio, S.; Laurent-Puig, P.; Bortoli, S.; Loriot, M.A.; Pallet, N. 6-mercaptopurine promotes energetic failure in proliferating T cells. *Oncotarget* **2017**, *8*, 43048–43060. [CrossRef]
27. Zaboli, M.; Raissi, H.; Zaboli, M. Investigation of nanotubes as the smart carriers for targeted delivery of mercaptopurine anticancer drug. *J. Biomol. Struct. Dyn.* **2022**, *40*, 4579–4592. [CrossRef]
28. Zhang, T.; Gan, Z.; Zhen, S.; Hu, Y.; Hu, X. Ratiometric fluorescent probe based on carbon dots and Zn-doped CdTe QDs for detection of 6-Mercaptopurine. *Opt. Mater.* **2022**, *134*, 113196. [CrossRef]

29. Koshy, S.T.; Desai, R.M.; Joly, P.; Li, J.Y.; Bagrodia, R.K.; Lewin, S.A.; Joshi, N.S.; Mooney, D.J. Click-Crosslinked Injectable Gelatin Hydrogels. *Adv. Healthc. Mater.* **2016**, *5*, 541–547. [CrossRef]
30. Andreazza, R.; Morales, A.; Pieniz, S.; Labidi, J. Gelatin-Based Hydrogels: Potential Biomaterials for Remediation. *Polymers* **2023**, *15*, 1026. [CrossRef]
31. Zhang, J.J.; Wang, J.; Zhang, H.; Lin, J.H.; Ge, Z.G.; Zou, X.N. Macroporous interpenetrating network of polyethylene glycol (PEG) and gelatin for cartilage regeneration. *Biomed. Mater.* **2016**, *11*, 035014. [CrossRef] [PubMed]
32. Raman, T.S.; Kuehnert, M.; Daikos, O.; Scherzer, T.; Krommelbein, C.; Mayr, S.G.; Abel, B.; Schulze, A. A study on the material properties of novel PEGDA/gelatin hybrid hydrogels polymerized by electron beam irradiation. *Front. Chem.* **2023**, *10*, 1094981. [CrossRef] [PubMed]
33. Gong, M.; Yang, J.; Li, Y.S.; Gu, J.L. Glutathione-responsive nanoscale MOFs for effective intracellular delivery of the anticancer drug 6-mercaptopurine. *Chem. Commun.* **2020**, *56*, 6448–6451. [CrossRef]
34. Kennedy, L.; Sandhu, J.K.; Harper, M.E.; Cuperlovic-Culf, M. Role of Glutathione in Cancer: From Mechanisms to Therapies. *Biomolecules* **2020**, *10*, 1429. [CrossRef]
35. Li, Y.; An, L.; Lin, J.; Tian, Q.; Yang, S. Smart nanomedicine agents for cancer, triggered by pH, glutathione, H_2O_2, or H_2S. *Int. J. Nanomed.* **2019**, *14*, 5729–5749. [CrossRef] [PubMed]
36. Justus, C.; Dong, L.; Yang, L. Acidic tumor microenvironment and pH-sensing G protein-coupled receptors. *Front. Physiol.* **2013**, *4*, 354. [CrossRef]
37. Deirram, N.; Zhang, C.H.; Kermaniyan, S.S.; Johnston, A.P.R.; Such, G.K. pH-Responsive Polymer Nanoparticles for Drug Delivery. *Macromol. Rapid. Comm.* **2019**, *40*, e1800917. [CrossRef]
38. Kim, J.H.; Kim, S.; So, J.H.; Kim, K.; Koo, H.J. Cytotoxicity of Gallium-Indium Liquid Metal in an Aqueous Environment. *ACS Appl. Mater. Inter.* **2018**, *10*, 17448–17454. [CrossRef]
39. Wang, M.O.; Etheridge, J.M.; Thompson, J.A.; Vorwald, C.E.; Dean, D.; Fisher, J.P. Evaluation of the In Vitro Cytotoxicity of Cross-Linked Biomaterials. *Biomacromolecules* **2013**, *14*, 1321–1329. [CrossRef]
40. Ji, G.F.; Zhang, Y.; Si, X.H.; Yao, H.C.; Ma, S.; Xu, Y.D.; Zhao, J.Y.; Ma, C.; He, C.L.; Tang, Z.H.; et al. Biopolymer Immune Implants' Sequential Activation of Innate and Adaptive Immunity for Colorectal Cancer Postoperative Immunotherapy. *Adv. Mater.* **2021**, *33*, e2004559. [CrossRef]
41. Wang, W.J.; Fang, C.J.; Wang, X.Z.; Chen, Y.X.; Wang, Y.N.; Feng, W.; Yan, C.H.; Zhao, M.; Peng, S.Q. Modifying mesoporous silica nanoparticles to avoid the metabolic deactivation of 6-mercaptopurine and methotrexate in combinatorial chemotherapy. *Nanoscale* **2013**, *5*, 6249–6253. [CrossRef] [PubMed]
42. Nezhad-Mokhtari, P.; Ghorbani, M.; Mahmoodzadeh, F. Smart co-delivery of 6-mercaptopurine and methotrexate using disulphide-based PEGylated-nanogels for effective treatment of breast cancer. *New J. Chem.* **2019**, *43*, 12159–12167. [CrossRef]
43. Jakubowski, M.; Kucinska, M.; Ratajczak, M.; Pokora, M.; Murias, M.; Voelkel, A.; Sandomierski, M. Zinc forms of faujasite zeolites as a drug delivery system for 6-mercaptopurine. *Microporous Mesoporous Mater.* **2022**, *343*, 112194. [CrossRef]
44. Gajendiran, M.; Kim, S.; Jo, H.; Kim, K. Fabrication of pH responsive coacervates using a polycation-b-polypropylene glycol diblock copolymer for versatile delivery platforms. *J. Ind. Eng. Chem.* **2020**, *90*, 36–46. [CrossRef]
45. Kim, S.; Lee, J.; Hwang, M.P.; Wang, Y.; Kim, K. Influence of fiber architecture and growth factor formulation on osteoblastic differentiation of mesenchymal stem cells in coacervate-coated electrospun fibrous scaffolds. *J. Ind. Eng. Chem.* **2019**, *79*, 236–244. [CrossRef]
46. Kim, K.; Chen, W.C.W.; Heo, Y.; Wang, Y. Polycations and their biomedical applications. *Prog. Polym. Sci.* **2016**, *60*, 18–50. [CrossRef]
47. Rehman, S.U.; Yaseen, Z.; Husain, M.A.; Sarwar, T.; Ishqi, H.M.; Tabish, M. Interaction of 6 Mercaptopurine with Calf Thymus DNA–Deciphering the Binding Mode and Photoinduced DNA Damage. *PLoS ONE* **2014**, *9*, e93913. [CrossRef] [PubMed]

gels

Article

A Light Scattering Investigation of Enzymatic Gelation in Self-Assembling Peptides

Stefano Buzzaccaro [1,*], Vincenzo Ruzzi [1], Fabrizio Gelain [2,3] and Roberto Piazza [1]

[1] Department of Chemistry, Materials Science, and Chemical Engineering (CMIC), Politecnico di Milano, Edificio 6, Piazza Leonardo da Vinci 32, 20133 Milano, Italy
[2] Unità di Ingegneria Tissutale, Fondazione IRCCS Casa Sollievo della Sofferenza, 71013 San Giovanni Rotondo, Italy
[3] Center for Nanomedicine and Tissue Engineering, ASST GOM Niguarda, 20162 Milano, Italy
* Correspondence: stefano.buzzaccaro@polimi.it

Abstract: Self-assembling peptides (SAPs) have been increasingly studied as hydrogel–former gelators because they can create biocompatible environments. A common strategy to trigger gelation, is to use a pH variation, but most methods result in a change in pH that is too rapid, leading to gels with hardly reproducible properties. Here, we use the urea–urease reaction to tune gel properties, by a slow and uniform pH increase. We were able to produce very homogeneous and transparent gels at several SAP concentrations, ranging from $c = 1\,\mathrm{g/L}$ to $c = 10\,\mathrm{g/L}$. In addition, by exploiting such a pH control strategy, and combining photon correlation imaging with dynamic light scattering measurements, we managed to unravel the mechanism by which gelation occurs in solutions of $(\mathrm{LDLK})_3$-based SAPs. We found that, in diluted and concentrated solutions, gelation follows different pathways. This leads to gels with different microscopic dynamics and capability of trapping nanoparticles. At high concentrations, a strong gel is formed, made of relatively thick and rigid branches that firmly entrap nanoparticles. By contrast, the gel formed in dilute conditions is weaker, characterized by entanglements and crosslinks of very thin and flexible filaments. The gel is still able to entrap nanoparticles, but their motion is not completely arrested. These different gel morphologies can potentially be exploited for controlled multiple drug release.

Keywords: gels; self-assembling peptide; photon correlation imaging; DLS; enzymatic gelation

1. Introduction

The spontaneous assembly of a wide variety of molecules, called gelators, dispersed in water, under the influence of different non-covalent forces such as hydrogen bonding, π-stacking, hydrophobic, and ionic forces [1–4], can lead to the formation of molecular hydrogels. These materials have sparked great interest for their possible use in controlled drug release [5–8], regenerative medicine [9], and tissue engineering [10–12].

In this context, the key strategy is to develop synthetic biomimetic hydrogels, that reproduce many of the properties of the extracellular matrix (ECM) [13–15]. In recent years, self-assembling peptides (SAPs) have been commonly used as gelators, because they form nanofibrous matrices that resemble the fibrillar matrix of the natural ECM [16]. In order to trigger the self-assembly, an external stimulus is usually needed [4,17], such as adding a co-solvent [18–21], irradiating the sample with UV light [22,23], varying the temperature [24,25], or changing the ionic strength [26] or the pH of the system [27–31].

In the case of SAPs that respond to a pH change, the gelators contain a pH-sensitive functionality. The degree of ionization of the functional group governs the solubility of these molecules. The gelators can be classified as acid-triggered or base-triggered [2], depending on the properties of the ionizable group. In early attempts, the pH was varied by adding a strong acid or base to the peptide liquid solution [30,31]. However, this led to a rapid change in pH, leading to heterogeneous gels, with properties that were difficult to replicate, because the rate of mixing of the components was slower than the rate of gelation [27,32]. To overcome this issue, it was suggested to use an additive that slowly hydrolyses with water, forming an acid or a base. If the dissolution of the additive is much faster than the hydrolysis, a homogeneous medium is generated, and a uniform pH variation throughout the system takes place. Because a larger number of SAPs can form gels when a solution at high pH is acidified, the first method that exploited this strategy used glucono-δ-lactone (GdL) [32]. The hydrolysis of GdL is slow and gives gluconic acid, which decreases the pH in a controllable way [33]. The use of a kinetically controlled acidification, resulted in reproducible and uniform gels, and the improvement in gel homogeneity translated into improved mechanical properties [32]. Only recently, a similar strategy was employed to control the gelation of base-triggered SAPs. In this case, a controlled alkalinization of the solution was achieved by using the urea–urease reaction [28], that involves hydrolysis of urea by urease and production of ammonia, increasing the pH [2]. While the concentration of GdL controls both the final gel pH and the rate of the gelation process, the use of the urea–urease reaction, allows these two aspects to be independently controlled. In fact, the hydrolysis rate depends on the concentration of urease, whereas the amount of urea sets the final pH. A further benefit of the use of enzyme-induced gelation, is that the rate of hydrolysis is sufficiently slow that observation of the SAP assembly process is possible [32,34].

While the micro-structure of peptide-based hydrogels, and their mechanical properties, have been extensively studied, with several techniques [21,35,36], such as rheometry [37–39], static small-angle scattering [40,41], and transmission electron microscopy [42,43], the kinetics of aggregation and the following gelation have been investigated much less. A relatively small number of works have investigated the assembly process using circular dichroism (CD) [44–47], Fourier-transform infrared spectroscopy (FTIR) [48], and thioflavin T fluorescence [34,49]. To our knowledge, light scattering studies of the SAP self-assembly kinetics, are still lacking. The main aim of this work, is to show that a fruitful combination of enzyme-controlled pH variation with photon correlation imaging (PCI) and dynamic light scattering (DLS) measurements, can help to elucidate some aspects of the mechanism that governs the gel formation in SAP solutions.

2. Results and Discussion

2.1. pH Evolution in the Urea–Urease Reaction: Optimizing Parameters to Obtain Homogeneous Gels

When dissolved in water, SAPs show an acidic behavior, characterized by a logarithmic decay of the solution pH with the peptide concentration (see Figure 1). This acidic behavior of the SAPs, is important to define the amount of acid to add to the solution in order to slow down the hydrolysis kinetics. To obtain a homogeneous gel, it is important that the peptide dissolution is significantly faster than the urea hydrolysis. This leads to a uniform pH variation throughout the system. It is well known that the activity of urease strongly depends on pH, with a maximum rate of conversion around $\text{pH} = 7$ [50,51]. For our purpose, it is important to work with a low initial pH of the solution, in order to reduce the activity of the enzyme. When the initial pH is below 4, the production of ammonia is limited. However, after a certain time, a rapid conversion to the high pH state occurs [52]. In these conditions, the urea–urease reaction is characterized by a lag-phase, whose duration can be controlled by the nature and concentration of the acid used [2]. We found that adding 0.012 mM of acetic acid to our solution, reduced the initial pH value to a value of 3.7, that is optimal for our purpose.

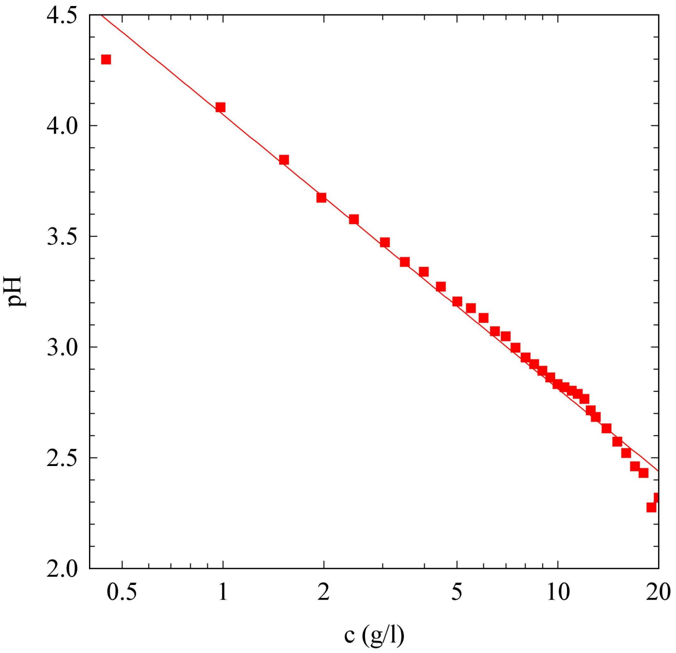

Figure 1. Dependence of the solution pH on the SAP concentration (log scale). The continuous line is a logarithmic fit, $\mathrm{pH} = -1.24\log(5.36 \times 10^{-4}c)$.

Panel (a) of Figure 2, shows the urea–urease pH kinetics at different values of urea and urease, at a fixed acetic acid concentration. In the absence of the enzyme, as expected, the pH of the solution does not change. When we add urease, the data show that the rate of alkalinization is slow below pH = 5. In fact, ammonia salts are formed and the acid is neutralized. Using acetic acid, a weak acid, we produce acetic acid–ammonium acetate, a buffer that resists the pH change [50]. The time evolution of the reaction is governed by the initial concentrations of urea and urease. Only the amount of urea sets the final pH: the larger the amount of urea, the higher the final pH. In strongly acidic conditions, the formation of ammonia–ammonium buffer limits the maximum pH that can be reached [2,50,53]. On the contrary, the value of the lag-time is related both to the amount of urea and urease [28,50]. If we compare the two samples with the same amount of urea (40 mM, squares and triangles in Figure 2), we note that the lag-time changes from 1000 s to 1300 s, on halving the enzyme concentration. If we focus on the curves with the same urease concentration (13 U/mL, triangles and full dots in Figure 2), we note that when doubling the amount of urea, the lag-time shows a thirty percent reduction. In order to obtain final gels with the same pH, we decided to work with a fixed concentration of urea, equal to 60 mM, and tune the lag-time, simply by changing the amount of enzyme we used.

Panel (b) of Figure 2, shows the urea–urease pH kinetics for different values of urease concentration. As expected, the initial values of pH are the same for all the samples, fixed by the acetic acid concentration. In addition, the final pHs are the same, and they are set by the amount of urea in solution. The lag-phase increases for lower concentrations of urease, because the production of ammonia is slower. We note that all the curves show a slow pH rate increase for $\mathrm{pH} < 5$, due to the acid–ammonium acetate buffer effect, a rapid increase in the rate between $5 < \mathrm{pH} < 8.5$, and a pronounced slowing down of the pH growth rate when the ammonia–ammonium buffer concentration is no longer negligible. To be more quantitative, in the inset of Figure 2b, we plot, for each urease concentration we studied, the times at which the samples reach pH values equal to 5, 6.5, and 8.5. In the limited range of urease concentrations we studied, the lag-time, arbitrarily defined as the time at which the sample reaches $\mathrm{pH} = 5$, decreases exponentially with the urease activity, and seems to reach an asymptotic value of about 9 min. Our data also clearly indicate that the duration of the phase of rapid increase in pH, is strongly dependent on the urease concentration. In fact, for a urease activity equal to 13 U/mL, the sample takes around 5 min to change from pH = 5 to pH = 8.5, whereas for the minimum urease concentration we studied, the system needs more than 30 min to show the same pH increase. In the following section, we focus on samples prepared with a urease concentration of 13 U/mL.

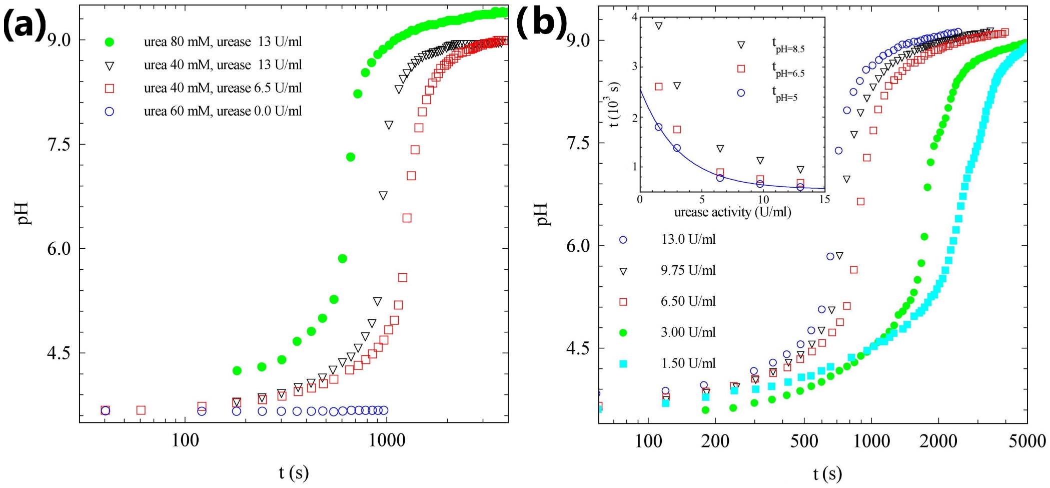

Figure 2. (**a**) Time evolution of the pH in the urea–urease reaction, for samples characterized by the same amount of acetic acid (0.012 mM) but different concentrations of urea and urease, as indicated in the legend. (**b**) Time evolution of the pH in the urea–urease reaction, for samples characterized by the same amount of acetic acid (0.012 mM) and urea (60 mM), but different urease activity. Inset: time needed to reach pH = 5 (circles), pH = 6.5 (squares), and pH = 8.5 (triangles). The continuous line is an exponential fit.

The preliminary study of the hydrolysis reaction kinetics in the presence of acetic acid, allowed us to find the best conditions to obtain homogeneous SAP gels. In fact, while the addition of NaOH resulted in an instantaneous pH jump, inducing a gelation that begins just after addition of the base, yielding a non-homogeneous and whitish gel, exploiting the urea–urease reaction to change the pH of the solution, allows us to obtain very transparent and homogeneous gels (panels (a) and (b) of Figure 3) at several SAP concentrations, ranging from $c = 1\,\mathrm{g/L}$ to $c = 10\,\mathrm{g/L}$. At higher SAP concentrations, and a fixed acetic acid dilution, the gelation kinetics were not reliable. This is probably due to an initial pH value that was too low to initiate the urea hydrolysis. In fact, urease loses activity at pH $\simeq$ 3 or below [2]. To obtain consistent results, it is important to keep the initial pH between 3.5 and 4. To emphasize the importance of the slow variation in the pH, in panel (c) of Figure 3, we show the speckle pattern measured for a gel obtained with the same urea, urease, and SAP concentrations as the sample in panel (b), but without the addition of the acetic acid. In this case, the initial pH is not sufficiently low, and the urea–urease reaction is so fast that the sample starts gelating during the mixing. The final gel, as expected, is not homogeneous, and keeps memory of the mixing dynamics.

In what follows, we will focus on two samples, characterized by the two SAP concentrations that bounded the interval we investigated: the sample at $c = 10\,\mathrm{g/L}$ will be referred to as Sample H and the less diluted sample, prepared at $c = 1\,\mathrm{g/L}$, will be referred to as Sample L.

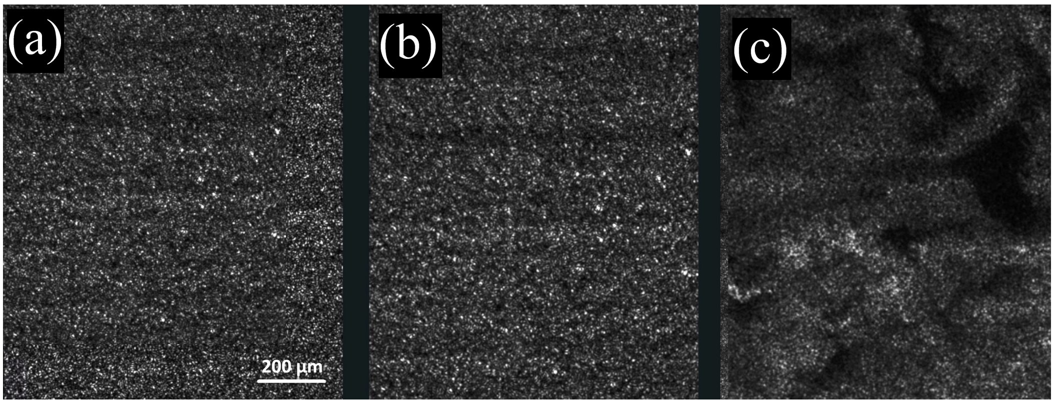

Figure 3. (**a**) Speckle pattern of sample H, two hours after its preparation. (**b**) Speckle pattern of sample L, two hours after its preparation. (**c**) Speckle pattern of a sample with the same composition as sample L, but without the addition of acetic acid, two hours after its preparation. In this case, a heterogeneous speckle pattern is clearly visible, demonstrating the sample's inhomogeneity.

2.2. Light Scattering Study of the SAPs' Aggregation Kinetics

2.2.1. Sample H

In panel (a) of Figure 4, we plot the evolution with time of pH, scattered intensity, and normalized degree of the time correlation $\hat{c}_I(\tau = 10\,\text{s}, t)$. After 2400 s, the data show a marked growth in the scattering intensity. Eventually the intensity reaches a value about 15 times larger than its initial value. This intensity increase takes places about 1000 s after the end of the pH lag-time. Interestingly, a small but continuous growth in the scattering intensity can also be observed during the pH lag-time. The variation in scattered light is due to a change in the sample structure factor, suggesting that the SAPs also start to slightly aggregate during the pH lag-time. It is therefore tempting to state, that the gel formation coincides with the abrupt increase in the scattering intensity.

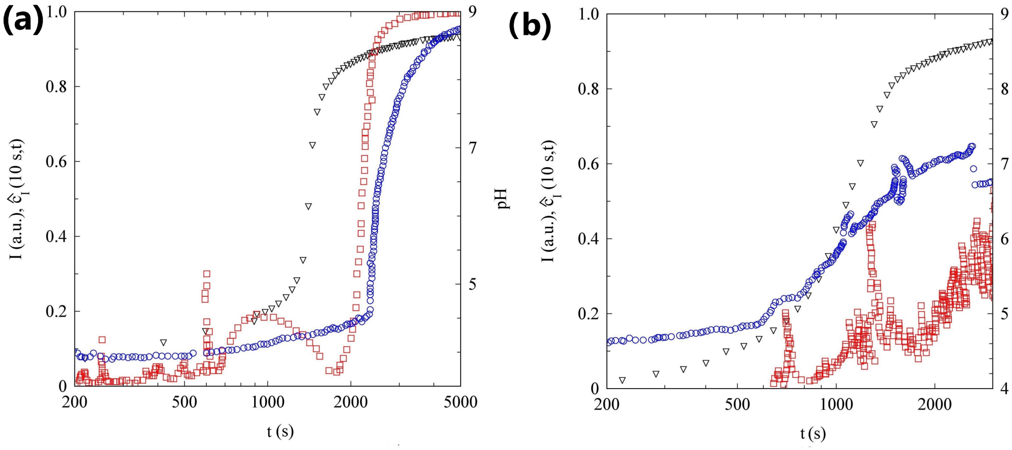

Figure 4. (**a**) Temporal evolution of pH (triangles), scattered intensity (circles), and $\hat{c}_I(10\,\text{s}, t)$ (squares) of sample H. (**b**) Temporal evolution of pH (triangles), scattered intensity (circles), and $\hat{c}_I(10\,\text{s}, t)$ (squares) of sample L.

However, the data in Figure 4a suggest a slightly different scenario. Before the sample gels, because the decay time of ICS for a fluid SAP is at least three orders of magnitude faster than 10 s, the correlation index is close to zero and quite noisy. However, around $t_g = 1800\,\text{s}$, $\hat{c}_I(\tau = 10\,\text{s}, t)$ shows a rapid increase, reaching a value of about 1 in a few minutes. A value close to 1, indicates that the speckle pattern is fully arrested on the time scale of 10 s. The whole sample turned quite rapidly into an arrested gel. It is important to stress that the sample gelation *anticipates* the rapid intensity growth, by about 10 min.

Unfortunately, the PCI temporal resolution does not allow us to monitor the sample dynamics during the pH lag-time phase and in the first phases of the gelation process. To overcome this limitation, we exploit the capability of DLS to monitor the fast dynamics of non-arrested systems. In panel (a) of Figure 5, we plot the ICFs measured at different times, starting 60 s after the sample preparation. Our data indicate that, before t_g, the ICFs have a contrast close to one and fully decorrelate, thus the sample is still liquid. In this phase the sample dynamics slow down, suggesting the formation of larger aggregates, in accordance with the slow growth in the scattering intensity, monitored by PCI. The contrast of the intensity correlation function decreases abruptly and goes to zero for $t > t_g$, suggesting that a non-ergodic arrested gel phase is formed.

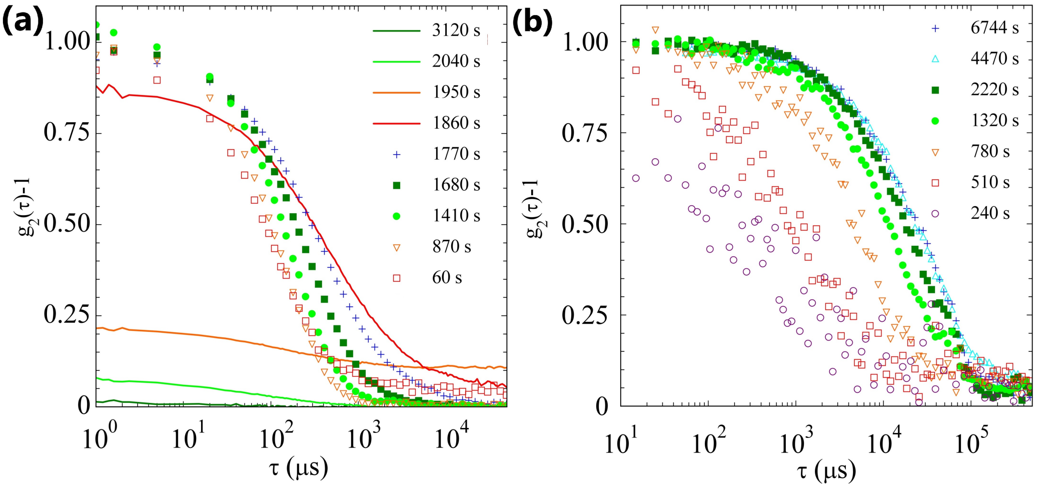

Figure 5. (**a**) ICFs at different times, indicated in the legend, for sample H. Symbols stand for ergodic samples, while continuous lines indicate ICFs taken after t_g, when the time averaged ICF is no longer reliable. (**b**) ICFs at different times, indicated in the legend, for sample L.

2.2.2. Sample L

In panel (b) of Figure 4, we plot the evolution with time of the pH, scattered intensity, and of the normalized degree of the time correlation $\hat{c}_I(\tau = 10\,\mathrm{s}, t)$, for sample L. The scattering intensity of this sample slowly increases with time, up to a factor of about 5. The data are rather noisy, because the sample concentration is an order of magnitude smaller than in the previous case: the light scattered by this sample is close to the detection limit of our PCI setup. The intensity growth rate still increases at the end of the pH lag-phase, but the rise is much milder than in the more concentrated sample. In addition, the variation in the correlation index is much more limited and the system is never fully arrested for $\tau = 10\,\mathrm{s}$. Removing the cell from the PCI setup and turning it upside down, suggests that a very viscous solution, possibly a gel with a very low yield stress, forms.

In this case too, we resort to DLS to better characterize the sample's dynamics. Panel (b) of Figure 5, shows the ICFs measured at several times, starting 240 s after the sample preparation. Initially, the scattered light is low and the correlation function is very noisy. The scattered intensity increases with time and the correlation functions are more reliable. Our data indicate a continuous slowing down of the dynamics, but without a detectable decrease in the contrast. The sample, at least at the q-vector we are probing, remains ergodic and never shows arrested dynamics.

2.2.3. Comparison of Samples' Dynamics

We report in Figure 6, the decay time of the ICFs, $\tau_{1/e}$, defined as $g_2(\tau_{1/e}) - 1 = e^{-1}$, measured for both samples H and L, as a function of time. The two samples, as already discussed, show a radically different behavior. For sample H, the decay time initially grows slowly, until it rapidly diverges at the gelation time. On the contrary, for the L sample, the value of $\tau_{1/e}$ increases with time, reaching a large but *finite* value, almost two orders of magnitude larger than the initial one. We note, quite unexpectedly, that when both the samples are still liquid, the dynamics of sample L are, at least, an order of magnitude slower than the dynamics of sample H. This suggests that the aggregates formed in the dilute solution are less dense but occupy a larger volume.

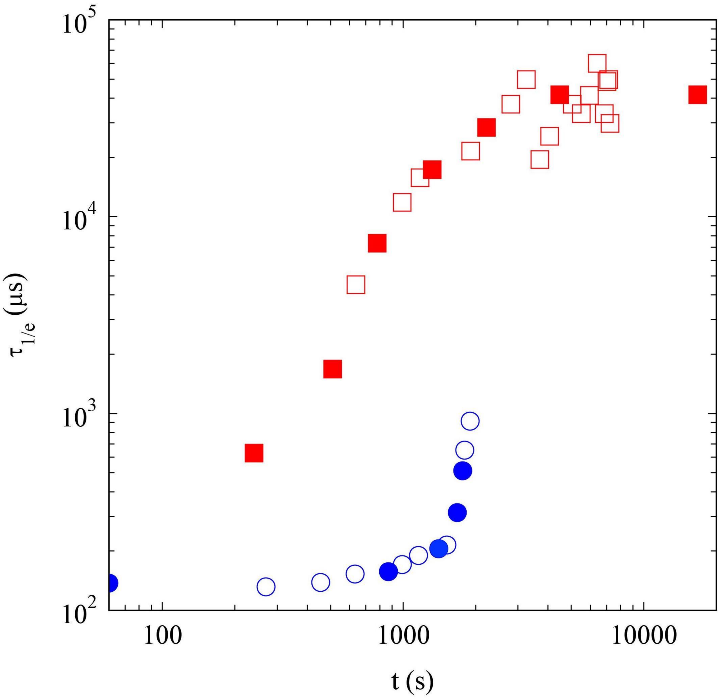

Figure 6. Decay times of the ICFs $\tau_{1/e}$ as a function of time, for samples H (circles) and L (squares). Full points refer to the ICFs shown in Figure 5.

2.3. Light Scattering Study of the SAPs Solution Seeded with Nanoparticles

The above results do not completely rule out the formation of an arrested phase for sample L. In fact, in principle, its dynamics could be arrested at lower q-vectors. Unfortunately, DLS experiments at low angles, where the dynamics are slower, in samples whose dynamics are not stationary in time, is a very challenging task, mainly because it is difficult to ensure that the duration, δt, of a DLS experiment is still much shorter than the characteristic timescale of the sample evolution. For this reason we decided to adopt a different and complementary approach. We seeded our sample with small colloidal particles, with a diameter of $\sigma = 192\,\mathrm{nm}$. If SAPs form an arrested phase, we would expect that the motion of the tracers would be limited, if not fully arrested.

2.3.1. Sample H

In the case of seeded samples, the scattered light mainly originates from the tracer particles. In our experiments we do not observe any signs of intensity variation, suggesting that the SAP aggregation does not promote particle clustering.

In panel (a) of Figure 7, we plot the temporal evolution of pH, $c_I(\tau = 0\,\mathrm{s}, t)$, and $\hat{c}_I(\tau = 10\,\mathrm{s}, t)$ for the more concentrated sample. We note that $c_I(\tau = 0\,\mathrm{s}, t)$, slightly increasing during the initial part of the experiment, shows a marked growth at $t = 1500\,\mathrm{s}$, about 500 s after the end of the lag-phase, and levels off when the pH growth rate rapidly decreases.

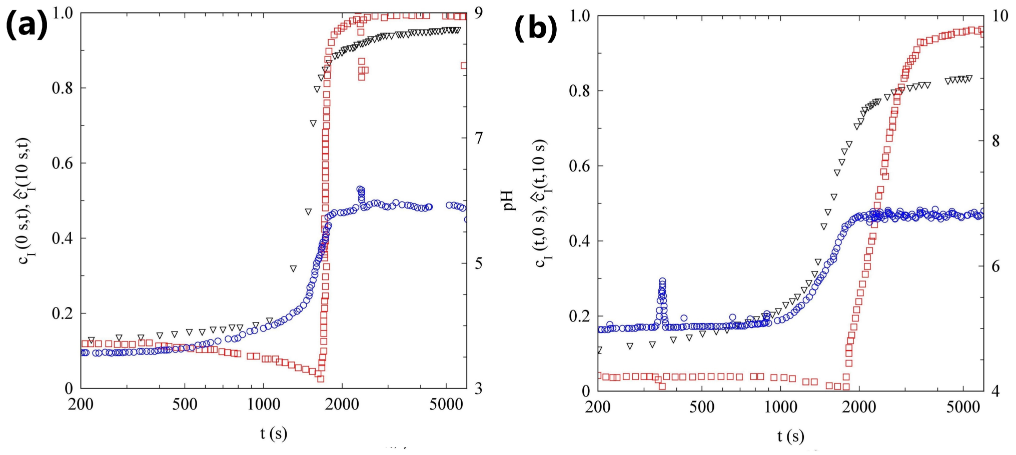

Figure 7. (**a**) Temporal evolution of the pH (triangles), $c_I(0\,\text{s}, t)$ (circles), and $\hat{c}_I(10\,\text{s}, t)$ (squares) of sample H seeded with PMMA nanoparticles. (**b**) Temporal evolution of the pH (triangles), $c_I(0\,\text{s}, t)$ (circles), and $\hat{c}_I(10\,\text{s}, t)$ (squares) of sample L seeded with PMMA nanoparticles.

Since our exposure time is $t_e = 10\,\text{ms}$, the marked increase in $c_I(\tau = 0\,\text{s}, t)$ indicates that the characteristic timescale of the tracer dynamics is smaller than 10 ms during the pH lag-phase, but rapidly increases approaching the gel phase. In fact, when $c_I(\tau = 0\,\text{s}, t)$ reaches a stationary value, suggesting that the dynamics appear static on the timescale of t_e, the $\hat{c}_I(\tau = 10\,\text{s}, t)$ starts to increase and in a few minutes reaches a value close to 1, indicating that the tracers are arrested inside the gel matrix.

This picture is confirmed by the ICF measured by DLS, shown in panel (a) of Figure 8. The sample dynamics become slower with time but the ICF completely decays to zero in less of 10 ms for $t < 1530\,\text{s}$. This is consistent with the PCI analysis, that shows a growth in $c_I(\tau = 0\,\text{s}, t)$ only for $t > 1500\,\text{s}$. After $t = 1620\,\text{s}$, the sample becomes non-ergodic and the contrast rapidly drops to zero in less than 3 min. The sample is fully arrested for $t > 1710\,\text{s}$, in accordance with the increase in $c_I(\tau = 10\,\text{s}, t)$ starting at $t = 1700\,\text{s}$.

2.3.2. Sample L

The data in panel (b) of Figure 8, that refer to the most diluted sample, show the temporal evolution of pH, $c_I(\tau = 0\,\text{s}, t)$, and $\hat{c}_I(\tau = 10\,\text{s}, t)$. If compared with panel (a) of Figure 7, samples H and L show strong analogies: the $c_I(\tau = 0\,\text{s}, t)$ increases at the end of the pH lag-phase and the tracer dynamics are fully arrested for $t > 4000\,\text{s}$. The only qualitative difference concerns the speed of the gelation process: while for the concentrated sample the $c_I(\tau = 10\,\text{s}, t)$ takes less than 2 min to change from 0 to 1, in the case of the more diluted sample, about 20 min are required.

Although the gelation of the two samples shares some similarities, the DLS measurements shown in panel (b) of Figure 8, allow us to observe a very important difference. The analysis of the ICFs, shows that the gelation process is characterized by three different stages: (I) For $t < 1050\,\text{s}$, the sample is fluid and ergodic, the contrast is equal to 1, and the dynamics slows with time; (II) for $t > 1050\,\text{s}$ the contrast slowly decreases, reaching a final value around 0.77 for $t = 2580\,\text{s}$. In this stage, the sample dynamics also slow down; (III) the contrast does not change anymore but the dynamics continue to slowly evolve. A final contrast of around 0.77, indicates that the motion of the tracers is not completely arrested at the probed length scale, the particles are, on average, bound to fixed positions, but they can still explore a region of the order of a few tens of nanometers. If we compare the sample evolution measured with DLS and PCI, we can see that the end of the first stage coincides with the time at which the $c_I(\tau = 0\,\text{s}, t)$ starts to increase. The end of the second stage takes place when $c_I(\tau = 10\,\text{s}, t)$ begins to level off.

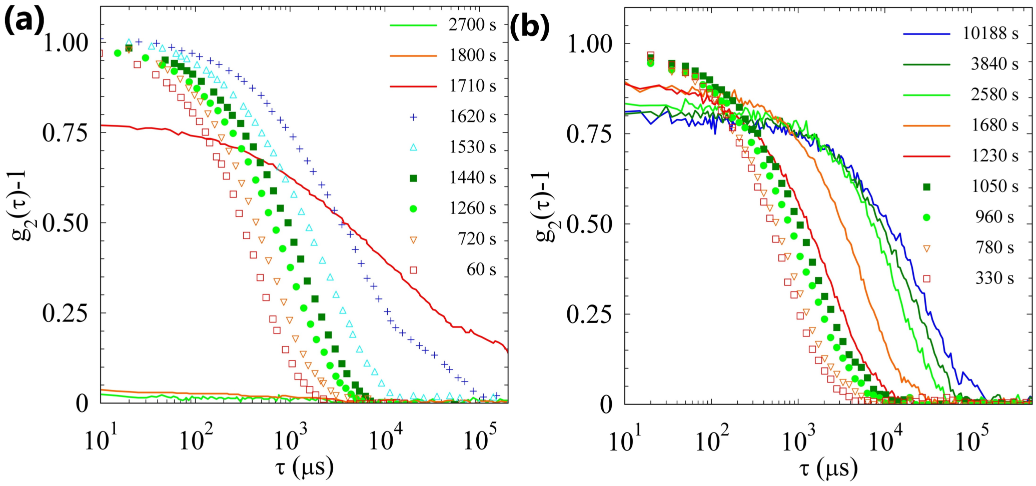

Figure 8. (**a**) ICFs at different times, indicated in the legend, for sample H seeded with PMMA nanoparticles. (**b**) ICFs at different times, indicated in the legend, for sample L seeded with PMMA nanoparticles. In both panels, symbols stand for ergodic samples, while continuous lines indicate ICFs taken after t_g, when the time averaged ICF is no longer reliable.

2.4. Discussion

Our results show that the approach to a gel phase follows different pathways in diluted and concentrated SAP solutions. Figure 4 shows that there is a delay of a few minutes between the pH jump and the gel formation. Several studies of similar fibril–former gelators, showed the existence of a lag-phase, during which the peptide aggregation is limited, followed by a stage in which the aggregate concentration rapidly increases [54–56]. It was concluded that, in these SAP solutions, the self-assembly process is characterized by a nucleated reaction, and several mechanisms were proposed to explain such a process [57–60]. Panels (b) of Figures 4 and 5, on the contrary, clearly indicate that, in a sufficiently diluted system, the raising of the pH *gives time* to the peptide aggregation. The difference becomes evident if we contrast the results of the DLS measurements, as shown in Figure 6. Sample L is characterized by a continuous slowing down of the dynamics, suggesting that quite large aggregates start to form from the beginning and their number and/or length increase with time. Conversely, in sample H, we note an initial very slow formation of smaller (and probably more compact) aggregates, as shown by the fact the decorrelation times are at least an order of magnitude lower than in the L sample. After a lag time of about 30 min, there is a rapid increase in the aggregate size and number, that leads to gelation. Interestingly, this aggregation process continues after the gel formation, as demonstrated by the increase in the scattered light measured by PCI, for at least one hour.

The concurrence of different mechanisms of self-assembly in hydrogel-forming peptides, whose rates depend on the monomer concentration, has been observed previously [34]. In particular, the first mechanism proposed for fibril formation, is the aggregation of monomers to form stable clusters [61,62]. The association of new monomers to the ends of existing protofibrils, is responsible for the measured increase in the fibril mass concentration. This aggregation mechanism, usually called *first nucleation*, is an entirely monomer-dependent mechanism, and it is described as a homogeneous, uncatalyzed reaction [55]. This mechanism favors the formation of long and thin fibrils. A second proposed mechanism of new fibril formation, is a self-catalyzed process. The pre-existing fibrils act as nuclei for the fibrillar formation. This is a *secondary nucleation* mechanism: gelators nucleate on the surface of the existing aggregates [63]. This lateral growth favors the formation of more compact aggregates. Our results suggest that primary nucleation is the favored mechanism of self-assembly in the diluted system, while secondary nucleation becomes dominant when the peptide concentration increases.

The gels' micro-structures and properties reflect these differences. At high concentration, a strong gel is formed, made of relatively thick and rigid branches that firmly entrap nanoparticles. On the scale of hundreds of nanometers probed by DLS, the system is completely arrested. In contrast, the gel formed in the diluted conditions is weaker, characterized by entanglements and crosslinks of very thin and flexible filaments. Between two crosslinked points, the motion of the strands is still possible and the dynamics is never arrested. The microscopic dynamics slows down with time, possibly reflecting the increase in filament stiffness as a consequence of the increase in diameter associated with monomers' lateral adhesion, that take place after the gel formation. Moreover, the gel is able to entrap nanoparticles, but their motion is not completely arrested and reflects the non-arrested motion of the filamentous matrix.

3. Conclusions

In this work, we have used urea–urease hydrolysis to control the gelation of a base-triggered SAP system. The use of the urea–urease reaction, allows the final pH and the gelation rate to be independently controlled: the final pH is controlled by the amount of urea, whereas the hydrolysis rate depends on the concentration of urease. We were able to produce very homogeneous and transparent gels at several SAP concentrations, ranging from $c = 1\,\mathrm{g/L}$ to $c = 10\,\mathrm{g/L}$. Better control on the gelation kinetic of SAPs, could be of crucial importance for several reasons: (1) it will improve the reproducibility of the scaffold mechanical properties; as a consequence (2) it will allow for a standardized reaction, related to the mechanical properties of a seeded cell in 3D cell culture systems, or scaffolds to be implanted; (3) slow gelation also opens the door to the inclusion of chemotactic agents following a specific spatial gradient, capable, for example, of triggering cell migration. Using a slow hydrolysis reaction to alter the pH, also allowed us to monitor the SAP aggregation process with light scattering methods, providing new insights into the gelation mechanism. We find that, in diluted and concentrated solutions gelation follows different pathways. This leads to gels with different microscopic dynamics and capability of trapping nanoparticles. Interestingly, well-controlled different gel morphologies within the scaffold, can also be used to achieve different kinetics of release of multiple drugs in vitro, where needed.

Further studies, combining the light scattering methods we used, with complementary techniques, such as time-resolved small-angle X-ray scattering [41], CD [46], and FTIR spectroscopy [48], are required, to shed full light on SAP gelation and to strengthen our findings.

The methodology we used in this work, can be extended to other base-triggered molecular gelators [19,20]. Understanding the possible effect of the urea–urease reaction in the self-assembly of urea-based SAPs [25], is particularly tempting. The fact that the gel we produced can be easily seeded with nanoparticles, is promising for possible application in drug delivery and tissue regeneration [8,64,65]. Particularly appealing, will be to study the dynamics of small objects, such as particles of different sizes [39,66], bacteria, viruses, and cells, embedded in weak gels, where microscopic motion is never completely arrested.

4. Materials and Methods

4.1. SAP Sample Preparation

In this investigation, we used the self-assembling peptide FAQRVPP-GGG-$(\mathrm{LDLK})_3\mathrm{NH}_2$ (Lot: $A020/3$, purity $> 99\,\%$) purchased from Nanomed3D Srl. This is a self-assembling peptide, making cross-beta structures. The peptides used in this work are derived from Ac-LDLKLDLKLDLK-CONH_2, in the sense that they share the same self-assembling backbone, viz. (LDLK_3). It has been fully characterized in the work of Gelain et al. [67]. SAPs were solid-phase microwave synthesized, by using the standard Fmoc approach. The molecular weight of the final product was evaluated through the MS technique. LC-MS spectra were recorded via a single quadrupole mass detector (Waters LC-MS Alliance 3100, Waters Corp., Milford, CT, USA), using a nebulizing nitrogen gas at 400 l/min and a temperature of 250 °C. The cone flow, capillary, and cone voltage, were respectively set at 40 mL/min, 3.5 kV, and 60 V. HPLC purification of the synthesized peptide, was performed using a Waters binary HPLC on a Restek (Restek Corp., Bellefonte, PA, USA) preparative C_18 column. The mobile phase consisted of a gradient of acetonitrile with 0.1% TFA and H_2O with 0.1% TFA, over 25 min. After HPLC purification and lyophilization, TFA salts were removed by dissolving the product (0.5% w/v) in 0.01 M HCl solution, and lyophilized again.

The SAP FAQRVPP-GGG-(LDLK)$_3$NH$_2$ we used, contains alternating charged hydrophilic and hydrophobic amino acid residues in its self-assembling backbone sequence, and is known to have a strong propensity to generate cross β-sheet structures. When the pH of the solution is sufficiently high, hydrophobic forces drive its assembly into cross-beta structures, yielding nanofibers featuring charged residues exposed to water, and hydrophobic ones buried in a hydrophobic inner pocket. Such molecular organization has been thoroughly described in the work of Gelain et al. [13].

Urea, urease (type III from Jack beans, U1500, Sigma Aldrich, St. Louis, MO, USA, 40, 150 U/g, Product Code: 1002597636) and acetic acid (Sigma Aldrich), were used without further purification.

The SAP stock solution, at 20 g/L, was prepared by suspending the SAP powder in deionized water and sonicating for at least 20 min, until a clear solution formed. The SAP stock solution was then filtered and kept in the fridge for a maximum of three days. Urease solutions were freshly prepared before use, dissolving the enzyme in distilled water and keeping it in the fridge for a maximum of 8 h. In this way, we minimized the denaturation of the urease. We verified that the activity of the dissolved urease, if kept at $T = 4\,^\circ$C, does not decrease appreciably in 10 h . To prepare the gel, the SAP stock solution, diluted in an aqueous solution of acetic acid, was firstly added to the measured quantities of the urea solution, to tune the final pH of the gel. Then, the sample was gently mixed in an Eppendorf 1.5 mL centrifuge tube. In a second phase, a controlled amount of a urease aqueous solution was added to the tubes using an electronic pipette. The whole solution was aspirated and dispersed back into the tube at least three times, in order to speed up and optimize the sample mixing. The entire mixing procedure lasted less than 30 s. At the end, the sample was split in two parts: The first one was poured in the cuvette inside the PCI setup, the other half was used to fill the DLS cell. The filling of the cells in the two setups was synchronized, in order to ensure the same pH evolution and gelation kinetics in both the experiments and simplify their comparison.

As detailed in Section 2.3, we also studied the gelation in samples with PMMA particle tracers, having diameter $\sigma = 192$ nm (microparticles Gmbh) and stabilized with Pluronic$^{®}$ F-127 (Sigma Aldrich). In this case, the previous sample preparation procedure was slightly modified, by initially diluting the SAP stock solution with an acetic acid solution seeded with the colloidal tracers.

4.2. Optical Methods: Dynamic Light Scattering and Photon Correlation Imaging

In a dynamic light scattering (DLS) experiment, the sample dynamics are probed on length scales of the order of the inverse of the scattering wave-vector $q = (4\pi n/\lambda)\sin(\vartheta/2)$, where ϑ is the scattering angle, n is the refractive index of the solvent, and λ is the laser wavelength in a vacuum, by measuring the (normalized) time correlation function of the scattered intensity I (ICF):

$$g_2(\tau;t) = \frac{\langle I(t)I(t+\tau)\rangle_{\delta t}}{\langle I(t)\rangle\langle I(t+\tau)\rangle_{\delta t}}, \tag{1}$$

where $\langle ... \rangle$ is experimentally a time average for a total duration δt, over the initial time t [68]. In all measurements we discuss, we have fixed $\vartheta = 90^\circ$. When the dynamics of the studied process change with time, such as during a gelation process, where the value of scattered intensity and microscopic dynamics depend on time, δt has to be kept smaller than the timescale of the material's time evolution.

When DLS is used to investigate arrested systems such as gels, it is important to recall some peculiar issues that characterize the ICF [69]. In fact, DLS is routinely used to study "fluid-like" materials, in which the scatterers are free to move in the solvent. With time, the system explores the full ensemble of possible configurations of the scatterer positions. The ICF previously defined, time-averaged over the duration of a single experiment, is equal to the ensemble average obtained repeating the experiment several times. If this condition is fulfilled, the material is known as *ergodic*. On the contrary, in gels and glasses, the scatterers move around fixed average positions. Due to this limited motion, these systems can only move in a limited region of the phase space and are known as *non-ergodic*. In this case, the time-averaged quantities measured on a particular sample, i.e., the ICF in a single DLS experiment, are temporal averages over only a subensemble of configurations. These averages do not correspond to the ones sampled over the whole of the phase space [70]. If we suppose that scattering volumes that are sufficiently large contain many uncorrelated regions, then the scattered electric field $E(t)$, is a complex Gaussian variable, whose mean value is equal to zero. In ergodic, fluid-like systems, the intensity sampled by the detector will fluctuate in time, because the scatterer positions change in time. If the experimental time, δt, is sufficiently long, the light field explores all the possible Gaussian fluctuations and the time and ensemble averages are the same. Due to Gaussian statistical properties, for $\tau = 0$, $g_2(0,t) - 1 = 1$, while for τ much longer than the characteristic time of the ICF, $I(t)$ and $I(t+\tau)$ are uncorrelated, so that $g_2(\tau,t) - 1 = 0$. Thus, the contrast of the ICF, defined as $g_2(0,t) - g_2(\infty,t)$, is maximum and equal to 1.

In the opposite case, of a sample that is completely arrested, the speckle pattern is rigid, because scatterers are frozen in a fixed configuration and the scattered light intensity measured by the detector is constant in time, so that $g_2(\tau,t) - 1 = 0$ for every delay time τ. We consider now the intermediate case, of a non-ergodic sample (like a gel or a glass), in which the motion of the scatterers is partially arrested. Here, the intensity pattern is characterized by both a fluctuating and non-fluctuating contribution. It is easy to demonstrate that, for $\tau = 0$ $g_2(0,t) - 1 < 1$, because only a part of all of the possible intensity fluctuations is probed. Conversely, at large delay times, $g_2(\tau,t) - 1 = 0$, because the fluctuations become uncorrelated, as in the ergodic case. The reduction in the contrast in a DLS experiment, is therefore a hallmark of the formation of a (partially) arrested system.

Recovering the true ensemble averaged ICF in a typical DLS experiment, is a tedious and time consuming procedure, that requires the sample or the detector to be moved across a large number of different positions [70,71]. To overcome this limitation, especially annoying in the case of time-varying samples, multi-speckle light scattering techniques have emerged in the past 20 years. Among them, photon correlation imaging (PCI) provides, in a single measurement, the ICFs of the scattered light at distinct points within the sample [72,73]. The light scattered by the sample at a given angle ϑ, is collected by a stopped-down optical system, forming a speckled image on a multi-pixel sensor. In this work, we renounce to spatial resolution, averaging the sample dynamics over all the pixels of the camera. This choice allows us to obtain a fast spatial averaging of the ICF for samples characterized by very slow dynamics. In analogy with the ICF defined for DLS, the correlation index $c_I(\tau;t)$, between two images taken at times t and $t+\tau$, is introduced

$$c_I(\tau;t) = \frac{\langle I_p(t) I_p(t+\tau) \rangle}{\langle I_p(t) \rangle \langle I_p(t+\tau) \rangle} - 1, \tag{2}$$

where $\langle \cdots \rangle$ is the spatial average over the whole image of the scattered intensity I_p, measured on each pixel. It is easy to show that $c_I(0;t)$, with the relative variance of the intensity in the image at time t. Usually, PCI is employed with samples with very slow dynamics, and the exposure time, t_e, of the camera, of the order of a few ms or less, is much shorter than the characteristic timescale of the speckle field evolution. In this case, $c_I(0;t)$ is constant during the experiment, and depends only on the setup configuration. To easily compare experiments obtained with different setups, it is useful to introduce the normalized degree of correlation, $\hat{c}_I(\tau;t) = c_I(\tau;t)/c_I(0;t)$. On the contrary, if the sample restructuring time is comparable with t_e and evolves in time, the value of $c_I(0;t)$ also changes during the experiment. In particular, if the decay time of the ICF is longer than t_e, the speckle pattern is frozen, and different pixels measure very different signals. Conversely, when the exposure increases, the visibility of the speckle pattern progressively decreases. Over the duration of an exposure, each pixel integrates the light intensity, that in the meantime fluctuates. If t_e is too long compared to the characteristic time of the sample restructuring, each pixel measures the same averaged value, and there is a limited spatial variation in the signal. Speckle-visibility spectroscopy [74] exploits this idea to characterize the sample dynamics. In our case, we monitor the variation in $c_I(0;t)$ for a fixed $t_e = 10\,\mathrm{ms}$, during the gelation process, in order to have access to a timescale much faster than the delay time between two PCI images.

The detailed properties of our experimental setup can be found in [75,76]. We simply recall, that the scattering vector that we probed in our PCI and DLS setups is $q \simeq 23\,\mu\mathrm{m}^{-1}$.

4.3. pH Measurement

A Thermo Scientific™ ORION™ 9810BN microelectrode, linked to an ORION™ bench-top 420A pH/mV meter, was used to follow the pH evolution during the gelation process (system pH accuracy of ±0.005). The microelectrode, filled with a filling solution of KCl 4 M and Ag/AgCl (ORION™ Cat. N. 900011), is characterized by a length of 120 mm, and a ceramic junction and tip of 37 × 1.3 mm. It could be used to investigate samples with a minimum volume of 500 nL. The small footprint of the electrode allowed us to insert the electrode inside the optical cell of the PCI setup, probing a region around 2 mm from the scattering volume. All measurements were conducted at room temperature. The microelectrode was stored according to the requirements of the producer and calibrated every three measures.

Author Contributions: Methodology, R.P., S.B. and F.G.; setup and software design, V.R. and S.B.; data collection S.B. and V.R.; data analysis, S.B.; writing—original draft preparation, S.B.; writing—review and editing, R.P., V.R., F.G. and S.B.; funding acquisition, R.P. and S.B.; resources, F.G. All authors have read and agreed to the published version of the manuscript.

Funding: This research was funded by The Italian Ministry of University and Research (PRIN Project 2017Z55KCW, *Soft Adaptive Networks*).

Data Availability Statement: The data underlying the results presented in this paper are not publicly available at this time, but may be obtained from the authors upon reasonable request.

Acknowledgments: We thank Sara Capitanio and Lucia Simoncelli for conducting preliminary experiments.

Conflicts of Interest: The authors declare no conflict of interest.

Abbreviations

The following abbreviations are used in this manuscript:

SAP	Self-assembling peptides
ECM	Extracellular matrix
GdL	Glucono-δ-lactone
CD	Circular dichroism
FTIR	Fourier-transform infrared spectroscopy
Fmoc	9-Fluorenylmethyloxycarbonyl
Tfa	Trifluoroacetate
HPLC	High-performance liquid chromatography
LC-MS	Liquid chromatography–mass spectroscopy
DLS	Dynamic light scattering
PCI	Photon correlation imaging
ICF	Intensity correlation function

References

1. Carlini, A.S.; Adamiak, L.; Gianneschi, N.C. Biosynthetic polymers as functional materials. *Macromolecules* **2016**, *49*, 4379–4394. [CrossRef] [PubMed]
2. Panja, S.; Adams, D.J. Urea-Urease Reaction in Controlling Properties of Supramolecular Hydrogels: Pros and Cons. *Chem.-Eur. J.* **2021**, *27*, 8928–8939. [CrossRef] [PubMed]
3. Estroff, L.A.; Hamilton, A.D. Water gelation by small organic molecules. *Chem. Rev.* **2004**, *104*, 1201–1218. [CrossRef]
4. Schweitzer-Stenner, R.; Alvarez, N.J. Short peptides as tunable, switchable, and strong gelators. *J. Phys. Chem. B* **2021**, *125*, 6760–6775. [CrossRef] [PubMed]
5. Wang, H.; Yang, Z. Short-peptide-based molecular hydrogels: Novel gelation strategies and applications for tissue engineering and drug delivery. *Nanoscale* **2012**, *4*, 5259–5267. [CrossRef]
6. Sutton, S.; Campbell, N.L.; Cooper, A.I.; Kirkland, M.; Frith, W.J.; Adams, D.J. Controlled release from modified amino acid hydrogels governed by molecular size or network dynamics. *Langmuir* **2009**, *25*, 10285–10291. [CrossRef] [PubMed]
7. Naskar, J.; Palui, G.; Banerjee, A. Tetrapeptide-based hydrogels: For encapsulation and slow release of an anticancer drug at physiological pH. *J. Phys. Chem. B* **2009**, *113*, 11787–11792. [CrossRef]
8. Raspa, A.; Carminati, L.; Pugliese, R.; Fontana, F.; Gelain, F. Self-assembling peptide hydrogels for the stabilization and sustained release of active Chondroitinase ABC in vitro and in spinal cord injuries. *J. Control. Release* **2021**, *330*, 1208–1219. [CrossRef]
9. Sangeetha, N.M.; Maitra, U. Supramolecular gels: Functions and uses. *Chem. Soc. Rev.* **2005**, *34*, 821–836. [CrossRef]
10. Genové, E.; Shen, C.; Zhang, S.; Semino, C.E. The effect of functionalized self-assembling peptide scaffolds on human aortic endothelial cell function. *Biomaterials* **2005**, *26*, 3341–3351. [CrossRef]
11. Gelain, F.; Luo, Z.; Zhang, S. Self-assembling peptide EAK16 and RADA16 nanofiber scaffold hydrogel. *Chem. Rev.* **2020**, *120*, 13434–13460. [CrossRef] [PubMed]
12. Loo, Y.; Wan, A.C.; Hauser, C.A.; Lane, E.B.; Benny, P. Xeno-free self-assembling peptide scaffolds for building 3D organotypic skin cultures. *FASEB BioAdvances* **2022**, *4*, 631–637. [CrossRef] [PubMed]
13. Gelain, F.; Bottai, D.; Vescovi, A.; Zhang, S. Designer self-assembling peptide nanofiber scaffolds for adult mouse neural stem cell 3-dimensional cultures. *PLoS ONE* **2006**, *1*, e119. [CrossRef] [PubMed]
14. Gelain, F.; Luo, Z.; Rioult, M.; Zhang, S. Self-assembling peptide scaffolds in the clinic. *NPJ Regen. Med.* **2021**, *6*, 9. [CrossRef] [PubMed]
15. Fu, K.; Wu, H.; Su, Z. Self-assembling peptide-based hydrogels: Fabrication, properties, and applications. *Biotechnol. Adv.* **2021**, *49*, 107752. [CrossRef] [PubMed]
16. Pugliese, R.; Gelain, F. Peptidic biomaterials: From self-assembling to regenerative medicine. *Trends Biotechnol.* **2017**, *35*, 145–158. [CrossRef]
17. Wang, H.; Yang, Z.; Adams, D.J. Controlling peptidebased hydrogelation. *Mater. Today* **2012**, *15*, 500–507. [CrossRef]
18. Amdursky, N.; Orbach, R.; Gazit, E.; Huppert, D. Probing the inner cavities of hydrogels by proton diffusion. *J. Phys. Chem. C* **2009**, *113*, 19500–19505. [CrossRef]
19. Diaferia, C.; Rosa, E.; Morelli, G.; Accardo, A. Fmoc-diphenylalanine hydrogels: Optimization of preparation methods and structural insights. *Pharmaceuticals* **2022**, *15*, 1048. [CrossRef]
20. Diaferia, C.; Rosa, E.; Gallo, E.; Morelli, G.; Accardo, A. Differently N-Capped Analogues of Fmoc-FF. *Chem.-Eur. J.* **2023**, e202300661. [CrossRef]
21. Majumder, L.; Chatterjee, M.; Bera, K.; Maiti, N.C.; Banerji, B. Solvent-assisted tyrosine-based dipeptide forms low-molecular weight gel: Preparation and its potential use in dye removal and oil spillage separation from water. *ACS Omega* **2019**, *4*, 14411–14419. [CrossRef]
22. Li, X.; Gao, Y.; Kuang, Y.; Xu, B. Enzymatic formation of a photoresponsive supramolecular hydrogel. *Chem. Commun.* **2010**, *46*, 5364–5366. [CrossRef] [PubMed]
23. Xiang, Y.; Mao, H.; Tong, S.c.; Liu, C.; Yan, R.; Zhao, L.; Zhu, L.; Bao, C. A Facile and Versatile Approach to Construct Photoactivated Peptide Hydrogels by Regulating Electrostatic Repulsion. *ACS Nano* **2023**, *17*, 5536–5547. [CrossRef]
24. Vegners, R.; Shestakova, I.; Kalvinsh, I.; Ezzell, R.M.; Janmey, P.A. Use of a gel-forming dipeptide derivative as a carrier for antigen presentation. *J. Pept. Sci. Off. Publ. Eur. Pept. Soc.* **1995**, *1*, 371–378. [CrossRef] [PubMed]
25. Xing, H.; Rodger, A.; Comer, J.; Picco, A.S.; Huck-Iriart, C.; Ezell, E.L.; Conda-Sheridan, M. Urea-modified self-assembling peptide amphiphiles that form well-defined nanostructures and hydrogels for biomedical applications. *ACS Appl. Bio Mater.* **2022**, *5*, 4599–4610. [CrossRef] [PubMed]
26. de Loos, M.; Friggeri, A.; van Esch, J.; Kellogg, R.M.; Feringa, B.L. Cyclohexane bis-urea compounds for the gelation of water and aqueous solutions. *Org. Biomol. Chem.* **2005**, *3*, 1631–1639. [CrossRef] [PubMed]
27. Helen, W.; De Leonardis, P.; Ulijn, R.V.; Gough, J.; Tirelli, N. Mechanosensitive peptide gelation: Mode of agitation controls mechanical properties and nano-scale morphology. *Soft Matter* **2011**, *7*, 1732–1740. [CrossRef]
28. Panja, S.; Adams, D.J. Maintaining homogeneity during a sol–gel transition by an autocatalytic enzyme reaction. *Chem. Commun.* **2019**, *55*, 47–50. [CrossRef]
29. Reddy, S.M.M.; Shanmugam, G.; Duraipandy, N.; Kiran, M.S.; Mandal, A.B. An additional fluorenylmethoxycarbonyl (Fmoc) moiety in di-Fmoc-functionalized L-lysine induces pH-controlled ambidextrous gelation with significant advantages. *Soft Matter* **2015**, *11*, 8126–8140. [CrossRef]

30. Zhang, Y.; Gu, H.; Yang, Z.; Xu, B. Supramolecular hydrogels respond to ligand- receptor interaction. *J. Am. Chem. Soc.* **2003**, *125*, 13680–13681. [CrossRef]
31. Mahler, A.; Reches, M.; Rechter, M.; Cohen, S.; Gazit, E. Rigid, self-assembled hydrogel composed of a modified aromatic dipeptide. *Adv. Mater.* **2006**, *18*, 1365–1370. [CrossRef]
32. Adams, D.J.; Butler, M.F.; Frith, W.J.; Kirkland, M.; Mullen, L.; Sanderson, P. A new method for maintaining homogeneity during liquid–hydrogel transitions using low molecular weight hydrogelators. *Soft Matter* **2009**, *5*, 1856–1862. [CrossRef]
33. Pocker, Y.; Green, E. Hydrolysis of D-glucono-. delta.-lactone. I. General acid-base catalysis, solvent deuterium isotope effects, and transition state characterization. *J. Am. Chem. Soc.* **1973**, *95*, 113–119. [CrossRef] [PubMed]
34. Braun, G.A.; Ary, B.E.; Dear, A.J.; Rohn, M.C.; Payson, A.M.; Lee, D.S.; Parry, R.C.; Friedman, C.; Knowles, T.P.; Linse, S.; et al. On the mechanism of self-assembly by a hydrogel-forming peptide. *Biomacromolecules* **2020**, *21*, 4781–4794. [CrossRef] [PubMed]
35. Nagarkar, R.P.; Schneider, J.P., Synthesis and Primary Characterization of Self-Assembled Peptide-Based Hydrogels. In *Nanostructure Design: Methods and Protocols*; Gazit, E., Nussinov, R., Eds.; Humana Press: Totowa, NJ, USA, 2008; pp. 61–77.
36. Pitz, M.E.; Nukovic, A.M.; Elpers, M.A.; Alexander-Bryant, A.A. Factors Affecting Secondary and Supramolecular Structures of Self-Assembling Peptide Nanocarriers. *Macromol. Biosci.* **2022**, *22*, 2100347. [CrossRef]
37. Yan, C.; Pochan, D.J. Rheological properties of peptide-based hydrogels for biomedical and other applications. *Chem. Soc. Rev.* **2010**, *39*, 3528–3540. [CrossRef]
38. Meleties, M.; Britton, D.; Katyal, P.; Lin, B.; Martineau, R.L.; Gupta, M.K.; Montclare, J.K. High-Throughput Microrheology for the Assessment of Protein Gelation Kinetics. *Macromolecules* **2022**, *55*, 1239–1247. [CrossRef]
39. Meleties, M.; Martineau, R.L.; Gupta, M.K.; Montclare, J.K. Particle-Based Microrheology As a Tool for Characterizing Protein-Based Materials. *ACS Biomater. Sci. Eng.* **2022**, *8*, 2747–2763. [CrossRef]
40. Guilbaud, J.B.; Saiani, A. Using small angle scattering (SAS) to structurally characterise peptide and protein self-assembled materials. *Chem. Soc. Rev.* **2011**, *40*, 1200–1210. [CrossRef]
41. McDowall, D.; Adams, D.J.; Seddon, A.M. Using small angle scattering to understand low molecular weight gels. *Soft Matter* **2022**, *18*, 1577–1590. [CrossRef]
42. Hule, R.A.; Nagarkar, R.P.; Altunbas, A.; Ramay, H.R.; Branco, M.C.; Schneider, J.P.; Pochan, D.J. Correlations between structure, material properties and bioproperties in self-assembled *β*-hairpin peptide hydrogels. *Faraday Discuss.* **2008**, *139*, 251–264. [CrossRef] [PubMed]
43. Liu, Y.; Ran, Y.; Ge, Y.; Raza, F.; Li, S.; Zafar, H.; Wu, Y.; Paiva-Santos, A.C.; Yu, C.; Sun, M.; et al. pH-sensitive peptide hydrogels as a combination drug delivery system for cancer treatment. *Pharmaceutics* **2022**, *14*, 652. [CrossRef] [PubMed]
44. Larsen, T.H.; Branco, M.C.; Rajagopal, K.; Schneider, J.P.; Furst, E.M. Sequence-dependent gelation kinetics of *β*-hairpin peptide hydrogels. *Macromolecules* **2009**, *42*, 8443–8450. [CrossRef]
45. Haines-Butterick, L.; Rajagopal, K.; Branco, M.; Salick, D.; Rughani, R.; Pilarz, M.; Lamm, M.S.; Pochan, D.J.; Schneider, J.P. Controlling hydrogelation kinetics by peptide design for three-dimensional encapsulation and injectable delivery of cells. *Proc. Natl. Acad. Sci. USA* **2007**, *104*, 7791–7796. [CrossRef] [PubMed]
46. Keiderling, T.A. Structure of condensed phase peptides: Insights from vibrational circular dichroism and Raman optical activity techniques. *Chem. Rev.* **2020**, *120*, 3381–3419. [CrossRef] [PubMed]
47. Bajpayee, N.; Vijayakanth, T.; Rencus-Lazar, S.; Dasgupta, S.; Desai, A.V.; Jain, R.; Gazit, E.; Misra, R. Exploring Helical Peptides and Foldamers for the Design of Metal Helix Frameworks: Current Trends and Future Perspectives. *Angew. Chem.* **2023**, *135*, e202214583. [CrossRef]
48. DiGuiseppi, D.; Kraus, J.; Toal, S.E.; Alvarez, N.; Schweitzer-Stenner, R. Investigating the formation of a repulsive hydrogel of a cationic 16mer peptide at low ionic strength in water by vibrational spectroscopy and rheology. *J. Phys. Chem. B* **2016**, *120*, 10079–10090. [CrossRef] [PubMed]
49. Chen, L.; Morris, K.; Laybourn, A.; Elias, D.; Hicks, M.R.; Rodger, A.; Serpell, L.; Adams, D.J. Self-assembly mechanism for a naphthalene- dipeptide leading to hydrogelation. *Langmuir* **2010**, *26*, 5232–5242. [CrossRef]
50. Hu, G.; Pojman, J.A.; Scott, S.K.; Wrobel, M.M.; Taylor, A.F. Base-catalyzed feedback in the urea- urease reaction. *J. Phys. Chem. B* **2010**, *114*, 14059–14063. [CrossRef]
51. Qin, Y.; Cabral, J.M. Kinetic studies of the urease-catalyzed hydrolysis of urea in a buffer-free system. *Appl. Biochem. Biotechnol.* **1994**, *49*, 217–240. [CrossRef]
52. Heuser, T.; Weyandt, E.; Walther, A. Biocatalytic feedback-driven temporal programming of self-regulating peptide hydrogels. *Angew. Chem.* **2015**, *127*, 13456–13460. [CrossRef]
53. Wrobel, M.M.; Bánsági, T.; Scott, S.K.; Taylor, A.F.; Bounds, C.O.; Carranza, A.; Pojman, J.A. pH wave-front propagation in the urea-urease reaction. *Biophys. J.* **2012**, *103*, 610–615. [CrossRef] [PubMed]
54. Arosio, P.; Cukalevski, R.; Frohm, B.; Knowles, T.P.; Linse, S. Quantification of the concentration of A*β*42 propagons during the lag phase by an amyloid chain reaction assay. *J. Am. Chem. Soc.* **2014**, *136*, 219–225. [CrossRef] [PubMed]
55. Arosio, P.; Knowles, T.P.; Linse, S. On the lag phase in amyloid fibril formation. *Phys. Chem. Chem. Phys.* **2015**, *17*, 7606–7618. [CrossRef]
56. Dudukovic, N.A.; Zukoski, C.F. Gelation of Fmoc-diphenylalanine is a first order phase transition. *Soft Matter* **2015**, *11*, 7663–7673. [CrossRef]

57. Zhang, H.; Luo, H.; Zhao, X. Mechanistic study of self-assembling peptide rada16-i in formation of nanofibers and hydrogels. *J. Nanotechnol. Eng. Med.* **2010**, *1*, 011007. [CrossRef]
58. Emamyari, S.; Kargar, F.; Sheikh-Hasani, V.; Emadi, S.; Fazli, H. Mechanisms of the self-assembly of EAK16-family peptides into fibrillar and globular structures: Molecular dynamics simulations from nano-to micro-seconds. *Eur. Biophys. J.* **2015**, *44*, 263–276. [CrossRef]
59. Pandya, M.J.; Spooner, G.M.; Sunde, M.; Thorpe, J.R.; Rodger, A.; Woolfson, D.N. Sticky-end assembly of a designed peptide fiber provides insight into protein fibrillogenesis. *Biochemistry* **2000**, *39*, 8728–8734. [CrossRef]
60. Lara, C.; Adamcik, J.; Jordens, S.; Mezzenga, R. General self-assembly mechanism converting hydrolyzed globular proteins into giant multistranded amyloid ribbons. *Biomacromolecules* **2011**, *12*, 1868–1875. [CrossRef]
61. Gurry, T.; Stultz, C.M. Mechanism of amyloid-β fibril elongation. *Biochemistry* **2014**, *53*, 6981–6991. [CrossRef]
62. Scheidt, T.; Łapińska, U.; Kumita, J.R.; Whiten, D.R.; Klenerman, D.; Wilson, M.R.; Cohen, S.I.; Linse, S.; Vendruscolo, M.; Dobson, C.M.; et al. Secondary nucleation and elongation occur at different sites on Alzheimer's amyloid-β aggregates. *Sci. Adv.* **2019**, *5*, eaau3112. [CrossRef] [PubMed]
63. Törnquist, M.; Michaels, T.C.; Sanagavarapu, K.; Yang, X.; Meisl, G.; Cohen, S.I.; Knowles, T.P.; Linse, S. Secondary nucleation in amyloid formation. *Chem. Commun.* **2018**, *54*, 8667–8684. [CrossRef] [PubMed]
64. Maleki, M.; Natalello, A.; Pugliese, R.; Gelain, F. Fabrication of nanofibrous electrospun scaffolds from a heterogeneous library of co-and self-assembling peptides. *Acta Biomater.* **2017**, *51*, 268–278. [CrossRef] [PubMed]
65. Pugliese, R.; Maleki, M.; Zuckermann, R.N.; Gelain, F. Self-assembling peptides cross-linked with genipin: Resilient hydrogels and self-standing electrospun scaffolds for tissue engineering applications. *Biomater. Sci.* **2019**, *7*, 76–91. [CrossRef]
66. Buzzaccaro, S.; Ruzzi, V.; Faleo, T.; Piazza, R. Microrheology of a thermosensitive gelling polymer for cell culture. *J. Chem. Phys.* **2022**, *157*, 174901. [CrossRef] [PubMed]
67. Gelain, F.; Cigognini, D.; Caprini, A.; Silva, D.; Colleoni, B.; Donega, M.; Antonini, S.; Cohen, B.; Vescovi, A. New bioactive motifs and their use in functionalized self-assembling peptides for NSC differentiation and neural tissue engineering. *Nanoscale* **2012**, *4*, 2946–2957. [CrossRef]
68. Berne, B.J.; Pecora, R. *Dynamic Light Scattering: With Applications to Chemistry, Biology, and Physics*; Mineola: Dover, NY, USA, 2000; Volume 376.
69. Joosten, J.G.; McCarthy, J.L.; Pusey, P.N. Dynamic and static light scattering by aqueous polyacrylamide gels. *Macromolecules* **1991**, *24*, 6690–6699. [CrossRef]
70. Pusey, P.N.; Van Megen, W. Dynamic light scattering by non-ergodic media. *Phys. A Stat. Mech. Its Appl.* **1989**, *157*, 705–741. [CrossRef]
71. Usuelli, M.; Cao, Y.; Bagnani, M.; Handschin, S.; Nyström, G.; Mezzenga, R. Probing the structure of filamentous nonergodic gels by dynamic light scattering. *Macromolecules* **2020**, *53*, 5950–5956. [CrossRef]
72. Duri, A.; Sessoms, D.A.; Trappe, V.; Cipelletti, L. Resolving long-range spatial correlations in jammed colloidal systems using photon correlation imaging. *Phys. Rev. Lett.* **2009**, *102*, 085702. [CrossRef]
73. Secchi, E.; Roversi, T.; Buzzaccaro, S.; Piazza, L.; Piazza, R. Biopolymer gels with "physical" cross-links: Gelation kinetics, aging, heterogeneous dynamics, and macroscopic mechanical properties. *Soft Matter* **2013**, *9*, 3931–3944. [CrossRef]
74. Bandyopadhyay, R.; Gittings, A.; Suh, S.; Dixon, P.; Durian, D.J. Speckle-visibility spectroscopy: A tool to study time-varying dynamics. *Rev. Sci. Instruments* **2005**, *76*, 093110. [CrossRef]
75. Piazza, R.; Campello, M.; Buzzaccaro, S.; Sciortino, F. Phase Behavior and Microscopic Dynamics of a Thermosensitive Gel-Forming Polymer. *Macromolecules* **2021**, *54*, 3897–3906. [CrossRef]
76. Filiberti, Z.; Piazza, R.; Buzzaccaro, S. Multiscale relaxation in aging colloidal gels: From localized plastic events to system-spanning quakes. *Phys. Rev. E* **2019**, *100*, 042607. [CrossRef]

gels

Article

Magnetic Ionotropic Hydrogels Based on Carboxymethyl Cellulose for Aqueous Pollution Mitigation

Andra-Cristina Enache, Ionela Grecu, Petrisor Samoila *, Corneliu Cojocaru and Valeria Harabagiu

Laboratory of Inorganic Polymers, "Petru Poni" Institute of Macromolecular Chemistry,
41A Grigore Ghica Voda Alley, 700487 Iasi, Romania
* Correspondence: samoila.petrisor@icmpp.ro

Abstract: In this work, stabilized ionotropic hydrogels were designed using sodium carboxymethyl cellulose (CMC) and assessed as inexpensive sorbents for hazardous chemicals (e.g., Methylene Blue, MB) from contaminated wastewaters. In order to increase the adsorption capacity of the hydrogelated matrix and facilitate its magnetic separation from aqueous solutions, sodium dodecyl sulfate (SDS) and manganese ferrite ($MnFe_2O_4$) were introduced into the polymer framework. The morphological, structural, elemental, and magnetic properties of the adsorbents (in the form of beads) were assessed using scanning electron microscopy (SEM), energy-dispersive X-ray analysis, Fourier-transform infrared spectroscopy (FTIR), and a vibrating-sample magnetometer (VSM). The magnetic beads with the best adsorption performance were subjected to kinetic and isotherm studies. The PFO model best describes the adsorption kinetics. A homogeneous monolayer adsorption system was predicted by the Langmuir isotherm model, registering a maximum adsorption capacity of 234 mg/g at 300 K. The calculated thermodynamic parameter values indicated that the investigated adsorption processes were both spontaneous ($\Delta G < 0$) and exothermic ($\Delta H < 0$). The used sorbent can be recovered after immersion in acetone (93% desorption efficiency) and re-used for MB adsorption. In addition, the molecular docking simulations disclosed aspects of the mechanism of intermolecular interaction between CMC and MB by detailing the contributions of the van der Waals (physical) and Coulomb (electrostatic) forces.

Keywords: carboxymethyl cellulose; manganese ferrite; sodium dodecyl sulfate; ionotropic hydrogels; magnetic beads; biosorbent; dye adsorption; molecular docking

1. Introduction

Water is a scarce and indispensable resource for our lives [1]. Notwithstanding this, the reality of global climate change and human activities have altered the quality of drinking water in recent decades [2,3]. Domestic, agricultural, and industrial activities, as well as hospital sewage and power generation, are just a few of the major contributors to water pollution [4]. Therefore, various hazardous compounds (organic, inorganic, radioactive pollutants, pathogens, nutrients, and others) are directly discharged into the water bodies [5,6]. As a consequence, more than 50 types of diseases arise as a result of drinking water contamination worldwide, which frequently leads to high mortality rates, particularly among children [7].

The synthetic dye-based industries (e.g., textiles, paper, pharmaceuticals, leather, and plastic materials) are one of the most concerning sectors when it comes to water contamination [8]. Every year, approximately 1,000,000 tons of different organic dyes are produced, and their release into the environment can endanger all life forms [8,9]. Among these, the cationic dyes have a tendency to be more harmful than the anionic dyes, as they have high tinctorial values (1 mg/L) [10] and can decompose into carcinogenic amine compounds under anaerobic conditions [11]. Methylene blue (MB) is a well-known heterocyclic cationic dye widely used in the pharmaceutical and medical fields, as well as in the textile and plastic industries [9,12]. However, MB is extremely destructive and a major threat to human health upon ingestion (damaging the neurological and visual systems) [13]. In addition, exposure to high doses of MB (>2 mg/kg) can cause other associated conditions, such as cardiopulmonary affections, nausea, Heinz body formation, tissue necrosis, jaundice, quadriplegia, breathing difficulties, and gastritis infections [9,14]. Additionally, MB's non-biodegradability and accumulation capacity make it highly problematic for the environment and aquatic life [12,15].

In order to reduce wastewater MB levels, different remediation methods have been investigated so far: adsorption [8], membrane separation [16], photodegradation [12], electrochemical treatment [17], coagulation-flocculation [18], constructed wetlands [19] and others. Besides being efficient, low-cost, and easy to design and operate, adsorption is one of the most attainable techniques in cationic dye removal. Other advantages of this method are the high selectivity for dyes of different concentrations and the relatively simple regeneration processes [20].

Therefore, in terms of economic feasibility and environmental impact, researchers have proven in recent years the efficiency of polysaccharide-based adsorbents (such as chitosan [8], alginate [21], kappa-carrageenan [22], cellulose [23], and others) for MB removal from aqueous solutions. Among these, carboxymethyl cellulose (CMC) was found to be a promising derivative of cellulose (the most prevalent natural polysaccharide in nature), as it is an anionic and water-soluble polyelectrolyte, ideal for cationic dye adsorption [23,24]. The main benefits of using CMC-based adsorbents for MB removal are their biodegradability, eco-friendliness, cost-effectiveness, gel-forming properties, and negatively charged surfaces (–CH_2COOH groups), which are suitable for binding cationic dyes through electrostatic interactions [25–27]. However, CMC has been shown to have poor mechanical qualities and limited adsorption capacity when used alone in wastewater applications. In consequence, physical and/or chemical modifications of the CMC or the incorporation of different types of particles in the CMC matrix (e.g., graphene oxide, metals, clays) in order to obtain composite materials have demonstrated improved capacities for MB adsorption [25,26,28].

Relying on the previously stated interest, this work proposes the development of sustainable, cost-effective, and non-toxic CMC-based sorbent in the form of beads with high added value through: (i) the preparation of hydrodynamically stabilized ionotropic hydrogels by cross-linking with iron cations; (ii) using sodium dodecyl sulfate (SDS) as a foaming agent and the freeze-drying method to improve the adsorption capacity; iii) facilitating the sorbent recovery through easy magnetic separation by adding manganese ferrite ($MnFe_2O_4$) to the polymer framework. As far as we are aware, this study is the first to describe the preparation of an ionotropic hydrogel based on Fe^{3+} cross-linked carboxymethyl cellulose with magnetic properties (provided by $MnFe_2O_4$ particles) in the form of freeze-dried beads. Furthermore, this is the first report on the use of these materials in the adsorption of cationic dyes, such as methylene blue, highlighting the adsorption mechanism, intermolecular interactions between MB and CMC, and sorbent-sorbate interaction energies through molecular docking computations.

2. Results and Discussion

2.1. Spinel Ferrite and Magnetic Beads Preparation

As a result of their low energy consumption, simple preparation procedure, and use of inexpensive and readily available raw materials, physical hydrogel formulations are considered promising materials for environmental applications [29]. However, environmental applications require certain aspects, such as the use of natural, biocompatible, and non-toxic materials, avoiding chemical leakage, increasing pollutant adsorption capacities, facilitating the recovery, reuse, etc.

Due to its eco-friendly properties and the abundance of reactive functional groups –COO^-, carboxymethyl cellulose (CMC) has been used in this work as a polymeric matrix for the preparation of adsorbent beads (as described in Table 1). A possible source of toxicity in ionotropic hydrogels is the leakage of crosslinking ions, which occurs especially when crosslinking with divalent ions (e.g., Ca^{2+}, Mg^{2+}) [30]. To avoid this drawback and to confer superior stability to the CMC-based hydrogels, trivalent Fe^{3+} cations were used to bind the carboxylic groups. The beads were prepared in an easy and inexpensive manner, as graphically represented in Figure 1, by drop-wise addition of CMC-based mixtures in a solution containing Fe^{3+} cations (0.1 M $Fe(NO_3)_3$). According to the literature [29], the instantaneous cross-linking mechanism involves the attachment of each Fe^{3+} trivalent cation to three polymeric chains of CMC, substituting Na^+ ions. Thus, the feasibility of selecting the ionotropic gelation of carboxymethyl cellulose (CMC) with iron cations (predominately stabilized by electrostatic interactions) can be considered a key factor for large-scale usage at minimal application cost.

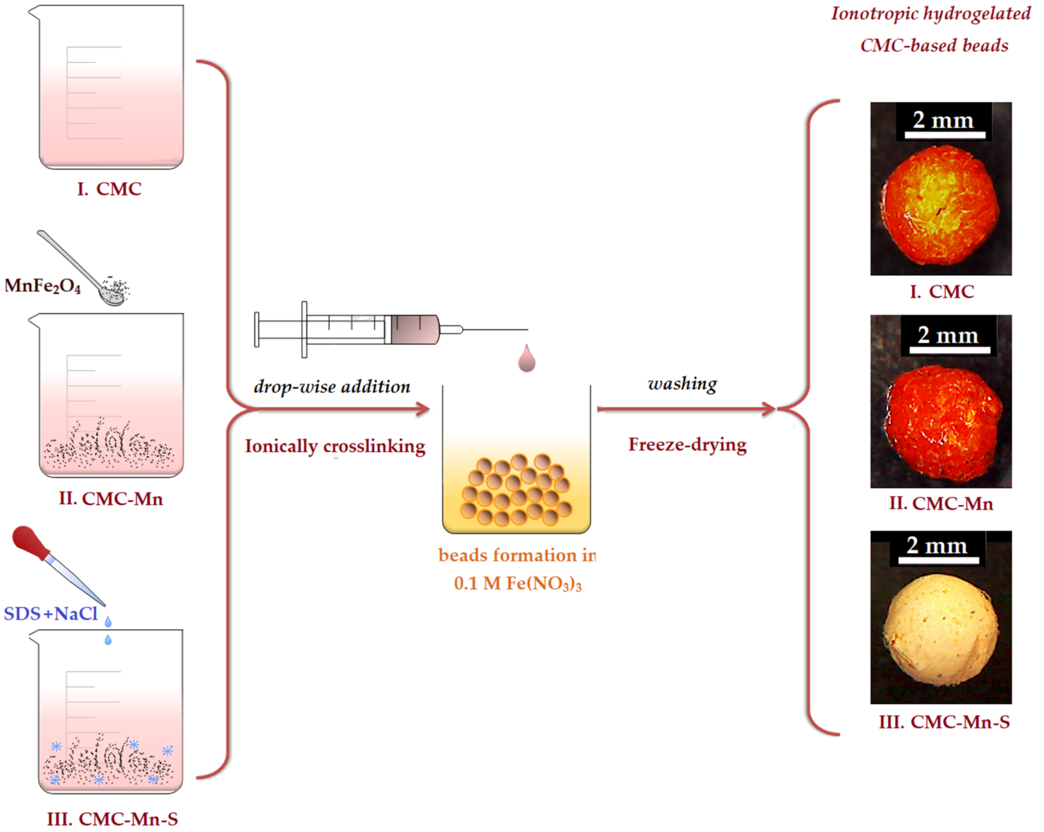

Figure 1. Schematic representation CMC-based bead preparation, where CMC is the 3% carboxymethyl cellulose solution (I); CMC-Mn is the magnetic dispersion of manganese spinel ferrite ($MnFe_2O_4$) in the CMC solution (II); and CMC-Mn-S represents the mixture after the addition of sodium dodecyl sulfate (SDS) into the magnetic dispersion (III). The beads obtained have the same annotation as the initial solutions.

Table 1. Chemical composition and characteristics of CMC-based beads.

Beads Code	Beads Composition [1]				Beads Size [2] (mm)	Magnetization at 30 kOe (emu/g)	Adsorption Capacity (*q*, mg/g)	Removal Efficiency (*Y*, %)
	CMC (g)	$MnFe_2O_4$ (% *w*/*w*)	SDS (% *w*/*w*)	NaCl (% *w*/*w*)				
CMC	3	–	–	–	2.60 ± 0.28	–	0.9	3.60
CMC-Mn	3	10	–	–	2.23 ± 0.36	2.07	0.77	3.06
CMC-Mn-S1	3	10	0.2	4	1.76 ± 0.25	1.39	6.82	27.10
CMC-Mn-S2	3	10	0.4	4	2.09 ± 0.24	1.50	18.22	72.38
CMC-Mn-S3	3	10	0.8	4	1.97 ± 0.27	1.26	12.92	51.33

[1] all the beads were prepared by using a stock solution of 3% CMC, and the crosslinking bath was 0.1 M $Fe(NO_3)_3$.
[2] average value (from 25 measurements) ± standard deviation.

One of the problems encountered in wastewater treatment generally deals with sorbent recovery from aqueous media [31]. As compared to traditional separation technologies (settling, centrifugation, and membrane filtration [32]), the ease of magnetic separation was investigated in this study by the introduction of manganese spinel ferrite ($MnFe_2O_4$) in the polymeric matrix. The $MnFe_2O_4$ inorganic particles were selected due to their extraordinary magnetic properties [33] and were synthesized by a flexible method, such as the sol-gel auto-combustion technique. This type of process uses an exothermic, self-sustaining anionic redox reaction in an aqueous solution of metal salts. The advantage of using nitrate salts as precursors is that they provide a water-soluble, low temperature oxidant source for synthesis. These salts (in this study, Mn^{2+} and Fe^{3+} nitrates) are classified as oxidizers. Citric acid serves as both a reductant and an oxygen source for the self-combustion stage.

In addition to the presence of $–COO^{-}$ functional groups in the CMC matrix that aid in the binding of cationic pollutants (e.g., Methylene Blue), the hydrogel matrix's ability to swallow dye solutions should also allow dye molecules to adsorb on its surface via van der Waals interactions or hydrogen bonds [34]. Moreover, to improve the adsorption capacity of the CMC hydrogel matrix, attempts were made to adjust the chemical structure and pore formation by adding different ratios of sodium dodecyl sulfate (SDS) surfactant and NaCl salt (see chemical composition in Table 1). The use of NaCl with SDS (Figure S1), before the crosslinking process, aimed to form larger micellar aggregates (the salt bridges stabilizing the micelles and increasing their size) [29]. The removal of these aggregates by washing with ethanol should lead to the appearance of a porous structure, with pore connections. Finally, the magnetic beads prepared by modification of CMC with SDS (CMC-Mn-S1, CMC-Mn-S2, and CMC-Mn-S3, respectively) were characterized by comparison with non-magnetic (CMC) and/or magnetic unmodified beads (CMC-Mn). After evaluation of adsorption capacities, the most promising material was subjected to in-depth examination, in order to provide a sustainable mitigation measure for methylene blue removal from aqueous solutions.

2.2. Manganese Ferrite Characterization

X-ray diffraction (XRD), Fourier-transform infrared spectroscopy (FTIR), vibrating-sample magnetometer (VSM), and transmission electron microscopy (TEM) were used to characterize the manganese ferrite ($MnFe_2O_4$) obtained by the sol-gel auto-combustion technique, as shown in Figure 2. According to the XRD pattern in Figure 2a, the $MnFe_2O_4$ sample is characterized by a crystalline structure. Peaks observed at 30.25°, 35.64°, 36.90°, 43.02°, 53.7°, 57.2°, and 62.85° confirm the pure cubic spinel structure of manganese ferrite (according to JCPDS card no. 10-0319) and correspond to the (220), (311), (222), (400), (422), (511), and (440) diffraction planes, respectively [35,36]. Figure 2b shows the FTIR spectra of $MnFe_2O_4$ registered in the range of 1000–400 cm^{-1}, which is in close agreement with the XRD findings about the spinel structure of the analyzed sample. Therefore, the band observed at 574 cm^{-1} is attributed to the vibration of the metal-oxigen bond in the tetrahedral sites of the spinel matrix, and the band at 468 cm^{-1} corresponds to the vibration of the metal-oxigen bond in the octahedral positions [35]. VSM was used to evaluate the magnetic properties of manganese ferrite nanoparticles at room temperature (Figure 2c). Considering the fact that the magnetization loop has no hysteresis, the obtained ferrite can be classified as superparamagnetic, with a magnetization value of 28.77 emu/g. This is also supported by coercivity and remanence values that are almost zero, indicating that the magnetization practically disappears with the removal of the external magnetic field. Similar behavior was also observed when manganese ferrite was synthesized by the co-precipitation technique [35]. The morphological features of $MnFe_2O_4$ nanoparticles were assessed by TEM, as highlighted in Figure 2d. Thus, the almost spherical-shaped nanoparticles can be observed, with a high tendency to agglomerate due to their magnetic properties. Based on the TEM image, particle size distribution was determined using Image J software (version 1.45s, National Institute of Health, Bethesda, MI, USA). According to the inset histogram (Figure 2d, upper left corner), the $MnFe_2O_4$ nanoparticles were found to be smaller than 18 nm in size. The selected electron diffraction pattern (Figure 2d, lower right corner) shows individualized, blurry rings, suggesting once again the crystallinity of the sample, as it is also shown in the XRD pattern.

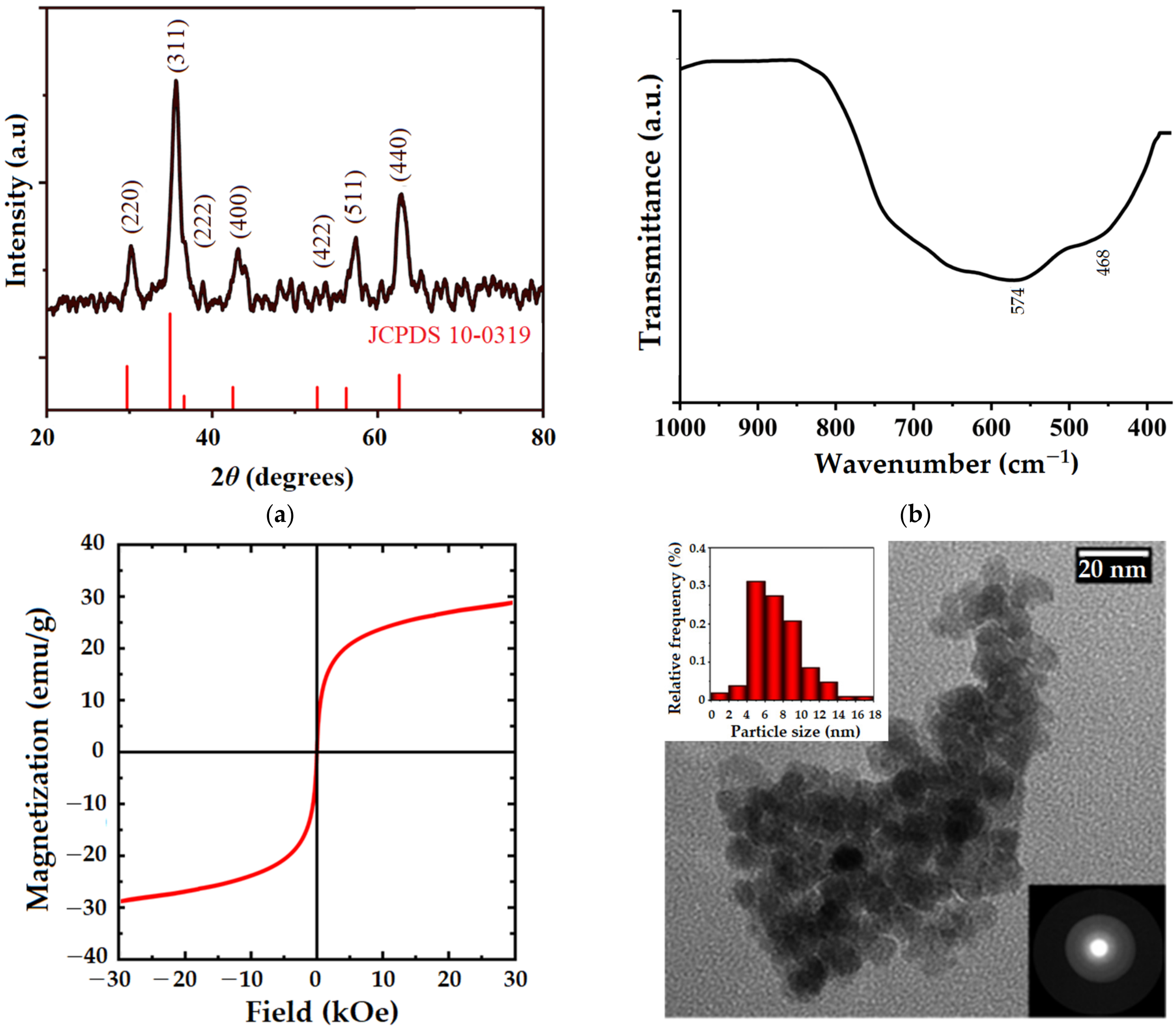

(**a**) (**b**)

(**c**) (**d**)

Figure 2. Manganese spinel ferrite analysis by (**a**) X-ray diffraction pattern compared to the standard XRD pattern of $MnFe_2O_4$ (JCPDS card no. 10-0319); (**b**) FT-IR spectrum; (**c**) VSM analysis; (**d**) representative TEM image, particle size distribution (upper left corner), and selected electron diffraction pattern (lower right corner).

2.3. CMC-Based Beads Characterization

2.3.1. Morphological Analysis

The surface and cross-section morphology of the CMC-based beads were analyzed by polarized light microscopy (PoLM) and scanning electron microscopy (SEM), as depicted in Figure 3 and Figure S2 (in Supplementary Materials), respectively. The PoLM images reveal the main modifications that occur in the CMC beads surface morphology (Figure 3a) induced by the addition of inorganic $MnFe_2O_4$ (Figure 3b) and SDS surfactant (Figure 3c–e). Thus, Figure 3a shows the uncompressed morphology of an unmodified CMC hydrogelated matrix, which allows the nanometric cellulosic fibrils to be seen. Moreover, the CMC beads are characterized by an orange color, provided by the cross-linking of the carboxylic groups with Fe^{3+} cations (also visible in Figure 1). These features are consistent with the cross-sectional morphology of the CMC granules (Figure S2, in Supplementary Materials), which show large pores and thin walls, typical of cellulosic hydrogels obtained by the freeze-drying process [37].

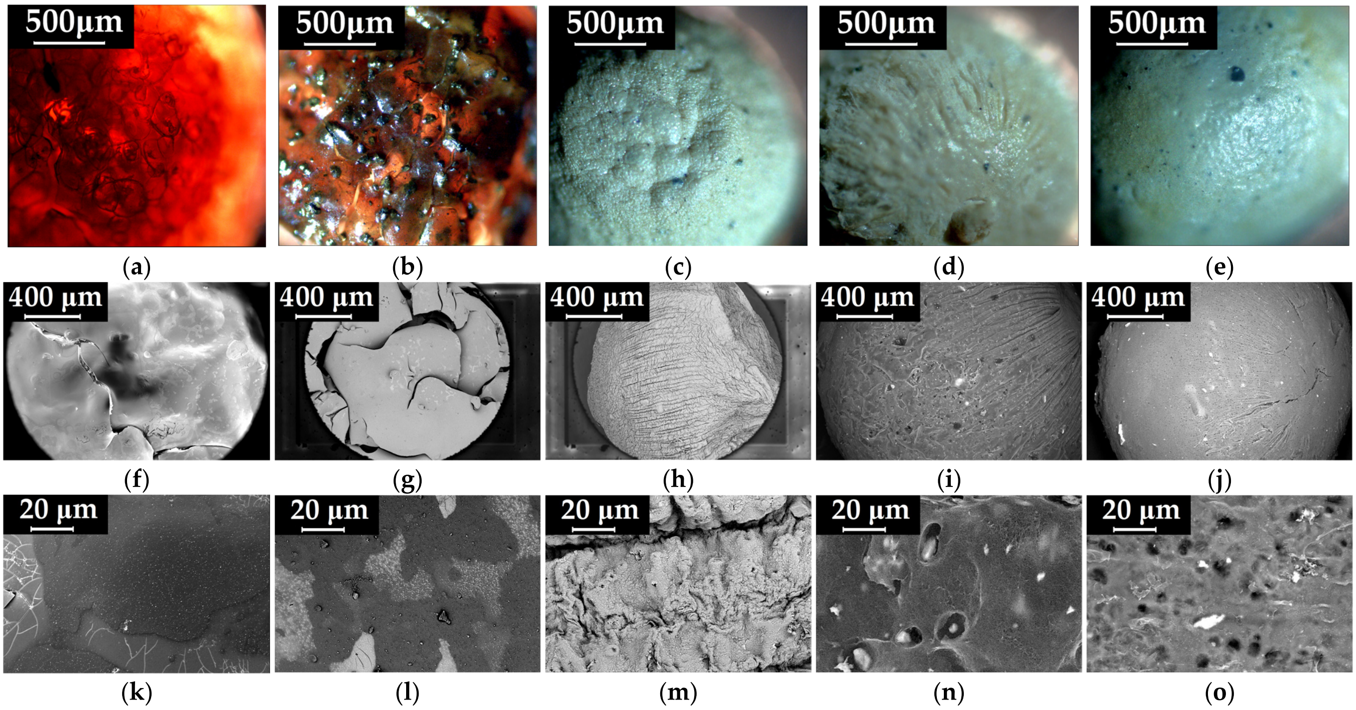

Figure 3. Surface morphology images of CMC (**a**,**f**,**k**), CMC-Mn (**b**,**g**,**l**), CMC-Mn-S1 (**c**,**h**,**m**), CMC-Mn-S2 (**d**,**i**,**n**), and CMC-Mn-S3 (**e**,**j**,**o**) beads, obtained by PoLM (**a**–**e**) and SEM (**f**–**o**) microscopy, respectively.

In comparison to the pristine CMC beads, the addition of ferrite nanoparticles into the polysaccharide matrix induced an irregular surface morphology of the CMC-Mn beads with a proclivity for the agglomeration of the magnetic component (Figure 3b). However, the cross-section of the beads revealed no significant morphological changes, as shown in Supplementary Materials (Figure S2b). When SDS and NaCl are added during the gelation process, the obtained CMC-Mn-S1, CMC-Mn-S2, and CMC-Mn-S3 beads acquire a whitish color and a specific morphology, both at the surface (Figure 3c–e) and in cross-section (Figure S2c–e). In addition, for SDS-modified beads, better dispersion of the magnetic nanoparticles in the polymer matrix was observed.

For an in-depth analysis of the morphological modifications of the beads, SEM microscopy was used (Figure 3f–j). It can be noticed that the images obtained by SEM are consistent with their analogues provided by polarized light microscopy (Figure 3a–e). Despite the cross-sectional morphology obtained by the freeze-drying process (large, elongated pores), the CMC and CMC-Mn beads present a non-porous and brittle surface morphology as a result of cross-linking with iron cations (Figure 3f,g,k,l).

Other authors demonstrated that the anionic surfactant SDS self-assembles into micelles in aqueous environments and forms micellar aggregates, mainly when NaCl salt is added in excess [29]. As expected, its use in the CMC hydrogel matrix led to the appearance of a porous surface, which should provide increased efficiency and adsorption capabilities to the obtained beads. Furthermore, the use of SDS led to a compact cross-sectional porous morphology (Figure S2h–j), which was needed for improved mechanical properties of the beads. This can be explained by the fact that the presence of SDS large micelles led to an in-depth, interconnected, crosslinked network. Note that the presence of iron is well observed in the bead's cross-section, as shown in Figure S2m–o. By comparison with CMC-Mn-S1, which has a folded surface, increasing the SDS content led to spherical beads with a highly porous and smoother surface, as observed for CMC-Mn-S2 and CMC-Mn-S3 samples.

The CMC polymeric matrix modifications were confirmed by changes occurring at the level of constituent elements, as highlighted in Supplementary Materials (Figure S3). The elemental mapping allowed the visualization of the elements in the analyzed samples. Figure S3d (corresponding to CMC beads) reveals the presence of carboxymethyl cellulose elements (C and O) as well as the crosslinking agent (Fe). It can be noticed that the Fe element is uniformly distributed as a result of the cross-linking process (Figure S3g). By comparison with pristine CMC beads, the insertion of manganese spinel ferrite was confirmed by the presence of the Mn element in both CMC-Mn and CMC-Mn-SDS samples (Figure S3e,h and f,I, respectively). Moreover, the presence of S, Na, and Cl elements confirms the addition of SDS and NaCl salts during the CMC gelling process (Figure S3f).

2.3.2. Structural Modifications

The structural properties of the CMC-based hydrogelated beads and the interactions at the polysaccharide functional groups were investigated using FTIR analysis, as shown in Figure 4. The spectrum of sodium carboxymethyl cellulose powder (NaCMC) revealed characteristic absorption bands: the broad band at 3465 cm^{-1} is related to O–H stretching vibrations (alcohol and intermolecular bonding); bands at 2920 cm^{-1} and 2878 cm^{-1} correspond to C–H (methylene) symmetric and asymmetric stretching vibrations, respectively; the typical bands for asymmetric and symmetric stretching of the $–COO^{-}Na^{+}$ carboxylate are found at 1622 cm^{-1} and 1426 cm^{-1}, respectively; the band at 1329 cm^{-1} is attributed to C–H bending, coupled with—OH bending, while the 1265 cm^{-1} band is given by C–H deformation; the region between 1200 and 930 cm^{-1} overlaps the stretching vibrations of the anhydroglucose units (C–O–C) with the C–O vibration from primary (C6–OH at 1020 cm^{-1}) and secondary alcohols (C2–OH at 1115 cm^{-1} and C3–OH at 1059 cm^{-1}); the glycosidic bonds (β1–4) vibration appears at 899 cm^{-1}; the band at 711 cm^{-1} is due to the monosubstituted out of plane =C–H bending, and the band at 590 cm^{-1} corresponds to C–C–O and O–C–O in plane deformation vibrations [23,37–40].

By comparison with pristine NaCMC, the cross-linking process with iron cations induced visible structural modifications in CMC beads (Figure 4). The adsorption bands corresponding to O–H (3486 cm^{-1}) and C–H stretching vibrations (2927 and 2887 cm^{-1}) were shifted to higher wavenumbers. The appearance of a new peak in the CMC spectrum (1735 cm^{-1}) is due to the carbonyl (–C=O) stretch, from the protonated –COOH group). This confirms the interactions between carboxylic groups in CMC and iron cations. Similar observations were made when CMC was crosslinked with Al^{3+} ions [29] or when a sodium carboxymethyl cellulose/sodium alginate blend was crosslinked with Fe^{3+} ions [41]. Shifting the absorption bands of $–COO^{-}$ asymmetric and symmetric stretching to lower wavenumbers (1600 and 1384 cm^{-1}, respectively), with the disappearance of the 1426 cm^{-1} band (assigned to carboxyl groups as salts), also suggests the existence of chemical interactions between carboxylate groups and iron cations [42]. The appearance of the shoulder at 1457 cm^{-1} is due to –CCH and –OCH bending vibrations of the pyranose ring [43]. The shifting of ΔO–H band from 1329 cm^{-1} to 1356 cm^{-1} in the CMC beads could also indicate the participation of polysaccharide hydroxyl groups in the formation of chelating structures with Fe^{3+}. This trend is also supported by the disappearance of the C6–OH band (1020 cm^{-1}), which suggests the interaction of the primary hydroxyl groups, and the increase in intensity of the C3–OH band (1061 cm^{-1}). The region 900–500 cm^{-1} has also undergone a few changes following the cross-linking of the CMC polysaccharide.

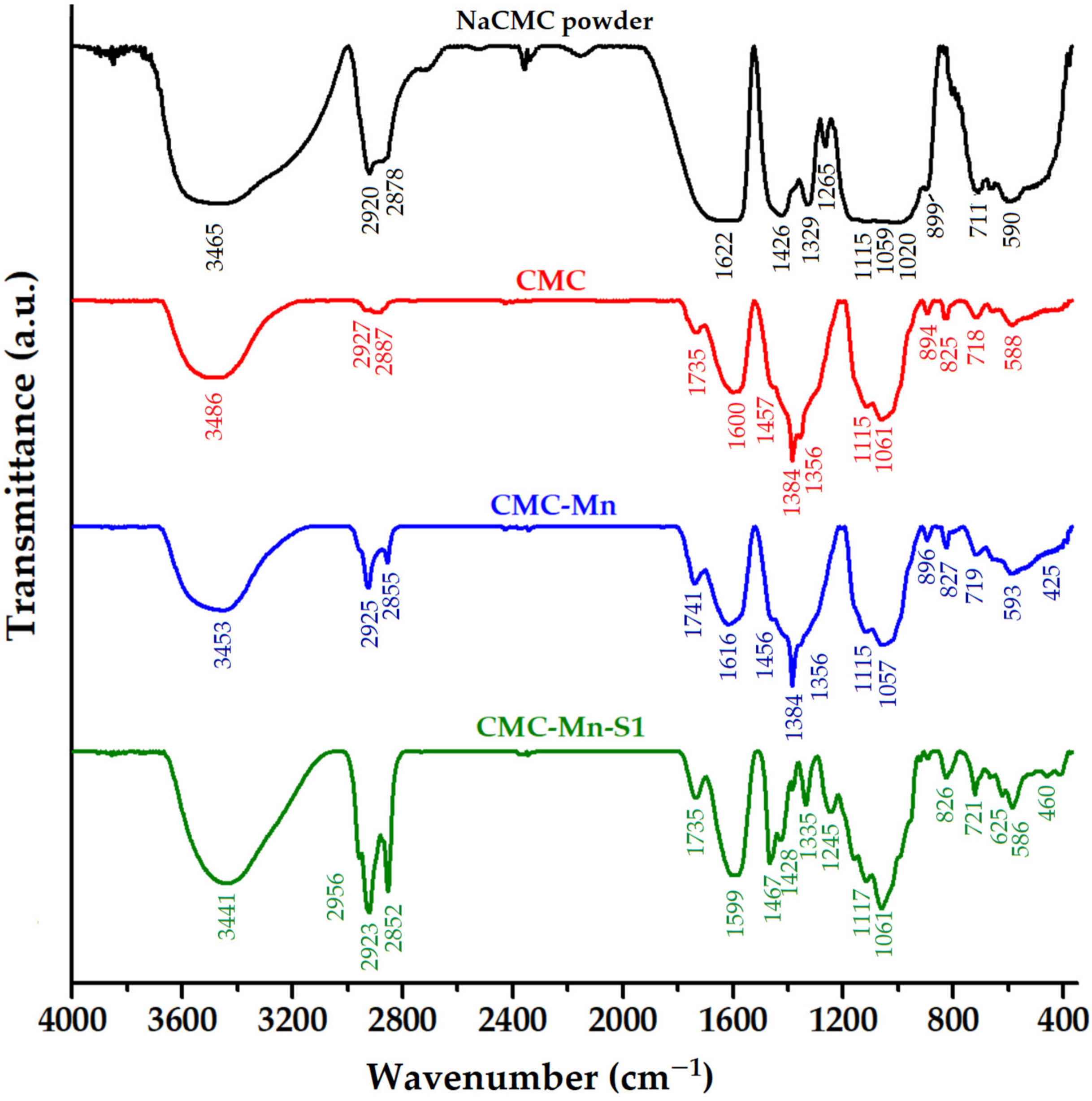

Figure 4. FTIR spectra of carboxymethyl cellulose powder (raw CMC powder) and of the investigated beads (CMC, CMC-Mn, and CMC-Mn-S1).

The CMC-Mn spectrum resembles the CMC spectrum (Figure 4), with slight displacement of the absorption bands. However, the presence of manganese spinel ferrite is confirmed by the presence of Fe–O and Mn–O characteristic absorption bands, which can be observed in the range of 600–400 cm^{-1}. By comparison with the CMC and CMC-Mn spectra, the use of SDS surfactant led to specific modifications. The bands corresponding to CMC-Mn structure are easily shifting, but new bands appear due to surfactant chemical structure, such as 2956 cm^{-1} (from CH_3 asymmetric stretching vibrations), 1467 and 1061 cm^{-1} (asymmetric and symmetric stretching νO=S=O of sulfonate groups), and 1245 cm^{-1} due to C–H bending vibrations [29]. However, the increase in intensity in the regions 3400–3000 and 1740–1500 could indicate a more reactive surface (–OH and –COO^{-} groups).

2.3.3. Magnetic Properties

The magnetization curves of $MnFe_2O_4$-loaded CMC beads (CMC-Mn and CMC-Mn-S1-3) were determined by using VSM, as shown in Figure 5. All the CMC-based magnetic beads presented magnetization loops similar to those of pure manganese ferrite (Figure 2c). Thus, the investigated beads keep their superparamagnetic character, as indicated by the lack of hysteresis as well as zero coercivity and remanence. However, the decrease of the magnetization values (registered at 30 kOe) from 28.77 emu/g (pure $MnFe_2O_4$) to values ranging from 1.2 to 2.1 emu/g should be mentioned, as given in Table 1. This can be attributed to the use of small amounts of ferrite (only 10%) in the polysaccharide matrix. For the same reason, the addition of SDS led to an additional proportional decrease in magnetization. However, an exception is made by the CMC-Mn-S2 beads, which have a slightly higher magnetization when compared to the beads with less SDS (CMC-Mn-S1), although the initial trend was the opposite. The magnetization values and the superparamagnetic properties of the beads are sufficient for providing easy separation from a solution when an external field is applied, even when the beads are charged with the adsorbed dye (as the lower right corner image from Figure 5 demonstrates).

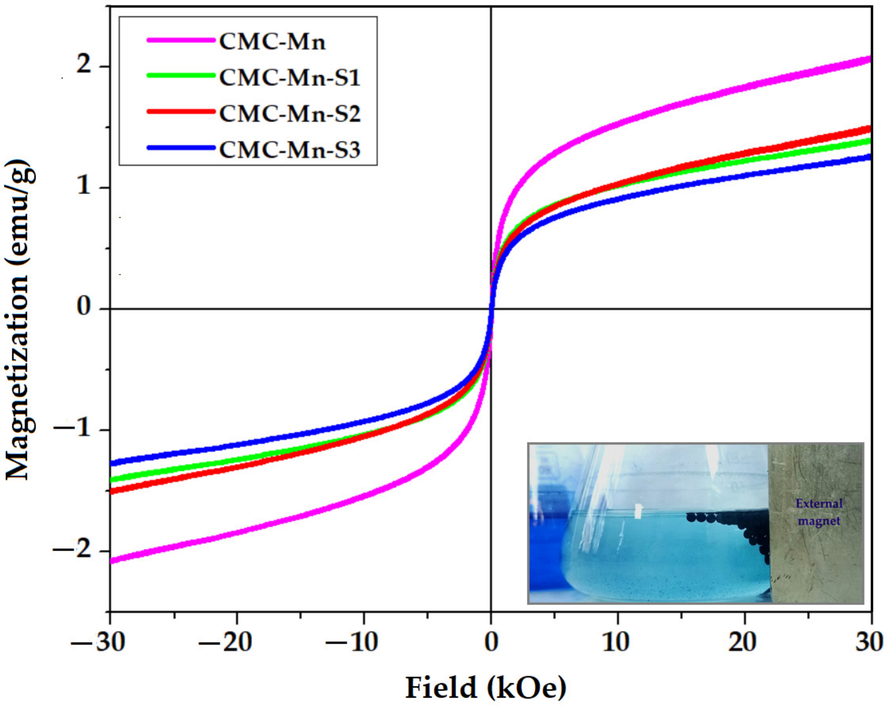

Figure 5. VSM analysis of manganese ferrite-loaded CMC beads (the inset image shows the separation of the MB-loaded beads from the aqueous solution under an external magnetic field).

2.4. Adsorption Tests of Methylene Blue (MB) Cationic Dye

2.4.1. Batch Adsorption Screening Test

In order to determine the adsorption performance of MB cationic dye from aqueous solutions under the same conditions onto the carboxymethyl cellulose-based beads (CMC, CMC-Mn, and CMC-Mn-S1-3), a batch adsorption screening test [44] was carried out. The preliminary results regarding the adsorption capacities (q, mg/g) and dye removal efficiency (Y, %) are highlighted in Figure 6. As expected, the addition of SDS surfactant during the gelling process of CMC led to increased adsorption capacities as compared with CMC and CMC-Mn beads (Table 1). This is attributed to the electrostatic repulsions of the $-O-SO_3^-$ groups from the SDS surfactant molecules and polyanionic CMC chains in the gelation process, which favor the formation of a more porous structure [29]. After SDS removal, the electrostatic interactions between the carboxylic groups of CMC (present on the beads' surface and within their pores) and MB molecules are expected to improve. Of these, CMC-Mn-S2 magnetic beads displayed the best adsorption performance, with the highest values of adsorption capacity (18.22 ± 0.23 mg/g) and color removal efficiency (72.38 ± 0.92%). The beads were dried after the adsorption assay, and their macroscopic images are shown in Figure 6. It should be noted that the color is more intense in CMC-Mn-S1 due to the shrinkage of the beads, whereas CMC-Mn-S2 retains its shape even after drying. The adsorption properties of CMC-Mn-S2 beads can also be correlated with their surface morphology (Figure 3d,i,n). In addition to these, the higher value of magnetization among SDS-containing samples recommends the use of CMC-Mn-S2 beads as adsorbents for subsequent tests (adsorption kinetics and isotherms).

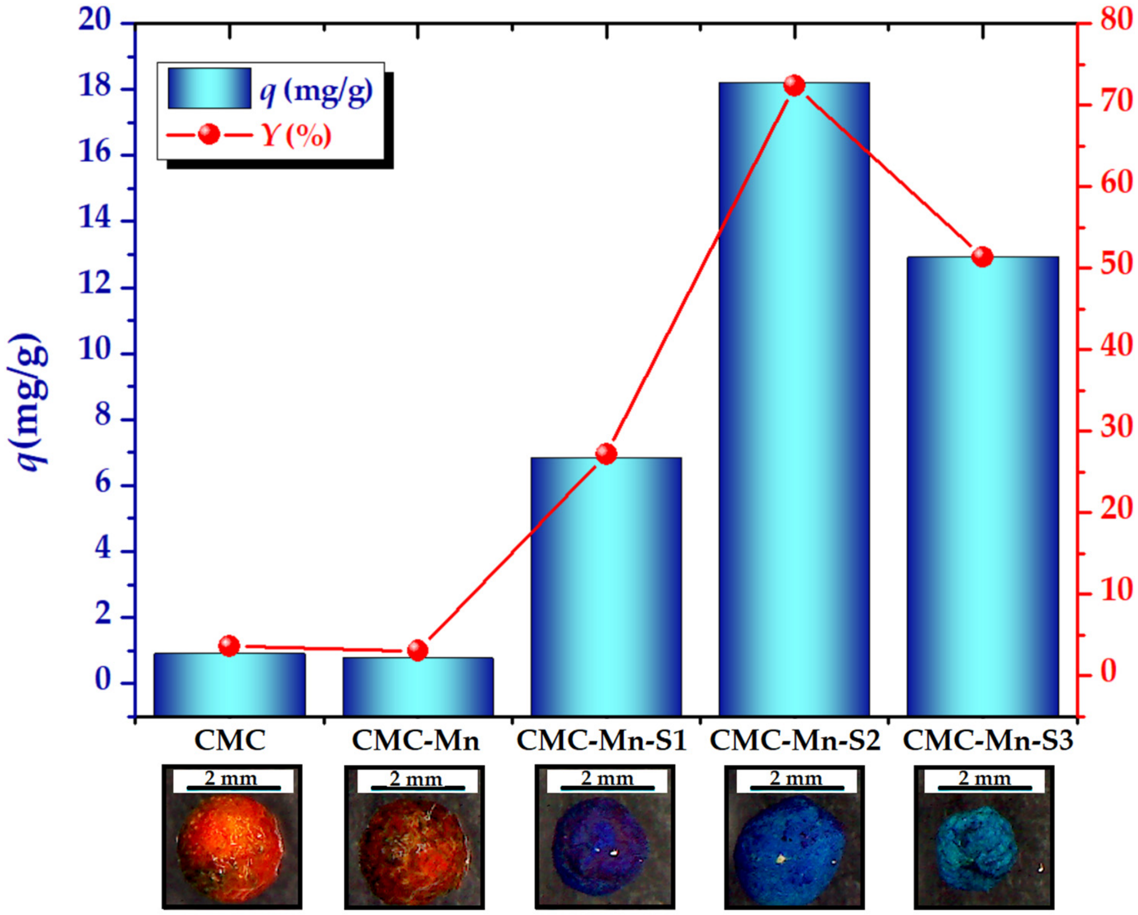

Figure 6. Batch screening test (adsorption capacity—*q*, mg/g, and color removal efficiency—*Y*, %) for Methylene Blue (MB) removal from aqueous solutions at room temperature (sorbent dose of 2 g/L, contact time of 1 h, MB initial concentration of 50 mg/L); macroscopic images of dried CMC-based beads after the adsorption process.

2.4.2. Kinetics and Isotherms

The effect of the contact time on the removal of MB from aqueous solutions is assessed since the dye's rate of adsorption is an important factor in the accurate evaluation of the adsorbent. As depicted in Figure 7a, the adsorption capacity (*q*, mg/g) of CMC-Mn-S2 hydrogelated beads was evaluated over time for different sorbent doses (*SD* = 0.5–3 mg/L). As expected, the adsorption of MB cationic dye is increasing with contact time, regardless of the sorbent dosage employed, due to the enhanced driving forces. As a result, a three-stage adsorption tendency was noticed [45], which is most noticeable when smaller amounts of sorbent are used. In the initial phase, a rapid increase is observed in the first 30 min, mainly due to the fast adsorption of MB on the CMC-Mn-S2 beads surface. Then, in the second stage (30–180 min), a slower adsorption is observed, which is more apparent when employing a lower dose of sorbent. The active adsorption sites on the surface of the beads are often limited at this point, and the MB molecules in the solid phase start to exhibit repulsive forces [29]. Following this stage, the dye molecules seek to diffuse into the pores of the beads and are slowly adsorbed by the deeper active sites until equilibrium is reached. In the third stage (>180 min), the adsorption capacity reaches a steady state due to the saturation of the carboxyl groups with MB molecules. This leads to the attainment of adsorption equilibrium.

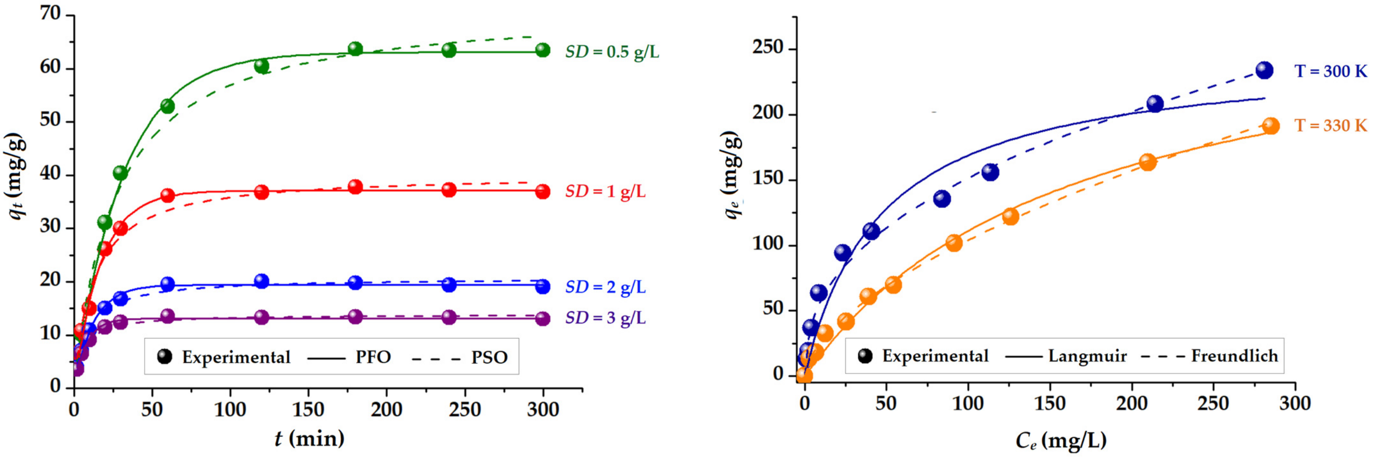

(**a**) (**b**)

Figure 7. Adsorption of Methylene Blue onto CMC-Mn-S2 adsorbent: (**a**) experimental data for different sorbent doses (0.5–3 g/L) and mathematical kinetic models (pseudo-first order and pseudo-second order); (**b**) experimental data at two temperatures (300 and 330 K) and isotherm models (Langmuir and Freundlich).

The impact of the sorbent dose (*SD*) on the adsorption capacity (*q*, mg/g) is also depicted in Figure 7a. Hence, it can be shown that after 6 h of the experiment, the increase in the sorbent dose led to a decrease in the adsorption capacity of MB. Consequently, a sorbent dose of 0.5 g/L resulted in the highest adsorption capacity of 63.46 mg/g, which was then decreased to 36.88 mg/g for *SD* = 1 g/L, 19.04 mg/g for *SD* = 2 g/L, and finally to 12.99 mg/g for *SD* = 3 g/L. This trend was also found by others [46] and is mainly attributed to the presence of excessive active sites as the sorbent dose is incremented.

For an in-depth investigation of the adsorption rate of the adsorption process [29], the experimental data were analyzed using two kinetic models: Lagergren's pseudo-first-order model (PFO) and Ho's pseudo-second-order model (PSO) [47]. Predictions according to the two models are represented in Figure 7 (by solid and dashed lines), while the corresponding non-linear equations and kinetic parameters are detailed in Table S1. The goodness-of-fit was employed to determine the better agreement of predicted data with the experimental ones by calculating the chi-squared (χ^2) statistical test (smaller values are better), as described by Equation (S1) in Supplementary Materials. According to Figure 7a and χ^2 values from Table S1, the PFO model best describes the adsorption kinetics of MB onto CMC-Mn-S2 hydrogelated beads [47]. Moreover, this model's assessment of the theoretical equilibrium adsorption capacity ($q_e^{(calc)}$) is consistent with the experimental findings ($q_e^{(obs)}$). A better fit given by PFO (compared to PSO) might be attributed to the fact that the separation process most probably involves a single main step, controlled by adsorption rather than diffusion. Similar findings were reported by other authors that investigated the adsorption of Cu(II) ions onto semi-interpenetrated polymer networks [48] or when the MB adsorption was evaluated on walnut-shell-based cellulosic materials [49].

The adsorption isotherms were investigated at 300 K and 330 K, respectively, in order to evaluate the relationship between the equilibrium concentrations (C_e, mg/L) of the cationic dye MB and the CMC-Mn-S2 adsorption capacities at equilibrium (q_e, mg/g). Considering the results obtained in the kinetic study (Figure 7a) for the determination of the adsorption isotherms, a contact time of 300 min was used to ensure the achievement of the adsorption equilibrium. The experimental data given in Figure 7b indicates a decrease in adsorption capacity at equilibrium with increasing temperature, from 234 mg/g (at 300 K) to 191 mg/g (at 330 K). This can be explained by the fact that when the temperature rises, the MB molecules acquire sufficient kinetic energy to overcome the electrostatic attraction and detach from the sorbent surface [45]. The faster and increased adsorption of MB on the CMC-Mn-S2 beads at lower temperatures can be an advantage when it comes to environmental applications (temperatures that are more similar to those of the environment).

The adsorption process and the affinity of CMC-Mn-S2 beads toward MB molecules were investigated by using the Langmuir and Freundlich isotherm models [29,50]. The experimental data were interpolated, and the calculated predictions are shown in Figure 7 with solid and dashed lines. Additionally, the chi-square (χ^2) test was performed, and the corresponding values are given in Table S2 (Supplementary Materials), along with the equations and parameters of the isotherms. Thus, the data in Table S2 show that the Langmuir equation is the most appropriate model for the investigated systems, suggesting monolayer dye adsorption (a smaller value of χ^2). The Langmuir isotherm model predicted a homogeneous monolayer adsorption system, indicating a finite number of equivalent sites and no interactions between MB molecules at the surface of the CMC-Mn-S2 beads [29]. Furthermore, a higher value of the Langmuir constant (K_L = 0.021 L/mg) indicates stronger interactions and increased affinity between the surface of the CMC-Mn-S2 beads and cationic dye molecules at a lower temperature (300 K). A further analysis can be expressed in terms of the dimensionless equilibrium parameter (R_L), to reveal the favorable adsorption of the Langmuir isotherm, in conformity with Equation (1):

$$R_L = \frac{1}{1 + K_L C_0}, \tag{1}$$

where K_L represents the Langmuir constant and C_0 is the initial dye concentration. The R_L is usually determined in order to confirm the nature of the adsorption process: irreversible adsorption (R_L = 0); favorable adsorption (0 < R_L < 1) and linear unfavorable adsorption (R_L = 1) [50,51]. As shown in Table S2, the calculated values of the R_L factor were 0.373 (300 K) and 0.614 (330 K) for initial dye concentrations (C_0) ranging from 10 to 400 mg/L. These results confirmed the favorable adsorption of MB cation dyes onto hydrogelated CMC-Mn-S2 adsorbent.

Furthermore, the Dubinin-Radushkevich (D-R) isotherm model was used to determine the type of adsorption process by calculating the mean free energy of adsorption, E_S (kJ/mol), as given in Table S2. The values of E_S make it possible to understand the nature of the adsorption process (physical, ion exchange, or chemisorption). Hence, values between 8 and 16 kJ/mol reflect an ion exchange process, while E < 8 kJ/mol characterizes a physical adsorption mechanism [52]. According to D-R data given in Table S2, the mean free energies of the investigated systems were 10.91 kJ/mol (at 300 K) and kJ/mol (at 330 K). This suggests that the adsorption of MB dye onto the CMC-Mn-S2 surface occurs mainly via strong electrostatic interactions (ion exchange mechanisms between the negatively charged carboxylic (–COO$^-$) groups of the adsorbent and positively charged amino groups from MB).

Figure 8a highlights the influence of sorbent dose (*SD*) and temperature on MB removal efficiency (*Y*). As discussed in the kinetic assay (Figure 7a), the increase in *SD* led to a decrease in adsorption capacity (*q*, mg/g). However, Figure 8a shows that by increasing the *SD* (at both 300 and 330 K temperatures), the removal efficiency of the MB dye from the aqueous solution is increasing. This behavior is explained by the fact that increasing the *SD* for a fixed number of MB molecules (50 mg/L) implies the availability of more adsorption sites. As a consequence, a larger amount of MB is adsorbed from the aqueous solution, but the amount of MB per unit mass of CMC-Mn-S2 adsorbent decreases. Because the MB dye is a well-known exogenous fluorophore [53], its homogeneous adsorption on the CMC-Mn-S2 surface was highlighted by using polarized light microscopy (Figure 8b). Moreover, the penetration into the depth of the beads of MB molecules was proved by the cross-section image (given in Figure S4, Supplementary Materials) due to the porous network created by the SDS surfactant's introduction during the gelation process. These results are in agreement with SEM morphology (discussed in Section 2.3.1). In addition, the presence of iron is well observed in the MB-loaded beads cross-section (Figure S4), confirming the absence of iron leakage during the adsorption process and the increased stability of the polymeric hydrogelated matrix.

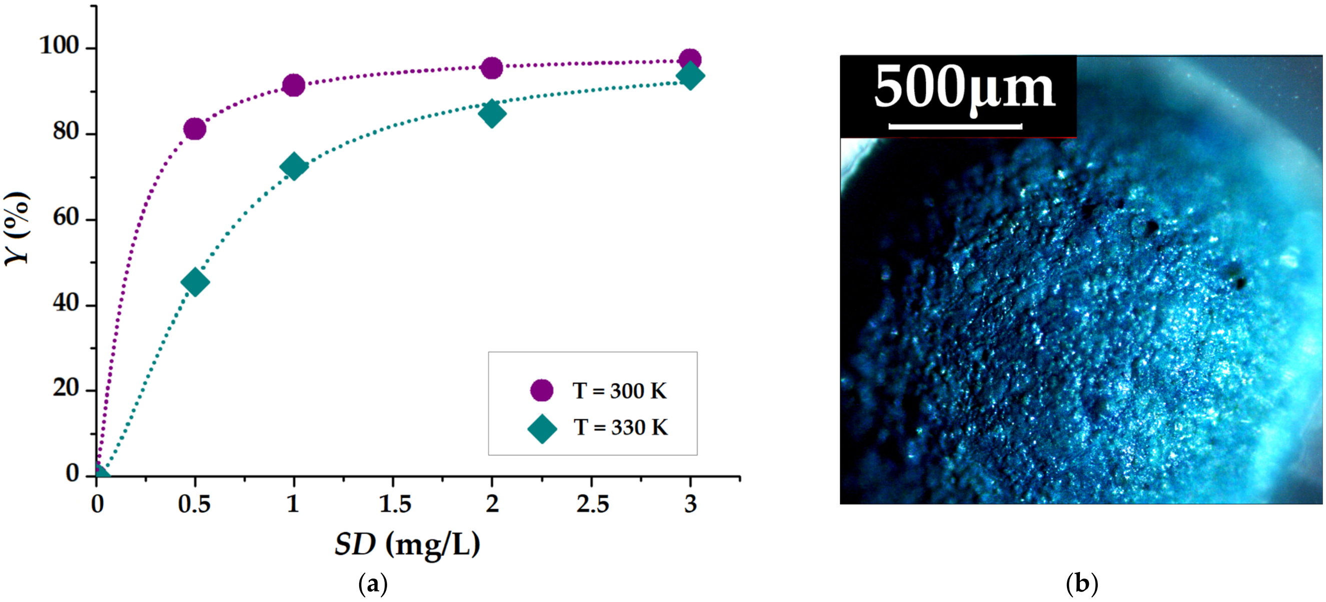

(a)

(b)

Figure 8. (**a**) Removal efficiency at equilibrium (%) of MB from aqueous solutions (C_0 = 50 mg/L) as a function of sorbent dose (*SD*); (**b**) Image obtained by polarized light microscopy of the CMC-Mn-S2 surface after MB adsorption.

Furthermore, we performed a comparative literature analysis on the efficacy of our CMC-based beads in comparison to existing CMC-based composite materials used to remove MB from aqueous solutions (maximum adsorption capacities are given in Table S3, Supplementary Materials). In contrast to CMC-based composites in the form of membranes [54], films [55], or (nano)particles [26,56], biosorbents in the form of aerogels [27,57] or (micro)granules [25,29,58,59] demonstrated higher MB adsorption capacities (between 75 and 245 mg/g). However, the maximum experimental MB adsorption capacity obtained in this study (234 mg/g) suggests that CMC-Mn-S2 beads are suitable materials for efficient removal of MB from aqueous solutions.

More than that, to demonstrate the suitability of CMC-Mn-S2 beads for cationic dye adsorption, other organic dyes were tested. Crystal violet (CV) and brilliant green (BG), two additional cationic dyes frequently employed in pharmaceutical applications [49,60], were examined for their ability to bind to these CMC-Mn-S2. Thus, Figure S5 points out the ability of CMC-Mn-S2 to adsorb high amounts of CV (62.4 mg/g) and BG (51.9 mg/g) from aqueous solutions after a contact time of 60 min. It should be noted that all adsorption studies were carried out at neutral pH $\approx$ 6 (by dissolving MB powder in distilled water), first to be suited for environmental applications and secondly because the adsorption capacities at more acidic or alkaline pH were found to be lower, as shown in Figure S6.

2.4.3. Thermodynamics

A detailed understanding of the underlying energy changes associated with the adsorption process can be obtained by determining thermodynamic parameters such as Gibbs free energy (ΔG), enthalpy (ΔH), and entropy (ΔS). The values of these thermodynamic parameters were calculated following the approach reported in our previous study [49]. For the adsorption process reported in this work, the thermodynamic parameters are summarized in Table 2.

Table 2. Values of various thermodynamic parameters for the adsorption of the MB cationic dye onto the CMC-Mn-S2 adsorbent.

Temperature	ΔG (kJ/mol)	ΔH (kJ/mol)	ΔS (J/K.mol)
300 K	−17.671	−34.572	−56.337
330 K	−15.981		−56.337

Taking into account the negative values of the Gibbs free energy ($\Delta G < 0$), it can be stated that the adsorption processes of MB onto an adsorbent have a spontaneous (exergonic) character. Because a more negative value of ΔG (−17,671 kJ/mol) was recorded at 300 k compared to the value at 330 K (−15,981 kJ/mol), it can be mentioned that a better affinity between the CMC-Mn-S2 adsorbent and MB molecules occurs at lower temperatures. It is important to note that these results are in agreement with the previous adsorption isotherm study (Figure 7b). Table 2 shows the negative enthalpy value ($\Delta H < 0$), suggesting exothermic effects of the adsorption. Additionally, the negative values of entropy indicate a rearrangement of the adsorption of MB on the CMC-Mn-S2 surface. As a result of the association between organic dye molecules and adsorbents, it appears that randomness at the solid-liquid interface decreases. A similar trend was observed when MB was adsorbed onto a CMC-based composite membrane [54].

2.4.4. Desorption Assay and Re-Use Test

The desorption experiments (in ethanol and acetone), followed by the MB re-adsorption (q, mg/g) on CMC-Mn-S2 recovered beads are discussed in detail in Supplementary Materials (Figure S7). However, it should be mentioned that desorption efficiency in acetone reaches 93%, implying a subsequent MB re-adsorption capacity of 48.6 mg/g (close to the initial adsorption values of about 52.9 mg/g). The possibility of being re-used is beneficial in environmental applications, and CMC-Mn-S2 can be considered an efficient adsorbent for removing MB from wastewater.

2.5. Molecular Docking

The molecular docking computations were performed to detail the intermolecular interactions between the cationic dye and the CMC-Mn-S2 adsorbent. The MB dye molecule (in cationic form) was used as the ligand for molecular docking, and the CMC oligomer (a tetramer) was used as the receptor. The YASARA-Structure program was used to create the structures of both the ligand (MB) and the receptor (CMC tetramer). The structures were then subjected to geometry optimization at the molecular mechanics theory level using the YASARA force field.

Then, for the molecular docking simulations, the optimal conformations (3-D structures) of the receptor and ligand were used. In order to achieve this, 100 docking poses were tested at the YASARA force field level. During molecular docking simulations, the receptor was regarded as a rigid body, whereas the ligand (the MB dye molecule) was treated as a flexible body. The YASARA-Structure program's "AutoSMILES" method was used to automatically generate the parameters for the modeled structures.

Figure 9 displays the outcomes of the molecular docking in the optimal docked complex pose, highlighting the intramolecular interactions between the ligand (MB) and the receptor (CMC tetramer). The hydrogen bonds (H-bonds), which are represented as dotted yellow lines in Figure 9, were found to be present inside the CMC receptor. Moreover, the intermolecular interactions between the MB molecule and the CMC tetramer are based on hydrophobic interactions (represented as solid green lines). These hydrophobic interactions can be linked to the physical adsorption of MB dye onto CMC (based on van der Waals forces). The docked complex CMC/MB presented a binding energy (E_b) of

−3.92 kcal/mol and a dissociation constant (K_d) of 1.33 mM, according to computational calculations. The dissociation of the docked complex is feasible due to the considerable value of the dissociation constant (K_d = 1.33 mM), which indicates that the connection between the MB ligand and the CMC receptor is not very strong.

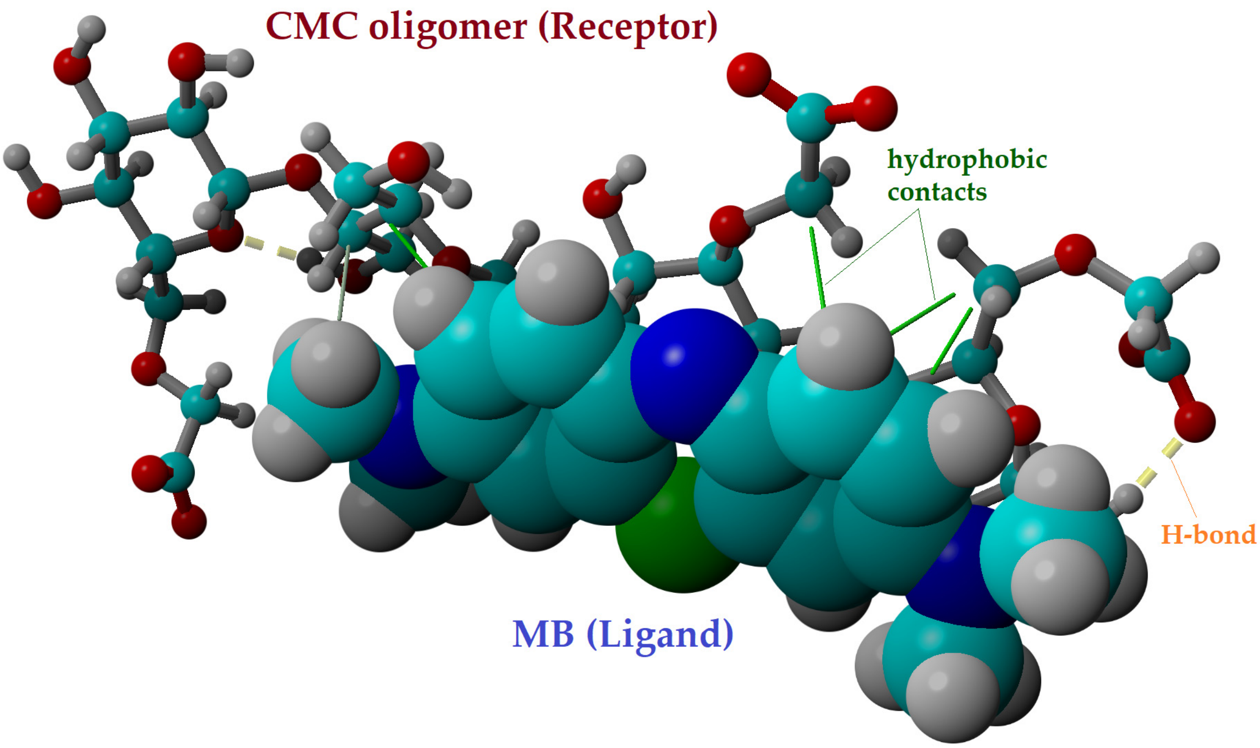

Figure 9. Molecular docking outcomes showing the best pose of the docked complex between the CMC tetramer receptor and MB ligand, as well as their interaction mode (E_b = −3.92 kcal/mol and K_d = 1.33 mM).

In order to take into account the contributions of the van der Waals and Coulomb (electrostatic) forces, the interaction energies between the ligand (MB dye) and CMC receptor were also computed at the level of the YASARA force field (molecular mechanics theory). According to the theoretical results, electrostatic Coulomb forces (ΔE_{CL} = −33.25 kcal/mol) are dominant compared to van der Waals forces (ΔE_{vdW} = −21.92 kcal/mol) in the mechanism of intermolecular interaction between MB dye and CMC oligomer. The docking results for the CMC/MB system were in good agreement with the D-R isotherm results, which suggested a mechanism of adsorption based on ion exchange (i.e., electrostatic interactions).

3. Conclusions

By ionically cross-linking with iron cations, sodium carboxymethyl cellulose (CMC) was used to create stabilized ionotropic hydrogels in the form of beads. In order to facilitate the magnetic separation of sorbents from aqueous solutions, $MnFe_2O_4$ nanoparticles (synthesized by the sol-gel auto-combustion method) were introduced into the hydrogelated matrix. In addition, SDS surfactant was used as a pore generator (porogen) to increase the adsorption capacity and hydrodynamic stability of the CMC-based beads. Therefore, magnetic beads were prepared by modification of CMC with SDS surfactant (CMC-Mn-S1, CMC-Mn-S2, and CMC-Mn-S3, respectively), and characterized (morphologically, structurally, and magnetically) by comparison with non-magnetic (CMC) and magnetic unmodified beads (CMC-Mn). After evaluation of adsorption capacities, CMC-Mn-S2 was found to be the most promising material and was further subjected to in-depth examination. The adsorption kinetics were best described by the PFO model, and the maximum adsorption capacity was registered at lower temperatures (234 mg/g at 300 K).

The isotherm data were best interpolated by the Langmuir isotherm model, suggesting a homogeneous monolayer adsorption mechanism. According to the thermodynamic parameters, it was found that the investigated adsorption processes occurred spontaneously ($\Delta G < 0$), revealing an exothermic nature ($\Delta H < 0$). After immersion in acetone, the sorbent was recovered (93% desorption efficiency) and successfully re-used for another adsorption test. In addition, molecular docking suggested that the interaction between MB dye and CMC was mainly based on electrostatic Coulomb forces ($\Delta E_{CL} = -33.25$ kcal/mol). These appeared between the negatively charged carboxylic ($–COO^-$) groups of the adsorbent and the positively charged amino groups in the MB molecule. Due to the fact that CMC-based physical hydrogel formulations fulfill certain aspects, such as the use of natural, biocompatible, and non-toxic materials, reduced chemicals leakage, increased pollutant adsorption capacities, and ease of recovery, the investigated hydrogelated beads can be considered a promising sorbent for environmental applications.

4. Materials and Methods

4.1. Materials

Manganese nitrate ($Mn(NO_3)_2 \cdot 6H_2O$), iron nitrate ($Fe(NO_3)_3 \cdot 9H_2O$), and citric acid ($C_6H_8O_7 \cdot H_2O$) were purchased from Merck Chemical (Saint Louis, MO, USA) and employed in manganese spinel ferrite synthesis. Sodium carboxymethyl cellulose (sodium salt, average M.W. 90000, DS = 0.7) was acquired from Acros Organics (Geel, Belgium), while sodium dodecyl sulfate (SDS), sodium chloride (NaCl), and Methylene Blue (MB) were supplied by Merck Chemical (Saint Louis, MO, USA). Ethanol was provided by Chemical Company (Iasi, Romania). These analytically graded materials were used without further purification.

4.2. Manganese Spinel Ferrite and CMC-Based Magnetic Beads Preparation

4.2.1. Synthesis of Manganese Spinel Ferrite ($MnFe_2O_4$)

The manganese spinel nanostructures were prepared by the sol-gel auto-combustion method [32]. In our case, the metal nitrate solutions ($Mn(NO_3)_2$ and $Fe(NO_3)_3$) were blended in stoichiometric proportions. Then the chelating agent was added. Thus, the molar ratio of cations to citric acid was 1:3. The procedure continued with the stirring and heating of the resulting solution in a water bath at 80 °C. Further, the sol developed into a dark-brown, porous, dry gel (Figure S8a). By gradually elevating the temperature up to 350 °C, self-propagating combustion was observed. This process was complete when loose black powder was formed (Figure S8b).

4.2.2. CMC-Based Beads Preparation

The preparation of CMC-based beads took place in an easy manner, as graphically represented in Figure 1. In a first phase, a stock solution of carboxymethyl cellulose (CMC) was prepared by dissolving 3% sodium carboxymethyl cellulose (NaCMC) in distilled water under continuous stirring at 45 °C for 24 h. In a second phase, the required amount of manganese spinel ferrite (10% by reference to CMC mass) was dispersed in 2 mL of distilled water by ultrasonication for 20 min (Emmi 12 HC, 100% ultrasonic efficiency). The obtained dispersion was added to the CMC solution, and the mixture was kept for another 60 min in the ultrasonic bath till homogenization was attained (CMC-Mn). In the third stage, in order to obtain porous magnetic beads, three different ratios of sodium dodecyl sulfate (SDS) and NaCl were added to the CMC-Mn mixture (CMC/SDS of 3/0.2, 3/0.4, and 3/0.8), while the amount of NaCl was maintained constant (4% by reference to polymer mass). The three mixtures containing SDS were named with increasing SDS concentrations: CMC-Mn-S1, CMC-Mn-S2, and CMC-Mn-S3, respectively.

The mixtures obtained in each phase were further subjected to an ionotropic gelling process by drop-wise addition in a 0.1 M $Fe(NO_3)_3$ bath using a LEGATO® 100 Syringe Pump (KD Scientific, Holliston, MA, USA). To remove the excess surfactant, the hydrogelated beads were carefully cleaned with ethanol multiple times before being washed with distilled water. In a final step, each type of bead was subjected to a freeze-drying process for 24 h (Christ Alpha 3–4 LSCbasic, Osterode, Germany), finally obtaining CMC, CMC-Mn, CMC-Mn-S1, CMC-Mn-S2, and CMC-Mn-S3 beads.

4.3. Characterization Methods

4.3.1. $MnFe_2O_4$ Characterization

The XRD pattern of the synthetized manganese ferrite was registered using a diffractometer Bruker D8 ADVANCE (Bruker, Karlsruhe, Germany) in the 2θ domain (20–80°), with a scanning step of 0.02° and a recording rate of 1 °/min. Infrared spectroscopy was performed in the wavenumber range of 4000–400 cm^{-1}, using a Bruker Vertex 70 FTIR spectrometer (Ettlingen, Germany) and the KBr pellet technique (at room temperature). Magnetic measurements were made on a LakeShore 8607 vibrating sample magnetometer (VSM, Shore Cryotronics, Westerville, OH, USA) at ambient temperature. The samples were demagnetized in an alternating field prior to each test. A Hitachi High-Tech HT7700 transmission electron microscope (TEM) (Hitachi High Technologies Company, Tokyo, Japan) was used to examine the morphology and microstructure. After being dispersed in acetone, the samples underwent 30 min of ultrasonication, drop casting on copper grids covered with Ted Pella carbon (Redding, CA, USA), and vacuum-assisted 60 °C drying.

4.3.2. CMC-Based Beads Characterization

The surface and cross-section morphology of CMC-based beads were investigated using a scanning electron microscope (SEM) with a resolution of 4 nm at 30 kV (FEI Quanta 200, Brno, Czech Republic). The chemical composition of the membranes was determined using the Quanta 200 system's energy-dispersive X-ray spectrometer (EDX). Using a polarized optical microscope (PoLM, Leica Microsystems, Wetzlar, Germany), beads morphology and MB dye adsorption onto the biosorbents were additionally observed. Structural and magnetic properties were investigated by FTIR and VSM (see Section 4.3.1).

4.3.3. Adsorption and Dessorption Assays of Methylene Blue Cationic Dye

The adsorption of Methylene Blue (MB) onto CMC-based beads was investigated using an orbital shaker-incubator, Biosan ES-20/60 (Riga, Latvia). A double-beam UV-VIS spectrophotometer, Hitachi U-U-2910 (Hitachi High Technologies Company, Tokyo, Japan), was used to measure the concentration of the cationic dye in the aqueous solutions at a wavelength of 664 nm.

The batch adsorption screening test was performed by immersing 0.1 g of adsorbent (SD = 2 g/L) in 50 mL of MB solution (C_0 = 50 mg/L) for 1 h. The final concentration was measured, and the adsorption capacity (q_t, mg/g) and removal efficiency (Y_t, %) were calculated according to Equations (2) and (3):

$$q\ (\text{mg/g}) = \frac{(C_0 - C_t)V}{m \cdot 1000}, \quad (2)$$

$$Y_t\ (\%) = \frac{C_0 - C_t}{C_0} \cdot 100, \quad (3)$$

where q_t (mg/g) is the amount of dye that has been adsorbed at time t, C_0 and C_t (mg/L) denote the dye concentrations in the initial and final solutions (after contact time t), respectively; V (mL) refers to the volume of the immersion medium, and m (g) represents the weight of the CMC-based beads. It should be noted that for the batch adsorption screening test, three measurements were performed for each system, and the values of adsorption capacity and removal efficiency shown in Figure 6 represent their average. The magnetic beads with the best adsorption performance were further employed in kinetics and isotherm studies. The kinetic adsorption was realized at T = 300 K, by immersion of different sorbent doses (corresponding to 0.5, 1, 2, and 3 g/L) in 50 mL of MB solution placed in the orbital shaker (initial concentration of 50 mg/L, 140 rpm, 6 h). The final dye concentration in solution was determined by taking aliquots from the dye solutions at various predetermined contact times, and the adsorption capacity at time t (q_t, mg/g) was calculated (based on Equation (2)). The adsorption isotherms were measured at 300 K and 330 K using the same sorbent dose (0.5 g/L) and varying the initial dye solution concentrations (10 and 400 mg/L). The contact time was set at 6 h to ensure the adsorption process's equilibrium at 180 rpm. The adsorption capacity (q_e, mg/g) and removal efficiency (Y, %) of MB dye at equilibrium from aqueous solution were calculated according to Equations (2) and (3) (by replacing the C_t concentration at time t with the C_e concentration at equilibrium).

After the adsorption processes, 0.025 g of used CMC-Mn-S2 were dried and subjected to desorption tests (0.025 g of sorbent each in 50 mL of ethanol, respectively in 50 mL of acetone), being left overnight (at a temperature of 300 K and 150 rpm). The desorption efficiency (%) was calculated as the ratio between the amount of MB desorbed and the amount of MB initially adsorbed (multiplied by 100). After recovering the samples (Figure 7b), they were subjected to a MB re-adsorption cycle, according to Equation (2).

4.3.4. Molecular Modeling

The molecular modeling simulations were performed on a Dell Precision workstation T7910 with 32 CPU threads. In this regard, the molecular docking computations were performed by using the AutoDock VINA algorithm [61] inbuilt into the YASARA-Structure program package (v.20.8.23) for modeling and visualization [62,63].

Supplementary Materials: The following supporting information can be downloaded at: https://www.mdpi.com/article/10.3390/gels9050358/s1, Figure S1: Chemical structure and 3D Conformer of SDS molecule; Figure S2: Cross-section morphology of CMC (a–c); CMC-Mn (d–f); CMC-Mn-S1 (g–i); CMC-Mn-S2 (j–l); CMC-Mn-S3 (m–o), obtained by polarized light microscopy and SEM, respectively; Figure S3: SEM images of CMC (a), CMC-Mn (b) and CMC-Mn-S1 (c) on the beads surface; corresponding elemental mapping and weight percentage of the constituent elements of the analyzed SEM surfaces (d–f), and the distribution of Fe (g), and Mn element in samples (h–i); Figure S4: Image obtained by polarized light microscopy of CMC-Mn-S2 cross-section after MB adsorption; Figure S5: Adsorption capacities of Methylene Blue (MB), Crystal Violet (CV), and Brilliant Green (BG) onto CMC-Mn-S2 beads (experimental conditions: SD = 0.025, C_0 = 50 mg/g, V = 50 mL, t = 60 min); Figure S6: Adsorption capacities of Methylene Blue (MB) from aqueous solutions of pH 2 (adjusted with 0.1 M H_2SO_4) and pH 11 (adjusted with 0.1 M NaOH); experimental conditions: SD = 0.025, C_0 = 50 mg/g, V = 50 mL, t = 60 min; Figure S7: (a) Desorption efficiency of MB in ethanol and acetone (experimental conditions: SD = 0.025, V = 50 mL, t = 24 h); and re-adsorption capacities (q, mg/g) of MB onto the recovered adsorbent (experimental conditions: SD = 0.025, C_0 = 50 mg/g, V = 50 mL, t = 60 min); (b) macroscopic images of CMC-based beads after desorption in ethanol (left) and acetone (right). Figure S8: Representative images of the obtained (a) xerogel and (b) loose dark nanoparticles of manganese ferrite; Table S1: Kinetic models non-linear equations and parameters for MB dye adsorption onto CMC-Mn-S2 adsorbent, using different sorbent doses (SD); experimental conditions: T = 300 K, C_0 = 50 mg/L; Table S2: Isotherm models, equations and parameters for MB dye adsorption onto CMC-Mn-S2 adsorbent (contact time: t = 300 min); Table S3. Comparison of the maximum adsorption capacities ($q_e^{(obs)}$) of CMC-based composite materials for retention of MB cationic dye.

Author Contributions: Conceptualization, A.-C.E., P.S. and C.C.; methodology, P.S., C.C., A.-C.E. and I.G.; software, C.C.; validation, A.-C.E., P.S., C.C. and V.H.; investigation, A.-C.E., I.G., P.S. and C.C.; resources, P.S. and V.H.; writing—original draft preparation, A.-C.E., P.S., C.C. and I.G.; writing—review and editing, P.S., C.C. and V.H.; supervision, V.H.; project administration, P.S. and C.C.; funding acquisition, P.S. All authors have read and agreed to the published version of the manuscript.

Funding: This work was supported by a grant from the Ministry of Research, Innovation and Digitization, CNCS-UEFISCDI, project number PN-III-P1-1.1-TE-2021-0030, within PNCDI III.

Institutional Review Board Statement: Not applicable.

Informed Consent Statement: Not applicable.

Data Availability Statement: Not applicable.

Conflicts of Interest: The authors declare no conflict of interest.

References

1. Walker, D.B.; Baumgartner, D.J.; Gerba, C.P.; Fitzsimmons, K. Surface Water Pollution. In *Environmental and Pollution Science*, 3rd ed.; Brusseau, M.L., Pepper, I.L., Gerba, C.P., Eds.; Academic Press: London, UK, 2019; pp. 261–292.
2. Abbass, K.; Qasim, M.Z.; Song, H.; Murshed, M.; Mahmood, H.; Younis, I. A review of the global climate change impacts, adaptation, and sustainable mitigation measures. *Environ. Sci. Pollut. Res.* **2022**, *29*, 42539–42559. [CrossRef] [PubMed]
3. Strokal, M.; Kroeze, C. Water, society and pollution in an urbanizing world: Recent developments and future challenges. *Curr. Opin. Environ. Sustain.* **2020**, *46*, 11–15. [CrossRef]
4. Madhav, S.; Ahamad, A.; Singh, A.K.; Kushawaha, J.; Singh Chauhan, J.; Sharma, S.; Singh, P. Water Pollutants: Sources and Impact on the Environment and Human Health. In *Sensors in Water Pollutants Monitoring: Role of Material*; Pooja, D., Kumar, P., Singh, P., Patil, S., Eds.; Springer: Singapore, 2020; pp. 43–62.
5. Mishra, B.; Varjani, S.; Iragavarapu, G.P.; Ngo, H.H.; Guo, W.; Vishal, B. Microbial Fingerprinting of Potential Biodegrading Organisms. *Curr. Pollut. Rep.* **2019**, *5*, 181–197. [CrossRef]
6. Claverie, M.; Garcia, J.; Prevost, T.; Brendlé, J.; Limousy, L. Inorganic and Hybrid (Organic–Inorganic) Lamellar Materials for Heavy Metals and Radionuclides Capture in Energy Wastes Management—A Review. *Materials* **2019**, *12*, 1399. [CrossRef]
7. Lin, L.; Yang, H.; Xu, X. Effects of Water Pollution on Human Health and Disease Heterogeneity: A Review. *Front. Environ. Sci.* **2022**, *10*, 880246. [CrossRef]
8. El-Kousy, S.M.; El-Shorbagy, H.G.; Abd El-Ghaffar, M.A. Chitosan/montmorillonite composites for fast removal of methylene blue from aqueous solutions. *Mater. Chem. Phys.* **2020**, *254*, 123236. [CrossRef]
9. Sivakumar, R.; Lee, N.Y. Adsorptive removal of organic pollutant methylene blue using polysaccharide-based composite hydrogels. *Chemosphere* **2022**, *286*, 131890. [CrossRef]
10. Ghoniem, M.G.; Ali, F.A.M.; Abdulkhair, B.Y.; Elamin, M.R.A.; Alqahtani, A.M.; Rahali, S.; Ben Aissa, M.A. Highly Selective Removal of Cationic Dyes from Wastewater by MgO Nanorods. *Nanomaterials* **2022**, *12*, 1023. [CrossRef] [PubMed]
11. Elwakeel, K.Z.; Abd El-Ghaffar, M.A.; El-kousy, S.M.; El-Shorbagy, H.G. Synthesis of new ammonium chitosan derivatives and their application for dye removal from aqueous media. *Chem. Eng. J.* **2012**, *203*, 458–468. [CrossRef]
12. Safardoust-Hojaghan, H.; Salavati-Niasari, M. Degradation of methylene blue as a pollutant with N-doped graphene quantum dot/titanium dioxide nanocomposite. *J. Clean. Prod.* **2017**, *148*, 31–36. [CrossRef]
13. Din, M.I.; Khalid, R.; Najeeb, J.; Hussain, Z. Fundamentals and photocatalysis of methylene blue dye using various nanocatalytic assemblies—A critical review. *J. Clean. Prod.* **2021**, *298*, 126567. [CrossRef]
14. Ginimuge, P.R.; Jyothi, S.D. Methylene blue: Revisited. *J. Anaesthesiol. Clin. Pharmacol.* **2010**, *26*, 517–520. [CrossRef]
15. Khan, I.; Saeed, K.; Zekker, I.; Zhang, B.; Hendi, A.H.; Ahmad, A.; Ahmad, S.; Zada, N.; Ahmad, H.; Shah, L.A.; et al. Review on Methylene Blue: Its Properties, Uses, Toxicity and Photodegradation. *Water* **2022**, *14*, 242. [CrossRef]
16. Tan, Y.; Sun, Z.; Meng, H.; Han, Y.; Wu, J.; Xu, J.; Xu, I.; Zhang, X. A new MOFs/polymer hybrid membrane: MIL-68(Al)/PVDF, fabrication and application in high-efficient removal of p-nitrophenol and methylene blue. *Sep. Purif. Technol.* **2019**, *215*, 217–226. [CrossRef]
17. Fadillah, G.; Saleh, T.A.; Wahyuningsih, S.; Ninda Karlina Putri, E.; Febrianastuti, S. Electrochemical removal of methylene blue using alginate-modified graphene adsorbents. *J. Chem. Eng.* **2019**, *378*, 122140. [CrossRef]
18. Ihaddaden, S.; Aberkane, D.; Boukerroui, A.; Robert, D. Removal of methylene blue (basic dye) by coagulation-flocculation with biomaterials (bentonite and Opuntia ficus indica). *J. Water Process. Eng.* **2022**, *49*, 102952. [CrossRef]
19. Jayalakshmi, R.; Soundaranayaki, K.; Subhash Kannan, M. Removal of Methylene Blue dye from textile wastewater using vertical flow constructed wetland. *Mater. Today Proc.* **2022**, *77*, 365–370. [CrossRef]
20. Yadav, S.; Asthana, A.; Singh, A.K.; Chakraborty, R.; Vidya, S.S.; Susan, M.A.B.H.; Carabineiro, S.A.C. Adsorption of cationic dyes, drugs and metal from aqueous solutions using a polymer composite of magnetic/β-cyclodextrin/activated charcoal/Na alginate: Isotherm, kinetics and regeneration studies. *J. Hazard. Mater.* **2021**, *409*, 124840. [CrossRef]
21. Chen, T.; Liu, H.; Gao, J.; Hu, G.; Zhao, Y.; Tang, X.; Han, X. Efficient Removal of Methylene Blue by Bio-Based Sodium Alginate/Lignin Composite Hydrogel Beads. *Polymers* **2022**, *14*, 2917. [CrossRef] [PubMed]
22. Duman, O.; Polat, T.G.; Diker, C.Ö.; Tunç, S. Agar/κ-carrageenan composite hydrogel adsorbent for the removal of Methylene Blue from water. *Int. J. Biol. Macromol.* **2020**, *160*, 823–835. [CrossRef]
23. Yan, H.; Zhang, W.; Kan, X.; Dong, L.; Jiang, Z.; Li, H.; Yang, H.; Cheng, R. Sorption of methylene blue by carboxymethyl cellulose and reuse process in a secondary sorption. *Colloids Surf. A Physicochem. Eng. Asp.* **2011**, *380*, 143–151. [CrossRef]
24. Rahman, M.S.; Hasan, M.S.; Nitai, A.S.; Nam, S.; Karmakar, A.K.; Ahsan, M.S.; Shiddiky, M.J.A.; Ahmed, M.B. Recent Developments of Carboxymethyl Cellulose. *Polymers* **2021**, *13*, 1345. [CrossRef] [PubMed]
25. Eltaweil, A.S.; Elgarhy, G.S.; El-Subruiti, G.M.; Omer, A.M. Carboxymethyl cellulose/carboxylated graphene oxide composite microbeads for efficient adsorption of cationic methylene blue dye. *Int. J. Biol. Macromol.* **2020**, *154*, 307–318. [CrossRef] [PubMed]

26. Zirak, M.; Abdollahiyan, A.; Eftekhari-Sis, B.; Saraei, M. Carboxymethyl cellulose coated Fe_3O_4@SiO_2 core–shell magnetic nanoparticles for methylene blue removal: Equilibrium, kinetic, and thermodynamic studies. *Cellulose* **2018**, *25*, 503–515. [CrossRef]
27. Hosseini, H.; Zirakjou, A.; McClements, D.J.; Goodarzi, V.; Chen, W.-H. Removal of methylene blue from wastewater using ternary nanocomposite aerogel systems: Carboxymethyl cellulose grafted by polyacrylic acid and decorated with graphene oxide. *J. Hazard. Mater.* **2022**, *421*, 126752. [CrossRef]
28. Liu, C.; Omer, A.M.; Ouyang, X. Adsorptive removal of cationic methylene blue dye using carboxymethyl cellulose/k-carrageenan/activated montmorillonite composite beads: Isotherm and kinetic studies. *Int. J. Biol. Macromol.* **2018**, *106*, 823–833. [CrossRef]
29. Benhalima, T.; Ferfera-Harrar, H.; Lerari, D. Optimization of carboxymethyl cellulose hydrogels beads generated by an anionic surfactant micelle templating for cationic dye uptake: Swelling, sorption and reusability studies. *Int. J. Biol. Macromol.* **2017**, *105*, 1025–1042. [CrossRef]
30. Massana Roquero, D.; Othman, A.; Melman, A.; Katz, E. Iron(III)-cross-linked alginate hydrogels: A critical review. *Mater. Adv.* **2022**, *3*, 1849–1873. [CrossRef]
31. Mamba, G.; Mishra, A. Advances in Magnetically Separable Photocatalysts: Smart, Recyclable Materials for Water Pollution Mitigation. *Catalysts* **2016**, *6*, 79. [CrossRef]
32. Samoila, P.; Cojocaru, C.; Cretescu, I.; Stan, C.D.; Nica, V.; Sacarescu, L.; Harabagiu, V. Nanosized Spinel Ferrites Synthesized by Sol-Gel Autocombustion for Optimized Removal of Azo Dye from Aqueous Solution. *J. Nanomater.* **2015**, *2015*, 1–13. [CrossRef]
33. Kanagesan, S.; Aziz, S.B.A.; Hashim, M.; Ismail, I.; Tamilselvan, S.; Alitheen, N.B.B.M.; Swamy, M.K.; Purna Chandra Rao, B. Synthesis, Characterization and in Vitro Evaluation of Manganese Ferrite ($MnFe_2O_4$) Nanoparticles for Their Biocompatibility with Murine Breast Cancer Cells (4T1). *Molecules* **2016**, *21*, 312. [CrossRef]
34. Gao, H.; Jiang, J.; Huang, Y.; Wang, H.; Sun, J.; Jin, Z.; Wang, J.; Zhang, J. Synthesis of hydrogels for adsorption of anionic and cationic dyes in water: Ionic liquid as a crosslinking agent. *SN Appl. Sci.* **2022**, *4*, 118. [CrossRef]
35. Haghiri, M.E.; Izanloo, A. Design and characterization of colloidal solution of manganese ferrite nanostructure coated with carboxymethyl chitosan. *Mater. Chem. Phys.* **2018**, *216*, 265–271. [CrossRef]
36. Ajibade, P.A.; Nnadozie, E.C. Synthesis and Structural Studies of Manganese Ferrite and Zinc Ferrite Nanocomposites and Their Use as Photoadsorbents for Indigo Carmine and Methylene Blue Dyes. *ACS Omega* **2020**, *5*, 32386–32394. [CrossRef] [PubMed]
37. Rahman, M.S.; Islam, M.M.; Islam, M.S.; Zaman, A.; Ahmed, T.; Biswas, S.; Sharmeen, S.; Rashid, T.U.; Rahman, M.M. Morphological Characterization of Hydrogels. In *Cellulose-Based Superabsorbent Hydrogels*, 1st ed.; Mondal, M.I.H., Ed.; Springer: Cham, Switzerland, 2019; pp. 819–863. [CrossRef]
38. Liu, X.; Tan, X.; Zhou, Y.; Li, Y.; Zhang, Z. Cu0NPs@CMC: An efficient recoverable nanocatalyst for decarboxylative A3 and A3 couplings under neat condition. *Res. Chem. Intermed.* **2019**, *45*, 3359–3378. [CrossRef]
39. Wang, Y.; Kretschmer, K.; Zhang, J.; Mondal, A.K.; Guo, X.; Wang, G. Organic sodium terephthalate@graphene hybrid anode materials for sodium-ion batteries. *RSC Adv.* **2016**, *6*, 57098–57102. [CrossRef]
40. Capanema, N.S.V.; Mansur, A.A.P.; Carvalho, I.C.; Carvalho, S.M.; Mansur, H.S. Bioengineered Water-Responsive Carboxymethyl Cellulose/Poly(vinyl alcohol) Hydrogel Hybrids for Wound Dressing and Skin Tissue Engineering Applications. *Gels* **2023**, *9*, 166. [CrossRef]
41. Swamy, B.Y.; Yun, Y.-S. In vitro release of metformin from iron (III) cross-linked alginate–carboxymethyl cellulose hydrogel beads. *Int. J. Biol. Macromol.* **2015**, *77*, 114–119. [CrossRef]
42. Mondal, M.I.H.; Yeasmin, M.S.; Rahman, M.S. Preparation of food grade carboxymethyl cellulose from corn husk agrowaste. *Int. J. Biol. Macromol.* **2015**, *79*, 144–150. [CrossRef]
43. Cuba-Chiem, L.T.; Huynh, L.; Ralston, J.; Beattie, D.A. In situ particle film ATR-FTIR studies of CMC adsorption on talc: The effect of ionic strength and multivalent metal ions. *Miner. Eng.* **2008**, *21*, 1013–1019. [CrossRef]
44. Mahu, E.; Samoila, P.; Ignat, M.; Cojocaru, C.; Harabagiu, V. Influence of fuel nature on sol–gel microwave-ignited combustion synthesis of nanosized cobalt and nickel spinel ferrites. *C. R. Chim.* **2020**, *25*, 189–202. [CrossRef]
45. Bouziane, N.; Aloui, A.; Behloul, S.; Zertal, A. Kinetic models of aqueous 2-mercaptobenzothiazole adsorption on local clay and activated carbon. *Rev. Roum. Chim.* **2021**, *66*, 479–491.
46. Tee, G.T.; Gok, X.Y.; Yong, W.F. Adsorption of pollutants in wastewater via biosorbents, nanoparticles and magnetic biosorbents: A review. *Environ. Res.* **2022**, *212*, 113248. [CrossRef]
47. Sahoo, T.R.; Prelot, B. Adsorption processes for the removal of contaminants from wastewater. In *Nanomaterials for the Detection and Removal of Wastewater Pollutants*; Bonelli, B., Freyria, F.S., Rossetti, I., Sethu, R., Eds.; Elsevier: Amsterdam, The Netherlands, 2020; pp. 161–222. [CrossRef]
48. Guaragnone, T.; Rossi, M.; Chelazzi, D.; Mastrangelo, R.; Severi, M.; Fratini, E.; Baglioni, P. pH-Responsive Semi-Interpenetrated Polymer Networks of pHEMA/PAA for the Capture of Copper Ions and Corrosion Removal. *ACS Appl. Mater. Interfaces* **2022**, *14*, 7471–7485. [CrossRef]
49. Enache, A.-C.; Samoila, P.; Cojocaru, C.; Apolzan, R.; Predeanu, G.; Harabagiu, V. An Eco-Friendly Modification of a Walnut Shell Biosorbent for Increased Efficiency in Wastewater Treatment. *Sustainability* **2023**, *15*, 2704. [CrossRef]
50. Demir, H.; Top, A.; Balköse, D.; Ülkü, S. Dye adsorption behavior of Luffa cylindrica fibers. *J. Hazard. Mater.* **2008**, *153*, 389–394. [CrossRef] [PubMed]

51. Alswieleh, A.M. Efficient Removal of Dyes from Aqueous Solution by Adsorption on L-Arginine-Modified Mesoporous Silica Nanoparticles. *Processes* **2022**, *10*, 1079. [CrossRef]
52. Blaga, A.C.; Tanasă, A.M.; Cimpoesu, R.; Tataru-Farmus, R.-E.; Suteu, D. Biosorbents Based on Biopolymers from Natural Sources and Food Waste to Retain the Methylene Blue Dye from the Aqueous Medium. *Polymers* **2022**, *14*, 2728. [CrossRef] [PubMed]
53. Jermain, P.R.; Fischer, A.H.; Joseph, L.; Muzikansky, A.; Yaroslavsky, A.N. Fluorescence Polarization Imaging of Methylene Blue Facilitates Quantitative Detection of Thyroid Cancer in Single Cells. *Cancers* **2022**, *14*, 1339. [CrossRef]
54. Radoor, S.; Karayil, J.; Parameswaranpillai, J.; Siengchin, S. Adsorption of methylene blue dye from aqueous solution by a novel PVA/CMC/halloysite nanoclay bio composite: Characterization, kinetics, isotherm and antibacterial properties. *J. Environ. Health Sci. Eng.* **2020**, *18*, 1311–1327. [CrossRef]
55. Radoor, S.; Karayil, J.; Jayakumar, A.; Parameswaranpillai, J.; Lee, J.; Siengchin, S. Ecofriendly and low-cost bio adsorbent for efficient removal of methylene blue from aqueous solution. *Sci. Rep.* **2022**, *12*, 20580. [CrossRef]
56. Zhou, Y.; Li, T.; Shen, J.; Meng, Y.; Tong, S.; Guan, Q.; Xia, X. Core-Shell Structured Magnetic Carboxymethyl Cellulose-Based Hydrogel Nanosorbents for Effective Adsorption of Methylene Blue from Aqueous Solution. *Polymers* **2021**, *13*, 3054. [CrossRef]
57. Zhu, W.; Jiang, X.; Jiang, K.; Liu, F.; You, F.; Yao, C. Fabrication of Reusable Carboxymethyl Cellulose/Graphene Oxide Composite Aerogel with Large Surface Area for Adsorption of Methylene Blue. *Nanomaterials* **2021**, *11*, 1609. [CrossRef]
58. Allouss, D.; Essamlali, Y.; Amadine, O.; Chakir, A.; Zahouily, M. Response surface methodology for optimization of methylene blue adsorption onto carboxymethyl cellulose-based hydrogel beads: Adsorption kinetics, isotherm, thermodynamics and reusability studies. *RSC Adv.* **2019**, *9*, 37858–37869. [CrossRef]
59. Liu, H.; Tian, X.; Xiang, X.; Chen, S. Preparation of carboxymethyl cellulose/graphene composite aerogel beads and their adsorption for methylene blue. *Int. J. Biol. Macromol.* **2022**, *202*, 632–643. [CrossRef] [PubMed]
60. Babalska, Z.Ł.; Korbecka-Paczkowska, M.; Karpiński, T.M. Wound Antiseptics and European Guidelines for Antiseptic Application in Wound Treatment. *Pharmaceuticals* **2021**, *14*, 1253. [CrossRef] [PubMed]
61. Trott, O.; Olson, A.J. AutoDock Vina: Improving the speed and accuracy of docking with a new scoring function, efficient optimization, and multithreading. *J. Comput. Chem.* **2010**, *31*, 455–461. [CrossRef] [PubMed]
62. Krieger, E.; Koraimann, G.; Vriend, G. Increasing the precision of comparative models with YASARA NOVA—A selfparameterizing force field. *Proteins* **2002**, *47*, 393–402. [CrossRef]
63. Krieger, E.; Vriend, G. YASARA View-molecular graphics for all devices-from smartphones to workstations. *Bioinformatics* **2014**, *30*, 2981–2982. [CrossRef]

gels

Article

Cross-Linked Gel Polymer Electrolyte Based on Multiple Epoxy Groups Enabling Conductivity and High Performance of Li-Ion Batteries

Wei Zhang †, Wansu Bae †, Lei Jin, Sungjun Park, Minhyuk Jeon, Whangi Kim and Hohyoun Jang *

Department of Applied Chemistry, Konkuk University, Chungju-si 27478, Republic of Korea
* Correspondence: 200417450@kku.ac.kr
† These authors contributed equally to this work.

Abstract: The low ionic conductivity and unstable interface of electrolytes/electrodes are the key issues hindering the application progress of lithium-ion batteries (LiBs). In this work, a cross-linked gel polymer electrolyte (C-GPE) based on epoxidized soybean oil (ESO) was synthesized by in situ thermal polymerization using lithium bis(fluorosulfonyl)imide (LiFSI) as an initiator. Ethylene carbonate/diethylene carbonate (EC/DEC) was beneficial for the distribution of the as-prepared C-GPE on the anode surface and the dissociation ability of LiFSI. The resulting C-GPE-2 exhibited a wide electrochemical window (of up to 5.19 V vs. Li^+/Li), an ionic conductivity (σ) of 0.23×10^{-3} S/cm at 30 °C, a super-low glass transition temperature (T_g), and good interfacial stability between the electrodes and electrolyte. The battery performance of the as-prepared C-GPE-2 based on a graphite/$LiFePO_4$ cell showed a high specific capacity of ca. 161.3 mAh/g (an initial Coulombic efficiency (CE) of ca. 98.4%) with a capacity retention rate of ca. 98.5% after 50 cycles at 0.1 C and an average CE of about ca. 98.04% at an operating voltage range of 2.0~4.2 V. This work provides a reference for designing cross-linking gel polymer electrolytes with high ionic conductivity, facilitating the practical application of high-performance LiBs.

Keywords: cross-linked gel polymer electrolyte; LiFSI; ionic conductivity; interfacial stability; Coulombic efficiency

1. Introduction

LiBs have been extensively used in consumer electronic and storage devices, owing to their high specific energy density, stable cycling performance, high open circuit potentials, low memory effects, light weight, and so forth [1–3]. Electrolytes play a critical role in high-performance LiBs. However, commercial liquid electrolytes (LEs) generate lithium dendrite, an unstable solid electrolyte interface (SEI), and leakage and flammability of the LE [4–6]. Polymer electrolytes have been extensively studied to solve this problem due to their significant advantages of low flammability, excellent processability, high electrochemical stability, good mechanical flexibility, and durability [7]. Gel polymer electrolytes (GPEs), which incorporate liquid plasticizers and lithium salts into polymer matrices, have been identified as one of the most promising candidates for cost-effective, safe, and long-lifespan LiBs [6,8]. GPEs are nonvolatile, have higher thermal and electrochemical stability than LEs, and, to some extent, alleviate problems derived from water [4,9]. Moreover, GPEs can be manufactured using the in situ polymerization method, which is compatible with the state-of-the-art LiB fabrication industry [10–12]. Among in situ-formed GPEs, polyethylene oxide (PEO), polymethyl methacrylate (PMMA), polyvinylidene fluoride (PVDF) [13,14], polyacrylonitrile (PAN) [10], poly (1,3-dioxlane) [15], and related co-block polymers are currently widely used as polymer hosts for the preparation of GPEs. Nevertheless, the ionic conductivity (σ) and battery performance of PEO-based GPEs still need to be improved, owing to the crystallinity of the as-prepared electrolyte and interfacial issues. For example, Xie et al. [16] present a dual-salt PEO-based cross-linked network electrolyte with a σ value of 0.57 × 10^{-3} S/cm at 30 °C, while Teng et al. [9] present a poly(ethylene oxide)-co-poly(propylene oxide)-based GPE that delivers a σ value of 2.8 × 10^{-3} S/cm at 30 °C, but polarization occurs due to anion accumulation. Our group's recent work employed LiFSI as an initiator and successfully polymerized a dual-epoxy group precursor through thermal cationic ring-opening technology [6,17,18]. The results showed tight interface compatibility between the electrolyte and electrode, which enables the σ and cycling performance of the battery.

Apart from LEs, GPEs with a certain amount of solvent might facilitate battery performance. For example, Lai et al. [19] report an in situ-formed GPE with 1 M $LiPF_6$ in EC/DEC/EMC that has a more stable deposition and dissolution behavior due to the uniform Li cation distribution on the anode surface. Wang et al. [20] present an in situ-formed solid-state polymer electrolyte based on poly(1,3-dioxolane) with a high σ (7.9 × 10^{-3} S/cm at room temperature), a high Li cation transference number (0.82), and low interfacial resistance. However, employing highly concentrated LiFSI (3.5 M) probably sacrifices cost-effectiveness and higher polymer electrolyte molecular weights due to rapid polymerization. Thus, a moderate condition needs to be considered. Furthermore, for comparison, LiTFSI-/$LiPF_6$-based GPEs [5,21–23] and LiFSI-based GPEs have the merits of higher σ of LiFSI [24,25], better interface compatibility with the electrodes, and better cycling performance due to the formation of the cathode–electrolyte interphase (CEI) [26] and solid–electrolyte interphase (SEI) layer [20] on the anode surface. From another aspect, the PEO-based SPEs face the challenges of poor ionic conductivity and interface issues by adding a plasticizer (e.g., fluoroethylene carbonate and succinonitrile) [15,27]. In contrast, cross-linked PEO-based GPEs could possess thermal ability, improved σ, and enhanced interfacial stability [14,28].

Epoxidized soybean oil (ESO), as a renewable raw material with multiple epoxy groups, has attracted great attention in recent years in both scientific and industrial areas, such as in fabricating lubricants, coatings, and bioplastics [29–31]. Research has explored the ring-opening polymerization of ESOs through boron trifluoride diethyl etherate ($BF_3.OEt_2$), and the epoxy group-based precursor can successfully achieve cationic ring-opening polymerization using Li salts, including LiFSI, $LiPF_6$, and lithium difluoro (oxalate) borate (LiDFOB) [4,17,22].

Herein, we attempted to prepare an in situ cross-linking gel polymer electrolyte (C-GPE), which consisted of low-concentrated LIFSI, environmentally friendly ESO, and EC/DEC solvent (1:1, by volume). The EC/DEC solvent could be beneficial for the dissociation of LiFSI and adjust the interfacial stability of the electrolyte and anode [32,33], while the ESO-based electrolyte probably provides a three-dimensional (3D) cross-linked structure, which improves ionic conductivity and provides more volume for ion mobility. In situ polymerization could also enhance battery performance by reducing interfacial resistance and generating intimate compatibility between the electrolyte and electrode [6,10–13]. In this work, we expect to provide a simple and practical method for designing C-GPEs with outstanding ionic conductivity, a wide electrochemical stability window, and low interfacial impedance for high-performance rechargeable LiBs.

2. Results and Discussion

2.1. Ionic Conductivity and Electrochemical Properties

As can be seen in Figure 1, the ionic conductivities of the as-synthesized C-GPEs are measured using Figure S1a–d of the Supplementary Materials (SM) and Equation (1), whose values are comparable to those of the reported GPEs. All as-prepared C-GPEs delivered a considerable σ (compared with Table S1 of the SM). At 30 °C, the typical σ values of the as-prepared C-GPEs—C-GPE-1, C-GPE-2, and C-GPE-3—were 0.21, 0.23, and 0.28 × 10^{-3} S/cm, respectively, while at 80 °C, the values of the corresponding σ were 0.3, 0.33, and 0.37 × 10^{-3} S/cm, respectively. Furthermore, a linear dependency of ln σ along with the temperature was displayed, which agrees with the typical Arrhenius plot [18].

Combined with battery performance, as shown below, these comparable σ values may be due to the increased distribution of free Li cations in the interface region [13], suggesting that EC/DEC facilitates the dissolution of Li ions, thereby improving the σ value.

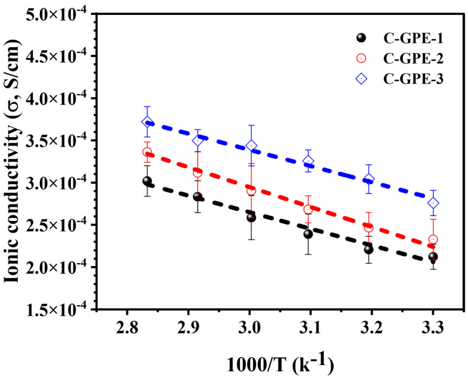

Figure 1. Plots of ionic conductivity vs. temperature based on dummy cells.

Figures 2a–c and S2 of the SM display the CV profiles of the as-prepared C-GPEs based on half-cells (Li/C-GPEs/$LiFePO_4$) and all clearly exhibit redox peaks. The CV peaks from C-GPE-1 and C-GPE-2 were found at 4.5 and 1.6 (Figure 2a) and 4.3 and 1.8 V (Figure 2b), respectively. These observations could indicate the de-lithiation and lithiation of the electrodes. Furthermore, the CV curves of C-GPE-2 overlap for three cycles, indicating the normal reversibility of the electrochemical reaction within the voltage range of −1.5~5 V. However, Figures 2c and S2 (C-GPE-4) of the SM show an extra peak at 0.2 V, which may be attributed to a side reaction due to the higher fraction of solvent (EC/DEC). Electrochemical anodic stability is a critical parameter of LiBs. As Figure 2d shows, the stable window values of the as-prepared C-GPEs based on Li | |SS cells for C-GPE-1, C-GPE-2, and C-GPE-3 were 5.0, 5.19, and 3.2 V, respectively. The as-prepared C-GPE-2-based cell exhibited a wide and stable voltage, which may be attributed to the good distribution of LiFSI and less to the solvation effect of EC/DEC [34,35].

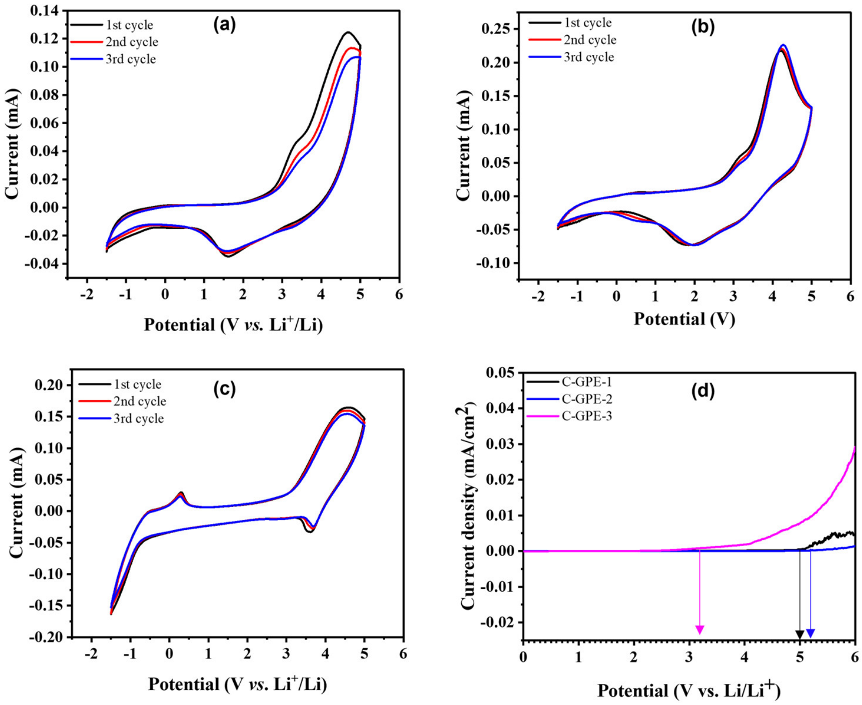

Figure 2. CV profiles of as-prepared (**a**) C-GPE-1, (**b**) C-GPE-2, and (**c**) C-GPE-3; (**d**) LSV traces of as-prepared C-GPEs based on Li//SS cells with a potential of 0–6 V and a scan rate of 0.1 mV/s.

2.2. Battery Performances

The rate performances of the as-prepared C-GPEs were tested using a full-cell configuration of graphite/C-GPEs/$LiFePO_4$ (LFP) with a potential range of 2.0–4.2 V at 0.1 C, 0.2 C, and 0.3 C, respectively. Figure 3a–c display variations in the discharge–charge (CD) capacity at 0.1–0.3 C. At 0.1 C, the initial charge- and discharge-specific capacities (C_{sp}) of C-GPE-1 were ca. 159.4 and 156.8 mAh/g, with an initial Coulombic efficiency (CE, η) of ca. 99.6%. Meanwhile, C-GPE-2 showed ca. 161.3 and 158.7 mAh/g with an η of ca. 98.4%, while C-GPE-3 showed ca. 160.3 and 151.5 mAh/g with an η of 94.5%, respectively. Furthermore, at 0.2 C, the C_{sp} of C-GPE-1, C-GPE-2, and C-GPE-3 were ca. 136.1, 137.5, and 135.2 mAh/g, respectively. At 0.3 C, the C_{sp} of C-GPE-1, C-GPE-2, and C-GPE-3 were ca. 106.7, 113.0, and 111.1 mAh/g, respectively. These good rate capacities of the as-prepared C-GPEs based on a full cell at 0.1–0.3 C could be attributed to the better interfacial compatibility between the cathode and electrolyte [36,37]. These observations are higher than or comparable with recent reported works (as shown in Table S1 of the SM). As can be seen in Figure 3d, the average η of the graphite/C-GPE-2/LFP battery is ca. 98.86%; nevertheless, the values of the C-GPE-1- and C-GPE-3-based full cells are ca. 98.04 and 91.97%, respectively, at 0.1 C after 50 CD cycles. The lower average η of the C-GPE-3 battery cell might be attributed to an unstable interface between the anode/C-GPE-3 (verified by Figure 2c). Furthermore, this result could be due to the solvation effect of Li ions [38]. It is worth noting that the slightly higher average η (98.86%) of the C-GPE-2 battery cell than that (98.04%) of the C-GPE-1 battery cell is probably due to the formation of a stable solid electrolyte layer on the graphite in the presence of LiFSI [6] and the suitable amount of EC/DEC adjusting the interfacial behavior on the graphite anode surface [32] with the increasing cycle number.

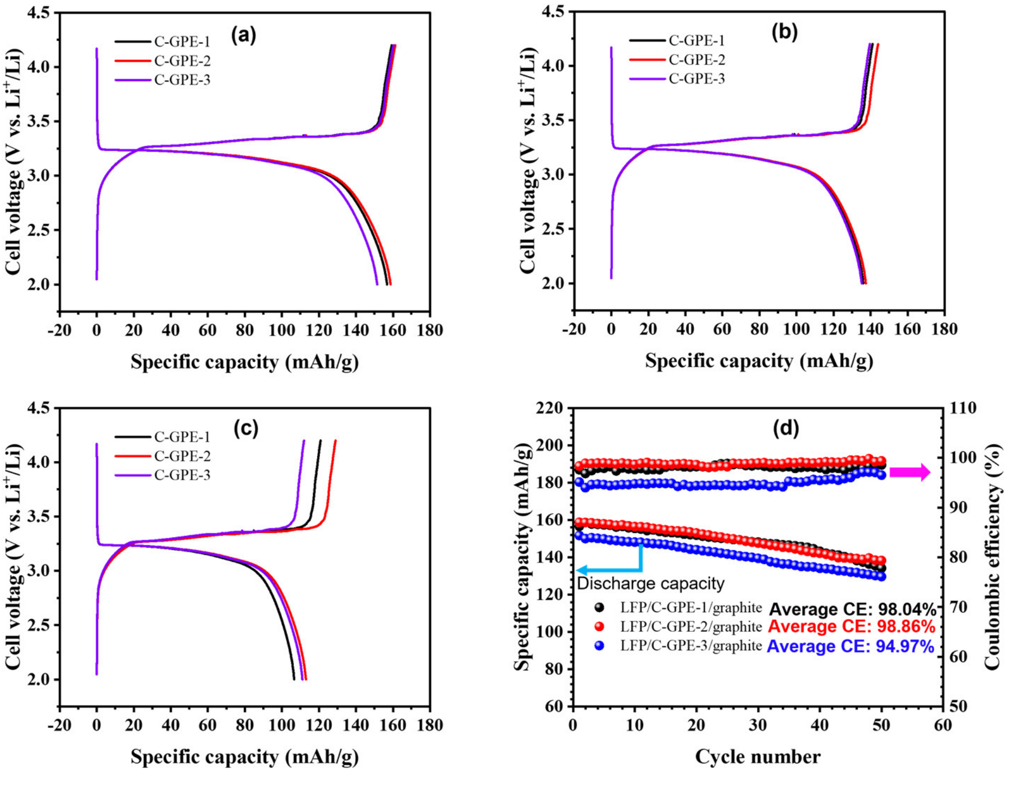

Figure 3. CD plots of graphite/C-GPEs/LFP cells at 0.1 C (**a**), 0.2 C (**b**), and 0.3 C (**c**) under 25 °C. (**d**) Plots of discharge-specific capacity as a function of CD cycles at 25 °C for as-prepared C-GPE-based graphite/C-GPEs/LFP full cells at 0.1 C.

Encouraged by the considerable performance in full-cell configuration (graphite/C-GPE-2/LFP), a half-cell (Li/C-GPE-2/LFP) was assembled to demonstrate its potential for large-scale applications. As shown in Figure 4a,b, the rate and cycling performance of the as-prepared C-GPE-2-based half-cell (Li/C-GPE-2/LFP) were investigated. The C_{sp} of the as-prepared C-GPE-2-based half-cell at 0.1, 0.2, and 0.3 C was ca. 146, 129.0, and 115.4 mAh/g, respectively. At the same time, there is less polarization potential (as displayed in Figure 4a). These findings indicate that C-GPE-2 may have good compatibility with Li metal anodes [32,33,39]. Figure 4b shows the C_{sp} and cyclability of the as-prepared C-GPE-2-based half-cell with 50 cycles at 2.5–4.2 V and 25 °C. This makes it clear that the slightly increasing value of η (up to 98.7%) could infer the generation of uniform Li^+ and a stabler SEI layer on the metallic Li anode surface. Compared to the initial C_{sp} (ca. 146.8 mAh/g) with an η of ca. 93.32%, the capacity retention of the Li/C-GPE-2/LFP battery was maintained at ca. 136.6 mAh/g (ca. 93.05%) after 50 cycles at 0.1 C and 25 °C.

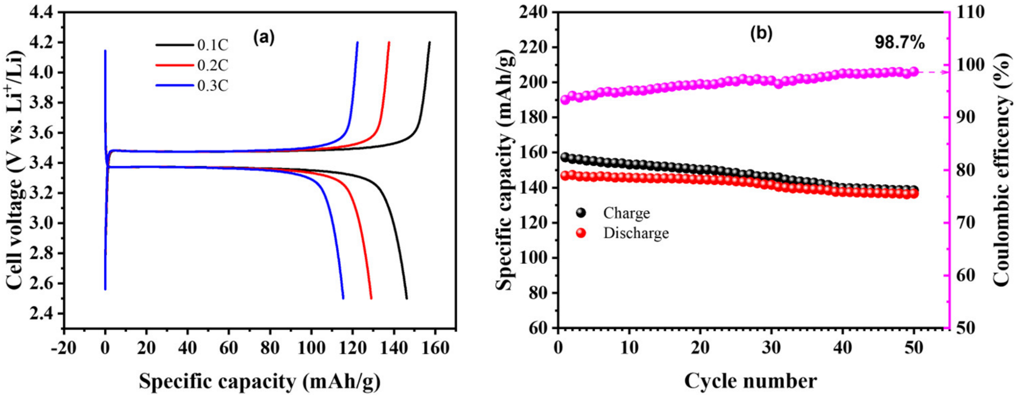

Figure 4. (**a**) Rate performances of Li/C-GPE-2/LFP half-cell at 0.1–0.3 C and 25 °C. (**b**) Discharge–charge capacities and CEs for Li/C-GPE-2/LFP half-cell at 0.1 C for 50 cycles at 25 °C.

2.3. Morphological Characterization

Figure 5a,b show the variations in the specific capacities and CEs vs. the CD cycling number of the as-prepared C-GPE-2 based on a full cell and a half-cell, respectively, at 0.2 C and 25 °C. The fade C_{sp} for the as-prepared C-GPE-2 based on the cells was ca. 18.8 and 14.4%, respectively, after 300 cycles. The corresponding average CE for the as-prepared C-GPE-2-based LiBs was ca. 98.8 and 96.9% after cycling. As can be seen, the monotonic increase in CE with the increasing CD cycling number can be attributed to the formation of an SEI layer on the graphite anode induced by the electrolyte [6]. Nevertheless, the average CE of the as-prepared C-GPE-2 electrolyte-based full cell is higher than that of the corresponding half-cell. This is possibly due to the better interface compatibility of graphite anodes compared to Li metal anodes. The full-cell interface stability of the LiBs based on C-GPE-2 was further investigated by analyzing the surface morphologies of the graphite anode. Figure 5c displays the FE-SEM image of the pristine graphite anode, and Figure 5d shows the FE-SEM image of the graphite anode of the as-prepared C-GPE-2-based full cell. After 300 CD cycles of the as-prepared C-GPE-2-based full cell, the graphite was recovered. It revealed that the as-prepared C-GPE-2 is capable of producing a dense, layered, and stable SEI layer on the graphite anode. This SEI layer can extend the interface stability of the electrolyte and electrode, which concurrently enhances the lifespan of LiBs [40]. The formation of the SEI layer was identified further by measuring the EDS elemental mapping of the graphite anode, as shown in Figure S5. The EDS elemental mapping clearly indicates the existence of a high density of the elements C, O, F, S, and N in the graphite anode.

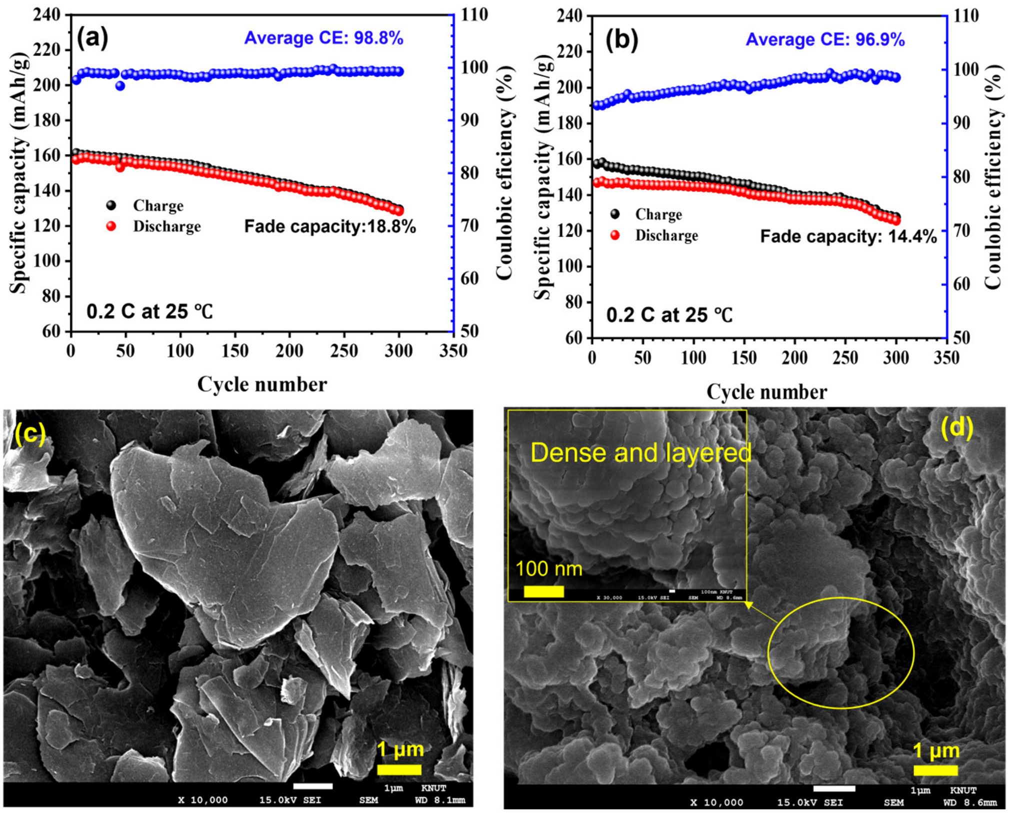

Figure 5. Variation in the specific capacity and the Coulombic efficiency as a function of CD cycling number of the corresponding full cell (**a**) and half-cell (**b**) at 0.2 C and 25 °C; FE-SEM images of (**c**) pristine graphite anode and (**d**) graphite anode based on C-GPE-2 electrolyte-contained LiBs (inset image shows the corresponding magnified FE-SEM image).

2.4. Characterization of As-Synthesized C-GPEs

Figure 6a,b show the FTIR spectra that were obtained to gain further insight into the structural characterization of the as-prepared C-GPEs. After completing polymerization for 24 h, all of the as-prepared C-GPEs display a broad peak (ca. 3505 cm^{-1}) of hydroxyl O–H stretching and reduced intensity of epoxy ring group stretching (ca. 902 cm^{-1}), suggesting that the ring-opening process was conducted. The peak at ca. 826 cm^{-1} is assigned to epoxy group stretching. These results are in good agreement with previously reported work [18,29]. Additionally, the stretching of C–H was found at a peak of ca. 2840–2946 cm^{-1}, and the peaks at ca. 1700–1800 cm^{-1} and ca. 1178 cm^{-1} of the as-prepared C-GPEs are attributed to the C=O stretching from EC/DEC [8] and the C–O–C deformation vibration [31,41], respectively.

Figure 6c shows the thermogravimetric analysis results of the LiFSI and the as-prepared C-GPEs. Obviously, the relative stable temperatures of the as-prepared C-GPE-2 and C-GPE-3 (up to ca. 174 °C) were similar, whereas the as-prepared C-GPE-1 (up to ca. 180 °C) exhibited a lower mass loss, which could mainly be attributed to moisture and the solvent (EC/DEC). After that, the degradation of the as-prepared C-GPEs was taken at a temperature range of ca. 180–480 °C. In contrast, the LiFSI had already decomposed at ca. 142 °C [42]. The enhanced thermal stability can be attributed to the conversion degree of the polymer and the cross-linked structure [20], which is also verified by the FTIR and DSC results. DSC measurements were conducted after the as-prepared C-GPEs were dried in a vacuum oven for 12h at 80 °C. As can be seen in Figure 6d, the glass transition temperatures (T_g) of the as-prepared C-GPEs—C-GPE-1, C-GPE-2, and C-GPE-3—were ca. −45.2, −46.5, and −46.2 °C, respectively. The super-low T_g values of the as-prepared C-GPEs are significantly linked to their highly amorphous network [41], which is confirmed by the XRD patterns.

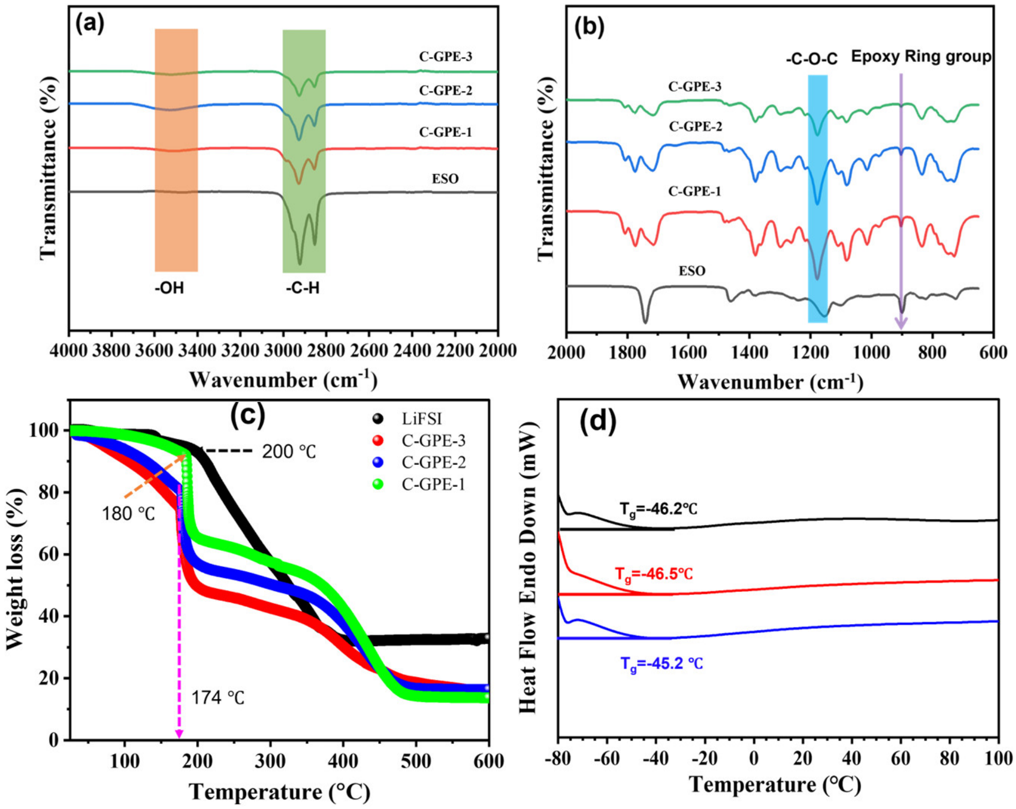

Figure 6. (**a**,**b**) FTIR spectra of as-prepared C-GPEs and ESO; (**c**) TGA traces of as-synthesized C-GPEs and LiFSI salt; (**d**) DSC plots of as-prepared C-GPEs.

2.5. In Situ Cross-Linking Gel Polymer Electrolytes

Figure 7a shows a plausible in situ cross-linking process and the proposed evolutionary network. Generally, in the first step, the homogeneous precursor solution containing the LiFSI, monomer (ESO), and solvent (EC/DEC) was injected into the assembled battery. Next, LiFSI provides Lewis acid H (FSIOH) under the heating condition of 40 °C [6], which attacks the cyclic epoxide ring and continues the propagation and cross-linking cationic ring-opening polymerization in the ESO chain in the presence of EC/DEC. Finally, the 3D cross-linked polymer network in the C-GPEs is formed in situ, directly inside the battery. Notably, this fabrication process is compatible with the current industrial application of LiBs. As additional initiators (e.g., LiTFSI and $LiBF_4$) [4,15,43,44] and cost-ineffective additives/plasticizers (e.g., FEC) [15] are unnecessary, this as-prepared C-GPE offers similar, or even lower, expense than the other reported works [45]. Figure 7b shows cross-sectional images investigating the close interface affinity between the cathode/as-prepared C-GPE-2/graphite anode, respectively. This tight contact between the cathode and the as-prepared electrolyte enables Li-ion communication and facilitates cycling performance [15,36,37]. Moreover, XRD tests were utilized to measure the crystallization of the as-prepared C-GPEs. As depicted in Figure 7c, all of the as-prepared C-GPEs showed a broad peak at around $2\theta = 21.6°$, suggesting a high-degree amorphous morphology with chain mobility [6,15]. The XRD analysis matches well with the T_g results of the as-prepared C-GPEs. Notably, the enhanced intensity of the amorphous peak should be due to the addition of EC/DEC, which enables the mobility of the polymer chain, as well as the increased FHMW.

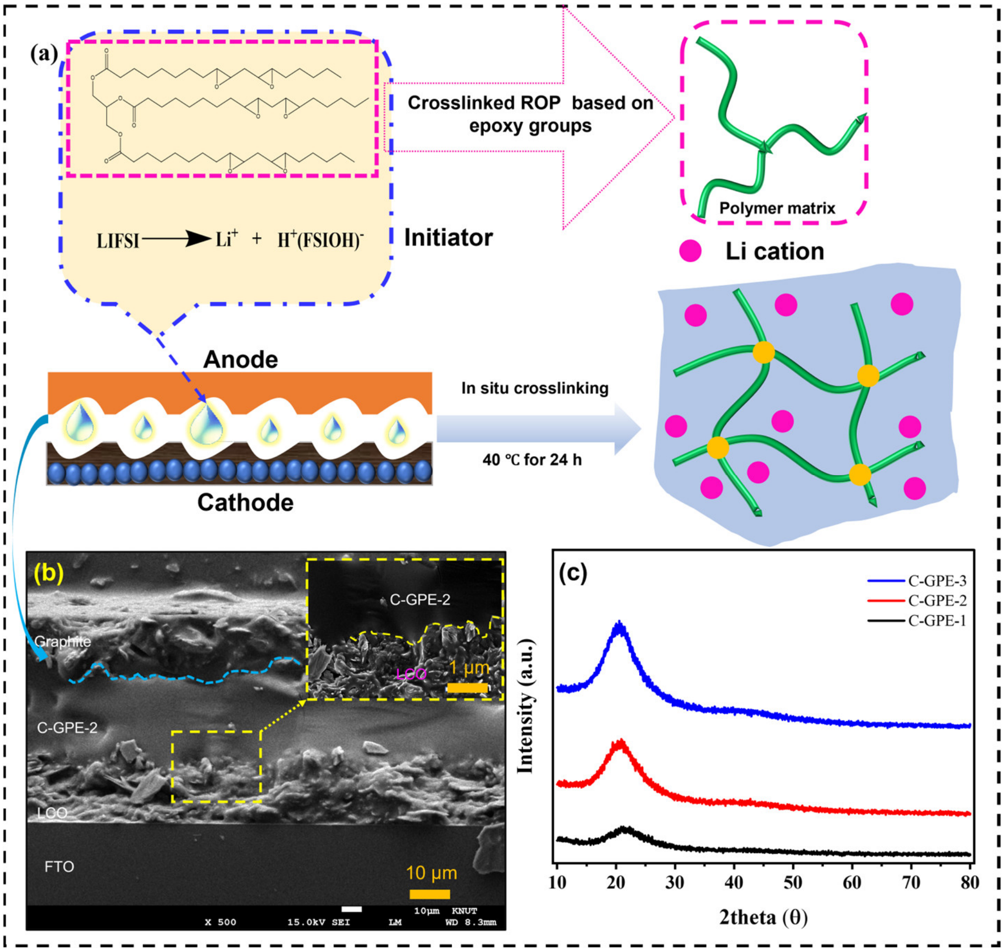

Figure 7. (**a**) Schematic diagram of in situ-fabricated C-GPEs. (**b**) Cross-sectional FE-SEM image of as-prepared C-GPE-2-based dummy cell (the inset is the enlarged area between the LCO cathode/the C-GPE-2). (**c**) XRD plots of as-prepared C-GPEs.

3. Conclusions

In summary, we report an in situ-formed C-GPE based on poly (ESO), which is successfully developed to simultaneously improve the interface adhesion and generate uniform distribution on an anode surface in the presence of 20% (*v*/*v*) solvent (EC/DEC). The as-synthesized C-GPEs exhibited good thermal stability (stable up to 180 °C), super-low T_g values, and considerable electrochemical properties. The FE-SEM images revealed a tight contact between the electrolyte and electrodes, which facilitates battery performance. Especially, the as-synthesized C-GPE-2 showed a T_g value of −46.5 °C, a comparable σ at 30 °C, and a broader electrochemical stability window (up to 5.19 V). As a result, the graphite/C-GPE-2/LFP full cell delivered an initial C_{sp} of ca. 158.7 mAh/g with an average η of 98.86% after 50 CD cycles at 0.1 C. Moreover, the as-prepared C-GPE-2-based Li//LFP half-cell delivered a capacity retention of ca. 93.05% after 50 CD cycles at 0.1 C. Additionally, the capacity retention of the as-prepared C-GPE-2-based cells was over 80% after 300 CD cycles. These results could provide an effective approach to improving anode stability and adjusting the distribution of electrolyte on electrode surfaces in lithium gel polymer batteries.

4. Materials and Methods

4.1. Sources

Epoxidized soybean oil (ESO), lithium bis(fluorosulfonyl)imide (LiFSI; 99.9%), diethyl carbonate (DEC; ≥99.9%), ethylene carbonate (EC; ≥99%), lithium cobalt(III) oxide ($LiCoO_2$;

$\geq$99.8%), N-methyl pyrrolidone (NMP; 99.5%), poly(vinylidene fluoride) (PVDF; average Mw~534,000), and carbon black (99.9%) were all ordered from Sigma-Aldrich (St. Louis, MO, USA), while the lithium iron(II) phosphate (LFP) power, graphite anode, and lithium were obtained from the MTI Company (Richmond, CA, USA).

4.2. Characterization and Measurements

The chemical structural properties of the as-synthesized polymer electrolyte were analyzed by Fourier-transform infrared spectra (FTIR) using a Nicolet iS5 (Thermo Fisher Scientific, Waltham, MA, USA) with a scanning range of 4000–650 cm^{-1}. The thermal properties were recorded using a Scinco TGA-N 1000 analyzer (Seoul, Republic of Korea) in the temperature range from 30 to 600 °C in an N_2 atmosphere at a heating rate of 10 °C/min. The differential scanning calorimetry (DSC) was conducted on a Pyris™ Diamond DSC (PerkinElmer Co., Ltd., Waltham, MA, USA) under a nitrogen atmosphere at a heating rate of 10 °C/min over a temperature range from −60 to 250 °C.

The interfacial morphology of the as-prepared electrolyte was characterized using a field-emission scanning electron microscope (FE-SEM; JSM-7610F; JEOL, Tokyo, Japan) along with energy dispersive X-ray (EDX; inCAx-sight7421; Oxford, UK) spectroscopy. The X-ray diffraction (XRD) analysis of the as-synthesized polymer electrolyte was recorded on D2 Phase (Bruker, Germany) in the angle range from 10 to 80° at a scanning rate of 1°/min at ambient temperature.

4.3. Electrochemical Measurements

Electrochemical impedance spectrometers (EISs) were used to measure the ionic conductivity (σ) of the as-prepared electrolyte using an IM6ex (Zahner Elektrik GmbH & Co. KG, Kronach, Germany) instrument (at a frequency range from 0.1 to 10^5 Hz and an AC amplitude of 5 mV in an open voltage). The fabricated asymmetrical dummy cells (Figure S3 of the SM) were allowed to reach thermal equilibrium for 30 min prior to each test. The temperature ranged from 30 to 80 °C, and each cell was recorded three times. Then, the received EIS spectra were fitted through Z-view software (version 3.1; Scribner Associates Inc., Southern Pines, NC, USA). The values of σ were calculated according to Equation (1), which is as follows:

$$\sigma = L/RS \tag{1}$$

where σ (S/cm) is the ionic conductivity, R (Ω) is the bulk resistance, L (cm) represents the distance between the electrodes, and S (cm^2) is the electrodes/electrolyte contact area.

All of the electrochemical performances of the cells were observed using Ivium-n-Stat (Ivium Technologies B.V., Eindhoven, The Netherlands). The cyclic voltammetry (CV) was examined from −1.5 to 5 V under a scan rate of 1 mV/s at 25 °C. The electrochemical anodic stability was determined by linear sweep voltammetry (LSV). CR2032-type coin cells were assembled with a stainless-steel (SS) disc as the working electrode and metallic Li as both the counter and reference electrode in the potential range from 0 to 6 V at a scan rate of 0.1 mV/s. The discharge–charge tests and cycling performances of the CR2032-type coin cells based on a graphite/C-GPEs/LFP configuration were carried out at 0.1, 0.2, and 0.3 C, respectively, under the operational voltage of 2.0 to 4.2 V and 25 °C. The C rate was defined based on the LFP cathode active material. For comparison, the half-cell of Li/C-GPE-2/LFP was assembled and examined at 0.1, 0.2, and 0.3 C, respectively, under a cell voltage of 2.5–4.2 V and 25 °C. All CR2032-type coin cells were assembled in an argon-filled glovebox (H_2O and $O_2 < 0.1$ ppm).

4.4. In Situ-Polymerized Cross-Linked Gel Polymer Electrolytes (C-GPEs)

The in situ polymeric electrolyte was prepared using ESO, LiFSI, and EC/DEC solvent. The digital pictures of the in situ-formed C-GPEs can be seen in Figure S4 and Video S1 of the SM for the as-prepared C-GPE-2. According to the polymerization tests, 2 M LiFSI in the electrolyte was applied in this work. First, 2 M LiFSI was added to the solution of ESO and EC/DEC (10% by *v*/*v*); the ratio in the mixture of EC/DEC is 5:5 by volume. After that, the obtained homogenous solution was placed at 40 °C in an Ar-filled glovebox for 24 h. Finally, the received electrolyte was named C-GPE-1. Similarly, based on the volume fraction of the solvent, the electrolytes with 20% and 30% solvent were denoted as C-GPE-2 and C-GPE-3, respectively. The detailed composition of the as-prepared CPEs can be seen in Table S2 in the SM. The asymmetric dummy cell was fabricated following our previous work [17] and was employed to evaluate the ionic conductivity of the as-prepared C-GPEs.

4.5. Preparation of LFP Cathode

The LFP cathode was composed of LFP, PVDF, and Super P at a ratio of (85:5:10)% by weight, respectively. NMP was added to the above mixture to form a homogenous slurry. Then, the slurry was coated on Al foil and dried in a vacuum oven at 120 °C for 12 h. Finally, the LFP cathode was cut into 14 mm discs and stored in a glove box before use. The loading mass of the LFP cathode was about 6 mg/cm^2.

Supplementary Materials: The following supporting information can be downloaded at https://www.mdpi.com/article/10.3390/gels9050384/s1, Figure S1: Nyquist plots of as-prepared C-GPE-1 (a), C-GPE-2 (b), and C-GPE-3 (c), and a corresponding equivalent circuit (d); Figure S2: CV profiles of C-GPE-4; Figure S3: Schematic illustration of an asymmetric dummy cell; Figure S4: Digital photos of in situ polymeric C-GPEs with varying concentrations of LiFSI; Table S1: Comparison of electrochemical properties of the polymer electrolyte with epoxy groups from reported works; Table S2: Detailed composition of the as-prepared CPEs; Figure S5: (a,b) Selected area of graphite anode of C-GPE-2 electrolyte-based LIB (inset shows the wt% of the elements C, N, O, F, and S), and (b–g) EDS elemental mapping of C, N, O, F, and S, respectively; Video S1: As-prepared C-GPE-2 after 24 h. [4,18,44,46–48].

Author Contributions: Conceptualization, W.Z. and W.K.; methodology and data curation, W.B.; software, L.J.; formal analysis, S.P.; resources, M.J.; writing—original draft preparation, W.Z.; writing—review and editing, H.J.; supervision, W.K.; project administration, H.J. All authors have read and agreed to the published version of the manuscript.

Funding: This research received no external funding.

Institutional Review Board Statement: Not applicable.

Informed Consent Statement: Not applicable.

Data Availability Statement: Not applicable.

Acknowledgments: This paper was supported by Konkuk University in 2022.

Conflicts of Interest: The authors declare no conflict of interest.

References

1. Liu, K.; Liu, Y.; Lin, D.; Pei, A.; Cui, Y. Materials for lithium-ion battery safety. *Sci. Adv.* **2018**, *4*, eaas9820. [CrossRef] [PubMed]
2. Xia, S.; Wu, X.; Zhang, Z.; Cui, Y.; Liu, W. Practical Challenges and Future Perspectives of All-Solid-State Lithium-Metal Batteries. *Chemistry* **2019**, *5*, 753–785. [CrossRef]
3. Liu, Q.; Cai, B.; Li, S.; Yu, Q.; Lv, F.; Kang, F.; Wang, Q.; Li, B. Long-cycling and safe lithium metal batteries enabled by the synergetic strategy of ex situ anodic pretreatment and an in-built gel polymer electrolyte. *J. Mater. Chem. A* **2020**, *8*, 7197–7204. [CrossRef]
4. Zhu, J.; Zhang, J.; Zhao, R.; Zhao, Y.; Liu, J.; Xu, N.; Wan, X.; Li, C.; Ma, Y.; Zhang, H.; et al. In situ 3D crosslinked gel polymer electrolyte for ultra-long cycling, high-voltage, and high-safety lithium metal batteries. *Energy Storage Mater.* **2023**, *57*, 92–101. [CrossRef]
5. Wan, J.; Xie, J.; Kong, X.; Liu, Z.; Liu, K.; Shi, F.; Pei, A.; Chen, H.; Chen, W.; Chen, J.; et al. Ultrathin, flexible, solid polymer composite electrolyte enabled with aligned nanoporous host for lithium batteries. *Nat. Nanotechnol.* **2019**, *14*, 705–711. [CrossRef]
6. Zhang, W.; Jin, L.; Lee, S.; Bae, W.; Park, S.; Jeon, M.; Kim, W.; Jang, H. In situ induced crosslinking highly conductive solid polymer electrolyte with intimated electrodes interfacial compatibility for safe Li-ion batteries. *J. Power Sources* **2023**, *557*, 232568. [CrossRef]
7. Long, L.; Wang, S.; Xiao, M.; Meng, Y. Polymer electrolytes for lithium polymer batteries. *J. Mater. Chem. A* **2016**, *4*, 10038–10069. [CrossRef]

8. Park, S.; Sohn, J.-Y.; Hwang, I.-T.; Shin, J.; Yun, J.-M.; Eom, K.; Shin, K.; Lee, Y.-M.; Jung, C.-H. In-situ preparation of gel polymer electrolytes in a fully-assembled lithium ion battery through deeply-penetrating high-energy electron beam irradiation. *Chem. Eng. J.* **2023**, *452*, 139339. [CrossRef]
9. Wu, K.; Cui, J.; Yi, J.; Liu, X.; Ning, F.; Liu, Y.; Zhang, J. Biodegradable Gel Electrolyte Suppressing Water-Induced Issues for Long-Life Zinc Metal Anodes. *ACS Appl. Mater. Interfaces* **2022**, *14*, 34612–34619. [CrossRef]
10. Liu, T.; Zhang, J.; Han, W.; Zhang, J.; Ding, G.; Dong, S.; Cui, G. Review—In Situ Polymerization for Integration and Interfacial Protection Towards Solid State Lithium Batteries. *J. Electrochem. Soc.* **2020**, *167*, 0700527. [CrossRef]
11. Liang, S.; Yan, W.; Wu, X.; Zhang, Y.; Zhu, Y.; Wang, H.; Wu, Y. Gel polymer electrolytes for lithium ion batteries: Fabrication, characterization and performance. *Solid. State Ion.* **2018**, *318*, 2–18. [CrossRef]
12. Ma, C.; Cui, W.; Liu, X.; Ding, Y.; Wang, Y. In situ preparation of gel polymer electrolyte for lithium batteries: Progress and perspectives. *InfoMat* **2021**, *4*, e12232. [CrossRef]
13. Chen, D.; Zhu, M.; Kang, P.; Zhu, T.; Yuan, H.; Lan, J.; Yang, X.; Sui, G. Self-Enhancing Gel Polymer Electrolyte by In Situ Construction for Enabling Safe Lithium Metal Battery. *Adv. Sci.* **2022**, *9*, e2103663. [CrossRef]
14. Xiao, Q.; Deng, C.; Wang, Q.; Zhang, Q.; Yue, Y.; Ren, S. In Situ Cross-Linked Gel Polymer Electrolyte Membranes with Excellent Thermal Stability for Lithium Ion Batteries. *ACS Omega* **2019**, *4*, 95–103. [CrossRef]
15. Ren, W.; Zhang, Y.; Lv, R.; Guo, S.; Wu, W.; Liu, Y.; Wang, J. In-situ formation of quasi-solid polymer electrolyte for improved lithium metal battery performances at low temperatures. *J. Power Sources* **2022**, *542*, 231773. [CrossRef]
16. Fu, F.; Zheng, Y.; Jiang, N.; Liu, Y.; Sun, C.; Zhang, A.; Teng, H.; Sun, L.; Xie, H. A Dual-Salt PEO-based polymer electrolyte with Cross-Linked polymer network for High-Voltage lithium metal batteries. *Chem. Eng. J.* **2022**, *450*, 137776. [CrossRef]
17. Zhang, W.; Yoon, S.; Jin, L.; Lim, H.; Jeon, M.; Jang, H.; Ahmed, F.; Kim, W. Lithium Salt Catalyzed Ring-Opening Polymerized Solid-State Electrolyte with Comparable Ionic Conductivity and Better Interface Compatibility for Li-Ion Batteries. *Membranes* **2022**, *12*, 330. [CrossRef]
18. Zhang, W.; Ryu, T.; Yoon, S.; Jin, L.; Jang, G.; Bae, W.; Kim, W.; Ahmed, F.; Jang, H. Synthesis and Characterization of Gel Polymer Electrolyte Based on Epoxy Group via Cationic Ring-Open Polymerization for Lithium-Ion Battery. *Membranes* **2022**, *12*, 439. [CrossRef]
19. Wang, Q.; Xu, X.; Hong, B.; Bai, M.; Li, J.; Zhang, Z.; Lai, Y. Molecular engineering of a gel polymer electrolyte via in-situ polymerization for high performance lithium metal batteries. *Chem. Eng. J.* **2022**, *428*, 131331. [CrossRef]
20. Cheng, H.; Zhu, J.; Jin, H.; Gao, C.; Liu, H.; Cai, N.; Liu, Y.; Zhang, P.; Wang, M. In situ initiator-free gelation of highly concentrated lithium bis(fluorosulfonyl)imide-1,3-dioxolane solid polymer electrolyte for high performance lithium-metal batteries. *Mater. Today Energy* **2021**, *20*, 100623. [CrossRef]
21. Castillo, J.; Santiago, A.; Judez, X.; Garbayo, I.; Coca Clemente, J.A.; Morant-Miñana, M.C.; Villaverde, A.; González-Marcos, J.A.; Zhang, H.; Armand, M.; et al. Safe, Flexible, and High-Performing Gel-Polymer Electrolyte for Rechargeable Lithium Metal Batteries. *Chem. Mater.* **2021**, *33*, 8812–8821. [CrossRef]
22. Niu, Y.-B.; Yin, Y.-X.; Wang, W.-P.; Wang, P.-F.; Ling, W.; Xiao, Y.; Guo, Y.-G. In Situ Copolymerizated Gel Polymer Electrolyte with Cross-Linked Network for Sodium-Ion Batteries. *CCS Chem.* **2020**, *2*, 589–597. [CrossRef]
23. Zhou, L.; Liu, S.; Li, W.; Song, H.; Du, L.; Cui, Z. Highly conductive Poly(ε-caprolactone) and chitosan based polymer electrolyte for lithium metal battery. *J. Power Sources* **2023**, *553*, 2322271. [CrossRef]
24. Hu, J.J.; Long, G.K.; Liu, S.; Li, G.R.; Gao, X.P. A LiFSI-LiTFSI binary-salt electrolyte to achieve high capacity and cycle stability for a Li-S battery. *Chem. Commun.* **2014**, *50*, 14647–14650. [CrossRef]
25. Cai, Y.; Zhang, H.; Cao, Y.; Wang, Q.; Cao, B.; Zhou, Z.; Lv, F.; Song, W.; Duo, D.; Yu, L. Synthesis, application and industrialization of LiFSI: A review and perspective. *J. Power Sources* **2022**, *535*, 231481. [CrossRef]
26. Bai, P.; Ji, X.; Zhang, J.; Zhang, W.; Hou, S.; Su, H.; Li, M.; Deng, T.; Cao, L.; Liu, S.; et al. Formation of LiF-rich Cathode-Electrolyte Interphase by Electrolyte Reduction. *Angew. Chem. Int. Ed. Engl.* **2022**, *61*, e202202731. [CrossRef]
27. Li, Z.; Liu, Q.; Deng, Y.; Zhou, M.; Tang, W.; Dong, H.; Zhao, W.; Liu, R. In situ cross-linked plastic crystal electrolytes toward superior lithium metal batteries. *Mater. Today Energy* **2023**, *31*, 101198. [CrossRef]
28. Wei, J.; Yue, H.; Shi, Z.; Li, Z.; Li, X.; Yin, Y.; Yang, S. In Situ Gel Polymer Electrolyte with Inhibited Lithium Dendrite Growth and Enhanced Interfacial Stability for Lithium-Metal Batteries. *ACS Appl. Mater. Interfaces* **2021**, *13*, 32486–32494. [CrossRef]
29. Qi, M.; Xu, Y.J.; Rao, W.H.; Luo, X.; Chen, L.; Wang, Y.Z. Epoxidized soybean oil cured with tannic acid for fully bio-based epoxy resin. *RSC Adv.* **2018**, *8*, 26948–26958. [CrossRef]
30. Liu, Z.; Erhan, S.Z. Ring-Opening Polymerization of Epoxidized Soybean Oil. *J. Am. Oil Chem. Soc.* **2009**, *87*, 437–444. [CrossRef]
31. Öztürk, C.; Küsefoğlu, S.H. Polymerization of epoxidized soybean oil with maleinized soybean oil and maleic anhydride grafted polypropylene mixtures. *J. Appl. Polym. Sci.* **2010**, *118*, 3311–3317. [CrossRef]
32. Zhang, H.; Arcelus, O.; Carrasco, J. Role of asymmetry in the physiochemical and electrochemical behaviors of perfluorinated sulfonimide anions for lithium batteries: A DFT study. *Electrochim. Acta* **2018**, *280*, 290–299. [CrossRef]
33. Wang, Y.; Cao, Z.; Ma, Z.; Liu, G.; Cheng, H.; Zou, Y.; Cavallo, L.; Li, Q.; Ming, J. Weak Solvent—Solvent Interaction Enables High Stability of Battery Electrolyte. *ACS Energy Lett.* **2023**, *8*, 1477–1484. [CrossRef]
34. Mackanic, D.G.; Michaels, W.; Lee, M.; Feng, D.; Lopez, J.; Qin, J.; Cui, Y.; Bao, Z. Crosslinked Poly(tetrahydrofuran) as a Loosely Coordinating Polymer Electrolyte. *Adv. Energy Mater.* **2018**, *8*, 1800703. [CrossRef]

35. Wang, Q.; Dong, T.; Zhou, Q.; Cui, Z.; Shangguan, X.; Lu, C.; Lv, Z.; Chen, K.; Huang, L.; Zhang, H.; et al. An in-situ generated composite solid-state electrolyte towards high-voltage lithium metal batteries. *Sci. China Chem.* **2022**, *65*, 934–942. [CrossRef]
36. Shin, H.; Choi, S.J.; Choi, S.; Jang, B.Y.; Jeong, J.; Cho, Y.-G.; Lee, S.-Y.; Song, H.-K.; Yu, J.H.; Kim, T.-H. In situ gel electrolyte network guaranteeing ionic communication between solid electrolyte and cathode. *J. Power Sources* **2022**, *546*, 231926. [CrossRef]
37. Chiu, L.-L.; Chung, S.-H. Composite gel-polymer electrolyte for high-loading polysulfide cathodes. *J. Mater. Chem. A* **2022**, *10*, 13719. [CrossRef]
38. Kang, P.; Chen, D.; Wu, L.; Yang, X.; Sui, G. Insight into poly(1,3-dioxolane)-based polymer electrolytes and their interfaces with lithium Metal: Effect of electrolyte compositions. *Chem. Eng. J.* **2023**, *455*, 140931. [CrossRef]
39. Lin, Y.; Wang, T.; Zhang, L.; Peng, X.; Huang, B.; Wu, M.; Zhao, T. In-situ forming lithiophilic-lithiophobic gradient interphases for dendrite-free all-solid-state Li metal batteries. *Nano Energy* **2022**, *99*, 107395. [CrossRef]
40. Ahmed, F.; Choi, I.; Ryu, T.; Yoon, S.; Rahman, M.M.; Zhang, W.; Jang, H.; Kim, W. Highly conductive divalent fluorosulfonyl imide based electrolytes improving Li-ion battery performance: Additive potentiating electrolytes action. *J. Power Sources* **2020**, *455*, 227980. [CrossRef]
41. Kasetaite, S.; De la Flor, S.; Serra, A.; Ostrauskaite, J. Effect of Selected Thiols on Cross-Linking of Acrylated Epoxidized Soybean Oil and Properties of Resulting Polymers. *Polymers* **2018**, *10*, 439. [CrossRef] [PubMed]
42. Kerner, M.; Plylahan, N.; Scheers, J.; Johansson, P. Thermal stability and decomposition of lithium bis(fluorosulfonyl)imide (LiFSI) salts. *RSC Adv.* **2016**, *6*, 23327–23334. [CrossRef]
43. Huang, S.; Cui, Z.; Qiao, L.; Xu, G.; Zhang, J.; Tang, K.; Liu, X.; Wang, Q.; Zhou, X.; Zhang, B.; et al. An in-situ polymerized solid polymer electrolyte enables excellent interfacial compatibility in lithium batteries. *Electrochim. Acta* **2019**, *299*, 820–827. [CrossRef]
44. Nair, J.R.; Shaji, I.; Ehteshami, N.; Thum, A.; Diddens, D.; Heuer, A.; Winter, M. Solid Polymer Electrolytes for Lithium Metal Battery via Thermally Induced Cationic Ring-Opening Polymerization (CROP) with an Insight into the Reaction Mechanism. *Chem. Mater.* **2019**, *31*, 3118–3133. [CrossRef]
45. Zhao, Q.; Liu, X.; Stalin, S.; Khan, K.; Archer, L.A. Solid-state polymer electrolytes with in-built fast interfacial transport for secondary lithium batteries. *Nat. Energy* **2019**, *4*, 365–373. [CrossRef]
46. Chen, B.; Xu, Q.; Huang, Z.; Zhao, Y.; Chen, S.; Xu, X. One-pot preparation of new copolymer electrolytes with tunable network structure for all-solid-state lithium battery. *J. Power Sources* **2016**, *331*, 322–331. [CrossRef]
47. Yao, W.; Zhang, Q.; Qi, F.; Zhang, J.; Liu, K.; Li, J.; Chen, W.; Du, Y.; Jin, Y.; Liang, Y.; et al. Epoxy containing solid polymer electrolyte for lithium ion battery. *Electrochim. Acta* **2019**, *318*, 302–313. [CrossRef]
48. Ma, Y.; Sun, Q.; Wang, S.; Zhou, Y.; Song, D.; Zhang, H.; Shi, X.; Zhang, L. Li salt initiated in-situ polymerized solid polymer electrolyte: New insights via in-situ electrochemical impedance spectroscopy. *Chem. Eng. J.* **2022**, *429*, 132483. [CrossRef]

gels

MDPI

Article

3D Co-Printing and Substrate Geometry Influence the Differentiation of C2C12 Skeletal Myoblasts

Giada Loi [1], Franca Scocozza [1], Flaminia Aliberti [2,3], Lorenza Rinvenuto [2], Gianluca Cidonio [4], Nicola Marchesi [2], Laura Benedetti [2], Gabriele Ceccarelli [2,†] and Michele Conti [1,*,†]

[1] Department of Civil Engineering and Architecture, University of Pavia, Via Adolfo Ferrata 3, 27100 Pavia, Italy; giada.loi01@universitadipavia.it (G.L.); franca.scocozza@unipv.it (F.S.)
[2] Human Anatomy Unit, Department of Public Health, Experimental and Forensic Medicine, University of Pavia, Via Forlanini 2, 27100 Pavia, Italy; flaminia.aliberti01@universitadipavia.it (F.A.); lorenza.rinvenuto01@universitadipavia.it (L.R.); nicola.marchesi01@universitadipavia.it (N.M.); laura.benedetti@unipv.it (L.B.); gabriele.ceccarelli@unipv.it (G.C.)
[3] Fondazione IRCCS Policlinico San Matteo, Center for Inherited Cardiovascular Diseases, Transplant Research Area, 27100 Pavia, Italy
[4] Center for Life Nano- & Neuro-Science (CLN2S), Fondazione Istituto Italiano di Tecnologia, 00161 Rome, Italy; gianluca.cidonio@iit.it
* Correspondence: michele.conti@unipv.it
† These authors contributed equally to this work.

Abstract: Cells are influenced by several biomechanical aspects of their microenvironment, such as substrate geometry. According to the literature, substrate geometry influences the behavior of muscle cells; in particular, the curvature feature improves cell proliferation. However, the effect of substrate geometry on the myogenic differentiation process is not clear and needs to be further investigated. Here, we show that the 3D co-printing technique allows the realization of substrates. To test the influence of the co-printing technique on cellular behavior, we realized linear polycaprolactone substrates with channels in which a fibrinogen-based hydrogel loaded with C2C12 cells was deposited. Cell viability and differentiation were investigated up to 21 days in culture. The results suggest that this technology significantly improves the differentiation at 14 days. Therefore, we investigate the substrate geometry influence by comparing three different co-printed geometries—linear, circular, and hybrid structures (linear and circular features combined). Based on our results, all structures exhibit optimal cell viability (>94%), but the linear pattern allows to increase the in vitro cell differentiation, in particular after 14 days of culture. This study proposes an endorsed approach for creating artificial muscles for future skeletal muscle tissue engineering applications.

Keywords: co-printing; murine myoblasts (C2C12); bioprinting; fibrinogen-based hydrogel; polycaprolactone

1. Introduction

Cells are subjected to and influenced by various biomechanical stimuli present in their physiological microenvironment [1]: several studies have shown that localized stresses, such as the stiffness [2–7], micropatterning [8–11], porosity [12,13], and geometry of the substrate [14–16], strongly influence cell proliferation and differentiation.

However, most of these studies have used 2D manufacturing techniques, such as microcontact printing, which do not allow us to mimic the real complexity of in vivo tissues impairing thus the capability to predict the actual cellular response [17]. In this context, techniques such as bioprinting (BioP) allow the production of in vitro 3D cellular microenvironments by depositing bioinks (i.e., a mixture of a biomaterial (usually hydrogel) and biological components (such as cells) [18]) in a spatially controlled way. In our previous study [19], we used BioP to recreate an in vitro muscle fiber model obtaining excellent cell differentiation, especially on the structure edges; however, the interplay between the bioprinted model and the substrate was not investigated, although it is known that this may have a crucial role on myoblast behavior [20–28]. In particular, the curvature feature, i.e., the use of circular, angled substrates with portions characterized by a certain radius of curvature, has been shown by several authors to improve cell proliferation [21–23]. Unfortunately, the effect of the geometrical curvatures on the process of myogenic differentiation is unclear and needs to be further elucidated. Therefore, finding the optimal substrate geometry that can improve myotube differentiation, alignment, and function is critical to engineering muscle tissues [29].

Among the manufacturing techniques suitable for this purpose, 3D co-printing emerges, which is a BioP technique that allows the simultaneous deposition of two materials of different natures, e.g., a thermoplastic material and a hydrogel [30,31], allowing us to obtain multi-material 3D constructs [32–35].

In this regard, the application of co-printing in the field of muscle regenerative medicine is already reported in the literature; in these studies, the co-printed engineered muscles showed high cell viability, good in vitro differentiation [36,37], and high in vivo regenerative effect [37,38]. However, none of these studies has yet investigated the possibility of making supports using this technique and of studying the influence of the support geometry and its biomechanical consequences on muscle cell differentiation.

Based on these considerations, the present study proposes the application of the co-printing technique to realize supports and understand how geometric cues maximize the differentiation of C2C12 murine myoblast cells. First, we evaluated the capability of the co-printing technique to realize substrates for cell-loaded materials by fabricating linear supports with a central channel made of polycaprolactone (PCL) and containing a fibrinogen-based hydrogel loaded with C2C12 cells that were previously selected [19]. Biological tests were carried out to evaluate cell viability and differentiation. Then, once the biocompatibility of the co-printing technique is verified, we moved on to its application to evaluate the substrate geometry influence on cell differentiation. To this aim, three different geometries, namely linear, circular with different outer diameters (OD), and hybrid structures (combining linear and circular features), were created.

2. Results and Discussion

2.1. Linear Structures: Bioprinted vs. Co-Printed

2.1.1. Gene Expression Analysis by Quantitative Real-Time PCR

As a preliminary test, the effect of co-printing on cell differentiation was tested. In this regard, we performed gene expression analyses comparing structures with the same geometry (linear) realized with different techniques, i.e., BioP and co-printing. Data related to bioprinted structures were derived from our previous study [19].

Gene expression analyses were performed at 7, 14, and 21 days of culture in differentiative conditions (Figure 1). The bioprinted constructs are named F, which stands for fibrinogen-based hydrogel, while the co-printed structures are named F + PCL, as the same hydrogel has been deposited on a PCL support. RT-qPCR was used to detect expression levels of myogenic genes in 3D structures; in particular, since there are first preliminary tests, we only considered the two muscle master genes, i.e., MyoD and MCK, normalized by the housekeeping PGK gene (Table S1). At 7 days, the MCK gene was significantly expressed by cells cultured in the co-printed linear structures (Figure 1a). At 14 days co-printing significantly improves the differentiation, showing high expression levels of both MyoD and MCK genes. At 21 days, no statistically significant differences in MCK expression were found; however, MyoD was differentially expressed in the bioprinted structures, showing a still early differentiation. Overall, at 21 days, MyoD gene expression decreased significantly; as expected, the expression of this gene is related to early myogenic differentiation, while, after 21 days of culture, the decreases are in favor of the expression of late genes involved in the myogenic commitment and cell elongation. These data show that the co-printing process significantly improves cell differentiation, in particular at 14 days.

For this reason, all the 3D structures that will be examined below in the discussion have been created through 3D co-printing.

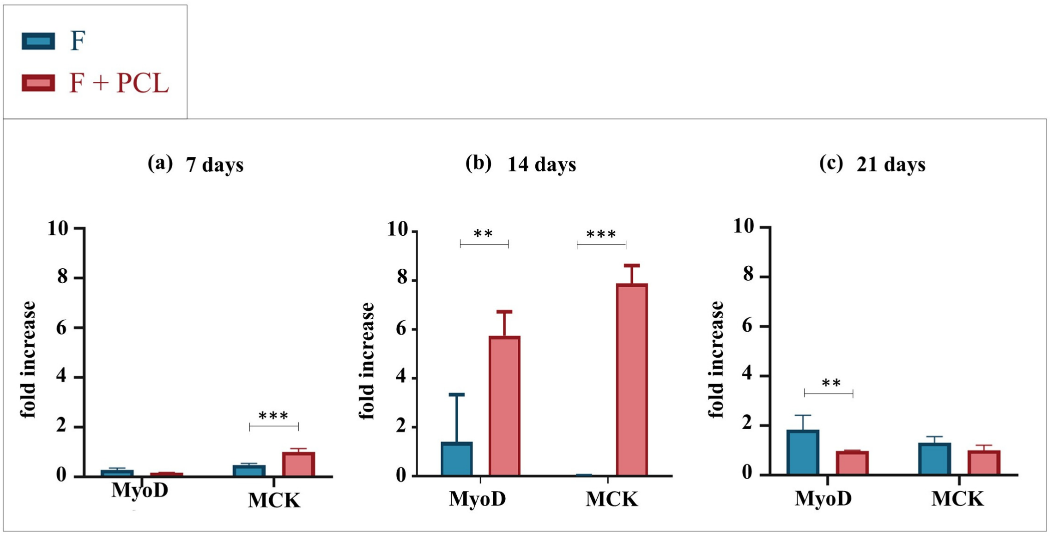

Figure 1. Gene expression analysis of C2C12 cells cultured into linear structures bioprinted (F) or co-printed (F+PCL) at 7, 14, and 21 days. (**a**) qRT-PCR at 7 days. (**b**) qRT-PCR at 14 days. (**c**) qRT-PCR at 21 days. Results are normalized to the housekeeping gene (3-phosphate dehydrogenase [PGK]). Statistically significant values are indicated as, ** $p < 0.01$ and *** $p < 0.001$. Analysis of variance test was performed to evaluate data significance.

2.2. Curvature Feature: Circular and Hybrid Structures

Gene Expression Analysis by Quantitative Real-Time PCR

To evaluate the effect of the curvature feature on cell differentiation, we performed gene expression analyses comparing the circular and serpentine-like structures realized by exploiting the co-printing technique. Analyses were performed at 7, 14, and 21 days of culture in differentiative conditions (Figure 2). Since, as mentioned in the introduction, the curvature feature has already been examined from the point of view of proliferation and not of differentiation, we decided to perform an in-depth differentiation analysis. For this reason, the expression levels of myogenic genes (i.e., MyoD, Myf5, Cyclin D1, Myh1, MCK, MCad, MyoG) in the 3D structures were detected by RT-qPCR normalized by the PGK gene.

At 7 days, no statistically significant differences are observed in the expression levels of the Cyclin D1 gene; all structures provide the same proliferative stimulus. The MyoD gene is differentially expressed in the serpentine-like structure compared to the circular ones. Otherwise, the Myf5 gene is differentially expressed in circular structures compared to the serpentine-like one.

At 14 days, as expected, Cyclin D1 expression starts to decrease for all structures; the proliferation process seems to reduce, and the differentiation increases. However, Cyclin D1 remains differentially expressed in the hybrid structure compared to the circular ones; so, this geometry promotes a proliferative process prolonged over time. The MyoG gene is differentially expressed in the circular structure with a small radius compared to the other cases examined, while the MyoD gene is differentially expressed in the serpentine-like structure.

Finally, at 21 days of culture, the Myh1 gene is differentially expressed in the circular structure with a small radius and in the hybrid structure compared to that with a large radius. The MCad and MCK genes are differentially expressed in the serpentine-like structure compared to the other analyzed cases. No statistically significant differences are observed for the MyoG, Cyclin D1, and Dysf genes (data not shown).

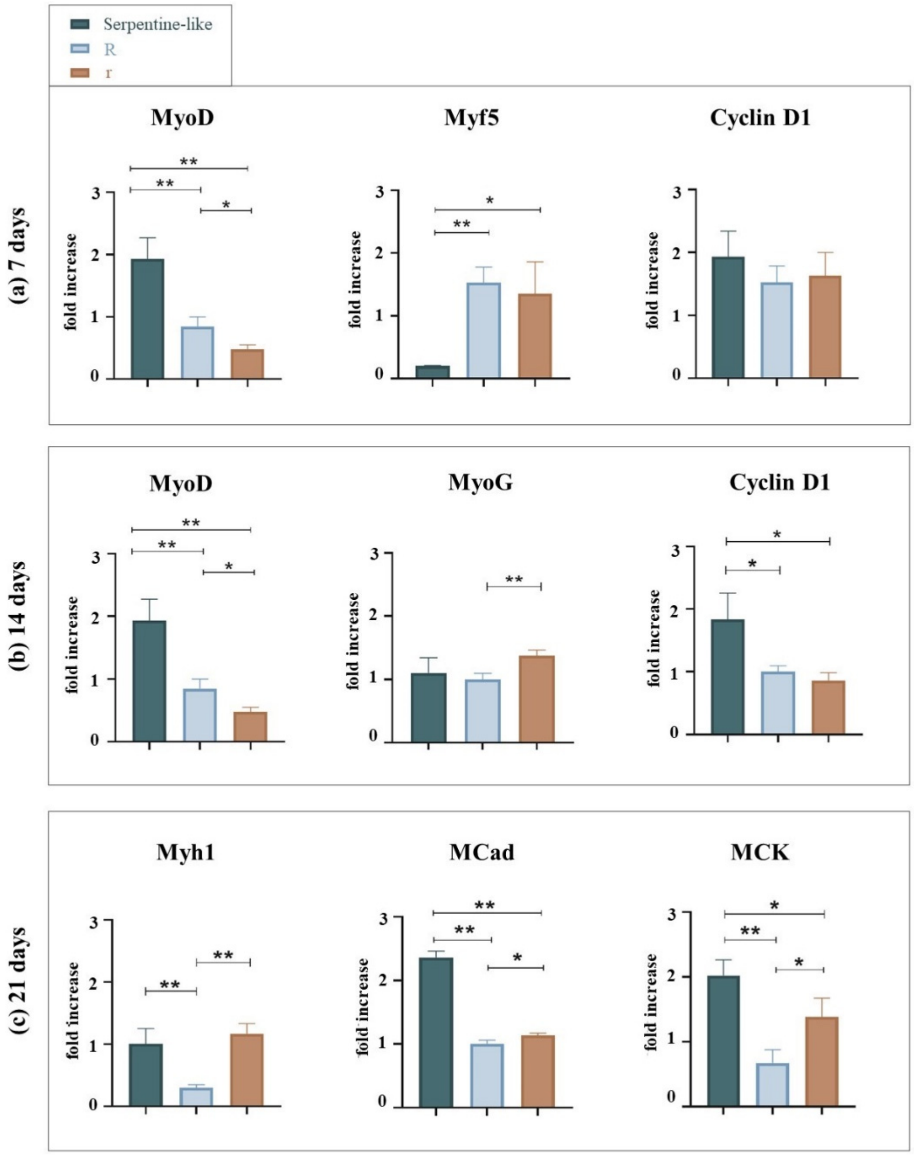

Figure 2. Gene expression analysis of C2C12 cultured into serpentine-like and circular (R, r) structures at 7, 14, and 21 days. (**a**) qRT-PCR at 7 days. (**b**) qRT-PCR at 14 days. (**c**) qRT-PCR at 21 days. Results are normalized to the housekeeping gene (3-phosphate dehydrogenase [PGK]). Statistically significant values are indicated as * $p < 0.05$, ** $p < 0.01$. Analysis of variance test was performed to evaluate data significance. R indicates structures with a 10 mm outer diameter while r indicates those with a 5 mm outer diameter.

In conclusion, regardless of geometry at 7 days, as expected, proliferation (indicated by cyclin D1 gene expression) is elevated and decreases with increasing culture period in favor of the differentiation process. At 14 days (short-term differentiation), the expression of cyclin D1 is still high in the serpentine-like constructs; instead, in the circular structures, it decreases favoring the expression of other differentiation genes. Finally, at 21 days (long-term differentiation), among the different geometries analyzed, at the same proliferation rate (i.e., same reduced expression of cyclin D1), the serpentine geometry is the one that showed greater differentiation and high expression of MCK and MCad genes.

2.3. Comparison of All Tested Geometries

Finally, to evaluate the effect of substrate geometry on cell behavior, we performed viability and gene expression analyses comparing all the considered geometries.

2.3.1. Live/Dead Staining

Live/dead staining was performed at different time points during the culture (1, 7, 14, and 21 days) (Figure 3). For all geometries, at 24 h after printing, cells are of a rounded shape and homogeneously distributed throughout the construct. Furthermore, at all time points and in all cases considered, cells demonstrated very high viability (>94%).

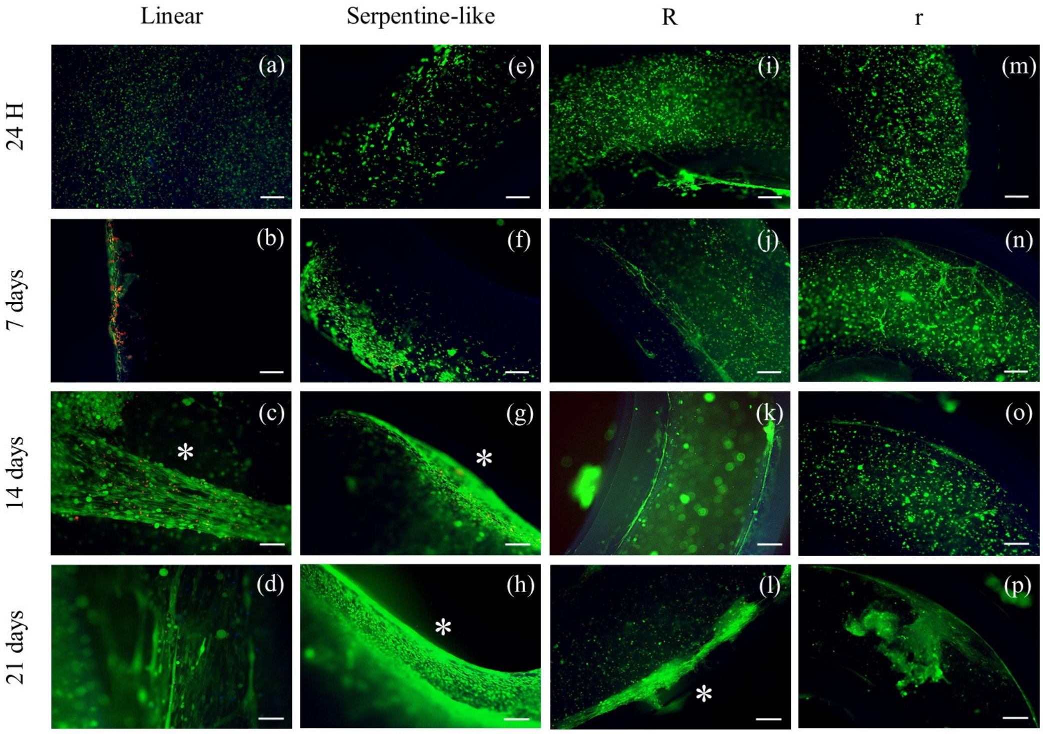

Figure 3. Live (green)/dead (red) images of different 3D geometries at specific time points in differentiative conditions. (**a**–**d**) Linear 3D constructs; (**e**–**h**) serpentine-like 3D constructs; (**i**–**l**) circular 3D constructs with OD 10 mm; (**m**–**p**) circular 3D constructs with OD 5 mm. Scale bar 50 µm. * highlights cell elongation. R indicates structures with a 10 mm outer diameter, while r indicates those with a 5 mm outer diameter.

On day 7, C2C12 cells remained mainly round-shaped in the center of the construct without merging to form myotubes. However, especially in linear constructs, an initial differentiation of C2C12 began at the edges of the 3D constructs, where cell elongation appeared. This is probably due to an inhomogeneous diffusion of the crosslinking solution or to lower oxygen and nutrient concentrations within the 3D constructs (Figure 3b).

Finally, at 14 and 21 days, C2C12 cells grown in linear and serpentine-like structures merged forming primordial myotubes even in the most central part of the 3D structure, and the alignment was promoted by the linear areas of the printed constructs (Figure 3d,h).

As for C2C12 cells grown in circular structures, at 7 and 14 days of culture, cells retain a rounded-shaped and slowly begin to elongate only at day 21, especially at the edges of the constructs (Figure 3l,p).

The elongation of C2C12 cells significantly decreased when printed in circular 3D structures (Figure 3i–p); otherwise, the linear structure appeared to significantly increase myotube formation, and the alignment of the myoblast is mainly located at the edges (Figure 3b–d).

Therefore, the live/dead results indicated that under differentiative conditions, the linear structure effectively induced the alignment of myoblasts in particular at the boundary of the structure with respect to the other geometries tested. An inhomogeneous diffusion of the crosslinker in the center of the construct and/or a lower diffusion of nutrients/oxygen could be responsible for insufficient cell elongation.

2.3.2. Gene Expression Analysis by Quantitative Real-Time PCR

Gene expression levels of C2C12 cells cultured under differentiative conditions in the different geometries at 7, 14, and 21 days were compared to evaluate the influence of the geometrical factor on the differentiation rate (Figure 4). The expression levels of the MyoD and MCK genes in the 3D co-printed structures were detected by RT-qPCR and normalized by the PGK gene. MyoD was analyzed for 7 and 14 days of culture to characterize early muscle differentiation, while MCK was analyzed for 21 days of culture as it indicates cell differentiation and maturation of muscle tissue.

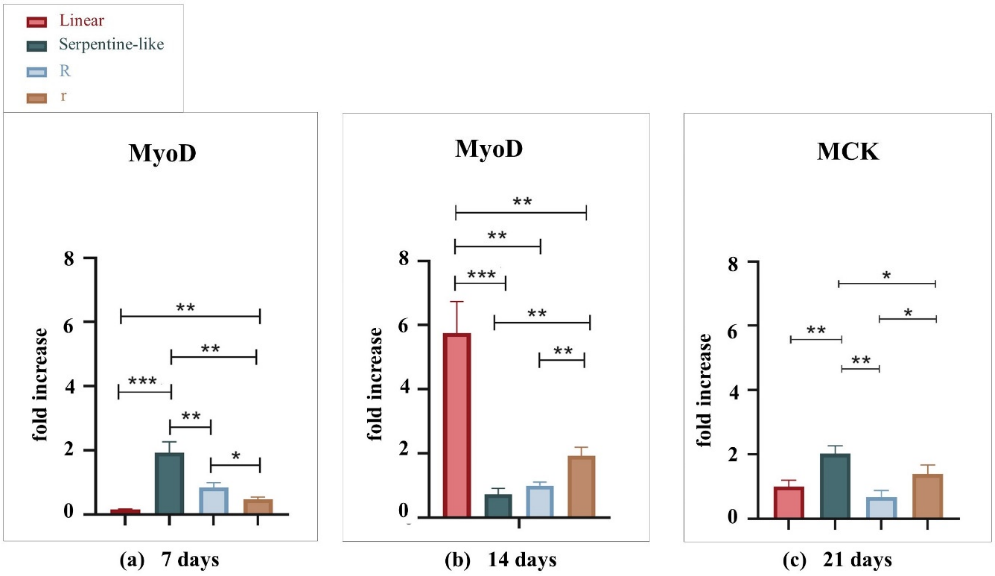

Figure 4. Gene expression analysis of C2C12 cultured into the different geometries tested (linear, serpentine-like, and circular) at 7, 14, and 21 days. (**a**) MyoD expression by qRT-PCR at 7 days. (**b**) MyoD expression by qRT-PCR at 14 days. (**c**) MCK expression by qRT-PCR at 21 days. Results are normalized to the housekeeping gene (3-phosphate dehydrogenase [PGK]). Statistically significant values are indicated as * $p < 0.05$, ** $p < 0.01$, and *** $p < 0.001$. Analysis of variance test was performed to evaluate data significance. R indicates structures with a 10 mm outer diameter while r indicates those with a 5 mm outer diameter.

At 7 days, the MyoD gene is differentially expressed in the serpentine-like structure. But, at 14 days, the linear geometry allows bursting cell differentiation, which reaches a very high gene expression value compared to all the other geometries examined. At 21 days, MCK is differentially expressed in the serpentine-like structure compared to the other ones. Thus, we obtained the best gene expression results at the 14-day time point, especially with the linear geometry, while the serpentine-like construct allows an improved late differentiation at 21 days. In conclusion, because one of our goals is to obtain a mature construct in the least time possible, linear geometry was selected. Indeed, it proves to be the best 3D structure to promote myoblast alignment along the printed filament in a short-time culture (14 days) and with the highest gene expression level.

2.4. Discussion

Cells are typically affected by biomechanical aspects of their micro-environment, such as substrate geometry. The curvature feature improves cell proliferation; however, its effect on differentiation is not clear and needs to be explored further [28,39].

Given these premises, in this study, we used the co-printing technique to create substrates and study the effect of their geometries on the differentiation of C2C12 murine myoblasts. Three different geometries—linear, circular with different outer diameters (OD 10 mm, OD 5 mm), and hybrid structures (linear and circular features in a serpentine-like construct)—were created by combining fibrinogen-based hydrogel loaded with C2C12 and PCL.

The results suggest that the co-printing technology does not impair cell viability and, indeed, significantly improves the differentiation at 14 days. However, following the excellent results obtained at 14 days, a decrease in both MyoD and MCK expression was observed at the subsequent 21-day time point. Considering MyoD, its expression significantly decreased, as we expected, because it is considered the master gene of early myogenic differentiation. While, regarding the MCK, we hypothesize that, following the high expression peak at 14 days, at 21 days, the translation process is favored compared to the transcription process.

Furthermore, all structures exhibited optimal cell viability (>94%). The linear pattern showed the best results as it allowed to increase in vitro cell differentiation after 14 days of culture.

Concerning biological experiments, contrary to other studies in the literature [15], statistically significant differences were observed in the gene expression of circular structures with different ODs. Specifically, at 21 days, the small radius structure showed a statistically significant differentiation compared to the large radius one. However, our structures are much larger than those previously studied [15], and therefore the results might not be comparable.

Furthermore, the linear geometry, as expected, showed a high degree of alignment, perhaps because the linear structure mimics as much as possible the structure of the muscle fiber. In several studies, myotube alignment has been modulated and guided by surface topography [27,28,40–42]. Instead, in our study, the alignment of cells was achieved on different geometries by using co-printing to create channels on the PCL supports for guiding the cells in them.

The selection of the linear structure is in contrast with other studies [15] which instead identified the hybrid ones as the best geometries for the C2C12 cell line. The reasons may be that in our serpentine architecture the curvature angle is greater (90°) compared to that of previous studies (30°) [15], and in the same structure we have included a discrete number of curvatures (three instead of one). Hence, we have less alignment and much more influence on the circular pattern due to the greater angle and number of the curvatures.

Finally, the application of this method allowed us to overcome some of the limitations that emerged in our previous study in which a bioprinted fiber muscle model had produced promising results [19]. In fact, in this work, the co-printing technique allowed us to create complex geometry supports for the bioink containment, which reduced the cell invasion on the Petri dish and will allow us in the future to introduce a mechanical stimulus that could improve the homogeneity of differentiation.

2.5. Limitations

Despite the success of the proposed co-printing strategy and the excellent results obtained, some limitations emerged. In particular, one of the main limitations concerns the inhomogeneous cell differentiation, located at the structure edges, probably both because structure edges are the areas where the stiffness and the crosslinking effect are greater and because cells need oxygen/nutrients and so they move to peripheral areas where the oxygen/nutrients concentration is higher. In this regard, given the significant impact of biomaterial stiffness on cell differentiation, this aspect will certainly be considered and investigated in future studies. Furthermore, structures with narrower channels could be designed to favor the formation of syncytia between cells. However, the bioprinter and hydrogel resolutions do not allow us to apply this solution. Therefore, to improve the homogeneity of differentiation, one solution is to apply mechanical stimulation. Several examples of mechanical stimulation-based bioreactors to improve muscle tissue maturation are reported in the literature [43–47]. This strategy could also reduce tissue maturation times which currently take up to 21 days. However, the PCL material selected for the support fabrication, due to its stiffness, does not allow mechanical stimulation. Furthermore, being a thermoplastic material it requires low printing speeds and consequently very long manufacturing times. For this reason, a solution may be to change the support material, which will have to be more elastic, autoclavable, and biocompatible. Finally, regarding co-printed linear structures, we obtained optimal results at 14 days of culture, but at the 21-day time point we observed a significant decrease in both MyoD and MCK gene expression (Figure 1c). The decrease in MyoD was an expected result since it is a gene expressed in early differentiation, as mentioned in Section 2.1.1, while the decrease in MCK, we hypothesize, may be related to a more advanced differentiation that favors the translation process to that of transcription. Therefore, this aspect will have to be further investigated and clarified in future studies.

3. Conclusions

Co-printing can be used to fabricate in vitro 3D models of muscle tissue with different architectures. We conclude that geometrical cues influence the differentiation process of C2C12 myoblasts. We investigated the viability and differentiation of C2C12 myoblasts on three main geometries—a linear, a circular, and a hybrid pattern, which combined linear and circular features in one geometrical unit. Our results clearly showed that the linear pattern, compared to the other structures, emerged as the optimal geometry to maximize the differentiation of C2C12 myotubes. After 14 days in culture, C2C12 cells were able to fuse forming aligned myotubes, in particular in the structure's edges, with high expression levels of specific skeletal muscle markers, such as MyoD.

Thanks to these findings, the results reported herein could have implications for improving skeletal muscle tissue engineering and the design of bioreactors for muscle–skeletal TE applications.

4. Materials and Methods

For the fabrication of skeletal muscle constructs, two commercial materials, i.e., a fibrinogen-based hydrogel (CELLINK® FIBRIN, Cellink AB, Göteborg, Sweden) and PCL pellets, and the mouse cell line C2C12 were used. The bioink was prepared by mixing the hydrogel and C2C12 cells. For the printing process, an extrusion-based pneumatic bioprinter (INKREDIBLE+®, Cellink AB, Göteborg, Sweden) with two print heads (PHs) was adopted. Both PHs were used for PCL and bioink co-printing: the first one (PH1) for printing PCL and the second one (PH2) for printing bioink. In the printed structures, viability and differentiation of C2C12 cells were analyzed at different time points (1, 7, 14, and 21 days) using, respectively, morphological tests by live/dead staining and gene expression analysis (by Real-Time PCR).

4.1. Cell Culture

C2C12 myoblasts (ATCC, CRL-1772™, Manassas, VA, USA) were cultured in Dulbecco's Modified Eagle's Medium (DMEM) supplemented with 10% fetal bovine serum, 1% penicillin/streptomycin (Sigma Aldrich, Burlington, MA, USA), 1% glutamine, and 2% sodium pyruvate at 37 °C in a humidified 5% CO_2 atmosphere. At about 80% of confluence, cells were used for the experiments. The cell concentration in the bioink was approximately 25×10^6 cells/mL, as previously selected [19]. Cell counting was performed using a Burker's chamber and an Eclipse TE200 microscope (Nikon, Minato, Tokyo, Japan).

4.2. Biomaterials and Crosslinker

Two commercial materials were used, a fibrinogen-based hydrogel (CELLINK® FIBRIN) and PCL pellets. The fibrinogen component of the selected hydrogel shown in our previous study was used to recreate a suitable microenvironment for the regeneration of muscle tissue in vitro [19]. Once printed, the bioink was ionically crosslinked using a calcium chloride ($CaCl_2$)-based solution to develop a suitable structural integrity. Instead, PCL was selected because it is one of the widely used biomaterials in BioP due to its biocompatibility and mechanical strength. This polymer allows manufacturing supports with complex geometries for bioink containment in long-term cell cultures.

4.3. 3D Bioprinter

To co-print the selected materials the 3D bioprinter Cellink INKREDIBLE + (Cellink AB, Sweden) was employed. It is a pneumatic extrusion-based 3D bioprinter equipped with two PHs, a UV LED curing system (365 and 405 nm), and a high-efficiency particulate air (HEPA) filter. The PHs temperature can be set up to a maximum of 130 °C. The printing chamber can guarantee the sterility necessary for cell-type experiments through the activation of the 365 nm UV light, the positive-pressure airflow, and the H13 HEPA filter.

4.4. Co-Printing Process and 3D Constructs Culture

Before the co-printing process, the bioprinter was placed under a biological sterile hood. An aluminum cartridge with a 0.5 mm metal nozzle was used for 3D printing the PCL. In detail, the cartridge was filled with PCL pellets, inserted into the PH1 and heated to 120 °C for 30 min before printing to sterilize the material. UV light was turned on for 1 h to sterilize all the surfaces. The bioink was prepared by mixing the hydrogel with C2C12 cells (10:1 ratio). The bioink was transferred to a plastic cartridge, then a conical nozzle (0.41 mm inner diameter) was connected, and, finally, the cartridge was inserted into the PH2. The PH1 and PH2 printing temperatures were respectively kept constant at 90 °C and room temperature (RT). The XYZ axes were homed, the Z axis was calibrated, and the pressure and printing speed were set according to the material guidelines (10–15 kPa and 600 mm/min for the hydrogel, 300 kPa and 45 mm/min for the PCL). The parameters set for this experiment are summarized in Table 1. The process starts with a virtual CAD model that is translated into PH coordinates (the G-code) by slicing software. In particular, the 3D CAD model of structures was designed using the Autodesk Inventor® software and then it was sliced using an open-source slicing software, Slic3r. The G-code was created and the 3D constructs were co-printed on a Petri dish. Then the constructs were crosslinked for 5 min at RT using a $CaCl_2$-based solution, which covered the whole 3D structure. The crosslinking solution was subsequently removed from the constructs and DMEM culture medium was added. 3D co-printed constructs were incubated at 37 °C in a humidified 5% CO_2 atmosphere and cultured for up to 21 days. The culture medium was refreshed every three days. Four days after co-printing, the differentiation process of C2C12-laden bioink was induced by using a differentiation medium composed of DMEM supplemented with 2% fetal bovine serum. Figure 5a shows a schematic representation of the 3D co-printing process described here.

Table 1. Summary of the operational parameters set for the study.

Operational Parameters	PCL	CELLINK FIBRIN
Extrusion pressure [kPa]	300	10–15
Conical nozzle diameter [mm]	0.5	0.41
Printing speed [mm/min]	45	600
Printing temperature [°C]	90	RT

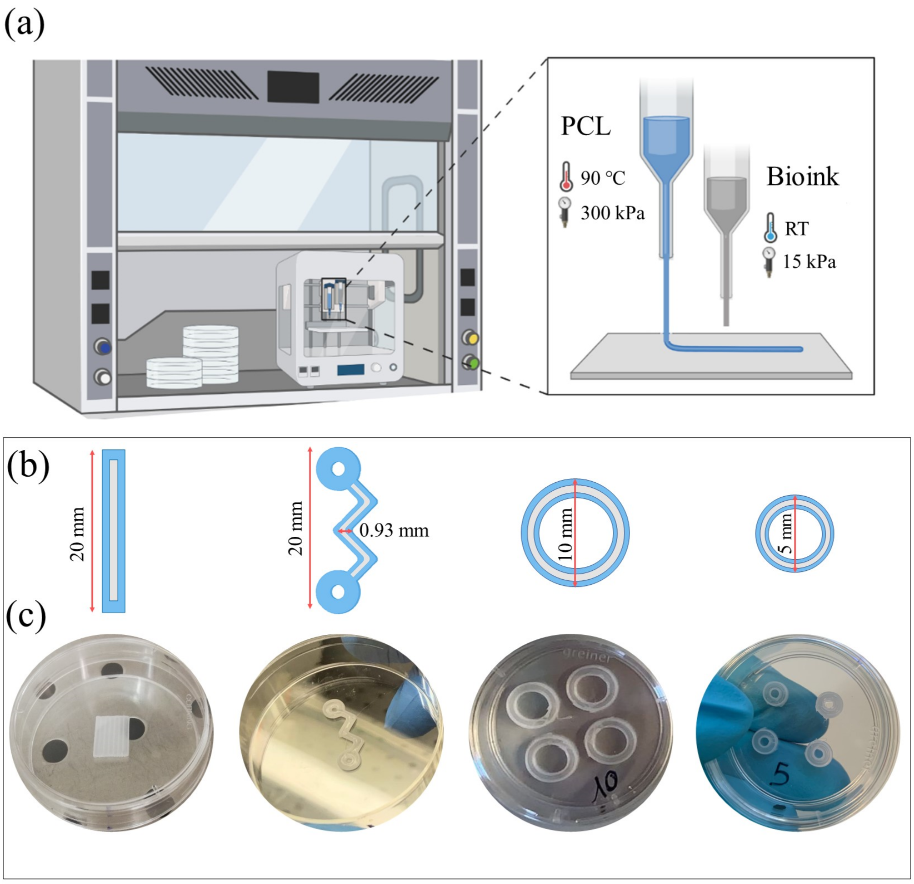

Figure 5. Design and fabrication of the different 3D constructs used in the study—linear, hybrid, and circular with different outer diameters (OD 10 mm, OD 5 mm). (**a**) Illustration showing the biofabrication process, selected materials, and printing parameters. (**b**) Schematic representation of the structures CAD design. (**c**) 3D-printed PCL constructs.

4.5. 3D Structure

To study the substrate geometry effect on murine myoblast differentiation, three different structures were co-printed: linear, hybrid, and circular with different ODs. Figure 5b,c summarize the geometries designed and used for the 3D co-printing experiments. Linear and serpentine-like structure length was set at 20 mm, while the OD of circular structures was set at 10 and 5 mm. The channel width was 0.93 mm for all geometries. This channel thickness was the minimum distance we were able to achieve when printing PCL substrates (data not shown).

4.6. Live/Dead Staining

Live/dead staining provides a two-color fluorescence cell viability assay that is based on the simultaneous determination of live (green) and dead (red) cells with two probes. This study used calcein and ethidium homodimer (EthD-1), optimal dyes for this application. Calcein is well retained within live cells, producing an intense, uniform green fluorescence. EthD-1 enters cells with damaged membranes and undergoes a 40-fold fluorescence enhancement upon binding to nucleic acids, producing a bright red fluorescence in dead cells. Therefore, live/dead staining (Invitrogen) was used to assess and monitor cell viability throughout the biological experiment. For this reason, it was performed at four different time points (1, 7, 14, and 21 days of cell culture). According to the protocol, a solution was prepared consisting of 1.5 mL of phosphate-buffered saline (PBS), 3 μL of ethidium homodimer-1 (EthD-1), and 1.5 μL of calcein. Three-dimensional constructs were covered with 500 μL of this solution and incubated for 45 min in the dark, and then the solution was removed. The image acquisition was performed by a semi-confocal microscope (ViCo confocal, Nikon).

4.7. Total RNA Extraction and Quantitative Real-Time PCR

Quantitative real-time PCR (RT-qPCR) is a technique used to analyze gene expression by evaluating mRNA from samples. It is a widely used technique indicating cell gene profiling that varies during time in biological experiments. In this study, RT-qPCR was used to analyze the expression levels of myogenic genes in the 3D co-printed constructs. At the different time points (7, 14, and 21 days in culture), cellular genetic material was isolated from each sample using 300 µL of lysis buffer (TRIzol Reagent). Then, total RNA was extracted using the Directzol RNA Miniprep reagents and the manufacturer's protocol (Zymo Research) and quantified by NanoDropTM (Thermo-Fisher Scientific). Reverse transcription of the cDNAs was performed using the iScript™ cDNA Synthesis Kit (Biorad). Then, to elucidate the C2C12 cell differentiation process, the gene expression of relevant myogenic differentiation markers was quantified. Specifically, different genes were selected according to the time points. MyoD, Myf5, and Cyclin D1 were analyzed at 7 days of culture, with MyoD and Myf5 as genes characterizing early muscle differentiation and Cyclin D1 for evaluating cell proliferation. At 14 days of culture, MyoD, MyoG, and Cyclin D1 were evaluated; MyoD was measured to study early differentiation, MyoG was measured for late differentiation, and, finally, Cyclin D1 was measured to evaluate cell proliferation. MCK, Myh1, and MCad were analyzed at 21 days of culture as genes indicating late differentiation and maturation of muscle tissue.

The reaction and data analysis were performed respectively by using Mini-Opticon Real-Time PCR System (BioRad Laboratories) and CFX Manager Software. The expression of each gene was studied in triplicate and normalized using the expression of a housekeeping gene, i.e., phosphoglycerate kinase (PGK). Relative gene expression was expressed in terms of fold increase calculated using the $2\hat{}(-\Delta\Delta Ct)$ method as described in this bibliography article [48]. The fold increase is a parameter that indicates how much a gene in the test condition considered is differently expressed compared to a control sample. The primer sequences used for gene expression analysis are listed in Table S1.

Supplementary Materials: The following supporting information can be downloaded at: https://www.mdpi.com/article/10.3390/gels9070595/s1, Table S1: Summary of primers used for qRT-PCR.

Author Contributions: M.C. and G.C. (Gabriele Ceccarelli) designed the study. G.L. and F.S. performed design and co-printing. G.L. performed the statistical and numerical analysis. F.A., L.R. and N.M. performed the biological experiments. G.C. (Gabriele Ceccarelli) and L.B. coordinated and supervised the laboratory activities. G.L. wrote the draft manuscript. G.C. (Gabriele Ceccarelli), M.C., F.S. and G.C. (Gianluca Cidonio) reviewed the document, and G.L. produced the final version of the manuscript. All authors have read and agreed to the published version of the manuscript.

Funding: This research received no external funding.

Institutional Review Board Statement: Not applicable.

Informed Consent Statement: Not applicable.

Data Availability Statement: Data will be made available on request.

Conflicts of Interest: The authors declare no conflict of interest.

References

1. Chen, C.S.; Tan, J.; Tien, J. Mechanotransduction at Cell-Matrix and Cell-Cell Contacts. *Annu. Rev. Biomed. Eng.* **2004**, *6*, 275–302. [CrossRef] [PubMed]
2. Bajaj, P.; Tang, X.; Saif, T.A.; Bashir, R. Stiffness of the substrate influences the phenotype of embryonic chicken cardiac myocytes. *J. Biomed. Mater. Res. A* **2010**, *95*, 1261–1269. [CrossRef] [PubMed]
3. Discher, D.E.; Janmey, P.; Wang, Y.-L. Tissue Cells Feel and Respond to the Stiffness of Their Substrate. *Science* **2005**, *310*, 1139–1143. [CrossRef]

4. Engler, A.J.; Griffin, M.A.; Sen, S.; Bonnemann, C.G.; Sweeney, H.L.; Discher, D.E. Myotubes differentiate optimally on substrates with tissue-like stiffness: Pathological implications for soft or stiff microenvironments. *J. Cell Biol.* **2004**, *166*, 877–887. [CrossRef]
5. Solon, J.; Levental, I.; Sengupta, K.; Georges, P.; Janmey, P.A. Fibroblast Adaptation and Stiffness Matching to Soft Elastic Substrates. *Biophys. J.* **2007**, *93*, 4453–4461. [CrossRef]
6. Yeung, T.; Georges, P.C.; Flanagan, L.A.; Marg, B.; Ortiz, M.; Funaki, M.; Zahir, N.; Ming, W.; Weaver, V.; Janmey, P.A. Effects of substrate stiffness on cell morphology, cytoskeletal structure, and adhesion. *Cell Motil. Cytoskelet.* **2005**, *60*, 24–34. [CrossRef] [PubMed]
7. Kim, K.; Dean, D.; Wallace, J.; Breithaupt, R.; Mikos, A.G.; Fisher, J.P. The influence of stereolithographic scaffold architecture and composition on osteogenic signal expression with rat bone marrow stromal cells. *Biomaterials* **2011**, *32*, 3750–3763. [CrossRef] [PubMed]
8. Chen, C.S.; Mrksich, M.; Huang, S.; Whitesides, G.M.; Ingber, D.E. Geometric Control of Cell Life and Death. *Science* **1997**, *276*, 1425–1428. [CrossRef] [PubMed]
9. Balaban, N.Q.; Schwarz, U.; Riveline, D.; Goichberg, P.; Tzur, G.; Sabanay, I.; Mahalu, D.; Safran, S.; Bershadsky, A.; Addadiand, L.; et al. Force and focal adhesion assembly: A close relationship studied using elastic micropatterned substrates. *Nat. Cell Biol.* **2001**, *3*, 466–472. [CrossRef]
10. Huang, N.F.; Patel, S.; Thakar, R.G.; Wu, J.; Hsiao, B.S.; Chu, B.; Lee, R.J.; Li, S. Myotube Assembly on Nanofibrous and Micropatterned Polymers. *Nano Lett.* **2006**, *6*, 537–542. [CrossRef]
11. Lee, L.H.; Peerani, R.; Ungrin, M.; Joshi, C.; Kumacheva, E.; Zandstra, P. Micropatterning of human embryonic stem cells dissects the mesoderm and endoderm lineages. *Stem Cell Res.* **2009**, *2*, 155–162. [CrossRef]
12. Yao, Y.-T.; Yang, Y.; Ye, Q.; Cao, S.-S.; Zhang, X.-P.; Zhao, K.; Jian, Y. Effects of pore size and porosity on cytocompatibility and osteogenic differentiation of porous titanium. *J. Mater. Sci. Mater. Med.* **2021**, *32*, 72. [CrossRef] [PubMed]
13. Han, Y.; Lian, M.; Wu, Q.; Qiao, Z.; Sun, B.; Dai, K. Effect of Pore Size on Cell Behavior Using Melt Electrowritten Scaffolds. *Front. Bioeng. Biotechnol.* **2021**, *9*, 629270. [CrossRef]
14. Kilian, K.A.; Bugarija, B.; Lahn, B.T.; Mrksich, M. Geometric cues for directing the differentiation of mesenchymal stem cells. *Proc. Natl. Acad. Sci. USA* **2010**, *107*, 4872–4877. [CrossRef] [PubMed]
15. Bajaj, P.; Reddy, B.; Millet, L.; Wei, C.; Zorlutuna, P.; Bao, G.; Bashir, R. Patterning the differentiation of C2C12 skeletal myoblasts. *Integr. Biol.* **2011**, *3*, 897–909. [CrossRef] [PubMed]
16. Vogel, V.; Sheetz, M. Local force and geometry sensing regulate cell functions. *Nat. Rev. Mol. Cell Biol.* **2006**, *7*, 265–275. [CrossRef]
17. Bahcecioglu, G.; Basara, G.; Ellis, B.W.; Ren, X.; Zorlutuna, P. Breast cancer models: Engineering the tumor microenvironment. *Acta Biomater.* **2020**, *106*, 1–21. [CrossRef]
18. Malda, J.; Visser, J.; Melchels, F.P.; Jüngst, T.; Hennink, W.E.; Dhert, W.J.A.; Groll, J.; Hutmacher, D.W. 25th Anniversary Article: Engineering Hydrogels for Biofabrication. *Adv. Mater.* **2013**, *25*, 5011–5028. [CrossRef]
19. Ronzoni, F.L.; Aliberti, F.; Scocozza, F.; Benedetti, L.; Auricchio, F.; Sampaolesi, M.; Cusella, G.; Redwan, I.N.; Ceccarelli, G.; Conti, M. Myoblast 3D bioprinting to burst in vitro skeletal muscle differentiation. *J. Tissue Eng. Regen. Med.* **2022**, *16*, 484–495. [CrossRef]
20. Bade, N.D.; Kamien, R.D.; Assoian, R.K.; Stebe, K.J. Curvature and Rho activation differentially control the alignment of cells and stress fibers. *Sci. Adv.* **2017**, *3*, e1700150. [CrossRef]
21. Rumpler, M.; Woesz, A.; Dunlop, J.W.; van Dongen, J.T.; Fratzl, P. The effect of geometry on three-dimensional tissue growth. *J. R. Soc. Interface* **2008**, *5*, 1173–1180. [CrossRef]
22. Bidan, C.M.; Kommareddy, K.P.; Rumpler, M.; Kollmannsberger, P.; Bréchet, Y.J.M.; Fratzl, P.; Dunlop, J.W.C. How Linear Tension Converts to Curvature: Geometric Control of Bone Tissue Growth. *PLoS ONE* **2012**, *7*, e36336. [CrossRef] [PubMed]
23. Bidan, C.M.; Kommareddy, K.P.; Rumpler, M.; Kollmannsberger, P.; Fratzl, P.; Dunlop, J.W.C. Geometry as a Factor for Tissue Growth: Towards Shape Optimization of Tissue Engineering Scaffolds. *Adv. Healthc. Mater.* **2013**, *2*, 186–194. [CrossRef] [PubMed]
24. Knychala, J.; Bouropoulos, N.; Catt, C.J.; Katsamenis, O.L.; Please, C.P.; Sengers, B.G. Pore Geometry Regulates Early Stage Human Bone Marrow Cell Tissue Formation and Organisation. *Ann. Biomed. Eng.* **2013**, *41*, 917–930. [CrossRef] [PubMed]
25. Guyot, Y.; Papantoniou, I.; Chai, Y.C.; Van Bael, S.; Schrooten, J.; Geris, L. A computational model for cell/ECM growth on 3D surfaces using the level set method: A bone tissue engineering case study. *Biomech. Model. Mechanobiol.* **2014**, *13*, 1361–1371. [CrossRef]
26. Guyot, Y.; Papantoniou, I.; Luyten, F.P.; Geris, L. Coupling curvature-dependent and shear stress-stimulated neotissue growth in dynamic bioreactor cultures: A 3D computational model of a complete scaffold. *Biomech. Model. Mechanobiol.* **2016**, *15*, 169–180. [CrossRef]
27. Werner, M.; Kurniawan, N.A.; Korus, G.; Bouten, C.V.C.; Petersen, A. Mesoscale substrate curvature overrules nanoscale contact guidance to direct bone marrow stromal cell migration. *J. R. Soc. Interface* **2018**, *15*, 20180162. [CrossRef]
28. Callens, S.J.; Uyttendaele, R.J.; Fratila-Apachitei, L.E.; Zadpoor, A.A. Substrate curvature as a cue to guide spatiotemporal cell and tissue organization. *Biomaterials* **2019**, *232*, 119739. [CrossRef]
29. Huang, Y.-C.; Dennis, R.G.; Larkin, L.; Baar, K. Rapid formation of functional muscle in vitro using fibrin gels. *J. Appl. Physiol.* **2005**, *98*, 706–713. [CrossRef]

30. Bari, E.; Scocozza, F.; Perteghella, S.; Sorlini, M.; Auricchio, F.; Torre, M.L.; Conti, M. 3D Bioprinted Scaffolds Containing Mesenchymal Stem/Stromal Lyosecretome: Next Generation Controlled Release Device for Bone Regenerative Medicine. *Pharmaceutics* **2021**, *13*, 515. [CrossRef]
31. Bari, E.; Scocozza, F.; Perteghella, S.; Segale, L.; Sorlini, M.; Auricchio, F.; Conti, M.; Torre, M.L. Three-Dimensional Bioprinted Controlled Release Scaffold Containing Mesenchymal Stem/Stromal Lyosecretome for Bone Regeneration: Sterile Manufacturing and In Vitro Biological Efficacy. *Biomedicines* **2022**, *10*, 1063. [CrossRef]
32. Izadifar, Z.; Chang, T.; Kulyk, W.; Chen, X.; Eames, B.F. Analyzing Biological Performance of 3D-Printed, Cell-Impregnated Hybrid Constructs for Cartilage Tissue Engineering. *Tissue Eng. Part C Methods* **2016**, *22*, 173–188. [CrossRef]
33. Kim, M.S.; Kim, G. Three-dimensional electrospun polycaprolactone (PCL)/alginate hybrid composite scaffolds. *Carbohydr. Polym.* **2014**, *114*, 213–221. [CrossRef] [PubMed]
34. Kim, Y.B.; Kim, G.H. PCL/Alginate Composite Scaffolds for Hard Tissue Engineering: Fabrication, Characterization, and Cellular Activities. *ACS Comb. Sci.* **2015**, *17*, 87–99. [CrossRef]
35. Merceron, T.K.; Burt, M.; Seol, Y.-J.; Kang, H.-W.; Lee, S.J.; Yoo, J.J.; Atala, A. A 3D bioprinted complex structure for engineering the muscle–tendon unit. *Biofabrication* **2015**, *7*, 035003. [CrossRef] [PubMed]
36. Choi, Y.-J.; Kim, T.G.; Jeong, J.; Yi, H.-G.; Park, J.W.; Hwang, W.; Cho, D.-W. 3D Cell Printing of Functional Skeletal Muscle Constructs Using Skeletal Muscle-Derived Bioink. *Adv. Health Mater.* **2016**, *5*, 2636–2645. [CrossRef]
37. Kang, H.-W.; Lee, S.J.; Ko, I.K.; Kengla, C.; Yoo, J.J.; Atala, A. A 3D bioprinting system to produce human-scale tissue constructs with structural integrity. *Nat. Biotechnol.* **2016**, *34*, 312–319. [CrossRef]
38. Kim, J.H.; Seol, Y.-J.; Ko, I.K.; Kang, H.-W.; Lee, Y.K.; Yoo, J.J.; Atala, A.; Lee, S.J. 3D Bioprinted Human Skeletal Muscle Constructs for Muscle Function Restoration. *Sci. Rep.* **2018**, *8*, 12307. [CrossRef] [PubMed]
39. Callens, S.J.P.; Fan, D.; van Hengel, I.A.J.; Minneboo, M.; Díaz-Payno, P.J.; Stevens, M.M.; Fratila-Apachitei, L.E.; Zadpoor, A.A. Emergent collective organization of bone cells in complex curvature fields. *Nat. Commun.* **2023**, *14*, 855. [CrossRef]
40. Wang, P.-Y.; Yu, H.-T.; Tsai, W.-B. Modulation of alignment and differentiation of skeletal myoblasts by submicron ridges/grooves surface structure. *Biotechnol. Bioeng.* **2010**, *106*, 285–294. [CrossRef]
41. Shimizu, K.; Fujita, H.; Nagamori, E. Alignment of skeletal muscle myoblasts and myotubes using linear micropatterned surfaces ground with abrasives. *Biotechnol. Bioeng.* **2009**, *103*, 631–638. [CrossRef]
42. Yamamoto, D.L.; Csikasz, R.I.; Li, Y.; Sharma, G.; Hjort, K.; Karlsson, R.; Bengtsson, T. Myotube Formation on Micro-patterned Glass: Intracellular Organization and Protein Distribution in C2C12 Skeletal Muscle Cells. *J. Histochem. Cytochem.* **2008**, *56*, 881–892. [CrossRef]
43. Feinberg, A.W.; Feigel, A.; Shevkoplyas, S.S.; Sheehy, S.; Whitesides, G.M.; Parker, K.K. Muscular Thin Films for Building Actuators and Powering Devices. *Science* **2007**, *317*, 1366–1370. [CrossRef] [PubMed]
44. Tanaka, Y.; Morishima, K.; Shimizu, T.; Kikuchi, A.; Yamato, M.; Okano, T.; Kitamori, T. An actuated pump on-chip powered by cultured cardiomyocytes. *Lab Chip* **2006**, *6*, 362–368. [CrossRef] [PubMed]
45. Tanaka, Y.; Morishima, K.; Shimizu, T.; Kikuchi, A.; Yamato, M.; Okano, T.; Kitamori, T. Demonstration of a PDMS-based bio-microactuator using cultured cardiomyocytes to drive polymer micropillars. *Lab Chip* **2006**, *6*, 230–235. [CrossRef] [PubMed]
46. Akiyama, Y.; Furukawa, Y.; Morishima, K. Controllable Bio-Microactuator Powered by Muscle Cells. In Proceedings of the 2006 International Conference of the IEEE Engineering in Medicine and Biology Society, New York, NY, USA, 5 March 2008; pp. 6565–6568. [CrossRef]
47. Herr, H.; Dennis, R.G. A swimming robot actuated by living muscle tissue. *J. Neuroeng. Rehabil.* **2004**, *1*, 6. [CrossRef]
48. Rao, X.; Huang, X.; Zhou, Z.; Lin, X. An improvement of the 2ˆ(–delta delta CT) method for quantitative real-time polymerase chain reaction data analysis. *Biostat. Bioinform. Biomath.* **2013**, *3*, 71–85.

gels

MDPI

Article

Study of Polyvinyl Alcohol Hydrogels Applying Physical-Mechanical Methods and Dynamic Models of Photoacoustic Signals

Roberto G. Ramírez-Chavarría [1], Argelia Pérez-Pacheco [2], Emiliano Terán [3] and Rosa M. Quispe-Siccha [2,*]

[1] Engineering Institute, National Autonomous University of Mexico, Mexico City 04510, Mexico; rramirezc@iingen.unam.mx
[2] Research and Technological Development Unit, Research Department, General Hospital of Mexico "Dr. Eduardo Liceaga", Mexico City 06726, Mexico; argeliapp@ciencias.unam.mx
[3] Faculty of Physical-Mathematical Sciences, Autonomous University of Sinaloa, Culiacan, Sinaloa 80040, Mexico; eteran@uas.edu.mx
* Correspondence: rosa.quispe@gmail.com

Abstract: This study aims to analyze the physical-mechanical properties and dynamic models of tissue-simulating hydrogels, specifically the photoacoustic (PA) response signals, by varying the concentrations of polyvinyl alcohol (PVA) and molecular weight (MW). A state-space model (SSM) is proposed to study the PVA hydrogels to retrieve the PA-related signal's damping ratio and natural frequency. Nine box-shaped PVA hydrogels containing saline solution were used, with five concentrations of PVA (7, 9, 12, 15, 20%) for MW1 and four for MW2. The results indicated that the concentration of PVA and MW played an important role in the PA wave's amplitude, arrival time, and speed of sound over the hydrogels. The SSM parameters showed that increasing PVA and MW concentrations improved the hydrogels' ability to absorb and transfer energy under the PA effect. These parameters were also found to be correlated with density and modulus of elasticity. Additionally, the concentrations of PVA and MW affected the absorption and optical scattering coefficients. The physical-mechanical properties, including porosity, density, and modulus of elasticity, improved as the concentration of PVA and MW increased. The ultimate goal of this study is to develop hydrogels as phantoms that can be used for tissue simulation and imaging.

Keywords: polyvinyl alcohol hydrogels; photoacoustic response signals; state-space model; physical-mechanical properties

1. Introduction

Over the past few years, tissue-simulating polyvinyl alcohol (PVA) hydrogels have shown their utility in various functions for biomedical optical and mechanical technologies [1–4]. The focus has been on developing hydrogels with optomechanical properties similar to those of tissue and using non-ionizing energy to provide a safer modality than X-ray images [5,6]. Regarding the studies of the mechanical properties of the hydrogels, the density, the speed of sound, the Poisson radius, and Young's modulus have been investigated, changing the number of freezing cycles [7,8]. Furthermore, experiments have been conducted on hydrogels that simulate various tissues, including breasts, to study their absorption and optical scattering coefficients under varying freezing cycles [5,9,10]. In addition, researchers have focused on photoacoustic (PA) wave propagation in hydrogels and biological environments using non-ionizing energy techniques, such as PA tomography. This technique combines photonics with ultrasound and focuses on obtaining images of PVA hydrogels with impurities and biological tissue [10–12]. PA tomography works by irradiating the tissue with low-energy laser pulses, the tissue absorbs the laser light and results in thermoelastic expansion, which generates broadband acoustic waves that emanate from the optical absorption volume; the amplitude of this acoustic perturbation is proportional to both local fluence and absorption [13]. Conventional ultrasound transducers can detect these acoustic waves to obtain physical parameters that characterize the sample through dynamic analysis of the PA signals [14] or an image related to the local optical absorption of the tissue [15].

Currently, there is an increasing trend to deploying attractive and robust methods for processing PA signals analysis in an automated way [16]. For instance, the time-domain analysis is commonly performed by seeking the signal amplitude, the envelope, and the time of arrival, which are related to the size, concentration, and distribution of light absorbers in tissue [14]. In contrast, frequency-domain methods analyze the signal power spectrum to relate its bandwidth, central frequency, and magnitude with the size of optical absorbers [17]. Machine learning or data-driven methods have become powerful tools to process PA data, mainly devoted to imaging [18]. However, more information is needed on data-driven methods for processing PA signals to retrieve automated and quantitative results using the raw signals [19,20]. Interestingly, as shown by [20], the PA signal can be considered the impulse response of a dynamical system. Nonetheless, this situation needs to be considered to analyze PA signals, and its applications are limited despite its powerfulness. Therefore, the hypothesis is that a PA signal could be thoroughly described using a dynamical systems approach coupled with data-driven methods [21–23].

This study aims to understand how the dynamic model of PA signals and the optomechanical properties of hydrogels vary with two molecular weights (MWs) and different concentrations of PVA. The study analyzed the peak-to-peak amplitude, arrival time, and speed of sound of the PA signals. The physical parameters and state-space models (SSM) were estimated from these signals to determine the damping ratio (absorption capacity), natural frequency (energy transfer through the sample), density, and modulus of elasticity. The optical absorption (μ_a) and scattering (μ_s) coefficients were determined using an integrating sphere. Apart from the SSM, the density and the modulus of elasticity were calculated using physical variables and a tensile device. Finally, the ImageJ program and MATLAB were used to calculate the porosity distribution of the microscopic images.

Dynamical Modeling of Photoacoustic Signals

According to the PA theory, the propagation of acoustic pressure $p(\vec{r},t)$ at position $\vec{r}$ and time t is governed by the wave equation:

$$\left(\nabla^2 - \frac{1}{c^2}\frac{\partial^2}{\partial t^2}\right)p(\vec{r},t) = -\frac{\beta}{C_P}\frac{\partial H(\vec{r},t)}{\partial t}, \tag{1}$$

where c is the speed of sound, β is the coefficient of thermal expansion, C_p is the specific heat capacity at constant pressure, and $H(\vec{r},t)$ is the thermal energy distributed within the heated region during radiation per unit time. By considering that thermal and stress confinement conditions were met [24] and following a point-source model [25], the generated PA wave at the surface ($\vec{r} = 0$) follows that:

$$\frac{\partial^2}{\partial t^2}p(t) + \alpha^2\frac{\xi + \frac{4}{3}\eta}{\rho}\frac{\partial}{\partial t}p(t) + a^2c^2p(t) = \Gamma\frac{\partial H(t)}{\partial t}, \tag{2}$$

where α is a propagation constant, ρ is the density, ξ is the bulk viscosity, η is the shear viscosity, and Γ is the Gruneisen parameter.

Interestingly, Equation (2) can be rewritten in terms of a linear-time-invariant (LTI) second-order mechanical system in the following form:

$$\frac{\partial^2}{\partial t^2}p(t) + \frac{b}{m}\frac{\partial}{\partial t}p(t) + \frac{k}{m}\,p(t) = \frac{u(t)}{m}, \tag{3}$$

where b is the damping coefficient, m is the mass, k is the spring constant, and $u(t)$ is an external force related to the optical illumination. By comparing Equations (2) and (3), it follows that the natural frequency is $\omega_n^2 = k/m = a^2c^2$, and the damping ratio is $\zeta = \frac{b}{2m} = \left(\alpha^2\xi + \frac{4}{3}\eta\right)/\rho$. Therefore, for PA signals, it is assumed that the system's response is underdamped, i.e., $\zeta < 1$. With the above procedure, we cast the PA problem into a simple dynamical system. Among the wide variety of dynamical model structures, SSM is flexible enough to describe LTI systems at high confidence levels; however, it preserves moderate complexity [26]. Thereby, the model for the PA signal in Equation (3) can be written in SSM form, given by the following equations:

$$\dot{x}(t) = Ax(t) + Bu(t) \tag{4}$$

$$y(t) = Cx(t) \tag{5}$$

where $x(t) \in \mathbb{R}^{n\times 1}$ is the state vector, $y(t) \in \mathbb{R}^{N\times 1}$ is the output sequence, $A \in \mathbb{R}^{n\times n}$ is the input matrix $B \in \mathbb{R}^{n\times 1}$ and the output matrix $C \in \mathbb{R}^{1\times n}$. Herein, the goal is to estimate the SSM matrices using a measured PA signal. For this purpose, system identification provides the tools to estimate the SSM and its parameters from measurements [27]. Following this rationale, by estimating the system-related matrices that produce the output sequence $y(t)$, it is possible to approximate the measured PA signal $y_{\mathrm{PA}}(t)$. Particularly, to estimate the SSM given in Equations (4) and (5), we used the numerical algorithm for the subspace state-space system identification (N4SID) method to estimate the set of matrices $\{A, B, C\}$. A detailed description of the N4SID is given in Section 2.3.

This research aims to provide researchers and clinicians with the tools for constructing hydrogels with varying densities and porosities by adjusting the concentration and molecular weight (MW) to mimic the macro and microenvironment of tissues and enable imaging development. A PVA-based photoacoustic hydrogel was developed using light absorption and speed of sound, optimizing concentration and molecular weight to obtain characteristic optical properties of tissue. The hydrogels were characterized by microscopic imaging methods, mechanical properties, and optical parameters to validate versatility in contrast with a dynamic model.

2. Results and Discussion

2.1. Photoacoustic Response Signals

Figure 1 shows the PA signals of the SS-containing hydrogels as a transmission medium for two MWs and different concentrations of PVA. As can be seen, the amplitude of the signals increases and shifts to longer times when the PVA concentration is higher. When the concentration is higher, the structural stability of the hydrogels improves due to the increase in the number and size of the crystalline regions. At higher MW, the porosity distribution improves due to increased polymer chain length. For example, the arrival time of the 7% and 9% hydrogels of molecular weight two (MW2) are close, and for the 12% and 15% hydrogels, the arrival time becomes very similar. The stability can also be observed in the standard deviation of the amplitude of the signals, and this will depend on the region of the hydrogel wall that the optoacoustic wave passes through until the sensor detects it.

When the PVA concentration increases, the hydrogel diameter expands, and there is a noticeable change in the time-of-arrival sensitivity of PA signals, as seen in Figure 1 and Table 1. Moreover, this time is related to the speed of sound; therefore, it also experiences a slight variation when changing the concentration of PVA, see Table 1. The amplitude of the PA signal is directly related to absorption. Therefore, an increase in PVA concentration results in a higher amplitude of the PA signal, as observed in Table 1.

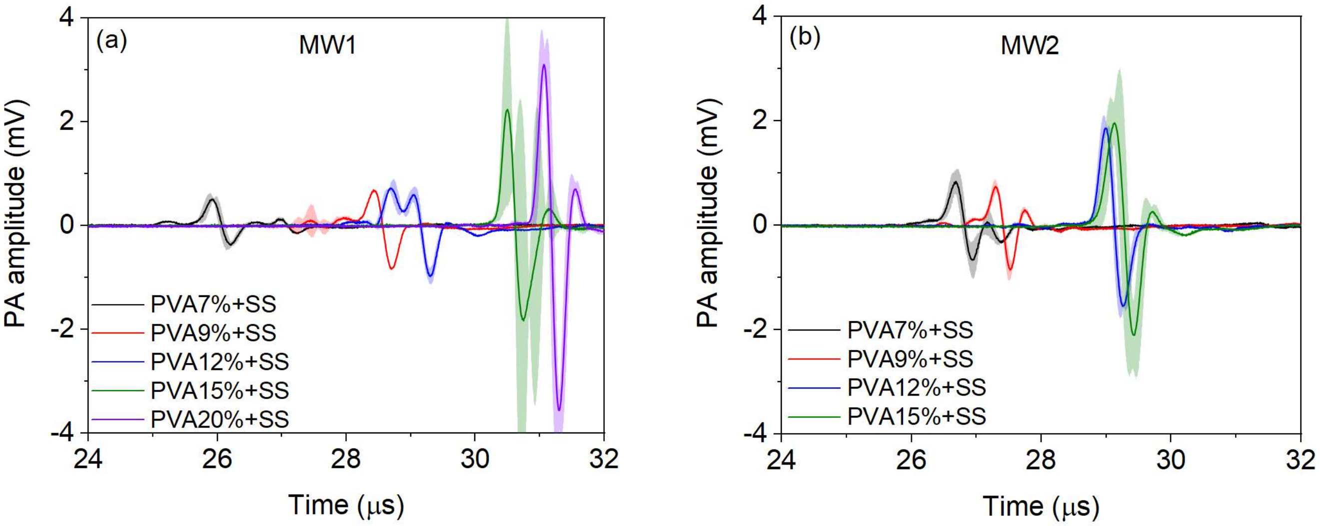

Figure 1. Signals of the PA response of the SS-containing hydrogels as a transmission medium for (**a**) Molecular weight one (MW1) of five PVA concentrations and (**b**) MW2 of four PVA concentrations. Each signal is an average of three measurements.

Table 1. Physical and optoacoustic variables of the photoacoustic signals of all the study hydrogels. The values are the average of three measurements plus their standard deviation.

		MW1		
PVA (%)	***D* (mm)**	**t_a(μs)**	***c* (m/s)**	***A* (mV)**
7	39.70 ± 1.34	25.60 ± 0.06	1551 ± 4.79	0.87 ± 0.06
9	43.16 ± 0.31	28.18 ± 0.02	1532 ± 0.60	1.51 ± 0.02
12	45.00 ± 0.24	28.45 ± 0.03	1582 ± 3.32	1.70 ± 0.14
15	46.22 ± 0.48	30.14 ± 0.06	1534 ± 6.38	4.07 ± 2.76
20	46.62 ± 0.26	30.82 ± 0.07	1513 ± 0.67	6.66 ± 0.41
		MW2		
7	40.20 ± 0.65	26.39 ± 0.06	1523 ± 2.62	1.50 ± 0.31
9	40.54 ± 2.00	27.08 ± 0.01	1497 ± 1.50	1.59 ± 0.17
12	43.84 ± 0.59	28.63 ± 0.04	1531 ± 0.15	3.41 ± 0.12
15	43.89 ± 0.22	28.67 ± 0.06	1531 ± 1.16	4.06 ± 0.63

The laser light passed through the different layers of the hydrogel depending on the PVA concentration and MWs. For higher concentrations, the source absorption was more significant in the first layers of the hydrogel wall due to the larger pore size in those areas than at different depths since there is greater lattice cross-linking at grander depths. However, the intensity of the PA wave did not decrease as it traveled from the absorbing source to the sensor. This was due to the fact that a propagation medium, saline solution (SS), minimized sound dispersion, and the hydrogel structure was more stable at higher concentrations in MWs. It is important to note that the arrival time of the PA signal is later due to the expansion of the hydrogel caused by the increase in the PVA concentration.

Our results are supported by studies showing consistent values for the speed of sound [7,28] and PA amplitude [29]. However, it is important to note that while other researchers changed freezing cycles to determine the speed of sound and PA amplitude, we varied the concentration of PVA.

2.2. Analysis of the Dynamical Model

The N4SID algorithm was applied to the measured signals to provide a dynamic model of the samples under study. According to the algorithm presented in Section 4.3, the model order is determined by the SVD of the block Hankel matrix. The N4SID algorithm retrieved a significant magnitude for the measured PA signals for two singular values [30]. The PA signals are fully described by two states of the SSM in Equations (4) and (5), which leads to a model-order $\hat{n} = 2$, for both MW. This makes sense since, according to the subspace identification, the magnitude of the singular values of the data monotonically decreases to zero after the second component. Moreover, this behavior only allows one to capture helpful information about the system and neglects the small singular value related to measurement artifacts and noise.

In order to evaluate the performance of the estimated SSM, the normalized root mean square error (NRMSE) was computed as follows:

$$NRMSE = \left(1 - \frac{\|y_{PA}(t) - y(t)\|}{\|y_{PA}(t) - \overline{y}_{PA}(t)\|}\right) \cdot 100, \tag{6}$$

where $y_{\mathrm{PA}}(t)$ is the measured signal, $y(t)$ is the output of the SSM, and $\overline{y}_{\mathrm{PA}}(t)$ its mean value. Figure 2 depicts the bar plots of the mean NRMSE for the two MWs to assess the similarity between the measured signal and the output of the SSM. In all cases, the estimation accuracy is higher than 95% (horizontal dashed line), thus indicating that a second-order SSM accurately approximates the PA signal for the PVA samples.

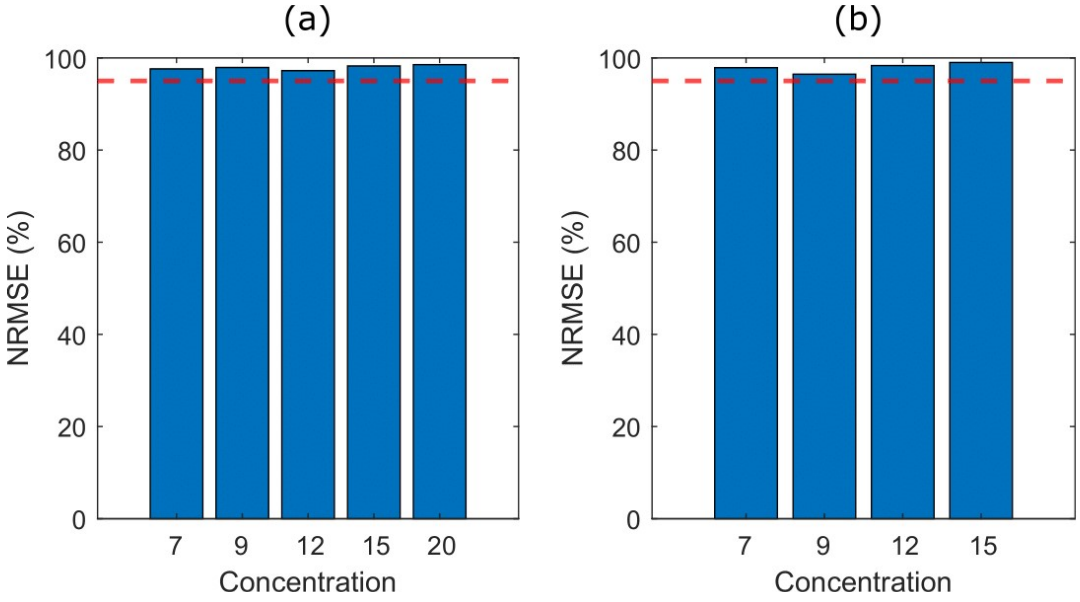

Figure 2. Bar plots of the normalized mean square error (NRMSE) to assess the accuracy of the estimated SSM for (**a**) MW1 of five PVA concentrations and (**b**) MW2 of four PVA concentrations. The horizontal red dashed line highlights the 95% NRMSE.

As the core of the SSM is the ability to capture information of a dynamic system in a structured form, it is also essential to analyze the parameters of the SSM to provide a physical meaning. Let us recall the SSM in Equations (4) and (5) and that the N4SID algorithm $\hat{n} = 2$ estimates the model order. Interestingly, this latter coincides with the order of the model in Equation (3) describing the PA effect. Thus, the PA model in Equation (3) can be explained by an SSM model with eigenvalues of the system matrix $\hat{A}$, given by

$\lambda = -\sigma \pm j\omega_n$. Moreover, it is well-known that the elements of $\hat{A}$ are related to the natural frequency ω_n and the damping factor ζ as follows:

$$\omega_n = |\ln(\lambda)| \backslash T_s \, , \, \zeta = -\cos(\angle ln(\lambda)), \tag{7}$$

these, in turn, are related to the parameters of Equation (3) as $\omega_n^2 = k/m$ and $\zeta = b/2m$. The estimated parameters encode useful parameters that could characterize the MW and concentration of PVA in the samples.

Figure 3 shows the relationship among the parameters ζ and ω_n retrieved by the SSM and the concentration of PVA for both MWs. Therein, the blue dots represent the sample mean of the estimated parameters, the vertical bars show the relative standard deviation, and the black line is the best fit in the least-squares sense.

In the following, we will discuss the influence of PVA concentrations on the PA signals and their relationship with the SSM parameters.

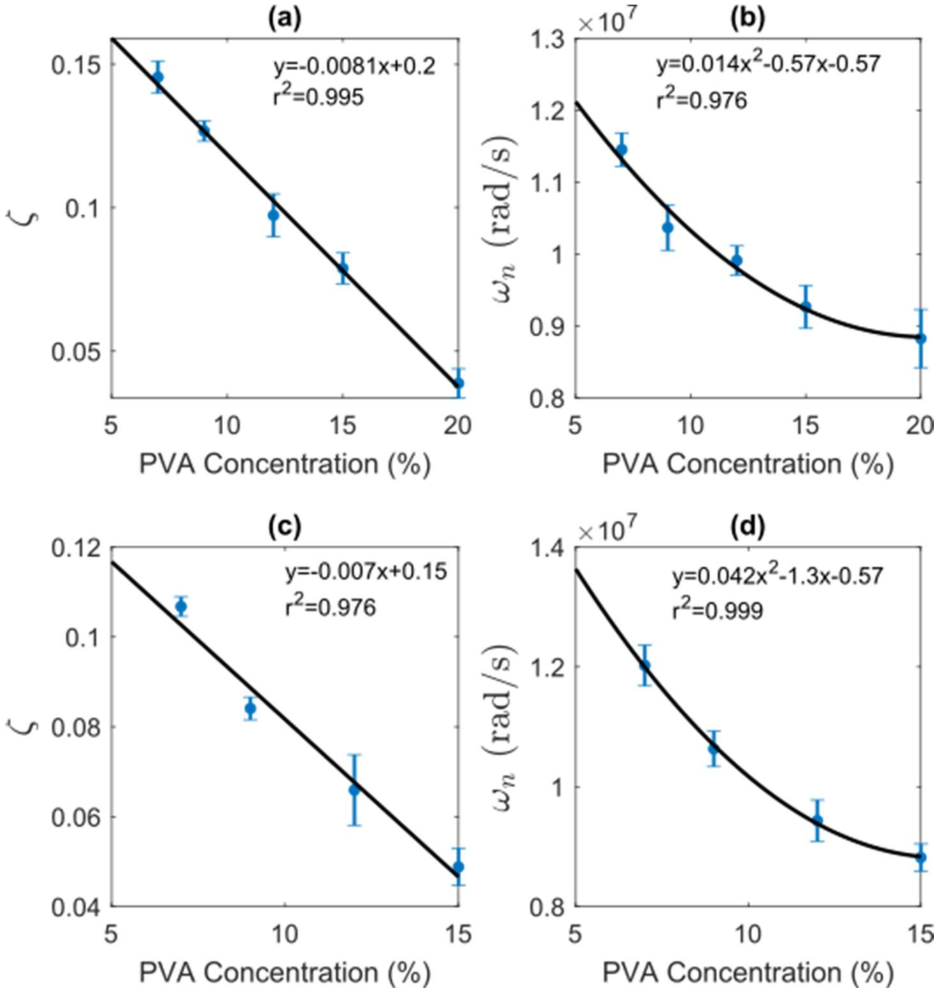

Figure 3. Relationship between state-space model parameters and PVA concentration. (**a**,**c**) show the damping ratio ζ for MW1 and MW2, respectively; (**b**,**d**) depict the natural frequency ω_n for MW1 and MW2.

2.2.1. Damping Ratio

The eigenvalues of the system matrix give the damping ratio. Physically, the damping ratio is dimensionless, defined as how much energy is consumed or how fast the pressure wave dissipates. Therefore, the damping represents the ability to absorb energy after the excited PVA sample. Interestingly, with the proposed SSM estimation, we can directly retrieve this mechanical feature for the measured samples using the PA effect. Figure 3a,c shows the relation between the damping ratio and PVA concentration for the MW1 and MW2, respectively. From there, one can see that ζ exhibits a linear relationship with the concentration of PVA, described by a linear model with above 97% accuracy. This trend could be explained by the fact that the damping ratio reflects the ability of the PVA sample to absorb energy from the pressure produced by the PA effect. Therefore, the PVA concentration could also be related to the elastic behavior of the samples.

2.2.2. Natural Frequency

The natural frequency parameter is retrieved using the imaginary component of the complex conjugate eigenvalue of the model. The natural frequency is related to the so-called resonant frequency, which corresponds to the frequency at which energy can freely transfer back and forth within the sample. Thus, it represents the oscillatory behavior of the PA signal and has a straightforward representation in the frequency domain through a spectrum peak. However, this parameter we show is also encoded by the SSM and is related to the PVA concentration, as shown in Figure 3b,d for MW1 and MW2, respectively. Therein, one can see that the parameter ω_n decreases as the percentage of PVA grows following a second-order degree trend, explained by fitting goodness above 96%. This situation could be attributed to the PA signal's information loss due to more PVA in the sample. Furthermore, from Figure 3b,d, it is possible to deduce that the MW impacts the bandwidth of the PA signal as it could be related to the density of the sample.

2.3. Analysis of Optical Coefficients

Table 2 shows PVA samples' μ_a and μ_s coefficients and anisotropic parameter (*g*) concerning the PVA concentration. The first column shows the PVA concentration, while the second and third columns display the μ_a and μ_s coefficients. The fourth column shows the reduced scattering coefficient (μ_s') and the final column outlines the *g* parameter. These values are derived from the optical properties listed in Table 2 in the methodology section.

Table 2. Sample's optical properties as a function of the PVA concentration.

		MW1		
PVA (%)	**μ_a (cm^{-1})**	**μ_s (cm^{-1})**	**μ_s' (cm^{-1})**	**g**
7	0.05 ± 0.00	54.94 ± 0.55	20.60 ± 0.21	0.62 ± 0.01
9	0.06 ± 0.00	55.30 ± 0.55	21.01 ± 0.21	0.62 ± 0.01
12	2.17 ± 0.00	51.82 ± 0.10	10.36 ± 0.02	0.80 ± 0.00
15	2.78 ± 0.02	52.57 ± 0.42	9.72 ± 0.08	0.82 ± 0.01
20	0.58 ± 0.01	53.15 ± 0.42	17.54 ± 0.14	0.67 ± 0.01
		MW2		
7	0.23 ± 0.01	12.86 ± 0.64	9.64 ± 0.48	0.25 ± 0.01
9	0.19 ± 0.02	9.88 ± 1.17	6.91 ± 0.83	0.30 ± 0.04
12	0.18 ± 0.02	11.01 ± 1.10	7.70 ± 0.77	0.30 ± 0.03
15	0.20 ± 0.02	10.35 ± 1.04	8.07 ± 0.81	0.22 ± 0.02

After analyzing the data from the MW1 samples, it was observed that μ_a increases significantly as the PVA concentration rises from 7% to 15%, reaching a peak value of 2.78 ± 0.02 cm^{-1} at 15% PVA. However, at 20% PVA, the μ_a drops to 0.58 ± 0.01 cm^{-1}. Additionally, there is a slight decrease in the μ_s with increased PVA concentration. The μ_s dropped from 54.94 ± 0.55 cm^{-1} at 7% PVA to 52.57 ± 0.42 cm^{-1} at 15% PVA and increased slightly to 53.15 ± 0.42 at 20% PVA. Similarly, μ_s' follows a similar trend and drops from 20.60 ± 0.21 cm^{-1} at 7% PVA to 9.72 ± 0.08 at 15% PVA and increases to 17.54 ± 0.14 cm^{-1} at 20% PVA. Finally, *g* shows significant changes between different concentrations of PVA, with values ranging from 0.62 ± 0.01 to 0.82 ± 0.01, which characterizes the angular distribution of scattered light.

Based on the MW1 sample data, it is clear that higher PVA concentrations lead to greater μ_a and lower μ_s and $\mu_s{}'$ coefficients. Additionally, changes in the g indicate that the direction of scattered light depends on PVA concentration. These results reinforce the PA response signals and provide helpful insight into the optical behavior of the samples. This knowledge can help optimize the design of optical biomaterial systems for various biomedical applications.

The μ_a values for the MW2 samples are relatively stable when the PVA concentrations are varied, with a slight decrease observed in the 12% PVA concentration. On the other hand, the μ_s values show a downward trend from 12.86 ± 0.64 to 10.35 cm^{-1} as the PVA concentration increases from 7% to 15%, with the most significant reduction observed in the 9% PVA concentration. Similarly, the $\mu_s{}'$ values show a negative trend from 9.64 ± 0.48 cm^{-1} to 8.07 ± 0.81 cm^{-1} from 7% to 15% PVA, with the minimum value observed in the 9% PVA concentration. The g values vary slightly, around 0.25, depending on the PVA concentration. Compared to the MW1 samples, the MW2 samples are somewhat more stable as the μ_a values do not vary much with increasing PVA concentration, even if the μ_s and $\mu_s{}'$ values decrease.

These findings reinforce the results of the PA response signal amplitudes for the MW2 samples since there is better stability. In that case, the 7 and 9% hydrogels showed similar amplitudes, and the 12 and 15% hydrogels showed comparable amplitudes when the PVA concentration was varied, with the most significant increase in amplitude being from the 9% PVA hydrogel to 12%.

The values of this study's μ_a and optical μ_s coefficients align with findings reported in other studies [5,6]. They determined the optical coefficients by changing the freezing cycles, and we determined them by varying the PVA concentration. The differences in the location of the sample and its internal structures may contribute to variations in the data observed.

Hydrogels' optical stability depends on their absorption and scattering capacity of near-infrared light, which varies with concentration. Increasing PVA concentration improved absorption capacity for both MWs. MW1 has a lower μ_a and higher μ_s coefficient for 7% and 9% concentrations, while higher concentrations of 12%, 15%, and 20% have higher μ_a and lower μ_s coefficients. MW2 has similar μ_a and μ_s coefficients for all concentrations except for 7% and 9%, with higher μ_a and lower μ_s coefficients than MW1. These hydrogels mimic tissue optical properties and aid in diagnosis and treatment using optical techniques such as PA and integrating sphere.

2.4. Analysis of Porosity Distribution

This section presents the results of the porosity distribution (number of pores versus diameter) for the MW1 and MW2 samples. The diameter range of the pores identified in the samples for different concentrations of PVA was from 10 to 80 µm. The increase in the concentration of PVA leads to a decrease in the diameter of the pores and, consequently, the number of pores. High MW samples have greater cross-linking due to more polymer chains; therefore, the pore diameter decreases. The porosity distribution for the samples of the two MWs fits a LogNormal curve with a value $R^2 = 0.998$, as shown in Figure 4a,b. Each measurement is the average of four samples.

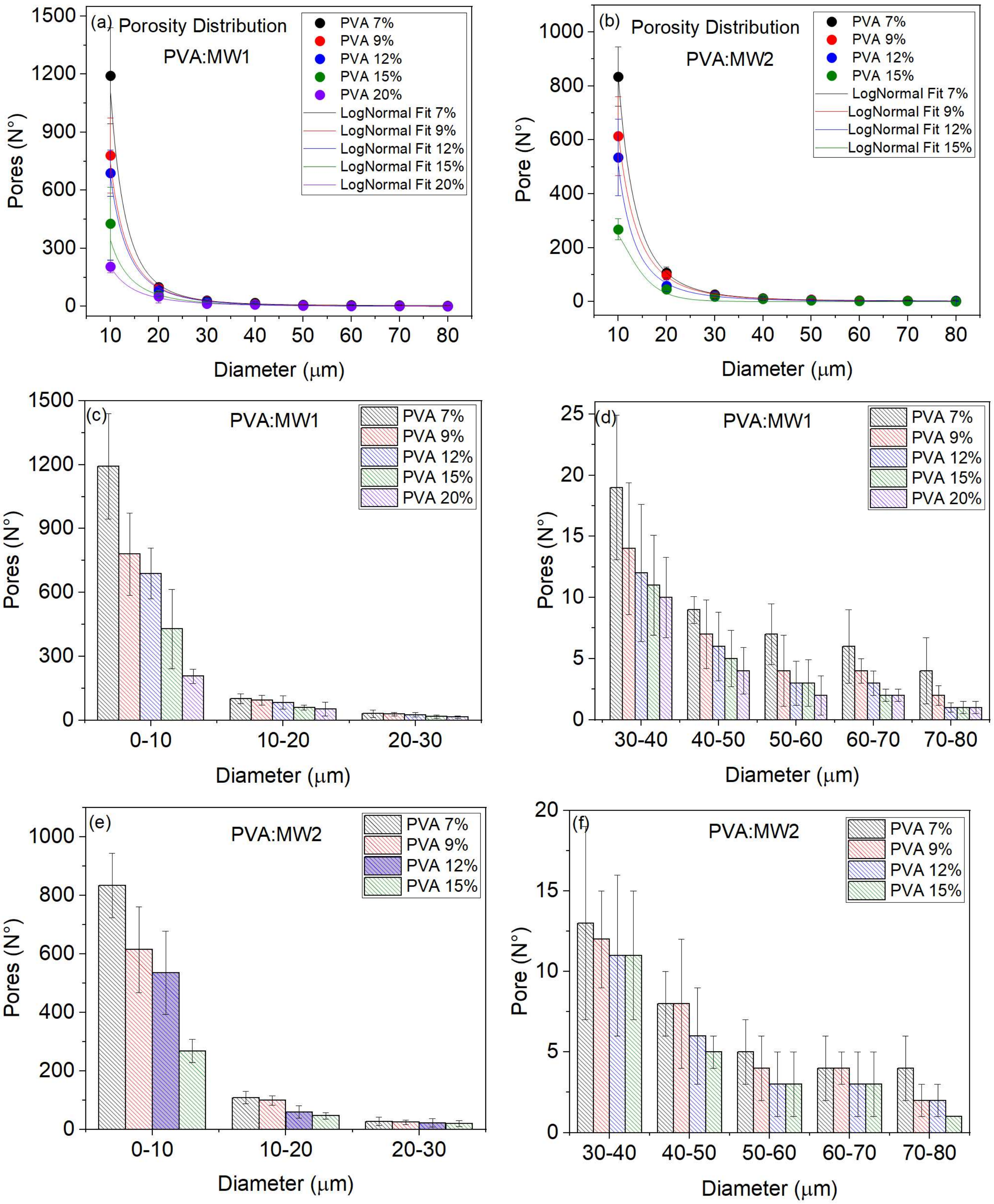

Figure 4. The behavior of the porosity distribution fitted to a LogNormal curve with R^2 = 0.998 for (**a**) MW1 samples and (**b**) MW2 samples. Additionally, the porosity distribution is displayed for both (**c**) small-diameter groups (0–10 μm, 10–20 μm, and 20–30 μm) and (**d**) large-diameter groups (30–40 μm, 40–50 μm, 50–60 μm, 60–70 μm, and 70–80 μm) for MW1 samples, and for the MW2 samples are (**e**) small-diameter groups and (**f**) large-diameter groups.

The histograms in Figure 4b,c display the distribution of porosity, categorized into two groups: small diameters ranging from 0–10 µm, 10–20 µm, and 20–30 µm, and larger diameters ranging from 30–40 µm, 40–50 µm, 50–60 µm, 60–70 µm, and 70–80 µm. The number of pores is higher for smaller diameters, notably within the 0–10 um range. As the concentration of PVA increases, the number and diameter of pores decrease. This trend is also observed in the MW2 samples, where increasing PVA concentration leads to fewer pores, as shown in Figure 4e,f. The differences in the measurements may be attributed to the composition of the various sample cuts.

When the samples have high concentrations and MW, their physical-mechanical properties improve and become more viscous. However, this also leads to a higher reduction in permeability. Our findings can assist in selecting the optimal parameters for PVA hydrogels in biopolymer applications.

2.5. Analysis of Density and Elasticity Modulus

Figure 5a shows that higher concentrations increase density due to decreased porosity, as previously discussed. The densities of MW2 are slightly higher than those of MW1. In both MWs, the densities of the 9% samples are slightly higher than those of 7%. However, the increase in density is more significant for the 12% and 15% samples compared to the 7% and 9% samples. The increase in density between 15% and 20% of MW1 is very smooth. The standard deviation of the density values is due to the porosity distribution of the four layers cut from the hydrogel wall for each concentration.

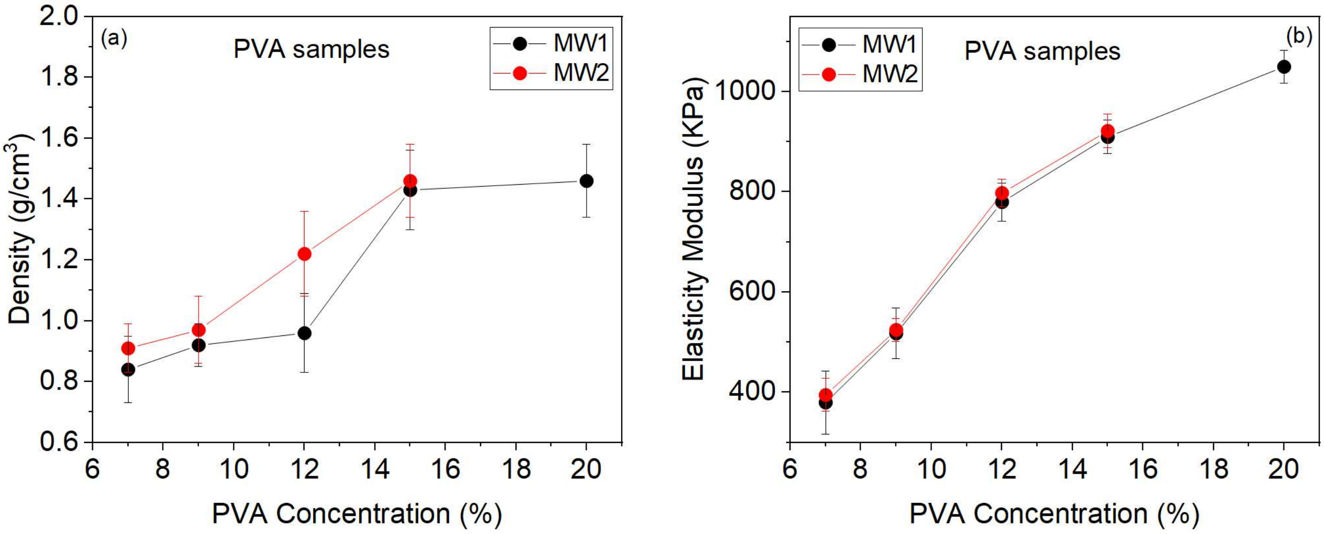

Figure 5. Mechanical properties of the PVA samples with two MWs and different concentrations. The density and elasticity modulus are plotted in (**a**,**b**), respectively.

The concentration of PVA directly impacts the modulus of elasticity and density. As the concentration of PVA increases, the modulus of elasticity also increases. The modulus of elasticity increases significantly for higher concentrations of PVA, as seen in Figure 5b. It is important to note that measurement variations may occur due to cutting different sections from the hydrogel wall.

Instead of measuring the modulus of elasticity with the number of freezing cycles, we report it based on concentration. Our findings are comparable to previous studies by [7,31]. It is important to note that the sample preparation methods, such as MW, concentration, freezing cycles, freezing time and temperature, and sample dimensions, play an essential role in the results. Our study's density and modulus of elasticity are consistent with the tissue simulant hydrogels' results for endoscopic ultrasound images due to using the same manufacturing methodology, as reported in [3].

After analyzing the modulus of elasticity, it was observed that the samples from MW2 are slightly higher than those of MW1. This means that the polymer with higher MW has more chains, resulting in fibers with greater tensile strength.

In this study, the mechanical stability of hydrogels depends on porosity, density, and modulus of elasticity. Low PVA concentrations (7% and 9%) result in greater pore diameter and number, leading to higher swelling and permeability but lower tensile strength. This behavior is similar for both MW1 and MW2. Hydrogels with higher PVA concentrations (12%, 15%, and 20%) have smaller pore diameters, higher density, and tensile strength, making them suitable for tissue simulation and image characterization.

2.6. Relationship of Dynamical Model and Mechanical Properties

For comparison purposes, we investigated the relationship of the elasticity modulus and density with the damping ratio and natural frequency, respectively, as shown in Figure 6. From Figure 6a, one can see that the damping ratio exhibits a quasi-linear inverse relationship with the elasticity modulus as the concentration grows for both MWs. This situation indicates that the concentration of PVA is related to the samples' elasticity; therefore, the damping ratio could be an effective parameter to characterize it using the PA effect. On the other hand, from Figure 6b, the natural frequency is inversely related to the sample density for different concentrations. In particular, using the natural frequency of the PVA samples, it is possible to infer the density of the samples, as suggested by the PA model in Equation (2).

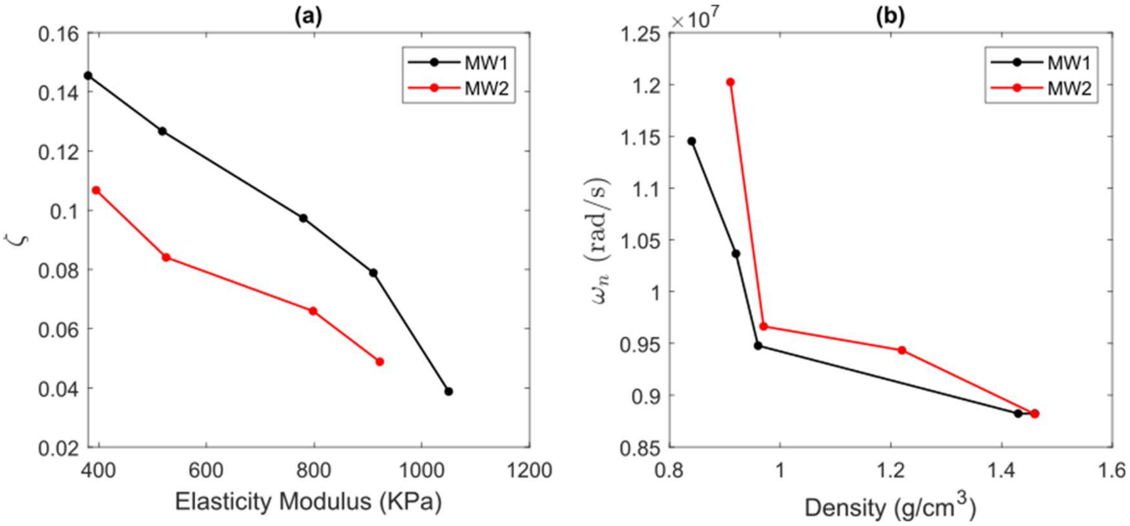

Figure 6. Relationship between state-space model parameters and mechanical properties of PVA samples for two MWs and different concentrations, (**a**) damping ratio versus elasticity modulus, and (**b**) natural frequencyversus density.

3. Conclusions

This study found that the concentration and MW changes affected the polymeric network's cross-linking and the hydrogels' dimensions. For that reason, the arrival time shifted toward longer times with increasing PVA concentration, and the amplitude of the PA signal increased, whereas the latter was due to the superior PVA absorption. A similar behavior was observed for the MW2 samples but with an amplitude slightly more pronounced. Moreover, as the speed of sound is related to arrival time, it displayed variations with increasing PVA concentration. Additionally, a subspace identification (SI) algorithm allowed for the recovery of state-space models from the temporal and frequency profile of the PA signals containing the sample's biophysical information. There was a similarity between the measured signal and the SSM signal using the NRMSE, which allowed for capturing valuable details about the system and depreciating small noise-related singular values. Based on the damping ratio, it was observed that an increased concentration of PVA resulted in higher energy absorption capacity of the hydrogels under the PA effect for both MWs. Concerning the natural frequency, it was observed that higher PVA concentration led to increased energy transfer in the hydrogels for both MW. Intriguingly, the damping ratio and natural frequency correlated with the modulus of elasticity and density. These properties were observed to increase with higher PVA concentration.

On the other hand, as the concentration of PVA increased, the μ_a coefficients also improved while the μ_s coefficient decreased slightly. Nevertheless, the MW2 samples exhibited minimal changes in their μ_a coefficients and optical μ_s, remaining almost steady. These results provide further evidence for the conclusions drawn from the PA method. From the distribution results of porosity, density, and modulus of elasticity, it can be concluded that the physical-mechanical properties of the hydrogels were improved as the concentration of PVA and MW increased. This study aimed to enhance the characterization of hydrogels with varying PVA concentrations and MW through diverse methods. The goal is to create hydrogels as phantoms that can be applied explicitly in tissue simulation and imaging.

4. Materials and Methods

4.1. PVA Hydrogels

In this study, nine PVA hydrogels shaped as hollow boxes were used. Five PVA boxes were obtained with concentrations of 7%, 9%, 12%, 15%, and 20% for MW1 = 85,000–124,000, and four PVA boxes with concentrations of 7%, 9%, 12%, and 15% for MW2 = 146,000–186,000. Regardless, the 20% PVA hydrogels could not be obtained due to the complexity of its preparation in the gel stage, which resulted in lumps.

This study chose a wide range of PVA concentrations to characterize the hydrogels through physical-mechanical techniques and analyzing PA signals using a dynamic model, in order that they can be applied as tissue simulators (organs and lesions) [3–6,28,32] and images [10,11,13,15,33].

To obtain the hydrogels with different concentrations, two steps were followed:

First step: PVA gel

For the preparation of PVA gel, powder with 99% hydrolysis (Sigma Aldrich, Saint Louis, MO, USA) was used, and to obtain the weight–concentration relationship, the following equation was used:

$$W_{PVA}(\mathrm{g}) = [PVA\ concentration\ (\%) \times H_2O\ volume\ (\mathrm{mL})]/100\% \quad (8)$$

The gel is obtained from the mixture of 150 mL pure water Milli-Q® (Merck, Darmstadt, Germany) and 10.5 mg of PVA powder corresponding to the concentration of 7% PVA by heating from 20 °C to 85 °C for approximately 90 min. The mixture was stirred with a bar magnet throughout the heating process to ensure a homogeneous solution. Then, this gel is left to rest to cool down and reach room temperature (20 °C) and eliminate air bubbles that may be trapped in the solution. The same procedure was followed for the rest of the concentrations, only changing the weight corresponding to each concentration.

Second Step: PVA hydrogel

The gel obtained in the first step is poured into a mold in the form of a box (coated steel) to undergo the process of freezing (−80 °C) using a freezer (Kaltis GV039M, Shanghai, China) during 1.5 h and thawing to room temperature (20 °C) during 4 h for four cycles. Finally, a PVA hydrogel is obtained, as shown in Figure 7a. To keep the hydrogel for a long time (even years), it is left submerged in pure water.

The hydrogel dimensions are represented in Figure 7b, where d_1 and d_3 are the thicknesses of the hydrogel walls, d_2 is the internal diameter, and D is the diameter. This hydrogel contains 12 mL of SS to propagate the PA wave when laser light irradiates.

The hydrogels' defined dimensions and hollow shape were due to two reasons: the area needed to be greater than the sensor's surface area to avoid laser light scattering, and the hydrogels needed to accommodate biological substances and tissue, such as mammary tumors, fibroadenomas, microcalcifications, etc.

Regarding microscopic images in Figure 7c, a 10 μm dehydrated film is shown. This was cut from a section of the hydrogel wall, and a drop of water on the dehydrated film is observed in Figure 7d.

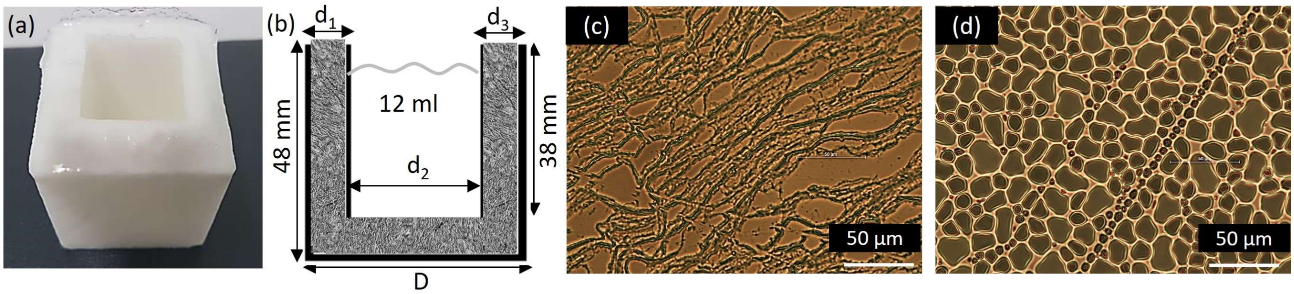

Figure 7. (**a**) PVA hydrogel image (MW1, 12%), (**b**) hydrogel cross-section dimensions (contains 12 mL of saline solution), (**c**) microscopic image of a 10 μm dehydrated film of the PVA hydrogel (scale, 50 μm), and (**d**) the same PVA film as (**c**) with a drop of water (Nikon optical microscope, Tokyo, Japan 40X objective, 10X eyepiece).

By increasing the concentration of PVA in the hydrogels, a slight expansion of their dimensions, d_1, d_2, and d_3, is observed in Table 3. This is a direct result of the greater crosslinking of the hydrogel, which leads to a higher degree of crystallinity and, subsequently, a higher resistance to mechanical stress.

Table 3. Dimensions of the PVA hydrogels for two MWs and different concentrations. The measurements are the average plus the standard deviation of three hydrogels.

PVA: MW1					
Diameter (mm)	**7%**	**9%**	**12%**	**15%**	**20%**
d_1	8.39 ± 0.07	9.82 ± 0.04	10.42 ± 0.18	10.88 ± 0.12	11.20 ± 0.52
d_2	22.60 ± 0.82	23.86 ± 0.14	24.44 ± 0.24	24.62 ± 0.23	24.32 ± 0.20
d_3	8.68 ± 0.52	9.47 ± 0.22	10.14 ± 0.30	10.72 ± 0.12	11.09 ± 0.46
D	39.70 ± 1.34	43.16 ± 0.31	45.00 ± 0.24	46.22 ± 0.48	46.62 ± 0.26
PVA: MW2					
d_1	8.88 ± 0.28	9.30 ± 1.12	10.62 ± 0.08	11.00 ± 0.22	-
d_2	21.88 ± 0.06	22.00 ± 1.77	23.32 ± 0.04	23.92 ± 0.26	-
d_3	9.01 ± 0.41	9.30 ± 0.26	9.56 ± 0.48	9.66 ± 0.04	-
D	40.20 ± 0.65	40.54 ± 2.00	43.84 ± 0.59	43.89 ± 0.22	-

Figure 7c shows a microscopic image (Nikon optical microscope, 40X objective, 10X eyepiece) of a 10 μm thick film that was obtained from the PVA hydrogel wall, and it was dehydrated for 24 h. Figure 1d shows the same film but hydrated with one drop of pure water, where it is observed how the pores are filled with this solution. The PA signals obtained in this study were from the empty hydrogel and with propagation medium, 12 mL of SS or sodium chloride (NaCl), 0.9% (Baxter, Jiutepec, Morelos, Mexico).

4.2. Photoacoustic Method

The PA signals of the PVA hydrogels of two MWs and different concentrations were obtained by the pulsed PA technique, as seen in Figure 2. The experimental setup consists of an Nd: YAG laser (Brilliant B, Quantel, Lannion, Côtes-d'Armor, France) with $\lambda = 1064$ nm, $\tau = 6$ ns, F = 10 Hz, and fluency = 33 mJ/cm^2 per pulse. An oscilloscope (DPO 5204B, Tektronix, Beaverton, OR, USA) with a bandwidth of 2 GHz and a sampling rate of 10 Gs/s to record the signals, a 100% reflectance mirror (NB1-K14, Thorlabs, Newton, NJ, USA) to reflect the laser beam, a 2.25 MHz immersion transducer (I-8 series, Olympus, Tokyo, Japan) to detect the ultrasonic signals, a Si photodetector amplified (PDA10A, Thorlabs, Newton, NJ, USA) from 200–1100 nm to detect the laser shot, and finally the PVA hydrogel with SS, which is adjusted laterally by two clamps to try to maintain the same sensor coupling with all hydrogels (Figure 8b).

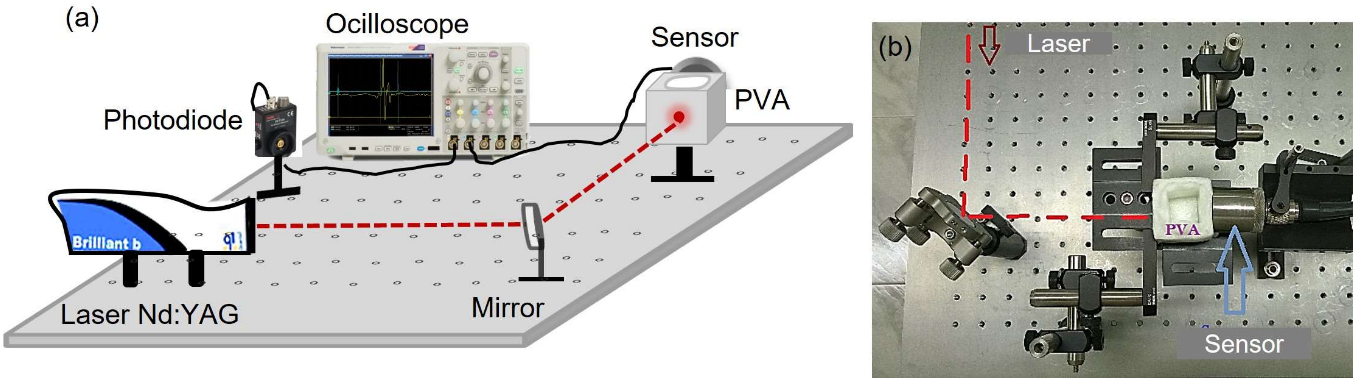

Figure 8. (**a**) Schema of the PA experimental setup to obtain the PA response signal of the hydrogels with two MWs and different PVA concentrations, (**b**) photography of the PA experimental setup.

This technique involves incising laser light on the hydrogel that is coupled directly to the sensor, part of this light is absorbed by the hydrogel, and the other part is scattered. Then, the absorbed part (absorption source) is heated, generating a thermoelastic effect and emitting optoacoustic waves that travel through the SS medium and are detected by an ultrasound sensor and recorded by the oscilloscope. Initially, the hydrogel is empty, and its PA signal is recorded. Then, 12 mL of SS is added, and the signal is recorded again. This process is repeated for each hydrogel three times.

As PVA hydrogels have high water absorption capacity, the coupling with immersion transducers is excellent since these are used to being in contact with water.

Photoacoustic Response Signals

In Figure 9, we can see the PA signals of an empty hydrogel and one containing SS (in this case, a PVA 7% hydrogel for MW1 and MW2). The empty hydrogel does not show a PA response since there is no medium for the acoustic waves generated in the hydrogel wall to propagate toward the sensor. However, it is important to understand that the acoustic wave is generated by the vibrations of the hydrogel structure when it absorbs electromagnetic energy. This structure is a 3D network containing water in its micropores and comprises a crystalline and amorphous phase. Therefore, increased PVA concentration and MW will be noted in the amplitude and delay time of the PA signal.

The image attached to Figure 3 shows that the beam impinges directly on the PVA wall, produces pressure waves, and travels through the medium SS until the sensor detects them.

By analyzing the PA signal, we can determine the arrival time of the pressure wave (t_a), which indicates how long it takes to travel from the source of absorption to the sensor. Peak-to-peak amplitude (A) can also be measured, directly related to absorption. Additionally, we can calculate the speed of sound (c) using the equation $c = D/t_a$, where (D) is the hydrogel diameter.

The PA signal amplitude is related to the PVA concentration and arrival time with the hydrogel's porosity distribution (number and diameter of pores) by varying the concentration.

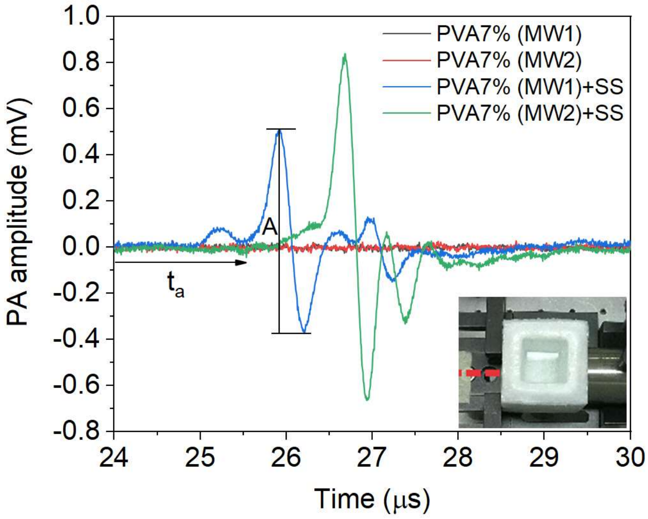

Figure 9. Amplitude versus time of PA signals for MW1 and MW2 of a PVA 7% hydrogel, both empty and with a saline solution medium.

4.3. Dynamical Model Identification

One of the most promising methods to derive data-driven models in an SSM structure is the SI approach [31]. SI aims to estimate the SSM in Equations (4) and (5) using structured measurements of input/output signals and orthogonal projections. Particularly, in this study, we appeal to the numerical algorithm for the N4SID method owing to its numerical stability. The N4SID is an algebraic in nature method working as follows. Let the measured PA signal $y_{PA}(t)$ be arranged in a block Hankel matrix defined as

$$\left[\frac{Y_p}{Y_f}\right] = \left[\begin{array}{ccc} y_0 & \cdots & y_{j-1} \\ \vdots & \ddots & \vdots \\ y_{i-1} & \cdots & y_{i+j-2} \\ \hline y_i & \cdots & y_{i+j-1} \\ \vdots & \ddots & \vdots \\ y_{2i-1} & \cdots & y_{2i+j-2} \end{array}\right], \tag{9}$$

where Y_p and Y_f are the matrices of past and future, respectively. Moreover, a shifted version of the Hankel matrix is constructed by moving the first block row of Y_f to the bottom of Y_p, thus leading to:

$$\left[\frac{Y_p^+}{Y_f^-}\right] = \left[\begin{array}{ccc} y_0 & \cdots & y_{j-1} \\ y_1 & \cdots & y_j \\ \vdots & \ddots & \vdots \\ y_i & \cdots & y_{i+j-1} \\ \hline y_{i+1} & \cdots & y_{i+j} \\ \vdots & \ddots & \vdots \\ y_{2i-1} & \cdots & y_{2i+j-2} \end{array}\right], \tag{10}$$

Similarly, the input signal and the state sequence can be arranged following the notation in Equations (9) and (10). Moreover, a regressor is formed by the combination of U_p and Y_p as $W_p = \left[U_p \; Y_p\right]^T$, which will be used further to solve the identification problem. Let us define the following:

$$\Gamma = \left[C \; CA \; CA^2 \; \cdots \; CA^{i-1}\right]^\top, \Delta = \left[A^{i-1}B \; A^{i-2}B \; \cdots \; B\right], \tag{11}$$

as the extended observability and controllability matrices, respectively. Finally, the impulse response is given by the following Toeplitz matrix:

$$H = \begin{bmatrix} 0 & 0 & \cdots & 0 \\ CB & 0 & \cdots & 0 \\ CAB & CB & \cdots & 0 \\ \vdots & \vdots & \ddots & 0 \\ CA^{k-2}B & CA^{k-3}B & \cdots & 0 \end{bmatrix} \tag{12}$$

At this point, two main assumptions should hold for our particular problem: (i) The system governing the PA signal is stable, observable, and controllable, and (ii) the input signal excites the useful modes to be modeled.

The problem here is, given a set of PA signal measurements, to estimate the parameters of the SSM using subspaces of the matrices presented above. For this purpose, the SSM can be rewritten in matrix notation as the following system of linear equations:

$$Y_p = \Gamma_i X_p + H_i U_p, \tag{13a}$$

$$Y_f = \Gamma_i X_f + H_i U_f, \tag{13b}$$

$$X_f = A^i X_p + \Delta_i U_p, \tag{13c}$$

where Equations (13a) and (13b) define past and future outputs as a linear combination of previous states and the extended observability matrix. On the other hand, Equation (13c) relates the future and past states given the system matrix A.

Now, the algorithm aims to estimate the subspaces of the matrix Γ and the state sequence X_f, which can be obtained from data projections. Let $\mathcal{O}_i$ be an orthogonal projection defined by $\mathcal{O}_i = \Gamma_i X_f$, which can be computed by the projection of the future output onto the subspace of past data in the direction of future input as:

$$\mathcal{O}_i = Y_f /_{U_f} W_p, \tag{14}$$

Thereafter, it can be factorized using singular value decomposition (SVD), in order that:

$$\mathcal{O}_i = U\Sigma V^\top = (U_1 U_2)\begin{pmatrix} S_1 & 0 \\ 0 & 0 \end{pmatrix}\begin{pmatrix} V_1^\top \\ V_2^\top \end{pmatrix} = U_1 S_1 V_1^\top, \tag{15}$$

where S_1 is a diagonal matrix containing the non-zero singular values of the matrix $\mathcal{O}_i$. Moreover, the required subspaces are computed as:

$$\Gamma_i = U_1 S_1^{1/2}, \tag{16}$$

which, in turn, is useful to solve the relationship in Equation (14). By construction, it holds that using Equations (14) and (16) is possible to estimate the state sequences given that:

$$\hat{X}_i = \Gamma_i^\dagger \mathcal{O}_i, \; \hat{X}_{i+1} = \Gamma_i^\dagger \mathcal{O}_{i+1}, \tag{17}$$

where the subscript † denotes the pseudo-inverse. Once the state sequences are estimated, the following set of equations can be solved:

$$\underbrace{\begin{pmatrix} \hat{X}_{i+1} \\ Y_i \end{pmatrix}}_{\mathcal{F}} = \underbrace{\begin{pmatrix} A & B \\ C & 0 \end{pmatrix}}_{\theta} \underbrace{\begin{pmatrix} \hat{X}_i \\ U_i \end{pmatrix}}_{M}, \tag{18}$$

which is a SSM in matrix notation. Interestingly, Equation (18) has a closed-form solution which can be algebraically computed. Thus, the optimal set of parameters $\theta^\star$, in the least-squares sense, is given by $\theta^\star = \mathcal{F}M^\top \left(MM^\top\right)^{-1}$, that corresponds to an estimate of the SSM matrices, $\hat{A}$, $\hat{B}$, and $\hat{\mathrm{C}}$. Thereby, the estimated SSM is related with the impulse response function governing the PA signal [32] and, in this way, one can perform a parametric analysis of PA, given the elements of the system-related matrices.

4.4. Optical Coefficients

The optical properties of the hydrogel's samples were investigated using a setup depicted by Teran et al. [34]. We utilized five different illumination beams to examine the diffuse reflectance and transmittance of these hydrogels. Each beam had a specific purpose: beam 1 provided diffuse illumination for reflection measurements (power detected, P_d); beam 2 offered collimated illumination (power detected, P_r); beam 3 accounted for the sample's specular reflection; beam 4 aided in transmission measurements with collimated illumination (power detected, P_t); and beam 5 represented the light that passed through the sample without scattering (power detected, P_{coh}). Switching between these beams was facilitated by removable mirrors.

For this setup, we utilized an integrating sphere (ISP-50-8-R-GT Ocean Optics) with an internal diameter of 13.46 cm and a wall reflection coefficient of $m = 0.98$. This sphere played a vital role in determining the power that the detector received under different illumination conditions. Using mathematical equations based on integrating sphere theory, we estimated this power for each beam and then determined the total reflectance and transmittance of the sample.

To determine the directional-diffuse reflectance, we compared the power reflected in a directional-diffuse illumination setup (beam 2) to the power detected in a diffuse-diffuse illumination setup (beam 1). This reflectance value is represented as:

$$R_{cd} = mP_r/P_d \tag{19}$$

On the other hand, we calculated the directional-diffuse transmittance (referred to as beam 4) by comparing the power detected in this configuration to the power detected in the diffuse-diffuse configuration:

$$T_{cd} = mP_t/P_d \tag{20}$$

We calculated the coherence transmittance by measuring both the incident power (P_o) and the directional light transmitted through the sample (P_{coh}):

$$T_c = P_{coh}/P_o \tag{21}$$

The relationships between reflectance and transmittance, including both coherent and diffuse measures, are crucial in determining the inherent optical properties of the samples.

Table 4 presents the optical properties of the hydrogel samples as a function of the PVA concentration, as described by Equations (19)–(21). The optical properties under consideration include diffuse-directional reflectance (R_{cd}), diffuse-directional transmittance (T_{cd}), and coherence transmittance (T_c)—each sample with a width of 100 μm.

Table 4. Sample's optical properties as a function of the PVA concentration with a width of 100 μm.

	PVA: MW1			PVA: MW2		
PVA (%)	R_{cd}	T_{cd}	T_c	R_{cd}	T_{cd}	T_c
7%	0.44 ± 0.01	0.47 ± 0.01	0.0	0.23 ± 0.05	0.34 ± 0.09	0.23 ± 0.08
9%	0.44 ± 0.01	0.44 ± 0.01	0.0	0.19 ± 0.12	0.34 ± 0.09	0.33 ± 0.12
12%	0.17 ± 0.00	0.42 ± 0.05	0.0	0.18 ± 0.10	0.34 ± 0.05	028 ± 0.06
15%	0.14 ± 0.01	0.41 ± 0.01	0.0	0.20 ± 0.10	0.29 ± 0.16	0.31 ± 0.08
20%	0.34 ± 0.01	0.44 ± 0.01	0.0	-	-	-

In the case of MW1 samples, it was noticed that the R_{cd} decreased as the concentration of PVA increased. This decrease was particularly significant at higher PVA concentrations, with the lowest value of 0.14 ± 0.01 observed at 15% PVA. However, at 20% PVA, the R_{cd} increased again to a value of 0.34 ± 0.01. These findings suggest that the concentration of PVA plays a crucial role in determining the reflectance behavior of the samples. Similarly, the T_{cd} showed a similar pattern, with a general decrease observed as the concentration of PVA increased. At 7% PVA, the T_{cd} was 0.47 ± 0.01, which gradually decreased to 0.41 ± 0.01 at 15% PVA. For the highest concentration of 20% PVA, the T_{cd} rose again to 0.44 ± 0.01. These results indicate that the PVA concentration affects the samples' transmission properties, with a decrease in transmission observed at higher concentrations. Furthermore, the T_c component of these samples is negligible.

The data analysis of MW2 samples shows similar trends to those observed in MW1. When the concentration of PVA increases from 7% to 15%, the R_{cd} reaches its lowest point at 12% and then slightly increases at 15%. This implies that there is a non-linear relationship between Rcd and PVA concentration. The T_{cd} remains stable at 0.34 ± 0.09 as the PVA concentration rises from 7% to 12%, indicating that changes in PVA concentration do not significantly impact this range. Nevertheless, at 15%, T_{cd} decreases to 0.29 ± 0.16, suggesting that higher PVA concentrations could significantly impact this parameter. Finally, Tc generally increases as PVA concentration increases, with a slight decrease at 12% followed by a rise at 15%.

The inverse Monte Carlo method [35] was then employed to calculate the hydrogels' (μ_a) and (μ_s) coefficients. This method compared the measured values of reflection (R_{cd}) and transmission (T_{cd} and T_c) coefficients with the ones generated by proposing a set of optical properties of the medium. The optimization was guided by the downhill simplex algorithm, emphasizing the importance of suitable initial parameter values for convergence.

4.5. Porosity Distribution

The number and diameter of pores were determined using microscopic images of PVA hydrogels (Nikon optical microscope, Tokyo, Japan 40X objective, 10X eyepiece). The images were processed using ImageJ and MATLAB programs, which utilized binarization and filters. The samples measured 1 cm × 1 cm × 50 μm and were obtained from sections of one wall of each hydrogel using a Leica Biosystems cryostat. As the concentration of PVA increases, the number of pores decreases due to a reduction in diameter. Figure 10 shows the histogram of the number of pores versus the diameter of the PVA MW1: 7% hydrogel. Each measurement is an average of four samples.

This study analyzes the distribution of porosity in nine hydrogels (MW1: 7%, 9%, 12%, 15%, 20%, and MW2: 7%, 9%, 12%, 15%). The results section displays histograms for all hydrogels analyzed.

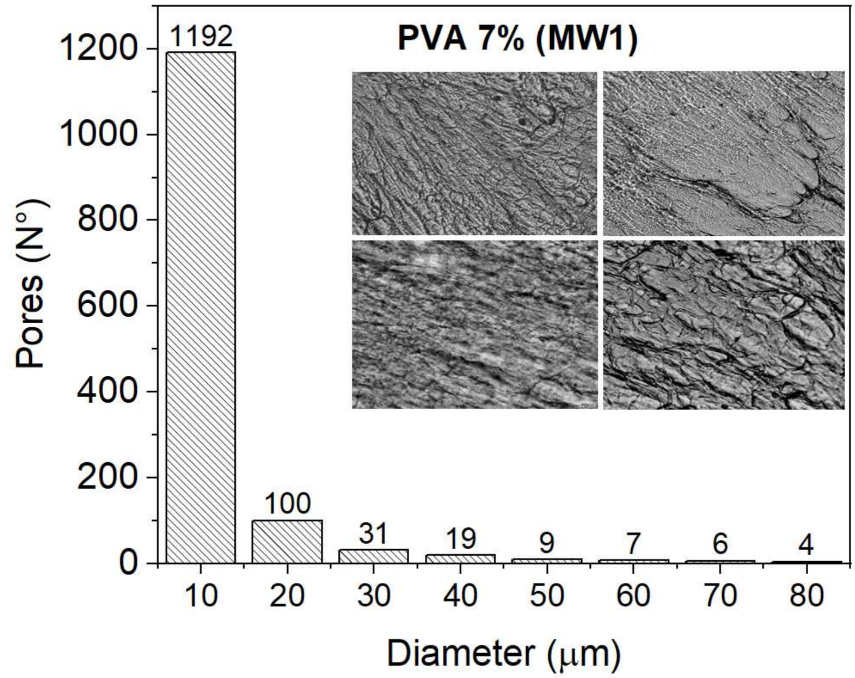

Figure 10. Histogram of the number of pores versus the diameter of the samples (measuring 1 cm × 1 cm × 50 μm) taken from a section of the wall of the PVA MW1: 7% hydrogel. Each measurement is an average of four samples.

4.6. Density and Elasticity Modulus

Four samples measuring 1 cm × 1 cm × 0.2 cm were cut from one of the PVA hydrogel walls to determine the density and elasticity modulus (Young's modulus). The density was measured using the equation $\rho = m/V$ according to Archimede's principle and the elasticity modulus of Young's modulus $(E = \sigma/\varepsilon)$ was determined using a traction device developed by the Research and Technological Development Unit of the General Hospital of Mexico "Dr. Eduardo Liceaga".

Author Contributions: Conceptualization, R.M.Q.-S., R.G.R.-C. and E.T.; methodology, R.M.Q.-S., A.P.-P. and E.T.; validation, R.M.Q.-S., R.G.R.-C. and E.T.; formal analysis, R.M.Q.-S., R.G.R.-C. and E.T.; investigation, R.M.Q.-S., A.P.-P. and E.T.; resources, R.M.Q.-S., A.P.-P., R.G.R.-C. and E.T.; data curation, R.M.Q.-S., R.G.R.-C. and E.T.; writing—original draft preparation, R.M.Q.-S. and R.G.R.-C.; writing—review and editing, R.M.Q.-S., R.G.R.-C., A.P.-P. and E.T.; visualization, R.M.Q.-S., R.G.R.-C. and E.T.; supervision, R.M.Q.-S. and R.G.R.-C.; project administration, R.M.Q.-S. and A.P.-P. All authors have read and agreed to the published version of the manuscript.

Funding: This paper was funded by the Research Department of the General Hospital of Mexico "Dr. Eduardo Liceaga" (DI/12/111/04/17) and by the grant DGAPA-UNAM-PAPIIT TA101423.

Institutional Review Board Statement: Not applicable.

Informed Consent Statement: Not applicable.

Data Availability Statement: Not applicable.

Acknowledgments: This paper was supported by Hospital General de México "Dr. Eduardo Liceaga" (DI/12/111/04/17) and Grants: CONACYT- 206574 and DGAPA-UNAM-PAPIIT TA101423. We also want to acknowledge the invaluable help from Patricia González Zavala, Ricardo Vera Graziano and Jocelin Correa Carranza for the design, advice, and porosity distribution of the hydrogels respectively. Similarly, Marco A. Durán Padilla and Alejandro K. Marquez Ramirez by providing us with the sections of PVA samples with the Leica Biosystems cryostat from Hospital General de México "Dr. Eduardo Liceaga".

Conflicts of Interest: The authors declare no conflict of interest.

References

1. Lamouche, G.; Kennedy, B.F.; Kennedy, K.M.; Bisaillon, C.-E.; Curatolo, A.; Campbell, G.; Pazos, V.; Sampson, D.D. Review of Tissue Simulating Phantoms with Controllable Optical, Mechanical and Structural Properties for Use in Optical Coherence Tomography. *Biomed. Opt. Express* **2012**, *3*, 1381–1398. [CrossRef]
2. Hernandez-Quintanar, L.; Rodriguez-Salvador, M. Discovering New 3D Bioprinting Applications: Analyzing the Case of Optical Tissue Phantoms. *Int. J. Bioprint.* **2019**, *5*, 1–11. [CrossRef] [PubMed]
3. Galvis-García, E.S.; Sobrino-Cossío, S.; Reding-Bernal, A.; Contreras-Marín, Y.; Solórzano-Acevedo, K.; González-Zavala, P.; Quispe-Siccha, R.M. Experimental Model Standardizing Polyvinyl Alcohol Hydrogel to simulate Endoscopic Ultrasound and Endoscopic Ultrasoundelastography. *World J. Gastroenterol.* **2020**, *26*, 5169–5180. [CrossRef] [PubMed]
4. Kamacı, U.D.; Kamacı, M. Preparation of polyvinyl alcohol, chitosan and polyurethane-based pH-sensitive and biodegradable hydrogels for controlled drug release applications. *Int. J. Polym. Mater. Polym. Biomater.* **2020**, *69*, 1167–1177. [CrossRef]
5. Kharine, A.; Manohar, S.; Seeton, R.; M Kolkman, R.G.; Bolt, R.A.; Steenbergen, W.; de Mul, F.F.M. Poly(Vinyl Alcohol) Gels for Use as Tissue Phantoms in Photoacoustic Mammography. *Phys. Med. Biol.* **2003**, *48*, 1–14. [CrossRef] [PubMed]
6. Xia, W.; Piras, D.; Heijblom, M.; Steenbergen, W.; van Leeuwen, T.G.; Manohar, S. Poly(Vinyl Alcohol) Gels as Photoacoustic Breast Phantoms Revisited. *J. Biomed. Opt.* **2011**, *16*, 075002. [CrossRef]
7. Fromageau, J.; Gennisson, J.L.; Schmitt, C.; Maurice, R.L.; Mongrain, R.; Cloutier, G. Estimation of Polyvinyl Alcohol Cryogel Mechanical Properties with Four Ultrasound Elastography Methods and Comparison with Gold Standard Testings. *IEEE Trans Ultrason. Ferroelectr. Freq. Control* **2007**, *54*, 498–508. [CrossRef] [PubMed]
8. Fukumori, T.; Nakaoki, T. Significant Improvement of Mechanical Properties for Polyvinyl Alcohol Film Prepared from Freeze/Thaw Cycled Gel. *Open J. Org. Polym. Mater.* **2013**, *03*, 110–116. [CrossRef]
9. Manohar, S.; Kharine, A.; van Hespen, J.C.G.; Steenbergen, W.; van Leeuwen, T.G. Photoacoustic Mammography Laboratory Prototype: Imaging of Breast Tissue Phantoms. *J. Biomed. Opt.* **2004**, *9*, 1172. [CrossRef] [PubMed]
10. Ermilov, S.A.; Khamapirad, T.; Conjusteau, A.; Leonard, M.H.; Lacewell, R.; Mehta, K.; Miller, T.; Oraevsky, A.A. Laser Optoacoustic Imaging System for Detection of Breast Cancer. *J. Biomed. Opt.* **2009**, *14*, 1–14. [CrossRef] [PubMed]
11. Su, Y.; Zhang, F.; Xu, K.; Yao, J.; Wang, R.K. A Photoacoustic Tomography System for Imaging of Biological Tissues. *J. Phys. D Appl. Phys.* **2005**, *38*, 2640–2644. [CrossRef]
12. Manohar, S.; Kharine, A.; Van Hespen, J.C.G.; Steenbergen, W.; Van Leeuwen, T.G. The Twente Photoacoustic Mammoscope: System Overview and Performance. *Phys. Med. Biol.* **2005**, *50*, 2543–2557. [CrossRef]
13. Xu, M.; Wang, L.V. Photoacoustic Imaging in Biomedicine. *Rev. Sci. Instrum.* **2006**, *77*, 1–22. [CrossRef]
14. Hysi, E.; Fadhel, M.N.; Moore, M.J.; Zalev, J.; Strohm, E.M.; Kolios, M.C. Insights into Photoacoustic Speckle and Applications in Tumor Characterization. *Photoacoustics* **2019**, *14*, 37–48. [CrossRef] [PubMed]
15. Rao, A.P.; Bokde, N.; Sinha, S. Photoacoustic Imaging for Management of Breast Cancer: A Literature Review and Future Perspectives. *Appl. Sci.* **2020**, *10*, 767. [CrossRef]
16. Yang, C.; Lan, H.; Gao, F.; Gao, F. Review of Deep Learning for Photoacoustic Imaging. *Photoacoustics* **2021**, *21*, 100215. [PubMed]
17. Song, X.; Zhou, X. Photoacoustic Microscopy Simulation Platform Based on K-Wave Simulation Toolbox. *Photon. Quantum* **2021**, *11844*, 1184415. [CrossRef]
18. Gonzalez, E.A.; Graham, C.A.; Lediju Bell, M.A. Acoustic Frequency-Based Approach for Identification of Photoacoustic Surgical Biomarkers. *Front. Photon.* **2021**, *2*, 716656. [CrossRef]
19. Li, X.; Ge, J.; Zhang, S.; Wu, J.; Qi, L.; Chen, W. Multispectral Interlaced Sparse Sampling Photoacoustic Tomography Based on Directional Total Variation. *Methods Programs Biomed.* **2022**, *214*, 1–13. [CrossRef] [PubMed]
20. Rathi, N.; Sinha, S.; Chinni, B.; Dogra, V.; Rao, N. Computation of Photoacoustic Absorber Size from Deconvolved Photoacoustic Signal Using Estimated System Impulse Response. *Ultrason. Imaging* **2021**, *43*, 46–56. [CrossRef] [PubMed]
21. Ramírez-Chavarría, R.G.; Alvarez-Serna, B.E.; Schoukens, M.; Alvarez-Icaza, L. Data-Driven Modeling of Impedance Biosensors: A Subspace Approach. *Meas Sci. Technol.* **2021**, *32*, 1–13. [CrossRef]
22. Salim, M.; Ahmed, S.; Khosrowjerdi, M.J. A Data-Driven Sensor Fault-Tolerant Control Scheme Based on Subspace Identification. *Int. J. Robust Nonlinear Control.* **2021**, *31*, 6991–7006. [CrossRef]
23. Jalanko, M.; Sanchez, Y.; Mahalec, V.; Mhaskar, P. Adaptive System Identification of Industrial Ethylene Splitter: A Comparison of Subspace Identification and Artificial Neural Networks. *Comput. Chem. Eng.* **2021**, *147*, 1–21. [CrossRef]
24. Ruiz-Veloz, M.; Martínez-Ponce, G.; Fernández-Ayala, R.I.; Castro-Beltrán, R.; Polo-Parada, L.; Reyes-Ramírez, B.; Gutiérrez-Juárez, G. Thermally Corrected Solutions of the One-Dimensional Wave Equation for the Laser-Induced Ultrasound. *J. Appl. Phys.* **2021**, *130*, 1–12. [CrossRef]
25. Gao, F.; Feng, X.; Zheng, Y. Photoacoustic Elastic Oscillation and Characterization. *Opt. Express* **2015**, *23*, 20617–20628. [CrossRef] [PubMed]
26. Saatci, E.; Saatci, E. State-Space Analysis of Fractional-Order Respiratory System Models. *Biomed. Signal Process. Control.* **2020**, *57*, 1–6. [CrossRef]
27. Ljung, L. *System Identification: Theory for the User*; Prentice Hall information and System Sciences Series; Prentice Hall PTR: Englewood Cliffs, NJ, USA, 1999; ISBN 9780136566953.
28. Surry, K.J.M.; Austin, H.J.B.; Fenster, A.; Peters, T.M. Poly(Vinyl Alcohol) Cryogel Phantoms for Use in Ultrasound and MR Imaging. *Phys. Med. Biol.* **2004**, *49*, 5529–5546. [CrossRef] [PubMed]

29. Arabul, M.U.; Heres, H.M.; Rutten, M.; van de Vosse, F.; Lopata, R. Optical Absorbance Measurements and Photoacoustic Evaluation of Freeze-Thawed Polyvinyl-Alcohol Vessel Phantoms. In Proceedings of the Photons Plus Ultrasound: Imaging and Sensing 2015, San Francisco, CA, USA, 11 March 2015; Volume 9323, p. 93232M. [CrossRef]
30. Gavish, M.; Donoho, D.L. The Optimal Hard Threshold for Singular Values Is $4/\sqrt{3}$. *IEEE Trans. Inf. Theory* **2014**, *60*, 5040–5053. [CrossRef]
31. Duboeuf, F.; Basarab, A.; Liebgott, H.; Brusseau, E.; Delachartre, P.; Vray, D. Investigation of PVA Cryogel Young's Modulus Stability with Time, Controlled by a Simple Reliable Technique. *Med. Phys.* **2009**, *36*, 656–661. [CrossRef]
32. Manohar, S.; Kharine, A.; Van Hespen, J.C.G.; Steenbergen, W.; De Mul, F.M.; Van Leeuwen, T.G. Photoacoustic Imaging of Inhomogeneities Embedded in Breast Tissue Phantoms. In *Biomedical Optoacoustics*; SPIE: Bellingham, WA, USA, 2003; Volume 4960, pp. 64–76. [CrossRef]
33. Zhang, R.; Zhao, L.; Zhao, C.; Wang, M.; Liu, S.; Li, J.; Zhao, R.; Wang, R.; Yang, F.; Zhu, L.; et al. Exploring the Diagnostic Value of Photoacoustic Imaging for Breast Cancer: The Identification of Regional Photoacoustic Signal Differences of Breast Tumors. *Biomed. Opt. Express.* **2021**, *12*, 1407–1421. [CrossRef]
34. Terán, E.; Méndez, E.R.; Quispe-Siccha, R.; Peréz-Pacheco, A.; Cuppo, F.L.S. Application of Single Integrating Sphere System to Obtain the Optical Properties of Turbid Media. *OSA Contin.* **2019**, *2*, 1791–1806. [CrossRef]
35. Terán, E.; Méndez, E.R.; Enríquez, S.; Iglesias-Prieto, R. Multiple Light Scattering and Absorption in Reef-Building Corals. *Appl. Opt.* **2010**, *49*, 5032–5042. [CrossRef] [PubMed]

gels

MDPI

Article

Modification of Acorn Starch Structure and Properties by High Hydrostatic Pressure

Luís M. G. Castro [1,2], Ana I. Caço [3], Carla F. Pereira [1], Sérgio C. Sousa [1], María E. Brassesco [1], Manuela Machado [1], Óscar L. Ramos [1], Elisabete M. C. Alexandre [2], Jorge A. Saraiva [2] and Manuela Pintado [1,*]

[1] CBQF-Centro de Biotecnologia e Química Fina—Laboratório Associado, Escola Superior de Biotecnologia, Universidade Católica Portuguesa, Rua Diogo Botelho 1327, 4169-005 Porto, Portugal; lgcastro@ucp.pt (L.M.G.C.); cpfpereira@ucp.pt (C.F.P.); sdsousa@ucp.pt (S.C.S.); mbrassesco@ucp.pt (M.E.B.); mmachado@ucp.pt (M.M.); oramos@ucp.pt (Ó.L.R.)

[2] LAQV-REQUIMTE—Laboratório Associado, Department of Chemistry, University of Aveiro, 3810-193 Aveiro, Portugal; elisabete.alexandre.pt@gmail.com (E.M.C.A.); jorgesaraiva@ua.pt (J.A.S.)

[3] Laboratório de Análises Térmicas, Department of Chemistry, University of Aveiro, 3810-193 Aveiro, Portugal; icaco@ua.pt

* Correspondence: mpintado@ucp.pt

Abstract: Despite being rich in starch, over half of acorn production is undervalued. High hydrostatic pressure was used to modify the properties of *Q. pyrenaica* (0.1 and 460 MPa for 20 min) and *Q. robur* (0.1 and 333 MPa for 17.4 min) acorn starches to obtain high-valued ingredients. Pressure significantly altered the span distribution and heterogeneity of the acorn starch granules depending on the species, but their morphology was unaffected. Pressurization increased the amylose/amylopectin ratio and damaged starch contents, but the effect was more prominent in *Q. pyrenaica* than in *Q. robur*. However, the polymorphism, relative crystallinity, gelatinization temperatures, and enthalpies were preserved. The pressure effect on the starch properties depended on the property and species. The solubility, swelling power, and acorn gels' resistance towards deformation for both species decreased after pressurization. For *Q. pyrenaica* starch, the in vitro digestibility increased, but the pseudoplastic behavior decreased after pressurization. No differences were seen for *Q. robur*. Regarding the commercial starch, acorn starches had lower gelatinization temperatures and enthalpies, lower in vitro digestibility, lower resistance towards deformation, superior pseudoplastic behavior, and overall higher solubility and swelling power until 80 °C. This encourages the usage of acorn starches as a new food ingredient.

Keywords: acorn; starch; extraction; modification; properties; high hydrostatic pressure

1. Introduction

Native to the Northern Hemisphere, oak trees of the *Quercus* spp. range from temperate to tropical latitudes in the Americas, Asia, Europe, and North Africa. They are evergreen, semi-deciduous, or deciduous trees that bear a small fruit called acorns [1]. There are large amounts of acorns in Portugal, and it is estimated that more than 400,000 tons are produced annually [2]. Despite being a novel food rich in resistant starch, more than half of the production is underused [3].

Native starch is formed by granules that are almost exclusively formed by amylose and amylopectin. Amylose is a linear chain of α-D-(1,4)-glucose residues, but amylopectin is highly branched since it has additional α-D-(1,6)-glucose bounds [4]. These structural differences cause amylose to have lower solubility, viscosity, gelatinization and melting temperatures, poorer thickening ability, adhesive forces, and freezing–thawing stability, but higher shear stability, a retrogradation tendency, and the ability to complex with lipids when compared to amylopectin [4]. Native starches are also a low-cost, renewable, and biodegradable resource with high availability. Still, their insolubility in cold water, fast easy aging, fast syneresis, fast retrogradation, low viscosity and shear stress resistance, and poor thermal properties and mechanical resistance limit their applicability [5]. To endow starch properties, they are usually chemically modified by the food industry through esterification, etherification, and oxidation methods to be used as food additives [6]. Oxidized starch, monostarch phosphate, distarch phosphate, phosphated distarch phosphate, acetylated distarch phosphate, acetylated starch, acetylated distarch adipate, hydroxypropyl starch, hydroxypropyl distarch phosphate, starch sodium octenyl succinate, acetylated oxidized starch, and starch aluminum octenyl succinate are the twelve authorized chemically modified starches used as food additives in the European Union [7]. However, the increasing awareness of consumers and the tendency to avoid modified starches make it necessary to produce clean-label starches [8].

High hydrostatic pressure (HP) is a non-thermal physical starch modification technology that endows starch properties from several botanical sources by using water and applying pressure levels from 100 to 600 MPa for 2 to 30 min at room temperature [9]. HP can inhibit the retrogradation of oat starch [10], increase the viscosity and obtain a highly structured profile of potato starch [11], and improve starch digestibility by decreasing the rapid and slowly digestible starch fractions and by increasing the resistant starch fraction of pea starch [12], and by increasing the swelling and solubility of corn and wheat starch [13]. HP has been gaining more attention since it does not use chemical reagents, is safer and of simple execution, and is more sustainable and environmentally friendly than the current chemical modification methods. As no chemical changes are induced, these starches do not need to be labeled as "modified starch" according to Annex I, paragraph 19 of Regulation (EC) 1333/2008 [7]. Thus, HP-modified starches can be more advantageous by attending to modern consumer demands. As HP is already used in the food industry, this study intends to use this technology to value natural resources existing in large quantities, such as acorns, to obtain food products or ingredients with high added value and great applicability, such as starch. In addition, this study also seeks to find out how the properties of these starches are comparable to commercial starch since it is familiar to the consumers and industry. Hence, this research aims to evaluate the effect of pressurization on the structure and properties of *Q. pyrenaica,* and *Q. robur* acorn starch and compare them to commercial corn starch.

2. Results and Discussion

2.1. Granular Morphology

Commercial starch granules occur in a range of shapes, as shown in Figure 1A, ranging from round, oval, and semicircular to triangular and trapezoidal–triangular, including granules with irregular shapes. Acorn starch granules were found to be round, oval, and semi-circular in shape, with some granules being triangular or trapezoidal–triangular in shape (Figure 1B–E), as reported in the literature [14–22]. Aside from the shape, commercial and acorn starch granules had a smooth surface without cracks and/or fissures, but a few granules had pits (Figure 1A–E) [14,17,19–21]. Pressurization did not affect the shapes and morphology of acorn starches of both *Q. pyrenaica* and *Q. robur* species, as previously observed for lily, chestnut, rice, and maize starches up to 500 MPa [9,23]. According to prior research, the outside layer of granules has a higher degree of order and appears to be more resistant to pressurization than the interior layer. This suggested that most changes occurred in the interior structure of the starch granule during pressurization [24]. Acorn starch granules had particles on the surface, which might be attributed to the presence of protein and/or fiber retained during extraction and sieving (Figure 1B–E) [14,16,25].

2.2. Granular Distribution and Particle Size

The size and shape of starch granules are related to their botanical origin and are genetically controlled. During their biosynthesis in amyloplasts or chloroplasts, the physical structures of plastids can give a certain shape to the granules and also affect the arrangement of amylose and amylopectin [26]. Hence, it is important to characterize them in terms of their distribution but also according to their size.

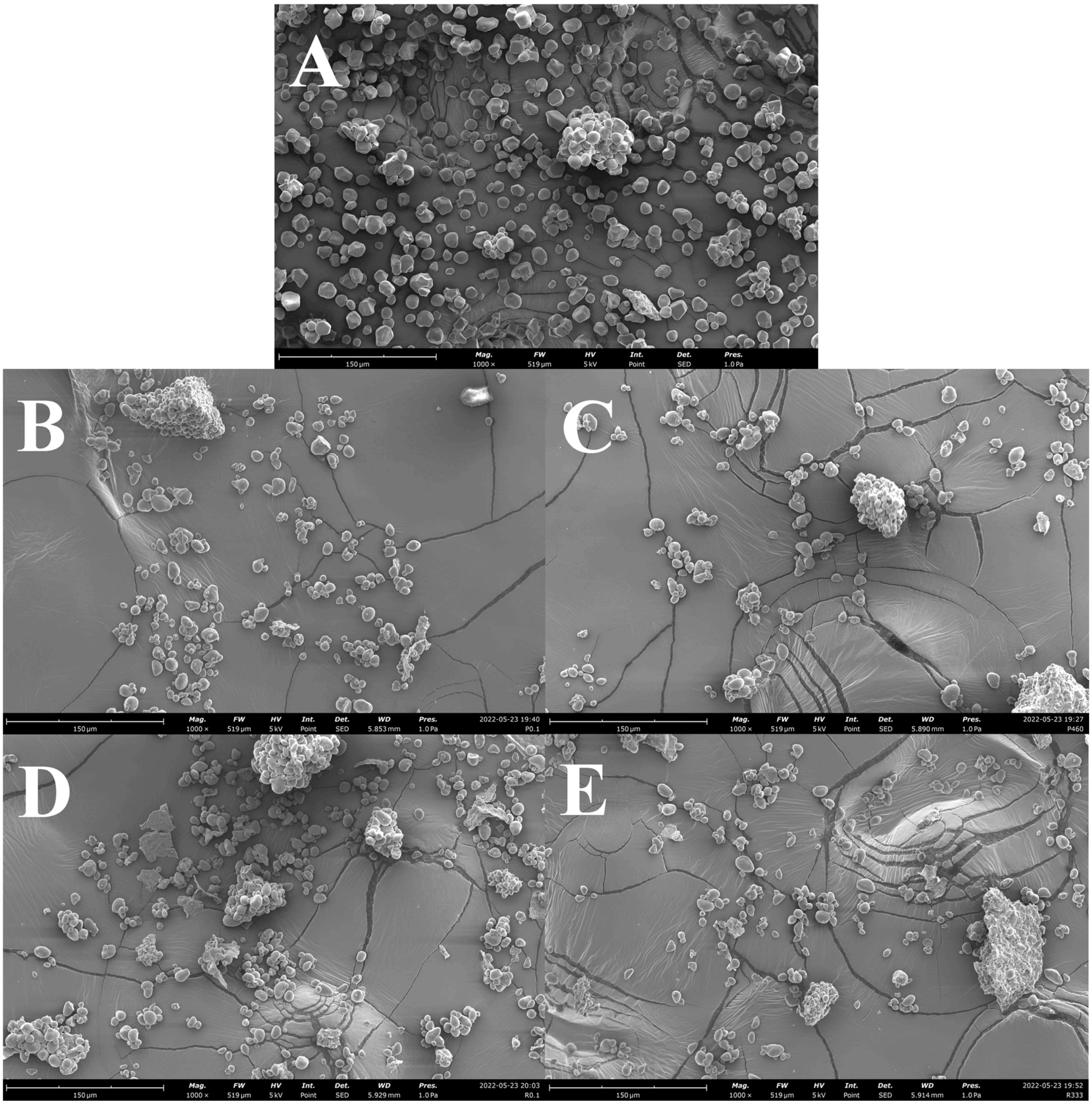

Figure 1. Scanning electron microscopy images at 1000× magnitude of (**A**) commercial starch; (**B**) *Q. pyrenaica* acorn starch extracted under control conditions (0.1 MPa for 20 min); (**C**) *Q. pyrenaica* acorn starch extracted under optimum conditions (460 MPa for 20 min); (**D**) *Q. robur* acorn starch extracted under control conditions (0.1 MPa for 17.4 min); (**E**) *Q. robur* acorn starch extracted under optimum conditions (333 MPa for 17.4 min).

In the case of *Q. pyrenaica*, the commercial and acorn starches (P0.1/t20 and P460/t20) had a non-normal distribution (Figure S1). While the acorn granule distribution was wider and flatter, the commercial granule distribution was narrow and taller. This finding is supported by the span values, which were lower for commercial starch (0.9 ± 0.0 µm) compared to the acorn starches (3.7 ± 0.1 µm for P0.1/t20 and 13.0 ± 0.4 µm for P46/t20). The P0.1/t20 and P46/t20 acorn starches had a statistically higher percentage of very small (<5 µm), small (5–10 µm), and large (>25 µm) granules than commercial starch (Table 1). However, commercial starch had a percentage of medium granules (10–25 µm) significantly higher (79.1 ± 0.0%) than acorn starches (44.0 ± 0.1% for P0.1/t20 and 37.1 ± 0.2 µm for P460/t20). The commercial starch showed a uniformity dispersion value of 0.3 ± 0.0, while acorn starches P0.1/t20 and P460/t20 showed a uniformity dispersion value of 1.4 ± 0.1 and 3.4 ± 0.1, respectively. The uniformity dispersion value is a measure of the size dispersion of the starch granules. Thus, a smaller uniformity dispersion value indicates a smaller size dispersion of the starch granules and, consequently, a greater similarity between granules [27]. Hence, the commercial starch granules are more homogeneous in size and more like each other than the acorn starch granules (Figure 1).

Table 1. Distribution and particle size characterization of the commercial, *Q. pyrenaica*, and *Q. robur* acorn starches extracted under control and optimum conditions.

Parameter	Commercial	P0.1/t20	P460/t20	R0.1/t17.4	R333/t17.4
<5 µm (%)	6.4 ± 0.0 ^{b}	9.3 ± 0.0 ^{e}	6.2 ± 0.0 ^{a}	8.2 ± 0.0 ^{c}	9.0 ± 0.0 ^{d}
5–10 µm (%)	12.4 ± 0.0 ^{a}	24.5 ± 0.1 ^{d}	17.1 ± 0.1 ^{b}	23.8 ± 0.0 ^{c}	26.1 ± 0.1 ^{e}
10–25 µm (%)	79.1 ± 0.0 ^{e}	44.0 ± 0.1 ^{d}	37.1 ± 0.2 ^{a}	37.9 ± 0.0 ^{b}	39.0 ± 0.1 ^{c}
>25 µm (%)	2.1 ± 0.0 ^{a}	22.2 ± 0.2 ^{b}	39.6 ± 0.3 ^{e}	30.1 ± 0.1 ^{d}	25.9 ± 0.3 ^{c}
Span (µm)	0.9 ± 0.0 ^{a}	3.7 ± 0.1 ^{b}	13.0 ± 0.4 ^{e}	7.2 ± 0.1 ^{d}	6.3 ± 0.2 ^{c}
UD (unitless)	0.3 ± 0.0 ^{a}	1.4 ± 0.1 ^{b}	3.4 ± 0.1 ^{e}	2.4 ± 0.1 ^{d}	2.0 ± 0.0 ^{c}
$D_{3,2}$ (µm)	8.7 ± 0.0 ^{c}	8.2 ± 0.0 ^{a}	11.3 ± 0.1 ^{e}	9.1 ± 0.0 ^{d}	8.6 ± 0.0 ^{b}
$D_{4,3}$ (µm)	14.0 ± 0.0 ^{a}	26.8 ± 0.8 ^{b}	73.3 ± 2.6 ^{e}	42.3 ± 1.2 ^{d}	34.6 ± 0.7 ^{c}
D_{10} (µm)	8.1 ± 0.0 ^{e}	5.2 ± 0.0 ^{a}	6.4 ± 0.0 ^{d}	5.5 ± 0.0 ^{c}	5.3 ± 0.0 ^{b}
D_{50} (µm)	14.0 ± 0.1 ^{b}	13.3 ± 0.1 ^{a}	18.5 ± 0.1 ^{d}	14.2 ± 0.0 ^{c}	13.2 ± 0.1 ^{a}
D_{90} (µm)	20.9 ± 0.0 ^{a}	53.8 ± 1.1 ^{b}	246.8 ± 9.0 ^{e}	107.3 ± 1.3 ^{d}	87.9 ± 3.1 ^{c}
SSA (m^2/kg)	687.2 ± 0.2 ^{c}	731.4 ± 1.6 ^{e}	533.3 ± 2.2 ^{a}	661.2 ± 0.6 ^{b}	695.7 ± 2.4 ^{d}

P0.1/t20: *Q. pyrenaica* acorn starch extracted under control conditions (0.1 MPa for 20 min); P460/t20: *Q. pyrenaica* acorn starch extracted under optimum conditions (460 MPa for 20 min); R0.1/t17.4: *Q. robur* acorn starch extracted under control conditions (0.1 MPa for 17.4 min); R333/t17.4: *Q. robur* acorn starch extracted under optimum conditions (333 MPa for 17.4 min); UD: uniformity dispersion; SSA: specific surface area. Significant differences between starches are represented by lower-case letters, and values in the same row with the same letters are not significant ($p > 0.05$).

Pressurization from P0.1/t20 to P460/t20 led to the transformation of a binomial to a trinomial distribution and flattened the distribution profile (Figure S1). The percentage of granules up to 25 µm decreased by 22% from P0.1/t20 to P460/t20 and the percentage of large granules (>25 µm) increased by 78%, which increased the span and uniformity dispersion values by 141 and 256%, respectively from P0.1/t20 to P460/t20 ($p < 0.05$) (Table 1). These results indicate that starch granule aggregation may have occurred from P0.1/t20 to P460/t20, resulting in the elongation of the granule distribution and greater heterogeneity of starch granules. The hypothesis of granular aggregation occurrence under pressurization from P0.1/t20 to P460/t20 is corroborated by the significant increases of the D_{10}, D_{50}, and D_{90} values by 23, 39, and 358%, respectively, indicating an increase in the maximum particle diameter below which 10, 50, and 90% of the starch granule volume exists, especially at D_{90}. Indeed, there was a significant increase in the De Brouckere diameter by 174%, a sensitive measurement of the presence of large particulates in the size distribution [28]. The significant variation of the Sauter diameter, defined as the diameter of a sphere with the same volume/surface area ratio as the particle of interest [29], indicates that the mean size of the starch granule distribution increased by 37%. The increase in the Sauter diameter could have been due to the significant decrease of the specific surface area by 27% (Table 1). The increase in D values, span, and uniformity dispersion after pressurization is what was previously observed for potato, lotus, lily, pea, maize, and quinoa starch [9,23,30,31].

Regarding *Q. robur*, the commercial and acorn starches (R0.1/t17.4 and R333/t17.4) had a non-normal distribution (Figure S1). These acorn granular distributions were also significantly wider and flatter (span value of 7.2 ± 0.1 µm for R0.1/t17.4 and 6.3 ± 0.1 µm for R333/t17.4) when compared to the commercial starch. The R0.1/t17.4 and R333/t17.4 acorn starches had a higher percentage of very small, small, and large granules than the commercial starch, which had more medium granules (Table 1). Since the commercial starch had a lower uniformity dispersion value than the R0.1/t17.4 and R333/t17.4 starches (2.4 ± 0.1 and 2.0 ± 0.0, respectively), the commercial granules were more homogeneous than the acorn starch granules. Pressurization maintained the binomial distribution of the starch granules from R0.1/t17.4 to R333/t17.4, even though there was a small narrowing (Figure S1). The percentage of granules up to 25 µm increased by 6% from R0.1/t17.4 to R333/t17.4 and the percentage of large granules (>25 µm) decreased by 14%, which significantly decreased the span and uniformity dispersion values by 15 and 12%, respectively. These results indicate that starch granule disassociation may have occurred, strengthening the distribution and yielding a higher homogeneity of granules. Such a hypothesis is found within the significant decrease of the D_{10}, D_{50}, and D_{90} values by 5, 7, and 18%, respectively, indicating an increase in the maximum particle diameter below which 10, 50, and 90% of the starch granule volume exists. Indeed, there was a significant increase in the De Brouckere diameter by 18%. Moreover, the significant variation of the Sauter diameter indicates that the mean size of the starch granule distribution decreased by 5%. The increase in the Sauter diameter could have been due to the significant increase of the specific surface area by 5% (Table 1).

The percentage of very small, small, medium, and large granules found for *Q. pyrenaica* (P0.1/t20; 9.3 ± 0.0, 24.5 ± 0.1, 44.0 ± 0.1, and 22.2 ± 0.2%, respectively) and *Q. robur* (R0.1/t17.4; 8.2 ± 0.0, 23.8 ± 0.0, 37.9 ± 0.0, and 30.1 ± 0.1%, respectively) were comparable to those found for *Q. wutaishanica* (10.6, 34.5, 40.8, and 14.14%) [16].

2.3. Amylose and Amylopectin

Regarding amylose, the commercial starch had a significantly lower content when compared to the P0.1/t20 and R0.1/t17.4 starches (Table 2).

Table 2. Characterization of the commercial, and *Q. pyrenaica* and *Q. robur* acorn starches extracted under control and optimum conditions.

Parameter	Commercial	P0.1/t20	P460/t20	R0.1/t17.4	R333/t17.4
Moisture (%)	9.6 ± 0.0 ^{a}	13.1 ± 0.3 ^{c}	11.5 ± 0.2 ^{b}	13.9 ± 0.1 ^{d}	16.5 ± 0.2 ^{e}
Total solids (%)	90.4 ± 0.0 ^{e}	86.9 ± 0.3 ^{c}	88.5 ± 0.2 ^{d}	86.1 ± 0.1 ^{b}	83.5 ± 0.2 ^{a}
Damaged starch (%)	1.01 ± 0.03 ^{b}	0.56 ± 0.01 ^{a}	3.83 ± 0.07 ^{c}	0.57 ± 0.01 ^{a}	1.09 ± 0.08 ^{b}
Amylose (%)	51.1 ± 0.1 ^{a}	53.2 ± 0.5 ^{b}	67.7 ± 0.0 ^{e}	58.2 ± 0.1 ^{c}	66.0 ± 0.0 ^{d}
Amylopectin (%)	45.0 ± 0.1 ^{e}	27.6 ± 0.5 ^{d}	19.8 ± 0.0 ^{b}	26.1 ± 0.1 ^{c}	15.0 ± 0.0 ^{a}
Amylose/Amylopectin (unitless)	1.14 ± 0.00 ^{a}	1.93 ± 0.05 ^{b}	3.41 ± 0.00 ^{d}	2.23 ± 0.01 ^{c}	4.40 ± 0.00 ^{e}

P0.1/t20: *Q. pyrenaica* acorn starch extracted under control conditions (0.1 MPa for 20 min); P460/t20: *Q. pyrenaica* acorn starch extracted under optimum conditions (460 MPa for 20 min); R0.1/t17.4: *Q. robur* acorn starch extracted under control conditions (0.1 MPa for 17.4 min); R333/t17.4: *Q. robur* acorn starch extracted under optimum conditions (333 MPa for 17.4 min); significant differences between starches are represented by lower-case letters and values in the same row with the same letters are not significant ($p > 0.05$).

The amylose content from *Q. pyrenaica* and *Q. robur* starch increased significantly by 27% from P0.1/t20 to P460/t20 and 13% from R0.1/t17.4 to R333/t17.4, respectively. Previous authors also observed an increase in the amylose starch content after pressurization for litchi, maize, mango, potato, sweet potato, buckwheat, and sorghum starches [9,32–34]. The amylose contents of *Q. pyrenaica* (P0.1/t20; 53.2 ± 0.5%) and *Q. robur* starches (R0.1/17.4; 58.2 ± 0.1%) were similar to those reported for *Q. rotundifolia* (53.7–54.5%) and *Q. suber* (57.9–59.4%) starches, respectively [35]. However, they were higher than those reported for *Q. ilex* (25.8%) [36], *Q. palustris* (31.4%) [18], *Q. serrata* (27.1%) [37], *Q. suber* (24.4%) [38], *Q. calliprinos* (29.2%) [39], *Q. suber* (34.4%) [36], *Q. acutissima* (30.6%) [15], *Q. ilex* (31%) [40], and *Q. wutaishanica* (31.4%) [16], *Q. ilex* (39.0%) [41], *Q. pubescens* (19.5%) [36], *Q. rotundifolia* (41.7%) [42], *Q. leucotrichophora* (15.6%) [14], *Q. brantii* (~18%) [21], *Q. coccifera* (36%) [40], and *Q. suber* (48.9%) [42] starches. The mechanical forces created during pressurization may have led to the cleavage of covalent bonds along the polymeric chains. Since amylopectin is more prone to degradation than amylose, the higher amylose content was associated with the cleavage of α-D-(1,6)-glucose bounds [43]. Indeed, the amylopectin contents decrease significantly after pressurization by 28% from P0.1/t20 to P460/t20 for *Q. pyrenaica* and 43% from R0.1/t17.4 to R333/t17.4 for *Q. robur*, respectively (Table 2).

2.4. Damaged Starch

For *Q. pyrenaica*, both P460/t20 and commercial starches had a significantly higher content when compared to the P0.1/t20 starch (Table 2). Pressurization from P0.1/t20 to P460/t20 increased significantly the damaged starch content by 584%, which may have been due to the rearrangement of amylose and amylopectin, leaving the chains more susceptible to enzymatic action and/or amylopectin degradation into amylose [30]. Previous authors also observed an increase in the damaged starch content from quinoa, lentils, potato, sweet potato, and maize starches under pressurized conditions [30,31,33,44,45]. For *Q. robur*, both commercial and R333/t20 starches had similar contents when compared to the R0.1/t17.4 starch, but the damaged starch content increased by 91% from R0.1/t17.4 to R333/t17.4. These results show that *Q. pyrenaica* starch is more susceptible to pressurization than *Q. robur* starch. For *Q. pyrenaica*, it is thought that a few short chains of amylopectin may be in the form of a double helix, causing water molecules to enter the crystalline zones of the starch granules more easily during pressurization and thus destroying the outer layer of the starch granule structure. Regarding *Q. robur*, a greater part of these chains may be associated with a double helix, which makes the penetration of water molecules difficult, making it necessary to apply higher pressure levels to destroy the crystalline structures [33]. However, future analyses of the distribution of different amylopectin sub-chains should be performed to obtain more detailed information and thus better explain the observed results.

2.5. Fourier Transform Infrared Spectroscopy

Starches showed similar FTIR spectra, but the spectra of pressurized acorn starches (P460/t20 and R333/t174) were more similar to the spectrum of the commercial starch than the corresponding native acorn starches (P0.1/t20 and R0.1/t174) (Figure S2).

Regarding the degree of short-range molecular order of *Q. pyrenaica*, both commercial and P460/t20 starches had similar but significantly lower 1047/1022 ratios when compared to P0.1/t20 starch (Table S1). Furthermore, the 1047/1022 ratio decreased significantly by 2% after pressurization from P0.1/t20 to P460/t20, which indicates a loss of the ordered structure. For *Q. robur*, the commercial starch had significantly lower 1047/1022 ratios when compared to both R0.1/t17.4 and R333/t17.4 starches. The 1047/1022 ratio also decreased significantly after pressurization R0.1/t17.4 and R333/t17.4 but by 10%, showing a higher loss of ordered structure (Table S1). The 1047/1022 ratios of *Q. pyrenaica* starch (P0.1/t20; 1.079 ± 0.001) were more similar to those previously reported for *Q. wutaishanica* (1.049) [16] and *Q. variabilis* starches (1.082) [17] than that of *Q. robur* starch (R0.1/17.4; 1.194 ± 0.007) found in the present paper.

Concerning the internal changes in the double helix degree of *Q. pyrenaica*, the commercial starch had statistically lower 995/1022 ratios than the P0.1/t20 and P460/t20 starches (Table S1). The 995/1022 ratio decreased significantly by 4% from P0.1/t20 to P460/t20, indicating a weakening hydrogen bond between amylopectin chains of double helix structures [10,46]. For *Q. robur*, the commercial starch also had statistically lower 995/1022 ratios than the R0.1/t17.4 to R333/t17.4 starches. The 995/1022 ratio also decreased significantly after pressurization from R0.1/t17.4 to R333/t17.4 but by 18%, which shows higher internal changes of the double helix. These results agree with each other since the loss of an ordered structure will also imply a loss of the double helix degree.

2.6. X-ray Diffraction

The crystalline structures of the amylopectin double chains can have different arrangements and can be mainly categorized as type-A, B, or C, according to the X-ray diffraction pattern [47]. The unit cell of type-A crystals is formed by seven double helices in a staggered monoclinic lattice with eight water molecules. In comparison, type-B consists of six double helices enclosing a large void that can harbor up to 36 water molecules. Type-C is believed to be a combination of type-A and type-B. The commercial starch had an unresolved doublet at 2θ = 17.3° and 18.1° and two peaks at 2θ = 15.3° and 23.2°, which is typical of the type-A diffraction pattern. Acorn starches showed a typical type-C diffraction pattern with four single diffraction peaks at 2θ = 5.7, 15.3, 17.3, and 23.0° with an additional faint peak at 2θ = 20.1° possibly due to starch–lipid complexes (Figure 2).

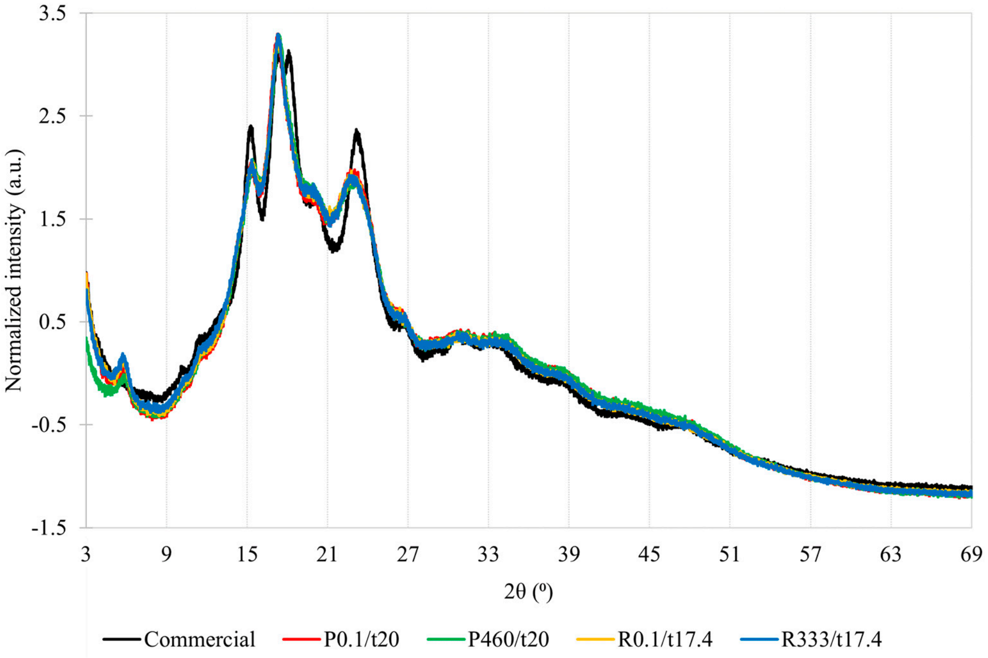

Figure 2. X-ray diffraction pattern of the commercial starch (black line); *Q. pyrenaica* acorn starch extracted under control conditions (red line; 0.1 MPa for 20 min—P0.1/t20); *Q. pyrenaica* acorn starch extracted under optimum conditions (green line; 460 MPa for 20 min—P460/t20); *Q. robur* acorn starch extracted under control conditions (yellow line; 0.1 MPa for 17.4 min—R0.1/t17.4); *Q. robur* acorn starch extracted under optimum conditions (blue line; 333 MPa for 17.4 min—R333/t17.4).

This diffraction pattern, observed for the current *Q. pyrenaica* and *Q. robur* starches, was also found for *Q. rotundifolia* [48], *Q. suber* [48], *Q. fabri* [22], *Q. brantii* [20], and *Q. wutaishanica* [16], but a type-A diffraction pattern was found for *Q. ilex* [49], *Q. glandulifera* [50], *Q. acutissima* [15], *Q. palustris* [18], *Q. suber* [51], and *Q. variabilis* [17]. According to the literature, the type-A and type-C patterns tend to shift towards type-B after pressurization whilst type-B is usually kept. Since the diffraction peaks and pattern were preserved after pressurization, it is thought that the compressive effect of pressure might have been felt on the amorphous regions and/or the pressure level was not sufficient to alter the crystalline structures of the amylopectin double chains due to the high amylose content [47,52].

Regarding relative crystallinity, commercial starch showed a significantly higher value than acorn starches, but pressurization had no impact on acorn starch from *Q. pyrenaica* and *Q. robur* (Table S1). The relative crystallinity values of *Q. pyrenaica* (P0.1/t20; 29.3 ± 1.3%) and *Q. robur* (R0.1/17.4; 22.4 ± 1.6%) starches were following the *Q. wutaishanica* (24.3%) [16], *Q. glandulifera* (23.5%) [50], and *Q. palustris* (22.3%) [18] starches, but were inferior to those found for *Q. variabilis* (30.6%) [17], *Q. rotundifolia* (43.1–46.6%) and *Q. suber* (43.1–44.0%) [48], *Q. fabri* (48.2%) [22], and *Q. brantii* (47.8%) [20]. These results may seem contradictory to those verified in the FTIR analysis; however, it is necessary to keep in mind that the crystallinity calculation in the X-ray analysis is relative since it is performed based on the integration of areas of crystalline and amorphous domains from the diffractogram. Therefore, this determination is thought to be less sensitive to minor variations than the one that is inferred based on the FTIR analysis.

2.7. Solubility and Swelling Power

The solubility values of the different starches increased with the corresponding swelling power values ($r^2 < 0.96$, $p > 0.05$), showing that solubilization and granular swelling occurred simultaneously, as previously reported for *Q. rotundifolia* and *Q. suber* [35]. Such can be justified by considering that a fraction of amylose can be entangled within the amylopectin, while the remaining fraction is free [14]. Concerning solubility, no solubilization was seen at 50 °C but solubilization increased significantly from 60 to 100 °C (Table 3).

Table 3. Solubility and swelling power values of the commercial, *Q. pyrenaica*, and *Q. robur* acorn starches extracted under control and optimum conditions.

Parameter	T (°C)	Commercial	P0.1/t20	P460/t20	R0.1/t17.4	R333/t17.4
Solubility (%)	50	n.d.	n.d.	n.d.	n.d.	n.d.
	60	0.83 ± 0.07^{aA}	2.36 ± 0.18^{aC}	1.60 ± 0.10^{aB}	1.46 ± 0.19^{aB}	1.82 ± 0.18^{aBC}
	70	4.71 ± 0.33^{bA}	8.97 ± 0.62^{bC}	6.22 ± 0.35^{bB}	4.52 ± 0.13^{bA}	5.07 ± 0.16^{bAB}
	80	7.58 ± 0.51^{cA}	11.79 ± 0.06^{cD}	10.33 ± 0.24^{cC}	8.79 ± 0.12^{cB}	7.71 ± 0.02^{cA}
	90	19.09 ± 0.08^{dC}	16.16 ± 0.21^{dA}	16.18 ± 0.26^{dA}	17.74 ± 0.36^{dB}	16.53 ± 0.40^{dA}
	100	22.88 ± 0.12^{eE}	17.82 ± 0.16^{eB}	16.66 ± 0.09^{eA}	19.71 ± 0.14^{eD}	18.74 ± 0.36^{eC}
Swelling power (g/g)	50	n.d.	n.d.	n.d.	n.d.	n.d.
	60	2.73 ± 0.11^{aA}	6.40 ± 0.10^{aB}	6.15 ± 0.02^{aB}	6.53 ± 0.09^{aB}	6.52 ± 0.37^{aB}
	70	8.73 ± 0.04^{bA}	10.10 ± 0.02^{bB}	9.05 ± 0.02^{bA}	8.64 ± 0.21^{bA}	8.82 ± 0.11^{bA}
	80	8.82 ± 0.05^{bA}	12.20 ± 0.09^{cC}	10.20 ± 0.34^{cB}	9.99 ± 0.31^{bB}	10.19 ± 0.37^{cB}
	90	15.68 ± 0.07^{cB}	15.71 ± 0.17^{dB}	13.31 ± 0.04^{dA}	15.39 ± 0.49^{cB}	15.79 ± 0.23^{dB}
	100	19.03 ± 0.42^{cC}	16.83 ± 0.03^{eB}	14.28 ± 0.26^{eA}	16.75 ± 0.60^{cB}	14.07 ± 0.17^{eA}

P0.1/t20: *Q. pyrenaica* acorn starch extracted under control conditions (0.1 MPa for 20 min); P460/t20: *Q. pyrenaica* acorn starch extracted under optimum conditions (460 MPa for 20 min); R0.1/t17.4: *Q. robur* acorn starch extracted under control conditions (0.1 MPa for 17.4 min); R333/t17.4: *Q. robur* acorn starch extracted under optimum conditions (333 MPa for 17.4 min); n.d.: not detected. Significant differences between starches are represented by lower-case letters and values in the same row with the same letters are not significant ($p > 0.05$). Significant differences between temperatures are represented by capital-case letters and values in the same column with the same letters are not significant ($p > 0.05$).

When heated under enough temperature, the crystalline regions of starch granules are broken and hydrogen bonds are formed between the water molecules and the free hydroxyl groups of amylose and amylopectin. This enhances the water absorption capacity and solubility, the latter due to amylose leaching [22]. For *Q. pyrenaica*, the solubility values of the P0.1/t20 and P460/t20 starches measured until 80 °C were higher than the commercial starch (Table 3). However, the solubility values of the P0.1/t20 and P460/t20 starches measured at 90–100 °C were lower than the commercial starch. The higher solubility values of acorn starch at lower temperatures in relation to the commercial starch encourages the usage of acorn starch as an food additive in fermented yoghurt and milk products [49]. Pressurization from P0.1/t20 to P460/t20 led to an overall significant decrease in the solubility values measured at 60–100 °C. Regarding *Q. robur*, solubility values at 60–80 °C of the R0.1/t17.4 and P333/t17.4 starches were statistically inferior and/or similar to the commercial starch (Table 3). The commercial starch had significantly higher solubility at 90–100 °C than the R0.1/t17.4 and P333/t17.4 starches. Pressurization from R0.1/t17.4 to P333/t17.4 did not change the solubility values until 70 °C, but they decreased significantly at 80–100 °C. It is considered that the reduction in solubility may be due to a greater entanglement of amylose caused by the increase in its content (Table 2).

In the matter of swelling power, no swelling power was seen at 50 °C. However, the swelling power increased significantly from 60 to 100 °C (Table 3). Concerning *Q. pyrenaica*, the swelling power of the commercial starch measured until 80 °C was significantly lower than those of the P0.1/t20 and P460/t20 starches. However, the commercial starch had significantly higher swelling power values at 90–100 °C than the P0.1/t20 and P460/t20 starches. Pressurization from P0.1/t20 to P460/t20 did not change the swelling power values until 60 °C, but a significant reduction was observed from 70 to 100 °C. Previous studies in the literature also report a decrease in both solubility and swelling power for lentils, wheat, quinoa, maize, potato, sweet potato, rice, kidney bean, corn, and waxy corn starch [27,33,44,53–55]. For *Q. robur*, the swelling power values of the commercial starch were generally lower than R0.1/t17.4 and R333/t17.4 starches up to 80 °C. However, the commercial starch showed higher values than both the R0.1/t17.4 and R333/t17.4 acorn starches at 100 °C. However, pressurization from R0.1/t17.4 to R333/t17.4 did not significantly alter the swelling power values up to 90 °C. However, there was a significant reduction at 100 °C.

Swelling power is a measurement of the granule water-holding capacity, i.e., water absorption and retention capacity of starch granules [56]. During pressurization, the amylose and amylopectin chains could have been altered, thus limiting the swelling power [55]. So, in other words, it is thought that the observed reduction in swelling power may have been caused by the decrease in solubility and/or cleavage of the amylopectin chains (Table 2). Granular disintegration (as evidenced by increased contents of damaged starch) could also inhibit amylose solubilization and lead to a lower solubility and swelling power [33]. The observed limited swelling power values from 60 to 100 °C could have been due to strong interactions between starch chains due to the high amylose content and/or the presence of amylose–lipid complexes [14,35] (Figure 2 and Table S1).

The solubility and swelling power values of *Q. pyrenaica* (P0.1/t20; 2.36 ± 0.18–17.82 ± 0.18% and 6.40 ± 0.10–16.83 ± 0.03 g/g, respectively) and *Q. robur* (R0.1/17.4; 1.46 ± 0.19–19.71 ± 0.14% and 6.53 ± 0.09–16.75 ± 0.60 g/g, respectively) starches diverged from those of *Q. brantii* (9.7% and 24.5 g/g, respectively) [20], *Q. fabri* (0.26–4.87% and 0.024–0.14 g/g, respectively) [22], *Q. brantii* (60–65% and 0.26–0.27 g/g, respectively) [21], *Q. rotundifolia* (9.1 g/g) [42], *Q. suber* (9.0 g/g) [42], and *Q. ilex* (0.2–14.0% and 8.95–13 g/g, respectively) [41].

2.8. Differential Scanning Calorimetry

It was verified that starch gelatinization is an endothermic phenomenon characterized by a positive increase in the enthalpies of the system (indicated by the black arrows in Figure 3).

Regarding the gelatinization temperatures, the commercial starch showed significantly higher T_o, T_p, and T_c temperatures than the acorn starches (Table S2). On the one hand, this shows that commercial starch requires higher temperatures to trigger gelatinization than acorn starches. Thus, the hydrogen bonds between amylose and/or amylopectin appear to be stronger in commercial starch than in acorn starches. These results agree with those in Table 2 since gelatinization (i.e., amylose leaching and solubilization) can occur only when the temperature used is equal to or higher than T_o. Furthermore, the solubility of the commercial starch at 60 °C was lower than the acorn starches due to differences in the T_o temperatures.

Pressurization did not affect the T_o, T_p, and T_c temperatures of both acorn starch species, as previously reported for chestnut flour [25]. The T_o, T_p, and T_c values found for *Q. pyrenaica* (P0.1/t205; 5.4 ± 0.3, 62.9 ± 0.4, and 68.6 ± 1.3 °C, respectively) and *Q. robur* (R0.1/17.4; 55.0 ± 0.4, 62.3 ± 0.2, and 66.8 ± 0.3 °C) starches were generally lower to those of *Q. wutaishanica* (60.1, 70.5, and 79.3 °C, respectively) [16], *Q. fabri* (60.5, 63.8, and 70.2 °C, respectively) [22], *Q. palustris* (65.0, 73.7, and (-) °C, respectively) [18], *Q. brantii* (60.5, 63.8, and 70.2 °C, respectively) [20], *Q. acutissima* (60.1, 69.5, and 80.6 °C, respectively) [15], *Q. glandulifera* (60.8, 66.5, and 73.8 °C, respectively) [50], *Q. ilex* (61.0–75.1, 17.8–88.1, and 98.0–120.0 °C, respectively) [41], *Q. rotundifolia* (58.7–60.9, 66.7–65.7, and 74.0–74.7 °C, respectively) [35], and *Q. suber* (58.4–58.6, 64.1–64.8, and 71.4–73.3 °C, respectively) [35] starches.

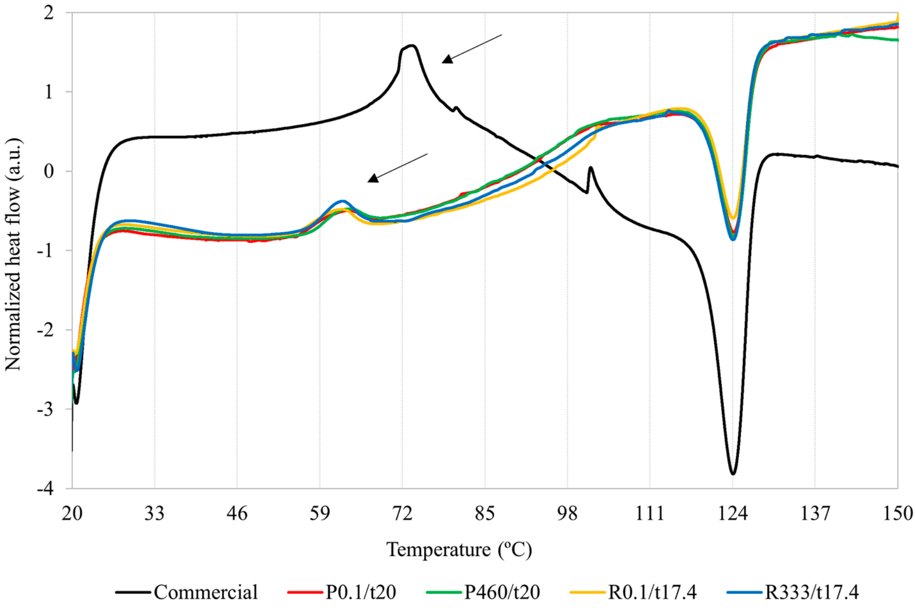

Figure 3. DSC thermograms of the commercial starch (black line); *Q. pyrenaica* acorn starch extracted under control conditions (red line; 0.1 MPa for 20 min—P0.1/t20); *Q. pyrenaica* acorn starch extracted under optimum conditions (green line; 460 MPa for 20 min—P460/t20); *Q. robur* acorn starch extracted under control conditions (yellow line; 0.1 MPa for 17.4 min—R0.1/t17.4); *Q. robur* acorn starch extracted under optimum conditions (blue line; 333 MPa for 17.4 min—R333/t17.4). The black arrows point to the endothermic phenomena corresponding to starches' gelatinization.

Since the gelatinization temperatures were not affected after pressurization, this reinforces the hypothesis that the decrease in solubility and swelling power of starches after pressurization could have been due to the formation of lipid–amylose complexes, as well as the scenario that the observed limited swelling power values were attributed due to strong interactions between amylose and/or amylopectin and/or the presences of amylose–lipid complexes [14,35].

Regarding gelatinization enthalpies, the commercial starch also showed significantly higher gelatinization enthalpies than the acorn starches (Table S2). This shows that commercial starch requires a higher energy input to disrupt the hydrogen intra-helix bonds of the crystalline regions (i.e., initiate and complete the gelatinization process) when compared to the acorn starches since the commercial starch had significantly higher gelatinization temperatures. Yet, pressurization did change the gelatinization enthalpies of acorn starches, as reported for chestnut flour [25]. The gelatinization enthalpies found for the *Q. pyrenaica* (P0.1/t20; 12.7 ± 1.5 J/g) and *Q. robur* (R0.1/17.4; 11.9 ± 1.3 J/g) starches are in accordance to those found for the *Q. brantii* (14.9 J/g) [20], *Q. acutissima* (9.7 J/g) [15], and *Q. fabri* (10.9 J/g) [22] acorn starches, but diverge from the *Q. palustris* (20.8 J/g) [18], *Q. suber* (4.2–4.3 J/g) [35], *Q. wutaishanica* (4.3 J/g) [16], *Q. glandulifera* (4.3 J/g) [50], and *Q. rotundifolia* (4.2–4.3 J/g) [35] starches.

It is thought that the commercial starch would have shown a greater relative crystallinity than the acorn starches since it had a lower amylose/amylopectin ratio (Tables 2 and S1). In other words, a lower amylose content makes it possible for amylopectin chains to form more crystalline domains. Since these interactions between chains involve the formation of hydrogen bonds, the gelatinization temperatures will be higher and, consequently, more energy will have to be supplied to break the hydrogen bonds (higher enthalpies of gelatinization) (Table S2).

2.9. *In Vitro Digestibility*

Concerning *Q. pyrenaica*, both P460/t20 and commercial starches were shown to have statistically more digestible starch than P0.1/t20 starch (Table 4). However, the P460/t20 starch had significantly more RDS, but less SDS and TDS than the commercial starch. Furthermore, the RDS, SDS, and TDS contents increased significantly by 176, 52, and 64%, respectively from P0.1/t20 to P460/t20, while the RS content decreased by 47%. In other words, the increase of RDS and SDS contents might have occurred by the transformation of RS. The decrease of the RS contents may have resulted from structural modifications and rupture of starch molecules, mainly the cleavage of α-(1,6)-glycosidic bonds of amylopectin (Table 2).

Table 4. In vitro digestibility characterization of the commercial, *Q. pyrenaica*, and *Q. robur* acorn starches extracted under control and optimum conditions.

Starch Content	Commercial	P0.1/t20	P460/t20	R0.1/t17.4	R333/t17.4
RDS (g/100g SM)	$16.6 \pm 0.4\ ^{c}$	$7.9 \pm 0.5\ ^{a}$	$21.8 \pm 0.5\ ^{d}$	$12.3 \pm 0.8\ ^{b}$	$13.0 \pm 1.0\ ^{b}$
SDS (g/100g SM)	$46.3 \pm 1.9\ ^{d}$	$18.2 \pm 0.4\ ^{a}$	$27.7 \pm 1.6\ ^{b}$	$38.1 \pm 1.9\ ^{c}$	$20.4 \pm 1.9\ ^{a}$
TDS (g/100g SM)	$86.9 \pm 0.4\ ^{d}$	$40.3 \pm 2.9\ ^{a}$	$65.9 \pm 3.5\ ^{c}$	$50.4 \pm 1.2\ ^{b}$	$49.4 \pm 2.4\ ^{ab}$
RS (g/100g SM)	$9.2 \pm 0.3\ ^{a}$	$40.5 \pm 1.4\ ^{d}$	$21.6 \pm 0.2\ ^{b}$	$33.9 \pm 0.1\ ^{c}$	$31.6 \pm 1.2\ ^{c}$
TS (g/100g SM)	$96.1 \pm 0.6\ ^{b}$	$80.8 \pm 4.3\ ^{a}$	$87.5 \pm 3.7\ ^{ab}$	$84.3 \pm 1.1\ ^{a}$	$81.0 \pm 1.2\ ^{a}$

P0.1/t20: *Q. pyrenaica* acorn starch extracted under control conditions (0.1 MPa for 20 min); P460/t20: *Q. pyrenaica* acorn starch extracted under optimum conditions (460 MPa for 20 min); R0.1/t17.4: *Q. robur* acorn starch extracted under control conditions (0.1 MPa for 17.4 min); R333/t17.4: *Q. robur* acorn starch extracted under optimum conditions (333 MPa for 17.4 min); RDS: rapidly digestible starch; SDS: slowly digestible starch; TDS: total digestible starch; RS: resistant starch; TS: total starch; SM: starchy material. Significant differences between starches are represented by lower-case letters and values in the same row with the same letters are not significant ($p > 0.05$).

These results are similar to those for wheat, potato, sweet potato, rice, kidney bean, corn, waxy wheat, waxy rice, and waxy corn starch [53,55,57,58]. Regarding *Q. robur*, there were no significant differences in the RS contents from R0.1/t17.4 to R333/t17.4, which were statistically higher than the RDS and SDS contents of the commercial starch. The pressure level applied may have been insufficient to destroy the starch granule structure [58]. No differences were also found in the RDS and TDS contents from R0.1/t17.4 to R333/t17.4, which were statistically lower than the RDS and TDS contents of the commercial starch. The commercial starch had a significantly higher SDS content than both *Q. robur* starches, but the SDS contents decreased by 46% from R0.1/t17.4 to R333/t17.4.

Pressurization may have stabilized amylopectin and double-amylose molecules by increasing the content of $^{4}C_{1}$ chair conformations and/or strengthening the Van der Waals and electrostatic forces of adjacent chains, which may have led to the reduction of interchain distances and surface area of both the amylopectin and double-amylose molecules [59]. These more compacted molecules can then be related to a decreased susceptibility of starch to amylolytic enzymes. These results indicate that the different starch fractions from *Q. pyrenaica* and *Q. robur* are affected differently when pressurized to the corresponding optimum extraction conditions. The RDS, SDS, and RS contents found for *Q. pyrenaica* (P0.1/t20; 7.9 ± 0.5, 18.2 ± 0.4, and 40.5 ± 1.4%, respectively) and *Q. robur* (R0./17.4; 12.3 ± 0.8, 38.1 ± 1.9, and 33.9 ± 0.1%, respectively) starches diverge from those of *Q. wutaishanica* (17.0, 22.4, and 60.6%, respectively) [16] and *Q. variabilis* starches (17.2, 23.8, and 59.0%, respectively) [17].

Concerning the total starch, no differences were found in the content between commercial and P460/t20 starches, nor between the P0.1/t20 and P460/t20 starches from *Q. pyrenaica* (Table 3). For *Q. robur*, the commercial starch presented a higher total content than the R0.1/t17.4 and R333/t17.4 starches. It is believed that such differences may be due to the presence of small contents of protein and/or fiber that may have been sieved along with the starch granules during extraction.

2.10. Steady Flow Behavior

The consistency coefficient and flow behavior index for all starches are summarized in Table 5. The consistency coefficient measures the starch fullness and can be seen as a viscosity criterion [54]. For *Q. pyrenaica*, the commercial and P460/t20 starches had similar consistency coefficient values concerning the P0.1/t20 starch. Pressurization from P0.1/t20 to P460/t20 significantly decreases the consistency coefficient by 34%. The same effect was observed for mango, maize, and quinoa starches [27,32]. This indicates a decrease in flow and shear stress resistance, which may have been due to the cleavage of α-(1,6)-glycosidic bounds (Table 2).

Table 5. Steady flow and dynamic oscillation characterization of the commercial, *Q. pyrenaica*, and *Q. robur* acorn starches extracted under control and optimum conditions.

Parameter	Commercial	P0.1/t20	P460/t20	R0.1/t17.4	R333/t17.4
σ					
K (Pa.s^{n})	0.020 ± 0.000^{a}	0.035 ± 0.001^{b}	0.020 ± 0.000^{a}	0.036 ± 0.004^{b}	0.031 ± 0.001^{b}
n (unitless)	0.859 ± 0.001^{b}	0.782 ± 0.003^{a}	0.859 ± 0.001^{b}	0.780 ± 0.023^{a}	0.778 ± 0.027^{a}
$\boldsymbol{\eta^*}$					
H (unitless)	-0.957 ± 0.004^{a}	-0.927 ± 0.005^{b}	-0.906 ± 0.007^{c}	-0.909 ± 0.008^{c}	-0.895 ± 0.004^{c}
G^* (Pa)	53.5 ± 2.6^{a}	53.9 ± 5.6^{a}	60.5 ± 2.3^{a}	58.2 ± 5.7^{a}	63.0 ± 11.8^{a}
$\boldsymbol{G^*}$					
n^* (unitless)	0.033 ± 0.002^{a}	0.071 ± 0.001^{b}	0.087 ± 0.001^{c}	0.091 ± 0.000^{c}	0.098 ± 0.001^{d}
K^* (Pa.s^{n})	328.5 ± 9.7^{a}	360.7 ± 4.6^{ab}	373.7 ± 1.9^{b}	411.3 ± 9.6^{c}	467.2 ± 11.3^{d}
$\boldsymbol{G'}$					
n' (unitless)	0.033 ± 0.001^{a}	0.071 ± 0.001^{b}	0.086 ± 0.001^{c}	0.091 ± 0.000^{d}	0.098 ± 0.001^{e}
K' (Pa.s^{n})	327.4 ± 9.7^{a}	358.0 ± 4.7^{ab}	390.7 ± 6.3^{bc}	407.7 ± 9.2^{c}	462.0 ± 12.0^{d}
$\boldsymbol{G''}$					
n'' (unitless)	0.096 ± 0.002^{a}	0.086 ± 0.008^{a}	0.126 ± 0.005^{b}	0.097 ± 0.003^{a}	0.114 ± 0.001^{b}
K'' (Pa.s^{n})	23.0 ± 1.5^{a}	42.2 ± 1.3^{b}	52.5 ± 2.1^{c}	47.3 ± 4.4^{ab}	61.1 ± 3.1^{d}

P0.1/t20: *Q. pyrenaica* acorn starch extracted under control conditions (0.1 MPa for 20 min); P460/t20: *Q. pyrenaica* acorn starch extracted under optimum conditions (460 MPa for 20 min); R0.1/t17.4: *Q. robur* acorn starch extracted under control conditions (0.1 MPa for 17.4 min); R333/t17.4: *Q. robur* acorn starch extracted under optimum conditions (333 MPa for 17.4 min); σ: shear stress; $\boldsymbol{\eta^*}$: complex viscosity; $\boldsymbol{G^*}$: complex modulus; $\boldsymbol{G'}$: elastic modulus; $\boldsymbol{G''}$: viscous modulus. Significant differences between starches are represented by lower-case letters and values in the same row with the same letters are not significant ($p > 0.05$).

For *Q. robur*, both R0.1/t17.4 and R333/t17.4 starches had significantly higher consistency values than the commercial starch, indicating that *Q. robur* acorn starches have superior resistance to flow and shear stress than the commercial starch. However, pressurization did not affect the consistency coefficient from R0.1/t17.4 to R333/t17.4. The consistency coefficient values of *Q. pyrenaica* (P0.1/t20; 0.035 ± 0.001 Pa.s^{n}) and *Q. robur* (R0.1/17.4; 0.036 ± 0.004 Pa.s^{n}) had a similar order of magnitude to that found for *Q. brantii* (0.011 Pa.s^{n}) [60].

Concerning the index of flow behavior, all analyzed starches had values lower than 1, indicating that starches were pseudoplastic fluids (Table 5). For *Q. pyrenaica*, the commercial and P460/t20 starches showed a similar index of flow behavior when compared to P0.1/t20 starch. Pressurization from P0.1/t20 to P460/t20 led to a significant increase in the flow behavior index by 10%. The same effect was observed for mango, maize, and quinoa starches [27,32]. This indicates an increase in fluidity (associated with the decrease of the consistency coefficient), thus weakening the pseudoplastic behavior.

Since *Q. pyrenaica* starch showed a much greater increase in amylose after pressurization than *Q. robur* starch (Table 2), the α-D-(1,4)-glucose chains of P460/t20 starch could not have the same anisotropic capacity as P0.1/t20 starch, decreasing the index values of flow behavior. In the case of *Q. robur*, both R0.1/t17.4 and R333/t17.4 starches had a significantly lower index of flow behavior than the commercial starch, indicating that *Q. robur* acorn starches have a superior pseudoplastic behavior. Pressurization had no effect on the index of flow behavior from R0.1/t17.4 to R333/t17.4. The index of the flow behavior of *Q. pyrenaica* (P0.1/t20; 0.782 ± 0.003) and *Q. robur* (R0.1/17.4; 0.780 ± 0.023) was in agreement with that found for *Q. brantii* (0.780) [60].

2.11. Dynamic Oscillation

Figure S3 shows the effect of pressurization on the complex modulus and complex viscosity of all starches analyzed. The complex viscosity measures the total resistance to the angular frequency [61]. The complex viscosity decreased linearly with angular frequency. Still, significant differences were found among the so-called *H* values, which corresponds to the linearization slopes for each of the starches. These values show how the complex viscosity decreases with frequency among the different starches (Table 5). Regarding *Q. pyrenaica*, the commercial starch had a lower *H* value than the P0.1/t20 and P420/t20 starches. Pressurization from P0.1/t20 to P420/t20 significantly increased the *H* values, showing that the complex viscosity of P420/t20 starch decreases more sharply with increasing frequency than the P0.1/t20 starch. This indicates that pressure treatment shifted the behavior from a viscoelastic solid to a viscoelastic fluid [9]. It is thought that this result may be related to the higher amylose increase and reduced amylopectin content since amylose has a linear structure while amylopectin is highly branched (Table 2). For *Q. robur*, the commercial starch had a lower *H* value than the R0.1/t17.4 and P333/t17.4 starches, but pressurization did not affect the *H* values. The *H* values of *Q. pyrenaica* (P0.1/t20; −0.927 ± 0.005) and *Q. robur* (R0.1/17.4; −0.909 ± 0.008) were similar to *Q. brantii* (−0.94) [62].

The complex modulus measures the overall resistance of materials to deformation [61]. According to Figure S3, the complex modulus of the analyzed starches increased with frequency, but significant differences were found in the complex index between starches (Table 5). For *Q. pyrenaica*, the complex index of the commercial starch was significantly lower than that presented by the P0.1/t20 and P420/t20 starches. However, pressurizing from P0.1/t20 to P420/t20 led to a significant increase in the complex index by 23%. This represents an increase in the dependence of the complex modulus with frequency, which, in other words, translates to a decrease in resistance towards deformation. For *Q. robur*, the complex index of the commercial starch was also significantly lower than that presented by the R0.1/t17.4 and P333/t17.4 starches. Pressurizing from R0.1/t17.4 to P333/t17.4 significantly increases the complex index by 8%. These results are lower than those found for quinoa [31]. It is thought that, as pressurization led to a greater increase in amylose content in *Q. pyrenaica* than in *Q. robur*, it is considered that amylose retrogradation may have been facilitated more in *Q. pyrenaica* than in *Q. robur*, leading to a distinct increase in the complex index (Table 2).

The complex modulus is the result of the contribution of the elastic (G') and viscous (G'') components of the materials. The former is the elastic modulus and measures the material's ability to store energy, whilst the latter is the dissipation module and measures the ability to dissipate energy [61]. All starches displayed a predominantly solid-like behavior in the studied frequency range of 0.1–10 Hz since that $G' > G''$, with no crossover (Figure S4). Both moduli increased with increasing frequency, as shown by the index values, but the increment of G'' was higher than that of G'. This indicates a slow development in the mechanical rigidity of the starch gels, as previously observed for chestnuts [25].

Regarding the elastic moduli, they behaved as the complex moduli counterparts (Table 5). In the case of *Q. pyrenaica*, pressurization from P0.1/t20 to P420/t20 significantly increases the elastic index by 21%. For *Q. robur*, pressurizing from R0.1/t17.4 to P333/t17.4 also significantly increases the elastic index by 8%. This indicates that the solid-like behavior of acorn starches decreased after pressurization, i.e., it was transformed from solid-like to a more liquid-like behavior [9]. Hence, the decrease in the overall resistance of the acorn starches to deformation can be explained by the loss of the starch's ability to store energy. The elastic index found for *Q. pyrenaica* (P0.1/t20; 0.071 ± 0.001) and *Q. robur* (R0.1/17.4; 0.091 ± 0.000) was higher than that found for *Q. brantii* (0.05) [62].

Concerning the viscous modulus, it behaved differently than the elastic moduli (Table 5). In the case of *Q. pyrenaica*, the viscous index value of the commercial starch was similar to the one presented by P0.1/t20. However, pressurizing from P0.1/t20 to P420/t20 led to a significant and sharper increase of the viscous index by 47%. For *Q. robur*, the viscous index value of the commercial starch was also similar to the one presented by R0.1/t17.4. Pressurizing from R0.1/t17.4 to P333/t17.4 also led to a significant and sharper increase of the index by 18%. This increase represents an increase in the dependence of the viscous modulus with frequency, which translates into a higher ability to dissipate energy. The viscous index of *Q. pyrenaica* (P0.1/t20; 0.086 ± 0.008) and *Q. robur* (R0.1/17.4; 0.097 ± 0.003) was much lower than that found for *Q. brantii* (0.45) [62].

3. Conclusions

Pressurized starch extraction from *Q. pyrenaica* and *Q. robur* acorns under optimal conditions led to significant structural and property changes, depending on the species. Pressure affected the span distribution and uniformity of acorn starch granules, but the granular morphology remained unaffected. Pressurization increased the amylose/amylopectin ratios and damaged starch contents, particularly in *Q. pyrenaica*. However, relative crystallinity, polymorphism, gelatinization temperatures, and enthalpies remained unchanged. The properties of acorn starches were affected by pressurization, with decreased solubility and swelling power due to amylopectin depolymerization and increased complex resistance to deformation. Pressurization increased in vitro digestibility and decreased pseudoplastic behavior in *Q. pyrenaica* starch, while no differences were observed in *Q. robur*. Acorn starches may be more advantageous than commercial corn starch due to lower gelatinization temperatures, enthalpies, in vitro digestibility, superior pseudoplastic behavior, and lower resistance to deformation, which encourages acorn starch to be used as a food ingredient or additive food product, thus valorizing acorn starches.

4. Materials and Methods

4.1. Acorn Sampling and Commercial Corn Starch

On 22 November 2018, acorns of the *Q. pyrenaica* and *Q. robur* species were harvested in Parque Nacional da Peneda-Gerês, Portugal, in Assento, Terras de Bouro, and Braga. The *Q. robur* oaks were located at Parque Cerdeira (41°45′46.0″ N; 8°11′24.2″ W) and the *Q. pyrenaica* oaks were found next to Rio Homem (41°45′49.7″ N; 8°11′55.9″ W). Acorns were hand collected from the entire area of ground covered by the canopy of various oak trees according to their quality (i.e., absence of putrefaction and no mechanical damage and/or spoilage by larvae were defined as quality controls). Acorns were brought to the laboratory facilities the same day in thermal plastic bags, washed with tap water to remove soil and foliage, cleaned with a fabric cloth, and stored at −20 °C until further use.

A commercial corn starch (Hacendado®, Zamora, Spain) was purchased from a local supermarket.

4.2. Acorn Starch Extraction

The acorn shells were removed by hand with a regular kitchen knife, and the cotyledons were grounded using a regular food processor, screened using 1 mm and 500 μm mesh sieves, and finally stored at −20 °C until further usage.

An 8% (*w*/*v*) acorn flour suspension was prepared with deionized water in low-permeability polyamide-polyethylene bags (IdeiaPack—Comércio de Embalagens, Lda, Viseu, Portugal). Bags were manually heat sealed with minimum air and placed inside the high hydrostatic pressure vessel with an inner diameter of 200 mm and 2000 mm in length (Hiperbaric 55, Hiperbaric, Burgos, Spain). The industrial equipment had a maximum operating pressure of 600 MPa and was connected to a refrigeration unit (RMA KH 40 LT, Ferroli, San Bonifacio, Italy) to control the temperature of the input water used as a pressurizing fluid. Starch extraction conditions were optimized using different pressure levels (0.1, 250, and 500 MPa) and extraction times (5, 12.5, and 30 min) by response surface methodology. The compression rate used was 250 MPa/min and the decompression was instantaneous. Suspensions were centrifuged at 3000× *g* for 20 min, and the pellets were screened using 180 and 40 µm diameter mesh sieves, thoroughly washed with water, and left to stand at 4 °C overnight. The starchy material was collected and dried at 45 °C in a ventilated oven-drying chamber until constant weight.

The optimum starch extraction condition from *Q. pyrenaica* acorns was 460 MPa during 20 min and from *Q. robur* acorns was 333 MPa during 17.4 min (Table 6). Control extraction was performed at 0.1 MPa for 20 min for *Q. pyrenaica* and at 0.1 MPa for 17.4 min for *Q. robur*. Extractions were performed in triplicate.

Table 6. Identification of the starch extraction conditions from *Q. pyrenaica* and *Q. robur* under optimum and control extraction conditions.

***Quercus* spp.**	**Pressure (MPa)**	**Time (min)**	**Nomenclature**
Q. pyrenaica	460	20.0	P460/t20
Q. robur	333	17.4	R333/t17.4
Q. pyrenaica	0.1	20.0	P0.1/t20
Q. robur	0.1	17.4	R0.1/t17.4

4.3. Structural Characterization

4.3.1. Scanning Electron Microscopy

Morphology was examined using a Phenom XL G2 (Thermo Fisher Scientific, Waltham, MA, USA) scanning electron microscope (SEM). Samples were placed on top of the observation pins covered with double-sided adhesive carbon tape (NEM tape; Nisshin, Japan). Afterwards, the samples were coated with gold/palladium on a sputter coater (Polaron, Germany) and visualized. SEM analyses were performed with the equipment operated at a high vacuum and an accelerating voltage of 20 kV using the secondary electron detector. Morphology was accessed according to the literature [63].

4.3.2. Particle Size

Measurements were performed in triplicate using a Mastersizer Hydro EV 3000 (Malvern Instruments Ltd., Worcestershire, UK) by laser diffraction with a constant paddle rotation of 2100 rpm. The absorption index used was 0.10 and the refractive indices of water and starch were 1.33 and 1.53, respectively. The D_{10}, D_{50}, and D_{90} represented the particle sizes at which 10, 50, and 90% of all the particles by volume were smaller, respectively, and the Sauter and De Brouckere mean diameters ($D_{3,2}$ and $D_{4,3}$, respectively) were recorded. Uniformity dispersion and span values were also registered. Granules were classified as large (>25 µm), medium (10–25 µm), small (5–10 µm), and very small (<5 µm) [26].

4.3.3. Damaged Starch, Amylose, and Amylopectin

Damaged starch was quantified in duplicate using a commercial kit from Megazyme, Wicklow, Ireland (REF: K-SDAM) based on the hydration of damaged granules and hydrolysis into maltosaccharides and α-limit dextrins with fungal α-amylase. Results were expressed in percentage (grams of damaged starch per 100 g of starchy material) on a dry basis.

Amylose was quantified in duplicate using a commercial kit from Megazyme International, Wicklow, Ireland (REF: K-AMYL) based on amylopectin precipitation by concanavalin A lectin. Amylopectin was computed by the difference between the total starch and the amylose content. Results were expressed in percentage (grams of amylose or amylopectin per 100 g of starchy material) on a dry basis.

4.3.4. Fourier Transform Infrared Spectroscopy

Measurements were performed in triplicate in the mid-infrared region with a resolution of 4 cm^{-1} using a Spectrum 100 FT-IR Spectrometer (PerkinElmer, MA, USA).

The measurement was conducted at room temperature, and spectra were recorded in the 400–4000 cm^{-1} range at 64 scans.

4.3.5. X-ray Diffraction

Diffractograms were obtained in duplicate using a MiniFlex 600 diffractometer (Rigaku, Tokyo, Japan) with Cu-Kα radiation using a voltage of 40 kV and a current of 15 mA. Starches were scanned from 3 to 70° at a rate of 3°/min at a 0.01° step. Relative crystallinity (RC) was computed according to Equation (1), where C_a is the crystalline area and A_a is the amorphous area.

$$\text{RC (\%)} = \left(\frac{C_a}{C_a + A_a}\right) \times 100 \tag{1}$$

4.4. Property Characterization

4.4.1. Solubility and Swelling Power

Solubility (S) and swelling power (SP) were measured in duplicate according to [35]. A starch suspension in water (1%, *w*/*v*) was incubated in a water bath for 30 min from 50 to 100 °C. Suspensions were then cooled and centrifuged at 4100× *g* for 30 min. The supernatants were freeze dried using a vertical freeze dryer BK-FD12P (Biobase, Shandong, China) and weighed, whilst gels were weighed as is. Solubility and swelling power were computed according to Equations (2) and (3), respectively, where W_{LS} is the weight of the lyophilized supernatant (g), W_S is the starch weight in dry basis (g), and W_G is the gel weight (g). Solubility and swelling power results were expressed in percentage (%; gram of solubilized starch per 100 g of starchy material on a dry basis) and gram of gel per g of non-solubilized starchy material on a dry basis (g/g SM), respectively.

$$\text{S (\%)} = \left(\frac{W_{LS}}{W_S}\right) \times 100 \tag{2}$$

$$\text{SP (g/g)} = \frac{W_G}{W_s \times \left(1 - \frac{S}{100}\right)} \tag{3}$$

4.4.2. Differential Scanning Calorimetry

Thermal characteristics were determined in triplicate using Diamond differential scanning calorimetry equipment (PerkinElmer, Shelton, CT, USA) [35]. The equipment was calibrated with indium and lead for temperature and heat capacity calibration. A mass of 3 mg of starch was weighed into a stainless-steal pan (REF: 03190218, PerkinElmer) and 11 µL of deionized water was added. After being hermetically sealed and left to equilibrate for 2 h at room temperature, the container was heated to 150 °C at 10 °C/min. An empty stainless-steal pan was used as a reference and the flow rate of the nitrogen was 40 mL/min. The onset (T_o; °C), peak (T_p; °C), and conclusion (T_c; °C) temperatures, and gelatinization enthalpy (ΔH) were obtained using the Pyris software (v13.4.0).

4.4.3. In Vitro Digestibility

The rapidly digestible starch (RDS), slowly digestible starch (SDS), total digestible starch (TDS), and resistant starch (RS) fractions were quantified in duplicate using a commercial kit from Megazyme, Wicklow, Ireland (REF: K-DSTRS). Total starch content was defined as the sum of the total digestible (TDS) and resistant starch (RS) fractions. Results were expressed in percentages (grams per 100 g of starchy material) on a dry basis.

4.4.4. Steady Flow Behavior

A starch suspension (1% d.b., *w*/*v*) was prepared in triplicate using deionized water and heated to 90 °C in a water bath for 30 min. Suspensions were cooled down in a water bath until room temperature [62]. A volume of 700 µL of suspension was loaded onto a controlled stress rheometer model CS-50 (Bohlin Instruments, Cranbury, NJ, USA) equipped with a cone–plate geometry (40 mm diameter, 4° cone angle, and 0.15 mm gap). The rheometer was programmed to increase the shear rate from 1 to 200 s^{-1} in 50 s and the experimental data were fitted into a power-law model using Equation (4), where σ is the shear stress (Pa), K is the consistency coefficient (Pa.s^n), $\dot{\gamma}$ is the shear rate (s^{-1}), and n is the flow behavior index (unitless).

$$\sigma = K \times \dot{\gamma}^n \quad (4)$$

4.4.5. Dynamic Oscillation

A starch suspension (8% d.b., w/v) was prepared in triplicate using deionized water and heated to 90 °C in a water bath for 30 min. Suspensions were cooled down in a water bath until room temperature [62]. The gelatinized starches were loaded onto a controlled stress rheometer model CS-50 (Bohlin Instruments, Cranbury, NJ, USA) equipped with a cone–plate geometry (40 mm diameter and 0.15 mm gap). The mechanical spectra were obtained by frequency sweep from 0.63–62.8 rad/s at a constant strain of 0.5% (within the linear viscoelastic region range). The complex modulus (G*), elastic modulus (G'), viscous modulus (G''), and complex viscosity (η*), were recorded as function frequency (ω) and fitted using Equations (5)–(8), where K*, K', and K'' are the consistency coefficients (Pa.s^n) and n*, n', and n'' are the index values (unitless).

$$G^* = K^* \times \omega^{n^*} \quad (5)$$

$$G' = K' \times \omega^{n'} \quad (6)$$

$$G'' = K'' \times \omega^{n''} \quad (7)$$

$$\eta^* = \frac{G^*}{\omega} \quad (8)$$

4.5. Statistical Analysis

Each sort of test involved the analysis of samples at random. After the Shapiro–Willk test confirmed that the data were normal, a one-way ANOVA was conducted to determine the statistical differences between the starches in all of the data. Data were reported as mean standard deviation, keeping the significant values permitted by the size of the standard deviation, and statistical tests were run using Tukey's test at a 5% significance level.

Supplementary Materials: The following supporting information can be downloaded at: https://www.mdpi.com/article/10.3390/gels9090757/s1, Table S1: FTIR and XRD characterization of the commercial starch, *Q. pyrenaica*, and *Q. robur* acorn starches extracted under control and optimum conditions; Table S2: Thermodynamical characterization of the commercial starch, *Q. pyrenaica*, and *Q. robur* acorn starches extracted under control and optimum conditions; Figure S1: Particle size distribution of the commercial starch (black line); *Q. pyrenaica* acorn starch extracted under control conditions (red line; 0.1 MPa for 20 min—P0.1/t20); *Q. pyrenaica* acorn starch extracted under optimum conditions (green line; 460 MPa for 20 min—P460/t20); *Q. robur* acorn starch extracted under control conditions (yellow line; 0.1 MPa for 17.4 min—R0.1/t17.4); *Q. robur* acorn starch extracted under optimum conditions (blue line; 333 MPa for 17.4 min—R333/t17.4); Figure S2: FTIR spectra of the commercial starch (black line); *Q. pyrenaica* acorn starch extracted under control conditions (red line; 0.1 MPa for 20 min—P0.1/t20); *Q. pyrenaica* acorn starch extracted under optimum conditions (green line; 460 MPa for 20 min—P460/t20); *Q. robur* acorn starch extracted under control conditions (yellow line; 0.1 MPa for 17.4 min—R0.1/t17.4); *Q. robur* acorn starch extracted under optimum conditions (blue line; 333 MPa for 17.4 min—R333/t17.4); Figure S3: Mechanical behavior regarding complex viscosity (η*; circle symbols) and complex modulus (G*; triangle symbols) of the commercial starch (black color); *Q. pyrenaica* acorn starch extracted under control conditions (red color; 0.1 MPa for 20 min—P0.1/t20); *Q. pyrenaica* acorn starch extracted under optimum conditions (green color; 460 MPa for 20 min—P460/t20); *Q. robur* acorn starch extracted under control conditions (yellow color; 0.1 MPa for 17.4 min—R0.1/t17.4); *Q. robur* acorn starch extracted under optimum conditions (blue color; 333 MPa for 17.4 min—R333/t17.4); Figure S4: Mechanical behavior regarding the elastic (G'; diamond symbols) and viscous (G''; square symbols) moduli of the commercial starch (black color); *Q. pyrenaica* acorn starch extracted under control conditions (red color; 0.1 MPa for 20 min—P0.1/t20); *Q. pyrenaica* acorn starch extracted under optimum conditions (green color; 460 MPa for 20 min—P460/t20); *Q. robur* acorn starch extracted under control conditions (yellow color; 0.1 MPa for 17.4 min—R0.1/t17.4); *Q. robur* acorn starch extracted under optimum conditions (blue color; 333 MPa for 17.4 min—R333/t17.4).

Author Contributions: Conceptualization, L.M.G.C., E.M.C.A., J.A.S. and M.P.; Data curation, L.M.G.C. and M.E.B.; Formal analysis, L.M.G.C., A.I.C., C.F.P., S.C.S., M.E.B. and M.M.; Funding acquisition, J.A.S. and M.P.; Investigation, L.M.G.C., E.M.C.A., J.A.S. and M.P.; Methodology, L.M.G.C., A.I.C., C.F.P., S.C.S. and M.M.; Project administration, J.A.S. and M.P.; Resources, L.M.G.C., E.M.C.A., J.A.S. and M.P.; Software, L.M.G.C., A.I.C., C.F.P., S.C.S. and M.M.; Supervision, E.M.C.A., J.A.S. and M.P.; Validation, L.M.G.C.; Visualization, L.M.G.C.; Writing—original draft, L.M.G.C.; Writing—review and editing, L.M.G.C., M.E.B., Ó.L.R., E.M.C.A., J.A.S. and M.P. All authors have read and agreed to the published version of the manuscript.

Funding: Authors L.M.G.C. (SFRH/BD/136882/2018 and COVID/BD/152756/2022) and M.M. (SFRH/BD/136701/2018) are grateful for the financial support provided by FCT through the Doctoral Grants. Author E.M.C.A. is grateful for the financial support of this work funded by national funds (OE), through FCT—Fundação para a Ciência e a Tecnologia, I.P., in the scope of the framework contract foreseen in the numbers 4, 5, and 6 of the article 23, of the Decree-Law 57/2016, of 29 August, changed by Law 57/2017 of 19 July.

Institutional Review Board Statement: Not applicable.

Informed Consent Statement: Not applicable.

Data Availability Statement: Data will be available upon request to the corresponding author.

Acknowledgments: All authors would like to acknowledge to the Universidade Católica Portuguesa by providing financial support to CBQF Associate Laboratory under the UID/Multi/50016/2021 FCT project and to Aveiro University and FCT/MCT for the financial support for the Laboratório Associado LAQV-REQUIMTE (UIDB/50006/2020) through national funds and, where applicable, co-financed by the FEDER, within the PT2020 Partnership Agreement.

Conflicts of Interest: The authors declare no conflict of interest.

References

1. Denk, T.; Grimm, G.W.; Manos, P.S.; Deng, M.; Hipp, A.L. An Updated Infrageneric Classification of the Oaks: Review of Previous Taxonomic Schemes and Synthesis of Evolutionary Patterns. In *Oaks Physiological Ecology. Exploring the Functional Diversity of Genus Quercus L.*; Gil-Pelegrín, E., Peguero-Pina, J.J., Sancho-Knapik, D., Eds.; Tree Physiology; Springer: Cham, Switzerland, 2017; Volume 7, pp. 261–302, ISBN 978-3-319-69098-8.
2. Silveira, T. Bolota: 55% da produção é desperdiçada. *Agro-Vida Vida Económica* **2017**, *1715*, 7.
3. Castro, L.M.G.; Ribeiro, T.B.; Machado, M.; Alexandre, E.M.C.; Saraiva, J.A.; Pintado, M. Unraveling the Effect of Dehulling Methods on the Nutritional Composition of Acorn *Quercus* spp. *J. Food Compos. Anal.* **2022**, *106*, 104354. [CrossRef]
4. Schirmer, M.; Jekle, M.; Becker, T. Starch gelatinization and its complexity for analysis. *Starch-Stärke* **2015**, *67*, 30–41. [CrossRef]
5. Adewale, P.; Yancheshmeh, M.S.; Lam, E. Starch modification for non-food, industrial applications: Market intelligence and critical review. *Carbohydr. Polym.* **2022**, *291*, 119590. [CrossRef]
6. Mortensen, A.; Aguilar, F.; Crebelli, R.; Di Domenico, A.; Dusemund, B.; Frutos, M.J.; Galtier, P.; Gott, D.; Gundert-Remy, U.; Lambré, C.; et al. Re-evaluation of oxidised starch (E 1404), monostarch phosphate (E 1410), distarch phosphate (E 1412), phosphated distarch phosphate (E 1413), acetylated distarch phosphate (E 1414), acetylated starch (E 1420), acetylated distarch adipate (E 1422), hydroxypropyl starch (E 1440), hydroxypropyl distarch phosphate (E 1442), starch sodium octenyl succinate (E 1450), acetylated oxidised starch (E 1451) and starch aluminium octenyl succinate (E 1452) as food additives. *EFSA J.* **2017**, *15*, 4911.
7. European Commission Regulation (EC) No 1333/2008. Available online: http://data.europa.eu/eli/reg/2008/1333/2022-10-31 (accessed on 31 October 2022).
8. Park, S.; Kim, Y.R. Clean label starch: Production, physicochemical characteristics, and industrial applications. *Food Sci. Biotechnol.* **2020**, *30*, 1–17. [CrossRef]
9. Castro, L.M.G.; Alexandre, E.M.C.; Saraiva, J.A.; Pintado, M. Impact of high pressure on starch properties: A review. *Food Hydrocoll.* **2020**, *106*, 105877. [CrossRef]
10. Zhang, J.; Zhang, M.; Zhang, Y.; Bai, X.; Wang, C. Effects of high hydrostatic pressure on the structure and retrogradation inhibition of oat starch. *Int. J. Food Sci. Technol.* **2022**, *57*, 2113–2125. [CrossRef]

11. Larrea-Wachtendorff, D.; Tabilo-Munizaga, G.; Ferrari, G. Potato starch hydrogels produced by high hydrostatic pressure (HHP): A first approach. *Polymers* **2019**, *11*, 1673. [CrossRef]
12. Liu, M.; Wu, N.N.; Yu, G.P.; Zhai, X.T.; Chen, X.; Zhang, M.; Tian, X.H.; Liu, Y.X.; Wang, L.P.; Tan, B. Physicochemical properties, structural properties, and in vitro digestibility of pea starch treated with high hydrostatic pressure. *Starch-Stärke* **2018**, *70*, 1700082. [CrossRef]
13. Heydari, A.; Razavi, S.M.A.; Hesarinejad, M.A.; Farahnaky, A. New Insights into Physical, Morphological, Thermal, and Pasting Properties of HHP-Treated Starches: Effect of Starch Type and Industry-Scale Concentration. *Starch-Stärke* **2021**, *73*, 2000179. [CrossRef]
14. Soni, P.L.; Sharma, H.; Dun, D.; Gharia, M.M. Physicochemical Properties of *Quercus leucotrichophora* (Oak) Starch. *Starch-Stärke* **1993**, *45*, 127–130. [CrossRef]
15. Yoo, S.H.; Lee, C.S.; Kim, B.S.; Shin, M. The properties and molecular structures of gusiljatbam starch compared to those of acorn and chestnut starches. *Starch-Stärke* **2012**, *64*, 339–347. [CrossRef]
16. He, M.; Ding, T.; Wu, Y.; Ouyang, J. Effects of Endogenous Non-Starch Nutrients in Acorn (*Quercus wutaishanica* Blume) Kernels on the Physicochemical Properties and In Vitro Digestibility of Starch. *Foods* **2022**, *11*, 825. [CrossRef]
17. Liu, M.; Yang, Q.; Wu, Y.; Ouyang, J. Effects of Endogenous Polyphenols in Acorn (*Quercus variabilis* Blume) Kernels on the Physicochemical Properties of Starch. *Starch-Stärke* **2022**, *74*, 2200005. [CrossRef]
18. Stevenson, D.G.; Jane, J.; Inglett, G.E. Physicochemical Properties of Pin Oak (*Quercus palustris* Muenchh.) Acorn Starch. *Starch-Stärke* **2006**, *58*, 553–560. [CrossRef]
19. Deng, M.; Reddy, C.K.; Xu, B. Morphological, physico-chemical and functional properties of underutilized starches in China. *Int. J. Biol. Macromol.* **2020**, *158*, 648–655. [CrossRef]
20. Molavi, H.; Razavi, S.M.A.; Farhoosh, R. Impact of hydrothermal modifications on the physicochemical, morphology, crystallinity, pasting and thermal properties of acorn starch. *Food Chem.* **2018**, *245*, 385–393. [CrossRef]
21. Bayati, A.; Javanmard, M.; Eikani, M.H.; Sharifi, A. The Effect of Starch Isolation Method on Morphological and Physicochemical Properties of Zagros Oak (*Quercus brantii* var. Persica) Starch. *Starch-Stärke* **2022**, *74*, 2200016. [CrossRef]
22. Zhang, Z.; Saleh, A.S.M.; Wu, H.; Gou, M.; Liu, Y.; Jing, L.; Zhao, K.; Su, C.; Zhang, B.; Li, W. Effect of Starch Isolation Method on Structural and Physicochemical Properties of Acorn Kernel Starch. *Starch-Stärke* **2020**, *72*, 1900122. [CrossRef]
23. Zhang, D.; Xu, H.; Jiang, B.; Wang, X.; Yang, L.; Shan, Y.; Ding, S. Effects of ultra-high pressure on the morphological and physicochemical properties of lily starch. *Food Sci. Nutr.* **2021**, *9*, 952–962. [CrossRef] [PubMed]
24. Błaszczak, W.; Valverde, S.; Fornal, J. Effect of high pressure on the structure of potato starch. *Carbohydr. Polym.* **2005**, *59*, 377–383. [CrossRef]
25. Ahmed, J.; Al-Attar, H. Structural properties of high-pressure-treated chestnut flour dispersions. *Int. J. Food Prop.* **2017**, *20*, S766–S778. [CrossRef]
26. Lindeboom, N.; Chang, P.R.; Tyler, R.T. Analytical, biochemical and physicochemical aspects of starch granule size, with emphasis on small granule starches: A review. *Starch-Stärke* **2004**, *56*, 89–99.
27. Li, G.; Zhu, F. Effect of high pressure on rheological and thermal properties of quinoa and maize starches. *Food Chem.* **2018**, *241*, 380–386. [CrossRef]
28. Leite, T.S.; Jesus, A.L.T.; Schmiele, M.; Tribst, A.A.L.; Cristianini, M. High pressure processing (HPP) of pea starch: Effect on the gelatinization properties. *LWT Food Sci. Technol.* **2017**, *76*, 361–369. [CrossRef]
29. Filippa, L.; Trento, A.; Álvarez, A.M. Sauter mean diameter determination for the fine fraction of suspended sediments using a LISST-25X diffractometer. *Meas. J. Int. Meas. Confed.* **2012**, *45*, 364–368. [CrossRef]
30. Zhang, D.; Mu, T.; Sun, H.; He, J. Effects of different high hydrostatic pressure-treated potato starch on the processing performance of dough-like model systems. *Food Res. Int.* **2019**, *120*, 456–463. [CrossRef]
31. Ahmed, J.; Thomas, L. Changes in structural, functional and antioxidant properties induced by high pressure on quinoa flour. *J. Food Meas. Charact.* **2020**, *14*, 401–410. [CrossRef]
32. Kaur, M.; Punia, S.; Sandhu, K.S.; Ahmed, J. Impact of high pressure processing on the rheological, thermal and morphological characteristics of mango kernel starch. *Int. J. Biol. Macromol.* **2019**, *140*, 149–155. [CrossRef]
33. Rahman, M.H.; Mu, T.H.; Zhang, M.; Ma, M.M.; Sun, H.N. Comparative study of the effects of high hydrostatic pressure on physicochemical, thermal, and structural properties of maize, potato, and sweet potato starches. *J. Food Process. Preserv.* **2020**, *44*, e14294. [CrossRef]
34. Sandhu, K.S.; Kaur, M.; Punia, S.; Ahmed, J. Rheological, thermal, and structural properties of high-pressure treated Litchi (*Litchi chinensis*) kernel starch. *Int. J. Biol. Macromol.* **2021**, *175*, 229–234. [CrossRef] [PubMed]
35. Correia, P.R.; Cristiana, M.; Beirão-da-Costa, M.L. The effect of starch isolation method on physical and functional properties of Portuguese nut starches. II. *Q. rotundifolia* Lam. and *Q. suber* Lam. acorns starches. *Food Hydrocoll.* **2013**, *30*, 448–455.
36. Cappai, M.G.; Alesso, G.A.; Nieddu, G.; Sanna, M.; Pinna, W. Electron microscopy and composition of raw acorn starch in relation to in vivo starch digestibility. *Food Funct.* **2013**, *4*, 917–922. [CrossRef]
37. Chung, D.-H.; Yu, T.-J.; Choi, B.-K. Studies on the Utilization of Acorn Starch—Part I. Properties of Acorn Starch. *J. Korean Agric. Chem. Soc.* **1975**, *18*, 102–108.
38. Irinislimane, H.; Belhaneche-Bensemra, N. Extraction and Characterization of Starch from Oak Acorn, Sorghum, and Potato and Adsorption Application for Removal of Maxilon Red GRL from Wastewater. *Chem. Eng. Commun.* **2017**, *204*, 897–906. [CrossRef]

39. Saleh, M.; Ajo, R.; Al-Ismail, K.; Ondier, G. Effects of hydrocolloids on acorn starch physical properties. *Starch-Stärke* **2016**, *68*, 1169–1179. [CrossRef]
40. Lassoued, R.; Abderrabba, M.; Mejri, J. Comparative chemical composition of two *Quercus* species seeds growing in Tunisia. *S. Afr. J. Bot.* **2022**, *146*, 71–76. [CrossRef]
41. Boukhelkhal, M.; Moulai-Mostefa, N. Physicochemical characterization of starch isolated from soft acorns of holm oak (*Quercus ilex* subsp. *ballota* (Desf.) Samp.) grown in Algeria. *J. Food Meas. Charact.* **2017**, *11*, 1995–2005. [CrossRef]
42. Correia, P.R.; Beirão-da-Costa, M.L. Effect of Drying Temperatures on Starch-Related Functional and Thermal Properties of Acorn Flours. *J. Food Sci.* **2011**, *76*, E196–E202. [CrossRef]
43. Pei-Ling, L.; Qing, Z.; Qun, S.; Xiao-Song, H.; Ji-Hong, W. Effect of high hydrostatic pressure on modified noncrystalline granular starch of starches with different granular type and amylase content. *LWT Food Sci. Technol.* **2012**, *47*, 450–458. [CrossRef]
44. Ahmed, J.; Thomas, L.; Taher, A.; Joseph, A. Impact of high pressure treatment on functional, rheological, pasting, and structural properties of lentil starch dispersions. *Carbohydr. Polym.* **2016**, *152*, 639–647. [CrossRef]
45. Ahmed, J.; Thomas, L.; Arfat, Y.A.; Joseph, A. Rheological, structural and functional properties of high-pressure treated quinoa starch in dispersions. *Carbohydr. Polym.* **2018**, *197*, 649–657. [CrossRef] [PubMed]
46. Jin, J.; Lin, H.; Yagoub, A.E.G.A.; Xiong, S.; Xu, L.; Udenigwe, C.C. Effects of high power ultrasound on the enzymolysis and structures of sweet potato starch. *J. Sci. Food Agric.* **2020**, *100*, 3498–3506. [CrossRef] [PubMed]
47. Yang, Z.; Chaib, S.; Gu, Q.; Hemar, Y. Impact of pressure on physicochemical properties of starch dispersions. *Food Hydrocoll.* **2017**, *68*, 164–177. [CrossRef]
48. Correia, P.M.R.; Cruz-Lopes, L.; Beirão-Da-Costa, L. Morphology and structure of acorn starches isolated by enzymatic and alkaline methods. *Open Agric.* **2021**, *6*, 37–46. [CrossRef]
49. Zarroug, Y.; Boulares, M.; Mejri, J.; Slimi, B.; Hamdaoui, G.; Djebi, S.; Saidi, F.; Nasri, H.; Sfayhi, D.T.; Kharrat, M. Extraction and Characterization of Tunisian *Quercus ilex* Starch and Its Effect on Fermented Dairy Product Quality. *Int. J. Anal. Chem.* **2020**, *2020*, 8868673. [CrossRef]
50. Li, S.; Zhou, Y.; Liu, M.; Zhang, Y.; Cao, S. Nutrient composition and starch characteristics of *Quercus glandulifera* Bl. seeds from China. *Food Chem.* **2015**, *185*, 371–376.
51. Zarroug, Y.; Boulares, M.; Sfayhi, D.; Slimi, B.; Stiti, B.; Zaieni, K.; Nefissi, S.; Kharrat, M. Structural and Physicochemical Properties of Tunisian *Quercus suber* L. Starches for Custard Formulation: A Comparative Study. *Polymers* **2022**, *14*, 556. [CrossRef]
52. Li, W.; Tian, X.; Liu, L.; Wang, P.; Wu, G.; Zheng, J.; Ouyang, S.; Luo, Q.; Zhang, G. High pressure induced gelatinization of red adzuki bean starch and its effects on starch physicochemical and structural properties. *Food Hydrocoll.* **2015**, *45*, 132–139. [CrossRef]
53. Bajaj, R.; Singh, N.; Ghumman, A.; Kaur, A.; Mishra, H.N. Effect of High Pressure Treatment on Structural, Functional, and In-Vitro Digestibility of Starches from Tubers, Cereals, and Beans. *Starch-Stärke* **2022**, *74*, 2100096. [CrossRef]
54. Wang, H.; Hu, F.; Wang, C.; Ramaswamy, H.S.; Yu, Y.; Zhu, S.; Wu, J. Effect of germination and high pressure treatments on brown rice flour rheological, pasting, textural, and structural properties. *J. Food Process. Preserv.* **2020**, *44*, e14604. [CrossRef]
55. Okur, I.; Ozel, B.; Oztop, M.H.; Alpas, H. Effect of high hydrostatic pressure in physicochemical properties and in vitro digestibility of cornstarch by nuclear magnetic resonance relaxometry. *J. Food Process. Eng.* **2019**, *42*, e13168. [CrossRef]
56. Kaur, M.; Oberoi, D.P.S.; Sogi, D.S.; Gill, B.S. Physicochemical, morphological and pasting properties of acid treated starches from different botanical sources. *J. Food Sci. Technol.* **2011**, *48*, 460–465. [CrossRef] [PubMed]
57. Hu, X.P.; Zhang, B.; Jin, Z.Y.; Xu, X.M.; Chen, H.Q. Effect of high hydrostatic pressure and retrogradation treatments on structural and physicochemical properties of waxy wheat starch. *Food Chem.* **2017**, *232*, 560–565. [CrossRef] [PubMed]
58. Zeng, F.; Li, T.; Gao, Q.; Liu, B.; Yu, S. Physicochemical properties and in vitro digestibility of high hydrostatic pressure treated waxy rice starch. *Int. J. Biol. Macromol.* **2018**, *120*, 1030–1038. [CrossRef]
59. Zhi-guang, C.; Jun-rong, H.; Hua-yin, P.; Qi, Y.; Chen-lu, F. The effects of HHP (high hydrostatic pressure) on the interchain interaction and the conformation of amylopectin and double-amylose molecules. *Int. J. Biol. Macromol.* **2020**, *155*, 91–102. [CrossRef]
60. Molavi, H.; Razavi, S.M.A. Steady Shear Rheological Properties of Native and Hydrothermally Modified Persian Acorn (*Quercus brantii* Lindle.) Starches. *Starch-Stärke* **2018**, *70*, 1700156. [CrossRef]
61. Mezger, T.G. Oscillatory tests. In *The Rheology Handbook*; Vincentz Network: Hannover, Germany, 2020; pp. 153–247.
62. Molavi, H.; Razavi, S.M.A. Dynamic Rheological and Textural Properties of Acorn (*Quercus brantii* Lindle.) Starch: Effect of Single and Dual Hydrothermal Modifications. *Starch-Stärke* **2018**, *70*, 1800086. [CrossRef]
63. Brown, G.H.; Louderback, L.A. Identification of starch granules from oak and grass species in the central coast of California. *J. Archaeol. Sci. Rep.* **2020**, *33*, 102549. [CrossRef]

gels

Article

Thermosensitive Hydrogel-Functionalized Mesoporous Silica Nanoparticles for Parenteral Application of Chemotherapeutics

Christina Voycheva [1], Marta Slavkova [1,*], Teodora Popova [1], Diana Tzankova [2], Denitsa Stefanova [3], Virginia Tzankova [3], Ivelina Ivanova [4], Stanislav Tzankov [4], Ivanka Spassova [5], Daniela Kovacheva [5] and Borislav Tzankov [1]

[1] Department Pharmaceutical Technology and Biopharmacy, Faculty of Pharmacy, Medical University—Sofia, 1000 Sofia, Bulgaria; hvoycheva@pharmfac.mu-sofia.bg (C.V.); tpopova@pharmfac.mu-sofia.bg (T.P.); btzankov@pharmfac.mu-sofia.bg (B.T.)
[2] Department of Pharmaceutical Chemistry, Faculty of Pharmacy, Medical University—Sofia, 1000 Sofia, Bulgaria; d.tsankova@pharmfac.mu-sofia.bg
[3] Department of Pharmacology, Pharmacotherapy and Toxicology, Faculty of Pharmacy, Medical University—Sofia, 1000 Sofia, Bulgaria; denitsa.stefanova@pharmfac.mu-sofia.bg (D.S.); vtzankova@pharmfac.mu-sofia.bg (V.T.)
[4] Faculty of Pharmacy, Medical University—Pleven, 5800 Pleven, Bulgaria; ivelinavasileva23@gmail.com (I.I.); stanislav_tzankov@abv.bg (S.T.)
[5] Institute of General and Inorganic Chemistry, Bulgarian Academy of Sciences, 1113 Sofia, Bulgaria; ispasova@svr.igic.bas.bg (I.S.); didka@svr.igic.bas.bg (D.K.)
* Correspondence: mslavkova@pharmfac.mu-sofia.bg

Abstract: Hydrogels can offer many opportunities for drug delivery strategies. They can be used on their own, or their benefits can be further exploited in combination with other nanocarriers. Intelligent hydrogels that react to changes in the surrounding environment can be utilized as gatekeepers and provide sustained on-demand drug release. In this study, a hybrid nanosystem for temperature- and pH-sensitive delivery was prepared from MCM-41 nanoparticles grafted with a newly synthesized thermosensitive hydrogel (MCM-41/AA-g-PnVCL). The initial particles were chemically modified by the attachment of carboxyl groups. Later, they were grafted with agar (AA) and vinylcaprolactam (VCL) by free radical polymerization. Doxorubicin was applied as a model hydrophilic chemotherapeutic drug. The successful formulation was confirmed by FT-IR and TGA. Transmission electron microscopy and dynamic light scattering analysis showed small particles with negative zeta potential. Their release behaviour was investigated in vitro in media with different pH and at different temperatures. Under tumour simulating conditions (40 °C and pH 4.0), doxorubicin was almost completely released within 72 h. The biocompatibility of the proposed nanoparticles was demonstrated by in vitro haemolysis assay. These results suggest the possible parenteral application of the newly prepared hydrogel-functionalized mesoporous silica nanoparticles for temperature-sensitive and pH-triggered drug delivery at the tumour site.

Keywords: hydrogel gatekeeper; mesoporous silica nanoparticles; stimuli-sensitive delivery; chemotherapy; doxorubicin

1. Introduction

Conventional chemotherapy is a mainstay of treatment for various cancer types [1]. It relies on the application of a variety of drug agents that can kill the cancerous cells. Unfortunately, their efficacy is usually hampered due to their inherent side effects on healthy tissues [2]. Another limitation is the need for frequent applications, which imposes an immense burden on the patients' quality of life. Therefore, significant trust and scientific effort has been put into the nanotechnological approach to overcome all the hurdles associated with chemotherapy. Various types of nanocarriers have been prepared and loaded with different chemotherapeutics, aiming to achieve improved antitumour efficacy, prolonged and sustained release, and to lessen the adverse events [3–8].

Hydrogels are a class of highly studied drug carriers with good biocompatibility and the possibility to be tuned for desirable properties and different routes of administration [9]. Hydrogels exhibit a three-dimensional structure of interconnected and crosslinked polymers that can absorb extensive amounts of water and yet do not dissolve in water [10]. Recently, attention has been directed towards intelligent hydrogels. They possess stimulus-sensitive behaviour triggered by alterations in the environmental conditions, such as temperature, pH, redox potential, light and others [11,12]. Amongst them, pH- and thermosensitivity have been exploited greatly in chemotherapy. This is mainly due to the fact that tumour cells are characterized by a specific microenvironment with an acidic medium and hyperthermia because of their intensive metabolism and vascularization [13,14]. Thus, a hydrogel with appropriate modifications can undergo reversible sol-gel transition at a specific desired temperature and release the loaded drug [15]. Depending on the temperature that causes the sol-gel transition, the hydrogels can have either a lower critical solution temperature (LCST) for the hydrophilic to hydrophobic transition or an upper critical solution temperature (UCST) for the opposite behaviour. In pharmaceutical applications, substances with LCST are widely used, such as poly(N-isopropyl acrylamide) (PNIPAM), poly(N-vinylcaprolactam) (PVCL), poly(N-vinylalkylamide), poly(2-hydroxyethylmethacrylate) (PHEMA), pluronic, chitosan, hyaluronic acid, etc. [16]. The specific temperature causing the on-demand drug release can be finely tuned by chemical or physical modifications of the parent polymer [15]. Nevertheless, there are some challenges in the application of hydrogels in chemotherapy, such as their lower mechanical strength and troublesome sustained release, especially in the case of hydrophilic drugs [17,18].

Developing composite systems for drug delivery has been shown to surmount the limitations of either one of their components on its own [19]. These are hybrid nanocarriers that combine the properties of different carriers, i.e., hydrogel and inorganic nanoparticles [20]. Different examples of their combinations can be found in the literature [21–23]. Thermosensitive hydrogels have been used by other researchers as gatekeepers to achieve sustained and specific drug delivery [16,24]. Some very suitable inorganic nanocarriers to be functionalized with appropriate hydrogel gatekeeper are mesoporous silica nanoparticles (MSNs) [19,25]. MSNs are characterized by a high specific surface area, an adjustable pore size, high hydrothermal stability, a large pore volume, biocompatibility and very low toxicity [19,26–29]. Moreover, their internal and external surface is highly covered with silanol groups, which can easily undergo functionalization [29]. The introduction of new chemical modalities (such as carboxylic groups) could be further utilized as a site for grafting with polymers, i.e., hydrogels [30].

Natural polymers are very attractive for modification because of their nontoxicity and biodegradability. Marine polysaccharides are extracted from renewable sources and are cost-effective [31]. Agar is a polysaccharide derived from algae which can form a strong biocompatible hydrogel. As an excipient, it is widely used in pharmaceutical practice in the role of a binder, filler, thickening agent, gelling agent, etc. [31,32]. Agar on its own does not possess thermosensitive properties, but can easily be modified by suitable grafting and result in a thermoresponsive hydrogel [33]. Therefore, agar was selected as a backbone for the gatekeeper modification of MSNs in the current study.

The present research aimed to obtain hydrogel-functionalized mesoporous silica nanoparticles for thermosensitive drug delivery. Doxorubicin was selected as a model drug due to its hydrophilic nature and versatile application in many forms of solid tumours and leukaemia [34]. It was hypothesized that the hybrid nanoparticles would be a suitable candidate for parenteral chemotherapy. The biocompatibility of the proposed nanocarrier was evaluated through its haemolytic potential.

2. Results and Discussion

The novel hydrogel AA-g-PnVCL was synthesized using a free-radical-initiated polymerization in a nitrogen atmosphere, as the amount of monomer and the concentration of the radical initiator were chosen on the basis of previous work. The rationale for the chosen ratios between the components of the hydrogel lies in the LCST (40 °C) of the obtained polymer together with its sufficient grafting efficiency (62.4%) [33]. The preparation of the hydrogel was based on the grafting-from strategy, where the polymerization occurs directly at the MSN's surface [35,36].

The LCST was chosen to be 40 °C, as solid tumours, in comparison with healthy tissue, are characterized by elevated temperatures (around 40–43 °C) [37,38]. In addition, this temperature is considered to be mild hyperthermia that can be applied locally alongside the chemotherapy and further improve the outcome with minimal discomfort to the patient [38].

2.1. Synthesis of Hydrogel-Functionalized Nanoparticles MCM-41/AA-g-PnVCL

Here, a two-step-controlled grafting method is proposed. First, functionalization (carboxylation) of the mesopores and the surface of MCM-41 was performed, followed by free radical polymerization of AA and nVCL in the presence of carboxyl modified MCM-41, using 2,2′-azobis(2,4-dimethylvaleronitrile) (AMVN) as a free radical initiator (Figure 1). The carboxyl modification of MCM-41 was carried out to provide reactive sites for attaching AA-g-PnVCL. The hydrogel was synthesized in the presence of carboxyl-modified MCM-41.

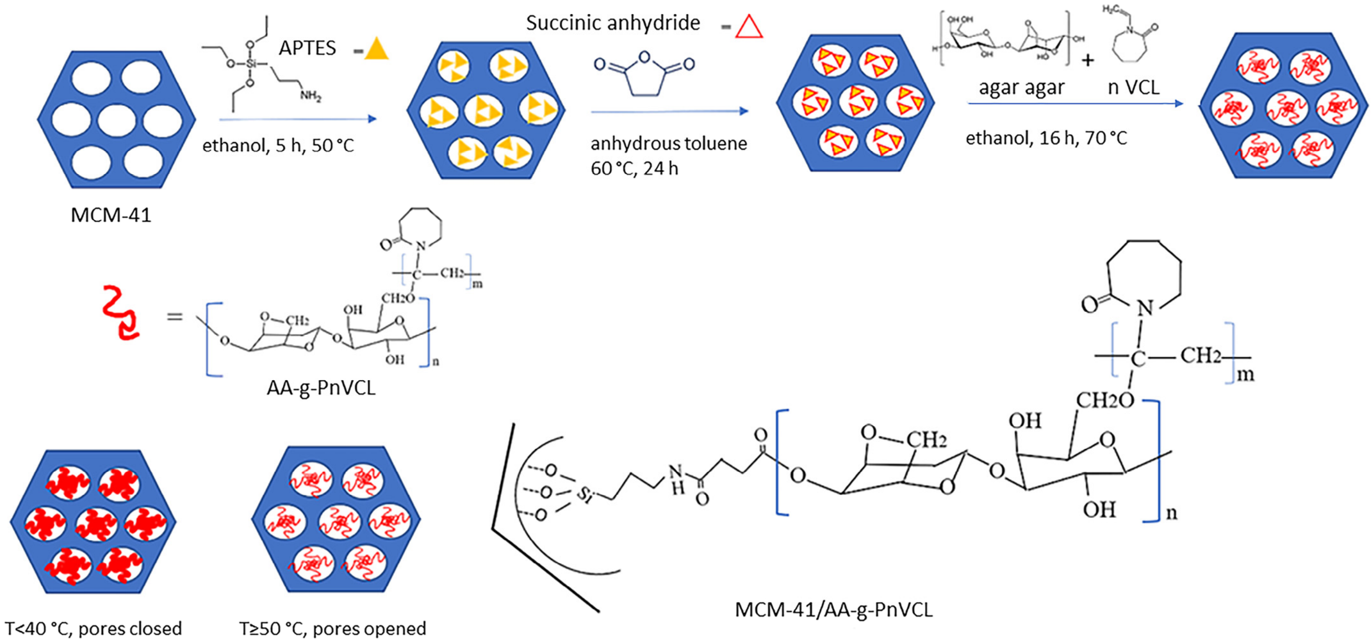

Figure 1. Synthesis of the hydrogel-functionalized silica nanoparticles.

2.2. Characterization of the AA-g-PnVCL and MCM-41/AA-g-PnVCL

2.2.1. FT-IR

The FT-IR spectra of all samples are presented in Figure 2. The parent silica MCM-41 materials were characterized by an intensive band at 1042 cm^{-1}, which was due to the asymmetric stretching vibration of the silica structure (Si–O–Si); the band at 962 cm^{-1} corresponded to the stretching vibrations of the surface Si–O groups [39,40]. After Dox loading onto MCM-41, no shifting of the silanol group bands was observed. It can be assumed that the Dox was physically entrapped in the nanocarriers. The significant shifting of the silanol group bands to 1069 cm^{-1} and 946 cm^{-1}, and the appearance of N-H bending at 1552 cm^{-1}, as well as the stretching vibration of the amide group at 1622 cm^{-1} (C=O) and the carboxylic groups (C=O) at 1728 cm^{-1} showed the successful attachment of COOH to the MCM-41 [41]. The reaction between APTES and succinic anhydride led to the formation of an amide bond, which was represented in the spectrum of MCM-41-COOH. A new peak also appeared from the attached COOH groups from the succinic anhydride.

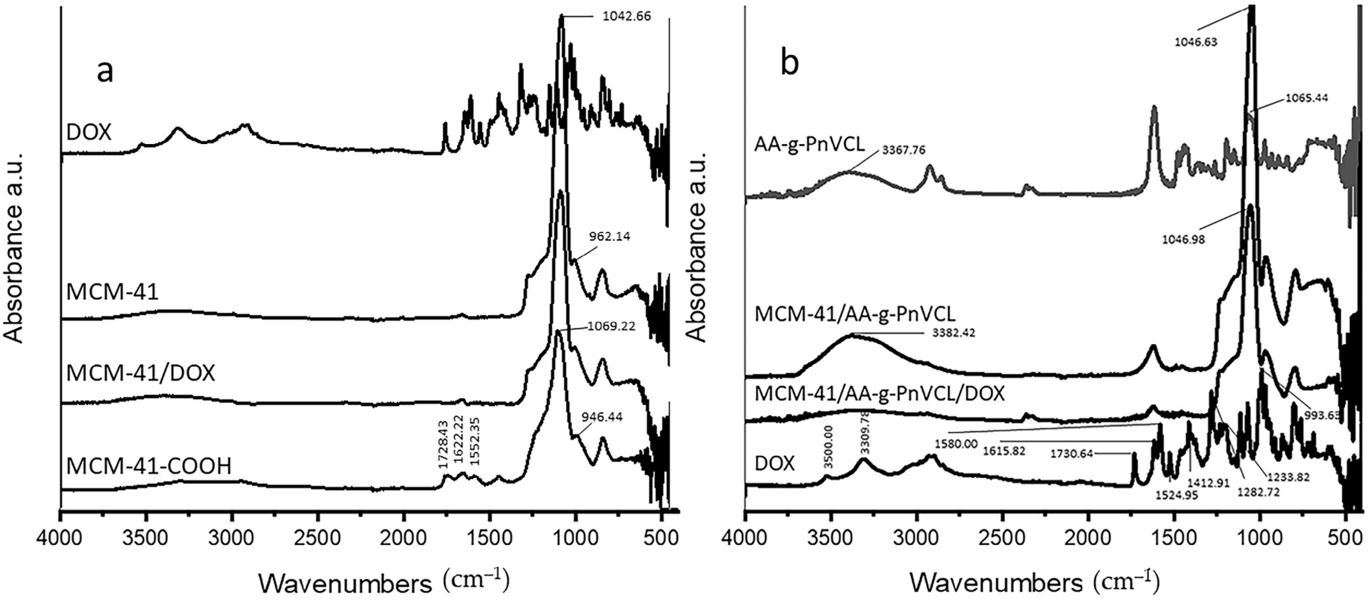

Figure 2. FT-IR spectra of (**a**) Dox, the parent MCM-41, Dox-loaded MCM-41 and carboxyl-modified MCM-41, and (**b**) Dox, AA-g-PnVCL, MCM-41/AA-g-PnVCL and loaded hydrogel-functionalized nanoparticles.

The shifting of the characteristic band of hydroxyl groups to 3382 cm^{-1} and the disappearance of the CH_2OH band visible at 1065 cm^{-1} in the spectrum of AA-g-PnVCL were evidence of the successful grafting of AA-g-PnVCL on MCM-41-COOH. Doxorubicin showed stretching vibrations of O-H and N-H bonds in the range of 3300–3550 cm^{-1}. The peak at 1730 cm^{-1} correlated with COOH groups, while those at 1615 cm^{-1} and 1580 cm^{-1} correlated with the ring (phenol), 1524 cm^{-1} correlated with the aromatic ring (C=C), 1412 cm^{-1} correlated with (N–H), 1282 cm^{-1} correlated with (C–C), 1233 cm^{-1} correlated with (C–N) and 993 cm^{-1} correlated with (C–OH), and were confirmed with literature data [42].

The spectrum of Dox loaded on the hybrid MCM-41/AA-g-PnVCL nanoparticles showed only a lowering of the intensities, but no significant shifting in the characteristic peaks. This fact suggests that doxorubicin was physically included in the MCM-41/AA-g-PnVCL particles.

2.2.2. TEM and SEM Analysis

TEM studies were performed for analysing the surface structure of MCM-41 and MCM-41/AA-g-PnVCL (Figure 3a–d). As seen in the figure, MCM–41 had the expected porous structure and spherical shape (Figure 3a,c). In accordance with the XRD data, the images of MCM-41/AA-g-PnVCL particles (Figure 3b,d) also showed some differences in the surface structure. This fact could be explained by pore blockage caused by the hydrogel modification of the particles. However, the hydrogel on the surface of silica particles did not significantly influence the morphology of MCM-41.

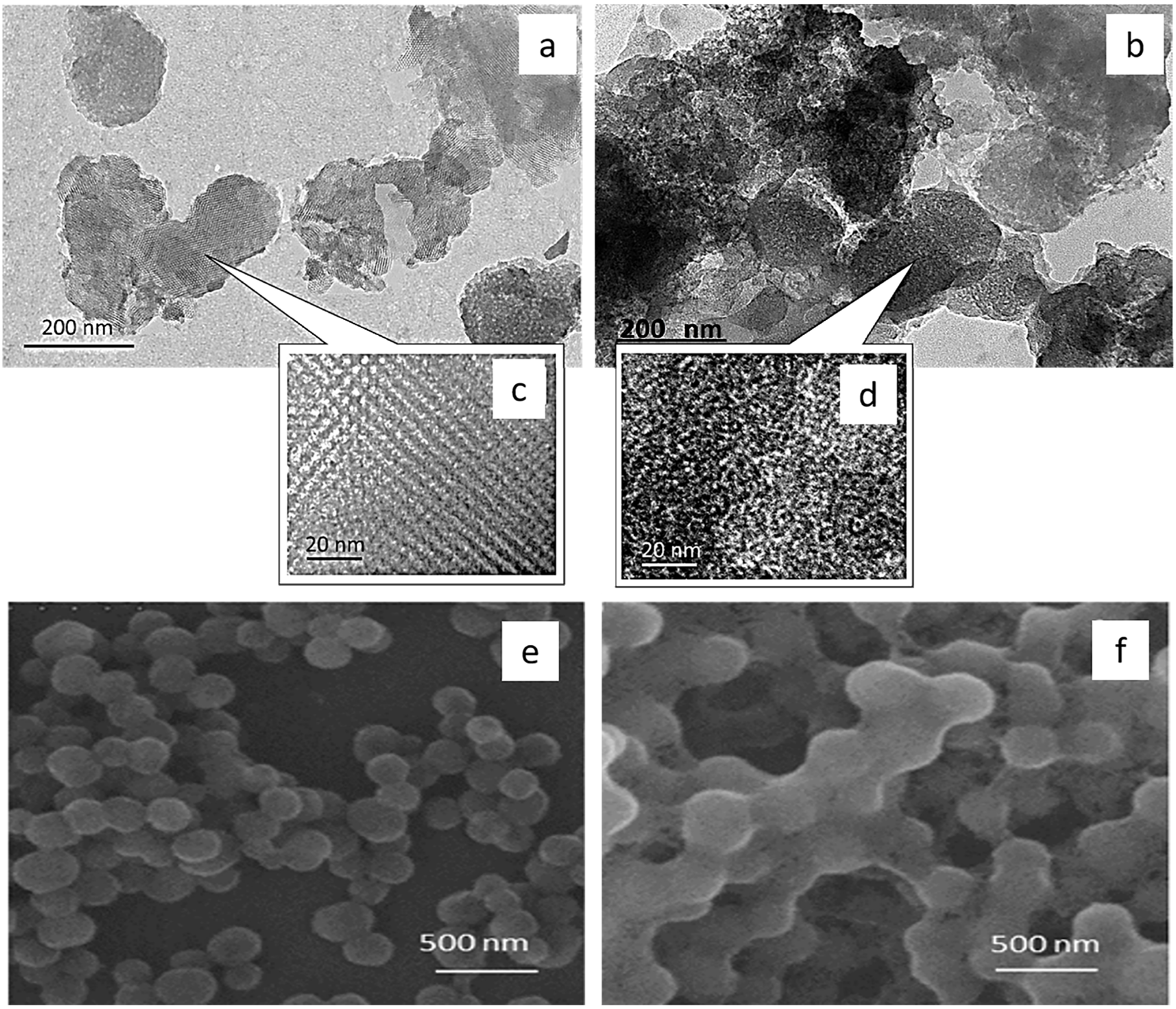

Figure 3. Transmission electron microscopy (**a**–**d**) and scanning electron microscopy (**e**,**f**) images of MCM-41 (**a**,**c**,**e**) and MCM-41/AA-g-PnVCL (**b**,**d**,**f**).

SEM images (Figure 3e,f) showed the spherical shape of the particles and sizes between 200 and 300 nm. The differences in the particles' size could be explained by the hydrogel crown formed around the MCM-41's surface due to grafting with AA-g-PnVCL (Figure 3f).

2.2.3. TGA

The attachment of AA-g-PnVCL on the MCM-41 particles could be evidenced by the thermogravimetric analyses shown in Figure 4. It presents the TG curves of MCM-41, the AA-g-PnVCL hydrogel and the hybrid system MCM-41/AA-g-PnVCL in the temperature range of 25–700 °C. Three main thermal steps were registered for the hydrogel.

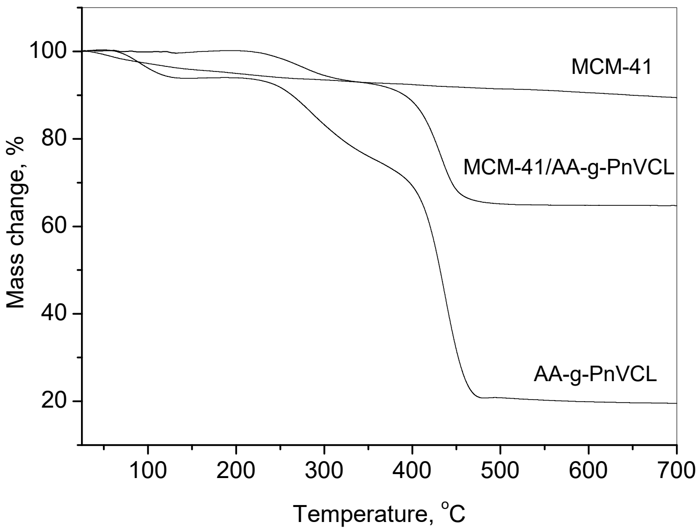

Figure 4. TG-curves of MCM-41 and MCM-41/AA-g-PnVCL and AA-g-PnVCL.

The first temperature weight loss ranged from 60 °C to about 120 °C, where the polymer lost about 8% of its mass due to dehydration. The second step was from 205 °C to 340 °C due to the depolymerization of the agar-agar, with a loss of about 25% of its mass. The third decomposition step occurred from about 340 °C to nearly 475 °C, where 35% of the material's mass was lost, probably due to the degradation of nVCL units with a full mass loss of nearly 80%. One could observe that the pure MCM-41 particles had a gradual and slight weight loss across the whole temperature range (10%), while the thermal decomposition stages of MCM-41/AA-g-PnVCL appeared at the same stages and temperatures as AA-g-PnVCL, and the difference between the mass loss of MCM-41 and MCM-41/AA-g-PnVCL was about 25%. The residue of pure AA-g-PnVCL was about 20%. The amount of attached polymer was calculated on the basis of the mass losses of the individual compounds and the MCM-41/AA-g-PnVCL sample. Since the residue of MCM at 700 °C was 90% and that of the AA-g-PnVCL was 20%, from the value obtained for the residue of the MCM-41/AA-g-PnVCL sample (65%), the quantity of the polymer bonded was found to be 36% of the initial mass. Hence, there was a successful attachment of the AA-g-PnVCL on the MCM-41 particles.

2.2.4. XRD

The small-angle parts of the XRD patterns of MCM-41 and MCM-41/AA-g-PnVCL and MCM-41/AA-g-PnVCL/Dox are presented in Figure 5. The X-ray powder diffraction pattern of the MCM-41 material exhibited four pronounced peaks, namely the most intense at (100) and the well-split (110) and (200), along with (210) reflections as an indication of the hexagonal pore structure with a high degree of ordering. The unit cell's parameter was 46.79(5) Å. The pattern of the MCM-41/AA-g-PnVCL showed a slight shift of the peaks towards higher degrees of 2 theta and peak asymmetry, which could be attributed to the changes in the pore walls' thickness due to the attachment of the AA-g-PnVCL on MCM-41. The pattern of the MCM-41/AA-g-PnVCL/Dox showed only one peak with low intensity, indicative of the filling of the mesopores with Dox, which was a confirmation of successful loading of the drug.

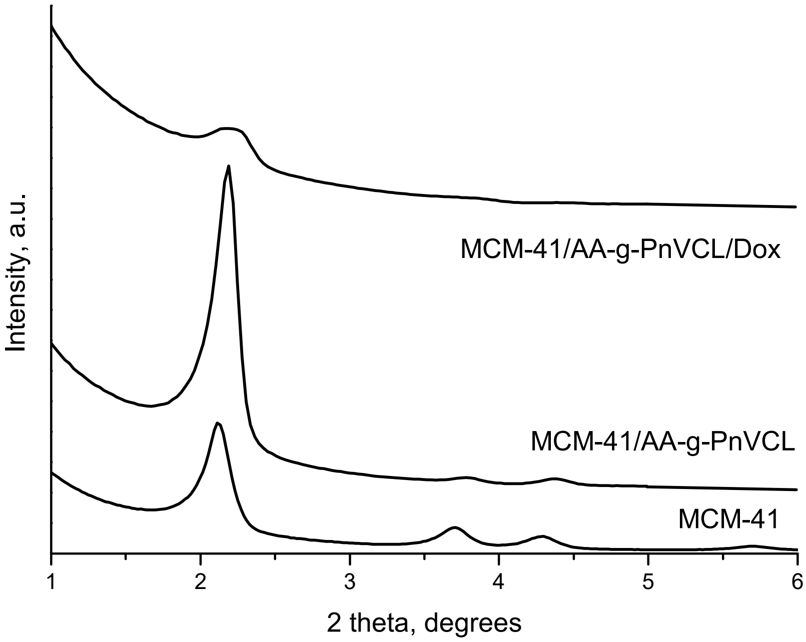

Figure 5. The small-angle part of the XRD patterns of MCM-41, MCM-41/AA-g-PnVCL and MCM-41/AA-g-PnVCL/Dox.

2.2.5. Temperature-Sensitive Behaviour

AA has no temperature sensitivity, while the LCST of PnVCL is 33 °C, as can be seen in Figure 6a. Nevertheless, this temperature is lower than the normal body temperature. Therefore, each of the components on their own did not provide sufficient thermoresponsive properties for modified drug release purposes. By grafting nVCL units on the AA hydrophilic backbone, the desirable thermosensitivity was achieved. Many researchers have discussed the application of nVCL in the development of thermosensitive drug delivery systems, e.g., microgels, hydrogels, nanogels and others [43]. It has been established that the change in the ratio of the hydrophilic polymer and the hydrophobic monomer gives different temperature behaviour of the polymers. The synthesized polymer AA-g-PnVCL (Figure 6a) at a predetermined ratio of the components had the characteristics necessary for the subsequent work with doxorubicin loading and achieving smart release at a temperature of 40 °C [33]. Other research groups have studied the grafting of different macromonomers with nVCL and their effect on the LCST of the resulting graft polymer. Chitosan was successfully used in combination with different ratios of PnVCL to produce a thermosensitive polymer with an LCST above normal body temperature for the delivery of 5-fluorouracil [44] or cisplatin [45]. Furthermore, the study of Banihasem et al. [45] showed that a coating of gold nanoparticles on the grafted chitosan–PnVCL polymer did not significantly affect the thermosensitive behaviour of the nanocarrier and allowed modified release of the chemotherapeutic.

Thermoresponsive polymers have a homogenous aqueous solution below the LCST and undergo a heterogeneous disperse system change above it. They prevent the release of the drug before the LCST is reached and stimulated the delivery of the active substance above LCST in larger quantities when the utility is the largest. The sharp changes from a swollen to a collapsed state are an opportunity to use this hydrogel as a gatekeeper and release the anticancer drug in a smart temperature-sensitive manner.

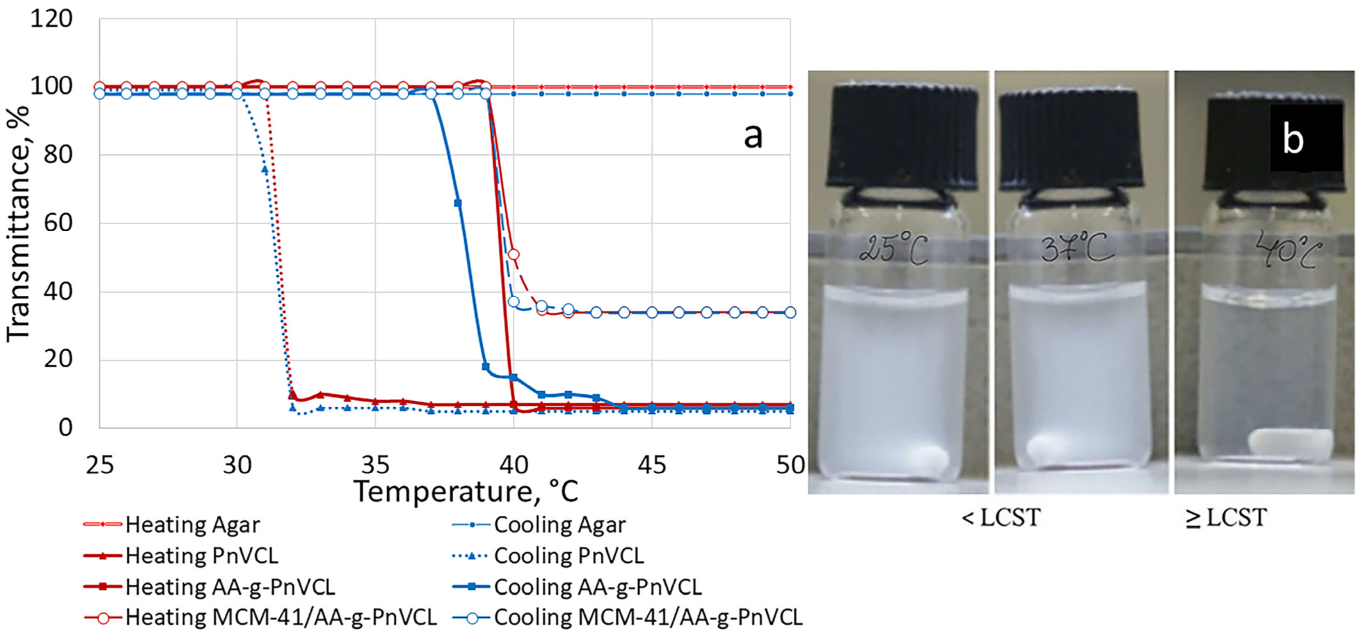

Figure 6. (**a**) UV transmittance at 500 nm as a function of the temperature of agar, PnVCL, AA-g-PnVCL and MCM-41-AA-g in a diluted aqueous dispersion (4 mg/mL). (**b**) Macroscopic photos of the corresponding hydrogel-functionalized nanoparticles' dispersion at various temperatures.

The grafting of MCM-41 nanoparticles with the synthesized thermosensitive hydrogel with a LCST value higher than usual body temperature could keep the API in the mesopores, preventing or drastically slowing its release below a certain temperature and hastening it if the local temperature is above the polymer's LCST. The thermoresponsive behaviour of hybrid nanoparticles is evident in Figure 6a,b. At 40 °C, the turbidity decreased sharply for both the hydrogel and the hydrogel-modified nanoparticles (Figure 6a). This observation gives us the reason to assume that MCM-41 does not significantly change the behaviour of AA-g-PnVCL after grafting. Similar results have been achieved by other authors. Karesoja et al. [46] investigated the thermosensitivity of mesoporous silica nanoparticles directly grafted with VCL and further modified with polyethylene oxide. The obtained nanoparticles possessed an LCST in the range of 35–37 °C. The closing of the pores of the mesoporous silica nanoparticles was also achieved by Sing et al. with the help of NIPAm-PEG [47]. The obtained system showed sustained of release Dox at temperatures below the LCST of the polymer and triggered its release above the LCST. The drug's release can be provoked by applying exterior heat to the field with the tumour tissue or by using the natural difference between healthy and tumour tissues, known as local tumour hyperaemia [37,38,48].

2.2.6. Dynamic Light Scattering (DLS)

Pristine MCM-41 nanoparticles are characterized by a small particle size and negative zeta potential, which is in accordance with the literature data [49,50]. The negative charge is due to the presence of silanol groups on their surface, which undergo deprotonation in an aqueous medium. Measurements performed by DLS analysis showed an increased particle size and polydispersity index after grafting of the polymer on the surface of the MCM-41 particles and a negative zeta potential above 20 mV (Table 1). The engagement of surface silanol groups in the graft with the thermosensitive polymer led to a decrease in the absolute value of zeta potential. Similar results after grafting were reported by other publications [49]. The value of the polydispersity index (PDI) showed the stability of the parent particles and the size distribution within narrow limits. The polymer graft predominantly affected the surface of the carboxyl-modified MCM-41, as can be seen from the TEM images as well (Figure 3b). Therefore, an increase in particle was observed, as expected due to the attached polymer chains. The increase in the PDI after preparation could be explained by the different number of grafted polymer molecules on each MCM-41-COOH particle. The decrease in the absolute zeta potential may also be a reason for the aggregation of particles and increased polydispersity. After Dox loading, the PDI and size of the particles remained in the same range as the ones of the Dox-free hybrid nanoparticles. These results suggested that Dox does not affect the size of the prepared hybrid nanoparticles, and no significant change was observed in their particle size distribution. The decrease in the absolute value of the zeta potential could be due to an electrostatic interaction between the nanocarrier and Dox. It is well known that Dox is a cationic drug (pKa = 8.3) which is positively charged in physiological conditions due to the presence of amine groups [51,52]. The results for the average size are in agreement with the TEM analysis.

Table 1. Average size, polydispersity index (PDI) and zeta potential from the DLS analysis; mean ± SD, *n* = 3.

Parameter	**MCM-41**	**MCM-41/AA-g-PnVCL**	**MCM-41/AA-g-PnVCL/Dox**
Size, nm	217 ± 7.3	360 ± 8.4	369 ± 3.3
PDI	0.31	0.86	0.83
Zeta potential, mV	−37.1 ± 3.7	−26.6 ± 3.6	−19.8 ± 2.4

2.2.7. Dox Loading Efficiency

API loading following post-surface grafting was chosen in the present study. According to the literature data, it has been suggested that during the numerous steps of grafting and extraction, Dox can be lost from the nanocarriers [53]. The loading of Dox onto unmodified MCM-41 was found to be 49%, while the loading efficiency on MCM-41/AA-g-PnVCL was calculated to be 59%. It was expected that the active substance was physically encapsulated in the grafted MCM-41 particles, according to the results of IR spectroscopy. The higher loading capacity of the hybrid particles was probably due to the formation of internal free volumes from the chains of AA-g-PnVCL attached to the surface of MCM-41.

2.2.8. Drug Release

The expected temperature- and pH-dependent release of Dox was monitored by performing an in vitro dissolution test in a buffer medium (pH 7.4 and 4.0) at 25 °C, 37 °C and 40 °C, corresponding to room temperature, normal body temperature and tumour hyperaemia. The results are presented in Figures 7 and 8.

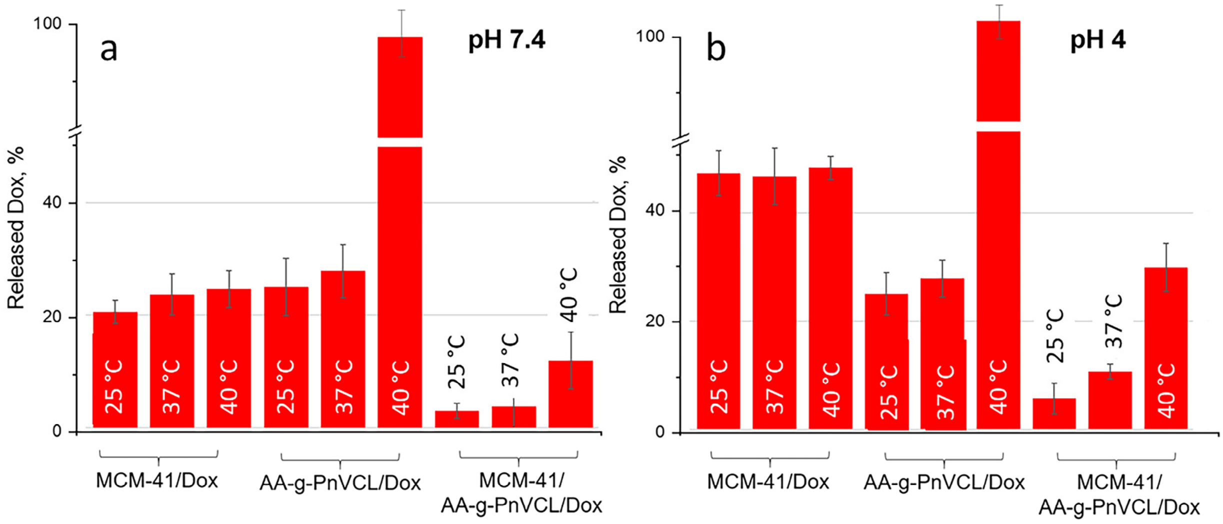

Figure 7. Amount of doxorubicin released (%) in the sixth hour during an in vitro dissolution test at pH 7.4 (**a**) and pH 4.0 (**b**) at different temperatures (25 °C; 37 °C; 40 °C); mean ± SD; n = 3.

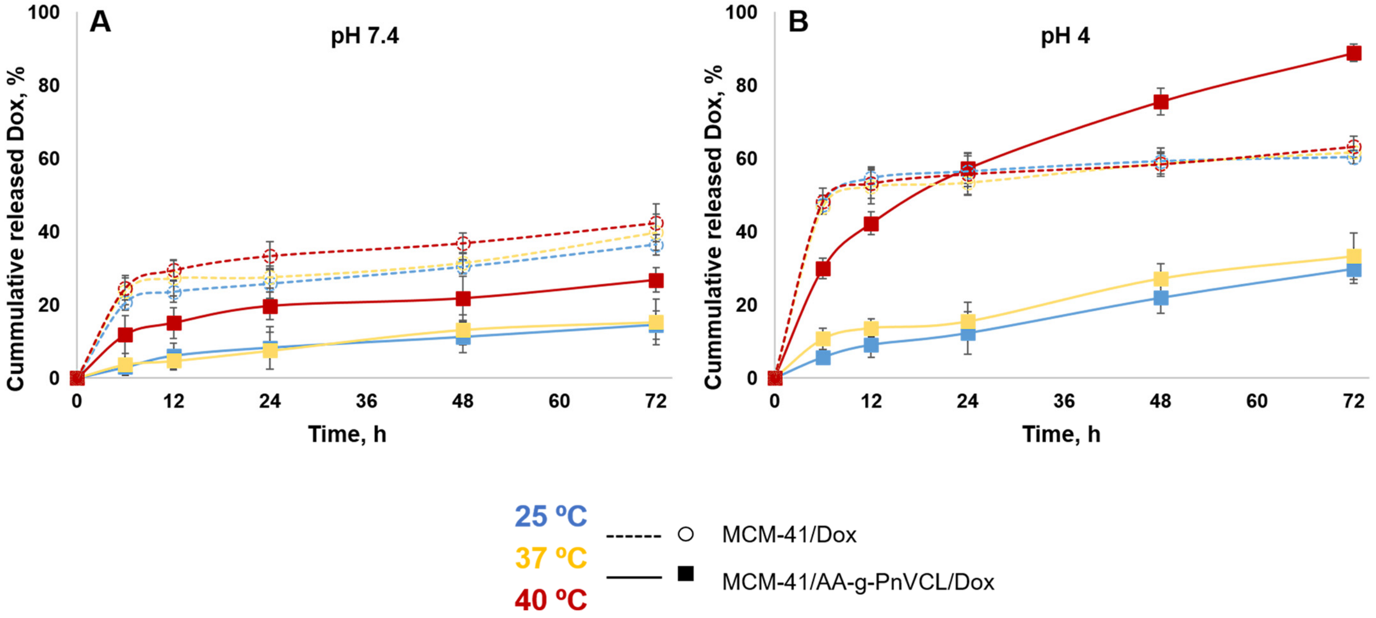

Figure 8. Release profiles of doxorubicin from MCM-41/AA-g-PnVCL and MCM-41 nanoparticles in a buffer medium with a pH of 7.4 (**A**) and a pH of 4 (**B**) at different temperatures (25 °C; 37 °C; 40 °C); mean ± SD; n = 3.

The release of doxorubicin from unmodified MCM-41/Dox at pH 7.4 was slow (20.6 ± 2.1%) within the first 6 h of the study (Figure 7a). At pH 7.4, the Dox molecules were partially protonated, as expected on the basis of their pKa = 8.22 [52,53]. Therefore, at this pH, Dox was positively charged while the MSN carrier's silanol groups were characterized by a negative charge. This led to electrostatic attraction between the carrier and the API, and the drug was retained. These results are in accordance with other studies [48–51]. In the 72nd hour at pH 7.4 (Figure 8A), regardless of the temperature, about 40% was released from the nonmodified particles (36.5 ± 2.8% at 25 °C; 39.8 ± 4.9% at 37 °C; 42.4 ± 5.2% at 40 °C). This suggests incomplete but still sufficient release of Dox at normal physiological conditions, which could cause toxic systemic effects.

At the same time, the thermosensitive AA-g-PnVCL/Dox showed complete release of Dox only at 40 °C (Figure 7a,b), regardless of the pH of the medium (97 ± 3.4% at pH

7.4 and 96.8 ± 3.8% at pH 4). The results obtained from the in vitro dissolution test for the hydrogel-functionalized nanoparticles at 25 °C and 37 °C showed a delayed release in the initial phase, as well as a slow release over time. Less than 5% (2.9 ± 1.3% and 3.7 ± 3.0% at 25 °C and 37 °C, respectively) of the active substance was released in the first 6 h (Figure 7a), followed by about 14.5 ± 3.9% and 15.3 ± 6.3%, respectively, at 25 °C and 37 °C being released by the 72nd hour (Figure 8A). This delay in the release was expected due to the swollen state of the hydrogel at room temperature and normal body temperature. This suggests the possibility for temperature-sensitive drug delivery at the tumour site, as shown in the literature [33]. The release of Dox from the hybrid nanoparticles at pH 7.4 and 40 °C was reported to be 11.9 ± 5.1% in the sixth hour (Figure 7a) and 26.8 ± 3.4% in the 72nd hour (Figure 8A). This temperature was above the LCST and the hydrogel on the surface of the particles was in its collapsed state, which allowed the opening of the pores and the release of the drug from the inside. The hydrogel acted as a gatekeeper, and Dox was released only after the required conditions had been met. There was statistically significant difference in the amount of Dox released from MCM-41/AA-gPnVCL at the three investigated temperatures. The ANOVA showed that the release at 40 °C was significantly different from the release at 25 °C ($p = 0.0060$) and at 37 °C ($p = 0.0061$). These findings suggest that the thermosensitive release was maintained in the preparation of hybrid nanoparticles.

At pH 4.0 (Figures 7b and 8B), all of the investigated nanocarriers exhibited increased release of Dox, which was expected due to its known better solubility in acidic media [54,55]. Such acidic conditions are expected for tumour cells because of their extensive metabolism [56]. The pristine MCM-41 loaded with Dox at pH = 4.0 showed a significant release with some burst effect in the first 6 h of dissolution (47.3 ±. 2.6% at 25 °C; 46.7 ± 2.0% at 37 °C; 48.3 ± 3.6% at 40 °C). There was no significant difference between the release at 40 °C and 25 °C ($p = 0.81$), as well as between the release at 40 °C and 37 °C ($p = 0.79$), and thus the unmodified nanoparticles possessed no temperature-sensitivity. Therefore, no actual sustained release was observed. In the acidic medium, the thermosensitive hydrogel AA-g-PnVCL loaded with Dox again completely released the API (96.8 ± 3.8%) within 6 h at 40 °C (Figure 7b). At temperatures lower than the LCST, a sustained release was observed, with lower amounts of Dox being released from the thermopolymer (25.3 ± 4.1% at 25 °C; 27.9 ± 3.5% at 37 °C). A comparison of the profiles between 25 °C and 40 °C as well as the ones between 37 °C and 40 °C showed significant differences ($p < 0.05$).

If we compare the release of Dox at 6 h at pH 4.0 from MCM-41, AA-g-PnVCL and MCM-41/AA-g-PnVCL (Figure 7b), sustained and temperature-triggered release from the hybrid nanoparticles was observed (29.9 ± 2.8%). The newly prepared hybrid nanoparticles under the simulated tumour conditions (pH = 4 and 40 °C) showed a sustained release without a burst effect in the initial phase (Figure 7b). Over time, a gradual controlled release was observed, and 88.9 ± 2.4% of the API was released within 72 h (Figure 8). This could lead to the assumption that no fluctuation in the concentration of Dox at the target site would be present. These findings support the expectations that combining two types of delivery systems, i.e., thermosensitive hydrogel and MSNs, will lead to superior properties and could improve the anticancer therapy.

On the basis of the data obtained, it can be assumed that the modification of MCM-41 particles with a thermopolymer allows a delayed and stimulus-triggered release compared with the hydrogel alone and unmodified particles. Providing very low drug release over time at a physiological pH of 7.4 at 37 °C (15.3 ± 6.3%) is a prerequisite for lowering the systemic toxicity of the novel MCM-41-AA-gPnVCL nanoparticles. Sustained and almost complete release (88.9 ± 2.4%) from the hybrid nanoparticles was observed only when an area with local tumour hyperaemia and an acidic pH was reached.

2.2.9. Haemolysis Assay

A haemolytic assay is a widely used primary screening method for in vitro biocompatibility testing of new drug substances. The haemolytic activity of the tested compounds was compared with the effects of Triton X-100, as shown in Figure 9. Triton X-100 induced complete haemolysis (by 100% vs. the control) after 1 h of incubation.

The experimental results showed the good hemocompatibility of all tested free carriers (MCM-41, AA-g-PnVCL and MCM-41/AA-g-PnVCL), because no haemolytic activity was observed, since the rate of haemolysis was lower than 5% (the accepted threshold level according to ISO 10993). Similarly, Dox (0.54, 2.75 and 10.87 μM) loaded in the nanoparticles (MCM-41-Dox, AA-g-PnVCL-Dox and MCM-41/AA-g-PnVCL-Dox) did not show a haemolytic effect, since the rate of haemolysis was lower than 5% (respectively, 1.6%, 3.3% and 1.8% vs. the untreated control). In contrast, the highest concentration of free Dox (10.87 μg/mL) was found to induce a slight increase in haemolysis by 8% vs. the untreated control.

In summary, empty nanoparticles and the Dox loaded in MCM-41, AA-g-PnVCL and MCM-41/AA-g-PnVCL did not show significant haemolytic effects. Our results are in accordance with the study of Saroj et al., who reported that pH-sensitive polyacrylic-acid-functionalized MCM-41 nanoparticles demonstrated hemocompatibility similar to that of the negative control group [57]. Zhao et al. reported the good biocompatibility of mesoporous silica nanoparticles MCM-41 with human erythrocytes compared with the highly haemolytic amorphous silica [58].

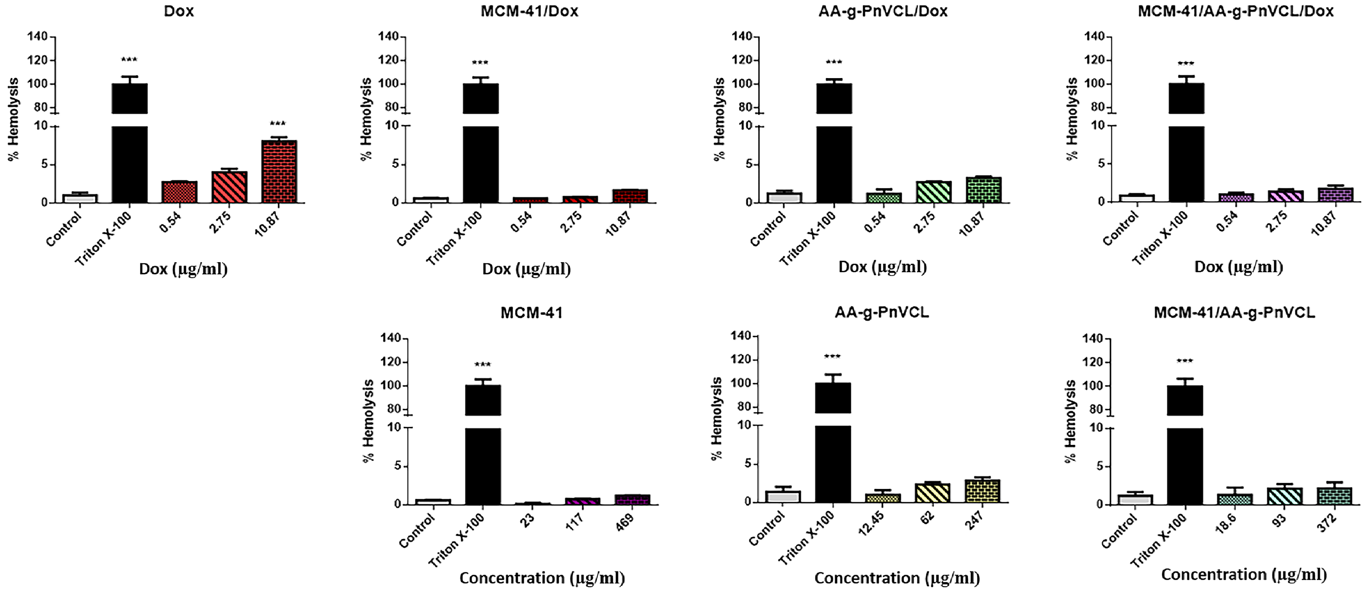

Figure 9. Haemolytic effects of free Dox (0.54–10.87 μM), Dox loaded in MCM-41, Dox loaded in AA-g-PnVCL, Dox loaded in MCM-41/AA-g-PnVCL (the concentrations of loaded Dox correspond to the concentrations of free Dox), and the free carriers MCM-41, AA-g-PnVCL and MCM-41/AA-g-PnVCL on human erythrocytes. The results are expressed as the mean ± SD of triplicate assays (n = 3). All groups were compared statistically vs. the untreated controls by one-way ANOVA with Dunnet's post-test *** $p < 0.001$ vs. control.

Thus, the results from our experiments confirmed the good hemocompatibility of the empty carriers, which is a promising perspective for parenteral application. Interestingly, we found that the loading of Dox in MCM-41, AA-g-PnVCL and MCM-41/AA-g-PnVCL nanoparticles improved its hemocompatibility compared with the effects of free Dox.

3. Conclusions

A hybrid, controlled drug delivery system based on AA grafted with PnVCL and attached to the surface of MCM-41 was obtained successfully. The newly synthesized hydrogel could efficiently serve as a gatekeeper of the MSNs, governing the drug's release in response to the environmental temperature and pH. The model drug doxorubicin was almost completely released only under the simulated cancer tissue conditions (40 °C and pH = 4.0). In addition, the hydrogel on the surface of the silica particles formed internal cavities for drug molecules, which allowed a high loading efficiency (59%). The release profile was prolonged within a 72 h timeframe, which could limit the frequency of treatment. The haemolysis assay demonstrated the good biocompatibility of empty and Dox-loaded nanoparticles, since no significant haemolysis of red blood cells was observed.

All the results presented here suggest that the developed hydrogel-functionalized MCM-41/AA-g-PnVCL-based platform is an attractive candidate for stimulus-triggered and controlled drug release for chemotherapeutic agents. Once the preparation, successful "smart" release properties and safety upon parenteral application are proven, further studies would be necessary to evaluate its therapeutic efficacy in vitro and in vivo.

4. Materials and Methods

4.1. Materials

MCM-41, 3-aminopropyltriethoxysilane (APTES), succinic anhydride, anhydrous toluene, agar-agar powder and N-vinyl caprolactam (nVCL) were purchased from Sigma Aldrich Inc. (St. Louis, MO, USA). The 2,2′-azobis(2,4-dimethylvaleronitrile) (AMVN) and hydroquinone were purchased from TCI Europe (Zwijndrecht, Belgium). Ethanol, disodium hydrogen phosphate dihydrate and potassium dihydrogen phosphate were all purchased from Merck (Darmstadt, Germany). Deionized water was obtained by ion exchange.

4.2. Synthesis of Hydrogel-Functionalized MCM-41 Nanoparticles

4.2.1. Synthesis of COOH-Modified MCM-41 Particles (MCM-41-COOH)

The carboxylation of MCM-41 was carried out in two steps. The first one included intermediate amination, in which 1 g of MSNs and 20 mL of 3-aminopropyltriethoxysilane (APTES) were mixed in ethanol for 5 h at 50 °C. Then a two-step washing process was conducted, first with ethanol and thereafter with deionized water. The resulting particles were dried at room temperature, followed by azeotropic dehydration. They were placed in toluene at 115 °C and the adsorbed water was removed.

The second step was the carboxylation of the amino-functionalized MCM-41. For this purpose, succinic anhydride (6.6 mmol) was added to the dispersion of the amino-modified MCM-41 in anhydrous toluene at 60 °C for 24 h. Carboxylation was performed by assuming that the MCM-41 was pre-functionalized with a 2 wt% amino content. The resulting modified particles were dried for 6 h by vacuum evaporation at 25 °C, and the obtained MCM-41-COOH particles were used for further thermopolymer attachment.

4.2.2. Synthesis of MCM-41-COOH/AA-g-PnVCL Nanoparticles

The formation of hydrogel containing AA and nVCL in a molar ratio of 20:1 by the free radical polymerization technique in the presence of AMVN as an initiator (AMVN: nVCL in a molar ratio of 1:20) is explained elsewhere [33]. To obtain the hybrid nanosystem, a modified direct polymerization method was applied according to the following procedure: AA (20 mg) was dissolved in 40 mL of distilled water at 90 °C with constant stirring. The MCM-41-COOH particles (250 mg) were homogeneously dispersed in the AA solution. Next, nVCL (140 mg) was dissolved in 40 mL of 95% ethanol and added to the mixture in a three-necked round bottomed flask in a nitrogen atmosphere for 60 min. Next, a solution of AMVN in 20 mL of 95% ethanol was added, and the nitrogen flow continued for another 15 min before the flask was closed. The reaction continued with ongoing stirring in a thermostatic paraffin bath (70 °C) for 16 h. Finally, the grafting procedure was terminated by adding a saturated solution of hydroquinone. The resulting MCM-41/AA-g-PnVCL particles were precipitated in acetone and separated by centrifugation (15,000 rpm). Removal of the homopolymer (PnVCL) was carried out by extraction with 95% ethanol for 24 h. Then the MCM-41/AA-g-PnVCL particles were dried under a vacuum to a constant weight and further subjected to characterization. A schematic representation of the procedure is shown in Figure 1.

4.3. Characterization of the Hydrogel, the MCM-41 Nanoparticles and the Hydrogel-Functionalized Nanoparticles (MCM-41/AA-g-PnVCL)

4.3.1. Fourier Transform Infrared Spectroscopy (FT-IR)

A Thermo-Nicolet 400 FT-IR instrument equipped with an attenuated total reflectance (ATR) device (Thermo Fischer Scientific, USA was used to collect the IR spectra in the range of 4000–400 cm^{-1} with a resolution of 4 cm^{-1} for the free components as well as the grafted products.

4.3.2. Transmission Electron Microscopy (TEM) and Scanning Electron Microscopy (SEM)

The size and structure of the gatekeeper-modified nanoparticles were characterized using transmission electron microscopy (JEOL JEM 2100 h STEM (200 kV; point resolution = 0.23 nm)). Samples were prepared by placing a water suspension of the nanoparticles on a polymer microgrid supported on a Cu grid. The water was further evaporated under a vacuum. The surface morphology was additionally examined on a scanning electron microscope (JSM 5510, JEOL, Tokyo, Japan) operating at 10 kV. Before imaging, the samples were coated with gold for 30 s using a sputter-coater (JSC 1200, JEOL, Tokyo, Japan) in an inert argon atmosphere.

4.3.3. Thermogravimetric Analysis (TGA)

A PerkinElmer TGA4000 thermogravimeter was used to perform the TGA, and the operating conditions were as follows: argon gas at 60 mL/min, a temperature range from 40 °C to 820 °C and a heating rate of 10 °C/min. Specialized software (Pyris v.11.0.0.0449) was used for data collection and processing.

4.3.4. X-ray Powder Diffraction (XRD)

XRD measurements were applied to characterize the nanoparticle crystallographic structure. The small-angle parts of the XRD patterns were collected from 0.3 to 8° 2θ using a knife-edge antiscatter screen attachment of the primary beam. Patterns were obtained on the Bruker D8 Advance diffractometer with Cu Kα radiation and a LynxEye detector (Bruker Corporation, Karlsruhe, Germany).

4.3.5. Determination of the Lower Critical Solution Temperature (LCST)

The characterization was performed via transmittance measurements on a UV spectrophotometer (Thermo Scientific Evolution 300, Madison, WI, USA) at 500 nm with a heating/cooling cycle step of 1 °C after incubating the samples for 5 min at each temperature. The light passed through the solution and the transmittance, as a percentage, was measured. At the LCST, a change in turbidity of the AA-g-PnVCL solution occurred.

4.3.6. Dynamic Light Scattering (DLS)

The nanoparticles' size, polydispersity index and zeta potential were determined using a Zetasizer (Zetasizer Nano ZS, Malvern Panalytical, Worcestershire, UK). The samples (0.1% w/v) were dispersed in distilled water, sonicated for 20 min and measured at a scattering angle of 90° and at 25 °C.

4.3.7. Drug Loading and Loading Efficiency

The wet mixing method was used for loading the model drug Dox into the hybrid MCM-41/AA-PnVCL particles. The particles were mixed with Dox at a weight ratio of 1:1

in 10 mL of water on a magnetic stirrer for 2 h at 40 °C. Then they were allowed to cool to room temperature. After incubation, the samples were centrifuged at 14,000 rpm for 20 min, washed three times with ethanol and dried under a vacuum for 24 h. Quantitative loading of Dox was determined by analysing the obtained supernatant by UV-vis absorption at 480 nm and was calculated by the formula

$$\text{Drug loading efficiency } (\%) = \frac{\text{A} - \text{B}}{\text{A}} \times 100 \tag{1}$$

where A is the total weight of Dox used for the drug-loading procedure and B is the weight of Dox which was present in the supernatant.

4.3.8. In Vitro Drug Release Study

All samples including MCM-41/Dox, AA-g-PnVCL/Dox and MCM-41/AA-PnVCL/Dox in amounts equal to approximately 6 mg of Dox were placed in a dialysis bag (MWCO: 6–8 kDa, Spectra/Por®) with 3 mL of a phosphate buffer solution (PBS) (pH 4.0 and pH 7.4) and were immersed in 20 mL of a buffered medium with the corresponding pH. Drug release was studied using an incubator shaker at 25 °C, 37 °C and 40 °C. Aliquots were withdrawn, analysed by UV-vis spectroscopy at $\lambda_{\max}$ = 480 nm and replaced with fresh medium at predetermined time points. A control experiment was conducted with free Dox to confirm that the selected dialysis membrane ensured unrestricted diffusion of the released drug. The highest drug concentration in the dialysate was below 10% of the drug's aqueous solubility, which is a prerequisite for "sink" conditions. The release study was performed in triplicate. The amount of Dox released was calculated on the basis of a previously obtained calibration curve in the corresponding PBS medium. One-way ANOVA was used to determine the significance of the differences in the amounts released. The significance level was set as $p < 0.05$.

4.3.9. Haemolysis Assay

The haemolytic potential of the test substances was evaluated following the protocol described by Evans et al. [59]. Blood samples from healthy volunteers were obtained from a certified clinical laboratory. The experimental procedures were conducted according to the rules of the Institutional Ethics Committee (KENIMUS) of the Medical University of Sofia, Bulgaria [60]. The erythrocytes were separated from the blood by repeated centrifugation in a 0.9% NaCl buffer. Then the blood cells were resuspended in a phosphate buffer (pH 7.4). The test substances (at appropriate concentrations), 20% Triton X-100 (used as a positive control group) and the phosphate buffer (used as a negative control group) were pipetted into 96-well plates, and the erythrocyte suspension in a phosphate buffer was added to them. Then the plates were incubated for 1 h at 37 °C and centrifuged for 5 min at 500× g. The supernatant was moved to new 96-well plates, in which the absorbance of haemoglobin was measured at 430 nm in a Synergy 2 plate reader (BioTek Instruments, Inc., Highland Park, Winooski, VT, USA). The results obtained were presented as the percentage of haemolysis relative to the haemoglobin's absorbance values in the positive controls; the haemoglobin absorbance of the negative controls was accepted as zero haemolysis. The substances that caused haemolysis below 5% (the acceptable haemolytic threshold is 5% according to ISO 10993-5) were considered to be biocompatible [61,62].

4.3.10. Statistical analysis

Statistical analysis was performed by one-way ANOVA followed by Dunnett's post hoc test. Statistical evaluation was performed using GraphPad 6 software. Differences were accepted to be significant at $p < 0.001$. All statistical analyses were carried out with Graph Pad 6 software. The results are expressed as the mean ± SD (n = 6) for 3 independent experiments.

Author Contributions: Conceptualization, C.V. and M.S.; methodology, T.P., D.T., D.S., V.T., I.S., S.T. and D.K.; software, D.S., D.T. and I.S.; formal analysis, D.T. and B.T. investigation, I.I.; resources, C.V.; data curation, I.I.; writing—original draft preparation, C.V. and M.S.; writing—review and editing, D.S., V.T., C.V. and M.S.; visualization, I.S., D.K., C.V. and M.S.; supervision, S.T., V.T. and B.T.; project administration, S.T. and C.V.; funding acquisition, S.T. and C.V. All authors have read and agreed to the published version of the manuscript.

Funding: I.I. and S.T. acknowledge the financial support of Medical University-Pleven, Commission for Financing Research Projects, with financing project 9/2021. C.V., M.S., T.P. and B.T. thank the funding provided by the European Union—Next Generation EU, through the National Recovery and Resilience Plan of the Republic of Bulgaria, Project No. BG-RRP-2.004-0004-C01.

Institutional Review Board Statement: Not applicable.

Informed Consent Statement: Not applicable.

Data Availability Statement: Data are available from the authors (see the email of the corresponding author).

Conflicts of Interest: The authors declare no conflict of interest.

References

1. Bukowski, K.; Kciuk, M.; Kontek, R. Mechanisms of Multidrug Resistance in Cancer Chemotherapy. *Int. J. Mol. Sci.* **2020**, *21*, 3233. [CrossRef]
2. Liu, Y.-Q.; Wang, X.-L.; He, D.-H.; Cheng, Y.-X. Protection against Chemotherapy- and Radiotherapy-Induced Side Effects: A Review Based on the Mechanisms and Therapeutic Opportunities of Phytochemicals. *Phytomedicine* **2021**, *80*, 153402. [CrossRef]
3. Niu, G.; Cogburn, B.; Hughes, J. Preparation and Characterization of Doxorubicin Liposomes. In *Cancer Nanotechnology: Methods and Protocols*; Methods in Molecular Biology; Grobmyer, S.R., Moudgil, B.M., Eds.; Humana Press: Totowa, NJ, USA, 2010; pp. 211–219, ISBN 978-1-60761-609-2.
4. Mal, A.; Prabhuraj, R.S.; Malhotra, R.; Valvi, S.K.; Ingle, A.; Srivastava, R.; De, A.; Bandyopadhyaya, R. pH-Responsive Sustained Delivery of Doxorubicin Using Aminated and PEGylated Mesoporous Silica Nanoparticles Leads to Enhanced Antitumor Efficacy in Pre-Clinical Orthotopic Breast Cancer Model. *J. Drug Deliv. Sci. Technol.* **2022**, *77*, 103800. [CrossRef]
5. Moraes, S.; Marinho, A.; Lima, S.; Granja, A.; Araújo, J.P.; Reis, S.; Sousa, C.T.; Nunes, C. Targeted Nanostructured Lipid Carriers for Doxorubicin Oral Delivery. *Int. J. Pharm.* **2021**, *592*, 120029. [CrossRef]
6. Valencia-Lazcano, A.A.; Hassan, D.; Pourmadadi, M.; Shamsabadipour, A.; Behzadmehr, R.; Rahdar, A.; Medina, D.I.; Díez-Pascual, A.M. 5-Fluorouracil Nano-Delivery Systems as a Cutting-Edge for Cancer Therapy. *Eur. J. Med. Chem.* **2023**, *246*, 114995. [CrossRef]
7. Shao, D.; Gao, Q.; Sheng, Y.; Li, S.; Kong, Y. Construction of a Dual-Responsive Dual-Drug Delivery Platform Based on the Hybrids of Mesoporous Silica, Sodium Hyaluronate, Chitosan and Oxidized Sodium Carboxymethyl Cellulose. *Int. J. Biol. Macromol.* **2022**, *202*, 37–45. [CrossRef]
8. Wei, G.; Wang, Y.; Yang, G.; Wang, Y.; Ju, R. Recent Progress in Nanomedicine for Enhanced Cancer Chemotherapy. *Theranostics* **2021**, *11*, 6370–6392. [CrossRef]
9. Nawaz, A.; Ullah, S.; Alnuwaiser, M.A.; Rehman, F.U.; Selim, S.; Al Jaouni, S.K.; Farid, A. Formulation and Evaluation of Chitosan-Gelatin Thermosensitive Hydrogels Containing 5FU-Alginate Nanoparticles for Skin Delivery. *Gels* **2022**, *8*, 537. [CrossRef]
10. Slavkova, M.; Tzankov, B.; Popova, T.; Voycheva, C. Gel Formulations for Topical Treatment of Skin Cancer: A Review. *Gels* **2023**, *9*, 352. [CrossRef]
11. Qureshi, D.; Nayak, S.K.; Maji, S.; Anis, A.; Kim, D.; Pal, K. Environment Sensitive Hydrogels for Drug Delivery Applications. *Eur. Polym. J.* **2019**, *120*, 109220. [CrossRef]
12. Li, L.; Scheiger, J.M.; Levkin, P.A. Design and Applications of Photoresponsive Hydrogels. *Adv. Mater.* **2019**, *31*, 1807333. [CrossRef] [PubMed]
13. Arneth, B. Tumor Microenvironment. *Medicina* **2020**, *56*, 15. [CrossRef] [PubMed]
14. Fu, S.; Chang, L.; Liu, S.; Gao, T.; Sang, X.; Zhang, Z.; Mu, W.; Liu, X.; Liang, S.; Yang, H.; et al. Temperature Sensitive Liposome Based Cancer Nanomedicine Enables Tumour Lymph Node Immune Microenvironment Remodelling. *Nat. Commun.* **2023**, *14*, 2248. [CrossRef]
15. Yu, Y.; Cheng, Y.; Tong, J.; Zhang, L.; Wei, Y.; Tian, M. Recent Advances in Thermo-Sensitive Hydrogels for Drug Delivery. *J. Mater. Chem. B* **2021**, *9*, 2979–2992. [CrossRef]
16. Thananukul, K.; Kaewsaneha, C.; Opaprakasit, P.; Lebaz, N.; Errachid, A.; Elaissari, A. Smart Gating Porous Particles as New Carriers for Drug Delivery. *Adv. Drug Deliv. Rev.* **2021**, *174*, 425–446. [CrossRef]
17. Bashir, S.; Hina, M.; Iqbal, J.; Rajpar, A.H.; Mujtaba, M.A.; Alghamdi, N.A.; Wageh, S.; Ramesh, K.; Ramesh, S. Fundamental Concepts of Hydrogels: Synthesis, Properties, and Their Applications. *Polymers* **2020**, *12*, 2702. [CrossRef]

18. Raghuwanshi, V.S.; Garnier, G. Characterisation of Hydrogels: Linking the Nano to the Microscale. *Adv. Colloid Interface Sci.* **2019**, *274*, 102044. [CrossRef]
19. Zhang, Z.; Wang, S.; Waterhouse, G.I.N.; Zhang, Q.; Li, L. Poly(N-Isopropylacrylamide)/Mesoporous Silica Thermosensitive Composite Hydrogels for Drug Loading and Release. *J. Appl. Polym. Sci.* **2020**, *137*, 48391. [CrossRef]
20. Rout, S.R.; Gowtham, K.; Sheikh, A.; Parvez, S.; Dandela, R.; Kesharwani, P. Chapter 15—Recent Advances and Future Prospective of Hybrid Drug Delivery Systems. In *Hybrid Nanomaterials for Drug Delivery*; Woodhead Publishing Series in Biomaterials; Kesharwani, P., Jain, N.K., Eds.; Woodhead Publishing: Cambridge, UK, 2022; pp. 357–374, ISBN 978-0-323-85754-3.
21. Zhang, M.; Qiao, X.; Han, W.; Jiang, T.; Liu, F.; Zhao, X. Alginate-Chitosan Oligosaccharide-ZnO Composite Hydrogel for Accelerating Wound Healing. *Carbohydr. Polym.* **2021**, *266*, 118100. [CrossRef]
22. Mamidi, N.; Delgadillo, R.M.V. Design, Fabrication and Drug Release Potential of Dual Stimuli-Responsive Composite Hydrogel Nanoparticle Interfaces. *Colloids Surf. B Biointerfaces* **2021**, *204*, 111819. [CrossRef]
23. Popescu, I.; Constantin, M.; Solcan, G.; Ichim, D.L.; Rata, D.M.; Horodincu, L.; Solcan, C. Composite Hydrogels with Embedded Silver Nanoparticles and Ibuprofen as Wound Dressing. *Gels* **2023**, *9*, 654. [CrossRef] [PubMed]
24. Zhang, Z.; Ji, Y.; Lin, C.; Tao, L. Thermosensitive Hydrogel-Functionalized Gold Nanorod/Mesoporous MnO2 Nanoparticles for Tumor Cell-Triggered Drug Delivery. *Mater. Sci. Eng. C* **2021**, *131*, 112504. [CrossRef] [PubMed]
25. Liu, C.-M.; Chen, G.-B.; Chen, H.-H.; Zhang, J.-B.; Li, H.-Z.; Sheng, M.-X.; Weng, W.-B.; Guo, S.-M. Cancer Cell Membrane-Cloaked Mesoporous Silica Nanoparticles with a pH-Sensitive Gatekeeper for Cancer Treatment. *Colloids Surf. B Biointerfaces* **2019**, *175*, 477–486. [CrossRef]
26. Bharti, C.; Nagaich, U.; Pal, A.K.; Gulati, N. Mesoporous Silica Nanoparticles in Target Drug Delivery System: A Review. *Int. J. Pharm. Investig.* **2015**, *5*, 124–133. [CrossRef]
27. Hu, X.; Hao, X.; Wu, Y.; Zhang, J.; Zhang, X.; Wang, P.C.; Zou, G.; Liang, X.-J. Multifunctional Hybrid Silica Nanoparticles for Controlled Doxorubicin Loading and Release with Thermal and pH Dual Response. *J. Mater. Chem. B* **2013**, *1*, 1109–1118. [CrossRef]
28. Voycheva, C.; Popova, T.M.; Tzankova, V.; Stefanova, D.; Tzankova, D.; Spassova, I.; Kovacheva, D.; Tzankov, B. Doxorubicin and Quercetin Double Loading in Modified MCM-41 Lowered Cardiotoxicity in H9c2 Cardioblast Cells In Vitro. *Bioengineering* **2023**, *10*, 637. [CrossRef]
29. Djayanti, K.; Maharjan, P.; Cho, K.H.; Jeong, S.; Kim, M.S.; Shin, M.C.; Min, K.A. Mesoporous Silica Nanoparticles as a Potential Nanoplatform: Therapeutic Applications and Considerations. *Int. J. Mol. Sci.* **2023**, *24*, 6349. [CrossRef]
30. Dumontel, B.; Conejo-Rodríguez, V.; Vallet-Regí, M.; Manzano, M. Natural Biopolymers as Smart Coating Materials of Mesoporous Silica Nanoparticles for Drug Delivery. *Pharmaceutics* **2023**, *15*, 447. [CrossRef]
31. Lomartire, S.; Gonçalves, A.M.M. Algal Phycocolloids: Bioactivities and Pharmaceutical Applications. *Mar. Drugs* **2023**, *21*, 384. [CrossRef]
32. Lee, W.-K.; Lim, Y.-Y.; Leow, A.T.-C.; Namasivayam, P.; Abdullah, J.O.; Ho, C.-L. Factors Affecting Yield and Gelling Properties of Agar. *J. Appl. Phycol.* **2017**, *29*, 1527–1540. [CrossRef]
33. Voycheva, C.; Slavkova, M.; Popova, T.; Tzankova, D.; Tosheva, A.; Aluani, D.; Tzankova, V.; Ivanova, I.; Tzankov, S.; Spassova, I.; et al. Synthesis and Characterization of PnVCL Grafted Agar with Potential Temperature-Sensitive Delivery of Doxorubicin. *J. Drug Deliv. Sci. Technol.* **2022**, *76*, 103725. [CrossRef]
34. Alam Khan, S.; Jawaid Akhtar, M. Structural Modification and Strategies for the Enhanced Doxorubicin Drug Delivery. *Bioorganic Chem.* **2022**, *120*, 105599. [CrossRef] [PubMed]
35. Frickenstein, A.N.; Hagood, J.M.; Britten, C.N.; Abbott, B.S.; McNally, M.W.; Vopat, C.A.; Patterson, E.G.; MacCuaig, W.M.; Jain, A.; Walters, K.B.; et al. Mesoporous Silica Nanoparticles: Properties and Strategies for Enhancing Clinical Effect. *Pharmaceutics* **2021**, *13*, 570. [CrossRef] [PubMed]
36. Zhang, L.; Bei, H.P.; Piao, Y.; Wang, Y.; Yang, M.; Zhao, X. Polymer-Brush-Grafted Mesoporous Silica Nanoparticles for Triggered Drug Delivery. *ChemPhysChem* **2018**, *19*, 1956–1964. [CrossRef] [PubMed]
37. Ghalehkhondabi, V.; Fazlali, A.; Soleymani, M. Temperature and pH-Responsive PNIPAM@PAA Nanospheres with a Core-Shell Structure for Controlled Release of Doxorubicin in Breast Cancer Treatment. *J. Pharm. Sci.* **2023**, *112*, 1957–1966. [CrossRef]
38. Ribeiro, T.P.; Moreira, J.A.; Monteiro, F.J.; Laranjeira, M.S. Nanomaterials in Cancer: Reviewing the Combination of Hyperthermia and Triggered Chemotherapy. *J. Control. Release* **2022**, *347*, 89–103. [CrossRef]
39. Takahashi, R.; Sato, S.; Sodesawa, T.; Kawakita, M.; Ogura, K. High Surface-Area Silica with Controlled Pore Size Prepared from Nanocomposite of Silica and Citric Acid. *J. Phys. Chem. B* **2000**, *104*, 12184–12191. [CrossRef]
40. Horcajada, P.; Rámila, A.; Férey, G.; Vallet-Regí, M. Influence of Superficial Organic Modification of MCM-41 Matrices on Drug Delivery Rate. *Solid State Sci.* **2006**, *8*, 1243–1249. [CrossRef]
41. Lai, Y.-L.; Cheng, Y.-M.; Yen, S.-K. Doxorubicin–Chitosan–Hydroxyapatite Composite Coatings on Titanium Alloy for Localized Cancer Therapy. *Mater. Sci. Eng. C* **2019**, *104*, 109953. [CrossRef]
42. Hu, S.H.; Fang, R.H.; Chen, Y.W.; Liao, B.J.; Chen, I.W.; Chen, S.-Y. Photoresponsive Protein-Graphene-Protein Hybrid Capsules with Dual Targeted Heat-Triggered Drug Delivery Approach for Enhanced Tumor Therapy. *Adv. Funct. Mater.* **2014**, *24*, 4144–4155. [CrossRef]
43. Cortez-Lemus, N.A.; Licea-Claverie, A. Poly(N-Vinylcaprolactam), a Comprehensive Review on a Thermoresponsive Polymer Becoming Popular. *Prog. Polym. Sci.* **2016**, *53*, 1–51. [CrossRef]

44. Rejinold, N.S.; Chennazhi, K.P.; Nair, S.V.; Tamura, H.; Jayakumar, R. Biodegradable and Thermo-Sensitive Chitosan-g-Poly(N-Vinylcaprolactam) Nanoparticles as a 5-Fluorouracil Carrier. *Carbohydr. Polym.* **2011**, *83*, 776–786. [CrossRef]
45. Banihashem, S.; Nezhati, M.N.; Panahia, H.A. Synthesis of Chitosan-Grafted-Poly(N-Vinylcaprolactam) Coated on the Thiolated Gold Nanoparticles Surface for Controlled Release of Cisplatin. *Carbohydr. Polym.* **2020**, *227*, 115333. [CrossRef] [PubMed]
46. Karesoja, M.; McKee, J.; Karjalainen, E.; Hietala, S.; Bergman, L.; Linden, M.; Tenhu, H. Mesoporous Silica Particles Grafted with Poly(Ethyleneoxide-Block-N-Vinylcaprolactam). *J. Polym. Sci. Part Polym. Chem.* **2013**, *51*, 5012–5020. [CrossRef]
47. Singh, N.; Karambelkar, A.; Gu, L.; Lin, K.; Miller, J.S.; Chen, C.S.; Sailor, M.J.; Bhatia, S.N. Bioresponsive Mesoporous Silica Nanoparticles for Triggered Drug Release. *J. Am. Chem. Soc.* **2011**, *133*, 19582–19585. [CrossRef]
48. Galhano, J.; Marcelo, G.A.; Duarte, M.P.; Oliveira, E. Ofloxacin@Doxorubicin-Epirubicin Functionalized MCM-41 Mesoporous Silica-Based Nanocarriers as Synergistic Drug Delivery Tools for Cancer Related Bacterial Infections. *Bioorg. Chem.* **2022**, *118*, 105470. [CrossRef]
49. Miao, Y.; Feng, Y.; Bai, J.; Liu, Z.; Zhao, X. Optimized Mesoporous Silica Nanoparticle-Based Drug Delivery System with Removable Manganese Oxide Gatekeeper for Controlled Delivery of Doxorubicin. *J. Colloid Interface Sci.* **2021**, *592*, 227–236. [CrossRef]
50. Yan, J.; Xu, X.; Zhou, J.; Liu, C.; Zhang, L.; Wang, D.; Yang, F.; Zhang, H. Fabrication of a pH/Redox-Triggered Mesoporous Silica-Based Nanoparticle with Microfluidics for Anticancer Drugs Doxorubicin and Paclitaxel Codelivery. *ACS Appl. Bio Mater.* **2020**, *3*, 1216–1225. [CrossRef]
51. Dasgupta, D.; Das, M.; Thakore, S.; Patel, A.; Kumar, S.; Seshadri, S. Development of a Controlled Sustainable Anticancer Drug Delivery Nanosystem Comprising Doxorubicin and Functionalized MCM-48. *J. Drug Deliv. Sci. Technol.* **2022**, *72*, 103419. [CrossRef]
52. Knežević, N.Ž.; Trewyn, B.G.; Lin, V.S.-Y. Light- and pH-Responsive Release of Doxorubicin from a Mesoporous Silica-Based Nanocarrier. *Chem. Weinh. Bergstr. Ger.* **2011**, *17*, 3338–3342. [CrossRef]
53. Sturgeon, R.J.; Schulman, S.G. Electronic Absorption Spectra and Protolytic Equilibria of Doxorubicin: Direct Spectrophotometric Determination of Microconstants. *J. Pharm. Sci.* **1977**, *66*, 958–961. [CrossRef] [PubMed]
54. Janssen, M.J.H.; Crommelin, D.J.A.; Storm, G.; Hulshoff, A. Doxorubicin Decomposition on Storage. Effect of pH, Type of Buffer and Liposome Encapsulation. *Int. J. Pharm.* **1985**, *23*, 1–11. [CrossRef]
55. Hakeem, A.; Zahid, F.; Zhan, G.; Yi, P.; Yang, H.; Gan, L.; Yang, X. Polyaspartic Acid-Anchored Mesoporous Silica Nanoparticles for pH-Responsive Doxorubicin Release. *Int. J. Nanomed.* **2018**, *13*, 1029–1040. [CrossRef]
56. Maghsoudi, M.; Abbasian, M.; Farhadi, K.; Mahmoodzadeh, F.; Ghorbani, M.; Hoseinzadeh, M. Mesoporous Si-MCM-41/Polymer as a pH-Responsive Drug Delivery System for Cancer Therapy. *ChemistrySelect* **2020**, *5*, 11901–11909. [CrossRef]
57. Saroj, S.; Rajput, S.J. Tailor-Made pH-Sensitive Polyacrylic Acid Functionalized Mesoporous Silica Nanoparticles for Efficient and Controlled Delivery of Anti-Cancer Drug Etoposide. *Drug Dev. Ind. Pharm.* **2018**, *44*, 1198–1211. [CrossRef] [PubMed]
58. Zhao, Y.; Sun, X.; Zhang, G.; Trewyn, B.G.; Slowing, I.I.; Lin, V.S.-Y. Interaction of Mesoporous Silica Nanoparticles with Human Red Blood Cell Membranes: Size and Surface Effects. *ACS Nano* **2011**, *5*, 1366–1375. [CrossRef]
59. Evans, B.C.; Nelson, C.E.; Yu, S.S.; Beavers, K.R.; Kim, A.J.; Li, H.; Nelson, H.M.; Giorgio, T.D.; Duvall, C.L. Ex Vivo Red Blood Cell Hemolysis Assay for the Evaluation of pH-Responsive Endosomolytic Agents for Cytosolic Delivery of Biomacromolecular Drugs. *J. Vis. Exp. JoVE* **2013**, *73*, e50166. [CrossRef]
60. Available online: https://mu-sofia.bg/nauka/nauka/etika-nauchni-izsledvania/ (accessed on 14 September 2023).
61. *ISO 10993-5:2009*; Biological Evaluation of Medical Devices—Part 5: Tests for In Vitro Cytotoxicity. ISO: Geneva, Switzerland, 2009. Available online: https://www.iso.org/standard/36406.html (accessed on 14 June 2023).
62. Romero, A.A.; Alba, M.D.; Zhou, W.; Klinowski, J. Synthesis and Characterization of the Mesoporous Silicate Molecular Sieve MCM-48. *J. Phys. Chem. B* **1997**, *101*, 5294–5300. [CrossRef]

gels

Article

Akkermansia muciniphila Encapsulated in Calcium-Alginate Hydrogelated Matrix: Viability and Stability over Aerobic Storage and Simulated Gastrointestinal Conditions

Daniela Machado †, Mariana Fonseca †, Rita Vedor, Sérgio Sousa, Joana Cristina Barbosa and Ana Maria Gomes *

Universidade Católica Portuguesa, CBQF—Centro de Biotecnologia e Química Fina—Laboratório Associado, Escola Superior de Biotecnologia, Rua Diogo Botelho 1327, 4169-005 Porto, Portugal; dmachado@ucp.pt (D.M.); s-marfonseca@ucp.pt (M.F.); rvedor@ucp.pt (R.V.); sdsousa@ucp.pt (S.S.); jcbarbosa@ucp.pt (J.C.B.)

* Correspondence: amgomes@ucp.pt

† These authors contributed equally to this work.

Abstract: *Akkermansia muciniphila* is considered a next-generation probiotic to be incorporated in new food and pharmaceutical formulations. Effective delivery systems are required to ensure high probiotic viability and stability during product manufacture, shelf-life, and post-consumption, namely, throughout digestion. Hydrogelated matrices have demonstrated promising potential in this dominion. Hence, this work aimed to evaluate the effect of a calcium-alginate hydrogelated matrix on *A. muciniphila* viability during 28-days refrigerated aerobic storage and when exposed to simulated gastrointestinal conditions, in comparison with that of free cells. *Akkermansia muciniphila* was successfully encapsulated in the calcium-alginate matrix via extrusion (60% encapsulation yield). Furthermore, encapsulated *A. muciniphila* exhibited high stability (a loss in viability lower than 0.2 log-cycle) after 28-days of refrigerated aerobic storage, maintaining its viability around 10^8 CFU/g. Prominently, as the storage time increased, encapsulated *A. muciniphila* revealed higher viability and stability regarding in vitro gastrointestinal conditions than free cells. This suggests that this encapsulation method may attenuate the detrimental effects of prolonged aerobic storage with a subsequent gastrointestinal passage. In conclusion, encapsulation via extrusion using a calcium-alginate hydrogelated matrix seems to be a promising and adequate strategy for safeguarding *A. muciniphila* from adverse conditions encountered during refrigerated aerobic storage and when exposed to the gastrointestinal passage.

Keywords: *Akkermansia muciniphila*; calcium-alginate hydrogelated matrix; encapsulation; extrusion; gastrointestinal passage; probiotic; storage; viability

1. Introduction

Probiotics are widely known as live microorganisms whose adequate consumption confers health-promoting effects on the host [1]. Traditionally, the microorganisms belonging to *Bifidobacterium* and former *Lactobacillus* genera (recently reclassified into 25 genera [2]) are recognized as well-studied and the most commercialized probiotics [3]. However, the growing trend and expansion of the probiotic market have led to a continuous search for the diversification of the available products. Taking this into account, several studies aiming at the selection of novel strains with different and specific functional properties have been conducted [4]. In this alignment, various bacterial species isolated from human gut microbiota, such as *Akkermansia muciniphila* and *Faecalibacterium* species, have been considered as novel probiotic candidates, also known as next-generation probiotics [3].

In the microbiology field, *A. muciniphila* is typically described as an oval-shaped, anaerobic, Gram-negative, and mucin-degrading bacterium that accounts for approximately 1 to 3% of the total fecal microbiota of healthy adults [5,6]. Recent evidence demonstrated that *A. muciniphila* plays a key role in the preservation of gut barrier integrity, modulation of the host immune response, and improvement of several metabolic pathways, making it a promising therapeutic tool in several metabolic, cardiovascular, neurological, and oncological disorders [7]. For *A. muciniphila* to be applied as a probiotic, effective delivery systems must be developed to guarantee the survival of this novel probiotic during manufacturing, the distribution chain, and shelf-life/storage. Additionally, these strategies must ensure protection throughout the gastrointestinal passage to guarantee that probiotic bacteria reach the intestine (target site) in adequate amounts to exert the desired health benefits [3].

Encapsulation techniques have been proposed as effective strategies to protect probiotic microorganisms against adverse conditions, as these methods may facilitate the controlled release and successful delivery of probiotics to the site of action [8]. Typically, it is defined as an entrapment process of substances (active ingredients) within another material (encapsulant). Several polymers may be used for probiotic encapsulation, including gelatin, chitosan, and alginate, the latter being one of the most commonly applied biomaterials. Alginate is a polyanionic polysaccharide, composed of (1–4)-linked β-D-mannuronate and C-5 epimer α-L-guluronate (G), which exhibits interesting properties in terms of a non-toxic nature, biocompatibility, high hydrophilicity, biodegradability, easy handling, being low in cost, a capability to form a strong gel structure through ionic crosslinking with calcium ions, and pH responsiveness (i.e., it is stable at lower pH levels and unstable at higher pH conditions which is advantageous in tailoring release profiles) [8,9]. Among the various encapsulation techniques, extrusion is recognized as the oldest and most popular methodology to encapsulate probiotics given its attractive characteristics, namely, simplicity, straightforwardness, employment of gentle conditions (without the involvement of organic/harmful solvents and extreme temperatures or pH values), low operational costs, and high probiotic viability [8]. In the extrusion process, probiotics are added and mixed into a biopolymer solution. Subsequently, the suspension is placed in an extruder (pilot scale) or a syringe needle (laboratory scale), which drips off into a hardening solution (most frequently calcium chloride) under gentle stirring [8]. Indeed, previous studies demonstrated that the entrapment of probiotic bacteria in calcium-alginate capsules offered protection against harsh conditions encountered during storage or when subjected to in vitro gastrointestinal conditions [10,11]. Based on this rationale, the present study aimed to evaluate the viability and stability of *A. muciniphila* DSM 22959 entrapped in calcium-alginate capsules produced via extrusion during refrigerated aerobic storage and when exposed to an in vitro gastrointestinal passage.

2. Results and Discussion

2.1. Capsules Morphology and Encapsulation Yield of Calcium-Alginate Capsules Entrapping *Akkermansia muciniphila*

Calcium-alginate hydrogelated capsules were selected as a strategy to study the viability and stability enhancement of *A. muciniphila* because, in general, these have good thermal stability and mechanical strength to withstand eventual food processing (mixing) and physiological digestion (passage through gastric conditions to finally release their content in the intestine).

Figure 1 shows the morphology of the *A. muciniphila*-loaded calcium-alginate hydrogelated capsules analyzed macroscopically under the naked eye (Figure 1a), under optical microscopy (Figure 1b,c), and scanning electron microscopy (Figure 1d). Morphologically, *A. muciniphila* capsules were presented mostly as spherical structures, with a continuous surface (Figure 1d), estimating a size of approximately 4 mm (Figure 1c).

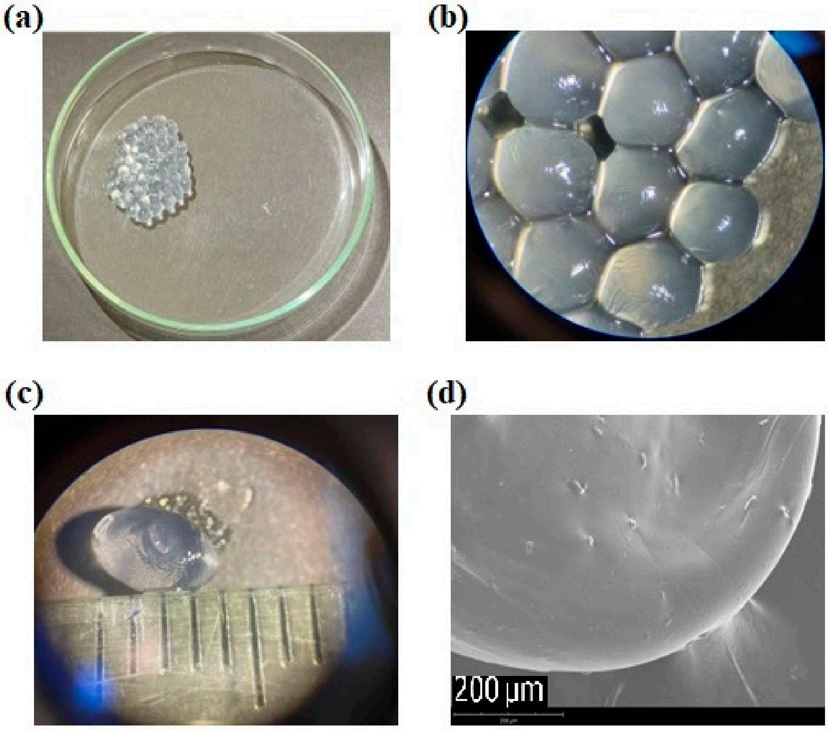

Figure 1. *Akkermansia muciniphila*-loaded capsules observed (**a**) under naked eye; (**b**) grouped under optical microscopy (magnification 20×); (**c**) individualized under optical microscopy (magnification 20×); (**d**) under scanning electron microscopy (magnification: 700×).

The encapsulation yield (EY) was 60% (±18%), calculated considering the initial *A. muciniphila* colony-forming units (CFU) number (suspension used for extrusion; 2.10×10^{10} CFU) and the final CFU number (calcium-alginate capsules; 1.26×10^{10} CFU). This value indicates that this encapsulation technique is suitable for *A. muciniphila* entrapment since the order of magnitude of the cell density (10^{10} CFU) was maintained. After comparing the obtained EY with other studies using similar encapsulation techniques but different probiotic strains, it falls within the reported range. For example, a study conducted by Amine et al. achieved EY values ranging from 31% to 65% for encapsulating *Bifidobacterium longum* ATCC 15708 using an extrusion procedure with sodium alginate and/or O-palmitoylated alginate at various concentrations [12]. Additionally, Frakolaki and coworkers implemented encapsulation via extrusion for *Bifidobacterium animalis* subsp. *lactis* BB-12® using alginate alone or in combination with other encapsulating agents, obtaining EY values ranging from 58.6% to 100%, depending on the employed encapsulating matrix [13].

Notably, van der Ark et al. were the pioneers in *A. muciniphila* encapsulation when these researchers reported an EY of 97.5% using a water-in-oil-in-water double emulsion technique. However, the encapsulated *A. muciniphila* suffered sharp viability reduction after 3 days of storage at 4 °C either under aerobic or anaerobic conditions [14]. Afterward, Marcial-Coba and colleagues encapsulated *A. muciniphila* DSM 22959 in a xanthan and gellan gum matrix, via the extrusion method, with a subsequent freeze-drying step, reporting an encapsulation efficiency ranging from 12.1% to 76.2%, depending on the employed cryoprotective agents [15]. Recently, Almeida and collaborators immobilized *A. muciniphila* DSM 22959, with a 64.4% entrapment efficacy, in a dual hydrocolloid matrix of alginate and denatured whey protein isolate by the emulsification/internal gelation method [16]. While the wide variety of encapsulating materials and techniques may explain the distinct values obtained in this work and in those described in the literature, our results suggest that the extrusion technique in the calcium-alginate matrix seems to be an efficient technological strategy for the entrapment of *A. muciniphila.*

2.2. Viability of Akkermansia muciniphila in Encapsulated and Free Forms during Refrigerated Aerobic Storage

Although there is no consensus regarding the minimum effective probiotic dose, it is usually accepted that probiotic products should have a minimum concentration of 10^6 CFU/mL or per gram and that a total of 10^8–10^9 probiotic microorganisms should be consumed daily to elicit health benefits [17]. For this reason, one of the major aspects when developing probiotic formulations refers to the ability of these to ensure the maintenance of probiotic viability throughout the manufacturing procedure and chain distribution until it reaches the consumer [3]. Additionally, in the literature, a refrigeration temperature of 4 °C has been related with a high viability level of *A. muciniphila*, either in free or encapsulated forms [15,16,18]. Taking this into account, free and encapsulated *A. muciniphila* were stored at 4 °C under aerobic conditions and their viability was assayed, at specific timepoints, for 28 days. As it can be observed in Figure 2a,b, encapsulated *A. muciniphila* exhibited a high stability in viability (loss lower than 0.2 log-cycle that corresponds to a normalized survival percentage of around 65%, see Figure 2b) after 28 days of refrigerated aerobic storage, maintaining its viability within the magnitude of 10^8 CFU/g. In contrast, free cell numbers decreased by approximately 1 log-cycle (corresponding to a normalized survival percentage of around 15%, see Figure 2b) within the same period. Notably, the present results concerning encapsulated *A. muciniphila* viability and stability throughout refrigerated aerobic storage contrast positively with those reported in the literature up to the present moment. In fact, van der Ark et al. reported a sharp viability reduction in *A. muciniphila* encapsulated in a water-in-oil-in-water double emulsion when stored at 4 °C for 72 h in both atmospheric conditions: anaerobiosis and aerobiosis [14]. Later, Marcial-Coba and colleagues evaluated the viability of *A. muciniphila* encapsulated via extrusion in a xanthan and gellan gum matrix with subsequent freeze-drying, throughout 30 days, in both aerobic and anaerobic storage conditions at temperatures of 4 °C and 25 °C. These researchers reported a significant decrease (of at least 0.5 log-cycle) in the viability of the freeze-dried microencapsulated *A. muciniphila* after 30 days of storage under both anaerobic and aerobic conditions, at both 4 °C and 25 °C, when compared with the initial concentration [15]. Chang and colleagues encapsulated *A. muciniphila* in a matrix of succinate-grafted alginate doped with epigallocatechin-3-gallate via spray-drying. The authors observed a protective effect of the matrix on the bacterial viability when comparing with the free cells; however, these observations are only verified for 12 days of anaerobic and refrigerated (4 °C) storage [19]. Another investigation conducted by Barbosa and coworkers explored the spray-drying encapsulation technique with different dairy-based matrices to enhance the viability of *A. muciniphila* over aerobic storage. The results indicated that the viability remained around 10^7 CFU/g up to 28 days at 4 °C under aerobic conditions, using a 10% skim milk matrix [18]. More recently, Almeida and colleagues encapsulated *A. muciniphila* in a dual hydrocolloid matrix containing alginate and denatured whey protein isolate by emulsification/internal gelation and they assessed the viability of the encapsulated bacteria and free counterpart over 95 days of refrigerated storage under aerobic and anaerobic conditions. These researchers reported that during the initial 30 days of refrigerated storage in both atmospheres, there was a similar reduction in the viability of both free and encapsulated cells. However, after 95 days of storage, the viability of the encapsulated *A. muciniphila* experienced a sharper decrease in both anaerobic and aerobic conditions [16]. Thus, our results suggest that extrusion in the calcium-alginate matrix ensures the maintenance of the viability of encapsulated *A. muciniphila* cells at levels around 10^8 CFU/g during 28 days under feasible household storage conditions, namely aerobic storage at 4 °C. However, the size of the capsules produced via extrusion is relatively high. For instance, the capsules' size produced herein was estimated at approximately 4 mm (Figure 1c). In the literature, the high dimension/size of the capsules obtained via extrusion is pointed to as one of the main drawbacks of this encapsulation technique [8]; nevertheless, such a drawback may be overcome by adapting their nature to the type of delivery food matrix.

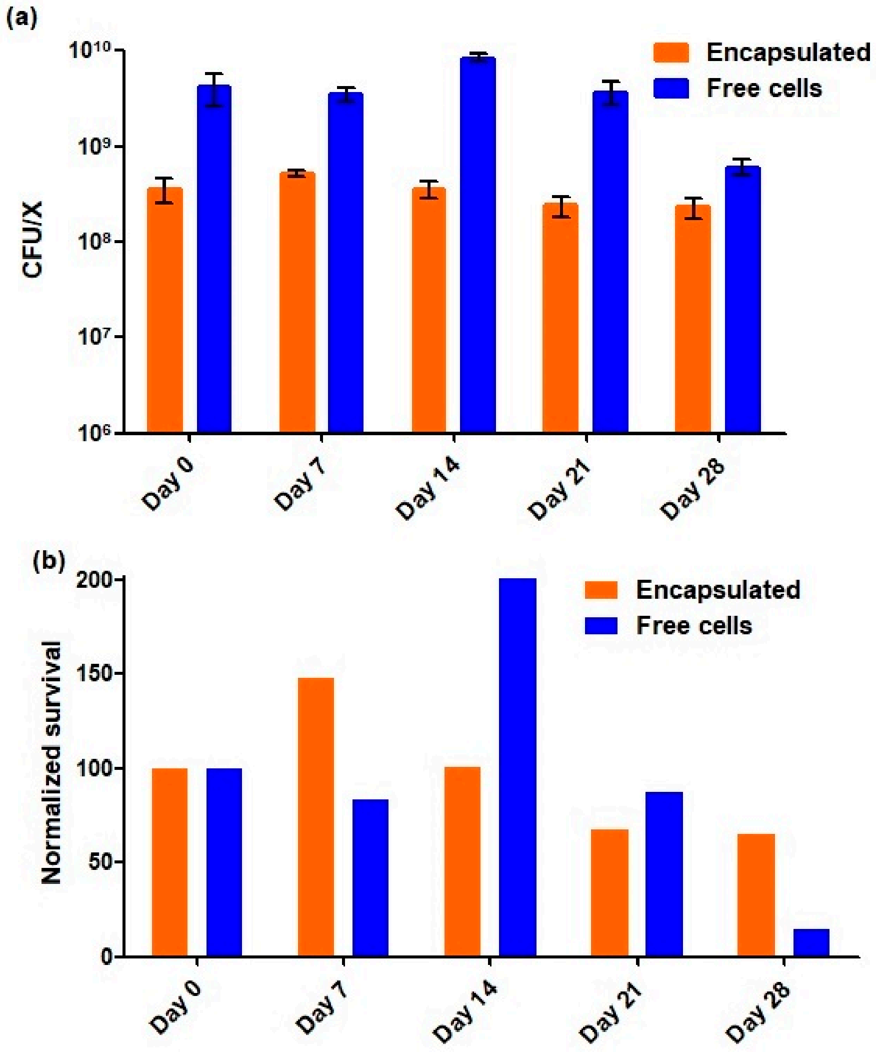

Figure 2. Viability of encapsulated (orange bars) and free cells (blue bars) of *A. muciniphila* DSM 22959 throughout 28 days of refrigerated aerobic storage (**a**) expressed in CFU/X in which X correspond to grams (g) and milliliters (mL) for encapsulated and free cells, respectively, and (**b**) expressed in terms of normalized survival in which the values of starting point (Day 0) were normalized to 100, and the subsequent time points were represented as ratios relative to this starting point.

2.3. Survival of *Akkermansia muciniphila* in Encapsulated and Free Forms When Exposed to In Vitro Simulated Gastrointestinal Conditions

It has been postulated that to elicit its beneficial effect, a probiotic microorganism must reach the target site in adequate viable numbers [1]. Therefore, it is important to ensure that delivery systems enclosing probiotic strains are resistant to the adverse gastrointestinal conditions, thus allowing the delivery of the probiotic strain in the optimal required conditions to the target site to trigger the expected benefits. In the present study, the survival of encapsulated and free *A. muciniphila* cells was assessed under simulated gastrointestinal conditions in the following timepoints: 1 and 28 days of refrigerated aerobic storage.

As presented in Table 1, on day 1 of storage, both encapsulated and free *A. muciniphila* maintained viability throughout the in vitro gastrointestinal passage, observing the maintenance of the order of magnitude with a viability of 10^8 CFU/g and 10^9 CFU/mL, respectively. In fact, in the literature it has been reported that *A. muciniphila* in its free form exhibits a certain resilience when exposed to gastrointestinal conditions [16,20]. This natural resilience observed in the early stage (at day 1) may be related with the reduced activity of bile salts against Gram-negative bacteria [21] and the presence of an acid resistance system on *A. muciniphila* cells [22].

Table 1. Evolution of viable cell numbers of *A. muciniphila* DSM 22959 in encapsulated (CFU/g) and free (CFU/mL) forms during in vitro gastrointestinal passage at 1 and 28 days of refrigerated aerobic storage. Data are shown as the mean ± standard deviation.

Condition	**Day 1**		**Day 28**	
	Encapsulated	**Free**	**Encapsulated**	**Free**
Initial Concentration	$(3.82 \pm 1.26) \times 10^8$	$(3.40 \pm 0.39) \times 10^9$	$(2.32 \pm 0.55) \times 10^8$	$(6.12 \pm 1.11) \times 10^8$
After gastric phase	$(2.74 \pm 1.17) \times 10^8$	$(2.57 \pm 0.31) \times 10^{10}$	$(1.15 \pm 0.12) \times 10^8$	$(7.46 \pm 6.91) \times 10^6$
After intestinal phase	$(1.57 \pm 0.33) \times 10^8$	$(4.83 \pm 0.36) \times 10^9$	$(2.93 \pm 1.09) \times 10^7$	<LOD [1]

[1] LOD means limit of detection, corresponding in CFU plating technique to 8×10^5 CFU/mL or /g.

Regarding the 28 days of storage, when exposed to the in vitro digestion protocol, the encapsulated bacteria reduced the number of viable cells by around 1 log-cycle (achieving a viability level in 10^7 CFU/g magnitude), while the free cells recorded a viability reduction of higher than 2 log-cycles (viability lower than 8×10^5 CFU/mL). These results showed a higher stability of encapsulated bacteria throughout the gastrointestinal passage compared to its free counterpart at the timepoint of 28 days of storage. In this alignment, a study conducted by Almeida et al. demonstrated that as the storage time increased, *A. muciniphila* encapsulated in an alginate of a denatured whey protein isolate matrix via emulsification/internal gelation showed higher stability when exposed to the gastrointestinal passage than its free counterpart. Specifically, these researchers recorded viability reductions in the free and encapsulated *A. muciniphila* of ca. 2 and lower than 1 log-cycle, respectively, at the timepoint of 30 days of refrigerated aerobic storage [16]. Still, in this context, Barbosa and coworkers showed that the encapsulation of *A. muciniphila* via spray-drying in 10% skim milk using inlet/outlet temperatures of 150/65 °C mitigated the detrimental effects of extended refrigerated aerobic storage for up 60 days, with the subsequent gastrointestinal passage allowing probiotic survival at levels of at least 10^{7} CFU/g [18]. Thus, our results suggest that the calcium-alginate capsules produced via extrusion seem to be a promising and adequate strategy to deliver *A. muciniphila* in an intestinal environment at recommended viability levels for probiotic products (above 10^6 CFU/g). Although the parameters related to *A. muciniphila* release from the capsules were not assayed, a possible mechanism of releasing these probiotic cells may be hypothesized. In the literature, it is described that alginate confers gastric-acid-protective effects on encapsulated probiotics [23,24]. In fact, the alginate capsules tend to shrink at a low pH (such as in a gastric environment), which prevents the release of encapsulated probiotic cells [8,25]. Once it passes to the higher pH of the intestinal environment, the alginate becomes a soluble alginic acid layer, allowing the release of probiotic cells [8].

3. Conclusions

This study showed that this extrusion technique, using a calcium-alginate encapsulating matrix, is an interesting and adequate strategy for *A. muciniphila* delivery. Indeed, this encapsulation technique guaranteed the efficient production of high-loaded capsules that maintained probiotic viability in a magnitude of 10^8 CFU/g throughout refrigerated aerobic storage for 28 days. Additionally, as the storage time increased, encapsulated *A. muciniphila* revealed higher viability and stability regarding in vitro gastrointestinal conditions than free cells. This finding suggests that this encapsulation procedure may attenuate the detrimental effects of prolonged aerobic storage with a subsequent gastrointestinal passage. At the same time, this extrusion method ensured *A. muciniphila* delivery at levels required for probiotic products (above 10^6 CFU/g), even after 28 days of refrigerated aerobic storage with a subsequent in vitro gastrointestinal passage. To enable the consolidation of the potential application of these probiotic calcium-alginate capsules in suitable food and pharmaceutical products, further studies on their size and morphology are required. Also, additional work assessing the viability and stability of encapsulated *A. muciniphila* under longer aerobic storage periods should be performed, to simulate the storage conditions of commercial probiotic products more realistically. Likewise, the rate and time of *A. muciniphila's* release from capsules should be determined to evaluate if a controlled release of *A. muciniphila* occurs and, consequently, its efficient delivery to the target site (intestine).

4. Materials and Methods

4.1. Bacterial Strain and Culture Conditions

Freeze-dried *A. muciniphila* DSM 22959 strain obtained from DSMZ collection (Leibniz Institute DSMZ—German Collection of Microorganisms and Cell Cultures, Braunschweig, Germany) was used in present study. For long-term storage, this strain was maintained frozen at −80 °C in PYG broth supplemented with 0.1% (m/v) mucin [PYGM; media composition as recommended by DSMZ [26] except that no resazurin was added], with 20% (v/v) glycerol (Fisher Scientific, Loughborough, UK). For each experiment, a glycerol stock of *A. muciniphila* DSM 22959 was thawed and grown in PYGM broth at 37 °C for 20–24 h under anaerobic conditions (85% N_2, 5% H_2, and 10% CO_2) achieved in an anaerobic incubator (Whitley A35 HEPA anaerobic workstation, Bingley, UK). The bacterial cultures were then propagated, at least two subsequent culturing steps, by inoculating fresh medium (PYGM broth) at 10% (v/v) and incubating under same growth conditions. The resulting cultures were centrifuged at 12,000× g for 30 min at 4 °C (Sorvall LYNX 4000 Superspeed Centrifuge, Thermo Fisher Scientific, Waltham, MA, USA) and washed once with the same volume of physiological saline solution (NaCl at 0.85% m/v). After centrifugation in the same previous conditions, the pelleted biomass was resuspended in physiological saline solution to reach a final cell concentration around 10^9 CFU/mL. This resulting bacterial suspension was either used directly as free cells control or for encapsulation procedure via extrusion (5 mL).

4.2. Extrusion Procedure

Encapsulation via the extrusion technique was based on Sousa and colleagues' protocol where optimum conditions were already adapted for different commercial probiotic strains [11]; herein, the protocol underwent some modifications. Briefly, *A. muciniphila* saline suspension (with a concentration of around 10^9 CFU/mL) was added at 10% (v/v) to 2% (m/v) sodium alginate with molecular weight ranging from 12,000–40,000 Daltons (Sigma-Aldrich, St. Louis, MO, USA). Afterwards, the alginate–culture mixtures (in a proportion of 45 mL alginate:5 mL bacterial suspension) were loaded in a 60 mL syringe (Enfa, Jiangsu Kanghua Medical Equipment Co., Ltd., Changzhou, China) coupled with a syringe needle (21 G × 1.5″, ICOplus 3, KD Medical GmbH Hospital Products, Berlin, Germany). This mixture (50 mL) was then extruded into 200 mL of 4% (m/v) $CaCl_2$ solution and stirred at 200 rpm (Heidolph MR 3001 magnetic stirrer; Heidolph Instruments GmbH and Co. KG, Schwabach, Germany). The extrusion rate was 4.0 mL/min. The flow rate was controlled using a syringe pump (Braintree Scientific BS-300 syringe pump, Braintree Scientific, Braintree, MA, USA). Afterward, the resulting capsules were left in contact with the $CaCl_2$ solution for 30 min at room temperature to ensure complete solidification. The $CaCl_2$ solution was subsequently removed by decanting and the capsules were suspended in physiological saline solution. Lastly, the capsules were recovered using a fine mesh strainer and they were stored according to conditions described in Section 4.6.

4.3. Enumeration of Free and Encapsulated Akkermansia muciniphila Cells

For the enumeration of free *A. muciniphila* cells, decimal dilutions were performed in PBS and spotted, in triplicate, on PYGM agar plates [PYGM broth supplemented with 1.5% (m/v) agar (BIOKAR Diagnostics, Beauvais, France)]. Plates were incubated for 5–7 days at 37 °C under anaerobic conditions, and results were expressed in CFU/mL. Concerning the encapsulated bacteria, the capsules were suspended in a tri-sodium citrate dihydrate (Merck KGaA, Darmstadt, Germany) solution at 2.28% (*m*/*v*) in a 1:9 (g/mL) ratio and subjected to the mechanical action of sterile pellet pestle (Sigma-Aldrich, St. Louis, MO, USA) assisted with vortexing for 5 min to allow the complete release of *A. muciniphila* cells from capsules. The resulting suspension was then serially diluted, as described for the free cells, and the results were expressed as CFU/g.

4.4. Encapsulation Yield Calculation

Encapsulation yield (EY) is a combined measurement of the efficacy of entrapment and survival of viable cells during the encapsulation procedure, and it was calculated according to the formula proposed by Martin and coworkers [27]:

$$\text{EY}\ (\%) = (\text{N}/\text{N0}) \times 100, \tag{1}$$

where N is the number of CFU released from capsules and N0 is the number of CFU present in bacterial suspension added to the alginate solution during the encapsulation procedure.

4.5. Capsules Morphology

The appearance of *A. muciniphila*-loaded capsules was analyzed under optical microscopy using an Olympus Stereo Microscope SZ60 (Olympus, Tokyo, Japan). Furthermore, capsules morphology was assessed through scanning electron microscopy. Initially, alginate capsules were fixed with a 2.5% (*v*/*v*) glutaraldehyde solution for 1 h. The samples were then washed with water, and dehydrated through immersion in a graded ethanol series (30, 50, 70, 80, 90, and 100% (*v*/*v*) for a minimum of 10 min each). Afterwards, capsules were swiftly dried by dripping hexamethyldisilazane on top and immediately evaporating under a gentle stream of nitrogen. The capsules were placed on observation pins, covered with double-sided adhesive carbon tape (NEM tape; Nisshin, Tokyo, Japan), sputter-coated with gold/palladium, and visualized using a Phenom XL G2 (Thermo Fischer Scientific, Waltham, MA, USA) scanning electron microscope. The micrographs were obtained at an accelerating voltage of 15 kV, utilizing the secondary electron detector.

4.6. Viability of Free and Encapsulated Akkermansia muciniphila Cells during Refrigerated Aerobic Storage

The effect of encapsulation via extrusion on *A. muciniphila* viability was assayed, in comparison to free cells, throughout refrigerated aerobic storage for 28 days. Free cells were stored as follows: equal portions (1 mL) of cell suspension were stored at 4 °C under aerobic conditions into 10 sterile microtubes, corresponding to two replicas for each sampling timepoint. Concerning the encapsulated bacteria, capsules were weighed into 50 mL sterile centrifuge tubes and suspended in physiological saline solution in a 1:9 (g/mL) ratio; these preparations were performed in duplicates for each sampling timepoint, and subsequently stored at 4 °C under aerobic conditions. The viability of free and encapsulated *A. muciniphila* cells was evaluated on the day of encapsulation and after 7, 14, 21, and 28 days of refrigerated aerobic storage, following the protocol previously described in Section 4.3.

4.7. Survival of Free and Encapsulated Akkermansia muciniphila Cells in In Vitro Simulated Gastrointestinal Passage

The viability of free and encapsulated *A. muciniphila* cells when exposed to in vitro simulated gastrointestinal conditions was determined 1 and 28 days after the extrusion procedure using a standardized digestion method [28] with minor changes. Briefly, either 0.5 mL of free cells in 0.85% (*m*/*v*) NaCl or 0.5 g of calcium-alginate capsules were distributed into independent tubes (two replicates per timepoint and condition). To simulate the temperature and peristaltic movements of the human digestion, an orbital shaker incubator (Wiggen Hauser, Berlin, Germany) was used at 37 °C and 200 rpm. For each assay, all enzyme solutions were freshly prepared. For the gastric phase, samples were exposed to

2 mL of simulated gastric fluid (pH 3) containing pepsin (2000 U/mL—from porcine gastric mucosa; Sigma Aldrich, St. Louis, MO, USA) for 2 h. Afterward, intestinal conditions were simulated for 3 h at pH 7 by adding 4 mL of simulated intestinal fluid containing pancreatin (based on the trypsin activity at 100 U/mL in the final mixture; Sigma Aldrich, St. Louis, MO, USA) and bile salts (Sigma Aldrich, St. Louis, MO, USA). To evaluate the effect of gastric and intestinal conditions on *A. muciniphila* viability (free and encapsulated forms), samples were collected at the end of each phase (gastric and intestinal) and cell enumeration was performed according to the procedure previously described in Section 4.3. Note that in vitro digestion protocol was performed under an aerobic atmosphere, while the PYGM agar plates were incubated under anaerobic conditions.

Author Contributions: Conceptualization, D.M., J.C.B. and A.M.G.; methodology, D.M. and A.M.G.; formal analysis, D.M., M.F., R.V. and S.S.; investigation, D.M., M.F., R.V. and S.S.; writing—original draft preparation, D.M. and M.F.; writing—review and editing, D.M., M.F., R.V., J.C.B. and A.M.G.; supervision, D.M., J.C.B. and A.M.G.; project administration, D.M. and A.M.G.; funding acquisition, D.M. and A.M.G. All authors have read and agreed to the published version of the manuscript.

Funding: This work was supported by the PROBIOCARE project (EXPL/BIA-MIC/0258/2021), financed by national funds through the Foundation for Science and Technology, I.P. (FCT). We would like to thank the scientific collaboration of CBQF (UIDB/50016/2020) and the Scientific Employment Stimulus—Individual Call (CEEC Individual—CEECIND/00520/2017/CP1404/CT0001).

Institutional Review Board Statement: Not applicable.

Informed Consent Statement: Not applicable.

Data Availability Statement: The data presented in this study are available in the article.

Conflicts of Interest: The authors declare no conflict of interest.

References

1. Hill, C.; Guarner, F.; Reid, G.; Gibson, G.R.; Merenstein, D.J.; Pot, B.; Morelli, L.; Canani, R.B.; Flint, H.J.; Salminen, S.; et al. Expert Consensus Document: The International Scientific Association for Probiotics and Prebiotics Consensus Statement on the Scope and Appropriate Use of the Term Probiotic. *Nat. Rev. Gastroenterol. Hepatol.* **2014**, *11*, 506–514. [CrossRef] [PubMed]
2. Zheng, J.; Wittouck, S.; Salvetti, E.; Franz, C.M.A.P.; Harris, H.M.B.; Mattarelli, P.; O'toole, P.W.; Pot, B.; Vandamme, P.; Walter, J.; et al. A Taxonomic Note on the Genus Lactobacillus: Description of 23 Novel Genera, Emended Description of the Genus *Lactobacillus beijerinck* 1901, and Union of *Lactobacillaceae* and *Leuconostocaceae*. *Int. J. Syst. Evol. Microbiol.* **2020**, *70*, 2782–2858. [CrossRef] [PubMed]
3. El Hage, R.; Hernandez-Sanabria, E.; Van de Wiele, T. Emerging Trends in "Smart Probiotics": Functional Consideration for the Development of Novel Health and Industrial Applications. *Front. Microbiol.* **2017**, *8*, 1889. [CrossRef] [PubMed]
4. de Melo Pereira, G.V.; de Oliveira Coelho, B.; Magalhães Júnior, A.I.; Thomaz-Soccol, V.; Soccol, C.R. How to Select a Probiotic? A Review and Update of Methods and Criteria. *Biotechnol. Adv.* **2018**, *36*, 2060–2076. [CrossRef]
5. Derrien, M.; Vaughan, E.E.; Plugge, C.M.; de Vos, W.M. *Akkermansia Municiphila* Gen. Nov., Sp. Nov., a Human Intestinal Mucin-Degrading Bacterium. *Int. J. Syst. Evol. Microbiol.* **2004**, *54*, 1469–1476. [CrossRef] [PubMed]
6. Derrien, M.; Collado, M.C.; Ben-Amor, K.; Salminen, S.; De Vos, W.M. The Mucin Degrader *Akkermansia muciniphila* Is an Abundant Resident of the Human Intestinal Tract. *Appl. Environ. Microbiol.* **2008**, *74*, 1646–1648. [CrossRef]
7. Pellegrino, A.; Coppola, G.; Santopaolo, F.; Gasbarrini, A.; Ponziani, F.R. Role of Akkermansia in Human Diseases: From Causation to Therapeutic Properties. *Nutrients* **2023**, *15*, 1815. [CrossRef]
8. Koh, W.Y.; Lim, X.X.; Tan, T.-C.; Kobun, R.; Rasti, B. Encapsulated Probiotics: Potential Techniques and Coating Materials for Non-Dairy Food Applications. *Appl. Sci.* **2022**, *12*, 10005. [CrossRef]
9. Lee, K.Y.; Mooney, D.J. Alginate: Properties and Biomedical Applications. *Prog. Polym. Sci.* **2012**, *37*, 106–126. [CrossRef]
10. Chandramouli, V.; Kailasapathy, K.; Peiris, P.; Jones, M. An Improved Method of Microencapsulation and Its Evaluation to Protect *Lactobacillus* Spp. in Simulated Gastric Conditions. *J. Microbiol. Methods* **2004**, *56*, 27–35. [CrossRef]
11. Sousa, S.; Gomes, A.M.; Pintado, M.M.; Malcata, F.X.; Silva, J.P.; Sousa, J.M.; Costa, P.; Amaral, M.H.; Rodrigues, D.; Rocha-santos, T.A.P.; et al. Encapsulation of Probiotic Strains in Plain or Cysteine-Supplemented Alginate Improves Viability at Storage below Freezing Temperatures. *Eng. Life Sci.* **2012**, *12*, 457–465. [CrossRef]
12. Amine, K.M.; Champagne, C.P.; Salmieri, S.; Britten, M.; St-Gelais, D.; Fustier, P.; Lacroix, M. Effect of Palmitoylated Alginate Microencapsulation on Viability of Bifidobacterium Longum during Freeze-Drying. *LWT Food Sci. Technol.* **2014**, *56*, 111–117. [CrossRef]

13. Frakolaki, G.; Giannou, V.; Topakas, E.; Tzia, C. Effect of Various Encapsulating Agents on the Beads' Morphology and the Viability of Cells during BB-12 Encapsulation through Extrusion. *J. Food Eng.* **2021**, *294*, 110423. [CrossRef]
14. Van der Ark, K.C.H.; Nugroho, A.D.W.; Berton-Carabin, C.; Wang, C.; Belzer, C.; de Vos, W.M.; Schroen, K. Encapsulation of the Therapeutic Microbe *Akkermansia muciniphila* in a Double Emulsion Enhances Survival in Simulated Gastric Conditions. *Food Res. Int.* **2017**, *102*, 372–379. [CrossRef]
15. Marcial-Coba, M.S.; Cieplak, T.; Cahú, T.B.; Blennow, A.; Knøchel, S.; Nielsen, D.S. Viability of Microencapsulated *Akkermansia muciniphila* and *Lactobacillus plantarum* during Freeze-Drying, Storage and in Vitro Simulated Upper Gastrointestinal Tract Passage. *Food Funct.* **2018**, *9*, 5868–5879. [CrossRef]
16. Almeida, D.; Machado, D.; Sousa, S.; Seabra, C.L.; Barbosa, J.C.; Andrade, J.C.; Gomes, A.M.; Freitas, A.C. Effect of Emulsification/Internal Gelation-Based Microencapsulation on the Viability of *Akkermansia muciniphila* upon Prolonged Storage and Simulated Gastrointestinal Passage. *Food Hydrocoll. Health* **2022**, *2*, 100084. [CrossRef]
17. Kechagia, M.; Basoulis, D.; Konstantopoulou, S.; Dimitriadi, D.; Gyftopoulou, K.; Skarmoutsou, N.; Fakiri, E.M. Health Benefits of Probiotics: A Review. *ISRN Nutr.* **2013**, *2013*, 481651. [CrossRef]
18. Barbosa, J.; Almeida, D.; Machado, D.; Sousa, S.; Freitas, A.; Andrade, J.; Gomes, A. Spray-Drying Encapsulation of the Live Biotherapeutic Candidate *Akkermansia muciniphila* DSM 22959 to Survive Aerobic Storage. *Pharmaceuticals* **2022**, *15*, 628. [CrossRef]
19. Chang, Y.; Yang, Y.; Xu, N.; Mu, H.; Zhang, H.; Duan, J. Improved Viability of *Akkermansia muciniphila* by Encapsulation in Spray Dried Succinate-Grafted Alginate Doped with Epigallocatechin-3-Gallate. *Int. J. Biol. Macromol.* **2020**, *159*, 373–382. [CrossRef]
20. Machado, D.; Almeida, D.; Seabra, C.L.; Andrade, J.C.; Gomes, A.M.; Freitas, A.C. Uncovering *Akkermansia muciniphila* Resilience or Susceptibility to Different Temperatures, Atmospheres and Gastrointestinal Conditions. *Anaerobe* **2020**, *61*, 102135. [CrossRef]
21. Begley, M.; Gahan, C.G.M.; Hill, C. The Interaction between Bacteria and Bile. *FEMS Microbiol. Rev.* **2005**, *29*, 625–651. [CrossRef] [PubMed]
22. Ottman, N.A. *Host Immunostimulation and Substrate Utilization of the Gut Symbiont Akkermansia muciniphila*; Wageningen University: Wageningen, The Netherlands, 2015.
23. Tan, L.L.; Ang, K.L.; Loo, S.C.J. Alginate Encapsulation Improves Probiotics Survival in Carbonated Sodas and Beers. *PLoS ONE* **2023**, *18*, e0283745. [CrossRef] [PubMed]
24. Zhang, Z.; Gu, M.; You, X.; Sela, D.A.; Xiao, H.; McClements, D.J. Encapsulation of Bifidobacterium in Alginate Microgels Improves Viability and Targeted Gut Release. *Food Hydrocoll.* **2021**, *116*, 106634. [CrossRef]
25. Chen, S.-C.; Wu, Y.-C.; Mi, F.-L.; Lin, Y.-H.; Yu, L.-C.; Sung, H.-W. A Novel PH-Sensitive Hydrogel Composed of N,O-Carboxymethyl Chitosan and Alginate Cross-Linked by Genipin for Protein Drug Delivery. *J. Control. Release* **2004**, *96*, 285–300. [CrossRef] [PubMed]
26. DSMZ Akkermansia muciniphila DSM 22959. Available online: https://www.dsmz.de/collection/catalogue/details/culture/DSM-22959 (accessed on 22 May 2023).
27. Martin, M.J.; Lara-Villoslada, F.; Ruiz, M.A.; Morales, M.E. Effect of Unmodified Starch on Viability of Alginate-Encapsulated *Lactobacillus fermentum* CECT5716. *LWT Food Sci. Technol.* **2013**, *53*, 480–486. [CrossRef]
28. Minekus, M.; Alminger, M.; Alvito, P.; Ballance, S.; Bohn, T.; Bourlieu, C.; Carrière, F.; Boutrou, R.; Corredig, M.; Dupont, D.; et al. A Standardised Static in Vitro Digestion Method Suitable for Food—An International Consensus. *Food Funct.* **2014**, *5*, 1113–1124. [CrossRef]

gels

MDPI

Article

Ultrashort Cationic Peptide Fmoc-FFK as Hydrogel Building Block for Potential Biomedical Applications

Enrico Gallo [1], Carlo Diaferia [2], Sabrina Giordano [1], Elisabetta Rosa [2], Barbara Carrese [1], Gennaro Piccialli [2], Nicola Borbone [2], Giancarlo Morelli [2], Giorgia Oliviero [3] and Antonella Accardo [2,*]

[1] IRCCS SYNLAB SDN, Via Gianturco 113, 80143 Naples, Italy; enrico.gallo@synlab.it (E.G.); sabrina.giordano@synlab.it (S.G.); barbara.carrese@synlab.it (B.C.)
[2] Department of Pharmacy, University of Naples "Federico II", Via D. Montesano 49, 80131 Naples, Italy; carlo.diaferia@unina.it (C.D.); elisabetta.rosa@unina.it (E.R.); gennaro.piccialli@unina.it (G.P.); nicola.borbone@unina.it (N.B.); gmorelli@unina.it (G.M.)
[3] Department of Molecular Medicine and Medical Biotechnologies, University of Naples "Federico II", Via S. Pansini 5, 80131 Naples, Italy; giorgia.oliviero@unina.it
* Correspondence: antonella.accardo@unina.it

Abstract: Fmoc-diphenylalanine (Fmoc-FF) is a low-molecular-weight peptide hydrogelator. This simple all-aromatic peptide can generate self-supporting hydrogel materials, which have been proposed as novel materials for diagnostic and pharmaceutical applications. Our knowledge of the molecular determinants of Fmoc-FF aggregation is used as a guide to design new peptide-based gelators, with features for the development of improved tools. Here, we enlarge the plethora of Fmoc-FF-based hydrogelated matrices by studying the properties of the Fmoc-FFK tripeptide, alone or in combination with Fmoc-FF. For multicomponent matrices, the relative weight ratios between Fmoc-FFK and Fmoc-FF (specifically, 1/1, 1/5, 1/10, and 1/20 *w*/*w*) are evaluated. All the systems and their multiscale organization are studied using different experimental techniques, including rheology, circular dichroism, Fourier transform infrared spectroscopy, and scanning electron microscopy (SEM). Preliminary profiles of biocompatibility for the studied systems are also described by testing them in vitro on HaCaT and 3T3-L1 cell lines. Additionally, the lysine (K) residue at the C-terminus of the Fmoc-FF moiety introduces into the supramolecular material chemical functions (amino groups) which may be useful for modification/derivatization with bioactive molecules of interest, including diagnostic probes, chelating agents, active pharmaceutical ingredients, or peptide nucleic acids.

Keywords: peptide materials; hydrogels; cationic peptide; Fmoc-FF analogues; soft materials

1. Introduction

Peptide aggregation behavior has a key role in biochemical research as the wide spectrum of supramolecular assemblies that may derive from the use of simple building blocks (short and ultra-short sequences of common and/or non-standard amino acids) offers inspiration for the generation of sophisticated devices to be applied in the biomedical sphere [1,2]. Among all peptide-based architectures (e.g., fibers [3], nanospheres [4], and micelles [5]), hydrogels (HGs) represent highly organized materials in which the network, generated by interconnected fibers, is able to retain, due to the hydrophilic portions of the amide skeleton, large amounts of water [6,7]. Thanks to their capabilities to accommodate active pharmaceutical ingredients (APIs) in their pores and to mimic the extracellular matrix because of their swollen structure, HGs have been successfully tested as drugs or contrast agents' reservoirs and as matrices for tissue engineering applications [8,9]. The chemical, physical and mechanical properties of the hydrogel can be easily modulated by the opportune design of the peptide sequence, since the choice of the length, the amino acid lateral side and the insertion of aromatic or aliphatic groups at the N-terminus have a significant impact on its gelation capability and HG features [10–13]. Moreover, the multicomponent strategy, which consists of the combination of peptides with other building blocks (like different peptides or polymers), may also offer some advantages for generating hydrogels with improved mechanical behaviors [14,15]. The homodimer Fmoc-FF (N^{α}-fluorenylmethoxycarbonyl-diphenylalanine) is one of the most studied peptide hydrogelators. Since the first analyses in 2006, this ultra-short sequence has been renowned for its displayed capability to form hydrogels in physiological conditions, combined with its synthetic accessibility [16,17]. Over the years, Fmoc-FF has represented the progenitor of a wide class of hydrogels, starting from analogues derived from the substitution of the fluorenyl moiety with other aromatic and non-aromatic groups to those made with changes to the peptide primary sequence [18]. Furthermore, a subclass of Fmoc-FF-derived materials is produced from the combination of Fmoc-FF with other chemical entities, according to the multicomponent strategy [19–21]. In this work, we describe the synthesis of a tripeptide originating from the addition of a lysine residue to the fluorenyl-protected diphenylalanine. The aminic group on the lysine side chain introduces a site accessible to its chemical functionalization, which at the same time, preserves the aromatic structure of the progenitor that is responsible for the aggregation. The derivatization of the Fmoc-FF base structure with an additional natural amino acid housing in its side chain, a positively charged functional group (Lys (K) or Arg (R)), has been recently tested by the group of He, Z [22,23]. The Fmoc-FFK and Fmoc-FFR tripeptides maintain the zwitterionic form, due to the fluorenyl end-capping of the N-terminus and give rise to different types of nanoarchitectures depending on the pH and the aliphatic lateral side. Moreover, the path of functionalization was performed by using Fmoc-FFR to immobilize gold nanoparticles (AuNPs) for nanocatalysis scopes, even though, in this case, the gelation capability of Fmoc-FFR was torn down by the alteration of the electrostatic balance along the peptide molecule after the derivatization of the NPs [24]. In our synthesis, the amidation of the C-terminus makes the tripeptide Fmoc-FFK cationic at a neutral pH, and no zwitterionic entity is accessible at any pH value. The gelation capability of this tripeptide was studied by exploiting the solvent switch method, which is one of the most used processes for hydrogel formulation and consists in the water dilution of a highly concentrated peptide solution in an organic solvent. Simultaneously, the possibility to generate multicomponent hydrogel matrices was also tested by combining Fmoc-FFK with Fmoc-FF at 1/1, 1/5, 1/10, and 1/20 weight/weight ratios. All the obtained matrices were fully characterized using a series of spectroscopic techniques, including fluorescence, Fourier transform infrared, circular dichroism, thioflavin T, and Congo red assays, scanning electron microscopy and optical microscopy. Rheological studies were also conducted to explore the mechanical properties of the resulting hydrogels. The biocompatibility of these matrices, together with their capability to support cell adhesion, was tested in vitro on HaCaT and 3T3-L1 cell lines.

2. Results and Discussion

2.1. Design and Synthesis of Fmoc-FFK

The Fmoc-FFK tripeptide (see chemical formula in Figure 1) represents the elongated analogue of the well-known Fmoc-FF hydrogelator. Unlike the latter, Fmoc-FFK contains a potentially reactive group (ε-NH_2), which can be opportunely used for functionalization with the desired moiety. The Lys residue has been positioned at the C-terminus which corresponds to the end of the aggregative group because the importance of the mutual steric proximity of both the Fmoc group and Phe residues for the self-assembly process and supramolecular organization has been demonstrated [25]. On the other hand, it is expected that any modification of the primary sequence could significantly alter the structural and functional properties of the material. Fmoc-FF generates a supramolecular assembly as consequence of an initial anti-parallel β-sheet secondary structure arrangement, with the anti-parallel π-stacking of the fluorenyl-protecting groups [26]. The additional lateral interlocking π–π interactions of four twisted anti-parallel β-sheets generates nanocylinders with an external diameter of ~3.0 nm.

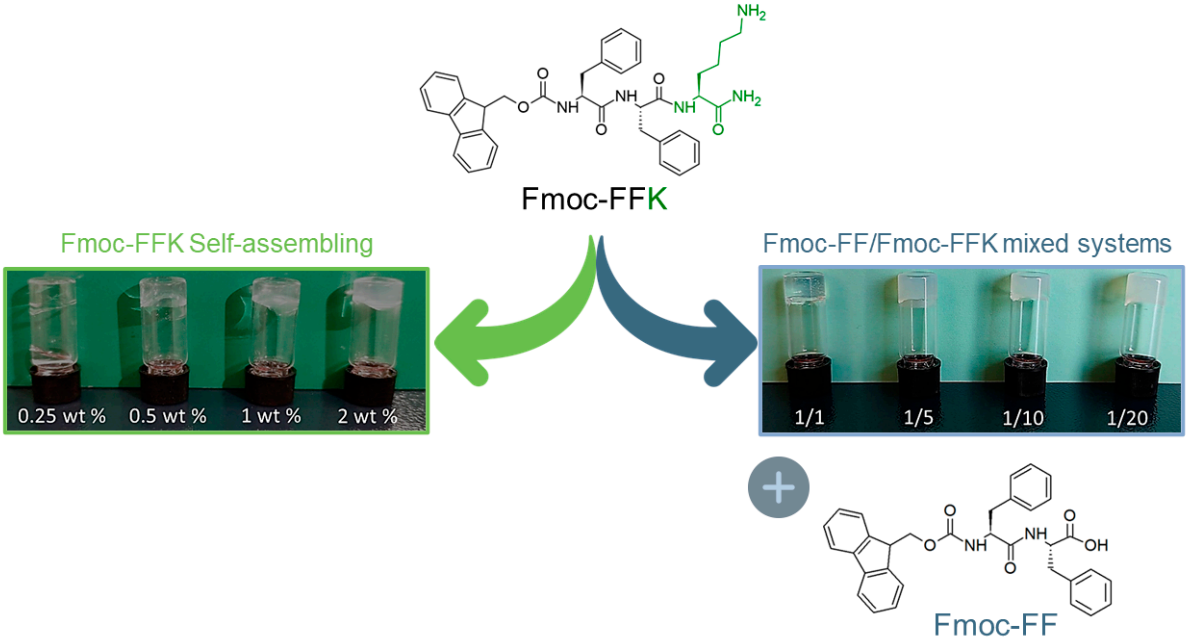

Figure 1. Schematic representation of the Fmoc-FFK tripeptide and the Fmoc-FF dipeptide. Inverted test tube of pure Fmoc-FFK hydrogel formulated at three different concentrations (0.5, 1.0, and 2.0 wt%) and the multicomponent Fmoc-FFK/Fmoc-FF hydrogels in which the two peptides are mixed in 1/1, 1/5, 1/10, and 1/20 (*w*/*w*) molar ratios.

The further adjacent self-associations of these structures allow for the formation of large, flat, twisted ribbons, which mutually block the water flow and form the hydrogel. The Fmoc-FFK tripeptide was synthetized according to solid-phase peptide synthesis (SPPS) protocols by using a Rink amide resin, which releases the peptide as an amide [27]. The capping of the carboxylic acid allows us to obtain only one potentially reactive group on the building block, thus reducing the reactive functions in the aggregate materials. Indeed, in a hypothetical post aggregative functionalization step, the lack of additional reactive groups, such as the carboxylic one, allows us to prevent collateral reactions, promoting a chemical control and increasing the selectivity of the reaction [28]. The crude peptide was purified via RP-HPLC chromatography, and its identity was assessed via an analytical HPLC characterization, ESI mass spectrometry, and ^{1}H-NMR spectroscopy (see Figures S1 and S2).

Initially, we evaluated the capability of the tripeptide to self-organize into a self-supporting hydrogel alone or in combination with the well-known hydrogelator Fmoc-FF at different weight/weight ratios (1/1, 1/5, 1/10 and 1/20 *w*/*w*). The hydrogel formation of ultrashort peptides can be generally induced using different approaches, like the pH-switch [29,30], the solvent switch [31,32], or the enzymatic one [33]. It is well documented that the choice of the method, as well as the solvent, the pH and the peptide concentration, can deeply affect the supramolecular architecture and the properties of the resulting material [34,35]. In our experiment, hydrogel formulation was achieved by using the solvent switch method, keeping the fraction of DMSO (ϕ_{DMSO} = 10%) unaltered. In this method, the gel formation is triggered by a physical stimulus, which is the addition of water to the peptide solution previously prepared in DMSO at a high concentration (100 mg/mL), with the formation of the peptide in a solvent–antisolvent mixture that induces the aggregation of monomers. After dilution in water, the sample is vortexed for few seconds to generate an opaque, uniform and metastable solution, then aged at room temperature. At the end of the preparation, the capability of the material to be self-supporting is macroscopically evaluated via the inverted test tube (Figure 1).

This test also allows for the determination of the critical gelation concentration (CGC), because the concentration is another important parameter for gel formation. The CGC for

Fmoc-FFK was established by using samples at different concentrations between 0.25 and 2.0 wt% (Figure 1; green arrow) and estimated to be in the 0.5–1.0 wt% range. Instead, mixed hydrogels at different weight/weight ratios were prepared at 1.0 wt% only. Under these conditions, the inverted test tube confirmed the gel state for all the samples. During the preparation of multicomponent hydrogels, we qualitatively observed a different gelation time as a function of the chosen ratio. To quantitatively estimate the kinetics of gelation, the decrease in the refractive index related to the transition of the metastable gel solution from opaque to limpid was measured via UV-vis spectroscopy. By plotting the absorbance at 600 nm (the long-range channel) as a function of time, a decrease in the optical density (OD) can be observed, which corresponds to the supramolecular organization of peptide building blocks into fibers having a size lower than that of the particles scattering the light. The gelation times (G_{ts}) were graphically extrapolated from the graph considering the flex concavity of the profiles (Table 1, Figure S6). Surprisingly, the gel kinetics significantly increase from 5 to 216 min with an increase in the Fmoc-FF ratio in the mixture. The capability of pure and mixed matrices to incorporate water (swelling) was estimated by performing a swelling test; the data were reported in terms of the swelling percentage (q). According to Equation (1), the q values are calculated by putting the gel in contact with water and determining the increase in weight that occurs. The swelling percentage ranged between 32 and 37% for all the samples (Table 1) and resulted to be slightly higher than the percentage determined for the pure Fmoc-FF hydrogel (29%) [36,37]. This value is in agreement with the ones observed for similar Fmoc-FF/tripeptide mixed systems. The relatively low swelling percentage may be due to the high hydrophobic component of the sequence, as a substantial aromatic part is present and may contribute to the low amount of entrapped water. Indeed, the addition of a more hydrophilic component results in an increase in the swelling ratio when compared to that of the pure Fmoc-FF (see Table S1) [36].

Table 1. Characterization of pure and mixed hydrogels at different *w*/*w* ratios. Swelling percentage, gelation time, storage modulus (G′), loss modulus (G″), and Tanδ.

System	Concentration (wt%)	Ratio (*w*/*w*)	Swelling (%)	G′ (Pa)	G″ (Pa)	tanδ	G_t (min)
Fmoc-FFK	0.5	-	32.4	5.8	1.3	0.224	75
	1.0	-	34.0	15.4	3.6	0.234	45
	2.0	-	37.5	24.3	5.6	0.230	30
Fmoc-FFK/Fmoc-FF	1.0	1/1	35.0	315	36	0.114	10
	1.0	1/5	35.1	6930	842	0.121	78
	1.0	1/10	33.8	9800	1195	0.122	138
	1.0	1/20	33.7	9412	495	0.0526	216

2.2. Scanning Electron Microscopy (SEM) Characterization

Morphological investigations on the pure and mixed hydrogels were carried out via scanning electron microscopy. Microphotos were acquired on xerogels prepared on aluminum stubs. The characterization performed on xerogels of pure Fmoc-FFK hydrogels at different concentrations (0.5, 1.0, and 2.0 wt%) shows that only the sample at 2.0 wt% had well-defined organization in its entangled fibers (Figure S4). On the contrary, no fibrillary networks, typical of hydrogel matrices, can be detected in the samples prepared at the other two lower studied concentrations (0.5 and 1.0 wt%). This result is in good agreement with the CGC previously found by the inverted test tube method. Instead, all the mixed hydrogels exhibit a similar morphology independently from the ratio between the two peptides (Figure 2).

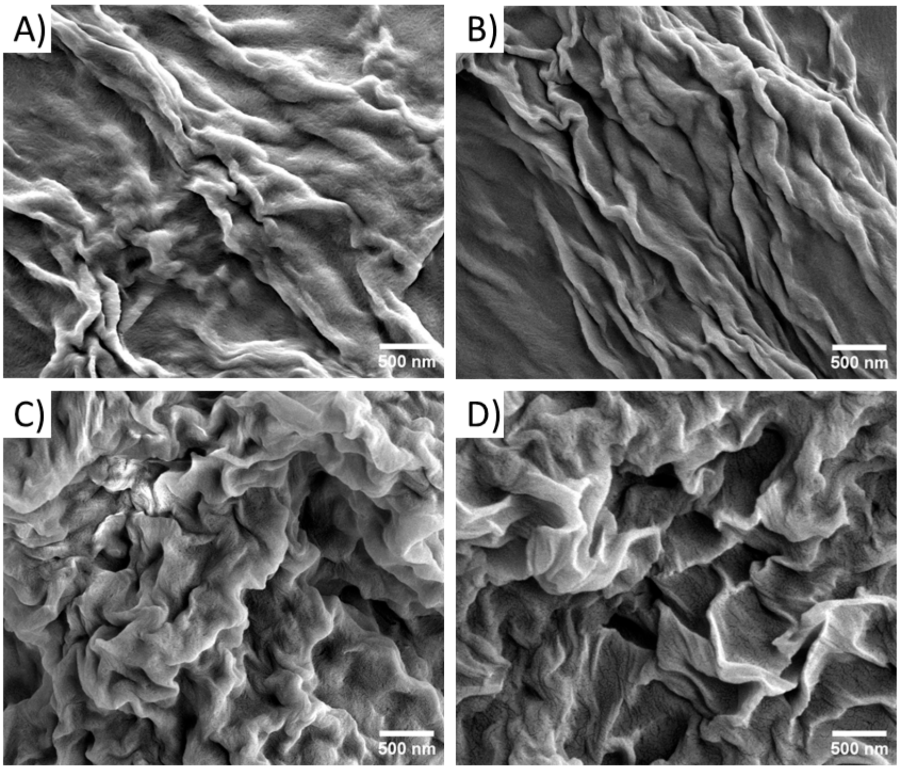

Figure 2. Selected microphotos of mixed xerogels: Fmoc-FFK/Fmoc-FF at 1/1 (**A**), 1/5 (**B**), 1/10 (**C**), and 1/20 (**D**). Scale bar: 500 nm.

2.3. Secondary Structural Characterization

The secondary structural organization of peptide units into the pure and mixed hydrogels was studied by using a combination of optical (microscopy and confocal) and spectroscopic (circular dichroism, Fourier transform infrared and fluorescence) techniques. A preliminary characterization of the arrangement of peptide sequences in the hydrogels was performed on samples in the solid state. Xerogels, prepared on glass from the corresponding hydrogels, were screened using two well-assessed assays (birefringence of Congo red and thioflavin T), which are commonly employed for revealing the presence of amyloid-like structures. Indeed, it has been demonstrated that both the CR and ThT undergo to a modification of their spectroscopic properties when they interact with β-sheet structures, with the appearance of an apple-green birefringence under cross-polarized light for the azoic CR dye and a fluorescence emission around 480 nm for ThT. From an inspection of Figure 3, it can be observed that both the pure and mixed Fmoc-FFK/Fmoc-FF xerogels stained with CR and ThT are positive to the assays, thus suggesting a β-sheet arrangement of peptides in the supramolecular matrices. The data gathered from spectroscopic techniques, like CD and FT-IR, can be combined to obtain information about the molecular organization within the hydrogel matrices. By comparing the shape of the CD spectra belonging to the mono-component Fmoc-FF and Fmoc-FFK HGs and the multi-component Fmoc-FFK/Fmoc-FF systems (with ratios of 1/1 and 1/20), provided in Figure 4A, it can be deduced that each matrix is affected by different organization modes. The secondary structure of Fmoc-FF has been widely analyzed and discussed [38]. The positive signal around 195 nm and the negative one centered at 206 nm are ascribable to $\pi \rightarrow \pi^*$ α-helix transitions. A super-helical arrangement of the phenylalanine residues is deduced by the 236 nm-centered broad band, attributed to $n \rightarrow \pi^*$ transitions.

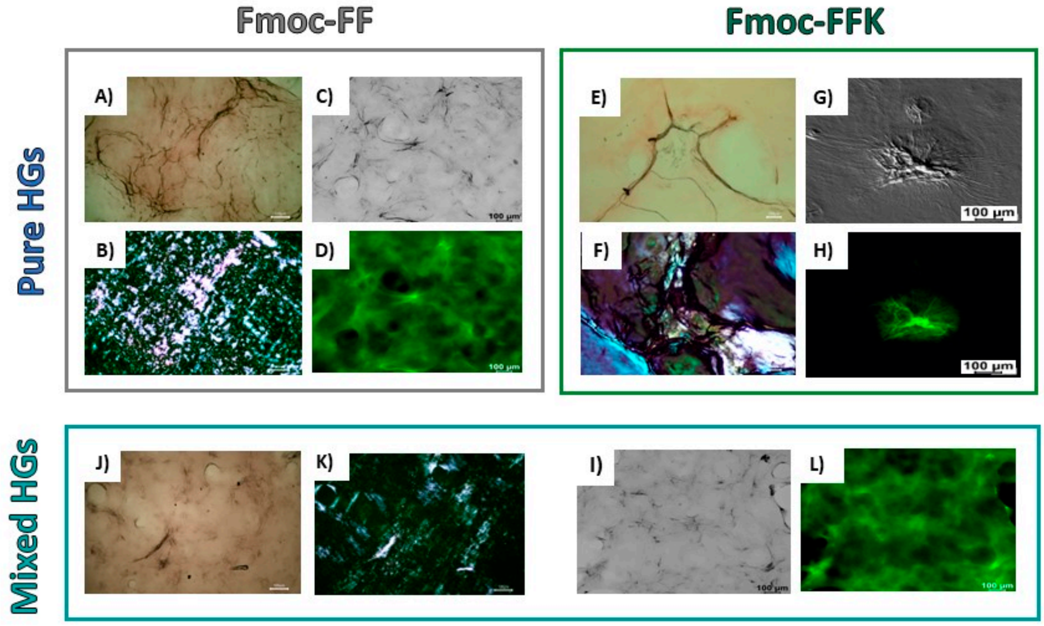

Figure 3. Birefringence CR assay and ThT assays for xerogels prepared by pure Fmoc-FF and Fmoc-FFK HGs (1.0 wt%) and mixed Fmoc-FFK/Fmoc-FF HGs (1.0 wt%, 1/5 *w*/*w*). Polarized optical microscopy images of air-dried samples stained with Congo red solution under bright-field microscopy (**A**,**E**,**J**) and between crossed polarizers (**B**,**F**,**K**). Confocal images of xerogels, stained with 50 µmol/L ThT solution, under bright-field microscopy (**C**,**G**,**I**) and in the green spectral region (GFP). λ_{exc} = 450 nm; 460 nm < λ_{em} < 600 nm (**D**,**H**,**L**).

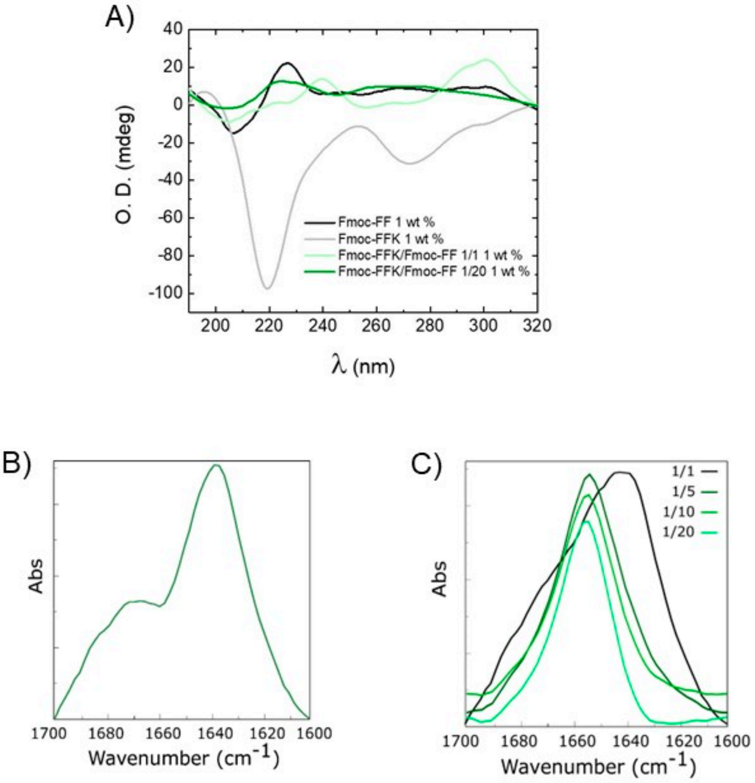

Figure 4. Secondary structure characterization of mixed hydrogels via CD and FTIR. (**A**) CD spectra in optical density of hydrogels at 1.0 wt%: Fmoc-FF (black line), Fmoc-FFK (grey line), Fmoc-FFK/Fmoc-FF (1/1) (light green line), and Fmoc-FFK/Fmoc-FF (1/20) (dark green line). FTIR spectra of pure Fmoc-FFK HGs (**B**) and mixed Fmoc-FFK/Fmoc-FF (**C**) at 1.0 wt% at all the weight/weight ratios.

By looking at the CD profile of the self-assembling Fmoc-FFK HG at the same 1 wt% peptide concentration, whose shape is analogous to that at the 2.0 wt% concentration (Figure S5), a β-sheet organization is clearly inferred by the positive signal at 196 nm ($\pi \rightarrow \pi^*$ transitions) and the negative one at 219 nm ($n \rightarrow \pi^*$ transitions). Moreover, the negative band in the spectral region of the Fmoc moiety (centered at 276 nm) is attributed to the π–π stacking of aromatic fluorenyl rings [39]. In the 1/1 multi-component HG, the weak negative bands at 204 and 226 nm suggest the occurrence of a negligible α-helix organization, while the more pronounced positive peak at 238 nm suggests an antiparallel orientation of β-sheets [40]. The π–π^* transitions of the fluorenyl are responsible for the generation of a positive signal at 301 nm [41]. By comparing the CD signature of this 1/1 mixed matrix with the one obtained by the arithmetic sum of the spectra of the two components alone, a co-assembly aggregation is inferred, as the two cited original and mathematical-derived spectra are different [42]. This ability of the components to arrange together gives rise to novel architectures, resulting from the interactions of the different building blocks with each other. This cannot be said for the Fmoc-FFK/Fmoc-FF 1/20 mixed matrix, for which the CD behavior seems to be driven by the Fmoc-FF, as the same previously cited peaks for the dipeptide have been noted. Even for the HGs in which the amount of Fmoc-FF is not so preponderant (at ratios of 1/5 and 1/10), the CD profiles follow the signature of Fmoc-FF, and thus, a similar secondary organization occurs (Figure S5). As the spectrum obtained by the sum of the optical density values of the two single components is similar to the one obtained by the analysis of the 1/20 HG, it can be deduced that in this kind of double-composed HG a self-sorting organization occurs, which means that the different building blocks are able to selectively recognize their mutual counterparts by generating mono-component supramolecular assemblies, interacting with the other singularly organized systems in the environment at a superior level [43]. To support the CD spectroscopic analyses, Fourier transform infrared (FT-IR) measurements were taken. The peptide signals in the amide I region (1700–1600 cm^{-1}), due, for the 80%, to the C=O stretching vibrations, can reveal the secondary structure arrangements [44]. For the Fmoc-FFK and the Fmoc-FFK/Fmoc-FF 1/1 mixed matrices, the band around 1640 cm^{-1} clearly indicates a β-sheet organization, as previously assessed via CD spectroscopy. The supplemental signal at 1672 cm^{-1} is attributable to the presence of TFA counterions (Figure 4B). Contrarily, for the mixed HG with a 1/20 ratio, the band centered around 1660 cm^{-1}, generally attributed to α-helix or super helical conformations, confirms the predominance of the Fmoc-FF structuration [21,45]. The same band was detected for the 1/5 and 1/10 ratios (Figure 4C). The progressive modification of the supramolecular arrangement is reinforced by a deconvolution analysis using weighted percentages of each mixed hydrogel (Table S2), indicating the increase in α-helix/super helical conformations with the increase in Fmoc-FF percentage in the mixed matrices.

2.4. Rheological Characterization

To confirm the gel status of all the samples, the storage modulus (G') and the loss modulus (G'') were evaluated by performing a rotational rheological analysis. The time sweep oscillatory measurements (20 min, 1.0 Hz, and 0.1 % strain; Figures 5 and S6) were carried out on the preformed samples, after the acquisition of both the frequency ($0.1 < \nu < 100$ Hz; Figures S7A and S8A) and strain sweeps ($0.1 < \omega < 100\%$; Figures S7B and S8B). As expected for hydrogels, the G' value is higher than the G'' one (Table 1), thus analytically confirming that all the studied samples are in the gel state.

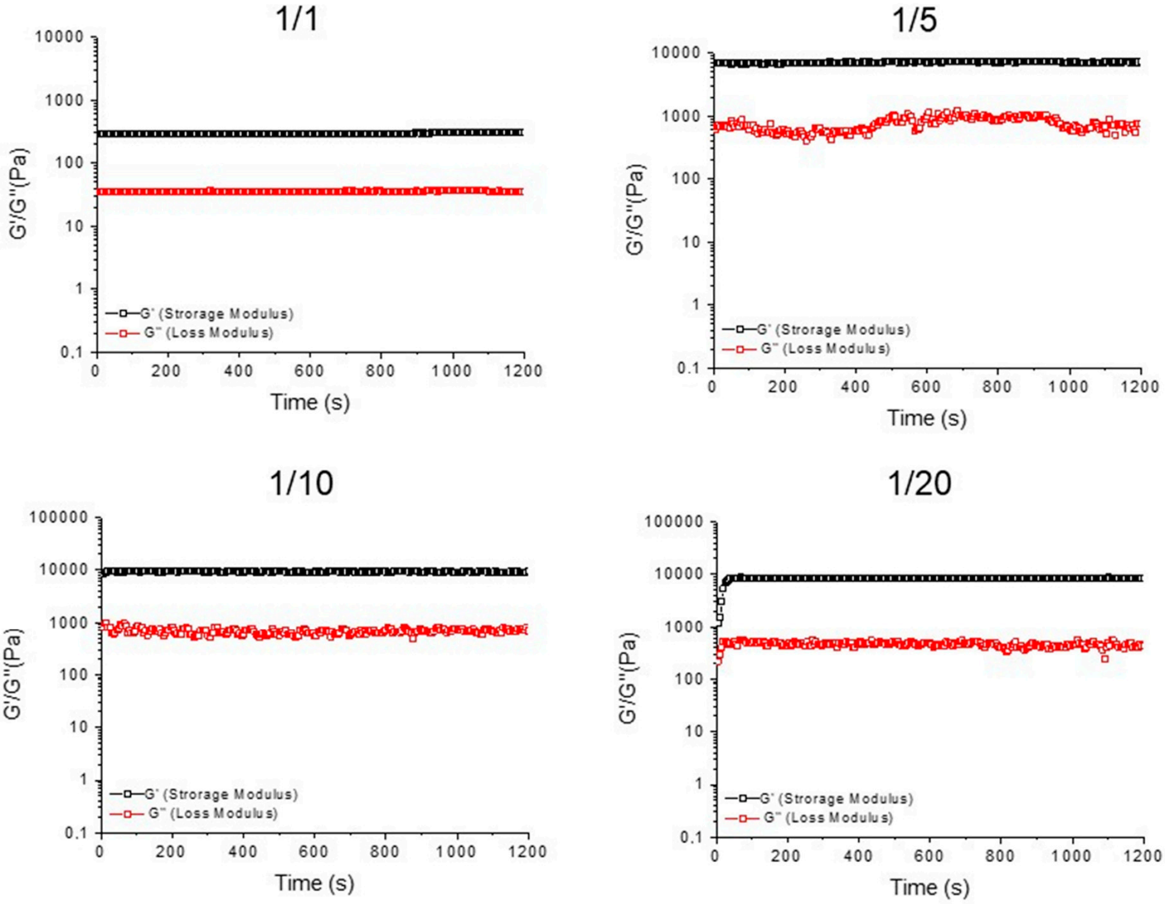

Figure 5. Time sweep (20 min) for mixed hydrogels Fmoc-FFK/Fmoc-FF at three different weight/weight ratios (1/1, 1/5, 1/10, and 1/20). The rheological analysis is reported in terms of G′ (storage modulus) and G″ (loss modulus).

From the inspection of the values in Table 1, it can be pointed out that the self-assembled Fmoc-FFK hydrogel has a very soft nature at all the studied concentrations (G′ = 5.8, 15.4, and 24.3 Pa for 0.5, 1.0, and 2.0 wt%, respectively). Additionally, a monotone increase in both G′ and G″ with the frequency was detected for the pure Fmoc-FFK matrices (Figure S9A). This trend is independent from the gel concentration, indicating an increase in the elastic response because of the decreasing dissipative stress time. Moreover, no creep oscillation value is detected for the pure Fmoc-FFK hydrogels (Figure S9B). The inclusion of the increasing amount of Fmoc-FF peptide into the formulation allows us to gradually improve the mechanical properties of the gel, with a significant rigidification of the matrix for the 1/10 and 1/20 ratios (G′ = 9800 and 9412 Pa). The existence of a strong matrix, with a prominent viscoelastic nature, is also confirmed by the loss tangent (tanδ = G″/G′) value, which is 0.0526 for Fmoc-FFK/Fmoc-FF (1/20, *w*/*w*). This increase in the mechanical features, which are well documented for other multicomponent matrices, seems to be related to the ability of the Fmoc-FF building block to govern and drive the gelation process, reducing the probable electrostatic repulsion in pure Fmoc-FFK gels [46]. These electrostatic repulsions may justify the low mechanical response of Fmoc-FFK hydrogels, as evidenced by the lower G′ values for multicomponent matrices with respect to the Fmoc-FF one (G′ = 23,160 Pa at 1.0 wt% and 1.0 Hz; rheological characterization reported in Figure S10).

2.5. Loading and Release of Naphthol Yellow S

The capacity of these hydrogels to retain drugs and to serve as reservoirs for controlled drug release was tested by encapsulating NYS in the matrices and evaluating its release over time. NYS is a water-soluble disodium salt of 5,7-dinitro-8-hydroxynaphthalene-2-sulfonic acid, a histological dye, herein used as drug model, easily shown via UV-vis spectroscopy. A total of 0.011 mol/L NYS was encapsulated within the hydrogel network during the rehydration step of the solvent switch formulation method. The gelation kinetics and the matrices' homogeneity were found to be not affected by the drug's inclusion. No syneresis was observed after the quantitative loading of the dye.

The release kinetics of NYS over 72 h are reported in Figure S11. The two more rigid Fmoc-FFK/Fmoc-FF 1/10 and 1/20 HGs were chosen to be compared with the mono-component Fmoc-FF precursor. Despite the significant difference in rigidity, Fmoc-FF and Fmoc-FFK/Fmoc-FF 1/20 exhibit a similar release behavior, with a NYS release around 25% of the initial amount over 72 h. On the other hand, a higher release (~35%) is observed for Fmoc-FFK/Fmoc-FF at the ratio of 1/10, which has the same rigidity as the other mixed hydrogel and a higher positive charge content. These results point out that additional factors, with respect to stiffness and electrostatic interactions, can play a role in drug retention.

A plausible explanation is that the escape tendency of the dye from HG could be affected by the different hydrophilic/hydrophobic natures of the matrix, which cause different levels of water accessibility.

2.6. Cytotoxicity and Cell Adhesion Assays

The cytotoxicity of the multicomponent hydrogels was evaluated in vitro on HaCaT (human fibroblasts) and 3T3-L1(mouse preadipocytes) cell lines by using an MTS assay, incubating the cells with the conditioned media up to 72 h. It was not possible to carry out the experiment for the 1.0 wt% or the 2.0 wt% self-assembled Fmoc-FFK hydrogels, as their high softness made them solve in few times in DMEM when incubated with the medium. No significant change in cell morphology was observed to be induced by the hydrogel treatment compared to the control.

As previously observed for Fmoc-FF hydrogels, a maximum toxicity was reached after 24 h (Figure 6), while the cell survival percentage had increased at the subsequent observation times [47]. This effect may be ascribed to a temporary cycle arrest at the S phase, followed by a complete recovery of the cells (negligible or no toxicity compared to the control for all the explored ratios) after 48 and 72 h (Figure 6). The capability of the matrices to work as scaffolds able to support cell adhesion and proliferation was evaluated by culturing HaCa T and 3T3-L1 cell lines on pre-casted hydrogels. The adhesion efficiency was measured up to 72 h after seeding and the results are expressed in terms of the percentage of adhered cells to the hydrogel compared to that of control cells (without the hydrogel). As shown in Figure 7, these adhesion percentages were found to be 73%, 71%, 50%, and 39% for the HaCaT cells and 74%, 72%, 58%, and 47% for the 3T3-L1 cells cultured on Fmoc-FFK at ratios of 1/1, 1/5, 1/10, and 1/20, respectively. An inverse correlation between the hydrogel rigidity and adhesion efficiency may be observed, since softer hydrogels seem to be better scaffolds for both of the tested cell lines.

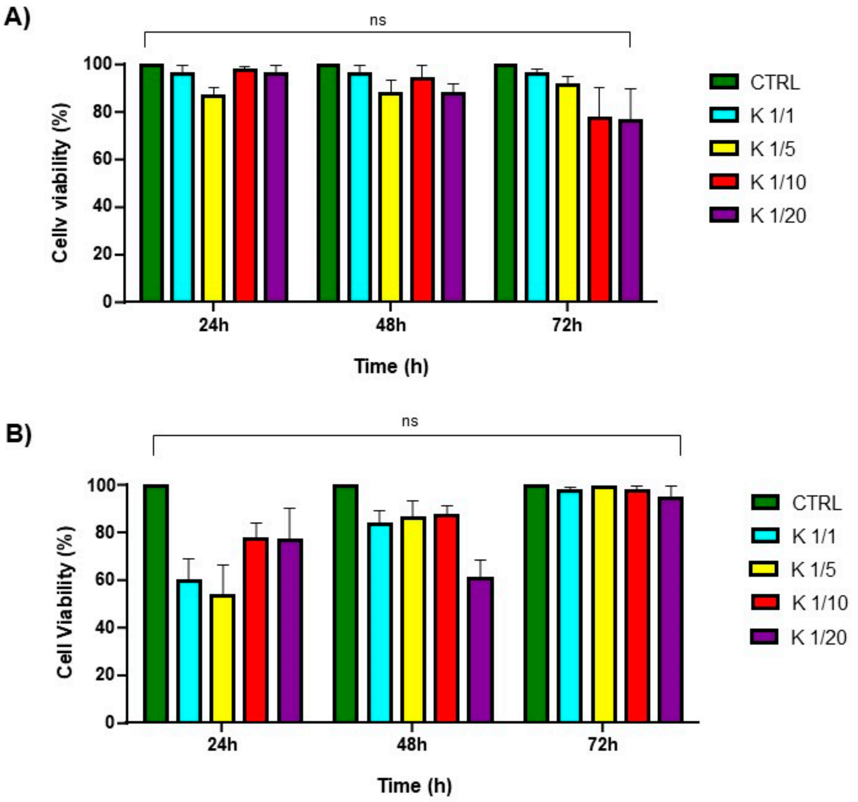

Figure 6. Cell viability assay. MTS assay of HaCaT (**A**) and 3T3-L1 (**B**) cell lines treated for 24, 48, and 72 h with hydrogel'sconditioned medium. ns: not significant versus control cells.

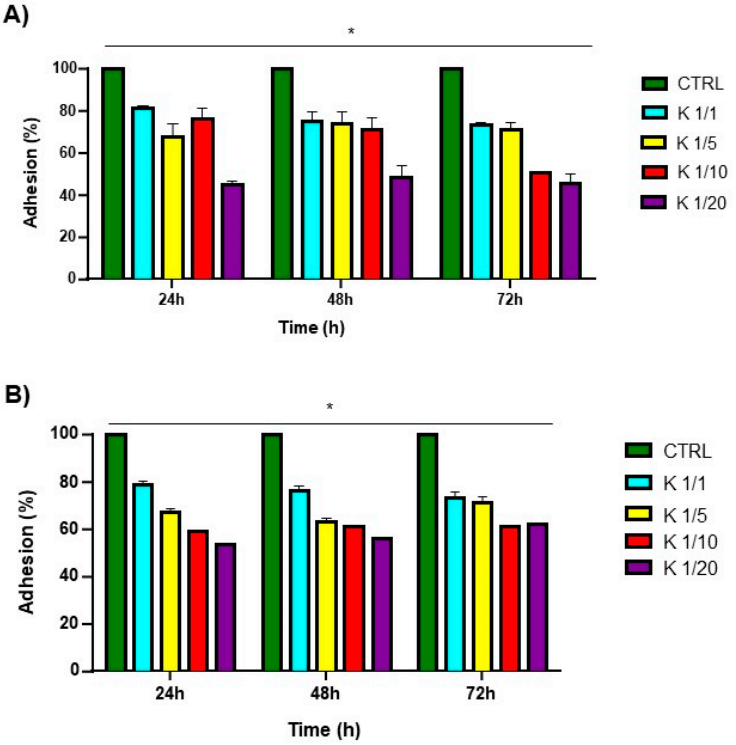

Figure 7. Adhesion test of HaCaT (**A**) and 3T3-L1 (**B**) cell lines for 24, 48, and 72 h on indicated mixed hydrogels. * $p < 0.05$, versus control cells.

3. Conclusions

In the last few years, short and ultrashort peptides have been identified as potential building blocks for the formulation of biocompatible materials, like nanotubes, fibers, nanospheres, and hydrogels. The main advantages offered by peptides are their low cost and the possibility to opportunely change the primary sequence to modulate their structure and function. Indeed, it is observed that the modification of the amino acid sequence can deeply alter the intermolecular interactions occurring in the supramolecular structure, with a consequent change in the structural properties that also affects the features of the material, like its mechanical rigidity, elasticity, and water content. These modifications in turn allow us to fabricate supramolecular systems, differing in morphology and performances, with a broad range of biomedical applications [48,49]. For instance, soft hydrogels are principally employed as injectable implants, whereas rigid ones are generally preferred for the regeneration of hard tissues, such as bone and cartilage. In this context, research on novel building blocks that are easy to synthetize is trending. The Fmoc-FF moiety represents a good starting point for the design of novel hydrogelators. Additionally, due to its high accessible gelation procedure (solvent switch), the combination of Fmoc-FF with other peptide sequences or polymers can allow for the development of novel materials. According to our findings, it can be observed that the Fmoc-FFK monomer, in which Fmoc-FF has been modified with a lysine residue at its C-terminus, is able to self-assemble and gel above the critical concentration of 1.0 wt%. The resulting self-supporting hydrogel exhibits a soft behavior with a G' value (24 Pa) that is very low with respect to that of the parental Fmoc-FF derivative (G' = 23,160 Pa). Considering that the two peptides share the same N-terminus sequence, their significantly different stiffness values are to be attributed to the positive charge that the Lys bears on the ε-NH. On the other hand, the co-aggregation of the novel Fmoc-tripeptide with Fmoc-FF at different weight/weight percentages (1/1, 1/5 1/10 and 1/20) allows us to produce matrices with enhanced mechanical properties with respect to Fmoc-FFK alone. The multicomponent hydrogels, exhibiting a similar structural organization and morphology with respect to those of a pure Fmoc-FF hydrogel, could potentially serve as platforms for post-gelation derivatization with bioactive molecules that bear a primary amine for diagnostic or therapeutic purposes.

4. Materials and Methods

4.1. Materials and Methods

Rink amide MBHA (4-methylbenzhydrylamine) resin, coupling reagents, and protected N^{α}-Fmoc-amino acid derivatives were supplied by Calbiochem-Novabiochem (Läufelfingen, Switzerland). Bachem (Bu-bendorf, Switzerland) provided the powder of Fmoc-FF peptide. Unless otherwise indicated, all other chemical items were used as specified by the manufacturers and were commercially accessible from Merck (Milan, Italy), Fluka (Bucks, Switzerland), or LabScan (Stillorgan, Dublin, Ireland). Samples and peptide-based hydrogels were prepared by weight using dimethyl sulfoxide (DMSO) and double distilled water, respectively. The crude peptides were purified via preparative reversed-phase high-performance liquid chromatography (RP-HPLC) on a Phenomenex (Torrance, CA, USA) C18 column. The LC8 Shimadzu HPLC system (Shimadzu Corporation, Kyoto, Japan) was employed, equipped with a UV Lambda-Max Model 481 detector. H2O/0.1% trifluoroacetic acid (TFA) (A) and CH3CN/0.1% TFA (B) were used as elution solvents. The concentrations were increased from 20% to 90% in 30 min at a flow rate of 20 mL min^{-1}. The purity of the products was assessed by analytical reversed-phase high-performance liquid chromatography (RP-HPLC) analysis performed by using Finnigan Surveyor MSQ single quadrupole electrospray ionization (Finnigan/Thermo Electron Corporation San Jose, CA, USA), with a C18-Phenomenex column eluting with H2O/0.1% TFA (A) and CH3CN/0.1% TFA (B) from 20% to 90% over 25 min at a flow rate of 1 mL min^{-1}. The identity of peptides was assessed by mass spectrometry using a LTQ XL Linear, ion trap mass spectrometer, ESI source (Finnigan/Thermo Electron Corporation, San Jose, CA, USA).

4.2. Solid-Phase Peptide Synthesis

Standard solid-phase peptide synthesis (SPPS) protocols were employed to synthesize the Fmoc-FFK peptide via an Fmoc/tBu strategy [50]. Essentially, *N*,*N*-dimethylformamide (DMF) was used as swelling solvent for Rink amide MBHA resin (substitution grade: 0.72 mmol g^{-1}) for 45 min. Fmoc cleavage was achieved by treating the solid support with a 20% *v*/*v* piperidine solution in DMF. Each amino acid was coupled by allowing the resin to react for 45 min with a two-fold molar excess of 1-hydroxybenzotriazole (HOBt) and HBTU (hexafluorophosphate benzotriazole tetramethyl uronium) (HBTU), as well as a four-fold molar excess of di-isopropylethylamine (DIPEA) in DMF as the reaction solvent. Using a TFA/triisopropylsilane (TIS)/H_2O (92.5/5.0/2.5 *v*/*v*/*v*) solution, the crude peptide was removed from the resin. The peptide was then precipitated in cold ether and freeze-dried three times. The crude peptide was found to be over 80% pure.

4.3. Fmoc-FFK Characterization

t_R = 18.31 min, MS (ESI+): *m*/*z*: calcd. for $C_{39}H_{42}N_4O_6$: 661.5 $[M+H]^+$; found: 662.5; ^{1}H NMR (700 MHz, DMSO) δ 8.15 (d, *J* = 7.9 Hz, 1H), 8.06 (d, *J* = 8.2 Hz, 1H), 7.95–7.86 (m, 3H), 7.62 (d, *J* = 7.5 Hz, 1H), 7.59 (dd, *J* = 11.8, 8.1 Hz, 2H), 7.46–7.38 (m, 3H), 7.32 (td, *J* = 7.4, 1.1 Hz, 1H), 7.30–7.22 (m, 10H), 7.21–7.13 (m, 3H), 7.11–7.05 (m, 1H), 4.56 (td, *J* = 8.4, 4.9 Hz, 1H), 4.27–4.16 (m, 3H), 4.15–4.07 (m, 2H), 3.07 (dd, *J* = 14.0, 4.9 Hz, 1H), 2.92 (dd, *J* = 13.8, 3.9 Hz, 1H), 2.86 (dd, *J* = 14.0, 9.1 Hz, 1H), 2.75 (t, *J* = 7.7 Hz, 3H), 2.70 (dd, *J* = 13.8, 10.8 Hz, 1H), 1.68 (td, *J* = 10.9, 5.4 Hz, 1H), 1.60–1.46 (m, 4H), 1.30 (tt, *J* = 16.4, 6.9 Hz, 3H).

4.4. Hydrogels Formulation

The DMSO/H_2O solvent switch approach was used to generate self-assembled hydrogels at four distinct weight/weight percentages: 0.25 wt%, 0.50 wt%, 1.0 wt%, and 2.0 wt%. A concentration of 1.0 weight percentage (10 mg mL^{-1}) of mixed hydrogels was prepared using the DMSO/H_2O solvent switch method. For mixed hydrogels, the ratios of 1/1, 1/5, 1/10, and 1/20 *w*/*w* were examined. The stock solution for each peptide was prepared in DMSO (100 mg mL^{-1}), mixed, vortexed, and then rehydrated with water. To improve sample homogeneity throughout the rehydration procedure, the solutions were also stirred for two seconds. The macroscopic assessment of hydrogel formation was conducted through the inverted tube test.

4.5. Hydrogel Swelling Studies

Hydrogel swelling ratios were determined by incubating each hydrogel sample (1.0 wt%, V = 300 µL) overnight at 25 °C upon the addition of 900 µL of doubly distilled water. Immediately after the removal of excess water, fully swollen hydrogels were weighed (*Ws*). Following freeze-drying, the hydrogels were weighed once again (*Wd*). The equation below states that the swelling behavior can be represented as the swelling ratio (*q*), which is the ratio between the weight of the swollen sample (*Ws*) and the weight of the freeze-dried hydrogel (*Wd*).

$$q = \frac{(Ws - Wd)}{Wd}\%$$

4.6. Circular Dichroism (CD) Studies

Jasco J-1500-150 spectropolarimeter equipped with a Jasco MCB-100 Mini Water Circulation Bath thermal controller unit (Peltier device) was used to gather the far-UV CD spectra of pure and mixed hydrogels, using a 0.2 mm quartz cell at 25 °C. Sample spectra were collected from 320 to 190 nm at various concentrations. Additional experimental parameters included the following: scan speed = 20 nm min^{-1}, sensitivity = 200 mdeg, time constant = 1 s, and bandwidth = 1 nm. Each spectrum was obtained by averaging three scans and correcting for the blank.

4.7. FT-IR Spectroscopy

The pure and mixed hydrogels (1.0 wt%) were examined through FT-IR spectroscopy. The spectra were obtained by using a Ge single crystal at a resolution of 4 cm^{-1} in attenuated total reflection mode on a Jasco FT/IR 4100 spectrometer (Easton, MD, USA). Every sample was scanned 100 times at a rate of 2 mm s^{-1} on a KBr background. The instrument integrated software immediately returned the amide I deconvolutions (in the 1600–1700 cm^{-1} area) as emissions after they were collected in transmission mode. A quantitative multivariate percentage analysis for secondary structure estimation (SEE) was achieved via method of principal component regression (PCR) with the Jasco SEE® dedicated software (Easton, MD, USA).

4.8. Thioflavin T (ThT) Spectroscopic Assay

ThT assay was used to assess the aggregation behavior of xerogels made by mixing hydrogels. Rapid interaction between thioflavin T and β-aggregated peptides results in enhanced emission at 482 nm [51]. Using the solvent switch approach, hydrogels were formulated by first diluting the peptide stock solution in DMSO (100 mg mL^{-1}) and then by adding water. Following the preparation of gels, samples were placed onto a clean glass coverslip, allowed to air dry, and then stained with 50 µL of a 50 µmol L^{-1} ThT solution. To prevent any corruption of the dried xerogels, the excess ThT solution on the samples was removed using filter paper. The dried stained films were examined in the GFP (green fluorescent protein) spectral region, with λ_{exc} = 488 nm and λ_{em} = 507 nm, under bright-field illumination. Fluorescence emission spectra were recorded between 460 and 600 nm after samples were excited at 450 nm. To acquire immunofluorescence pictures, scale bars were recorded at a resolution of 100 µm for each photograph, by means of a Leica MICA microhub fluorescent microscope with a 10× magnification.

4.9. Birefringence CR Assay

Owing to its ability to bind amyloid-like fibers, CR dye is frequently used to identify β-aggregated peptides [52]. To prepare the samples, ≈40 µL of each preformed peptide hydrogel was drop-cast onto a glass microscope slide. HGs were immediately ready for analysis, as previously mentioned. A total of 2 µL of a saturated CR solution dissolved in H_2O/ethanol (80/20, *v*/*v*) and saturated with NaCl was added to the hydrogels during the formulation step. Subsequently, the hydrogel was placed onto a glass microscope slide and air-dried overnight at room temperature. The obtained dried films were examined using an Optech BM80 Pol microscope (Milan, Italy) for both crossed polars and bright-field lighting.

4.10. Rheological Studies

Freshly preformed hybrid hydrogels (500 µL) underwent rheological assessments employing 1.5 cm diameter flat-plate geometry (PU20-PL61) and a rotational controlled-stress rheometer (Malvern Kinexus, UK). Each measurement was carried out in a humidity chamber with a 1.0 mm gap interval at 25 °C. Initial optimization parameters were carried out using strain sweep (0.1–100%) and oscillation frequency (0.1–100 Hz). Subsequently, an oscillatory time-sweep study lasting 15 min was carried out at 25 °C, 0.1% strain, and 1.0 Hz frequency. Rheological profiles were plotted as storage or elastic modulus (G') and shear loss or viscous modulus (G''). The profiles were reported in Pascal (Pa).

4.11. Scanning Electron Microscopy (SEM)

Xerogels were morphologically analyzed using field-emission SEM (Phenom_XL, Alfatest, Milan, Italy). A total of 10 µL of hydrogel was drop-cast and allowed to air dry on an aluminum stub to prepare the samples. For 75 s, a thin layer of palladium and gold was sputtered at a current of 25 mA. Following the introduction of the sputter-coated samples into the specimen chamber, pictures were taken using a secondary electron detector (SED) at an accelerating voltage of 10 kV.

4.12. Encapsulation and Release of Naphthol Yellow S

Naphthol yellow S (NYS) encapsulating HGs were prepared in 1.5 mL conical tubes, following the procedure previously described. An NYS water solution was used to rehydrate the DMSO solution of each peptide at a concentration of 0.012 mol L^{-1} (final NYS concentration: 0.011 mol L^{-1}). UV-Vis spectroscopy was used to analytically quantify the concentration of NYS solution (ε_{430} = 9922 L·cm^{-1}). A total of 800 μL of water was poured over each hydrogel, and 400 μL of this solution was removed and replaced with 400 μL of fresh water at predetermined intervals. UV-vis spectroscopy was carried out to estimate the quantity of NYS in each fraction, which was then expressed as a percentage of the ratio between the original amount that was encapsulated and the released NYS.

4.13. Cell Lines

The IRCCS SYNLAB SDN Biobank, Naples, Italy (10.5334/ojb.26, 13 Feb 2017) provided the human aneuploid immortal keratinocyte HaCaT and the mouse pre-adipocyte 3T3-L1 cell lines. The cells were cultured in Dulbecco's modified Eagle medium with 10% fetal bovine serum and 1% L-glutamine added. Seeds were placed in 100 mm culture dishes and the cells were incubated at 37 °C with 5% CO_2.

4.14. Cell Viability and Survival Test

Both HaCaT and 3T3-L1 cell lines were seeded at a density of 1.5×10^3 cells per well in 96-well plates for the adhesion test. Each well was filled with 50 μL of the designated hydrogels prior to seeding. Using a light microscope, adhering cells were counted, and the percentage of adherent cells relative to the number of plated cells was determined at increasing times (24, 48, and 72 h). The MTS (3-(4,5-dimethylthiazol-2-yl)-5-(3-carboxymethoxyphenyl)-2-(4-sulfophenyl)-2H-tetrazolium) assay (Cell Titer 96 Aqueous One Solution Cell Proliferation Assay, Promega, Italy) was used to test the toxicity of hydrogels conditioned media. The procedure was carried out according to the manufacturer's instructions, wherein cells were seeded at a density of 1.5×10^3 HaCaT and 3T3-L1 cells per well in 24-well plates, and the medium was incubated for 24, 48 and 72 h. To obtain the conditioned medium, hydrogels were formulated in a 200 μL hollow plastic chamber [53]. In brief, hydrogels were created in a plastic support that was sealed with a porous membrane at one end. They were then incubated for 16 h at room temperature in sterile conditions with 2 mL of the final mixture. After incubation, there was no noticeable shift in the media's color, and a pH value of 7.5–7.8 was found to be suitable to culture the cell lines seeded into the wells. The cells were grown in the conditioned media for 24, 48, and 72 h. Following the manufacturer's recommendations, the MTS test was used every 24 h to determine cell viability [54]. The Victor Nivo Multimode Microplate Reader (PerkinElmer San Jose, USA) was used to examine the samples at an absorbance of 490 nm. The percentage of viable cells in the presence of hydrogels was used to represent cell survival in comparison to that of control cells cultivated without them. Both assays were carried out in triplicate and repeated twice with comparable outcomes.

Supplementary Materials: The following supporting information can be downloaded at: https://www.mdpi.com/article/10.3390/gels10010012/s1, Figure S1: Physicochemical characterization of Fmoc-FFK peptide; Figure S2: ^{1}HNMR spectrum of Fmoc-FFK; Figure S3: Gelation kinetics of gels via UV-vis; Figure S4: SEM microphotos of Fmoc-FFK; Figure S5: CD spectra of mixed Fmoc-FFK/Fmoc-FF HGs; Figures S6–S10: rheological characterization of pure and mixed HGs; Figure S11: release kinetics of NYS from mixed HGs. Table S1: swelling test results. Table S2: A quantitative multivariate percentage analysis for secondary structure estimation (SEE).

Author Contributions: Conceptualization, E.G., C.D. and A.A.; Methodology, E.G., C.D., S.G., E.R. and G.O.; Software, E.G., C.D., S.G., E.R. and A.A.; Validation, E.G., C.D., B.C., N.B., G.O. and A.A.; Formal analysis, E.G., C.D., S.G., B.C., N.B. and A.A.; Investigation, E.G., C.D., S.G., B.C. and A.A.; Resources, G.O., G.M. and A.A.; Data curation, E.G., C.D., S.G., E.R., G.O. and A.A.; Writing—original draft, E.G., C.D., E.R., B.C., G.P., G.M., G.O. and A.A.; Supervision, E.G., C.D., G.M., G.O. and A.A.;

Project administration, E.G., C.D. and A.A.; Funding acquisition, A.A. All authors have read and agreed to the published version of the manuscript.

Funding: This work was supported by the Italian Ministry of Health-Ricerca Corrente Project and by MUR—Italian Ministry of University and Research (Italy) (grant number 2022TSLMHR), with Carlo Diaferia as the principal investigator.

Institutional Review Board Statement: The HaCaT and 3T3-L1 cell lines used for the in vitro experiments were obtained from IRCCS SYNLAB SDN Biobank (10.5334/ojb.26).

Informed Consent Statement: Not applicable.

Data Availability Statement: All data and materials are available on request from the corresponding author. The data are not publicly available due to ongoing research.

Conflicts of Interest: The authors declare no conflicts of interest.

References

1. Chen, J.; Zou, X. Self-assemble peptide biomaterials and their biomedical applications. *Bioact. Mater.* **2019**, *4*, 120–131. [CrossRef] [PubMed]
2. Levin, A.; Hakala, T.A.; Schnaider, L.; Bernardes, G.J.L.; Gazit, E.; Knowles, T.P.J. Biomimetic peptide self-assembly for functional materials. *Nat. Rev. Chem.* **2020**, *4*, 615–634. [CrossRef]
3. Rosa, E.; de Mello, L.; Castelletto, V.; Dallas, M.L.; Accardo, A.; Seitsonen, J.; Hamley, I.W. Cell Adhesion Motif-Functionalized Lipopeptides: Nanostructure and Selective Myoblast Cytocompatibility. *Biomacromolecules* **2023**, *24*, 213–224. [CrossRef] [PubMed]
4. Gallo, E.; Diaferia, C.; Balasco, N.; Sibillano, T.; Roviello, V.; Giannini, C.; Vitagliano, L.; Morelli, G.; Accardo, A. Fabrication of fluorescent nanospheres by heating PEGylated tetratyrosine nanofibers. *Sci. Rep.* **2021**, *11*, 2470. [CrossRef] [PubMed]
5. Barrett, J.C.; Tirrell, M.V. Peptide Amphiphile Micelles for Vaccine Delivery. *Methods Mol. Biol.* **2018**, *1798*, 277–292. [PubMed]
6. Fu, K.; Wu, H.; Su, Z. Self-assembling peptide-based hydrogels: Fabrication, properties, and applications. *Biotechnol. Adv.* **2021**, *49*, 107752. [CrossRef] [PubMed]
7. Ahmes, E.M. Hydrogel: Preparation, characterization, and applications: A review. *J. Adv. Res.* **2015**, *6*, 105–121.
8. Shariati Pour, S.R.; Oddis, S.; Barbalinardo, M.; Ravarino, P.; Cavallini, M.; Fiori, J.; Giuri, D.; Tomasini, C. Delivery of active peptides by self-healing, biocompatible and supramolecular hydrogels. *Molecules* **2023**, *28*, 2528. [CrossRef]
9. Di Gregorio, E.; Rosa, E.; Ferrauto, G.; Diaferia, C.; Gallo, E.; Accardo, A.; Terreno, E. Development of cationic peptide-based hydrogels loaded with iopamidol for CEST-MRI detection. *J. Mater. Chem. B* **2023**, *11*, 7435–7441. [CrossRef]
10. Martin, A.D.; Thordarson, P. Beyond Fmoc: A review of aromatic peptide capping groups. *J. Mater. Chem. B* **2020**, *8*, 863–877. [CrossRef]
11. Pramanik, B. Short peptide-based smart thixotropic hydrogels. *Gels* **2022**, *8*, 569. [CrossRef]
12. Hiew, S.H.; Lu, Y.; Han, H.; Gonçalves, R.A.; Alfarano, S.R.; Mezzenga, R.; Parikh, A.N.; Mu, Y.; Miserez, A. Modulation of Mechanical Properties of Short Bioinspired Peptide Materials by Single Amino-Acid Mutations. *J. Am. Chem. Soc.* **2023**, *145*, 3382–3393. [CrossRef]
13. Bordi, F.; Paradossi, G.; Rinaldi, C.; Ruzicka, B. Chemical and physical hydrogels: Two casesystems studied by quasi elastic light scattering. *Phys. A Stat. Mech. Appl.* **2002**, *304*, 119–128. [CrossRef]
14. Afami, M.E.; El Karim, I.; About, I.; Krasnodembskaya, A.D.; Laverty, G.; Lundy, F.T. Multicomponent Peptide Hydrogels as an Innovative Platform for Cell-Based Tissue Engineering in the Dental Pulp. *Pharmaceutics* **2021**, *13*, 1575. [CrossRef]
15. Falcone, N.; Shao, T.; Andoy, N.M.O.; Rashid, R.; Sullan, R.M.A.; Sun, X.; Kraatz, H.-B. Multi-component peptide hydrogels—A systematic study incorporating biomolecules for the exploration of diverse, tuneable biomaterials. *Biomater. Sci.* **2020**, *8*, 5601–5614. [CrossRef]
16. Jayawarna, V.; Ali, M.; Jowitt, T.A.; Miller, A.F.; Saiani, A.; Gough, J.E.; Ulijn, R.V. Nanostructured Hydrogels for Three-Dimensional Cell Culture through Self-Assembly of Fluorenylmethoxycarbonyl–Dipeptides. *Adv. Mater.* **2006**, *18*, 611–614. [CrossRef]
17. Mahler, A.; Reches, M.; Rechter, M.; Cohen, S.; Gazit, E. Rigid, self-assembled hydrogel composed of a modified aromatic dipeptide. *Adv. Mater.* **2006**, *18*, 1365–1370. [CrossRef]
18. Wang, Y.; Geng, Q.; Zhang, Y.; Adler-Abramovich, L.; Fan, X.; Mei, D.; Gazit, E.; Tao, K. Fmoc-diphenylalanine gelating nanoarchitectonics: A simplistic peptide self-assembly to meet complex applications. *J. Colloid. Interface Sci.* **2023**, *636*, 113–133. [CrossRef]
19. Halperin-Sternfeld, M.; Ghosh, M.; Sevostianov, R.; Grigoriants, I.; Adler-Abramovich, L. Molecular co-assembly as a strategy for synergistic improvement of the mechanical properties of hydrogels. *Chem. Commun.* **2017**, *53*, 9586–9589. [CrossRef]
20. Gong, X.; Branford-White, C.; Tao, L.; Li, S.; Quan, J.; Nie, H.; Zhu, L. Preparation and characterization of a novel sodium alginate incorporated self-assembled Fmoc-FF composite hydrogel. *Mater. Sci. Eng. C Mater. Biol. Appl.* **2016**, *58*, 478–486. [CrossRef]
21. Ji, W.; Yuan, C.; Chakraborty, P.; Gilead, S.; Yan, X.; Gazit, E. Stoichiometry-controlled secondary structure transition of amyloid-derived supramolecular dipeptide co-assemblies. *Commun. Chem.* **2019**, *2*, 65. [CrossRef]

22. Fan, Y.; Xing, Q.; Zhang, J.; Wang, Y.; Liang, Y.; Qi, W.; Su, R.; He, Z. Self-Assembly of Peptide Chiral Nanostructures with Sequence-Encoded Enantioseparation Capability. *Langmuir* **2020**, *36*, 10361–10370. [CrossRef]
23. Xing, Q.; Zhang, J.; Xie, Y.; Wang, Y.; Qi, W.; Rao, H.; Su, R.; He, Z. Aromatic Motifs Dictate Nanohelix Handedness of Tripeptides. *ACS Nano* **2018**, *12*, 12305–12314. [CrossRef]
24. Zhang, Y.; Liu, X.; Wang, M.; Zhaoa, Y.; Qi, W.; Suabc, R.; He, Z. Co-assembly of Fmoc-tripeptide and gold nanoparticles as a facile approach to immobilize nanocatalysts. *RSC Adv.* **2017**, *7*, 15736–15741. [CrossRef]
25. Tang, C.; Ulijn, R.V.; Saiani, A. Effect of Glycine Substitution on Fmoc–Diphenylalanine Self-Assembly and Gelation Properties. *Langmuir* **2011**, *27*, 14438–14449. [CrossRef]
26. Smith, A.M.; Williams, R.J.; Tang, C.; Coppo, P.; Collins, R.F.; Turner, M.L.; Saiani, A.; Ulijn, R.V. Fmoc-Diphenylalanine Self Assembles to a Hydrogel via a Novel Architecture Based on π–π Interlocked β-Sheets. *Adv. Mater.* **2008**, *20*, 37–41. [CrossRef]
27. Coin, I.; Beyermann, M.; Bienert, M. Solid-phase peptide synthesis: From standard procedures to the synthesis of difficult sequences. *Nat. Protoc.* **2007**, *2*, 3247–3256. [CrossRef]
28. White, A.M.; Palombi, I.R.; Malins, L.R. Umpolung strategies for the functionalization of peptides and proteins. *Chem. Sci.* **2022**, *13*, 2809–2823. [CrossRef]
29. Sun, Y.; Li, X.; Zhao, M.; Chen, Y.; Xu, Y.; Wang, K.; Bian, S.; Jiang, Q.; Fan, Y.; Zhang, X. Bioinspired supramolecular nanofiber hydrogel through self-assembly of biphenyl-tripeptide for tissue engineering. *Bioact. Mater.* **2022**, *8*, 396–408. [CrossRef]
30. Tang, C.; Smith, A.M.; Collins, R.F.; Ulijn, R.V.; Saiani, A. Fmoc-diphenylalanine self-assembly mechanism induces apparent pKa shifts. *Langmuir* **2009**, *25*, 9447–9453. [CrossRef]
31. Dudukovic, N.A.; Hudson, B.C.; Paravastu, A.K.; Zukoski, C.F. Self-assembly pathways and polymorphism in peptide-based nanostructures. *Nanoscale* **2018**, *10*, 1508–1516. [CrossRef]
32. Levine, M.S.; Ghosh, M.; Hesser, M.; Hennessy, N.; DiGuiseppi, D.M.; Adler-Abramovich, L.; Schweitzer-Stenner, R. Formation of peptide-based oligomers in dimethylsulfoxide: Identifying the precursor of fibril formation. *Soft Matter* **2020**, *16*, 7860–7868. [CrossRef]
33. Chronopoulou, L.; Sennato, S.; Bordi, F.; Giannella, D.; Di Nitto, A.; Barbetta, A.; Dentini, M.; Togna, A.R.; Togna, G.I.; Moschinic, S.; et al. Designing unconventional Fmoc-peptide-based biomaterials: Structure and related properties. *Soft Matter* **2014**, *10*, 1944–1952. [CrossRef]
34. Diaferia, C.; Rosa, E.; Morelli, G.; Accardo, A. Fmoc-Diphenylalanine Hydrogels: Optimization of Preparation Methods and Structural Insights. *Pharmaceuticals* **2022**, *15*, 1048. [CrossRef]
35. Raeburn, J.; Pont, G.; Chen, L.; Cesbron, Y.; Levy, R.; Adams, D.J. Fmoc-diphenylalanine hydrogels: Understanding the variability in reported mechanical properties. *Soft Matter* **2012**, *8*, 1168–1174. [CrossRef]
36. Giordano, S.; Gallo, E.; Diaferia, C.; Rosa, E.; Carrese, B.; Borbone, N.; Scognamiglio, P.L.; Franzese, M.; Oliviero, G.; Accardo, A. Multicomponent peptide-based hydrogels containing chemical functional groups as innovative platforms for biotechnological applications. *Gels* **2023**, *9*, 903. [CrossRef]
37. Raeburn, J.; Mendoza-Cuenca, C.; Cattoz, B.N.; Little, M.A.; Terry, A.E.; Cardoso, A.Z.; Griffiths, P.C.; Adams, D.J. The effect of solvent choice on the gelation and final hydrogel properties of Fmoc–diphenylalanine. *Soft Matter* **2015**, *11*, 927–935. [CrossRef]
38. Ryan, K.; Beirne, J.; Redmond, G.; Kilpatrick, J.I.; Guyonnet, J.; Buchete, N.-V.; Kholkin, A.L.; Rodriguez, B.J. Nanoscale Piezoelectric Properties of Self-Assembled Fmoc–FF Peptide Fibrous Networks. *ACS Appl. Mater. Interf.* **2015**, *7*, 12702–12707. [CrossRef]
39. Reddy, S.M.M.; Shanmugam, G.; Duraipandy, N.; Kiranb, M.S.; Mandal, A.B. An additional fluorenylmethoxycarbonyl (Fmoc) moiety in di-Fmoc-functionalized l-lysine induces pH-controlled ambidextrous gelation with significant advantages. *Soft Matter* **2015**, *11*, 8126–8140. [CrossRef]
40. Micsonai, A.; Wien, F.; Kernya, L.; Lee, Y.H.; Goto, Y.; Réfrégiers, M.; Kardos, J. Accurate secondary structure prediction and fold recognition for circular dichroism spectroscopy. *Proc. Natl. Acad. Sci. USA* **2015**, *112*, E3095–E3103. [CrossRef]
41. Thornton, K.; Abul-Haija, Y.M.; Hodsonc, N.; Ulijn, R.V. Mechanistic insights into phosphatase triggered self-assembly including enhancement of biocatalytic conversion rate. *Soft Matter* **2013**, *9*, 9430–9439. [CrossRef]
42. Makam, P.; Gazit, E. Minimalistic peptide supramolecular co-assembly: Expanding the conformational space for nanotechnology. *Chem. Soc. Rev.* **2018**, *47*, 3406–3420. [CrossRef]
43. Chen, C.H.; Palmer, L.C.; Stupp, S.I. Self-sorting in supramolecular assemblies. *Soft Matter* **2021**, *17*, 3902–3912. [CrossRef]
44. Haris, P.I.; Chapman, D. The conformational analysis of peptides using Fourier transform IR spectroscopy. *Biopolymers* **1995**, *37*, 251–263. [CrossRef]
45. Brauner, J.W.; Flach, C.R.; Mendelsohn, R. A Quantitative Reconstruction of the Amide I Contour in the IR Spectra of Globular Proteins: From Structure to Spectrum. *J. Am. Chem. Soc.* **2005**, *127*, 100–109. [CrossRef]
46. Halperin-Sternfeld, M.; Netanel Liberman, G.; Kannan, R.; Netti, F.; Ma, P.X.; Arad, S.M.; Adler-Abramovich, L. Thixotropic Red Microalgae Sulfated Polysaccharide-Peptide Composite Hydrogels as Scaffolds for Tissue Engineering. *Biomedicines* **2022**, *10*, 1388. [CrossRef]
47. Smaldone, G.; Rosa, E.; Gallo, E.; Diaferia, C.; Morelli, G.; Stornaiuolo, M.; Accardo, A. Caveolin-Mediated Internalization of Fmoc-FF Nanogels in Breast Cancer Cell Lines. *Pharmaceutics* **2023**, *15*, 1026. [CrossRef]
48. Kurbasic, M.; Parisi, E.; Garcia, A.M.; Marchesan, S. Self-Assembling, Ultrashort Peptide Gels as Antimicrobial Biomaterials. *Curr. Top. Med. Chem.* **2020**, *20*, 1300–1309. [CrossRef]

49. Liu, X.; Sun, X.; Liang, G. Peptide-based supramolecular hydrogels for bioimaging applications. *Biomater. Sci.* **2021**, *9*, 315–327. [CrossRef]
50. Hansen, P.R.; Oddo, A. Fmoc Solid-Phase Peptide Synthesis. *Methods Mol. Biol.* **2015**, *1348*, 33–50.
51. LeVine, H., 3rd. Thioflavine T interaction with synthetic Alzheimer's disease beta-amyloid peptides: Detection of amyloid aggregation in solution. *Protein Sci.* **1993**, *2*, 404–410. [CrossRef]
52. Espargaró, A.; Llabrés, S.; Saupe, S.J.; Curutchet, C.; Luque, F.J.; Sabaté, R. On the Binding of Congo Red to Amyloid Fibrils. *Angew. Chem. Int. Ed. Engl.* **2020**, *59*, 8104–8107. [CrossRef]
53. Diaferia, C.; Ghosh, M.; Sibillano, T.; Gallo, E.; Stornaiuolo, M.; Giannini, C.; Morelli, G.; Adler-Abramovich, L.; Accardo, A. Fmoc-FF and hexapeptide-based multicomponent hydrogels as scaffold materials. *Soft Matter* **2019**, *15*, 487–496. [CrossRef]
54. Mosmann, T. Rapid colorimetric assay for cellular growth and survival: Application to proliferation and cytotoxicity assays. *J. Immunol. Methods.* **1983**, *65*, 55–63. [CrossRef]

gels

Article

Self-Assembly of a Novel Pentapeptide into Hydrogelated Dendritic Architecture: Synthesis, Properties, Molecular Docking and Prospective Applications

Stefania-Claudia Jitaru [1], Andra-Cristina Enache [2,*], Corneliu Cojocaru [2], Gabi Drochioiu [1], Brindusa-Alina Petre [1,3] and Vasile-Robert Gradinaru [1]

[1] Faculty of Chemistry, "Alexandru Ioan Cuza" University, 11 Carol I Bd., 700506 Iasi, Romania; jitaru.stefania@yahoo.com (S.-C.J.); gabi.drochioiu@gmail.com (G.D.); brindusa.petre@uaic.ro (B.-A.P.); robert.gradinaru@uaic.ro (V.-R.G.)
[2] "Petru Poni" Institute of Macromolecular Chemistry, 41-A Grigore Ghica Voda Alley, 700487 Iasi, Romania; cojocaru.corneliu@icmpp.ro
[3] TRANSCEND-Regional Institute of Oncology, 700483 Iasi, Romania
* Correspondence: humelnicu.andra@icmpp.ro

Abstract: Currently, ultrashort oligopeptides consisting of fewer than eight amino acids represent a cutting-edge frontier in materials science, particularly in the realm of hydrogel formation. By employing solid-phase synthesis with the Fmoc/tBu approach, a novel pentapeptide, FEYNF-NH_2, was designed, inspired by a previously studied sequence chosen from hen egg-white lysozyme (FESNF-NH_2). Qualitative peptide analysis was based on reverse-phase high performance liquid chromatography (RP-HPLC), while further purification was accomplished using solid-phase extraction (SPE). Exact molecular ion confirmation was achieved by matrix-assisted laser desorption–ionization mass spectrometry (MALDI-ToF MS) using two different matrices (HCCA and DHB). Additionally, the molecular ion of interest was subjected to tandem mass spectrometry (MS/MS) employing collision-induced dissociation (CID) to confirm the synthesized peptide structure. A combination of research techniques, including Fourier-transform infrared spectroscopy (FTIR), fluorescence analysis, transmission electron microscopy, polarized light microscopy, and Congo red staining assay, were carefully employed to glean valuable insights into the self-assembly phenomena and gelation process of the modified FEYNF-NH_2 peptide. Furthermore, molecular docking simulations were conducted to deepen our understanding of the mechanisms underlying the pentapeptide's supramolecular assembly formation and intermolecular interactions. Our study provides potential insights into amyloid research and proposes a novel peptide for advancements in materials science. In this regard, in silico studies were performed to explore the FEYNF peptide's ability to form polyplexes.

Keywords: peptide; self-assembling; supramolecular gels; β-sheet; molecular docking; polyplexes

1. Introduction

In recent years, the spotlight in the realms of biology, chemistry, and medicine has intensified on short peptides, which have captivated the scientific community with their distinctive features [1,2]. Apart from their low molecular weight and facile synthesis, these types of peptides are recognized for their biocompatibility and the ability to target specific cells or organelles with minimal side effects [3]. These distinct attributes make them exceptionally well suited for an extensive array of applications, such as cell culture [4], tissue regeneration processes [5], drug delivery [6], and biosensors [7]. Noteworthy is that short peptides were proven to play pivotal roles in the advanced gene therapy area [8,9]. Peptides can serve as smart delivery vehicles due to their capability to bind, conjugate, or encapsulate DNA or RNA [9]. Additionally, they are utilized in diagnostic imaging due to their inherent targeting ability [10,11].

Self-assembly represents an innate and intricate mechanism observed across numerous essential biological processes, underscoring its fundamental role in nature [12]. Within this context, peptides demonstrate a remarkable capability to autonomously organize and undergo self-assembly, particularly under specific environmental conditions [1–4]. The molecular self-assembly process implies the formation of physical hydrogels, also known as supramolecular hydrogels [13]. The predominant mechanism in peptide supramolecular gelation is primarily catalyzed by fundamental physical forces, such as hydrogen bonding, hydrophobic interactions, aromatic π–π stacking interactions, and electrostatic interactions, which are weak and reversible [14]. Such noncovalent interactions are known for imparting order and directionality to peptide self-assembly into fibril-like structures and hence play a critical role in building the final 3D architecture [15,16]. The inherent biocompatibility, high water content, and exceptional hydrogelation propensity brought on by the unidirectional amide H-bonding and π–π stacking interactions can provide peptide-based hydrogels significant unique properties [17]. These special features, when harmonized with the inherent bioactivity intrinsic to the peptide sequences, pave the way for the creation of distinct and specialized biomaterials.

It was previously reported that peptides consisting of fewer than eight amino acids can spontaneously self-assemble into hydrogels [18]. The ability of peptides consisting of only two amino acids (shortest self-assembling motif of peptides) to form linear dipeptide hydrogels was also shown, employing different synthesis strategies [13]. Chemical synthesis of peptides can be achieved either by solution- or solid-phase strategies. However, the solid-phase peptide synthesis (SPPS) method (in which a peptide is anchored to an insoluble solid support, typically made of a polymer matrix), has lately seen consistent advancements and refinements in order to produce peptides with high purity [19]. Thus, the exploration of amino acids and their ability to form specific sequences and implicitly supramolecular structures have paved the way for pioneering advancements in materials science [20,21].

Due to the intriguing structures formed by short hybrid peptides, there is growing interest in leveraging self-assembly principles to design and forecast peptide hydrogels. Therefore, understanding the underlying mechanisms and microscopic behavior involved in peptide self-assembly is essential. Computational techniques have increasingly become instrumental in elucidating the interplay between molecular structures, as well as the potential for supramolecular gelation [22]. Furthermore, the computational methodologies are expected to be critical for researchers exploring and innovating in the realm of peptide hydrogel materials.

Therefore, this research aims to explore the synergistic relationship between the synthesis of a new short-peptide, its self-assembly capacity, and its potential therapeutic applications. Accordingly, the synthesis of a new highly pure amidated pentapeptide was envisaged, specifically, FEYNF-NH_2, comprised of F (phenylalanyl), E (glutamyl), Y (tyrosyl), and N (asparaginyl) residues. In addition to examining the morphostructural properties of the peptide, this study emphasized the significance of computational techniques, notably molecular docking simulations, to: (i) undertake an in-depth investigation into the driving forces and structural intricacies driving the self-assembly of the FEYNF peptide; (ii) forecast its inclination towards adopting a β-sheet structure and potential for supramolecular gel formation; and (iii) conduct a computational assessment (in silico study) to evaluate the FEYNF peptide's capability to form polyplexes, serving as an initial step toward exploring potential future applications.

2. Results and Discussion

2.1. Solid-Phase Synthesis of Novel FEYNF-NH_2 Pentapeptide

Certain peptides have the inherent capability to undergo self-assembly, leading to the formation of gels characterized by adjustable properties under specific environmental conditions [12]. In a previous study, we demonstrated the propensity of a pentapeptide inspired by the hen egg-white lysozyme, specifically, FESNF (where F-phenylalanyl, E-glutamyl, S-seryl, and N-asparaginyl), to self-assemble into ordered and dense fibrils [23]. Given the fact that aromatic amino acid side chains (e.g., phenylalanine, tyrosine, tryptophan, and histidine) are likely to participate in π-stacking interactions [24], we suggested substituting the serine (S) in the FESNF peptide with the aromatic amino acid tyrosine (Y). This led to the synthesis of a novel amidated peptide, FEYNF, with the chemical structure (2D geometry) represented in Figure 1a.

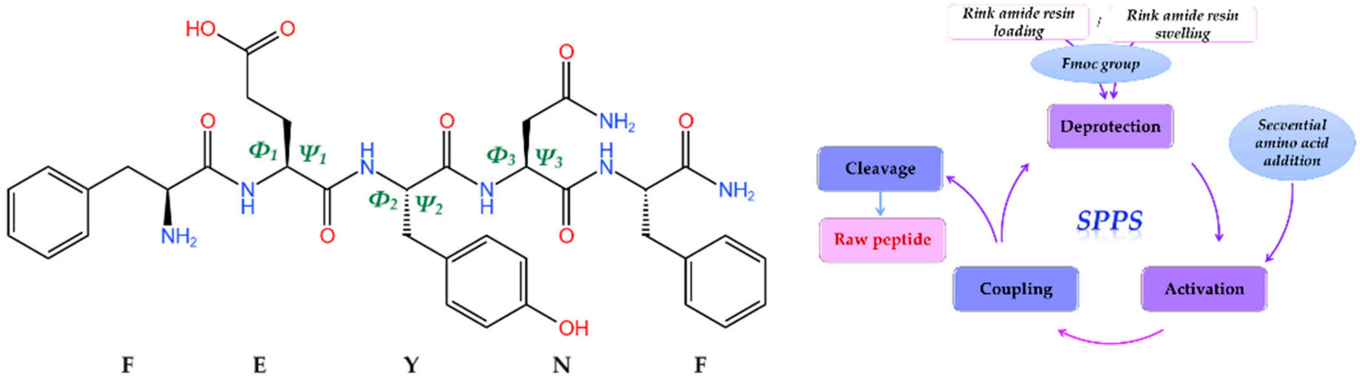

(**a**) (**b**)

Figure 1. (**a**) Chemical structure depiction (2D geometry) of the FEYNF-NH_2 pentapeptide (KingDraw V3.0.2.) highlighting Φ (Phi) and Ψ (Psi) torsion angles; where $\Phi = C(j-1) - N(j) - C\alpha(j) - C(j)$ and $\Psi = N(j) - C\alpha(j) - C(j) - N(j+1)$; j—atom index in the backbone sequence; (**b**) schematic representation of the solid-phase peptide synthesis (SPPS) protocol (adapted from [19]).

The synthesis of the FEYNF-NH_2 pentapeptide was effectively achieved using the solid-phase peptide synthesis (SPPS) approach, rooted in the established Fmoc/tBu methodology [15,16,25,26]. As illustrated in Figure 1b, the SPPS technique primarily entailed employing a Rink amide resin to optimize the peptide synthesis environment, along with Fmoc group deprotection, coupling of activated Fmoc–amino acids, and subsequent detachment of the peptide from the resin. It is noteworthy that amino acids with suitable protective groups were selected to ensure alignment with the 9-fluorenylmethoxycarbonyl/tert-butyl (Fmoc/t-butyl) approach for solid-phase peptide synthesis (SPPS). In addition, the amidation at the peptide's C-terminal is expected to diminish its net charge, potentially resulting in reduced solubility. Nevertheless, this alteration augments the peptide's stability, aligning it more closely with native proteins, thereby enhancing its biological relevance [27].

2.2. Qualitative FEYNF-NH_2 Peptide Analysis and Purification

Reverse-phase high-performance liquid chromatography (RP-HPLC) was used to analyze and separate the crude mixture of synthesized peptide. The HPLC profile of the raw peptide mixture FEYNF-NH_2 is given in Figure 2. To detect the peptide bond specifically, a targeted wavelength of 215 nm was used during the analysis. The initial separation of the raw peptide mixture followed a clearly defined pattern guided by a linear gradient, as clearly depicted in Figure S1 (in Supplementary Materials). This approach facilitated the systematic fractionation of components within the mixture, allowing for discernible identification and characterization of individual compounds based on their distinct retention times.

The chromatographic analysis within the initial 5 min window revealed the presence of peaks attributed primarily to acetic acid and potential residual solvents employed during the synthesis process. However, a distinct compound, detected at 9.09 min of retention time, was unequivocally identified via mass spectrometry as the FEYNF peptide. The considerable intensity of this peak strongly indicates a successful synthesis process. Notably, a secondary peak appearing at 10.05 min of retention time, albeit with lower intensity, corresponds to a synthesis by-product demonstrating heightened hydrophobicity. This phenomenon, characterized by a marginally extended elution time, is a commonly observed occurrence in solid-phase peptide synthesis (SPPS) using Rink amide as solid support [28].

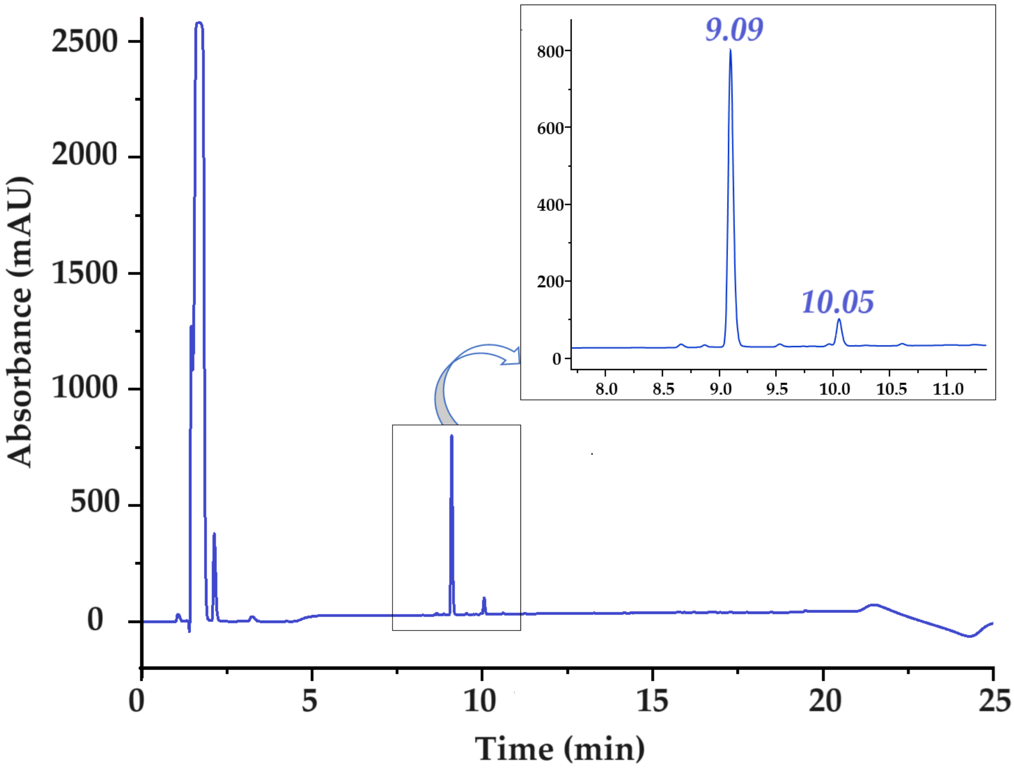

Figure 2. HPLC chromatogram of raw FEYNF-NH_2 pentapeptide. The chromatogram was recorded at a wavelength of 215 nm. Injected volume: 90 µL.

In this investigation, we employed a purification methodology for the FEYNF peptide via RP-SPE chromatography with gradient elution, a technique adapted from [29]. Notably, our protocol differed by introducing a crucial modification: after peptide elution with acetic acid, the mixture underwent adjustment to an optimal intermediate pH of 4.5, in accordance with the column cartridge specifications. This adjustment, within the pH range of 2–8 to prevent denaturation of the stationary phase, served a dual purpose: ensuring the integrity of the stationary phase and eliminating the need for a time-consuming freeze-drying step typically required to remove excess acetic acid. By preventing denaturation and obviating extended drying procedures, this adaptation streamlined our purification process, significantly enhancing efficiency and expediting the overall workflow.

It should be mentioned that the determined purity of the pentapeptide FEYNF-NH_2 was assessed immediately after synthesis (raw product) and quantified at an impressive 95.47%. Moreover, the compounds eluted within the initial 5 min of the chromatography predominantly stem from the presence of acetic acid used for solubilization/during the washing step and residual solvents originating from the synthesis process, as well as the injection peak [30]. To guarantee the utmost quality of the peptide, a meticulous purification step was executed through solid-phase extraction. This rigorous process yielded a confirmed purity of 99.54% for the pentapeptide used in the experiments. Importantly, this achieved purity underwent thorough validation through subsequent HPLC analysis, as illustrated in Figure S2 (in Supplementary Materials).

2.3. Molecular Mass Confirmation (MALDI-ToF MS and MS/MS)

Molecular mass determination was obtained by using a MALDI-ToF MS instrument (Bruker, Billerica, MA, USA). Crystals were characterized by distinctive morphologies when the peptide was associated (co-crystalized) with HCCA and DHB matrices, as depicted in Figure S3 (in Supplementary Material) and observed through the MALDI-ToF camera. Consistent with both experimental findings and existing literature, co-crystals originating from the DHB matrix exhibit a needle-like, acicular structure, while those formed from the HCCA matrix display a compact, amorphous appearance [31]. Upon mass spectrometry analysis of the first peak, the molecular ion $[M + H]^+$ of the pentapeptide was identified at m/z 718.40 with the DHB matrix (Figure 3a) and slightly shifted to m/z 718.55 with HCCA (Figure 3b). Notably, alongside the protonated molecular ion, the detection of sodium ($[M + Na]^+$) adduct ions at m/z 740.41 and m/z 740.50, contingent upon the specific matrix employed, was evident. The peptide appears to demonstrate a distinct tendency to produce sodium ions, possibly due to interactions between the sodium ion and carboxyl oxygen and/or amide nitrogen. This interplay could achieve stability through the aromatic ring of the tyrosine side chain, a hypothesis previously supported by previous research studies [32]. Furthermore, potassium species ($[M + K]^+$) were observed at m/z 756.51 and 756.58, as depicted in Figure 3a,b.

Further analysis involved collision-induced dissociation (CID) of the molecular ion $[FEYNF + H]^+$ (m/z 718.55), yielding multiple b^+ and y^+ molecular fragments, providing valuable insights into the fragmentation patterns of the FEYNF-NH_2 pentapeptide and enhancing our understanding of its structural characteristics (Figure 3c). The tandem mass spectrum exhibits several distinct fragments, notably featuring ions abundant due to the elimination of ammonia: $y_2{}^+$-NH_3 at m/z 261.87, $y_3{}^+$-NH_3 at m/z 424.99, $b_4{}^+$-NH_3 at m/z 537.99, and $y_4{}^+$-NH_3 at m/z 553.61. Additionally, water loss correlates with the glutamate moiety, while carbon dioxide release likely originates from the decarboxylation of the same moiety.

Notably, at m/z 672.93 ($[M + H]^+$—46), the observed 46 Da discrepancy is postulated to correspond to the elimination of a CO_2 and a H_2 molecule. Moreover, scrutiny of the tandem MS spectra reveals that the equitable distribution of aromatic residues along the peptide backbone induces fragmentation at all amide bonds. This diverges from our earlier investigations, wherein the mutant peptide FESNY-NH_2 characterized by aromatic residues solely at the termini exhibited a marked predilection for fragmentation in those regions [33]. The inclusion of phenylalanine and tyrosine residues, endowed with a relatively high electron density, is conjectured to facilitate fragmentation by promoting charge localization and augmenting susceptibility to dissociation processes in tandem MS spectra [34].

2.4. Self-Aggregation of FEYNF-NH_2 Investigations

2.4.1. Fourier-Transform Infrared Spectroscopy (FTIR)

The investigation into peptide self-assembly and its correlation with secondary structure, particularly the formation of β-sheet structures, involved the use of FTIR spectroscopy analysis. To elucidate the secondary structure of the FEYNF-NH_2 peptide, the examination focused on the amide bands, specifically, the amide I band. Figure S4 in the Supplementary Materials illustrates the broad shape of the amide I band, attributed to overlapping bands from distinct secondary structures, primarily consisting of peptide backbone C=O stretching vibrations [35]. Additionally, the amide II region (Figure S4) mainly reflects N–H and C–N bending modes [36], with the absorption band at 1511 cm^{-1} potentially linked to the tyrosine residue's aromatic ring, according to De Meutter et al., which suggests its occurrence at higher wavenumbers in free amino acids [37].

For a detailed assessment of the FEYNF-NH_2 peptide's secondary structure, quantitative Gaussian peak fitting was applied to the FTIR data (Figure 4), utilizing OriginPro 8.5.0 SR1 software (OriginLab Corporation, Northhampton, MA, USA). Following a linear baseline subtraction for the amide I band (Figure S4), the second derivative was calculated to identify the position and number of absorption bands essential for peak fitting, employing a 20-point Savitzky–Golay smoothing function [38]. Subsequently, Gaussian peaks were introduced into the amide I band based on positions indicated by the second derivative spectrum, and the corresponding structures were identified referencing literature [35–38], as shown in Figure 4.

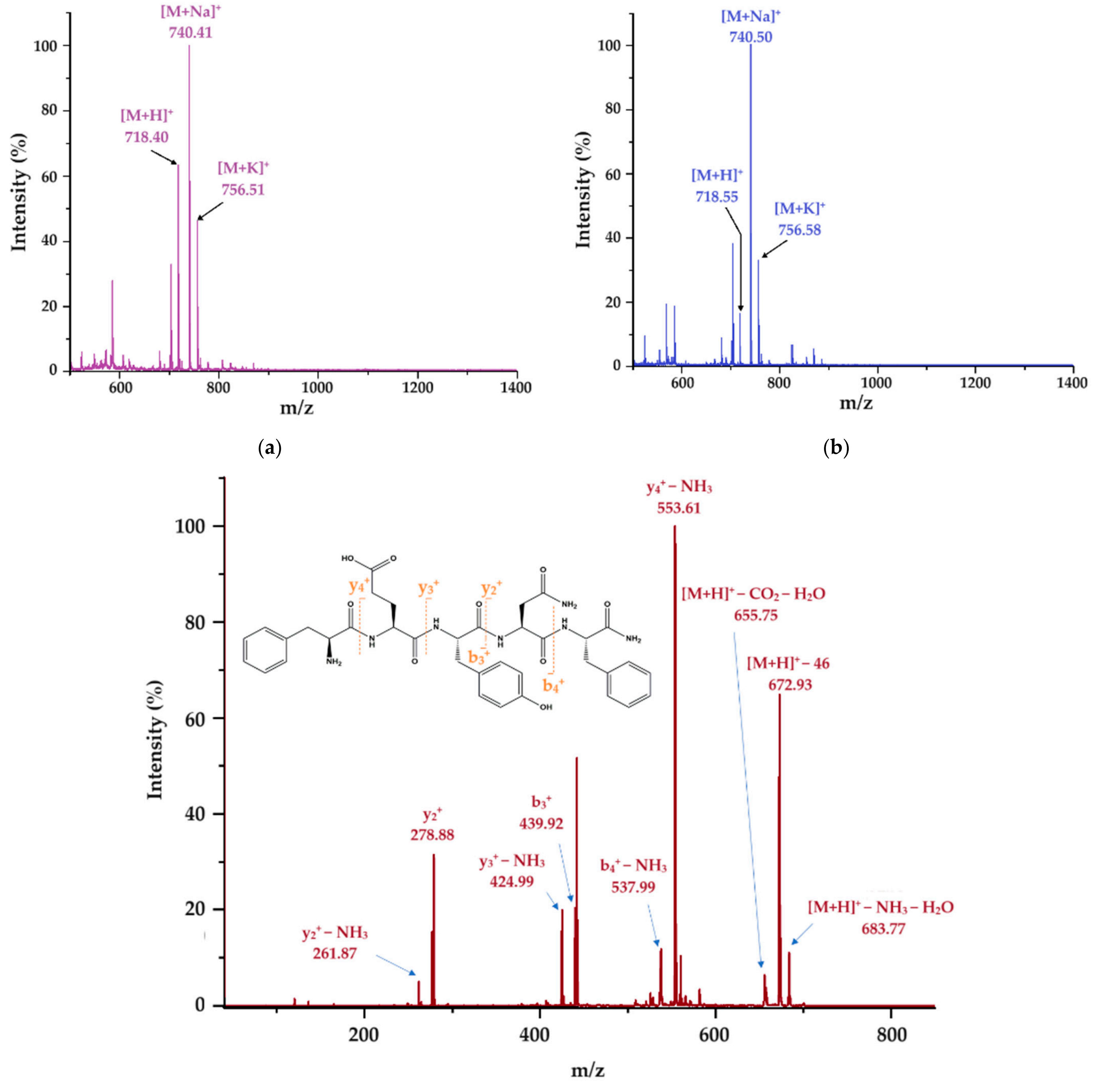

(**a**)

(**b**)

(**c**)

Figure 3. MS spectrum of the eluted fraction at 9.09 min confirming *m*/*z* corresponding to FEYNF-NH$_2$ with two different matrices: (**a**) DHB and (**b**) HCCA; (**c**) assignment of *m*/*z* signals resulting from MALDI-ToF MS/MS tandem mass spectrometry analysis; fragmentation of the molecular ion [FEYNF + H]$^+$ (*m*/*z* 718.55) was performed by collision-induced dissociation (CID).

One may see that most notable absorption bands are located at 1633 cm^{-1} and 1672 cm^{-1}, corresponding to β-sheet and β-turn structures, respectively. This observation is supported by the data presented in Table S1 from the Supplementary Materials, where it is revealed that the peaks associated with β-sheet/turn structures contribute significantly to the overall area of the amide I band. However, while the self-assembly of FEYNF-NH$_2$ peptide is primarily driven by the formation of β-sheet structures, it is noteworthy that FTIR spectrum may also exhibit signals indicative of α-helix and side chain structures.

Nevertheless, as indicated by FTIR analysis, the primary structural pattern observed in the self-assembly of peptides is linked to the formation of β-sheets. As a result, further analysis will be employed to deepen and understand the intricacies of FEYNF-NH_2 peptide self-assembly.

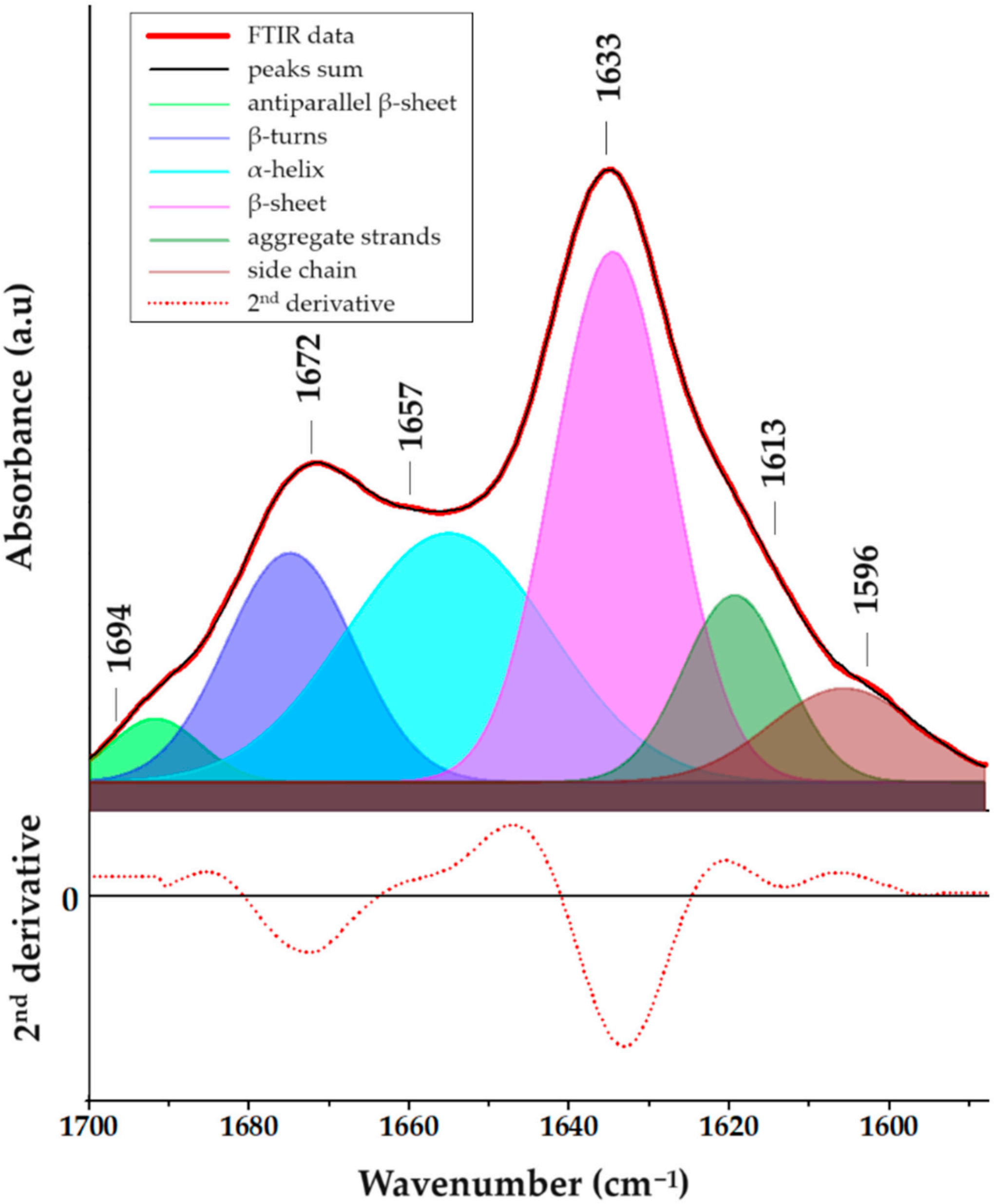

Figure 4. FTIR spectrum corresponding to the amide I region evidencing the secondary structures of FEYNF-NH_2 peptide in the solid state, achieved through deconvolution (Gaussian curves positioned at peaks predetermined by the second derivative spectrum of the initial data).

2.4.2. Fluorescence Studies

The fluorescence studies conducted in sodium acetate at pH 7.4, along with the concentration-dependent experiments, provide essential contributions to understanding the dynamics of self-assembly. To universally excite the two aromatic amino acids, phenylalanine and tyrosine, embedded within the peptide backbone, an excitation wavelength of 275 nm was employed [39]. As represented in Figure 5, the noticeable decline in fluorescence intensity at 304 nm, coupled with the concurrent decrease in the shoulder within the 322–335 nm range after 20 min, alongside a reduction in fluorescence intensity in the violet-blue region (390–450 nm), collectively signifies significant changes in the microenvironment enveloping the aromatic amino acids (phenylalanine and tyrosine). These observed alterations strongly suggest a compelling correlation with the gelation process [40]. Furthermore, the dityrosine formation characterized by a emission signal at around 409 nm cannot be excluded [41].

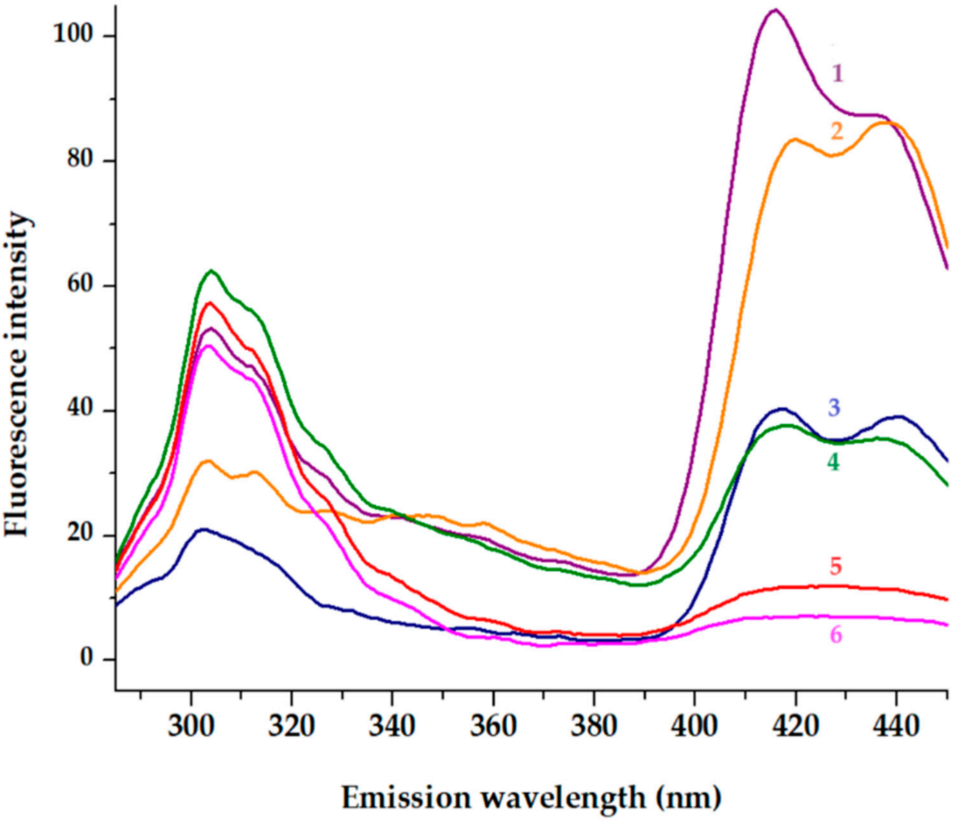

Figure 5. Fluorescence emission spectra recorded at λ_{ex} = 275 nm. The initial spectra (1, 4) of peptide at 27 µM respectively 0.5 mM are displayed. The emission spectra of peptide after 10 min (2 and 5) and 20 min (3 and 6) incubation at room temperature (20 degrees) are presented.

Expanding the investigation to include the violet-blue region is particularly insightful. The violet-blue region encompasses emissions from both phenylalanine and tyrosine, revealing additional nuances in their fluorescence behavior. This broader spectral analysis allows discerning changes in the electronic environment, potential shifts in molecular conformations, or alterations in the interactions among aromatic amino acids during gelation. The reduction in fluorescence intensity in the violet-blue region suggests a complex interplay of factors affecting the electronic states of both phenylalanine and tyrosine. This could include changes in solvent accessibility, local structural rearrangements, or variations in intermolecular interactions, all of which contribute to the observed fluorescence behavior. By considering these additional spectral features, the understanding of the molecular events associated with gelation becomes more nuanced and provides valuable insights into the intricate dynamics of the peptide's structural transformation.

This quenching phenomenon was observed within a brief timeframe for two distinct concentrations of the FEYNF-NH_2 peptide: 27 µM and 0.5 mM (Figure 5). The quenching effect in fluorescence, observed in the blue region of emission spectra, can be attributed to a multitude of factors, encompassing alterations in fluorophore proximity and interactions with neighboring molecules. Particularly, in the context of gelation, the formation of a three-dimensional network is believed to foster heightened interactions among aromatic amino acids, thereby influencing their fluorescence properties [42,43]. It is well known that tyrosine quenching and a tyrosine–tyrosine homotransfer might be interconnected [44]. Further insights into these intricate dynamics can be crucial for a comprehensive understanding of the peptide's behavior under different concentrations and temporal conditions.

2.4.3. Transmission Electron Microscopy (TEM)

In both solid and solution phases, under specific conditions, peptide subunits engage in intricate noncovalent interactions, leading to the formation of self-assembled architectures. These supramolecular constructs subsequently undergo further self-association, culminating in diverse nano- and micro-architectures pivotal for the advancement of functional materials [45]. Consequently, to evaluate the morphological features of the newly synthesized FEYNF-NH_2 peptide, transmission electron microscopy (TEM) was employed (Figure S5a,b, Supplementary Material). In addition, the elemental composition and the purity of the synthetized peptide were confirmed by the presence of characteristic C, N, and O elements (see Figure S5c,d in Supplementary Materials), using energy-dispersive X-ray spectrometry (EDX) coupled with TEM. It should be noted that the differences in C intensities are mainly due to the use of TEM carbon grids.

The TEM images of the pentapeptide (previously dispersed in phosphate buffer solution and dimethyl sulfoxide (DMSO)) are depicted in Figure S5a (in Supplementary Material). One may see the self-assembled peptide as a highly extended nanotape with overlapping areas. This could be attributed to an increase in the density of transitory noncovalent contacts between self-assembled nanostructures [46]. In addition, this arrangement (flat, extended shape) is characteristic of β-sheets. The corresponding TEM image for the dehydrated peptide after incubation is delineated in Figure S5b (Supplementary Materials). In contrast to Figure S5a, the incubation of the FEYNF peptide appears to instigate the development of structures resembling fibrils, along with some regions exhibiting tape-like characteristics.

2.4.4. Polarized Optical Light Microscopy (POM)

A major factor determining the physical and chemical properties of self-assembled peptides (and amino acids) is molecular orientation [21]. Polarization-based optical analysis is very useful in molecular analysis, mainly when it comes to molecular orientation. Thus, in order to have a more in-depth perspective on the morphology of the peptide after incubation, polarized light microscopy was used. Accordingly, in Figure 6, the images obtained at two different polarizing angles (0° and 90°) and also at two different magnifications are represented. One may see that the self-assembled FEYNF peptide reveals intricate hyperbranched architecture, characterized by expansive dendritic patterns. Figure 6c highlights the increased visibility of short branches that have formed and are oriented nearly perpendicular to the nanofiber axis. This behavior was reported by Chakraborty et al., revealing the presence of entangled fibers following gelation, a characteristic of supramolecular hydrogels [17].

The FEYNF morphology can be mainly attributed to the presence of a tyrosine amino acid residue. It is well known that within physiological parameters (pH 7.4), the tyrosine residue likely retains its neutral state, facilitating pivotal interactions for the initiation of fibrillogenesis [47]. When juxtaposed with the previously studied peptide (FESNF-NH_2) under analogous pH conditions [23], the introduction of tyrosine led to morphological changes for FEYNF-NH_2. Hence, although the formation of fibrils was absolutely absent in the case of the initial FESNF-NH_2 peptide at pH 7.4, and the newly synthetized FEYNF-NH_2 peptide possesses a distinctive capability at the physiological pH: the formation of dendritic-like fibrils (Figure 6). This structural variation predominantly stems from the tyrosine's aromatic ring and the presence of an adjacent hydroxyl moiety. Thus, in addition to the Phe–Phe interaction (previously shown to ensure π–π stacking and hydrophobic interactions), tyrosine may similarly contribute to peptide self-assembly. Interestingly, the theoretical calculated isoelectric point of the FEYNF peptide (6.94) closely aligns with the native FESNF peptide isoelectric point (6.99). Nonetheless, FEYNF-NH_2 exhibits resemblances in fibril formation with the amyloid-beta peptide (Aβ), especially when contextualized within the vicinity of its isoelectric point [48]. This noteworthy characteristic not only holds potential for designing related compounds but also offers fresh insights into the role of amino acids in triggering the emergence of gel aggregates.

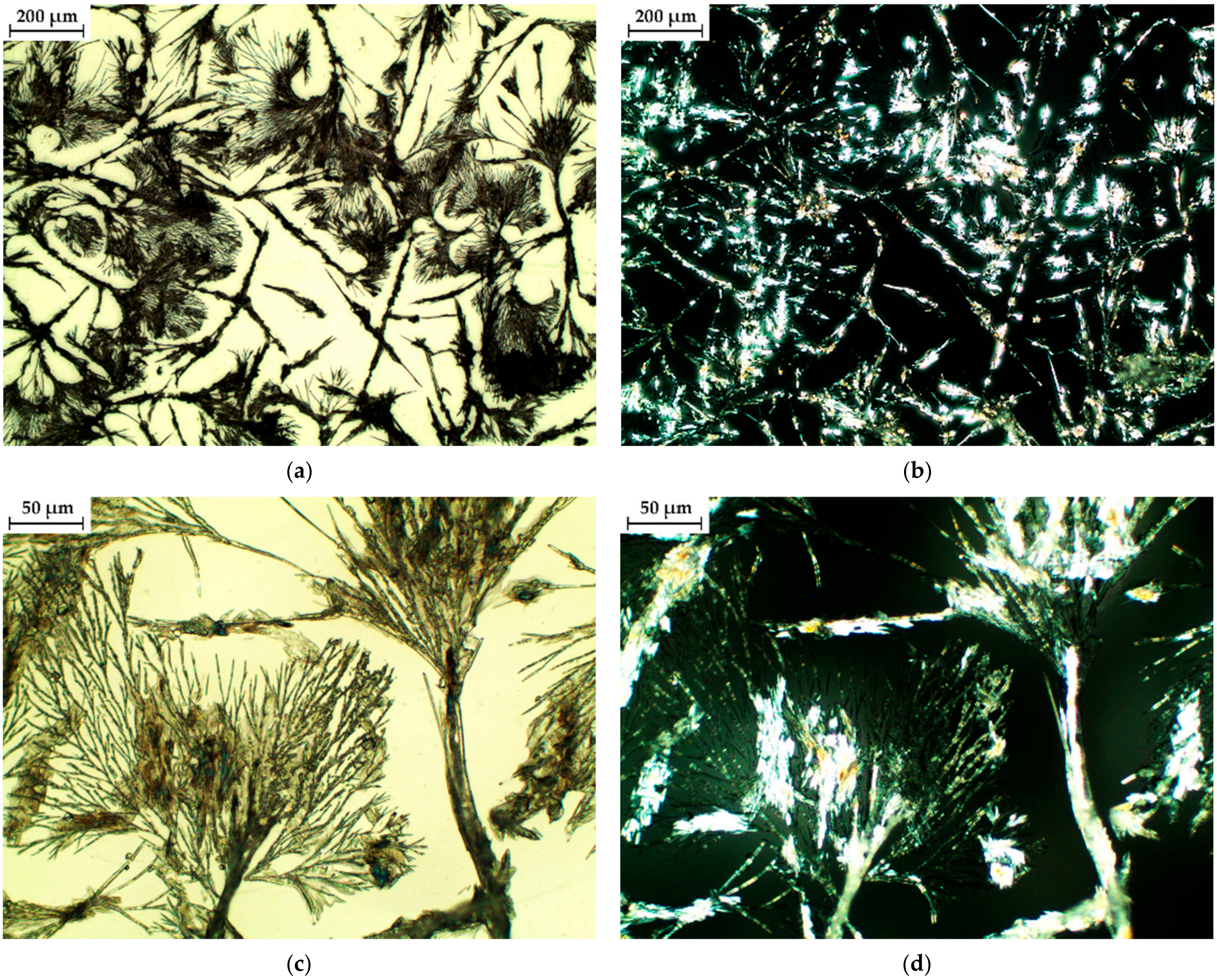

(**a**) (**b**)

(**c**) (**d**)

Figure 6. Microscopic images of dehydrated specimens derived from incubated solutions (3 mM) of FEYNF-NH_2 at a physiological pH of 7.4 and a temperature of 37 °C, captured under two polarization angles: 0 degrees (**a**,**c**), and 90 degrees (**b**,**d**) and at two different scales (50 and 200 μm).

An interesting aspect is visible in Figure 6b,d registered at a polarization angle of 90°. Under polarized light, the self-assembled FEYNF peptide exhibits birefringence. This indicates the self-assembly governed by the presence of peptide β-sheets, which led to well-organized, crystalline structures. It has been shown by others that temperature can also influence peptide self-assembly, resulting in bundles of aligned peptide nanofibers. These bundles can produce macroscopic birefringent domains on the order of tenths of millimeters [21,49].

To further investigate using polarized light microscopy, we evaluated the Congo red staining assay. Congo red is acknowledged for its affinity to bind with β-sheets and adhere to amyloid structures, characterized by either complete or partial composition of β-folded sheets. In the context of this study, Lembré et al. observed that amyloid peptides tend to exhibit a distinctive "apple-green" birefringence upon Congo red staining when examined under polarized light [50]. However, the perceived dichroism in amyloid structures, particularly the apple-green color, is considered potentially misleading as it is specific to stained fibrils perfectly aligned with the polarized light beam. Minor deviations, such as changes in the polarized light angle, can result in the manifestation of "anomalous" colors [51]. Our findings align with this perspective, as the microscopic images of Congo red-stained FEYNF-NH_2 peptide were captured under different incidence angles (0°—Figure S6a and 90°—Figure S6b). Thus, comparison with Figure S6a,b indicates the presence of dichroic birefringence. This supports the existence of peptide β-sheets, essential in governing the self-assembly of the peptide.

2.5. Molecular Docking Simulation

The process of self-assembled supramolecular gelation operates across multiple scales, with atomic-scale interactions dictating the properties of macroscopic hydrogel materials. As a result, a variety of computational methods with varying levels of precision are essential to gathering information at distinct scales [22]. Commonly employed within computational simulations, the molecular docking technique is extensively utilized for scrutinizing interactions between a ligand, typically an organic molecule, and a receptor, such as oligomers, proteins, DNA, RNA, or other macromolecules. More precisely, this in silico method enables: (i) the anticipation of the ligand's spatial arrangement within a binding site, commonly known as its "pose"; (ii) the evaluation of the binding affinity in the ligand–receptor complex through two parameters, namely, binding energy and dissociation constants; and (iii) the identification of the interactions likely to occur between the ligand and the receptor [52]. The AutoDock-VINA algorithm (included in the YASARA Structure v.20.8.23 program) is more like a "machine-learning" approach, amalgamating the merits of knowledge-based potentials and empirical scoring functions [53–55]. This approach is employed to evaluate the binding energy associated with a specific ligand pose within the binding site of the receptor.

2.5.1. Insights into FEYNF-NH_2 Self-Assembling Mechanism

The computer-aided molecular docking simulation was performed herein in order to gain comprehensive insights into the peculiar mechanism governing the self-assembly of the amidated FEYNF peptide. Assuming the chemical structure (2D) of the pentapeptide given in Figure 1a, its spatial conformer (3D) was built directly in the YASARA-Structure program using the "BuildMol" command. Subsequently, the initial generated 3D geometry of FEYNF-NH_2 underwent optimization using the molecular mechanics method at the YASARA force field level [56]. The optimized 3D arrangement of the atoms in the FEYNF-NH_2 structure (following energy minimization) is illustrated in Figure 7a. One may observe that the hydrophilic and hydrophobic peptide side chains are found on opposite sides of the peptide backbone. The optimized conformation from Figure 7a was then utilized in molecular docking simulations, serving dual roles as both a flexible ligand and a rigid receptor, to spot the self-assembling mechanism by assessing the peptide–peptide interactions during the dimer formation (Figure 7b).

Molecular docking simulations were carried out by assessing 100 docked complexes (poses) of the dimer (FEYNF@FEYNF), using the VINA algorithm. The numerical data obtained for all 100 poses (plotted in Figure 7c) elucidate the correlation between binding energy (E_b) and dissociation constant (K_d) for each docked model. As shown in Figure 7c, an increased value of the dissociation constant for a given docked model corresponds to a higher associated binding energy. Nevertheless, the relationship (K_d vs. E_b) is non-linear and characterized by a monotonically increasing trend. After clustering the 100 peptide dimer conformations, 11 distinct and representative docked models (clusters) were identified. The clusters differ from each other in terms of root-mean-square deviation (RMSD) of atomic positions of at least 5.0 Å. Subsequently, Table S2 (in Supplementary Materials) provides detailed information on binding energy (E_b), dissociation constant (K_d) values, and the amino acid residues involved in the peptide–peptide interaction for each cluster. The relation between the binding energy (E_b) and dissociation constant (K_d) after the clustering analysis is represented in Figure 7d. Generally, the lower the values for E_b and K_d, the better the affinity, and the peptide–peptide interaction is more favorable, indicating a higher docking score. Consequently, according to Figure 7d and Table S2 (Supplementary Materials) data, the optimum pose for the peptide dimer complex was associated with the lowest binding energy ($E_b = -5.38$ kcal/mol) and dissociation constant ($K_d = 113.87$ µM). The calculated values indicate a strong and stable noncovalent binding interaction between the peptide molecules. This can be attributed to the fact that each distinctive amino acid residue from the FEYNS-NH_2 structure (PHE1 (F), GLU2 (E), TYR3 (Y), ASN4 (N), and PHE5 (F)) is involved in the peptide–peptide interaction, as indicated by the data in Table S2.

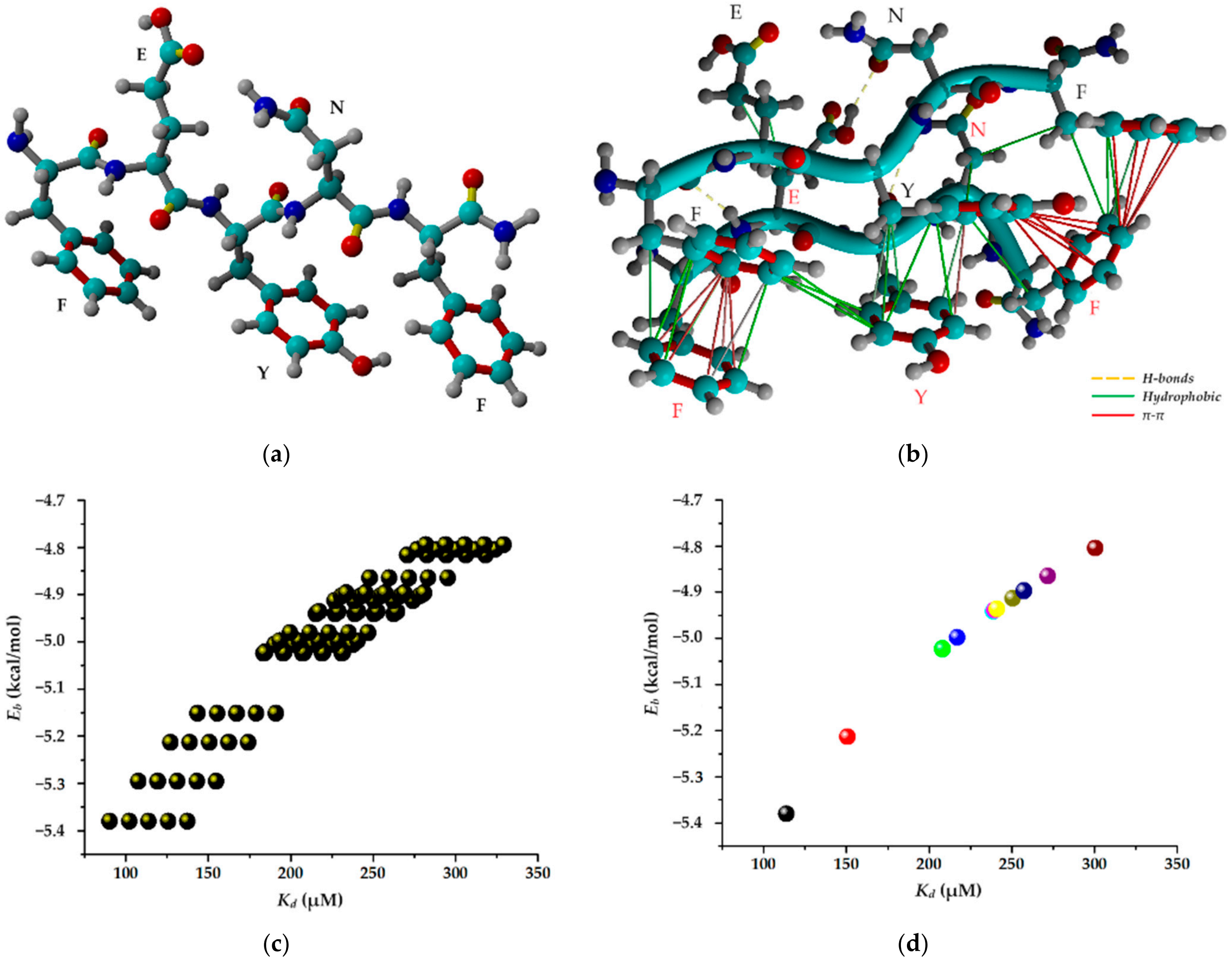

(**a**) (**b**)

(**c**) (**d**)

Figure 7. (**a**) Optimized conformer (3D structure) of FEYNF-NH_2 pentapeptide at the level of YASARA force field (atom colors: cyan—carbon, blue—nitrogen, red—oxygen, and gray—hydrogen); (**b**) best docked FEYNF@FEYNF dimer complex (peptide ligand–black annotations and peptide receptor–red annotations); (**c**) data for all 100 docked poses of FEYNF@FEYNF dimer complex demonstrating the relationship between binding energy and dissociation constant; (**d**) data for clustering analysis for the 11 representative docked models (clusters).

Hence, the best docked FEYNF@FEYNF dimer complex conformation and the corresponding binding interactions are highlighted in Figure 7b. One may see that the peptide structures are oriented in the same direction (parallel), and the intermolecular interactions between the peptide molecules are based on hydrophobic interactions, π–π stacking, and H-bonds (detailed in Table S3, Supplementary Materials). The presence of multiple interacting sites is ideal for the formation of supramolecular gels.

Appropriate intermolecular alignment and interactions between side chains are required for a certain peptide conformation with the assembly of nanofibers into a hydrogel. As anticipated, in concordance with findings from a previous investigation [23], the presence of terminal PHE side chains (PHE1 and PHE5) in the peptide's structure facilitates their engagement in π–π stacking interactions. Such interactions are recognized for imparting order and directionality to the peptide self-assembly into fibril-like structures, playing a pivotal role in shaping the final 3D architecture [23,57]. However, in the present study, the introduction of the TYR3 (tyrosyl, Y) moiety into the peptide structure resulted in additional π–π stacking interactions with the PHE5 terminal residue (Figure 7b and Table S3). Thus, in addition to the available PHE terminal sequences, which promote linear aggregation via the hydrophobic effect, the TYR3 sequence offers the possibility of branched growth. This can explain the self-assembling of the FEYNF-NH_2 peptide into a hydrogelated dendritic architecture, as evidenced above in Figure 6 (under polarized light).

2.5.2. Investigation of β-Sheet Structure Formation

It is important to note that one important criterion for determining whether peptides can self-assemble into hydrogelated structures is their tendency toward a β-sheet conformation [22]. Given the fact that the optimal conformation of the FEYNF peptide (Figure 7a) revealed the distribution of the hydrophilic and hydrophobic side chains on the opposite sides of the peptide backbone, it is expected that β-strand formation will occur [58]. In this context, the best pose for FEYNF@FEYNF dimer complex was further investigated considering its protonated form (-NH^{3+}). Thus, the modeled peptide–peptide complex carried a net charge equal to (+2) by protonation of one amine group for each peptide chain at the opposite end. The molecular conformation of the protonated dimer complex was then subjected to energy minimization by molecular mechanics theory at the level of the YASARA force field. Consequently, the optimal conformation of the modeled protonated dimer (FEYNF@FEYNF(+2)) is depicted in Figure 8.

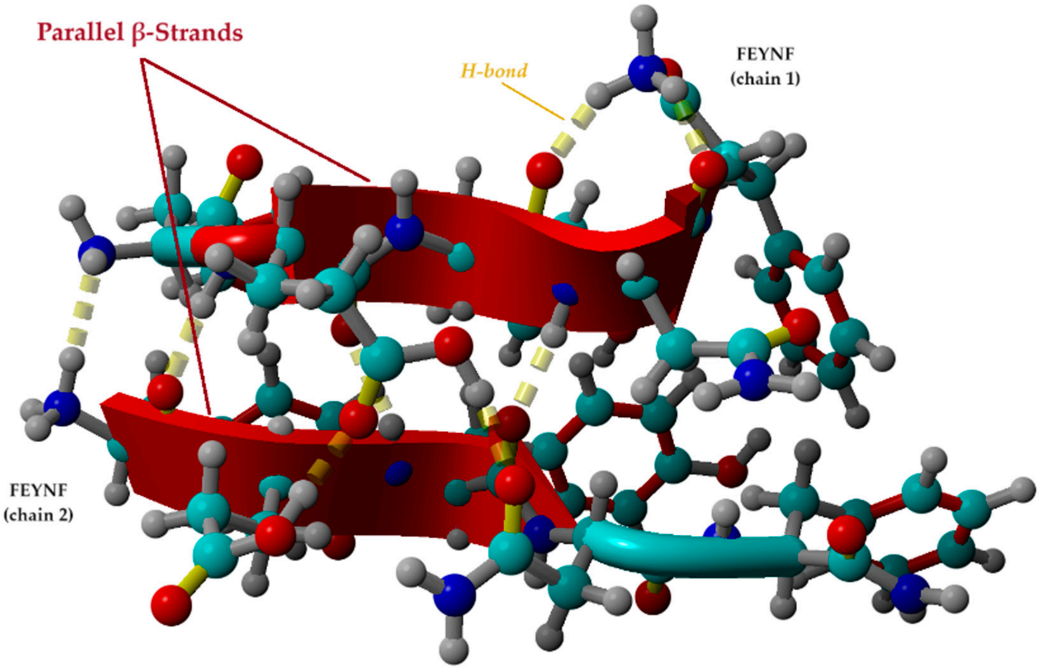

Figure 8. Optimal conformation of the protonated dimmer (FEYNF@FEYNF(+2)) computed at the level of the YASARA force field, suggesting the self-assembling and gelation pathway of FEYNF toward an β-sheet structure (atom colors: cyan—carbon, blue—nitrogen, red—oxygen, and gray—hydrogen).

Hence, following energy minimization, the tertiary structure of the peptides forms two β-strands with the same N to C orientation (parallel configuration). The β-strands given in Figure 8 are mainly formed by the backbone in an extended conformation of the GLU2, TYR3, and ASN4 for chain 1 of the FEYNF peptide. For the second chain, the β-strand starts from the C-(C=O) group of the PHE1 and continues with the GLU2 and TYR3 backbone.

In the depicted conformation (Figure 8), the amidated FEYNF peptide exhibits the capacity to assume a β-sheet structure, as the two represented β-strands are laterally connected by H-bonds. This phenomenon facilitates the extension of β-sheets with an increase in size, particularly as the oligomer expands, inherently implying the formation of a fibril. To confirm the β-sheet formation in the dimer conformation optimized by molecular mechanics at the level of the YASARA force field (Figure 8), the dihedral (torsion) angles Φ (Phi) and Ψ (Psi) were calculated for each chain, and their values are given in Table 1. The Φ torsion angle is characteristic for the $N - C\alpha$ bond, while the Ψ angle corresponds to $C\alpha - C$ bond (as shown in Figure 1a), both types of bonds being flexible and free to rotate. The values for the torsion angles can lead to the determination of the 3D shape of the polypeptide backbone, in accordance with the Ramachandran plot [59].

Table 1. Values of the torsion angles (Φ—*Phi* and Ψ—*Psi*) for the two FEYNF peptide chains in the optimized dimer conformation.

FEYNF Peptide Chain	**Torsion Angles** [1]					
	$\boldsymbol{\Phi_1}$	$\boldsymbol{\Psi_1}$	$\boldsymbol{\Phi_2}$	$\boldsymbol{\Psi_2}$	$\boldsymbol{\Phi_3}$	$\boldsymbol{\Psi_3}$
Chain-1	−137.069°	144.980°	−137.509°	123.895°	−126.403°	151.016°
Chain-2	−81.123°	132.445°	−139.163°	116.446°	−43.919°	−52.269°

[1] The determined torsion angles (dihedrals) correspond to the ones represented in Figure 1a.

The torsion angles, as outlined in Table 1, validate the existence of an elongated conformation conducive to β-sheet formation. The pair values (Φ,Ψ), depicted in Figure S7 (in Supplementary Materials), align with the β-sheet region of the Ramachandran plot [59]. An exception is observed in the case of the pair (Φ_3,Ψ_3) for the FEYNF chain 2. This is attributed to the absence of the ASN4 residue in the β-strand formed within the FEYNF chain 2 (as also observed in Figure 8). However, the amidated FEYNF peptide sequences' β-strand conformation confirm their ability to engage in the self-assembly process, generating hydrogelated architectures with a β-sheet tertiary structure.

2.6. Potential Use of FEYNF Self-Assembling Aggregates in Polyplex Formation

Polyplexes are a special type of macromolecular complex that have garnered significant attention in recent decades owing to their potential applications in gene therapy. These specialized complexes arise through the interaction of (macro)molecular entities, such as polypeptides and polycations, with nucleic acids (DNA or RNA) [60]. Gene delivery systems are currently divided into two primary directions: viral and non-viral vector systems. Given the substantial risks associated with viral vectors, increased focus has shifted toward non-viral systems, predominantly relying on the use of cationic lipids, cationic polymers, or cationic polypeptides [61]. For example, it was demonstrated the efficiency of dendritic amino acid-conjugated polyamidoamines as carriers for human adipose-derived mesenchymal stem cells (AD-MSCs), as they exhibit lower immunogenicity and cytotoxicity, as well as higher transfection efficiency [62]. Peptide-based non-viral vectors are also considered ideal candidates for gene therapy, mainly due to their cell-penetrating capacity [63]. In this context, the polyplex formation capacity of the FEYNF peptide was investigated by molecular docking simulations (in silico study).

Hence, the optimized protonated FEYNF@FEYNF dimer complex (shown in Figure 8) was employed in a second molecular docking simulation study using a DNA oligonucleotide sequence as the receptor. To this end, the Drew–Dickerson dodecamer d(CGCGAAT TCGCG)2 was used as a model for the short DNA helix simulation [60,64]. Details regarding the molecular structure of the dodecamer are given in Figure S8 (in Supplementary Materials).

Hence, the protonated peptide dimer (FEYNF@FEYNF(+2)) was modeled as a rigid ligand, while the negatively charged Drew–Dickerson dodecamer (DDD (−25)) was modeled as a rigid receptor. In this instance, after running 100 poses for the polyplex conformation, 12 representative docked models (clusters) were identified. The results of the molecular docking calculations, encompassing information on binding energy, dissociation constant, and contact residues, are comprehensively presented in the Supplementary Material (Table S4 and Figure S9).

The optimal docking pose between the protonated dimer complex (FEYNF@FEYNF(+2)) and the DNA oligonucleotide sequence (DDD (−25)) is shown in Figure 9. Consequently, the most favorable affinity was observed at the lowest binding energy ($E_b = -12.49$ kcal/mol) and the smallest dissociation constant ($K_d = 0.694$ nM). Notably, the nanometric order of the dissociation constant value indicates the formation of a highly stable docked complex, affirming the successful formation of the polyplex. As illustrated in Figure 9, polyplex formation relies on noncovalent interactions, such as hydrophobic interactions, inter- and intramolecular H-bonds, π–π stacking, and cation–π interactions. The attractive π–π interactions primarily occur between the π bonds of the PHE1 aromatic ring in the peptide dimer and the fused-ring molecules of the DNA purine nucleobases (G4-guanine and A5-adenine). Additionally, Figure 9 also highlights cation–π interactions involving the positively charged amino group at PHE5 (chain 1 of the docked dimer) and the π–electron cloud of aromatic rings in adenine (A6) and thymine (T7). All these noncovalent interactions significantly contribute to the stabilization of the polyplex.

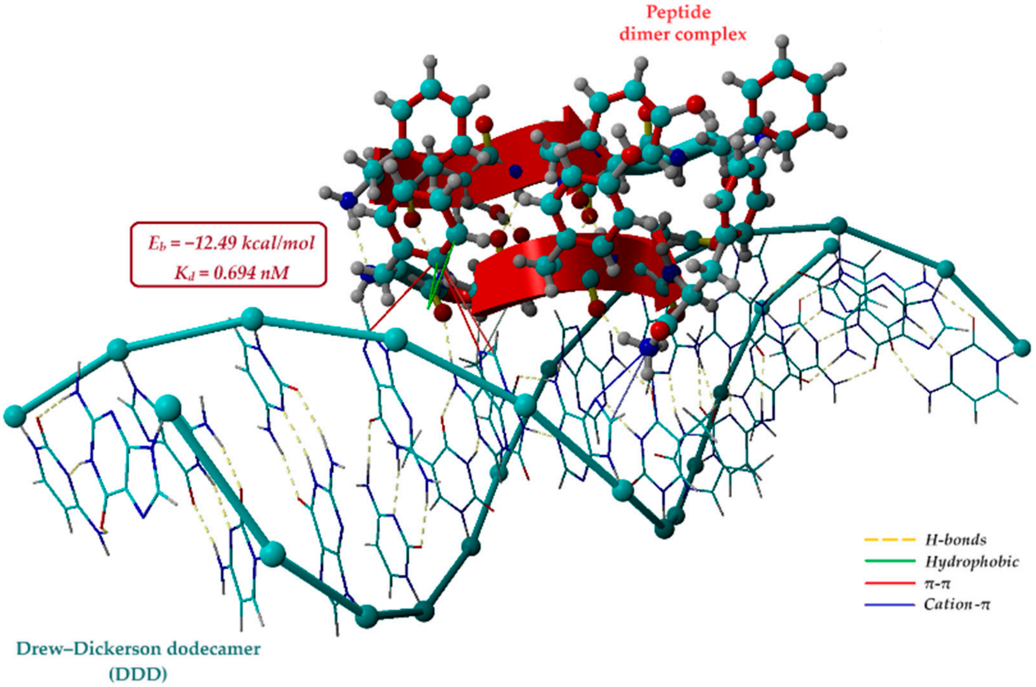

Figure 9. Best conformation of the polyplex resulting from molecular docking simulation showing the noncovalent interactions between the protonated dimer (FEYNF@FEYNF) as ligand and the Drew–Dickerson dodecamer d(CGCGAATTCGCG)2 as receptor (atom colors: cyan—carbon, blue—nitrogen, red—oxygen, and gray—hydrogen).

The supramolecular assembly of FEYNF peptides demonstrates the potential to compact nucleic acids, transforming B-form DNA into a more condensed sequence specific to polyplexes. This plays a pivotal role in gene therapy. This compaction process serves to safeguard nucleic acids, shielding them from premature degradation, and facilitates their transportation across the plasma membrane, particularly through cellular processes like endocytosis. Consequently, this enhances cell absorption.

3. Conclusions

This comprehensive multi-approach study has successfully undertaken the synthesis, characterization, and separation of a de novo peptide sequence capable of spontaneous self-assembly into unique intricately branched dendritic structures under physiological conditions. Initially, the peptide was synthesized through solid-phase peptide synthesis (SPPS) employing the Fmoc/tBu strategy and was effectively characterized using RP-HPLC and MALDI-ToF MS. FTIR analysis revealed that the FEYNF-NH_2 peptide self-assembly is primarily driven by the formation of β-sheet structures. The fluorescence analysis showed the presence of a quenching phenomenon, observed within a brief timeframe for two distinct concentrations of the FEYNF-NH_2 peptide. In addition, the microscopic examination through POM and TEM imaging provided valuable insights into the elaborate framework, revealing its potential for forming gel-like structures. For future research, one may consider exploring alternative methods to gain additional insights into the intricate dynamics of peptide behavior under various conditions.

The application of in silico studies employing molecular docking simulation (using the AutoDock-VINA algorithm included in YASARA-Structure) has unveiled critical insights into the peptide–peptide interactions and the conformational behavior of the protonated dimer (FEYNF@FEYNF(+2)). These computational methods have not only illuminated the self-assembling pathway but have also shed light on the intriguing gelation process. The prevalence in FEYNF to a β-sheet structure is an essential disclosure, indicating the structural evolution of the peptide and its capacity to form organized, sheet-like arrangements.

Moreover, the revelation of noncovalent interactions between the FEYNF peptide's protonated dimer (as a ligand) and the widely acknowledged Drew–Dickerson dodecamer d(CGCGAATTCGCG)2 holds paramount importance. This DNA sequence, often employed as a key model in structural and molecular biology research, underscores the practical applicability of the FEYNF peptide. This discovery not only validates the versatility of the FEYNF peptide but also marks a significant advancement, connecting peptide self-assembly with DNA recognition. This linkage opens promising avenues for the development of innovative biomaterials and targeted therapeutics.

4. Materials and Methods

4.1. Reagents

Fmoc-L-phenylalanine, Fmoc-L-glutamic acid 5-tert-butyl ester, and N-α-Fmoc-N-ß-trityl-L-asparagine were procured from Fluka (Buchs, Switzerland), while Fmoc-O-tert-butyl-L-tyrosine was sourced from Roth (Karlsruhe, Germany). Furthermore, Rink amide resin (4-(2′,4′-dimethoxyphenyl-Fmoc-aminomethyl)phenoxy resin, PEPTIPURE®, 100–200 mesh, 0.3–0.8 $mmol \cdot g^{-1}$, 1% DVB) purchased also from Roth was used as a solid support. Various chemical reagents essential for experimental procedures were obtained from reputable suppliers. Dimethyl sulfoxide (DMSO, EMSURE ACS), diethyl ether (EMSURE ACS), N,N-dimethylformamide (DMF), piperidine (PYP), triisopropylsilane (TIS), acetic acid, benzotriazol-1-yl-oxytripyrrolidino phosphonium hexafluorophosphate (PyBOP), N-methylmorpholine (NMM), 2,5-dihydroxybenzoic acid (DHB), α-cyano-4-hydroxycinnamic acid (HCCA), and NaH_2PO_4 were acquired from Merck (Darmstadt, Germany). Dichloromethane (DCM) was sourced from Scharlab (Barcelona, Spain), while methanol, acetonitrile (ACN, HPLC grade), and trifluoroacetic acid (TFA) were obtained from Carl Roth (Karlsruhe, Germany). All solutions were prepared meticulously using water of high purity with a resistivity of 18.2 $M\Omega \cdot cm$, generated through a Millipore Milli-Q system (Bedford, MA, USA).

4.2. Solid-Phase Synthesis of FEYNF-NH_2 Pentapeptide

The amidated peptide FEYNF-NH_2 (depicted in Figure 1a) was obtained using the solid-phase peptide synthesis (SPPS) method, employing the Fmoc/t-butyl strategy, as described in the literature [15,16,24,25]. A Rink amide resin with a coarse mesh served as the primary solid support during the synthesis. The key procedures consisted of two primary steps for coupling amino acids to the peptide chain. In the initial step, the deprotection of the Fmoc group was assessed for durations of 2, 2, 5, and 10 min using a 20% PYP in DMF solution. Subsequently, the bromophenol blue assay was used to evaluate the effectiveness of deprotection, in accordance with the methodology proposed by Krchnak et al. [65]. The second stage entailed coupling activated Fmoc–amino acids dissolved in DMF (to the exposed amino group on the resin) using PyBOP and NMM as coupling reagents. The coupling reaction lasted 50 min to guarantee the full integration of each amino acid into the emerging peptide chain. To ensure the reliability of the process, each amino acid underwent a double-coupling process. Following each deprotection phase, rigorous resin washing was conducted, involving six washes with 2 mL of DMF and an additional three washes between the first and second coupling reactions. To address time constraints, the synthesis was briefly paused by washing the resin with DCM before the next deprotection phase. Essential resin swelling was performed for 30 min in DMF before both initiating and resuming the synthesis process.

Upon completion of synthesis, a cleavage solution comprised of TFA, TIS, and deionized water (in a volumetric ratio of 18:1:1, $v/v/v$) was employed to release the peptide from the resin. This process was conducted at room temperature for 3 h under stirring. Subsequent to cleavage, the crude product was precipitated in cold diethyl ether and isolated using a fritted glass filter funnel (Porosity 4). The raw peptide fractions were then eluted using 50% and 5% aqueous acetic acid solutions, respectively.

4.3. Reverse-Phase High-Performance Liquid Chromatography

The raw pentapeptide underwent qualitative examination using an HPLC Dionex UltiMate 3000 UHPLC system from Thermo Fisher Scientific (Waltham, MA, USA). The nonpolar stationary phase consisted of an AcclaimTM C18 column measuring 100 mm × 4.6 mm (5 μm silica, 120 Å pore size). Two eluents were used in the mobile phase: A (0.1% TFA in MilliQ water) and B (0.1% TFA in a mixture of ACN and MilliQ water, 80:20 v/v), prepared by adapting a method described by Körsgen et al. [30]. The column temperature was maintained at 25 °C throughout the entire analytical procedure.

4.4. Solid-Phase Extraction of FEYNF-NH$_2$ Peptide

The purification of the newly synthesized FEYNF-NH$_2$ peptide was accomplished through reverse-phase solid-phase extraction (RP-SPE). The purification methodology for the FEYNF peptide was RP-SPE chromatography with gradient elution, a technique adapted from Insuasty Cepeda et. al. [29]. Thus, a Waters™ Sep-Pak™ cartridge syringe (Milford, MA, USA) equipped with a hydrophobic C18 stationary phase was used [29]. A concentrated peptide fraction was eluted with 50% glacial acetic acid and adjusted to pH 4.5 with a 1 M NaOH solution. For reproducibility, the column was solvated with methanol and equilibrated with eluent a (0.1% TFA in MilliQ water). The solution containing the pentapeptide was gently loaded onto the column at a low flow rate to enhance the analyte–sorbent interaction. An additional rinsing step with MilliQ water was performed to effectively eliminate unwanted salts or residual agents. Elution involved a stepwise gradient of eluent B in eluent A ranging from 5% to 60% (see eluents described in Section 4.3). Following the assessment of purity through HPLC analysis, the eluted samples underwent freeze-drying using Christ Alpha 3–4 equipment (LSCbasic, Osterode, Germany). Consequently, the FEYNF-NH$_2$ peptide was obtained as a solid.

4.5. Mass Spectrometry Analysis (MALDI-ToF MS and MS/MS)

The confirmation of the molecular ion was conducted using matrix-assisted laser desorption–ionization mass spectrometry (MALDI-ToF MS), employing two distinct matrices: HCCA and DHB. In this context, a Bruker Ultraflex MALDI ToF/ToF mass spectrometer was used. Peptide mapping was assessed by using a semi-saturated DHB solution (36 mg/mL) mixed with a 3:2 ratio of ACN: 0.1% TFA (in MilliQ water). In addition, a supra-saturated HCCA matrix solution was prepared in the same solvent. Following room-temperature drying, the sample was co-crystallized with each matrix in a 1:1 ratio on a 348-spot target plate. MALDI-ToF MS spectra were acquired in positive ion mode under defined conditions: 25 kV acceleration voltage, a delay of 140 ns, 50% grid voltage, and a low mass gate of 500 Da (500–1400 Da mass range). For MS calibration, a Bruker Peptide Calibration STD II containing nine reference peptides from 700 to 3500 Da was employed. Furthermore, the specific molecular ion underwent tandem mass spectrometry (MS/MS) using collision-induced dissociation (CID). The investigation of peptide fragmentation aimed to ensure precise data acquisition.

4.6. Fluorescence Analysis

A stock peptide solution (3 mM) was freshly prepared in Milli-Q water. Subsequently, the peptide was further diluted to two distinct final concentrations (27 μM and 0.5 mM, respectively) using a 30 mM sodium acetate solution with a pH of 7.4. Fluorescence spectra were acquired using a JASCO FP-8350 spectrofluorometer (Jasco Inc., Tokyo, Japan), with 2D spectra recorded in the emission range of 285–450 nm and an excitation wavelength of 275 nm. To ensure accuracy, each measurement was systematically repeated ten times at three distinct time intervals: initially, after 10 min, and finally, after 20 min. The peptide exhibited intrinsic fluorescence at 303 nm attributed especially to one tyrosine residue positioned in the center of the pentapeptide primary sequence. The emission could be also attributed to deep-blue autofluorescence (around 440 nm) observed prior formation of well-defined structures involving mainly phenylalanine residues positioned at the extremities and less to the tyrosyl moiety [66].

4.7. Sample Preparation Protocol for Incubation in Physiological Conditions

A 3 mM pentapeptide solution, formulated in a solvent mix of 10 mM phosphate buffer solution (pH 7.4) and 1% dimethyl sulfoxide (DMSO), underwent a controlled incubation at 37 °C for 20 h using the Eppendorf Thermomixer Compact (Eppendorf SE, Hamburg, Germany). Following incubation, a 5 μL aliquot of the aged solution was meticulously deposited onto a microscope slide and allowed to desiccate at room temperature. The resultant dried sample was then examined in ATR mode, by using a Bruker Vertex 70 FTIR spectrometer (Bruker, Ettlingen, Germany). In addition, a polarized optical microscope from Leica Microsystems (Wetzlar, Germany) was used for morphological analysis of the pristine peptide in solid state, as well as to observe its morphology after Congo red staining. For the latter, a 0.5% solution of Congo red was applied onto the microscope slide containing the dried peptide, followed by an additional incubation period of 30 min at 37 °C in an Orbital Shaker-Incubator ES-20/60 (Biosan, Riga, Latvia). In addition, a Hitachi High-Tech HT7700 transmission electron microscope equipped with an energy-dispersion X-ray spectroscopy modulus (Hitachi High Technologies Company, Tokyo, Japan) was employed to investigate the FEYNF peptide before and after incubation.

4.8. Molecular Docking

The molecular docking simulations were conducted on a Dell Precision workstation T7910 equipped with 32 CPU threads. The AutoDock VINA technique, available in the YASARA-Structure software package (version 20.8.23), was utilized for modeling and visualization [41–44]. Within the YASARA-Structure software, the spatial conformers in 3D of the FEYNF pentapeptide and Drew–Dickerson dodecamer were constructed using the "BuildMol" function. Specifically, the FEYNF 3D conformation incorporated the amino acids F-phenylalanyl, E-glutamyl, Y-tyrosyl, and N-asparaginyl. The dodecamer was formed using the nucleotide sequences of a sense strand 5′-CGCGAATTCGCG-3′ and a complementary anti-sense strand 3′-GCGCTTAAGCGC-5′. The 3D structures were subjected to energy minimization (for geometry optimization) at the level of molecular mechanics theory using the YASARA force field.

Supplementary Materials: The following supporting information can be downloaded at https://www.mdpi.com/article/10.3390/gels10020086/s1. Figure S1: The gradient protocol used in HPLC analysis; Figure S2: HPLC chromatogram of the FEYNF-NH$_2$ peptide following purification through solid-phase extraction, revealing a calculated purity of 99.54%. The chromatogram was generated using an injection volume of 5 μL, and the data were recorded at a detection wavelength of 215 nm. The observed peak patterns and their intensities affirm the successful purification, highlighting the peptide's exceptional purity achieved through the solid-phase extraction process; Figure S3: Visualization of the crystals formed by the HCCA and DHB matrices (a,b) and the co-crystals with the FEYNF samples on the target (c,d). Images obtained by means of the camera equipped with the MALDI-ToF mass spectrometer. Retention times are reported based on HPLC analysis; Figure S4: FTIR spectrum of FEYNF-NH$_2$ peptide evidencing the amide I–amide II spectral range and the baseline applied for data processing; Table S1: The content of secondary structures (%) of the FEYNF-NH$_2$ revealed from FTIR spectrum analysis; Figure S5: TEM images of FEYNF-NH$_2$ before (a) and after 20 h of incubation at physiological pH of 7.4 and a temperature of 37 °C; EDX spectra for FEYNF peptide sample before (c) and after incubation (d); Figure S6: Microscopic images of FEYNF-NH$_2$ sample after Congo red staining captured under two polarization angles: 0 degrees (a), and 90 degrees (b); Table S2: Representative clusters of the docking simulation for the FEYNF@FEYNF dimer complex, highlighting the amino acid residues involved in the peptide–peptide interaction, binding energy (E_b) and dissociation constant (K_d) values; Table S3: Intermolecular and intramolecular interactions occurring in the FEYNF@FEYNF dimer complex, with corresponding amino acid residues involved; Figure S7: Graphical representation of $(\Phi j,\Psi j)$ plot (Chain 1: (Φ_1,Ψ_1)—red, (Φ_2,Ψ_2)—green, (Φ_3,Ψ_3)—blue; Chain 2: (Φ_4,Ψ_4)—cyan, (Φ_5,Ψ_5)—magenta, (Φ_6,Ψ_6)—yellow) based on determined torsion angles; Figure S8: Graphical representation of Drew–Dickerson dodecamer sequence (d(CGCGAATTCGCG)2) with molecular structures of corresponding nitrogenous bases (C-cytosine, G-guanine, A-adenine, T-tymine) and sugar-phosphate backbone (KingDraw V3.0.2.); Table S4: Representative clusters of the docking simulation for the investigated polyplex (binding energy (E_b), dissociation constant (K_d) and contacting residues); Figure S9: Molecular docking outcomes for the polyplex formation: (a) data for all 100 docked poses of polyplex conformation (binding energy vs. dissociation constant); (b) data for the 12 representative clusters (obtained from clustering analysis).

Author Contributions: Conceptualization, S.-C.J., A.-C.E., B.-A.P. and V.-R.G.; methodology, S.-C.J., A.-C.E. and C.C.; software, C.C.; validation, A.-C.E., G.D., B.-A.P. and V.-R.G.; formal analysis, C.C.; investigation, S.-C.J. and A.-C.E.; writing—original draft preparation, S.-C.J. and A.-C.E.; writing—review and editing, C.C., G.D., B.-A.P. and V.-R.G.; supervision, B.-A.P. and V.-R.G. All authors have read and agreed to the published version of the manuscript.

Funding: This research received no external funding.

Institutional Review Board Statement: Not applicable.

Informed Consent Statement: Not applicable.

Data Availability Statement: Data are contained within the article and supplementary material.

Conflicts of Interest: The authors declare no conflicts of interest.

References

1. Sun, B.; Tao, K.; Jia, Y.; Yan, X.; Zou, Q.; Gazit, E.; Li, J. Photoactive properties of supramolecular assembled short peptides. *Chem. Soc. Rev.* **2019**, *48*, 4387–4400. [CrossRef] [PubMed]
2. Abbas, M.; Ovais, M.; Atiq, A.; Ansari, T.M.; Xing, R.; Spruijt, E.; Yan, X. Tailoring supramolecular short peptide nanomaterials for antibacterial applications. *Coord. Chem. Rev.* **2022**, *460*, 214481. [CrossRef]
3. Ellert-Miklaszewska, A.; Poleszak, K.; Kaminska, B. Short peptides interfering with signaling pathways as new therapeutic tools for cancer treatment. *Future Med. Chem.* **2017**, *9*, 199–221. [CrossRef]
4. Restu, W.K.; Yamamoto, S.; Nishida, Y.; Ienaga, H.; Aoi, T.; Maruyama, T. Hydrogel formation by short D-peptide for cell-culture scaffolds. *Mater. Sci. Eng. C Mater. Biol. Appl.* **2020**, *111*, 110746. [CrossRef]
5. Ross, A.; Sauce-Guevara, M.A.; Alarcon, E.I.; Mendez-Rojas, M.A. Peptide Biomaterials for Tissue Regeneration. *Front. Bioeng. Biotechnol.* **2022**, *10*, 893936. [CrossRef] [PubMed]
6. Yang, S.; Wang, M.; Wang, T.; Sun, M.; Huang, H.; Shi, X.; Duan, S.; Wu, Y.; Zhu, J.; Liu, F. Self-assembled short peptides: Recent advances and strategies for potential pharmaceutical applications. *Mater. Today Bio* **2023**, *20*, 100644. [CrossRef] [PubMed]

7. Sfragano, P.S.; Moro, G.; Polo, F.; Palchetti, I. The Role of Peptides in the Design of Electrochemical Biosensors for Clinical Diagnostics. *Biosensors* **2021**, *11*, 246. [CrossRef]
8. Riley, M.K.; Vermerris, W. Recent Advances in Nanomaterials for Gene Delivery—A Review. *Nanomaterials* **2017**, *7*, 94. [CrossRef]
9. Tarvirdipour, S.; Huang, X.; Mihali, V.; Schoenenberger, C.A.; Palivan, C.G. Peptide-Based Nanoassemblies in Gene Therapy and Diagnosis: Paving the Way for Clinical Application. *Molecules* **2020**, *25*, 3482. [CrossRef]
10. Habibi, N.; Kamaly, N.; Memic, A.; Shafiee, H. Self-assembled peptide-based nanostructures: Smart nanomaterials toward targeted drug delivery. *Nano Today* **2016**, *11*, 41–60. [CrossRef]
11. Wang, W.; Hu, Z. Targeting Peptide-Based Probes for Molecular Imaging and Diagnosis. *Adv. Mater.* **2019**, *31*, 1804827. [CrossRef] [PubMed]
12. Petit, N.; Dyer, J.M.; Gerrard, J.A.; Domigan, L.J.; Clerens, S. Insight into the self-assembly and gel formation of a bioactive peptide derived from bovine casein. *BBA Adv.* **2023**, *3*, 100086. [CrossRef] [PubMed]
13. Li, L.; Xie, L.; Zheng, R.; Sun, R. Self-Assembly Dipeptide Hydrogel: The Structures and Properties. *Front. Chem.* **2021**, *9*, 739791. [CrossRef] [PubMed]
14. Webber, M.J.; Pashuck, E.T. (Macro)molecular Self-Assembly for Hydrogel Drug Delivery. *Adv. Drug Deliv. Rev.* **2021**, *172*, 275–295. [CrossRef]
15. Hansen, P.R.; Oddo, A. Methods in Molecular Biology; Fmoc Solid-Phase Peptide Synthesis. In *Peptide Antibodies*; Houen, G., Ed.; Humana Press: New York, NY, USA, 2015; Volume 1348, pp. 33–50. [CrossRef]
16. Behrendt, R.; White, P.; Offer, J. Advances in Fmoc solid-phase peptide synthesis. *J. Pept. Sci.* **2016**, *22*, 4–27. [CrossRef] [PubMed]
17. Chakraborty, P.; Tang, Y.; Yamamoto, T.; Yao, Y.; Guterman, T.; Zilberzwige-Tal, S.; Adadi, N.; Ji, W.; Dvir, T.; Ramamoorthy, A.; et al. Unusual Two-Step Assembly of a Minimalistic Dipeptide-Based Functional Hypergelator. *Adv. Mater.* **2020**, *32*, 1906043. [CrossRef] [PubMed]
18. Seow, W.Y.; Hauser, C.A. Short to ultrashort peptide hydrogels for biomedical uses. *Mater. Today* **2014**, *17*, 381–388. [CrossRef]
19. Martin, V.; Egelund, P.H.G.; Johansson, H.; Le Quement, S.T.; Wojcik, F.; Pedersen, D.S. Greening the synthesis of peptide therapeutics: An industrial perspective. *RSC Adv.* **2020**, *10*, 42457–42492. [CrossRef]
20. Gazit, E. Self-Assembled Peptide Nanostructures: The Design of Molecular Building Blocks and Their Technological Utilization. *Chem. Soc. Rev.* **2007**, *36*, 1263–1269. [CrossRef]
21. Handelman, A. Optical Polarization-Based Measurement Methods for Characterization of Self-Assembled Peptides' and Amino Acids' Micro- and Nanostructures. *Molecules* **2022**, *27*, 1802. [CrossRef]
22. Zhou, P.; Yuan, C.; Yan, X. Computational approaches for understanding and predicting the self-assembled peptide hydrogels. *Curr. Opin. Colloid Interface Sci.* **2022**, *62*, 101645. [CrossRef]
23. Jitaru, S.-C.; Neamtu, A.; Drochioiu, G.; Darie-Ion, L.; Stoica, I.; Petre, B.-A.; Gradinaru, V.-R. A Diphenylalanine Based Pentapeptide with Fibrillating Self-Assembling Properties. *Pharmaceutics* **2023**, *15*, 371. [CrossRef] [PubMed]
24. Lucas, X.; Bauzá, A.; Frontera, A.; Quiñonero, D. A thorough anion–π interaction study in biomolecules: On the importance of cooperativity effects. *Chem. Sci.* **2016**, *7*, 1038–1050. [CrossRef] [PubMed]
25. Amblard, M.; Fehrentz, J.A.; Martinez, J.; Subra, G. Methods and protocols of modern solid phase peptide synthesis. *Mol. Biotechnol.* **2006**, *33*, 239–254. [CrossRef] [PubMed]
26. Wellings, D.A.; Atherton, E. Standard Fmoc protocols. *Methods Enzymol.* **1997**, *289*, 44–67. [CrossRef] [PubMed]
27. Arispe, N.; Diaz, J.C.; Flora, M. Efficiency of histidine-associating compounds for blocking the Alzheimer's Aβ channel activity and cytotoxicity. *Biophys. J.* **2008**, *95*, 4879–4889. [CrossRef] [PubMed]
28. Guzmán, F.; Aróstica, M.; Román, T.; Beltrán, D.; Gauna, A.; Albericio, F.; Cárdenas, C. Peptides, solid-phase synthesis and characterization: Tailor-made methodologies. *Electron. J. Biotechnol.* **2023**, *64*, 27–33. [CrossRef]
29. Insuasty Cepeda, D.S.; Pineda Castañeda, H.M.; Rodríguez Mayor, A.V.; García Castañeda, J.E.; Maldonado Villamil, M.; Fierro Medina, R.; Rivera Monroy, Z.J. Synthetic peptide purification via solid-phase extraction with gradient elution: A simple, economical, fast, and efficient methodology. *Molecules* **2019**, *24*, 1215. [CrossRef]
30. Ruderman, G.; Caffarena, E.R.; Mogilner, I.G.; Tolosa, E.J. Hydrogen Bonding of carboxylic acids in aqueous solutions—UV spectroscopy, viscosity, and molecular simulation of acetic acid. *J. Solut. Chem.* **1998**, *27*, 935–948. [CrossRef]
31. Körsgen, M.; Pelster, A.; Dreisewerd, K.; Arlinghaus, H.F. 3D ToF-SIMS analysis of peptide incorporation into MALDI matrix crystals with sub-micrometer resolution. *J. Am. Soc. Mass Spectrom.* **2015**, *27*, 277–284. [CrossRef]
32. Moyer, S.C.; VonSeggern, C.E.; Cotter, R.J. Fragmentation of cationized phosphotyrosine containing peptides by atmospheric pressure MALDI/Ion trap mass spectrometry. *J. Am. Soc. Mass Spectrom.* **2003**, *14*, 581–592. [CrossRef] [PubMed]
33. Jitaru, S.C.; Enache, A.C.; Drochioiu, G.; Petre, B.A.; Gradinaru, V.R. Dendritic-like Self-Assembling Pentapeptide with Potential Applications in Emerging Biotechnologies. In Proceedings of the IFMBE Proceedings Series, Bucharest, Romania, 9–10 November 2023.
34. Zhang, Z. Prediction of low-energy collision-induced dissociation spectra of peptides. *Anal. Chem.* **2004**, *76*, 3908–3922. [CrossRef] [PubMed]
35. Bagińska, K.; Makowska, J.; Wiczk, W.; Kasprzykowski, F.; ChmurzyńSKI, L. Conformational studies of alanine-rich peptide using CD and FTIR spectroscopy. *J. Pept. Sci.* **2008**, *14*, 283–289. [CrossRef] [PubMed]

36. Seo, J.; Hoffmann, W.; Warnke, S.; Huang, X.; Gewinner, S.; Schöllkopf, W.; Bowere, M.T.; von Helden, G.; Pagel, K. An infrared spectroscopy approach to follow β-sheet formation in peptide amyloid assemblies. *Nat. Chem.* **2016**, *9*, 39–44. [CrossRef] [PubMed]
37. De Meutter, J.; Goormaghtigh, E. Amino acid side chain contribution to protein FTIR spectra: Impact on secondary structure evaluation. *Eur. Biophys. J.* **2021**, *50*, 641–651. [CrossRef]
38. Barreto, M.S.C.; Elzinga, E.J.; Alleoni, L.R.F. The molecular insights into protein adsorption on hematite surface disclosed by in-situ ATR-FTIR/2D-COS study. *Sci. Rep.* **2020**, *10*, 13441. [CrossRef] [PubMed]
39. Angelerou, M.G.F.; Markus, R.; Paraskevopoulou, V.; Foralosso, R.; Clarke, P.; Alvarez, C.V.; Chenlo, M.; Johnson, L.; Rutland, C.; Allen, S.; et al. Mechanistic investigations into the encapsulation and release of small molecules and proteins from a supramolecular nucleoside gel in vitro and in vivo. *J. Control. Release* **2020**, *317*, 118–129. [CrossRef]
40. Creasey, R.C.; Mostert, A.B.; Solemanifar, A.; Nguyen, T.A.; Virdis, B.; Freguia, S.; Laycock, B. Biomimetic peptide nanowires designed for conductivity. *ACS Omega* **2019**, *4*, 1748–1756. [CrossRef]
41. Radomska, K.; Wolszczak, M. Spontaneous and Ionizing Radiation-Induced Aggregation of Human Serum Albumin: Dityrosine as a Fluorescent Probe. *Int. J. Mol. Sci.* **2022**, *23*, 8090. [CrossRef]
42. Zhang, L.; Li, Y.; Mu, G.; Yang, L.; Ren, C.; Wang, Z.; Guo, Q.; Liu, J.; Yang, C. Structure of self-assembled peptide determines the activity of aggregation-induced emission luminogen-peptide conjugate for detecting alkaline phosphatase. *Anal. Chem.* **2022**, *94*, 2236–2243. [CrossRef]
43. Xiong, Y.; Shi, C.; Li, L.; Tang, Y.; Zhang, X.; Liao, S.; Zhang, B.; Sun, C.; Ren, C. A review on recent advances in amino acid and peptide-based fluorescence and its potential applications. *New J. Chem.* **2021**, *45*, 15180–15194. [CrossRef]
44. Lakowicz, J.R. *Principles of Fluorescence Spectroscopy*, 3rd ed.; Springer: New York, NY, USA, 2013.
45. Konda, M.; Bhowmik, S.; Mobin, S.M.; Biswas, S.; Das, A.K. Modulating Hydrogen Bonded Self-Assembled Patterns and Morphological Features by a Change in Side Chain of Third Amino Acid of Synthetic γ-Amino Acid Based Tripeptides. *ChemistrySelect* **2016**, *1*, 2586–2593. [CrossRef]
46. Gelain, F.; Luo, Z.; Zhang, S. Self-Assembling Peptide EAK16 and RADA16 Nanofiber Scaffold Hydrogel. *Chem. Rev.* **2020**, *120*, 13434–13460. [CrossRef] [PubMed]
47. DiCostanzo, A.C.; Thompson, J.R.; Peterson, F.C.; Volkman, B.F.; Ramirez-Alvarado, M. Tyrosine residues mediate fibril formation in a dynamic light chain dimer interface. *JBC* **2012**, *287*, 27997–28006. [CrossRef] [PubMed]
48. Tian, Y.; Viles, J.H. pH Dependence of Amyloid-β Fibril Assembly Kinetics: Unravelling the Microscopic Molecular Processes. *Angew. Chem. Int. Ed.* **2022**, *61*, e202210675. [CrossRef] [PubMed]
49. Zhang, S.; Greenfield, M.A.; Mata, A.; Palmer, L.; Bitton, R.; Mantei, J.R.; Aparicio, C.; de la Cruz, M.O.; Stupp, S.I. A self-assembly pathway to aligned monodomain gels. *Nat. Mater.* **2010**, *9*, 594–601. [CrossRef]
50. Lembré, P.; Di Martino, P.; Vendrely, C. Amyloid peptides derived from CsgA and FapC modify the viscoelastic properties of biofilm model matrices. *Biofouling* **2014**, *30*, 415–426. [CrossRef]
51. Dapson, R.W. Amyloid from a histochemical perspective. A review of the structure, properties and types of amyloid, and a proposed staining mechanism for Congo red staining. *Biotech. Histochem.* **2018**, *93*, 543–556. [CrossRef]
52. Cojocaru, C.; Clima, L. Binding assessment of methylene blue to human serum albumin and poly (acrylic acid): Experimental and computer-aided modeling studies. *J. Mol. Liq.* **2019**, *285*, 811–821. [CrossRef]
53. Trott, O.; Olson, A.J. AutoDock Vina: Improving the speed and accuracy of docking with a new scoring function, efficient optimization, and multithreading. *J. Comput. Chem.* **2010**, *31*, 455–461. [CrossRef]
54. Krieger, E.; Koraimann, G.; Vriend, G. Increasing the precision of comparative models with YASARA NOVA—A self-parameterizing force field. *Proteins* **2002**, *47*, 393–402. [CrossRef] [PubMed]
55. Krieger, E.; Vriend, G. YASARA View—Molecular graphics for all devices—From smartphones to workstations. *Bioinformatics* **2014**, *30*, 2981–2982. [CrossRef] [PubMed]
56. Schlegel, H.B. Geometry optimization. *Wiley Interdiscip. Rev. Comput. Mol. Sci.* **2011**, *1*, 790–809. [CrossRef]
57. Gazit, E. A possible role for π-stacking in the self-assembly of amyloid fibrils. *FASEB J.* **2002**, *16*, 77–83. [CrossRef] [PubMed]
58. Arakawa, C.K.; DeForest, C.A. Polymer Design and Development. In *Biology and Engineering of Stem Cell Niches*; Elsevier: London, UK, 2017; pp. 295–314. [CrossRef]
59. Choudhuri, S. Chapter 8–Additional Bioinformatic Analyses Involving Protein Sequences. In *Bioinformatics for Beginners*, 1st ed.; Choudhuri, S., Ed.; Academic Press: Cambridge, MA, USA, 2014; pp. 183–207. [CrossRef]
60. Cojocaru, C.; Neamtu, A.; Vasiliu, T.; Isac, D.; Pinteala, M. Molecular Dynamics Simulations and In Silico Analysis of Supramolecular Self-Assembled Structures. In *New Trends in Macromolecular and Supramolecular Chemistry for Biological Applications*, 1st ed.; Abadie, M.J., Pinteala, M., Rotaru, A., Eds.; Springer: Cham, Switzerland, 2021; pp. 357–371. [CrossRef]
61. Ita, K. Polyplexes for gene and nucleic acid delivery: Progress and bottlenecks. *Eur. J. Pharm. Sci.* **2020**, *150*, 105358. [CrossRef]
62. Bae, Y.; Lee, S.; Green, E.S.; Park, J.H.; Ko, K.S.; Han, J.; Choi, J.S. Characterization of basic amino acids-conjugated PAMAM dendrimers as gene carriers for human adipose-derived mesenchymal stem cells. *Int. J. Pharm.* **2016**, *501*, 75–86. [CrossRef]
63. Yang, J.; Luo, G.-F. Peptide-Based Vectors for Gene Delivery. *Chemistry* **2023**, *5*, 1696–1718. [CrossRef]
64. Vasiliu, T.; Cojocaru, C.; Rotaru, A.; Pricope, G.; Pinteala, M.; Clima, L. Optimization of Polyplex Formation between DNA Oligonucleotide and Poly(L-Lysine): Experimental Study and Modeling Approach. *Int. J. Mol. Sci.* **2017**, *18*, 1291. [CrossRef]

65. Krchňák, V.; Vágner, J.; Šafář, P.; Lebl, M. Noninvasive continuous monitoring of solid-phase peptide synthesis by acid-base indicator. *Collect. Czechoslov. Chem. Commun.* **1988**, *53*, 2542–2548. [CrossRef]
66. Niyangoda, C.; Miti, T.; Breydo, L.; Uversky, V.; Muschol, M. Carbonyl-based blue autofluorescence of proteins and amino acids. *PLoS ONE* **2017**, *12*, e0176983. [CrossRef]

gels

MDPI

Article

Ag^0–Ginger Nanocomposites Integrated into Natural Hydrogelated Matrices Used as Antimicrobial Delivery Systems Deposited on Cellulose Fabrics

Florentina Monica Raduly [1], Valentin Raditoiu [1,*], Alina Raditoiu [1], Maria Grapin [1], Mariana Constantin [1,2], Iuliana Răut [1], Cristian Andi Nicolae [1] and Adriana Nicoleta Frone [1]

[1] Laboratory of Functional Dyes and Related Materials, National Research and Development Institute for Chemistry and Petrochemistry—ICECHIM, 202 Splaiul Independentei, 6th District, 060021 Bucharest, Romania; monica.raduly@icechim.ro (F.M.R.); coloranti@icechim.ro (A.R.); maria.grapin@icechim.ro (M.G.); mariana.calin@icechim.ro (M.C.); iulia_rt@yahoo.com (I.R.); ca_nicolae@yahoo.com (C.A.N.); ciucu_adriana@yahoo.com (A.N.F.)

[2] Faculty of Pharmacy, Titu Maiorescu University, Bd. Gh. Sincai, No.16, 040441 Bucharest, Romania

* Correspondence: vraditoiu@icechim.ro

Abstract: In the textile, medical, and food industries, many of the applications have targeted the use of textile fabrics with antimicrobial properties. Obtaining eco-friendly coatings is of wide interest, especially for applications related to wound dressing or to food packaging. In order to obtain coatings with antimicrobial properties through environmentally friendly methods, a series of experiments were carried out on the use of natural polymers loaded with silver nanoparticles. In this study, coatings with antimicrobial properties were obtained by depositing natural composites based on rice flour, carob flour, or alginate on cotton fabrics. These antimicrobial coatings were multicomponent systems, in which the host matrix was generated via hydration of natural polymers. The nanocomposite obtained from the phytosynthesis of silver particles in ginger extract was embedded in hydrogel matrices. The multicomponent gels obtained by embedding silver nanoparticles in natural polymer matrices were deposited on cotton fabric and were studied in relation to nanoparticles and the type of host matrix, and the antimicrobial activity was evaluated. Fabrics coated with such systems provide a hydrophilic surface with antimicrobial properties and can therefore be used in various areas where textiles provide antibacterial protection.

Keywords: nanocomposites; natural gels; silver nanoparticles; hydrogels; natural antimicrobials

1. Introduction

Migration events determined by population growth in recent years and the free movement of people after the fall of several dictatorial systems in Asia and Africa, as well as technological development, have led, among other things, to the appearance of new types of pathogens in certain regions or the increase in the resistance of already known pathogens to classic treatments [1–3]. Thus, the search for new types of antimicrobial treatments, such as photodynamic therapy [4,5], disinfection with UV light [6], the combined use of several known antimicrobial agents [7], or finding new compounds with antifungal activity, was considered a priority. From the last category, a series of natural compounds, polyphenolic derivatives, chitosan, tannins, and essential oils were studied [8–12], and new antibiotics [11,13] or nanomaterials, such as graphene oxide, metallic oxides, and metallic particles [8,14–16], were synthesized. All these newly discovered antimicrobial agents must be packaged under different formulations or delivery platforms in order to be used in as many fields as possible. The development and diversification of the segment that refers to the materials from which various objects for domestic use or use in specific fields are formed have led to the demand for researchers' imagination to create and obtain composites that make it possible to apply new compounds with antimicrobial activity on these surfaces. At the same time, the circumstances related to the reduction in pollution and the promotion of the circular economy support the development of new less polluting and cheaper technologies [17–19]. To obtain such results, new methods of recovering active products from food waste [20,21] or obtaining new natural binders or biopolymers were sought [22–25]. In their studies, the researchers' attention was drawn to flours and starches that contain polysaccharides, gums, protein, lipids with adhesive properties and swelling properties, minerals, polyphenolic derivatives, or flavonoids with antioxidant activity [26]. Cereal flours (wheat, rice, corn) are traditionally used in the processes of obtaining bakery products [27–29] and in the field of fabric dyeing [30–32]. Their new applications have been introduced in the food industry or in the restoration of paintings as thickening or gelling agents (tapioca, alginate, carob) [29,33], and many of them, such as rice flour and chitosan, are already used in the cosmetic and pharmaceutical fields and carob flour in the biomedical field [26,34].

From the variety of natural polymers presented, in this paper, three types of agents, namely rice flour, carob flour, and alginate, were chosen, which represented the delivery base of Ag^0–ginger nanocomposites obtained following the process of reducing silver ions through phytosynthesis in the presence of ginger extract. In this sense, following the gelation process of the flours in the presence of water, the Ag^0–ginger nanocomposites were embedded in hydrogel matrices and resulted in three types of composites that were deposited by printing on cotton fabric. In this way, three types of fabrics (G1, G2, and G3) were obtained, with antimicrobial properties confirmed using silver ion release tests and tests on *Staphylococcus aureus*, *Escherichia coli*, and *Candida albicans* cultures. The realization of these fabrics covered with eco-composites aimed at obtaining, through an environmentally friendly and economic method, cellulosic materials with antimicrobial properties that can be used in the food field for food packaging, in the medical field for dressings, or for specific clothing.

2. Results and Discussion

The benefits of natural ginger extract are well-known, and it has been used since ancient times in the field of traditional medicine [35]. Bioactive compounds and polyphenol derivatives extracted most often in alcohol or water and used as reducing systems to obtain silver nanoparticles have been thoroughly studied [36–38]. In this work, based on the results from the literature, we chose to synthesize silver nanoparticles according to El Refai's recipe [38] from aqueous ginger extract and aqueous silver nitrate solution (Scheme 1A), the presence of which was confirmed via UV–Vis analysis (Scheme 1B). The Ag^0–ginger nanocomposites were integrated into three types of hydrogel matrices based on rice flour, alginate, and carob flour (Scheme 1A(a–c)). The resulting natural hydrogels were deposited by printing on cotton fabric (G1, G2, and G3). In order to study the influence and necessity of the presence of silver nanoparticles in hydrogels rich in bioactive compounds, we compared the G3-0 fabric, which was covered with the same type of composite as G3 but lacked silver nanoparticles, and the G3-1 fabric, which contained twice as much Ag^0–ginger nanocomposite compared to G3.

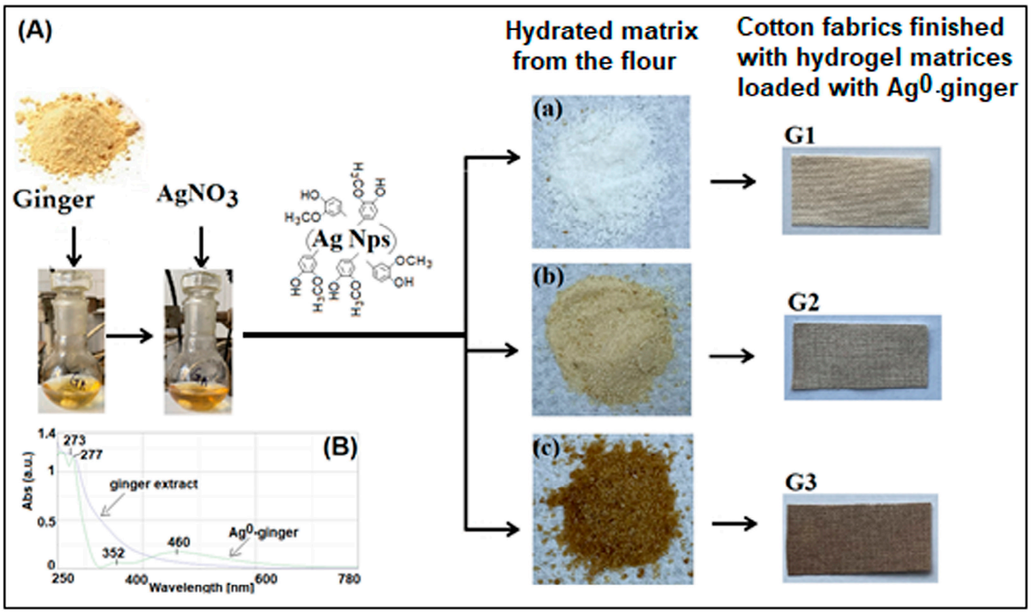

Scheme 1. The main stages of obtaining (**A**) the gelled composites based on rice (**a**), alginate (**b**), and carob (**c**) for antimicrobial coatings on cellulose support (G1, G2, G3) and the UV-Vis spectrum of the initial ginger extract and the nanocomposite with metallic silver (**B**).

2.1. Characterization of the Cellulose Fabrics Finished with Natural Hydrogels

2.1.1. FTIR Spectroscopy

The basic structure of cellulose is made up of D-glucose units linked β(1-4) whose infrared spectral signals will be found in the FTIR spectra of the three fabrics finished with eco-composites (Figure 1). The FTIR peaks present at 3330 and 3270 cm^{-1} were attributed to O–H stretching vibrations, while at 2900, 1426, and 1314 cm^{-1}, the peaks corresponding to the C–H stretch were identified. The band at 1640 cm^{-1} was attributed to the O–H bond of adsorbed water, while the peaks at 1107, 1052, and 1030 cm^{-1} belong to C–O vibrations and the peak at 1160 cm^{-1} is attributed to the C–O–C stretching mode. The bands shown at 1107 and 895 cm^{-1} are characteristic of the C–O stretching vibration on the polysaccharide skeleton [39]. In the case of the cellulose supports covered with natural hydrogel, in the FTIR analysis of each sample analyzed, the presence of polysaccharides will lead to the broadening of the characteristic O–H stretching bands around 3300 and 2900 cm^{-1}, which correspond to C–H stretching vibrations. At the same time, the hydroxyl [40], carboxylic [41], or methylene [26,42] functional groups grafted on the glycoside residues and the auxiliary compounds that are found in the biopolymer component presented characteristic bands of the coating types. Starch is one of the major constituents of rice flour. It has as main components amylose and amylopectin, which give characteristic spectral bands in the range of 1500–800 cm^{-1} (fingerprint region). In the specialized literature, the IR spectrum of rice flour presents bands at 1540 cm^{-1} attributed to the NH bending vibration due to the protein content, at 1640 cm^{-1} due to the HOH bending vibration mode of water [40], and at 1740 cm^{-1} attributed to carbonyl group stretching vibration due to the content of lipids or oils. During the hydration of the starch matrix, the hydrogel spectrum showed an intense band at 1730 cm^{-1}, and the bands at 1640 and 1540 cm^{-1} decreased in intensity and broadened, which proved that proteins are involved in the hydration process [27]. The FTIR-ATR spectrum of alginate has a wide band at about 3200 cm^{-1}, which was attributed to the overlapping of O–H stretching vibrations due to the strong intra-molecular and intermolecular hydrogen bonds. The two bands at 1600 and 1410 cm^{-1}, respectively, correspond to the asymmetrical and symmetrical stretching vibrations of carboxylic ion [41]. The involvement of carboxylic groups in the process of hydration of the alginate matrix is confirmed in the G2 spectrum by the decrease in the intensity of the two characteristic bands. The appearance of an intense band at 1730 cm^{-1}, similar to the one observed in the case of G1, can be assigned to the ester groups, as was already reported [43].

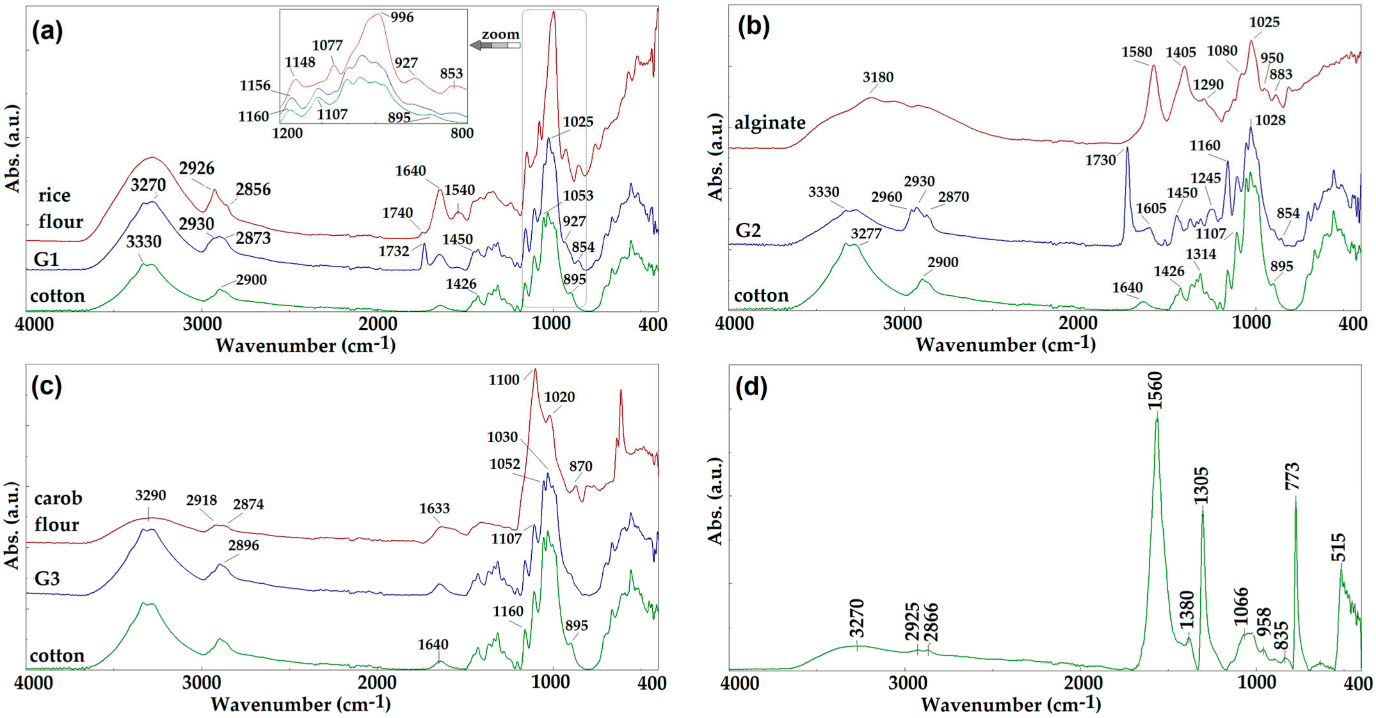

Figure 1. FTIR-ATR spectra for raw flour of rice (**a**), alginate (**b**), carob (**c**), and cotton fabrics coated with their hydrogels and Ag^0–ginger nanocomposites (**d**).

The FTIR absorption spectrum of the carob flour has a wide band at 3290 cm^{-1}, attributed to the O–H and N–H stretching vibrations of protein groups, while the signals at 2918 and 2874 cm^{-1} correspond to the asymmetrical and symmetrical stretching vibrations of CH_2. The wide band at 1633 cm^{-1} corresponds to the stretching or bending vibrations of the NH bonds belonging to the protein residues [42]. It is observed that the structure of the carob flour is similar to that of cellulose, so that the hydrated matrix deposited on the textile support (G3) does not bring significant structural changes in the IR spectrum.

In Figure 1, the FTIR absorption spectrum of the Ag^0–ginger nanocomposite shows at 3270 cm^{-1} the characteristic band of H–O stretching vibration, while the region at 2925–2866 cm^{-1} is attributed to C–H stretching vibrations. The band at 1560 cm^{-1} corresponds to amide groups, at 1380 cm^{-1} is a band which corresponds to the CH stretching vibration, and the band at 1305 cm^{-1} was attributed to the O–H bond. The band at 1066 cm^{-1} is characteristic of the stretching vibrations of the C–O bonds, while the signal at 773 cm^{-1} corresponds to a vibration characteristic of aromatic rings [36].

2.1.2. X-ray Diffraction Analysis of Fabrics Finished with Hydrogel Matrices

The textile materials finished with natural hydrogels show the presence of the characteristic lines of cellulose in Figure 2a, due to its polymorphism, according to data from the literature [44]. The amorphous region in cellulose was signaled by the appearance of a distinctive peak at $2\theta = 32°$, corresponding to the lattice plane (004), according to the specifications of JCPDS card no. 00-056-1718 for cellulose Iβ. For the fabric (G3) covered with hydrogels containing AgNPs, the XRD diffraction pattern showed the presence of two diffraction maxima at 38° and 44° corresponding to the diffraction planes (111), and (200) confirming the presence of Ag, in a cubic crystalline system (ICDD PDF No. 01-087-0719). Besides these lines, two other diffraction maxima at 26° and 32° corresponding to (110) and (111) diffraction planes were identified and attributed to Ag_2O in the cubic crystalline system (ICDD PDF. No. 01-078-5867), which was formed after oxidation of the silver nanoparticles.

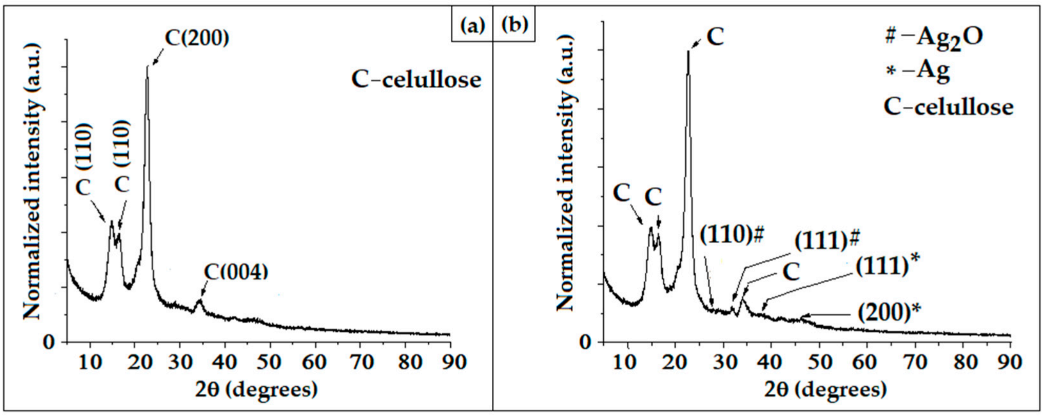

Figure 2. X-ray diffraction pattern of the G3-0 (**a**) and G3 (**b**) samples.

2.1.3. SEM-EDX Analysis of Fabrics Finished with Hydrogel Matrices

For the study of the natural matrices used as delivery systems, three types of flour characterized by different saccharide structural sequences were chosen (Figure 3). These, following the gelation process, generate networks with their own architecture and specific characteristics of the resulting gels. Thus, starch, the major component in rice, has the property of swelling and can easily retain interstitial water [28], while the carboxylic groups contained on the polysaccharide chain favor cross-linking processes in the presence of divalent ions [30]. Carob flour has a larger ramified polysaccharide sequence, called galactomannan, which, together with the proteins and fibers contained, manifests itself as gum [26]. The SEM images (Figure 4) of the three types of hydrogels loaded with AgNPs, which were deposited on the cellulosic fabrics, were analyzed, and it was observed that the biopolymer through its structure influences the final gelled compositions. In the case of composites G1 and G3, the starch content of rice flour [28] and the galactomannans from carobs [26], respectively, formed homogeneous mixtures, and the silver particles were well-dispersed in the gelled matrices. Therefore, the type of polysaccharides contained and the initial milling treatments to obtain flour directly influence their solubility [26,28], rheology, viscosity, the gelation process, and water absorption [25–30]. The architecture of the gels resulting from the hydration of rice and carob polysaccharides favors a good dispersion of the nanocomposite loaded in the natural polymer network.

Moreover, as can be seen in Figure 4, in the case of G2, the hydrogelated matrixinfluences the compatibility between the host alginate and the guest (AgNPs). The tendency of silver nanoparticles to agglomerate is favored by the architecture of the macromolecular matrices formed by (1-4)-linked β-D-mannuronate and (1-4)-linked α-D-guluronateunits which through the carboxyl groups establish intramolecular hydrogen bonds [45,46] and intermolecular bonds with the hydroxyl and methoxy groups grafted on the aromatic residues of the organic structures in the Ag^0–ginger nanocomposite.

The composites were analyzed by energy-dispersive X-ray (EDX) method to identify the elemental composition of the materials (Figure 5). EDX spectra of multicomponent gels authenticated the presence of elemental silver (Table 1). All three types of flour have polysaccharides as main components, confirmed by qualitative elemental analysis, recorded by EDX measurements. The difference between them is represented by the content of minerals: Mg in rice, Na, and K in alginate and carob flour, and Ca in all three types of aggregates. Carob flour has the most complex content compared to the other two biopolymers, and in addition, already found in the composition are fibers, tannins, and fatty acids. The presence of sulfur in EDX measurements proves the content of proteins that form aggregates through covalent bonds and disulfide bridges [47].

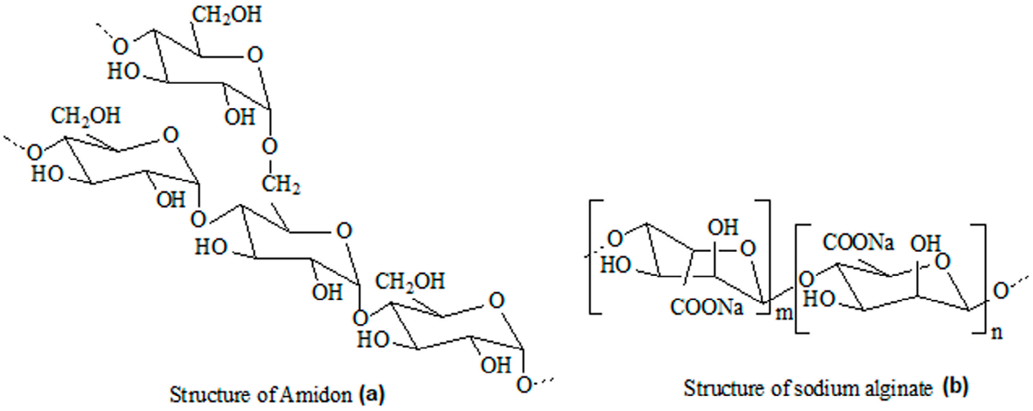

Structure of Amidon **(a)**

Structure of sodium alginate **(b)**

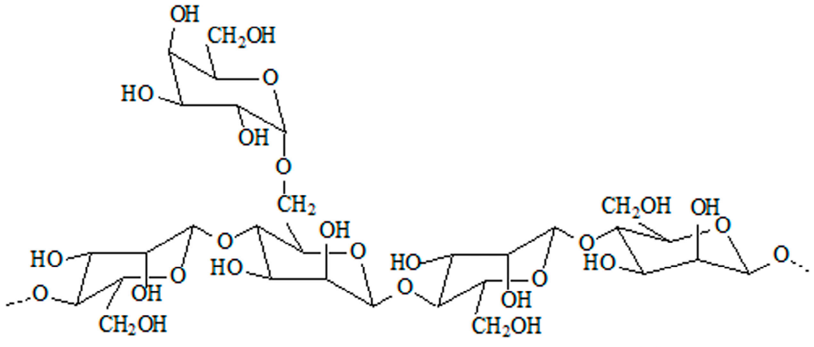

Structure of Galactomannan Carob **(c)**

Figure 3. Polysaccharide sequences that constitute the natural polymer matrices from rice flour (**a**), sodium alginate (**b**), and carob (**c**).

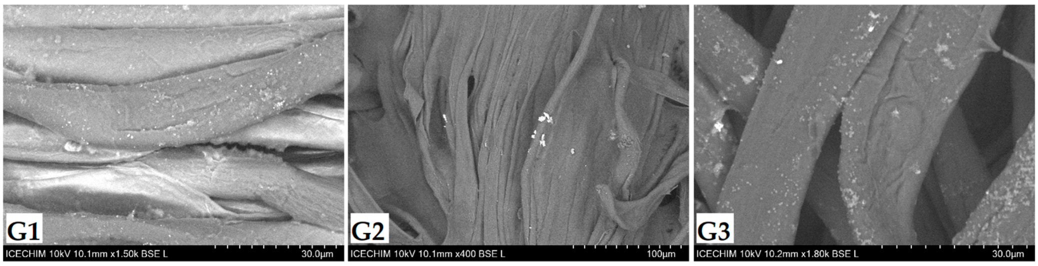

(**a**) (**b**) (**c**)

Figure 4. SEM images of the cellulose fabrics finished with natural hydrogels: G1-rice matrix (**a**); G2-alginate matrix (**b**) and G3-carob matrix (**c**).

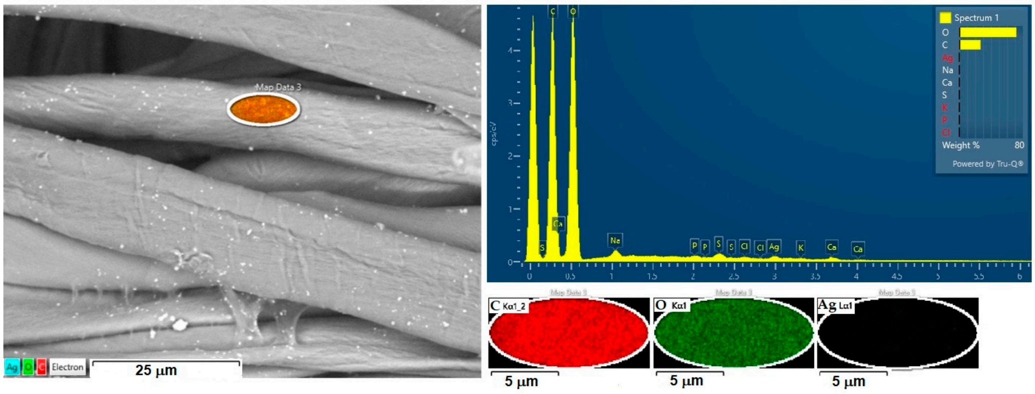

Figure 5. Elemental mapping images (Map Data 3) and EDX spectrum of G3.

Table 1. Percentage weight of elements using SEM-EDX.

Element	Line Type	G1 Weight%	G2 Weight %	G3 Weight %
C	K series	26.68	26.96	26.72
O	K series	72.03	72.03	71.82
S	K series	-	-	0.20
Mg/Na	K series	0.06	-	0.28
Ca	K series	0.41	0.20	0.25
Ag	L series	0.56	0.61	0.52
P	K series	0.07	-	0.07
Cl	K series	-	-	0.07
K	K series	-	0.20	0.07

2.1.4. Thermogravimetric Analysis

By thermogravimetric analysis (Figure 6), we evaluated the stability of multicomponent systems consisting of coated fabrics in comparison with the original cellulosic support. The fabrics present four stages of thermal decomposition, with maximum temperatures directly influenced by the morphological structure of the hydrogel used to finish the fabric. The first stage of decomposition takes place up to 128 °C when the mass loss is about 2–3.4% and is attributed to the processes of water evaporation. The second stage of decomposition takes place up to 232 °C, but in each case, maximum temperature differs depending on the polymer matrix. This stage is attributed to the evaporation processes of the interstitial water sequestered following the hydration processes of the natural polymer matrices. G3 has the lowest mass loss, of about 2%, which correlates with the high content of other bioactive compounds in the composition of the natural matrix and supports the hypothesis of the formation of a hydrogel network with increased density [45]. The organization of the hydrogel resulting from the hydration of the alginate matrix, in a robust network supported by intermolecular hydrogen bonds, makes the maximum temperature of this stage of decomposition the highest, approximately 228 °C, and the mass loss percentage is 2.4%, comparable to G3. The gelation of the starch in G1 leads to a high retention of water in the hydrogel matrix, shown by amass loss of 5.2%, double compared to G2 and G3. The weak starch hydrogel network has the maximum decomposition temperature for this stage at 147 °C, being the lowest among the three samples. The next stage of decomposition takes place around the maximum temperature of 346 °C and is directly related to the decomposition processes of the cellulosic support, where the raw fabric has a mass loss of 85%. For G1 and G2, the maximum temperature is reached at 341 °C, but the mass loss is lower for G1 (76%) compared to 82% in the case of G2. The differences are due to the different content of excipients in the natural polymer matrices confirmed by EDX analysis. The last stage of decomposition is characterized by a greater mass loss for G1 and G3, of 16% and 22%, respectively, in which the auxiliary organic residues of the biopolymer matrix, represented by fatty acids, phospholipids, and polysaccharide residues left from the collapsed hydrogel network are decomposed. The maximum temperature of this stage is the highest in the case of G3 and is influenced by the content of the natural matrix obtained using carob flour. At the end of the thermal decomposition of fabrics covered with hydrogels, a low residue of 0.7–2% was obtained consisting of inorganic compounds resulting from the thermal decomposition of the analyzed multicomponent systems.

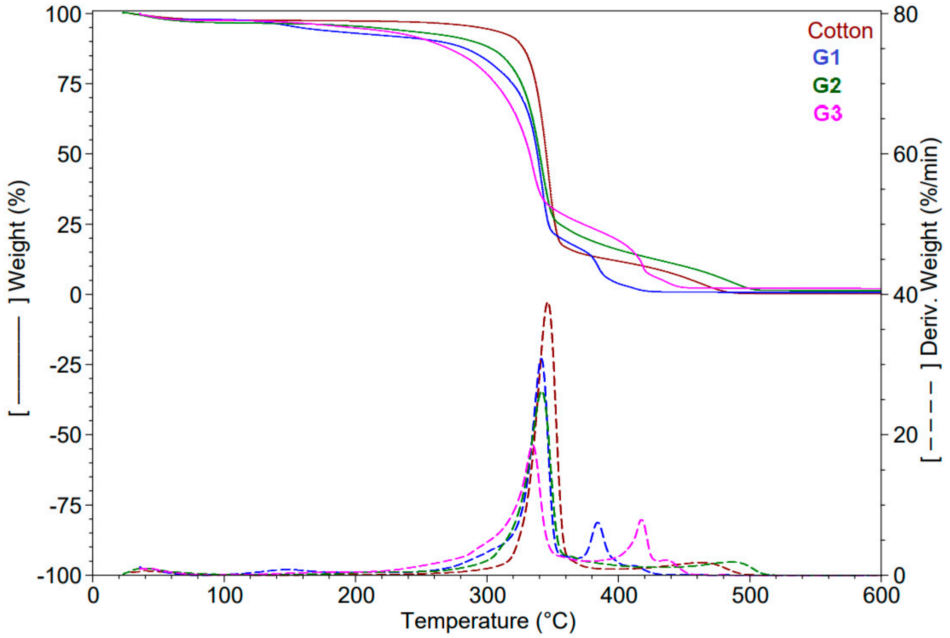

Figure 6. Thermogravimetric curves of cotton finished with natural biopolymers containing AgNPs.

2.1.5. Color Parameters in CIEL*a*b* System and Water Contact Angle Measurements

The chromatic characterization of the fabrics finished with natural hydrogels loaded with silver nanoparticles was carried out by comparing the color coordinates L*, a*, b*. The measurements were made in a three-dimensional colorspace consisting of three axes using as parameters 10○ observer and D65 illuminant. Comparing the coordinates measured for the initial polymer matrix with those of the resulting hydrogel and deposited on the cellulosic support, it was observed that in the case of G1 and G3, coatings with higher brightness, L* = 68.01 and L* = 76.42, respectively, are obtained. A slight change in shade to yellow is obtained for G1 (b* = 4.77), as a result of the hydrogen bonds established between the hydrated matrix and the Ag^0–ginger nanocomposite. The shade of G3 turns towards blue due to the drastic decrease in b* from 21.45 in the initial matrix to b* = 3.63 for hydrogel. In the case of fabric G2, its brightness L* = 68.81 does not differ much from that of the initial alginate matrix L* = 63.68. The modified hue towards yellow is significant due to the displacement of the value of alginate powder b* = 21.64 to low values b* = 7.04 due to the hydrogen bonds established in the hydrogel matrix, with the AgNP hosting compound and the intermolecular ones established between the hydrogels and the cellulosic fibers [48–50].

These intermolecular bonds established between the natural hydrogels and the cotton fabric lead to stable and resistant coatings with relatively good adhesion performance in both dry and wet conditions (Table 2) [51].

Table 2. Color parameters in the CIEL*a*b* system and water contact angle for natural polymers and finished cellulosic fabrics.

Sample	Color Parameters			Rubbing Fastness (Grade) ISO 105 X12		Water Contact Angle (Standard Deviation)
	L*	a*	b*	Dry	Wet	(°)
Cotton fabric	82.94	−0.07	−1.14	–	–	0
Rice flour	90.51	−0.57	3.44	–	–	–
G1	68.01	2.62	4.77	2–3	1–2	107 ± 9.67
Alginate	63.68	9.13	21.64	–	–	–
G2	68.81	5.76	7.04	3	2–3	75 ± 10.02
Carob flour	83.50	4.69	21.45	–	–	–
G3	76.42	1.89	3.63	3–4	2–3	85 ± 3.60

The fabrics finished with multicomponent systems based on polysaccharide networks in which AgNPs were embedded are characterized by good hydrophilicity, having contact angles between 75° and 107°, and a high rate of adsorption of water droplets due to the OH groups that were found in the structure of hydrogel matrices.

2.2. Spectrophotometric Determination of Silver Ions by the Dithizone Method

Another study was carried out regarding the ability of the gelled matrices deposited on the textile support to release silver ions from the network. The presence of silver ions in the aqueous system was confirmed by Shah's method [51] based on silver ion complexation with dithizone (DTZ). This is a sensitive method for determining metal ions (Ag^+, Cd^+, Hg^+) by complexing them with DTZ. The concentration of complexed ions is determined spectrophotometrically by measuring the molar absorbance of the solution in the presence of a nonionic or cationic surfactant. The method involves the detection of silver ions complexed with dithizone, a process that can be detected visually due to the change in color from green to brick red. The color change was evaluated by absorption spectroscopy (peaks characteristic of DTZat ~456 and 620 nm) at about 0.97 mM concentration, where the solution obeys Beer's law (Figure 7). After one hour of hydration of the coated textile samples, the concentration of Ag ions in the aqueous solution was measured spectrophotometrically. Comparing the absorbance recorded for the three samples to the calibration curve for known concentrations of Ag^+, it was found that the related solution G1 had a concentration of 7.3 ppm [Ag^+], the G2 solution had 6.8 ppm, while for G3, a concentration of 9.4 ppm [Ag^+] was found. The results confirmed that Ag^+ ions can migrate through the gel network and can be released into the external environment, where they can exhibit an antimicrobial effect.

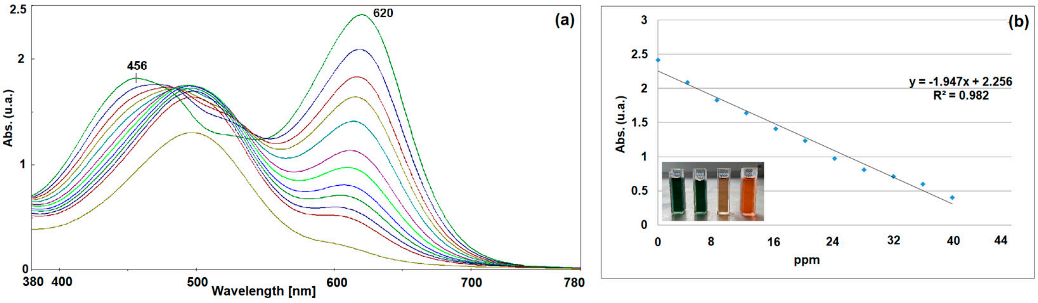

Figure 7. Absorption spectra of dithizone solution (DTZ) and effect of silver–dithizone complex on the absorbance at λ_{max} 620 nm (**a**). Calibration graph of DTZ standard solution (0.97 mM) with increasing amounts of Ag+ (0–40 ppm) (**b**).

2.3. Antimicrobial Study

The antimicrobial activity of silver nanoparticles has been confirmed in a significant number of articles that can be found in the specialized literature [37,38]. In the present work, it was observed how AgNPs keep their antimicrobial properties and their efficiency after being loaded into hydrogel matrices. These aspects are important to know in order to be able to further develop new fields of application or to diversify the delivery matrices of silver nanoparticles.

Specimens from each cotton fabric finished with natural hydrogel loaded with the Ag^0–ginger nanocomposite were evaluated regarding the antifungal and antibacterial activity by the "Agar diffusion plate test" (Table 3). According to the method presented in the literature [52,53] and in ISO 20645:2004 [54], each fabric sample was placed on a wet culture of microbial cells. The samples were moistened, and the silver ions diffused, reaching the culture of bacteria/fungi, where they affected their growth more or less in relation to the concentration of ions released from the multicomponent system. After 24 h of incubation, the test results showed that specimens G1 and G3 have a moderate antimicrobial activity (at the limit of effectiveness), showing rather a bacteriostatic and fungistatic effect, while for G2, a "strong growth" of microbial cells was observed after the removal of the textile specimen (Figure 8). The results of the antimicrobial activity are in accordance with the measurements obtained when evaluating the capacity to release Ag^+ from the hydrogel network, where G3 recorded the highest concentration of released ions. The hydrophilic properties of the fabrics favor the adhesion of the biofilm on the surface, and the formation of AgNP agglomerates in the alginate hydrogel matrix determined a weak antimicrobial activity in the case of G2. Considering that the best results were obtained in the case of the carob matrix, the uncharged matrix and the hydrogel system with different loadings of silver nanoparticles were evaluated. Taking into account the literature data regarding the antioxidant and antimicrobial effects given by the content of polyphenols, tannins, and other bioactive compounds [34] of carob flour, it was tested whether the cellulose support covered with carob hydrogel (G3-0) showed antimicrobial properties. Encouraged by the initial results obtained, the increase in the effectiveness of the antimicrobial activity of the fabric was studied if the amount of Ag^0–ginger nanocomposite were doubled (G3-1). The evaluation after the incubation time was carried out visually and under the microscope, and no antimicrobial activity was observed in the case of G3-0 against either fungi or bacteria (Figure 9a–c). For specimen G3-1, the results showed a lack of growth of microbial cells under the textile substrate. Therefore, G3-1 had a very good antimicrobial activity, best observed against *S. aureus* cells, where a halo formed around the fabric at a distance of 1 mm. However, the enrichment of the carrier matrix with silver nanoparticles, by increasing the amount of Ag^0–ginger nanocomposite, led to a decrease in the viscosity of the multicomponent system and had the effect of its partial yielding from the fabric, in wet conditions, as can be seen for G3-1 in Figure 8. G3-0 and G3-1 were also evaluated by electron microscopy; the SEM images obtained, shown in Figure 9, confirm the adhesion of microbial cells on the surface of cellulose fibers coated with hydrogelated matrices, while in the case of hydrogel coatings with AgNPs embedded in the network, they are untouched by Gram-positive and Gram-negative cells and fungi.

Table 3. Evaluation of microbial cells grown under the textile specimens.

Sample	Growth of Bacteria/Fungi under the Specimen		
	S. aureus	*E. coli*	*C. albicans*
G1	none/slight	none/slight	slight
G2	heavy	moderate/heavy	moderate/heavy
G3	none	none/slight	none

Adopted from ISO 20645:2004: none = good effect; slight = limit of efficacy; moderate = insufficient effect; heavy = insufficient effect.

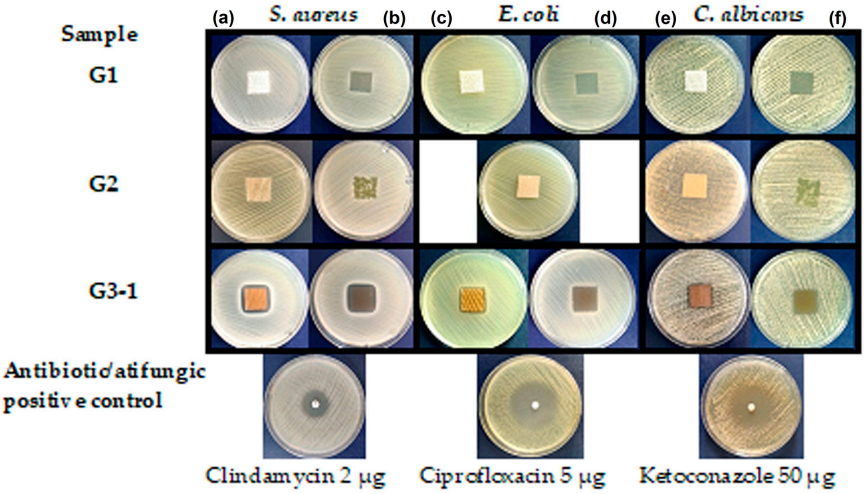

Figure 8. Images of the textile specimens inoculated on microbial strains (*S. aureus* (**a**), *E. coli* (**c**), *C. albicans* (**e**)) and bacteriostatic/fungistatic effect after removing the textiles covered with the multicomponent composites (*S. aureus* (**b**), *E.coli* (**d**), *C. albicans* (**f**)).

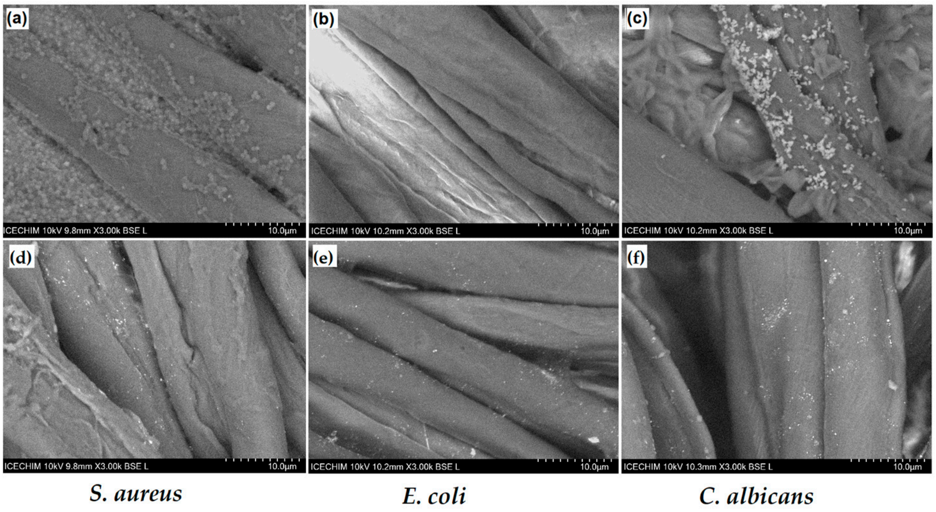

Figure 9. SEM images of the adhered microorganisms on the cotton coated with hydrogel without AgNPs (G3-0, (**a**–**c**) and the one with AgNP content (G3-1, (**d**–**f**)).

Considering that textile surfaces evaluated by electron microscopy are very small and to support the results obtained regarding the antimicrobial activity of multicomponent coatings, counts of cells grown on fabrics exposed to Gram-positive bacteria were performed. The comparison of the effectiveness of the antimicrobial activity of G3-type fabrics covered with hydrogel with/without Ag nanoparticles was performed on the most strongly inhibited *S. aureus* strain. For the three specimens (G3-0, G3, G3-1), viable cells were counted on the specimen fabrics after 24 h of contact with the inoculated microorganism. The evaluation of the effectiveness of finished fabrics covered with hydrogel matrices from carob flour with varying content of silver nanoparticles showed that for G3-0 at dilutions of 10^{-5}, CFU/mL = 4.32 × 10^8, and for G3 at dilutions of 10^{-5}, CFU/mL = 3.24 × 10^8, there is a bacteriostatic effect, causing a moderate multiplication of bacteria. In the case of sample G3-1 at the dilution of 2 × 10^{-6}, no colonies were observed on the surface of the culture medium, which confirms once again that G3-1 has a bactericidal effect (kills 99.9% of bacteria). Its activity is due to the presence of silver ions that diffused through the network of the hydrogel in which it was loaded (Figure 10).

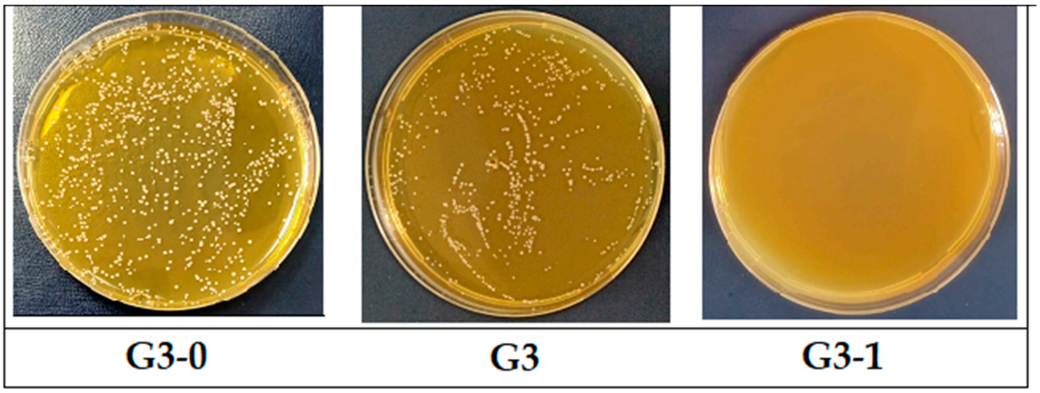

Figure 10. Evaluation by the method of counting cells grown after exposure to Gram-positive bacteria of cotton finished with carob hydrogel matrices (G3-0) and loaded with different concentrations of Ag^0–ginger nanocomposite (G3, dilution of 10^{-5} and G3-1, dilution of 2 × 10^{-6}).

In this way, it is confirmed that the hydrogel network through its architecture influences the polydisperse system of natural composites, and at the same time, the amount of silver nanoparticles embedded in the gelled matrix affects the antimicrobial properties of the multicomponent system.

3. Conclusions

Obtaining multicomponent gels with antimicrobial properties consisted of incorporating Ag^0–ginger nanocomposites in natural polymer matrices using an eco-friendly method. Ag^0–ginger nanocomposites result from the phytosynthesis process of reducing silver ions to metallic nanoparticles in the presence of bioactive compounds from ginger extract. By using natural matrices of different plant origin, in which the nanocomposites were loaded at low temperature, three types of multicomponent system were obtained and deposited on the cotton fabric. The finished surfaces showed hydrophilic properties and a good adhesion to the cellulosic substrate. Tests performed on finished textile materials regarding the release of silver ions highlighted the influence of the gelled matrix structure on the migration capacity of the ions from the multicomponent system to the external environment. All fabrics finished with natural composites showed bacteriostatic and fungistatic effects. By optimizing the amount of Ag^0–ginger nanocomposite loaded in the gelled matrix, fabrics with antimicrobial effect were obtained.

4. Materials and Methods

4.1. Materials

The extract of active compounds was prepared by mixing 5 g of ginger powder purchased from the local company Organic India (Bucharest, Romania) and 100 mL of alcoholic aqueous solution (30%) under stirring on a magnetic stirrer, at 60 °C for 30 min. The resulting mixture was cooled to 25 °C and separated using a Büchner funnel (Jena, Germany) and Whatman no. 1 filter paper (Merck, Darmstadt, Germany). The obtained yellow liquid was stored in a 100 mL flask and completed with deionized water. In a 100 mL flask, 20 mL of ginger extract from the stock solution and 20 mL of silver nitrate aqueous solution (1 mmol) were added under continuous stirring. The obtained nanoparticles were synthesized according to the method reported by El Refai [38] with a slight modification. The reaction mixture in an equimolar ratio of (1:1) plant extracts to silver nitrate solution was kept under stirring for another four hours at room temperature, when the color of the mixture turned brown. Thus, silver nanoparticles in ginger extract (Ag^0—ginger) were synthesized through an eco-friendly method.

Natural polymer gels were obtained by dissolving 2 g of alginate/6 g of rice flour/6 g of carob flour bought from a local supermarket in 100 mL of deionized water, each under stirring and at a temperature of 80–90 °C, for one hour. Over 8 g of the gelled matrices were added to 2 g of Ag^0–ginger nanocomposite, stirring continuously. After incorporating the solution containing silver particles into the gelled matrices, three types of homogeneous gels were obtained, and they were deposited on 2 g cotton fabric by the screen printing method. The finished fabrics were dried at 25 °C for 2 h, the nat 105 °C for 1 h in a thermofixation oven (Biobase, Shandong, China). The fabric used as a support for the natural hydrogels was100% cotton (Matasea Romana, Romania) with the following characteristics: specific weight = 161.98 g/m^2, 79.4 ends, 65.4 picks, yarn count of 23.4 × 22 tex; it was originally scoured and chemically bleached.

4.2. Methods

The cellulosic fabrics finished with the natural composites loaded with silver nanoparticles were analyzed to confirm the presence of silver by recording XRD diffractograms in the range 2θ, 2–90° with a RigakuSmartLab equipment (Rigaku Corporation, Tokyo, Japan). The diffractograms were interpreted using the PDXL software (ver. 2.7.2.0, Rigaku Corporation, Tokyo, Japan), provided by Rigaku, and the identification of the silver and silver oxide present at the textile surface was performed by comparison with the ICDD (International Centre for Diffraction Data) database entries. The structural analysis of the three types of biopolymers and the interactions between their hydrogel matrix and cotton was carried out by FTIR measurements. Spectra were recorded in the range 400 to 4000 cm^{-1}, making 128 accumulations at a resolution of 4 cm^{-1} with a JASCO FT-IR 6300 instrument (Jasco Int. Co. Ltd., Tokyo, Japan), which was equipped with a Specac ATR Golden Gate (Specac Ltd., Orpington, UK) with KRS5 lens. SEM images of coated fabrics with natural hydrogels and those inoculated in microbiologic medium were obtained with a TM4000Plus equipment (HITACHI, Tokyo, Japan) using the following operating conditions: acceleration voltage of 10 kV and magnifications up to 1800×. The thermal stability of the natural composites was studied by thermogravimetric analysis (TGA) performed with a TGA Q5000IR instrument (TA Instruments, New Castle, DE, USA). The quantity of the samples subjected to thermal decomposition was about 3.5–4 mg each, and it was weighed in platinum pans and analyzed under the following conditions: heating ramp 10 °C/min up to 600 °C, Synthetic Air (99.999%) used as purge gas at a 50 mL/min flow rate. To evaluate the colors of finished textile samples and raw flours, total color differences were measured in the CIELAB system, using a 10° standard observer and illuminant D65, with V570 UV-VIS-NIR equipment (Jasco Int. Co. Ltd., Tokyo, Japan) equipped with an integrating sphere (JASCO ILN-472 (150 mm)), using spectralon as reference material. The hydrophilic properties of the coatings were evaluated by measuring the water contact angle with a CAM 200 (KSV Instruments, Helsinki, Finland) equipped with a high-resolution camera (Basler A602f, Basler, Ahrensburg, Germany) and an autodispenser. Water contact angles were measured in air, at 25° C and ambient humidity, 2 s after the drop contacted the surface of the coatings. Drops of 6 µL deionized water were dispensed on each sample, and the value of the reported water contact angles was the average of six measurements. Natural coated fabrics were evaluated for rubbing fastness according to ISO-105X12 [51].

The evaluation of the antibacterial activity of cotton finished with natural composites was carried out on bacterial strains, *Staphylococcus aureus* (ATCC 25923) and *Escherichia coli* (ATCC 25922), and strain of fungi, *Candida albicans* (ATCC 10231), from the Microbial Collection of National Research and Development Institute for Chemistry and Petrochemistry-ICECHIM. For the evaluation of the antimicrobial activity, we used the "Agar diffusion plate test" method with coated fabric samples (2×2 cm^2) on the Sabouraud medium for fungi and Muller Hinton medium for bacteria, respectively, inoculated into the cloth with the tested microorganisms. Antimicrobial activity was evaluated according to ISO 20645:2004 [54] by measuring the diameter of the clear area (halo) that appeared around the textile specimens. The working inoculum was represented by a suspension made from a fresh culture in AFS (sterile physiological water), developed on a solid TSA (Tryptic Soy Agar) medium, with a density of 1.5×10^8 CFU/mL, nephelometrically adjusted (McFarland standard 0.5 = 1.5×10^8 CFU/mL). The plates were incubated for 24 h at the optimal temperature (28 °C for fungi and 37 °C for bacteria) and then the cell cultures were examined. Following the evaluation of cellular microorganisms, it was observed that the best results were in the case of *S. aureus* cultures and the tests were continued by counting viable cells. The viable cells on the textile samples were counted after 24 h of contact of the textile sample with the inoculated microorganism by the method presented below. The textile sample was transferred into 20 mL of AFS and vortexed to help detach the bacterial cells from the textile support. The supernatant was serially diluted up to 10^{-5} dilution and inoculated with 100 µL of each on TSA medium. After 24 h of incubation, the colonies were counted. The number of viable bacteria was reported as colony forming units, CFU/mL.

Author Contributions: Conceptualization, F.M.R. and V.R.; methodology, F.M.R. and V.R.; validation, A.R.; formal analysis, A.N.F.; C.A.N.; M.C. and I.R.; investigation, M.G.; writing—original draft preparation, A.R. and M.G.; writing—review and editing, F.M.R.; visualization, A.R.; supervision, V.R. All authors have read and agreed to the published version of the manuscript.

Funding: This work was carried out through the PN 23.06 Core Program—ChemNewDeal within the National Plan for Research, Development and Innovation 2022–2027, developed with the support of Ministry of Research, Innovation, and Digitization, project no. PN 23.06.01.01.

Institutional Review Board Statement: Not applicable.

Informed Consent Statement: Not applicable.

Data Availability Statement: The data are not publicly available due to their containing information that could compromise the privacy of research participants.

Acknowledgments: SEM analysis was carried out on equipment acquired in the frame of a grant from the Romanian Ministry of Research, Innovation, and Digitization, CNCS/CCCDI–UEFISCDI, NeXT-BExcel 15PFE/2021.

Conflicts of Interest: The authors declare no conflicts of interest.

References

1. Tang, K.W.K.; Millar, B.C.; Moore, J.E. Antimicrobial Resistance (AMR). *Br. J. Biomed.* **2023**, *80*, 11387. [CrossRef]
2. Salam, M.A.; Al-Amin, M.Y.; Salam, M.T.; Pawar, J.S.; Akhter, N.; Rabaan, A.A.; Alqumber, M.A.A. Antimicrobial Resistance: A Growing Serious Threat for Global Public Health. *Healthcare* **2023**, *11*, 1946. [CrossRef]
3. Bassetti, M.; Garau, J. Current and future perspectives in the treatment of multidrug-resistant Gram-negative infections. *J. Antimicrob. Chemother.* **2021**, *76*, 23–37. [CrossRef]
4. Karaiskos, I.; Lagou, S.; Pontikis, K.; Rapti, V.; Poulakou, G. The "Old" and the "New" Antibiotics for MDR Gram-Negative Pathogens: For Whom, When, and How. *Front. Public Health* **2019**, *7*, 151. [CrossRef]
5. Sperandio, F.F.; Huang, Y.Y.; Hamblin, M.R. Antimicrobial photodynamic therapy to kill Gram-negative bacteria. *Recent Pat. Anti-Infect. Drug Discov.* **2013**, *8*, 108–120. [CrossRef]
6. Lorenzo-Leal, A.C.; Tam, W.; Kheyrandish, A.; Mohseni, M.; Bach, H. Antimicrobial Activity of Filtered Far-UVC Light (222nm) against Different Pathogens. *BioMed Res. Int.* **2023**, *8*, 2085140. [CrossRef]
7. Yi, H.; Yuan, G.; Li, S.; Xu, X.; Guan, Y.; Zhang, L.; Yan, Y. Drug Combinations to Prevent Antimicrobial Resistance: Various Correlations and Laws, and Their Verifications, Thus Proposing Some Principles and a Preliminary Scheme. *Antibiotics* **2022**, *11*, 1279. [CrossRef]
8. Parmanik, A.; Das, S.; Kar, B.; Bose, A.; Dwivedi, G.R.; Pandey, M.M. Current Treatment Strategies Against Multidrug-Resistant Bacteria: A Review. *Curr. Microbiol.* **2022**, *79*, 388. [CrossRef]
9. Gyawali, R.; Ibrahim, S.A. Natural products as antimicrobial agents. *Food Control* **2014**, *46*, 412–429. [CrossRef]
10. Beristain-Bauza, S.D.C.; Hernández-Carranza, P.; Cid-Pérez, T.S.; Ávila-Sosa, R.; Ruiz-López, I.I.; Ochoa-Velasco, C.E. Antimicrobial Activity of Ginger (*Zingiber Officinale*) and Its Application in Food Products. *Food Rev. Int.* **2019**, *35*, 407–426. [CrossRef]
11. Farid, N.; Waheed, A.; Motwani, S. Synthetic and natural antimicrobials as a control against food borne pathogens: A review. *Heliyon* **2023**, *9*, 17021. [CrossRef] [PubMed]
12. Raduly, F.M.; Raditoiu, V.; Raditoiu, A.; Purcar, V. Curcumin: Modern Applications for a Versatile Additive. *Coatings* **2021**, *11*, 519. [CrossRef]
13. Matlock, A.; Garcia, J.A.; Moussavi, K.; Long, B.; Liang, S.Y.T. Advances in novel antibiotics to treat multidrug-resistant gram-negative bacterial infections. *Intern. Emerg. Med.* **2021**, *16*, 2231–2241. [CrossRef]
14. Bhatt, S.; Pathak, R.; Punetha, V.D.; Punetha, M. Recent advances and mechanism of antimicrobial efficacy of graphene-based materials: A review. *J. Mater. Sci.* **2023**, *58*, 7839–7867. [CrossRef] [PubMed]
15. Yılmaz, G.E.; Göktürk, I.; Ovezova, M.; Yılmaz, F.; Kılıç, S.; Denizli, A. Antimicrobial Nanomaterials: A Review. *Hygiene* **2023**, *3*, 269–290. [CrossRef]
16. Karypidis, M.; Karanikas, E.; Papadaki, A.; Andriotis, E.G. A Mini-Review of Synthetic Organic and Nanoparticle Antimicrobial Agents for Coatings in Textile Applications. *Coatings* **2023**, *13*, 693. [CrossRef]
17. Technology and Innovation for Cleaner and More Productive and Competitive Production. Available online: www.unctad.org (accessed on 20 December 2023).
18. Coccia, M. New technological trajectories to reduce fossil-fuel pollution and support sustainable socioeconomic systems. *Res. Sq.* **2022**. [CrossRef]
19. Söderholm, P. The green economy transition: The challenges of technological change for sustainability. *Sustain. Earth* **2020**, *3*, 6. [CrossRef]
20. Leichtweis, M.G.; Oliveira, M.B.P.P.; Ferreira, I.C.F.R.; Pereira, C.; Barros, L. Sustainable Recovery of Preservative and Bioactive Compounds from Food Industry Bioresidues. *Antioxidants* **2021**, *10*, 1827. [CrossRef]
21. Messinese, E.; Pitirollo, O.; Grimaldi, M.; Milanese, D.; Sciancalepore, C.; Cavazza, A. By-Products as Sustainable Source of Bioactive Compounds for Potential Application in the Field of Food and New Materials for Packaging Development. *Food Bioprocess. Technol.* **2023**, *6*, 1–22. [CrossRef]
22. Vaishnavee, G.J.; Deepu, S. A Review of Natural Binders as Pharmaceutical Excipient in The Novel Drug Delivery System. *IJPPR Hum. Human.* **2021**, *21*, 84–99.
23. Ruschhaupt, P.; Varzi, A.; Passerini, S. Natural Polymers as Green Binders for High-Loading Supercapacitor Electrodes. *ChemSusChem* **2020**, *13*, 763–770. [CrossRef]
24. Lacoste, C.; El Hage, R.; Bergeret, A.; Corn, S.; Lacroix, P. Sodium alginate adhesives as binders in wood fibers/textile waste fibers biocomposites for building insulation. *Carbohydr. Polym.* **2018**, *184*, 1–8. [CrossRef]

25. Xiong, R.; Grant, A.M.; Ma, R.; Zhang, S.; Tsukruk, V.V. Naturally-derived biopolymer nanocomposites: Interfacial design, properties and emerging applications. *Mater. Sci. Eng.* **2018**, *125*, 1–41. [CrossRef]
26. Sharma, P.; Sharma, S.; Ramakrishna, G.; Srivastava, H.; Gaikwad, K. A comprehensive review on leguminous galactomannans: Structural analysis, functional properties, biosynthesis process and industrial applications. *Crit. Rev. Food Sci. Nutr.* **2021**, *62*, 443–465. [CrossRef]
27. Suklaew, P.O.; Chusak, C.; Adisakwattana, S. Physicochemical and Functional Characteristics of RD43 Rice Flour and Its Food Application. *Foods* **2020**, *9*, 1912. [CrossRef]
28. Amagliani, L.; O'Regan, J.; Kelly, A.L.; O'Mahony, J.A. Chemistry, structure, functionality and applications of rice starch. *J. Cereal Sci.* **2016**, *70*, 291–300. [CrossRef]
29. Raya, M.A.A.; Ghoneem, G.A.A.; Blasim, H.A. Effect of Addition Corn Flour on Chemical, Physical, Rheological and Sensory Properties of Iraq Bread. *J. Food Dairy Sci.* **2022**, *13*, 95–100. [CrossRef]
30. Wang, L.; Zhu, F.; Lu, D. Rheological properties of sodium alginate and xanthan pastes on cotton with reactive dye in screen printing. *Text. Res. J.* **2013**, *83*, 1873–1884. [CrossRef]
31. Abdou, E.S.; El-Hennawi, H.M.; Ahmed, K.A. Preparation of Novel Chitosan-Starch Blends as Thickening Agent and Their Application in Textile Printing. *J. Chem.* **2013**, *8*, 595810. [CrossRef]
32. Ebrahim, S.A.; Hassabo, A.G.; Osman, H.A. Natural Thickener in Textile Printing. *J. Text. Color. Polym. Sci.* **2021**, *18*, 55–64. [CrossRef]
33. Geetha, R.; Sankari, A.; Pugalendhi, L.; Vennila, P.; Swarnapriya, R.; Thangamani, C. Studies on functional properties of cassava var. Yethapur Tapioca-2 for its suitability as an ideal industrial substitute for the grain starches. *J. Pharm. Innov.* **2021**, *10*, 9–12.
34. Ikram, A.; Khalid, W.; Zafar, K.W.; Ali, A.; Afza, M.F.; Aziz, A.; Rasool, I.F.; Al-Farga, A.; Aqlan, F.; Koraqi, H. Nutritional, biochemical, and clinical applications of carob: A review. *Food Sci. Nutr.* **2023**, *11*, 3641–3654. [CrossRef]
35. Al-Awwadi, N.A.J. Potential health benefits and scientific review of ginger. *J. Pharmacogn. Phytother.* **2017**, *9*, 111–116. [CrossRef]
36. Venkatadri, B.; Shanparvish, E.; Rameshkumar, M.R.; Arasu, M.V.; Al-Dhabi, N.A.; Ponnusamy, V.K.; Agastian, P. Green synthesis of silver nanoparticles using aqueous rhizome extract of Zingiberofficinale and Curcuma longa: In-vitro anti-cancer potential on human colon carcinoma HT-29 cells. *Saudi J. Biol. Sci.* **2020**, *27*, 2980–2986. [CrossRef] [PubMed]
37. Vanlalveni, C.; Lallianrawna, S.; Biswas, A.; Selvaraj, M.; Changmai, B.; Rokhum, S.L. Green synthesis of silver nanoparticles using plant extracts and their antimicrobial activities: A review of recent literature. *RSC Adv.* **2021**, *11*, 2804. [CrossRef] [PubMed]
38. El-Refai, A.A.; Ghoniem, G.A.; El-Khateeb, A.Y.; Hassaan, M.M. Eco-friendly synthesis of metal nanoparticles using ginger and garlic extracts as biocompatible novel antioxidant and antimicrobial agents. *J. Nanostruct. Chem.* **2018**, *8*, 71–81. [CrossRef]
39. Parihar, A.; Vongsvivut, J.; Bhattacharya, S. Synchrotron-Based Infra-Red Spectroscopic Insights on Thermo-Catalytic Conversion of Cellulosic Feedstock to Levoglucosenone and Furans. *ACS Omega* **2019**, *4*, 8747–8757. [CrossRef]
40. Ishikawa, D.; Yang, J.; Ichikawa, C.; Fujii, T. Evaluation of solid state of rice flours produced by different milling processes using ATR-FTIR spectroscopy. *Biosci. Biotechnol. Biochem.* **2021**, *85*, 1056–1062. [CrossRef]
41. Costaa, H.S.; Dias, M.R. Alginate/Bioactive Glass Beads: Synthesis, Morphological and Compositional Changes Caused by SBF Immersion Method. *Mater. Res.* **2021**, *24*, e20200587. [CrossRef]
42. Christou, C.; Agapiou, A.; Kokkinofta, R. Use of FTIR spectroscopy and chemometrics for the classification of carobs origin. *J. Adv. Res.* **2018**, *10*, 1–8. [CrossRef]
43. Erceg, T.; Stupar, A.; Cvetinov, M.; Vasi, V.; Risti, I. Investigation the correlation between chemical structure and swelling, thermal and flocculation properties of carboxymethylcellulose hydrogels. *J. Appl. Polym. Sci.* **2021**, *138*, 50240. [CrossRef]
44. Fawcett, T.G.; Crowder, C.E.; Kabekkodu, S.N.; Needham, F.; Kaduk, J.A.; Blanton, T.N.; Petkov, V.; Bucher, E.; Shpanchenko, R. Reference materials for the study of polymorphism and crystallinity in cellulosics. *Powder Diffr.* **2013**, *28*, 18–31. [CrossRef]
45. Eskens, O.; Villani, G.; Amin, S. Rheological Investigation of Thermoresponsive Alginate-Methylcellulose Gels for Epidermal Growth Factor Formulation. *Cosmetics* **2021**, *8*, 3. [CrossRef]
46. Urbanova, M.; Pavelkova, M.; Czernek, J.; Kubova, K.; Vyslouzil, J.; Pechova, A.; Molinkova, D.; Vyslouzil, J.; Vetchy, D.; Brus, J. Interaction Pathways and Structure—Chemical Transformations of Alginate Gels in Physiological Environments. *Biomacromolecules* **2019**, *20*, 4158–4170. [CrossRef]
47. Aydın, S.; Özdemir, Y. Development and Characterization of Carob Flour Based Functional Spread for Increasing Use as Nutritious Snack for Children. *J. Food Qual.* **2017**, *7*, 5028150. [CrossRef]
48. Glowacki, E.D.; Irimia-Vladu, M.; Bauerb, S.; Sariciftci, N.S. Hydrogen-bonds in molecular solids—From biological systems to organic electronics. *J. Mater. Chem. B* **2013**, *1*, 3742. [CrossRef]
49. Raduly, F.M.; Rădițoiu, V.; Rădițoiu, A.; Frone, A.N.; Nicolae, C.A.; Răut, I.; Constantin, M.; Grapin, M. Multifunctional Finishing of Cotton Fabric with Curcumin Derivatives Coatings Obtained by Sol-Gel Method. *Gels* **2023**, *9*, 369. [CrossRef] [PubMed]
50. Fleischmann, C.; Lievenbrück, M.; Ritter, H. Polymers and Dyes: Developments and Applications. *Polymers* **2015**, *7*, 717–746. [CrossRef]
51. *ISO 105-X12*; ISO Textiles—Tests for Colour Fastness—Part X12: Colour Fastness to Rubbing. International Organization for Standardization: Geneva, Switzerland, 2016.
52. Shah, R.; Devi, S. Spectrophotometric determination of microquantities of silver(I) using dithizone in the presence of cetyltrimethylammonium bromide. *Indian J. Chem.* **1995**, *34*, 925–927.

53. Pinho, E.; Magalhães, L.; Henriques, M.; Oliveira, R. Antimicrobial activity assessment of textiles: Standard methods comparison. *Ann. Microbiol.* **2011**, *61*, 493–498. [CrossRef]
54. Ivankovic, T.; Rajic, A.; Ercegovic, R.S.; du Roscoat, R.S.; Skenderi, Z. Antibacterial Properties of Non-Modified Wool, Determined and Discussed in Relation to ISO 20645:2004 Standard. *Molecules* **2022**, *27*, 1876. [CrossRef] [PubMed]

gels

Article

In Situ Gelling Behavior and Biopharmaceutical Characterization of Nano-Silver-Loaded Poloxamer Matrices Designed for Nasal Drug Delivery

Nadezhda Ivanova [1,*], Neli Ermenlieva [2], Lora Simeonova [3], Neli Vilhelmova-Ilieva [3], Kameliya Bratoeva [4], Georgi Stoyanov [5] and Velichka Andonova [1]

[1] Department of Pharmaceutical Technologies, Faculty of Pharmacy, Medical University of Varna, 9000 Varna, Bulgaria; velichka.andonova@mu-varna.bg
[2] Department of Microbiology and Virology, Faculty of Medicine, Medical University of Varna, 9000 Varna, Bulgaria; neli.ermenlieva@mu-varna.bg
[3] Department of Virology, Stephan Angeloff Institute of Microbiology, Bulgarian Academy of Sciences, 26 G. Bonchev Str., 1113 Sofia, Bulgaria; losimeonova@gmail.com (L.S.); nelivili@gmail.com (N.V.-I.)
[4] Department of Physiology and Pathophysiology, Faculty of Medicine, Medical University of Varna, 9000 Varna, Bulgaria; k_brat@abv.bg
[5] Clinical Pathology, Complex Oncology Center, 9700 Shumen, Bulgaria; georgi.geesh@gmail.com
* Correspondence: nadejda.ivanova@mu-varna.bg

Abstract: A combination of Poloxamer 407 (P407) and hydroxypropyl methylcellulose (HPMC) hydrosols is proposed as an in situ thermo-gelling vehicle for the nasal drug delivery of chlorhexidine–silver nanoparticles conjugates (SN-CX). Optimization of the formulation was carried out by applying varying ratios of P407 and HPMC in the presence and absence of SN-CX so that gelation would occur in the temperature range of the nasal cavity (30–34 °C). Mechanisms for the observed gelation phenomena were suggested based on viscosimetry, texture analysis, and dynamic light scattering. Tests were carried out for sprayability, washout time, in vitro drug release, ex vivo permeation, and antimicrobial activity. When applied separately, HPMC was found to lower the P407 gelation temperature (T_g), whereas SN-CX increased it. However, in the presence of HPMC, SN-CX interfered with the P407 micellar organization in a principally contrasting way while leading to an even further decrease in T_g. SN-CX-loaded nasal formulations composed of P407 16% and HPMC 0.1% demonstrated a desired gelation at 31.9 °C, good sprayability (52.95% coverage of the anterior nasal cavity), mucoadhesion for 70 min under simulated nasal clearance, expedient release and permeation, and preserved anti-infective activity against seasonal Influenza virus and beta-coronavirus, *Pseudomonas aeruginosa, Klebsiella pneumoniae, Staphylococcus aureus* and other pathogens. Our findings suggest that the current development could be considered a potential formulation of a protective nasal spray against respiratory infections.

Keywords: silver nanoparticles; chlorhexidine; Kolliphor P407; thermogelation; phase transition; sol–gel transition; protective nasal spray; respiratory infections; prophylaxis; virucidal activity

1. Introduction

In situ gelling pharmaceutical formulations find broad application as drug delivery systems when prolongation of the retention time at the site of administration is required to improve the therapeutic result. Upon reaching the designated biological compartment, these polymeric systems undergo sol-to-gel transition initiated by different stimuli such as changes in the temperature, pH, ionic environment, or others [1–3]. Thereby, they ensure drug immobilization into a highly viscous layer, adherence to the target region, and a sustainable effect. The usage of in situ gelling vehicles is highly appropriate in the development of nasal dosage forms for local, systemic, or nose-to-brain drug delivery [1,4–6].

The protective nasal formulations are a subject of growing interest in this post-COVID-19 pandemic period [7]. Since society's self-awareness of complying with the public health culture principles was provoked, scientists have become more and more engaged in developing new, alternative, and more efficient ways for reducing the spread of infectious respiratory diseases [8]. The protective nasal sprays may exhibit different mechanisms of action, but, in general, they concentrate on supporting the natural defense capacity of the nasal mucosa, enhancing the biophysical barrier function of the mucus, and/or exerting microbicidal activity at the site of the pathogen's entry [9]. An effective protective nasal formulation is required to possess good sprayability; to form stable, even, and retentive film on the mucosa; to not harm the nasal cilia; and to preserve the active ingredients' activity by ensuring physical and chemical stability, compatibility, and adequate drug liberation [1,9].

The thermo-sensitive Poloxamer 407 (poly(ethylene oxide)-poly(propylene oxide)-poly(ethylene oxide) triblock copolymer)—P407—was selected as the main constituent in the composition of in situ gelling nasal spray for protection against respiratory infections. The polymer is known for its low toxicity, good tolerability, great chemical inertness, and drug–polymer compatibility [2,10]; because of its amphiphilic nature, P407 self-assembles into micelles, which aggregate with the increase in temperature and forms a crystal network (micelles order into a hexagonal crystalline packing and form a solid gel) [11,12]. The gelation temperature (T_g) of P407 solutions depends on the polymer's concentration and the presence of additives such as active pharmaceutical ingredients and excipients [11]; in any case, the gelation of P407 $\geq 15\ w/w\%$ aqueous solutions occurs in a temperature range appropriate for biomedical applications [13,14].

Often, P407 is combined with other polymers in order to improve the formulation's adhesiveness and gel strength (e.g., cellulose derivatives, chitosan, carbomer, and poly(vinyl)pyrrolidone) [14,15]. In this study, we focused on hydroxypropyl methylcellulose (HPMC)—a polymer with thermoreversible gelation manifesting at much higher than physiological temperature (>65 °C) but with good bioadhesive properties [14,16,17]. It was hypothesized that a P407-HPMC combination could be obtained with eligibility for nasal application, adhesive properties, low viscosity, good sprayability at the ambient temperature, and gelation point in the temperature range of the nasal cavity (30–34 °C) [4,18].

Ultimately, this study aimed to result in the establishment of a suitable vehicle for the nasal delivery of chlorhexidine–silver nanoparticles conjugates (SN-CX) as an active ingredient. SN-CX were previously synthesized in our laboratories and characterized with explicit antimicrobial properties against Influenza Type A, *Staphylococcus aureus, Escherichia coli*, and *Candida albicans* [19]. Our ongoing research follows the activity of SN-CX against these and other respiratory pathogens (seasonal beta-coronavirus, *Pseudomonas aeruginosa,* and *Klebsiella pneumoniae*) when in the composition of the co-polymeric solution and the biopharmaceutical characteristics of so-obtained nasal spray. Although several research papers have reported the inclusion of silver nanoparticles (SN) into P407-based thermogelling vehicles [20–25], the mechanisms by which nano-silver colloids interfere with the P407 micellization and gelation have not yet been widely explored. We attempted a stepwise investigation of the SN-CX impact on the micellar arrangement and point of solidification of P407 hydrosols and combined P407-HPMC hydrosols.

2. Results and Discussion

2.1. Optimization of the In-Situ Gelling Nasal Composition Based on Viscosimetry, T_g, Textural, and Colloidal Properties

2.1.1. Viscosimetry

The viscosimetry revealed an increase in viscosity and a sol–gel transition with the rise in temperature up to 45 °C for all test formulations; exceptions were made for the HPMC 0.5% solutions, whose inherent temperature-dependent viscosity was not significantly affected by the presence of SN-CX (within the test temperature range), and the P407 15.5% solutions, combined with HPMC. P407 20% hydrosol was found to undergo gelation at 22.7 °C, while P407 20% hydrosol containing conjugates of silver nanoparticles with chlorhexidine (SN-CX) solidified at 26.1 °C. There are very few reports in the literature that we could relate this result to. Although widely formulated within Poloxamer-containing drug delivery vehicles, to the best of our knowledge, neither form of silver nanoparticles has yet been investigated with respect to interaction with the polymer's gelation. However, several surveys on other types of nanoparticles in Poloxamer formulations and their effects on gelation are available, and expectedly, they report divergent trends [26]. For example, poly(isobutyl cyanoacrylate) (PIBCA) nanoparticles coated with a mixture of chitosan and thiolated chitosan did not show substantial influence on P407 gelation in the study of Pradines et al. [27]; Laponite-silicate nanoparticles [28], chitosan nanoparticles [29], and ZnO nanoparticles [30] were demonstrated to lower T_g and/or improve the strength of poloxamer gels, while solid lipid nanoparticles (SLN) increase the T_g [31].

HPMC 0.1%-enriched P407 solutions showed a decrease in T_g as compared to pure P407 solutions with the same concentration. These findings are in accordance with other reports from original studies on the subject [2,14,32,33].

Based on the results from this primary screening, the test formulations were obtained by mixing stock solutions of both hydrosols—P407 20% and HPMC 0.5%—in varying ratios; upon this procedure, formulations with gradiently dropping P407 and raising HPMC concentrations were yielded. As the proportion of the HPMC hydrosol in the formulation increased, expectedly, gelation was observed at higher temperatures due to the stepwise dilution of the P407 hydrosol [33]. Interestingly, when SN-CX was present in the mixtures, a lower gelation point was recorded at all P407-HPMC ratios (Figure 1).

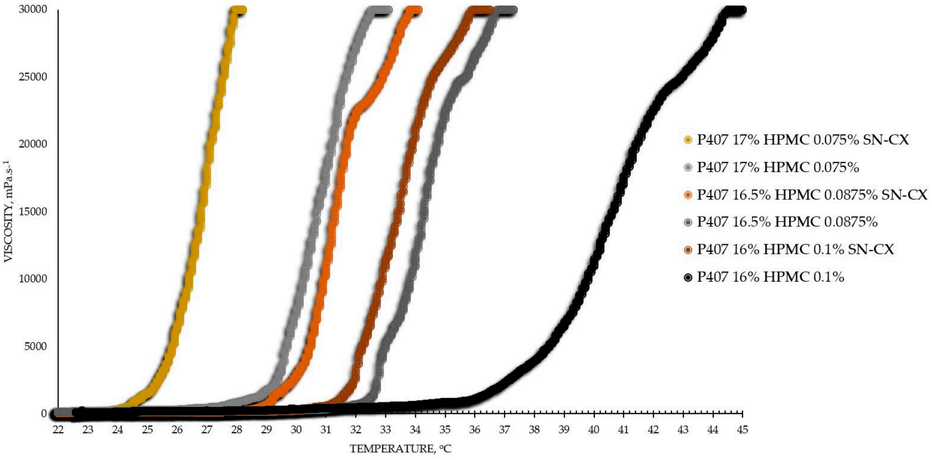

Figure 1. Viscosity–temperature curves of SN-CX-loaded and drug-unloaded P407-HPMC test formulations.

As a practical contribution of this analysis, the formulation P407 16% HPMC 0.1% SN-CX was selected as an appropriate in situ gelling formulation for nasal administration because of its favorable T_g at 31.9 °C; the temperature in the nasal cavity is reported to be in the range of 30–34 °C [4,18]. Furthermore, the formulation in question was characterized as suitable for spaying low viscosity at room temperature (120 mPa.s, Table 1) [4].

From an analytical point of view, we found that separately, SN-CX increased the T_g of P407, and HPMC decreased it. Still, when applied to a combined P407-HPMC solution, the colloidal particles further potentiated the gelation and decreased the T_g. To investigate these phenomena, a DLS analysis was performed, and a mechanism for the occurrence of this controversy was proposed (Figures 2 and 3).

Table 1. Viscosity, T_g, DLS analysis, and textural analysis of the test formulations.

Formulation	Viscosity (25 °C), mPa·s ± SD	T_g, °C	DLS at 15 °C				Texture Analysis at 34 °C			pH
			Z-Average, nm ±SD	Diffusion Coefficient, $\mu m^2 \cdot s^{-1}$ ± SD	d_{90} ±SD	Span ±SD	Firmness, g ± SD	Adhesiveness, g·s ± SD	Cohesiveness, g·s ± SD	
P407 20%	>29 999	22.7	28.85 ± 2.13	12.79 ± 0.83	4.37 ± 0.53	0.47 ± 0.021	109.33 ± 22.09	23.03 ± 7.26	135.43 ± 29.94	6.5
HPMC 0.5%	4.87 ± 0.09	n.a.	412.07 ± 35.26	0.90 ± 0.05	478.28 ± 51.92	0.52 ± 0.022	n.a.	n.a.	n.a.	n.a.
P407 17% HPMC 0.075%	258.31 ± 14.69	29.2	n.a.	n.a.	n.a.	n.a.	n.a.	n.a.	n.a.	n.a.
P407 16.5% HPMC 0.088%	161.45 ± 13.07	32.3	n.a.	n.a.	n.a.	n.a.	n.a.	n.a.	n.a.	n.a.
P407 16% HPMC 0.1%	130.27 ± 2.84	38.0	170.04 ± 20.77	2.17 ± 0.15	4.38 ± 0.53	0.53 ± 0.026	110.67 ± 10.84	24.97 ± 4.58	119.53 ± 14.29	6.0
P407 15.5% HPMC 0.113%	60.00 ± 0.00	>45	n.a.	n.a.	n.a.	n.a.	n.a.	n.a.	n.a.	n.a.
P407 16%	30.53 ± 3.97	43	n.a.	n.a.	n.a.	n.a.	n.a.	n.a.	n.a.	n.a.
SN-CX	n.a.	n.a.	394.84 ± 42.86	0.93 ± 0.06	344.05 ± 42.02	0.50 ± 0.020	n.a.	n.a.	n.a.	n.a.
P407 20% SN-CX	7 011.64 ± 1125.73	26.1	77.12 ± 5.80	4.78 ± 0.27	4.76 ± 0.42	0.67 ± 0.025	100 ± 16.97	20.9 ± 7.50	113.33 ± 17.96	6.0
HPMC 0.5% SN-CX	4.67 ± 0.15	n.a.	864.52 ± 60.39	0.43 ± 0.02	772.28 ± 83.84	0.51 ± 0.020	n.a.	n.a.	n.a.	n.a.
P407 17% HPMC 0.075% SN-CX	1664.15 ± 713.43	25.3	n.a.	n.a.	n.a.	n.a.	n.a.	n.a.	n.a.	n.a.
P407 16.5% HPMC 0.088% SN-CX	147.87 ± 7.83	29.5	n.a.	n.a.	n.a.	n.a.	n.a.	n.a.	n.a.	n.a.
P407 16% HPMC 0.1% SN-CX	120.00 ± 0.00	31.9	655.54 ± 71.16	0.56 ± 0.04	694.93 ± 84.87	0.65 ± 0.029	105.33 ± 5.57	24.83 ± 3.18	115.77 ± 14.14	6.0
P407 15.5% HPMC 0.113% SN-CX	30.00 ± 0.00	>45	n.a.	n.a.	n.a.	n.a.	n.a.	n.a.	n.a.	n.a.

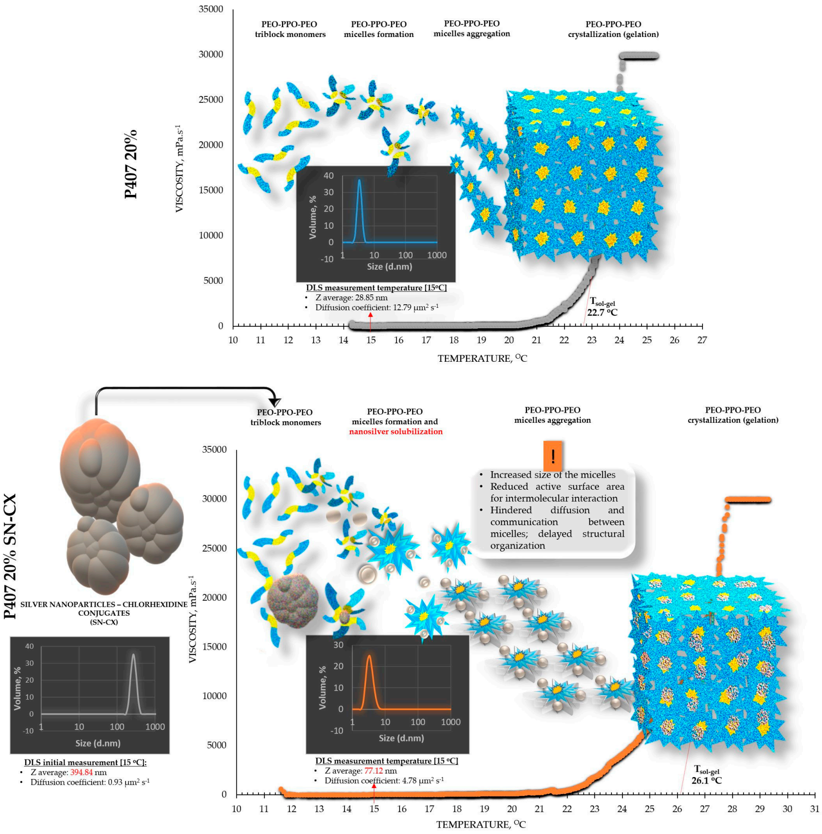

DLS measurement temperature [15°C]
- Z average: 28.85 nm
- Diffusion coefficient: 12.79 μm² s-1

DLS initial measurement [15 °C]:
- Z average: 394.84 nm
- Diffusion coefficient: 0.93 μm² s-1

DLS measurement temperature [15 °C]
- Z average: 77.12 nm
- Diffusion coefficient: 4.78 μm² s-1

- Increased size of the micelles
- Reduced active surface area for intermolecular interaction
- Hindered diffusion and communication between micelles; delayed structural organization

Figure 2. Speculative illustration of the mechanism of gelation of P407 sols and SN-CX-loaded P407 sols.

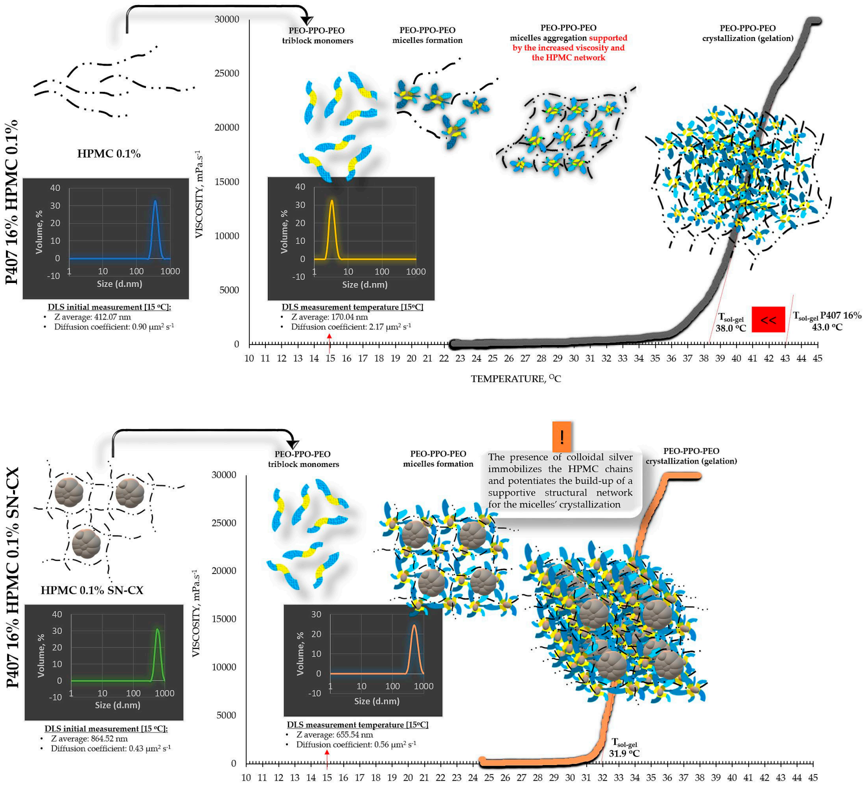

DLS initial measurement [15 °C]:
- Z average: 412.07 nm
- Diffusion coefficient: 0.90 μm² s-1

DLS measurement temperature [15°C]
- Z average: 170.04 nm
- Diffusion coefficient: 2.17 μm² s-1

DLS initial measurement [15 °C]:
- Z average: 864.52 nm
- Diffusion coefficient: 0.43 μm² s-1

DLS measurement temperature [15°C]
- Z average: 655.54 nm
- Diffusion coefficient: 0.56 μm² s-1

The presence of colloidal silver immobilizes the HPMC chains and potentiates the build-up of a supportive structural network for the micelles' crystallization

Figure 3. Speculative illustration of the mechanism of gelation of P407-HPMC combined sols and SN-CX-loaded P407-HPMC combined sols.

2.1.2. Dynamic Light Scattering (DLS)

DLS analysis was carried out for all single components and mixtures of interest. A decision was made to perform the tests at a temperature low enough to ensure a sol state of all samples—15 °C. The results from the front angle (12.78°) scans were considered as they demonstrated eligibility for comparative purposes for all materials. Under these conditions, the hydrodynamic diameter (d_H, Z-average, nm) of the colloidal SN-CX conjugates was found to be 394.84 ± 42.86 nm; visibly, d_H drastically decreased when the nanoparticles were introduced into the P407 20% solution (77.12 ± 5.80 nm), thus suggesting micelle-assisted solubilization and localization amongst the hydrophilic P407 regions [34,35]; solubilization in the hydrophobic micellar cores is unlikely because of the prevailingly hydrophilic nature of the superficial silver ions and chlorhexidine diacetate. On the contrary, when the same concentration of SN-CX was included in an HPMC 0.5% solution, a more than two-fold increase in d_H (864.52 ± 60.39 nm) revealed adsorption of the negatively charged polymer (−) onto the positive (+) colloidal surface of SN-CX (ζ = +44.59 [19,36]). Indeed, the visual appearance of both SN-CX-carrying solutions was compliant with this result since P407 20% SN-CX appeared as a fully transparent yellow solution, while HPMC 0.5% SN-CX possessed an orange-brown color and a slight opalescence. When SN-CX was placed in a combined solution of P407 16%-HPMC 0.1%, the obtained d_H values of 655.54 ± 71.16 nm eloquently testified that the silver nanoparticles' solubilization is limited by the HPMC shield on the particles' surface and their respective enlargement.

The colloids' diffusion coefficients were derived because of their straight relation to the particles' mobility, interaction, and ability to assemble into organized structures (determining the point of gelation); they were all found to correspond well with the average hydrodynamic size in the system. Because of the complexity and heterogeneity of the colloidal mixtures, d_{90} and span values were also considered; the first parameter indicates the size limit within the predominant part of 90% of the sample, while the latter is a measure of the size distribution within the sample (span = $(d_{90} - d_{10})/d_{50}$). The interpretation of d_{50} and d_{10} is analogous with $d_{90.}$ Although all test formulations were of a complex nature and obtained by mixing different-sized colloids, the resulting samples exhibited a low span value of <0.7, indicating a relatively narrow size distribution within the sample's volume. All data from the DLS analysis are presented in Table 1.

Based on the viscosimetry and DLS results, the following suggestions were made to explain the observed gelation phenomena: 1. When SN-CX are added to P407 hydrosol, they are shown to solubilize and therefore lead to an increased size of the micelles; thus, the active surface area for intermolecular interaction is reduced, the diffusion and communication between the micelles is hindered, delayed structural organization and gelation at higher temperature is observed; 2. When HPMC is added to P407 hydrosol, the latter crystallizes at a lower temperature, likely due to an increase in viscosity and structural support of the micellar organization by the HPMC chains [14,32]; 3. When SN-CX are added to P407-HPMC combined hydrosols, our results suggest the occurrence of two events: a. the negatively charged HPMC adsorbs on the positively charged SN-CX and prevents their micellar solubilization; b. the presence of colloidal silver immobilizes the HPMC chains and potentiates the build-up of a supportive structural network for the micelles' crystallization.

2.1.3. Texture Analysis

HPMC was chosen as a second polymeric ingredient in the thermo-gelling nasal vehicle in order to improve the formulation's adhesiveness and gel strength. When P407 20% and HPMC 0.5% solutions were mixed in an 80:20 ratio (in order to form a vehicle with an appropriate gelation point—31.9 °C), a final concentration of P407 16% HPMC 0.1% was obtained. Textural analysis of P407 20% and P407 16% HPMC 0.1% in the presence and absence of SN-CX was performed. Although the addition of HPMC solution decreased the P407 concertation from 20% to 16%, it was proven to not only retain but also slightly increase the firmness and adhesiveness of the formed gel at 39 °C while reducing the cohesiveness. The same observation was made in the presence of SN-CX, except for the cohesiveness; the latter was relatively lower for SN-CX-enriched gels as compared to the drug-unloaded gels and was not significantly different for both P407 20% SN-CX and P407 16% HPMC 0.1% SN-CX formulations. This result is likely due to the hypothesized conformational changes in the system caused by the integration of silver nanoparticles in the hydrophilic micellar regions and corresponds with the observed effect of SN-CX on P407 gelation. In addition, the presence of SN-CX weakly reduced the firmness and adhesiveness of both test gels as well, as compared to the drug-unloaded analogs (Figure 4, Table 1).

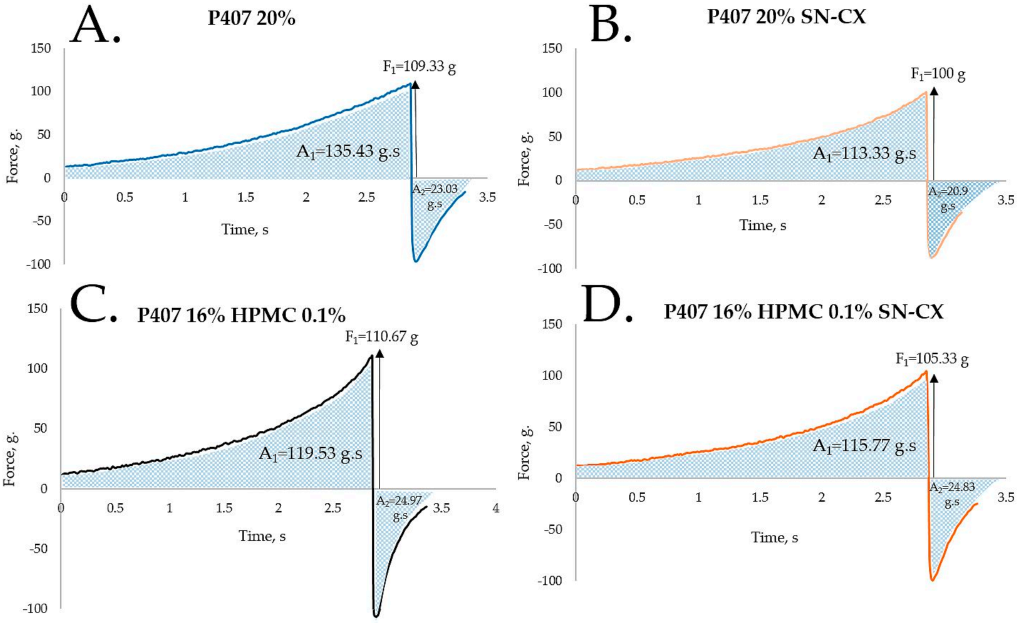

Figure 4. Texture analysis of (**A**) P407 20% hydrogel, (**B**) P407 20% SN-CX hydrogel, (**C**) P407 16% HPMC 0.1% hydrogel, and (**D**) P407 16% HPMC 0.1% SN-CX hydrogel at 34 °C.

2.2. Sprayability

The proposed nasal formulation—P407 16% HPMC 0.1% SN-CX—was tested against a water solution in order to follow the influence of the polymeric mixture on the solution's ability to be sprayed and spread along the anterior nasal cavity. This was carried out using an original methodology for the purpose, and the obtained results testify to its applicability for comparative purposes. Both the test and the control samples were colored in advance with a water-soluble red dye so that the sprayed-on material could be color-analyzed. The loss of sprayability due to an increased viscosity of the test formulation was calculated to be only 12.55% as compared to the performance of pure water injected with the same spraying device. This result was achieved after three-in-a-row injections of the formulations in the nasal cavity model. We should acknowledge that the difference in the covered area between the test and control spray was greater and not as satisfactory when one or two-in-a-row injections were applied. An advantage of the polymeric solution was the better retention on site and the lack of leakage to the throat. It should be noted that the proposed methodology did not allow simulation and consideration of the airflow forces arising upon the recommended sharp inhale while spraying in the nose. We reckon that this method of sprayability testing could be applied as an easy and affordable to reproduce alternative technique in the process of pharmaceutical development; this should be only carried out when better simulation models (such as 3D printed nasal casts or software-assisted models for digital simulations [37,38]) are not available. The results from the sprayability test are presented in Figure 5. Color analysis was performed, as shown in Figure 6.

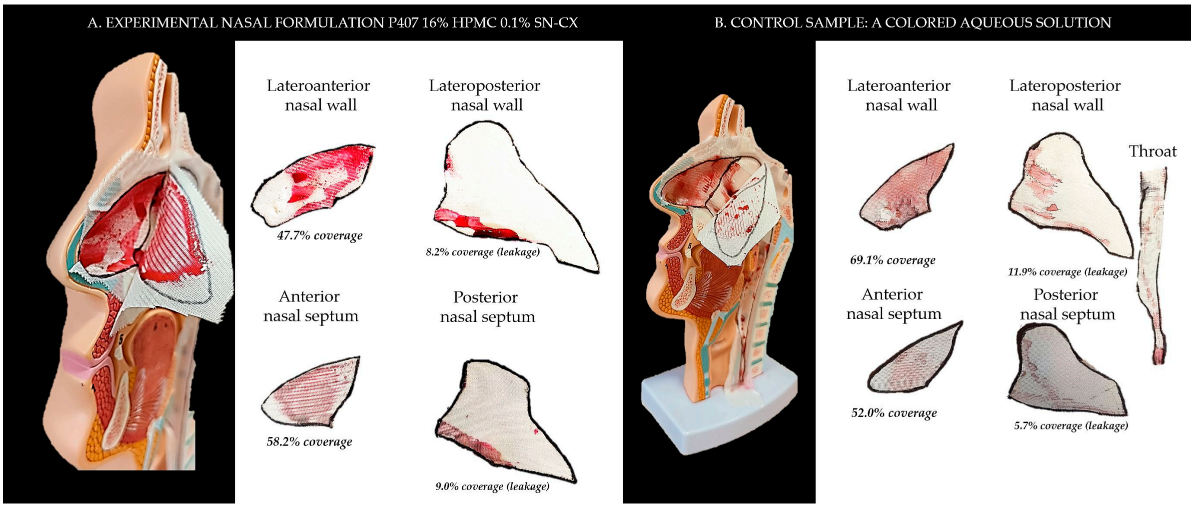

Figure 5. Sprayability of (**A**) P407 16% HPMC 0.1% SN-CX against (**B**) colored water solution, assessed by the area covered (%) in a simulated nasal cavity model: the role of the delivery vehicle.

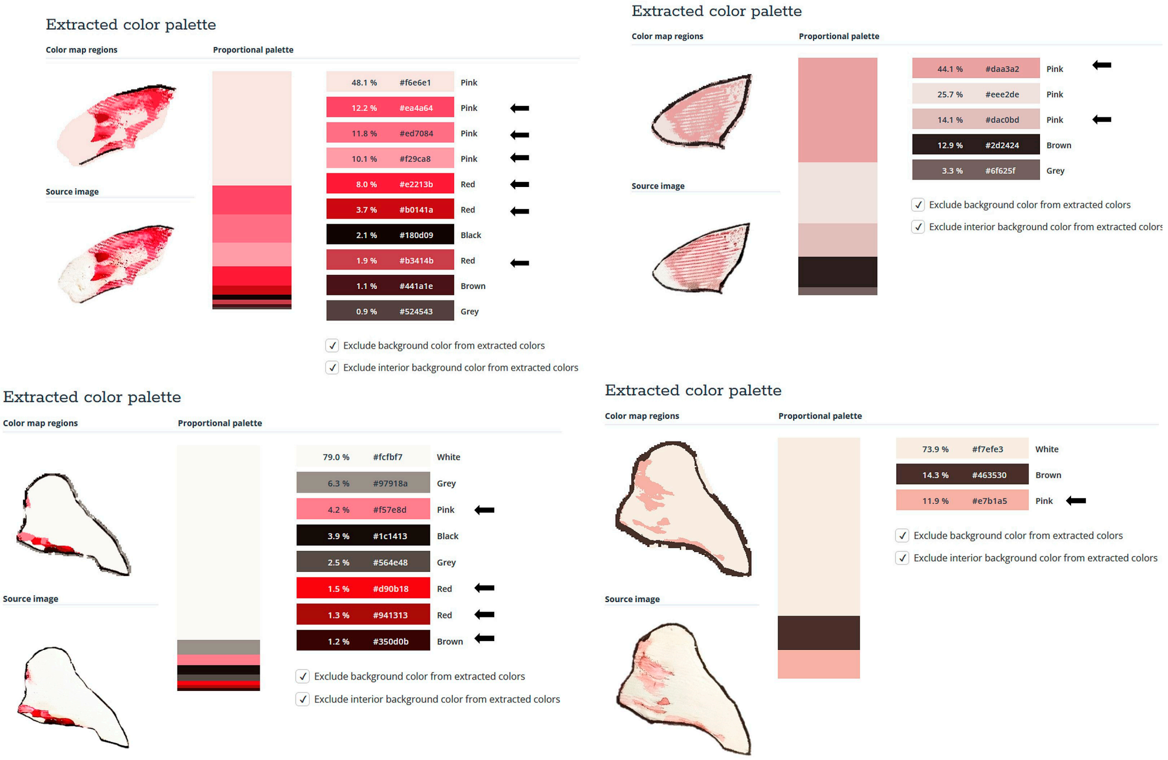

Extracted color palette

48.1 %	#f6e6e1	Pink	
12.2 %	#ea4a64	Pink	←
11.8 %	#ed7084	Pink	←
10.1 %	#f29ca8	Pink	←
8.0 %	#e2213b	Red	←
3.7 %	#b0141a	Red	←
2.1 %	#180d09	Black	
1.9 %	#b3414b	Red	←
1.1 %	#441a1e	Brown	
0.9 %	#524543	Grey	

☑ Exclude background color from extracted colors
☑ Exclude interior background color from extracted colors

Extracted color palette

44.1 %	#daa3a2	Pink	←
25.7 %	#eee2de	Pink	
14.1 %	#dac0bd	Pink	←
12.9 %	#2d2424	Brown	
3.3 %	#6f625f	Grey	

☑ Exclude background color from extracted colors
☑ Exclude interior background color from extracted colors

Extracted color palette

79.0 %	#fcfbf7	White	
6.3 %	#97918a	Grey	
4.2 %	#f57e8d	Pink	←
3.9 %	#1c1413	Black	
2.5 %	#564e48	Grey	
1.5 %	#d90b18	Red	←
1.3 %	#941313	Red	←
1.2 %	#350d0b	Brown	←

☑ Exclude background color from extracted colors
☑ Exclude interior background color from extracted colors

Extracted color palette

73.9 %	#f7efe3	White	
14.3 %	#463530	Brown	
11.9 %	#e7b1a5	Pink	←

☑ Exclude background color from extracted colors
☑ Exclude interior background color from extracted colors

Figure 6. Color analysis of sprayed and dried artificial tissues performed online at https://labs.tineye.com (accessed on 1 February 2024).

2.3. Washout Time/Mucosal Retention

In this study, we aimed to emphasize the role of HPMC in the composition and compared the mucosal retention of the optimized nasal formulation—P407 16% HPMC 0.1% SN-CX—with the one of P407 20% SN-CX. This was carried out upon vertical positioning and fixation of the mucosal tissue and under simulated nasal flow. The time to complete washout was recognized with the aid of methylene blue dye added to the samples in advance. For P407, 20% SN-CX, it was registered to be approximately 40 min, and for P407, 16% HPMC 0.1% SN-CX—70 min. The photographs in Figure 7 demonstrate the beginning and end points of the experiment and the washout zone determined by the path of the drops.

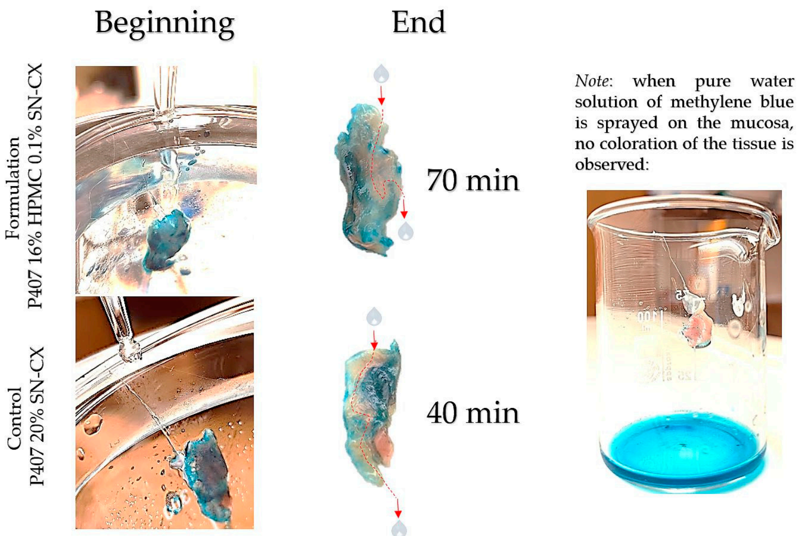

Note: when pure water solution of methylene blue is sprayed on the mucosa, no coloration of the tissue is observed:

Figure 7. Washout zone and retention time of test formulation P407 16% HPMC 0.1% SN-CX against control formulation P407 20% SN-CX: the role of the mucoadhesive HPMC polymer.

Since warm water (34 °C) was used as a washing fluid in this test and a flow rate comparable to the average physiological nasal secretion debit was maintained (2000 mL per day) [39], we may reckon that the obtained results relate to an extreme case scenario in which the nasal mucus would acquire a viscosity comparable to water under high shear rates typical for sniffing, sneezing, etc. [40].

2.4. In Vitro Drug Release and Ex Vivo Mucosal Permeation

The drug liberation from P407 16% HPMC 0.1% SN-CX and the actual permeation through nasal mucosa did not show any notable differences of practical significance. Indeed, the ex vivo study allowed a higher concentration of silver ions in the receptor compartment as compared to the quantity released through the artificial dialysis membrane. Most importantly, neither of the membranes allowed permeation of silver nanoparticles; likely due to the complex structure and the larger hydrodynamic diameter of the nanoparticles in the composition, SN-CX were still undetectable in the receptor media by UV-Vis spectrophotometry after the 3rd hour of the experiments. Despite the broad-spectrum activity, the lack of biodegradation of silver nanoparticles is considered the main disadvantage of this type of nanotechnology [41]. Hence, this result fits a desired case scenario—formulated SN-CX release their active components, i.e., chlorhexidine and silver ions, by dissociation and degradation, respectively, but do not penetrate the mucosa and do not set a prerequisite for cumulation and absorption into the bloodstream (Figure 8).

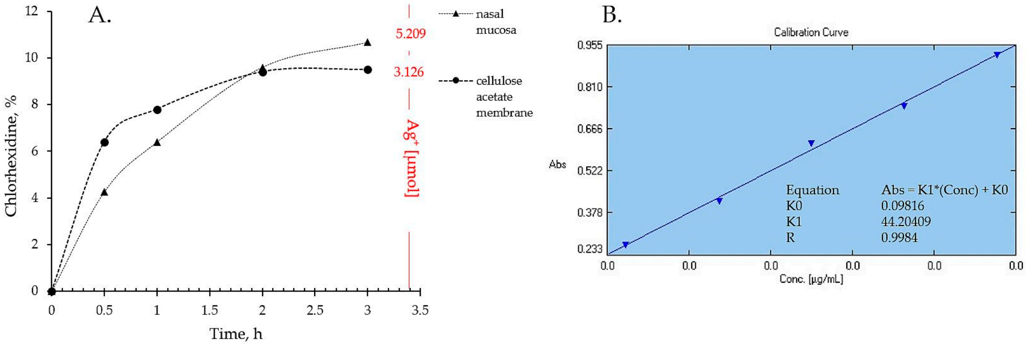

Figure 8. (**A**) Drug liberation and mucosal permeation from P407 16% HPMC 0.1% SN-CX formulation; (**B**) calibration curve of chlorhexidine diacetate in purified water.

2.5. Antimicrobial Activity

2.5.1. Antibacterial and Antifungal Activity

The SN-CX conjugates were previously proven with antimicrobial activity against *S. aureus*, *C. albicans*, and *E. coli*, and minimal bactericidal/fungicidal concentrations were found at 28.6 $\mu g \cdot mL^{-1}$, 28.6 $\mu g \cdot mL^{-1}$, and 14.3 $\mu g \cdot mL^{-1}$, respectively (these values relate to the total active concentration of silver nanoparticles plus the equivalent concentration of chlorhexidine linked) [19]. These results were taken into consideration when choosing the active concentration in the nasal formulation (57.19 $\mu g \cdot mL^{-1}$). Herein, the antimicrobial potency of SN-CX was assessed within the polymeric solution and compared with the activity of the non-formulated SN-CX colloid. To the test pathogens were added *Pseudomonas aeruginosa* and *Klebsiella pneumoniae* because of their high relevance to respiratory infections and complications [42,43]. Judging by the zones of inhibition on Mueller–Hinton agar, P407 16% HPMC 0.1% SN-CX demonstrated the strongest antimicrobial activity against *C. albicans* (d = 21 mm), followed by *K. pneumoniae* (d = 20 mm), *S. aureus* (d = 17 mm), *P. aeruginosa* (d = 14 mm), and *E. coli* (d = 12 mm). The zones of inhibition obtained with the pure SN-CX solution at the same concentration were found to be either the same or not more than 2 mm wider as compared to the ones achieved with the SN-CX-loaded nasal formulation (Figure 9, Table 2). Such a slightly decreased effect is expected upon the application of viscous dosage forms due to a retarded drug release and diffusion [44].

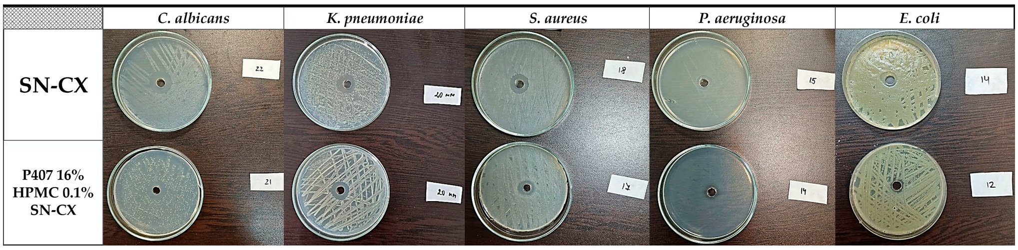

Figure 9. Inhibitory zones of P407 16% HPMC 0.1% SN-CX and SN-CX in seeds of *P. aeruginosa*, *K. pneumoniae*, *S. aureus*, *C. albicans*, and *E. coli*.

Table 2. Inhibitory zones of P407 16% HPMC 0.1% SN-CX and SN-CX in seeds of *P. aeruginosa*, *K. pneumoniae*, *S. aureus*, *C. albicans*, and *E. coli*.

Pathogen	P407 16% HPMC 0.1% SN-CX, mm	SN-CX, mm
C. albicans	21	22
K. pneumoniae	20	20
S. aureus	17	18
P. aeruginosa	14	15
E. coli	12	14

2.5.2. Antiviral and Virucidal Activity

In order to be able to claim that the effect of the test sample on the cell monolayer during the antiviral experiments is due to viral replication, but not to the cytotoxicity, its cytotoxicity against the cell lines was previously determined. When examining the toxicity of P407 16% HPMC 0.1% SN-CX against the HCT-8 cell line over a period of 120 h (the time required to determine the antiviral effect in the HCov-OC-43 strain), it was found that the test sample was significantly more cytotoxic compared to the reference substance Remdesivir (REM) used (Table 3).

Regarding cytotoxicity evaluation in MDCK cells, P407 16% HPMC 0.1% SN-CX showed considerably higher toxicity than the reference oseltamivir (OS) 450 $\mu g \cdot mL^{-1}$. These data are in accordance with our previous report on SN-CX toxicity, although, herein, in the polymeric milieu, the toxicity against MDCK cells slightly decreases (Table 4) [19].

Table 3. Cytotoxicity of the test sample P407 16% HPMC 0.1% SN-CX against the HCT-8 cell line.

Compound	**HCT-8 Cell Line**	
	CC_{50} [a] Mean ± SD [b] [$\mu g \cdot mL^{-1}$]	**MTC [c] [$\mu g \cdot mL^{-1}$]**
P407 16% HPMC 0.1% SN-CX	47.5 [d] ± 2.8	9.2 [d]
REM	2500.0 ± 4.3	1000.0

[a] CC_{50}—cytotoxic concentrations 50%; [b] SD—standard deviation; [c] MTC—maximum tolerable concentration; [d] total active concentration silver nanoparticles plus the equivalent concentration of chlorhexidine.

Table 4. Cytotoxicity of the test sample P407 16% HPMC 0.1% SN-CX against MDCK cell line.

Compound	**MDCK Cell Line**	
	CC_{50} [a] Mean ± SD [b] [$\mu g \cdot mL^{-1}$]	**MTC [c] [$\mu g \cdot mL^{-1}$]**
P407 16% HPMC 0.1% SN-CX	4.68 [d] ± 2.8	3.0 [d]
SN-CX [19]	4.20 [d] ± 0.6 [19]	-
OS	450.0 ± 1.3	360.0

[a] CC_{50}—cytotoxic concentrations 50%; [b] SD—standard deviation; [c] MTC—maximum tolerable concentration; [d] total active concentration of silver nanoparticles plus the equivalent concentration of chlorhexidine bound

When determining the effect on the replication of HCov-OC-43 and IAV A/Panama/07/99 (H3N2), it was found that P407 16% HPMC 0.1% SN-CX, like pure SN-CX, had no effect on this stage of viral reproduction compared to REM (IC_{50} = 12.5 ± 0.9 $\mu g \cdot mL^{-1}$; selectivity index (SI) = 200.0) and OS (IC_{50} = 1.8 $\mu g \cdot mL^{-1}$; SI = 250).

The virucidal effect (effect on the viability of extracellular virion particles of corona and influenza virus) of P407 16% HPMC 0.1% SN-CX at its MTC was also investigated. It was found that in the first two incubation time intervals (15 and 30 min), the effect was low and comparable for both viruses (up to 1 Δlg). It slightly increased with the extension of the exposure time, and at 60 min, the viability of HCov-OC-43 and influenza virions was reduced by Δlg = 1.5 and Δlg = 1.25, respectively (Tables 5 and 6).

Table 5. Virucidal activity against coronavirus virions strain HCoV-OC-43.

Compound	**Δlg**			
	15 Min	**30 Min**	**45 Min**	**60 Min**
P407 16% HPMC 0.1% SN-CX	0.25	0.75	1.25	1.50
Ethanol 70%	5.0	5.0	5.0	5.0

Table 6. Virucidal activity against influenza virus virions strain A/Panama/07/99 (H3N2).

Compound	**Δlg**			
	15 Min	**30 Min**	**45 Min**	**60 Min**
P407 16% HPMC 0.1% SN-CX	0.25	0.50	1.00	1.25
SN-CX [19]	0	0	0.33	0.33
Ethanol 70%	4.0	4.0	4.0	4.0

The registered virucidal effect against corona and influenza virus is present but weak (compared to standard ethanol 70%) due to the very low MTC of the formulation on HCT-8 and MDCK cell lines. The latter drastically limits the active concentrations to be applied and tested. Still, the obtained results show an increase in the virucidal potency of the nasal formulation in comparison to non-formulated SN-CX [19].

3. Conclusions

An in situ gelling vehicle composed of P407 and HPMC for the nasal drug delivery of silver nanoparticles–chlorhexidine conjugates (SN-CX) was developed, and the effects of this active complex on the formulation's thermo-gelling and mechanical properties were investigated. A DLS-based analysis allowed us to propose a mechanism for the arising phenomena, which, namely, were 1. SN-CX's undergo solubilization in the P407 sols and suppress the micelles' crystallization, which leads to an increase in the gelation temperature; 2. HPMC potentiates the P407 gelation, and their mixture acquires lower gelation temperature compared to only P407-containing sols with corresponding concentrations; 3. When SN-CX and HPMC are both present in the composition of the P407 hydrosols, an additional potentiation of the gelation of P407 is observed, and thus even lower gelation temperatures are registered. This interesting finding could be explained by the SN-CX's significantly enlarged hydrodynamic size when HPMC adsorbs on their surface and the subsequent lack of micellar solubilization. Because of these findings, we hypothesized that instead of acting as a conformational obstacle for the micelles' organization, SN-CX structurally supports the HPMC-mediated intermolecular communication within the P407-HPMC solutions.

Within the scope of this study, we propose two original methodologies for comparative sprayability assessment and comparative mucosal retention time assessment. Both methodologies are easily reproducible and do not require specific and expensive equipment. Therefore, we consider they could be used as accessible alternatives in the stages of preliminary nasal dosage forms development.

The optimized drug-loaded P407 16% HPMC 0.1% SN-CX test nasal formulation possessed several desirable qualities for its designation: a gelation temperature at 31.9 °C; a better adhesiveness and mucosal retention as compared to P407 compositions without HPMC; a good sprayability ensuring a 52.95% coverage of the anterior nasal cavity; an effective Ag^+ and chlorhexidine release and mucosal permeation to which we devote the established antimicrobial activity against *Pseudomonas aeruginosa, Klebsiella pneumoniae, Staphylococcus aureus*, *Escherichia coli*, and *Candida albicans* and the weak but present after the 45th minute of contact virucidal effect on influenza and coronavirus virions. According to this study, the proposed formulation has shown eligibility for in situ gelling protective nasal spray on all aspects. As a prospect, an improvement might be sought in terms of lower colloidal size and an even less pronounced shielding effect on antiviral activity.

4. Materials and Methods

4.1. Materials

Silver nitrate (>99.9%), sodium hydroxide (>98%), and ammonium thiocyanate (>98%) were supplied from Thermo Fisher Scientific, Oxford, UK. Chlorhexidine diacetate salt hydrate (≥98%, Mw 625.55 g/mol) was purchased from Sigma Aldrich, Burlington, MA, USA; Kolliphor® P407, hydroxypropyl methylcellulose (HPMC) (80–120 cps), and Ammonium iron(III) sulfate dodecahydrate were obtained from Sigma-Aldrich, St. Louis, MO, USA; all organic solvents were supplied from Sigma-Aldrich, St. Louis, MI, USA in analytical grade.

4.2. Silver Nanoparticles–Chlorhexidine Conjugates (SN-CX)

Aqueous solutions of $AgNO_3$ at 2 mM were reduced with green tea-derived phenolic fraction, and silver nanoparticles were obtained; further, the latter were conjugated with chlorhexidine diacetate (CX) following an already established procedure [19,43]. The obtained colloidal solutions were purified by a dialysis method and standardized with a concentration of 700 $\mu g \cdot mL^{-1}$ nano-silver and 1130 $\mu g \cdot mL^{-1}$ conjugated CX [19]. The total active concentration of the stock SN-CX solution was considered the sum of SN and CX—1830 $\mu g \cdot mL^{-1}$. SN-CX samples were stored at room temperature under light protection and used within a safe period of 7 days [45].

4.3. Preparation of In Situ Gelling Test Formulations

A stock solution of P407 20% *w/w* was prepared by dispersing the polymer in purified water under static conditions, keeping the so-obtained mixture in a refrigerator for at least 24 h, and gentle homogenization thereafter. Where needed, P407 16% *w*/*w* solution was prepared from P407 20% *w*/*w* stock solution by proper dilution.

A stock solution of HPMC 0.5% *w*/*w* was prepared by dispersing the polymer in preheated purified water at 80 °C under continuous stirring, keeping the so-obtained mixture in a refrigerator for at least 24 h, and homogenization thereafter.

Stock solutions of SN-CX-enriched hydrosols with a concentration of 57.19 $\mu g \cdot mL^{-1}$ were prepared by the addition of SN-CX stock solution (3.13% *w*/*w*) to previously obtained with a re-calculated quantity of purified water hydrosols of P407 or HPMC so that the final polymeric concentration would be the same as for the drug-unloaded hydrosols—20% *w*/*w* for P407 and 0.5% *w*/*w* for HPMC, respectively.

All polymeric stock solutions were stored in a refrigerator before their use. The drug-unloaded test formulations were obtained by mixing stock solutions of P407 20% *w*/*w* and HPMC 0.5% *w*/*w* in varying ratios—90:10, 85:15, 80:20, and 75:25. SN-CX-loaded test formulations were obtained likewise by using SN-CX-enriched P407 20% *w*/*w* and HPMC 0.5% *w*/*w* stock hydrosols.

All samples that were subjected to antimicrobial studies were prepared under aseptic conditions in a laminar-flow box (UVT-B-AR, DNA/RNA UV-cleaner box, BIOSAN, Riga, Latvia) and with the aid of previously sterilized (autoclaved; 121 °C, 30 min) distilled water. All recommendations for aseptic pharmaceutical preparation were met.

4.4. pH Measurement

The pH of the test formulations was measured using Filtres Fioroni pH indicator paper (Filtres Fioroni, Yorkshire, UK), which has a pH measurement range of 5.0–9.0.

4.5. Viscosimetry

Viscosity analysis of the test formulations was performed on IKA® Rotavisc lo-vi, IKA®-Werke GmbH & Co. KG, Staufen, Germany. Spindle№ 4 (SP-4) was used at a rotation speed of 20 rpm, determining a viscosity range detection up to 30,000 mPa·s. The test samples were introduced in a large volume of 500 mL. The temperature was controlled with the aid of an external water bath, and the change in viscosity as a function of the actual sample's temperature was plotted. Values were registered up to 45 °C. The obtained data were processed using Microsoft Excel® (Microsoft office 2016 professional plus), and the gelation temperature was determined by the trend line passing the ascending region of the curve at minimum R^2 = 0.95 (the tangential), as shown in the example in Figure 10.

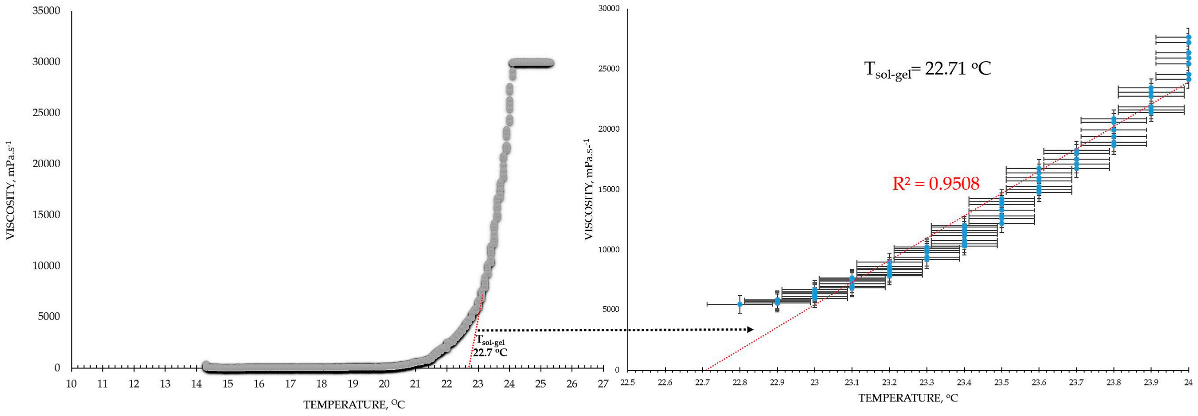

Figure 10. Mathematical extrapolation of the gelation temperature (T_g) based on the gelation curve's tangential [46–48].

Exception from this methodology made the viscosimetry of HPMC 0.5% solutions because of their significantly lower viscosity and lack of sol–gel transition in the investigated temperature interval. They were assessed with the aid of spindle SP-1 at 50 rpm, which allowed the best obtainable sensitivity in the expected low viscosity range.

The viscosity at 25 °C was calculated for all test formulations as an average of all viscosity values received in the temperature interval between 24.5 and 25.5 °C during the measurements.

4.6. Texture Analysis

The samples of interest were previously filled in appropriate for the test containers and tempered at 34 °C in a climatic chamber, Climatest CH 150, ArgoLab, Arezzo, Italy, for at least an hour. The texture analysis was performed on a Belle texture analyzer (Agrosta Overseas, Serqueux, France). The apparatus was equipped with a conical probe with a diameter of 40 mm. The motion of the probe was set at 3 $\text{mm}\cdot\text{s}^{-1}$ at pre-test and test runs; the insertion depth was 5 cm [49]. The means of three replicates were considered. The graphs were built based on the average values.

4.7. Dynamic Light Scattering (DLS)

Zetasizer Ultra Red, $\lambda = 632.8$ nm (Malvern Panalytical Ltd., Malvern, UK) was used for the DSL measurements. Multi-angle dynamic light scattering (MADLS) technique was applied at 15 °C. Data were processed and obtained using ZS XPLORER 3.2.0.84 software. Parameters such as average hydrodynamic diameter (d_H, Z-average), diffusion coefficient, d_{90}, and span were obtained. All measurements were repeated in triplicate.

4.8. Sprayability

The experimental setting for sprayability testing was built with the aid of a real-sized plastic 3D nasal cavity anatomical model. The surface from the inside was covered with a white synthetic silk surgical tape to allow retention and visibility of the sprayed formulation and removal of the tissue thereafter; the same material was applied as an improvised nasal septum. The four main zones of the nasal cavity, i.e., lateroanterior nasal wall, lateroposterior nasal wall, anterior septum, and posterior septum, were outlined with a black permanent marker. The spraying device was inserted in the nostril and the angles of spraying were determined thereof (Figure 11). The sprayability of the test nasal formulation was assessed against pure water solution; both the test and the control solutions were colored with a water-soluble red dye in advance so that a color analysis could be performed for estimation of the covered area. Each solution was sprayed thrice by using the same spraying device. At least an hour before spraying and right after spraying, the prepared nasal cavity model was kept at 34 °C in a climatic chamber, Climatest CH 150, ArgoLab, Italy. The artificial lining was removed after drying up the sprayed material, cut along the contours, and taped on a blank paper sheet in order for contrast photographs to be taken and color analyzed. The pictures were taken with a realme 11 Pro+ 32 MP camera without magnification. The color analysis was carried out with the aid of the online color extraction platform of TinEye https://labs.tineye.com/color/ (accessed on 1 February 2024). The ability of the formulation to be sprayed was evaluated by the percentage covered area. The loss of sprayability of the test formulation due to the increased viscosity was calculated as follows:

$$\frac{\textbf{Coverage of the lateroanterior nasal wall},\ \%\ (\textbf{Test}) + \%\ \textbf{Coverage of the anterior nasal septum},\ \%\ (\textbf{Test})}{\textbf{Coverage of the lateroanterior nasal wall},\ \%\ (\textbf{Control}) + \%\ \textbf{Coverage of the anterior nasal septum},\ \%\ (\textbf{Control})}\cdot\mathbf{100} \quad (1)$$

4.9. Isolation of Nasal Mucosa Explants

The method for nasal mucosa preparation was selected according to Wadell et al.'s methodology [50]. The tissues were obtained from the porcine snout of a pig weighing 80–90 kg and aged 7–8 months in a certified slaughterhouse (Varna, Bulgaria). The snout was opened by pathologists using forceps and a scalpel, and the pieces of nasal mucosa were isolated from the cavity mucosa and placed on ice during transport to the laboratory. Within 60 min of removal, pieces of nasal mucosa were carefully cut with a scalpel of appropriate size for the mucosal retention test and the ex vivo permeation test.

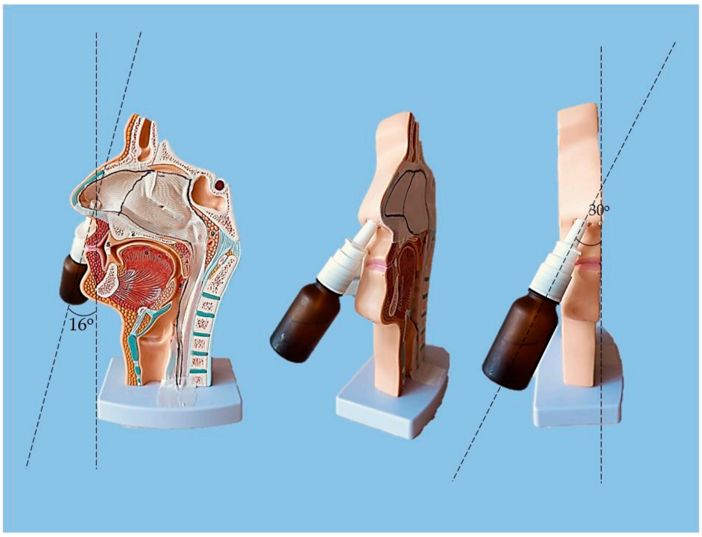

Figure 11. Experimental setting for sprayability testing.

4.10. Determination of Mucosal Retention Time/Washout Time

The experimental setting for mucosal retention time was based on vertical fixation of the mucosal explants, spraying of the test formulations, initiation of simulated nasal flow, and detection of the time required for the appearance of a washed-out zone (Figure 12). Subjects to this test were P407-HPMC drug-loaded optimized formulation and HPMC-free equivalent formulation. Both test samples were colored with methylene blue before spraying on the mucosa. A pure water solution of methylene blue was used as a negative control in order to establish the compound's lack of coloring potential when not in the composition of a viscous and mucoadhesive form. Nasal mucosa explants with an approximate size of 1 × 2 cm were fixated to the upper inner side of an empty beaker glass with the aid of silicone glue. The tissue's temperature was adjusted to 34 °C by ensuring tight contact with an external water bath, as shown in Figure 12. So prepared, the setting was allowed to condition for an hour before performing the experiment. A single spray of each formulation was applied to the mucosal explants. A simulation of nasal flow was initialized by using warm water (34 °C)-loaded burettes positioned right above the medial axis of the sprayed mucosal pieces. A flow rate of 1.4 $\text{mL}\cdot\text{min}^{-1}$ (30 drops per minute) resembling the physiological nasal secretion debit (2000 mL per day) was set [39]. The time required for the appearance of a clear washed-out zone was recorded. The mucosal explants were gently dried with the aid of a filter paper at the end of the experiment, and photographs were taken (realme 11 Pro+ 32 MP camera without magnification).

4.11. In Vitro Drug Release

The in vitro drug release (permeation) study was carried out on Franz diffusion with a receptor volume of 8.0 mL and an orifice of 0.98 cm^2 (PermeGear, Hellertown, PA, USA); Spectra/Por® cellulose membrane (MWCO: 12–14 kDa) was used for the purpose. The receptor compartment was filled nearly to the upper limit with distilled water, and the cell was conditioned at 34 ± 0.5 °C with a circulating thermostatic bath. A 0.83 g test hydrosol (corresponding to 1.0 mL formulation at 25 °C) was introduced in the donor compartment, and the receptor volume was adjusted to the top. A stirring rate of 1000 rpm was set. A sample of 0.5 mL was withdrawn on 0.5, 1, 2, and 3 h from the receptor media for quantification of SN-CX and CX. UV-Vis spectrophotometric analysis (at λ = 439 nm for SN-CX and λ = 231 nm for CX [19]) was applied for the purpose, and a standard curve calculation was used. The analyzed sample was returned to the receptor compartment and if an adjustment of the volume to the top was needed, distilled water was used. At the end of the experiment titrimetric assay of silver ions (Ag^+) was performed by using an adjusted pharmacopoeial method with ferric ammonium sulfate 100 $mg \cdot mL^{-1}$ as indicator and ammonium thiocyanate 0.01 mM as titrant [51].

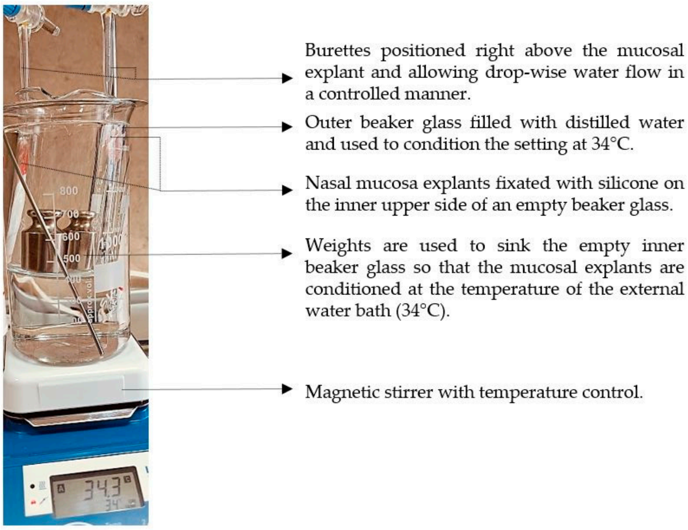

Figure 12. Experimental setting for mucosal retention time testing.

4.12. *Ex Vivo Drug Permeation*

The ex vivo permeation study was carried out by using nasal mucosa explant as a membrane on Franz diffusion cell; the applied procedure followed the same specifications as described above (Section 4.11). The mucosal tissue was positioned in the cell with the aid of a fixation ring, as shown in Figure 13. The mucosal integrity was checked before starting the experiment with a bubble test.

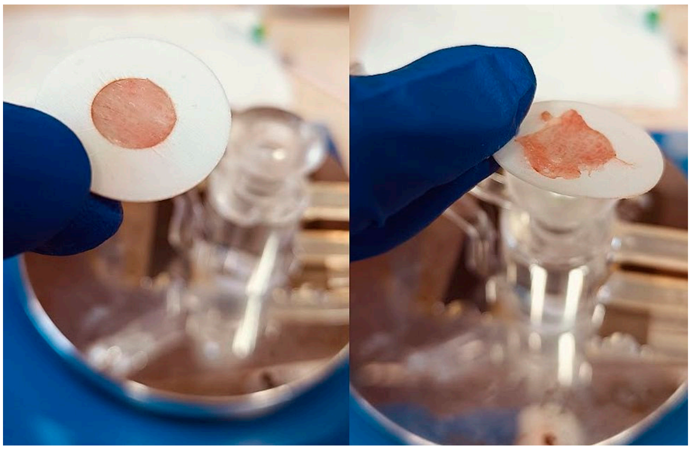

Figure 13. Fixation of the nasal mucosa for the ex vivo permeation study.

4.13. *Antimicrobial Activity*

4.13.1. Antibacterial and Antifungal Activity

A cup–plate technique was applied for evaluation of the antimicrobial activity of SN-CX and SN-CX-loaded test nasal formulation against *Staphylococcus aureus* (ATCC 25923), *Escherichia coli* (ATCC 25922), *Candida albicans* (ATCC 10231), *Pseudomonas aeruginosa* (ATCC 10145), and *Klebsiella pneumoniae* (ATCC 10031)—MicroSwabs, Ridacom, Bulgaria. Dense seeds of 0.5 MF standardized microbial suspensions were made on Mueller–Hinton agar (HiMedia®, Ridacom, Sofia, Bulgaria). After drying, using a sterile borer, a 7 mm wide well was carved in the center of each Petri's agar and filled with 100 µL of the test formulation. The Petri dishes were incubated aerobically at 37 °C for 24 h for the bacterial cultures and at 35 °C for 48 h for *C. albicans*; after that, the emerged inhibition zones were measured in diameter.

4.13.2. Cytotoxicity, Antiviral, and Virucidal Activity

Cells

Permanent HCT-8 [HRT-18] (ATCC-CCL-244™, LGC Standards, Middlesex, UK) was kept at 5% CO_2 and 37 °C in RPMI 1640 (Roswell Park Memorial Institute Medium, ATCC-30-2001) to which L-glutamine 0.3 $g \cdot L^{-1}$ (Sigma-Aldrich, Darmstadt, Germany), Penicillin 100 UI, horse serum 10% (ATCC-30-2021), and Streptomycin 0.1 $mg \cdot mL^{-1}$ (Sigma-Aldrich, Darmstadt, Germany) were added. Madine–Darby canine kidney MDCK (ATCC-CCL-34™) cell line was a gift from Dr. Cyril Bharbesange, National Reference Center for Influenza, Sciensano, Belgium. Cells were grown in DMEM (Gibco, Washington, DC, USA) containing fetal bovine serum (FBS) 5%, (Gibco), sodium bicarbonate 3.7 $mg \cdot mL^{-1}$, HEPES buffer 10 µM (AppliChem GmbH, Darmstadt, Germany), Penicillin 100 $U \cdot mL^{-1}$, and Streptomycin 100 $\mu g \cdot mL^{-1}$. Both cell lines were seeded at a density of 2.5 × 105/mL at 37 °C in a 5% CO_2 incubator Thermo Forma 310 (Thermo Fisher Scientific, Waltham, MA, USA), in 96-well plates (Corning® Costar®, New York, NY, USA), Amphotericin B 25 $\mu g \cdot mL^{-1}$ for 24 h until monolayer confluency is reached.

Viruses

Human coronavirus OC-43 (HCoV-OC43) (ATCC: VR-1558) strain was propagated in HCT-8 cells in a RPMI 1640 maintenance solution; the medium was supplemented with horse serum 2%, Penicillin 100 U/mL, and Streptomycin 100 $\mu g \cdot mL^{-1}$. The cells were lysed by 2 freeze and thaw cycles 5 days after infection; the virus was titrated according to the Reed and Muench formula [52]. The infectious titer of the stock virus was $10^{6.0}$ cell culture infectious doses 50% in 1 mL ($CCID50.mL^{-1}$).

Allantoic fluid and MDCK-derived seasonal influenza A virus (IAV) strain A/Panama/07/99 (H3N2) (National Center for Infectious and Parasitic Diseases—NCIPD, Sofia, Bulgaria) were used. The infectious titer of the stock virus was $T = 10^{-5.0}$ lg $CCID50.mL^{-1}$ and used as a stock suspension or at a working dose of 100 CCID50 mL^{-1}.

Cytotoxicity assay

Cytotoxicity at the 72nd hour on HCT-8 and MDCK cells was evaluated first by visual microscopic observation and then by cell viability assessment after treatment with varying concentrations of test samples following neutral red (NR) dye uptake assay as described previously [53]. As a reference antiviral inhibitor of coronavirus replication, the stock solution of Veklury® (Gilead Science Inc., Cork, Ireland UC) with a concentration of 150 $mg \cdot mL^{-1}$ was used; it was prepared in double distilled water at a final remdesivir (REM) concentration of 8.3×10^{-3} M. As a reference antiviral inhibitor of influenza virus replication, oseltamivir phosphate (OS) (Hoffman-LaRoche, Basel, Switzerland) was used.

Antiviral activity assay

The cells were cultivated in 96-well plates. After a confluent monolayer was formed, cell infection with 0.1 mL viral suspension in tenfold falling dilutions was carried out. The non-adsorbed virus was eliminated after an hour, and 0.1 mL/well maintenance medium was added to the cells. The plates were incubated at 33 °C for 5 days for HCoV-OC43 and at 37 °C for 3 days in a 5% CO_2 atmosphere for IAV. Unintended cells were used as control, cultivated under the same conditions (cells infected with the maximum concentration of the virus demonstrating the maximum cytopathic effect). Microscopic monitoring of the cellular monolayer was used to determine the infectious viral titer. The visually defined cytopathic effect (CPE) was confirmed by NR Uptake Assay [53]. The optical density (OD) of each well was reported at 540 nm in a microplate reader (Biotek Organon, West Chester, PA, USA).

The antiviral activity of the test formulation was evaluated with the aid of a CPE inhibition test. A 100-cell culture infectious dose of 50% (CCID50) in 0.1 mL (containing a different virus strain) was applied to infect a confluent cell monolayer in 96-well plates. The non-adsorbed virus was removed after an hour of virus adsorption for IAV or 2 h for HCov-OC-43, and the test formulation was added in various concentrations; incubation was carried out for 48 h at 37 °C and 5% CO_2 for IAV, or 120 h at 33 °C and 5% CO_2 for HCov-OC-43. The CPE was determined using a neutral red uptake assay, and the percentage of CPE inhibition for each concentration of the test sample was calculated according to a protocol described previously [19]. IC_{50} (the 50% inhibitory concentration) was defined as the concentration causing 50% viral replication inhibition as compared to the virus control.

Virucidal Assay

The test formulation was used in its maximum tolerated concentration (MTC) and combined in a 1:1 ratio with 1 mL containing virus (10^5 CCID50). The samples were stored at room temperature for different time intervals (15, 30, 45, and 60 min). The residual infectious virus content in each sample was determined by the end-point dilution method, and Δlgs compared to the untreated controls were evaluated.

Statistical analysis

Data were recorded using Gen5® and further processed by Excel® Microsoft. The values of CC_{50} were calculated using non-linear regression analysis (GraphPad Software, San Diego, CA, USA). The values were presented as means ± SD from three independent experiments.

Author Contributions: Conceptualization, N.I.; methodology, N.I., N.E., L.S., N.V.-I., K.B. and G.S.; software, N.I.; validation, V.A., N.E., K.B. and L.S; formal analysis, N.I., N.E. and L.S; investigation, N.I. and K.B.; resources, N.I.; data curation, N.I. and L.S.; writing—original draft preparation, N.I., L.S. and K.B; writing—review and editing, V.A.; visualization, N.I.; supervision, V.A.; project administration, N.I. and V.A.; funding acquisition, V.A. All authors have read and agreed to the published version of the manuscript.

Funding: This research was funded by the Medical University of Varna, Bulgaria.

Institutional Review Board Statement: A porcine snout was supplied from a certified slaughterhouse (Varna, Bulgaria). HCT-8 cells (ATCC- CCL-244™) & MDCK ATCC- CCL-34™ cells were supplied from LGC Standards and The Dr. Cyril Barbesange, National Reference Center for Influenza, Sciensano, Belgium, respectively. Seasonal influenza A virus (IAV) strain A/Panama/07/99 (H3N2) was supplied by the National Center for Infectious and Parasitic Diseases—NCIPD, Sofia, Bulgaria).

Informed Consent Statement: The origin of the abovementioned cell lines and the porcine snout is described in Section 4 but they are not a subject of an ethical approval.

Data Availability Statement: The data presented in this study are openly available in article.

Acknowledgments: We would like to express our gratefulness to the National program "Young scientists and post-doctoral researchers-2", Bulgaria.

Conflicts of Interest: The authors declare no conflicts of interest. The funders had no role in the design of the study; in the collection, analyses, or interpretation of data; in the writing of the manuscript; or in the decision to publish the results.

References

1. Vigani, B.; Rossi, S.; Sandri, G.; Bonferoni, M.C.; Caramella, C.M.; Ferrari, F. Recent Advances in the Development of In Situ Gelling Drug Delivery Systems for Non-Parenteral Administration Routes. *Pharmaceutics* **2020**, *12*, 859. [CrossRef] [PubMed]
2. Brambilla, E.; Locarno, S.; Gallo, S.; Orsini, F.; Pini, C.; Farronato, M.; Thomaz, D.V.; Lenardi, C.; Piazzoni, M.; Tartaglia, G. Poloxamer-Based Hydrogel as Drug Delivery System: How Polymeric Excipients Influence the Chemical-Physical Properties. *Polymers* **2022**, *14*, 3624. [CrossRef] [PubMed]
3. Madan, M.; Bajaj, A.; Lewis, S.; Udupa, N.; Baig, J.A. In situ forming polymeric drug delivery systems. *Indian J. Pharm. Sci.* **2009**, *71*, 242–251. [CrossRef] [PubMed]
4. Perkušić, M.; Nižić Nodilo, L.; Ugrina, I.; Špoljarić, D.; Jakobušić Brala, C.; Pepić, I.; Lovrić, J.; Safundžić Kučuk, M.; Trenkel, M.; Scherließ, R.; et al. Chitosan-Based Thermogelling System for Nose-to-Brain Donepezil Delivery: Optimising Formul tion Properties and Nasal Deposition Profile. *Pharmaceutics* **2023**, *15*, 1660. [CrossRef] [PubMed]

5. Suhagiya, K.; Borkhataria, C.H.; Gohil, S.; Manek, R.A.; Patel, K.A.; Patel, N.K.; Patel, D.V. Development of mucoadhesive in-situ nasal gel formulation for enhanced bioavailability and efficacy of rizatriptan in migraine treatment. *Results Chem.* **2023**, *6*, 101010. [CrossRef]
6. Riaz, M.; Zaman, M.; Hameed, H.; Sarwar, H.S.; Khan, M.A.; Irfan, A.; Shazly, G.A.; Paiva-Santos, A.C.; Jardan, Y.A.B. Lamotrigine-Loaded Poloxamer-Based Thermo-Responsive Sol–Gel: Formulation, In Vitro Assessment, Ex Vivo Permeation, and Toxicology Study. *Gels* **2023**, *9*, 817. [CrossRef] [PubMed]
7. Williamson, S.; Dennison, L.; Greenwell, K.; Denison-Day, J.; Mowbray, F.; Richards-Hall, S.; Smith, D.; Bradbury, K.; Ainsworth, B.; Little, P.; et al. Using nasal sprays to prevent respiratory tract infections: A qualitative study of online consumer reviews and primary care patient interviews. *BMJ Open* **2022**, *12*, e059661. [CrossRef]
8. Alsaqqa, H.H. Building the Culture of Public Health as a Positive Reflection from the COVID-19 Crisis. *Risk Manag. Healthc. Policy* **2022**, *15*, 1683–1693. [CrossRef]
9. Ivanova, N.; Sotirova, Y.; Gavrailov, G.; Nikolova, K.; Andonova, V. Advances in the Prophylaxis of Respiratory Infections by the Nasal and the Oromucosal Route: Relevance to the Fight with the SARS-CoV-2 Pandemic. *Pharmaceutics* **2022**, *14*, 530. [CrossRef]
10. Bellotti, D.; D'Accolti, M.; Pula, W.; Huang, N.; Simeliere, F.; Caselli, E.; Esposito, E.; Remelli, M. Calcitermin-Loaded Smart Gels Activity against *Candida albicans*: A Preliminary In Vitro Study. *Gels* **2023**, *9*, 165. [CrossRef]
11. Cook, M.T.; Haddow, P.; Kirton, S.B.; McAuley, W.J. Polymers Exhibiting Lower Critical Solution Temperatures as a Route to Thermoreversible Gelators for Healthcare. *Adv. Funct. Mater.* **2020**, *31*, 2008123. [CrossRef]
12. Djabourov, M. Gels. In *NMR and MRI of Gels*; Deene, Y.D., Ed.; Royal Society of Chemistry: London, UK, 2020; pp. 1–44. [CrossRef]
13. Russo, E.; Villa, C. Poloxamer Hydrogels for Biomedical Applications. *Pharmaceutics* **2019**, *11*, 671. [CrossRef] [PubMed]
14. da Silva, J.B.; Cook, M.T.; Bruschi, M.L. Thermoresponsive systems composed of poloxamer 407 and HPMC or NaCMC: Mechanical, rheological and sol-gel transition analysis. *Carbohydr. Polym.* **2020**, *240*, 116268. [CrossRef] [PubMed]
15. Pagano, C.; Giovagnoli, S.; Perioli, L.; Tiralti, M.C.; Ricci, M. Development and characterization of mucoadhesive-thermoresponsive gels for the treatment of oral mucosa diseases. *Eur. J. Pharm. Sci.* **2020**, *142*, 105125. [CrossRef] [PubMed]
16. Perez-Robles, S.; Carotenuto, C.; Minale, M. HPMC Hydrogel Formation Mechanisms Unveiled by the Evaluation of the Activation Energy. *Polymers* **2022**, *14*, 635. [CrossRef] [PubMed]
17. Joshi, S.C. Sol-Gel Behavior of Hydroxypropyl Methylcellulose (HPMC) in Ionic Media Including Drug Release. *Materials* **2011**, *4*, 1861–1905. [CrossRef] [PubMed]
18. Abla, K.K.; Domiati, S.; El Majzoub, R.; Mehanna, M.M. Propranolol-Loaded Limonene-Based Microemulsion Thermo-Responsive Mucoadhesive Nasal Nanogel: Design, In Vitro Assessment, Ex Vivo Permeation, and Brain Biodistribution. *Gels* **2023**, *9*, 491. [CrossRef] [PubMed]
19. Ivanova, N.; Ermenlieva, N.; Simeonova, L.; Kolev, I.; Slavov, I.; Karashanova, D.; Andonova, V. Chlorhexidine–Silver Nanoparticle Conjugation Leading to Antimicrobial Synergism but Enhanced Cytotoxicity. *Pharmaceutics* **2023**, *15*, 2298. [CrossRef] [PubMed]
20. Francisco, P.; Neves Amaral, M.; Neves, A.; Ferreira-Gonçalves, T.; Viana, A.S.; Catarino, J.; Faísca, P.; Simões, S.; Perdigão, J.; Charmier, A.J.; et al. Pluronic® F127 Hydrogel Containing Silver Nanoparticles in Skin Burn Regeneration: An Experimental Approach from Fundamental to Translational Research. *Gels* **2023**, *9*, 200. [CrossRef]
21. Liu, T.; Aman, A.; Ainiwaer, M.; Ding, L.; Zhang, F.; Hu, Q.; Song, Y.; Ni, Y.; Tang, X. Evaluation of the anti-biofilm effect of poloxamer-based thermoreversible gel of silver nanoparticles as a potential medication for root canal therapy. *Sci. Rep.* **2021**, *11*, 12577. [CrossRef]
22. Wunnoo, S.; Bilhman, S.; Waen-ngoen, T.; Yawaraya, S.; Paosen, S.; Lethongkam, S.; Kaewnopparat, N.; Voravuthikunchai, S.P. Thermosensitive hydrogel loaded with biosynthesized silver nanoparticles using Eucalyptus camaldulensis leaf extract as an alternative treatment for microbial biofilms and persistent cells in tissue infections. *J. Drug Deliv. Sci. Technol.* **2022**, *74*, 103588. [CrossRef]
23. Wunnoo, S.; Lorenzo-Leal, A.C.; Voravuthikunchai, S.P.; Bach, H. Advanced biomaterial agent from chitosan/poloxamer 407-based thermosensitive hydrogen containing biosynthesized silver nanoparticles using Eucalyptus camaldulensis leaf extract. *PLoS ONE* **2023**, *18*, e0291505. [CrossRef]
24. Bates, M.G.; Risselada, M.; Peña-Hernandez, D.C.; Hendrix, K.; Moore, G.E. Antibacterial activity of silver nanoparticles against Escherichia coli and methicillin-resistant Staphylococcus pseudintermedius is affected by incorporation into carriers for sustained release. *Am. J. Vet. Res.* **2024**, *85*, 1–11. [CrossRef] [PubMed]
25. Salem, H.F.; Nafady, M.M.; Ewees, M.G.E.-D.; Hassan, H.; Khallaf, R.A. Rosuvastatin calcium-based novel nanocubic vesicles capped with silver nanoparticles-loaded hydrogel for wound healing management: Optimization employing Box–Behnken design:in vitroandin vivoassessment. *J. Liposome Res.* **2021**, *32*, 45–61. [CrossRef]
26. Abou-Shamat, M.A.; Calvo-Castro, J.; Stair, J.L.; Cook, M.T. Modifying the Properties of Thermogelling Poloxamer 407 Solutions through Covalent Modification and the Use of Polymer Additives. *Macromol. Chem. Phys.* **2019**, *220*, 1900173. [CrossRef]
27. Pradines, B.; Bories, C.; Vauthier, C.; Ponchel, G.; Loiseau, P.M.; Bouchemal, K. Drug-Free Chitosan Coated Poly(isobutylcyanoacrylate) Nanoparticles Are Active Against Trichomonas vaginalis and Non-Toxic Towards Pig Vaginal Mucosa. *Pharm. Res.* **2014**, *32*, 1229–1236. [CrossRef]

28. Wu, C.; Schmidt, G. Thermosensitive and Dissolution Properties in Nanocomposite Polymer Hydrogels. *Macromol. Rapid Commun.* **2009**, *30*, 1492–1497. [CrossRef] [PubMed]
29. Timur, S.S.; Şahin, A.; Aytekin, E.; Öztürk, N.; Polat, K.H.; Tezel, N.; Gürsoy, R.N.; Çalış, S. Design and in vitro evaluation of tenofovir-loaded vaginal gels for the prevention of HIV infections. *Pharm. Dev. Technol.* **2017**, *23*, 301–310. [CrossRef]
30. Lupu, A.; Rosca, I.; Gradinaru, V.R.; Bercea, M. Temperature Induced Gelation and Antimicrobial Properties of Pluronic F127 Based Systems. *Polymers* **2023**, *15*, 355. [CrossRef] [PubMed]
31. Dorraj, G.; Dadashzadeh, S.; Erfan, M.; Moghimi, H.R. Controlled SLN Delivery by Thermoresponsive In-situ Forming Erodible Gels; A Whole-body and Organ Imaging Study. *Curr. Drug Deliv.* **2018**, *15*, 510–519. [CrossRef]
32. Chen, L.-C.; Lin, S.-Y.; Cheng, W.-J.; Sheu, M.-T.; Chung, C.-Y.; Hsu, C.-H.; Lin, H.-L. Poloxamer sols endowed with in-situ gelability and mucoadhesion by adding hypromellose and hyaluronan for prolonging corneal retention and drug delivery. *Drug Deliv.* **2023**, *30*, 2158964. [CrossRef] [PubMed]
33. Fakhari, A.; Corcoran, M.; Schwarz, A. Thermogelling properties of purified poloxamer 407. *Heliyon* **2017**, *3*, e00390. [CrossRef] [PubMed]
34. Tatarchuk, V.V.; Bulavchenko, A.I.; Druzhinina, I.A. Kinetics of dissolution of silver nanoparticles inside triton N-42 reversed micelles. *Russ. J. Inorg. Chem.* **2009**, *54*, 1678–1683. [CrossRef]
35. Huang, F.; Gao, Y.; Zhang, Y.; Cheng, T.; Ou, H.; Yang, L.; Liu, J.; Shi, L.; Liu, J. Silver-Decorated Polymeric Micelles Combined with Curcumin for Enhanced Antibacterial Activity. *ACS Appl. Mater. Interfaces* **2017**, *9*, 16880–16889. [CrossRef] [PubMed]
36. Ko, Y.-B.; Park, Y.-H.; MubarakAli, D.; Lee, S.-Y.; Kim, J.-W. Synthesis of antibacterial hydroxypropyl methylcellulose and silver nanoparticle biocomposites via solution plasma using silver electrodes. *Carbohydr. Polym.* **2023**, *302*, 120341. [CrossRef]
37. Williams, G.; Suman, J.D. In Vitro Anatomical Models for Nasal Drug Delivery. *Pharmaceutics* **2022**, *14*, 1353. [CrossRef] [PubMed]
38. Du, J.; Shao, X.; Bouteiller, J.-M.C.; Lu, A.; Asante, I.; Louie, S.; Humayun, M.S.; Lazzi, G. Computational optimization of delivery parameters to guide the development of targeted Nasal spray. *Sci. Rep.* **2023**, *13*, 4099. [CrossRef]
39. Beule, A.G. Physiology and pathophysiology of respiratory mucosa of the nose and the paranasal sinuses. *GMS Curr. Top. Otorhinolaryngol. Head Neck Surg.* **2010**, *9*, Doc07. [CrossRef]
40. Leal, J.; Smyth, H.D.C.; Ghosh, D. Physicochemical properties of mucus and their impact on transmucosal drug delivery. *Int. J. Pharm.* **2017**, *532*, 555–572. [CrossRef]
41. Pernakov, M.; Ermini, M.L.; Sulaieva, O.; Cassano, D.; Santucci, M.; Husak, Y.; Korniienko, V.; Giannone, G.; Yusupova, A.; Liubchak, I.; et al. Complementary Effect of Non-Persistent Silver Nano-Architectures and Chlorhexidine on Infected Wound Healing. *Biomedicines* **2021**, *9*, 1215. [CrossRef]
42. Jones-Nelson, O.; Hilliard, J.J.; DiGiandomenico, A.; Warrener, P.; Alfaro, A.; Cheng, L.; Stover, C.K.; Cohen, T.S.; Sellman, B.R. The Neutrophilic Response to Pseudomonas Damages the Airway Barrier, Promoting Infection by Klebsiella pneumoniae. *Am. J. Respir. Cell Mol. Biol.* **2018**, *59*, 745–756. [CrossRef] [PubMed]
43. Riquelme, S.A.; Ahn, D.; Prince, A. Pseudomonas aeruginosa and Klebsiella pneumoniae Adaptation to Innate Immune Clearance Mechanisms in the Lung. *J. Innate Immun.* **2018**, *10*, 442–454. [CrossRef] [PubMed]
44. Binder, L.; Mazál, J.; Petz, R.; Klang, V.; Valenta, C. The role of viscosity on skin penetration from cellulose ether-based hydrogels. *Skin Res. Technol.* **2019**, *25*, 725–734. [CrossRef] [PubMed]
45. Ivanova, N.; Andonova, V.; Jelev, I.; Dimova, G. Synthesis of silver nanoparticles with green tea-extracted reductants: A preliminary study for optimization of the preparation technique. *Scr. Sci. Pharm.* **2021**, *8*, 17–26. [CrossRef]
46. Liu, Y.; Dai, C.; Wang, K.; Zhao, M.; Zhao, G.; Yang, S.; Yan, Z.; You, Q. New insights into the hydroquinone (HQ)–hexamethylenetetramine (HMTA) gel system for water shut-off treatment in high temperature reservoirs. *J. Ind. Eng. Chem.* **2016**, *35*, 20–28. [CrossRef]
47. Lahrech, K.; Safouane, A.; Peyrellasse, J. Sol state formation and melting of agar gels rheological study. *Phys. A Stat. Mech. Appl.* **2005**, *358*, 205–211. [CrossRef]
48. Zhao, J.; An, X.; Qiao, S. The extraction effect of CO2 injection on the flow properties of crude oil. *Petrol. Sci. Technol.* **2019**, *37*, 710–717. [CrossRef]
49. Sotirova, Y.; Gugleva, V.; Stoeva, S.; Kolev, I.; Nikolova, R.; Marudova, M.; Nikolova, K.; Kiselova-Kaneva, Y.; Hristova, M.; Andonova, V. Bigel Formulations of Nanoencapsulated St. John's Wort Extract—An Approach for Enhanced Wound Healing. *Gels* **2023**, *9*, 360. [CrossRef] [PubMed]
50. Wadell, C.; Björk, E.; Camber, O. Nasal drug delivery—Evaluation of an in vitro model using porcine nasal mucosa. *Eur. J. Pharm. Sci.* **1999**, *7*, 197–206. [CrossRef]
51. European Directorate for the Quality of Medicines & HealthCare of the Council of Europe (EDQM). *European Pharmacopoeia*; Council of Europe: Strasbourg, France, 2019; Volume 10, pp. 3790–3791.
52. Reed, L.J.; Muench, H.A. Simple method of estimating fifty percent endpoints. *Am. J. Hyg.* **1938**, *27*, 493–497.
53. Repetto, G.; del Peso, A.; Zurita, J.L. Neutral red uptake assay for the estimation of cell viability/cytotoxicity. *Nat. Protoc.* **2008**, *3*, 1125–1131. [CrossRef] [PubMed]

gels

MDPI

Article

Development of Polyvinyl Alcohol Hydrogels for Controlled Glucose Release in Biomedical Applications

Rosa M. Quispe-Siccha [1,*], Osvaldo I. Medina-Sandoval [2], Abraham Estrada-Tinoco [2], Jorge A. Pedroza-Pérez [2], Adolfo Martínez-Tovar [3], Irma Olarte-Carrillo [3], Rafael Cerón-Maldonado [3], Arturo Reding-Bernal [4] and Juan C. López-Alvarenga [5]

[1] Research and Technological Development Unit, Research Department, General Hospital of Mexico, "Dr. Eduardo Liceaga", Mexico City 06726, Mexico
[2] Interdisciplinary Biotechnology Professional Unit, National Polytechnic Institute, Mexico City 07340, Mexico; oimsipn@gmail.com (O.I.M.-S.); abraham_et_ma@live.com.mx (A.E.-T.); alan.japp3@gmail.com (J.A.P.-P.)
[3] Hematology Laboratory, General Hospital of Mexico "Dr. Eduardo Liceaga", Mexico City 06726, Mexico; mtadolfo@gmail.com (A.M.-T.); irma.olarte@salud.gob.mx (I.O.-C.); cmrafael.bh@gmail.com (R.C.-M.)
[4] Research Department, General Hospital of Mexico "Dr. Eduardo Liceaga", Mexico City 06726, Mexico; arturo.reding@salud.gob.mx
[5] Population Health & Biostatistics, School of Medicine, University of Texas Rio Grande Valley, Edinburgh, TX 78539, USA; juan.lopezalvarenga@utrgv.edu
* Correspondence: rosa.quispe@salud.gob.mx or rosa.quispe@gmail.com

Abstract: Polyvinyl alcohol (PVA) hydrogels have a wide range of applications in the pharmaceutical and biomedicine fields due to their exceptional biophysical properties. The study focuses on preparing and characterizing capsule-shaped PVA hydrogels to enhance their biocompatibility and porosity for controlled glucose release and cell proliferation. The hydrogels were prepared using different concentrations (Cs) and molecular weights (MWs) of PVA, with two different lengths, A (10 mm) and B (20 mm), to control glucose release over 60 min. The preparation process involved PVA gel preparation and PVA hydrogel formation. A total of 500 µL of glucose was injected into all dehydrated hydrogels in groups A and B. Glucose release was studied by immersing the hydrogels in saline at 37 °C with stirring at 500 rpm. The SUP-B15 cell line was grown in six A1 hydrogels for biocompatibility testing. The results indicate that all hydrogels remained stable at 37 °C without degrading. Those with a higher C and MW exhibited a denser and less porous structure, lower glucose storage capacity, and higher elongation at break. Significant differences in glucose release, diffusion speed, and flux were observed, which were more evident in A1 > A4, B1 > B4, and B1 > A1 over 60 min. A1 and B1 had higher values because their higher porosity distribution allowed glucose to diffuse more easily. B1, being larger, has more glucose due to its increased length. The cell growth response and viability at 48 h in contact with the hydrogels was similar to that of the control (4.5×10^5 cells/mL, 98.5% vs. 4.8×10^5 cells/mL, 99.7% viability), thus demonstrating biocompatibility. The hydrogels effectively released glucose over 60 min, with variations based on porosity, C, MW, and length, and demonstrated good biocompatibility with the cell line.

Keywords: polyvinyl alcohol hydrogel; dehydration; storage capacity; thermal resistance; permeability; glucose release; diffusion speed; flow; cell growth

1. Introduction

Polyvinyl alcohol (PVA) hydrogels exhibit various physical and chemical properties that significantly influence drug release, making them versatile for multiple biomedical applications. The freeze–thaw (F/T) method commonly used to prepare PVA hydrogels affects their swelling ability and stability, affecting drug release [1]. For example, hydrogels with fewer F/T cycles and higher freezing temperatures show higher swelling rates, which improves their ability to release drugs over extended periods [1].

Mechanical properties such as tensile stress and Young's modulus are also critical; for example, PVA hydrogels subjected to stretching cycles between F/T cycles exhibit higher crystallinity and stiffness, which can improve the drug release rate [2]. The molecular weight and concentration of PVA further influence the hydrogel's ability to absorb and transfer energy, affecting the release kinetics of the encapsulated drugs [3].

The elongation at the break of PVA hydrogels is a crucial aspect of their characterization because it measures their ductility or ability to deform plastically before breaking [3]. This is important in applications requiring flexibility and adaptability, such as dressings or implants [4]. Additionally, the storage modulus, known as Young's modulus (G'), and the loss modulus (G'') are important for characterizing viscoelastic materials like PVA hydrogels and composites with other materials [2,5–7]. G' describes a material's stiffness or elasticity, while G'' is associated with damping or viscoelastic behavior.

The storage capacity of substances in a PVA hydrogel depends on its porous structure and ability to absorb water. PVA hydrogels are highly porous materials with a great capacity to retain water. The pores in PVA hydrogels act as reservoirs, absorbing and holding liquids, including water and dissolved substances [1,3]. This property is crucial for controlled drug release or tissue engineering [8–10]. Additionally, PVA hydrogels are known for their excellent thermal stability compared to other materials, providing greater resistance to degradation when exposed to temperature changes [11,12]. Their thermal resistance allows them to be used in environments with temperature fluctuations, such as dressings or controlled drug-release systems and tissue engineering [8,13,14].

The concentration of PVA is crucial for determining the distribution of porosity in hydrogels [2,15,16] and their degree of swelling [1,3,17]. By adjusting the concentration and optimizing cross-linking, their properties can be controlled for specific applications. For instance, it can change the release rate of substances in controlled-release applications according to therapeutic needs [8,18]. In tissue regeneration, PVA hydrogels serve as scaffolds for cell growth, promoting cell adhesion and proliferation in a three-dimensional environment through the diffusion of nutrients and oxygen [3,19–23]. These properties are also vital in applications such as medical dressings, which aim to keep a wound moist to facilitate healing [4,9,14,24]. Additionally, PVA hydrogels are used in sensors and actuators, such as pH or glucose sensors [25–27].

PVA is more biomimetic compared to other synthetic polymers and can be used as matrices in tissue engineering applications, as well as a vehicle for controlled drug release [8,20,28,29]. Additionally, PVA hydrogels can create scaffolds capable of housing various types of cells, such as pancreatic and corneal cells. This facilitates the implantation of cells to carry out their functions without triggering adverse reactions from the transplantation [3,30]. For instance, a bioartificial pancreas can shield transplanted islets from the recipient's immune response by enveloping them with a semipermeable membrane or hydrogel barrier. The bioartificial pancreas prevents immunocompetent cells, antibodies, or complement from breaching the semipermeable barrier, ultimately providing immunoprotecting. Furthermore, the device can respond to blood glucose levels by releasing insulin [19,20].

Blending PVA with other polymers can enhance its mechanical properties. When combined with chitosan (CT), PVA can improve hydrogels' tensile strength, flexibility, bulk, and surface hydrophilicity [31]. For instance, incorporating CT into PVA hydrogels results in a more homogeneous network structure, enhancing mechanical stability, reducing porosity, and being more bioabsorbable. This is crucial for maintaining cell viability during preservation [32,33]. Additionally, when PVA is mixed with polyethylene glycol (PEG), it can achieve controlled drug release. A higher PEG content leads to the reduced swelling of hydrogels [8]. Moreover, modifying PVA with cellulose powder and poly (ethylene glycol) (PEG) has been shown to enhance the hydrogels' biocompatibility and cytocompatibility, making them suitable for cell growth and tissue engineering applications [34]. Moreover, uniform PVA microparticles can be utilized to microencapsulate drugs through membrane emulsification and chemical cross-linking, allowing a higher drug content storage [14,35].

PVA mixed with Ag nanoparticles has an improved antibacterial effect for wound dressing applications [14]. However, in some cases, blending PVA with other polymers can be counterproductive and even toxic, especially when chemically induced cross-linking occurs [36].

The combined physical and chemical properties, such as swelling behavior, mechanical strength, porosity, and presence of additional materials, determine the effectiveness and rate of substance release from PVA hydrogels. This makes them well-suited for specific drug delivery systems, cell preservation, and survival, and effective as scaffolds. In this study, we constructed and characterized PVA hydrogels as capsules of two lengths. We varied their concentration (C) and molecular weight (MW) to examine their porosity distribution (pores number versus diameter) and to assess their release behavior from the inside to the outside of the hydrogel, diffusion speed, and diffusion flow of glucose in a time interval of 60 min. The hydrogels were physically cross-linked using freeze/thaw techniques, eliminating the need for toxic chemicals and mixing with other polymers, ensuring biocompatibility and immunoprotection [36]. Based on this study's findings, combining them with different polymers is possible in future studies. This study developed a method for producing hydrogels that can release substances, such as glucose, from the interior to the exterior of a hydrogel within 60 min. These hydrogels have been shown to be biocompatible with the SUP-B15 cell line, supporting their preservation and proliferation. This presents new possibilities for future research involving other cell lines to assess their preservation and cell viability through a nutrient exchange.

2. Results and Discussion

This section presents the results obtained from the PVA hydrogels of Groups A and B. Group A comprises hydrogels with a length of 10 mm, while Group B consists of hydrogels with a length of 20 mm. The formulations for these groups are as follows: A1 and B1 (C1, MW1); A2 and B2 (C2, MW1); A3 and B3 (C1, MW2); and A4 and B4 (C2, MW2), as detailed in the methodology.

2.1. Dehydration

Table 1 shows the percentage of water mass lost (W_L) as a function of C and MW for the A and B group hydrogels due to dehydration. The results are an average of 4 hydrogels for each experiment, which is 32 hydrogels.

Table 1. The percentage of water mass loss (W_L) in all PVA hydrogel formulations during dehydration.

Hydrogels (A Group)	W_L (%)	Hydrogels (B Group)	W_L (%)
A1	7.79 ±1.72	B1	10.6 ± 0.55
A2	4.23 ± 2.17	B2	6.80 ± 2.80
A3	6.25 ± 1.12	B3	7.46 ± 1.02
A4	3.94 ± 2.11	B4	3.98 ± 1.54

The purpose of dehydrating the hydrogels was to increase their storage capacity for glucose. The dehydration time was carefully chosen for each group to prevent their original length and shape from being compromised when injected with glucose. Group B hydrogels lost more water mass than Group A hydrogels because they were larger. Hydrogels with higher C and MW tend to experience lower water mass loss due to a greater porosity distribution but smaller pore size. These results are related to the following studies [37].

The dehydration percentage of our hydrogels was kept low compared to other studies to preserve the original structure when rehydrating them with glucose filling [37,38]. Dehydrated hydrogels can be utilized for controlled drug release by slowly rehydrating them to enable sustained drug release [37]. In biomedical applications, dehydrated hydrogels can be used for cell preservation and transport, being rehydrated at the time of use [23].

2.2. Swelling Ratio

The data presented in Table 2 show that the hydrogels' swelling ratio (W_s) varies depending on the C and MW of PVA. The results indicate that the W_s decreases as the C and MW increase. This trend is observed in both groups of hydrogels A and B, with group B exhibiting a larger W_s due to its larger size. The results represent an average of four hydrogels for each PVA hydrogel formulation.

Table 2. Results of the swelling ratio (W_s) in all PVA hydrogel formulations.

Hydrogels (A Group)	W_s (%)	Hydrogels (B Group)	W_s (%)
A1	121 ±25	B1	141 ± 13
A2	96 ± 7	B2	110 ± 12
A3	115 ± 17	B3	130 ± 9
A4	103 ± 4	B4	115 ± 6

The distribution and interconnection of pores in a material are mainly influenced by the composition of the polymer chains and the cross-linking density. When the polymer concentration in a given volume increases, the number of organized polymer chains increases, leading to decreased porosity within the material. High MW polymers typically have a finer pore structure due to longer and cross-linked chains, which may explain their reduced water retention capacity [3,37].

Hydrogel swelling is a crucial characteristic that can be controlled by adjusting the C and MW of PVA, the freeze–thaw time, and the number of freeze–thaw cycles. By regulating hydrogel swelling, it is possible to use them as controlled release systems and create a favorable environment for cells, enabling cell adhesion [3].

2.3. Storage Capacity and Thermal Resistance

The storage capacity of the milk–green dye mixture within the A1 hydrogels averaged 430 ± 12 µL, and for the B1 hydrogels, it was 450 ± 10 µL. Additionally, both hydrogels demonstrated thermal resistance at 37 °C with a constant rotation of 500 rpm without deformation, as shown in Figure 1. When stretched, they did not break. Furthermore, the mixture decreased after three intervals: the original state, 20 min, and 30 min.

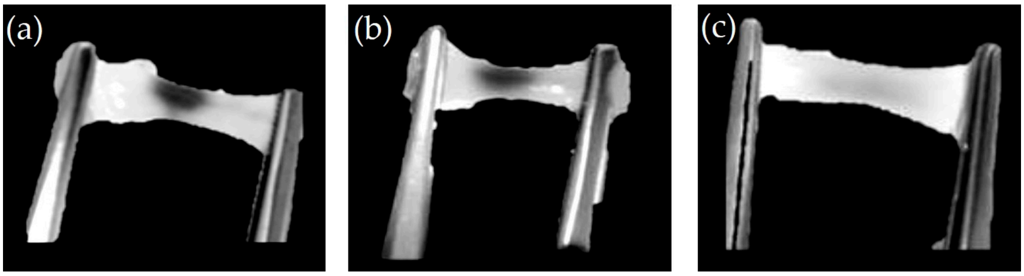

Figure 1. The hydrogel at different stages of exposure to temperature and stirring. The hydrogel is in its original state before being subjected to heat and stirring (**a**), the hydrogel was exposed to 37 °C and constant stirring of 500 rpm for 20 min (**b**), and the hydrogel after being exposed to 37 °C and continuous stirring at 500 rpm for 30 min (**c**).

The experiment was conducted on two types of hydrogels, A1 and B1, which have lower C and MW values, resulting in a lower density. These hydrogels can endure temperatures of 37 °C and constant agitation at 500 rpm. In that case, it is expected that other hydrogels with higher C and MW values will also be able to endure these conditions due to their higher density [3,7].

After confirming that the PVA hydrogel in capsule form can store substances and withstand body temperatures under constant agitation, we obtained the results for the target substance of this study, which is the volume of glucose supported by two groups of hydrogels, A and B, that were previously dehydrated. Table 3 shows the glucose storage capacity of group A and B hydrogels. The results represent an average of five hydrogels for each PVA hydrogel formulation.

Table 3. The volume of glucose supported by the hydrogels of groups A and B.

Hydrogels (A Group)	**Volume (Units)**	**Hydrogels (B Group)**	**Volume (Units)**
A1	42.10 ± 8.08	B1	44.90 ± 8.10
A2	37.20 ± 8.06	B2	38.50 ± 8.14
A3	39.25 ± 6.08	B3	40.80 ± 6.80
A4	34.15 ± 6.05	B4	35.85 ± 6.10

The maximum average volume supported by hydrogel A1 of group A was 42.10 ± 8.08 glucose units, equivalent to 421 μL. In comparison, hydrogel B1 of group B supported 44.90 ± 8.10 units, equivalent to 449 μL, with a conversion rate of 10 units to 100 μL. It is important to note that the hydrogels in group B are longer than those in group A, which affords them a greater storage capacity. However, as the C and MW increase, the difference in glucose volume between the hydrogels of both groups becomes shorter. This is because denser hydrogels have a lower storage capacity, but their ability to retain substances improves due to their strengthened structure [3,37].

As explained in the methodology, the glucose injection needle was inserted at the center of the hydrogel to maximize each hydrogel's storage capacity. This ensured an even pressure distribution throughout the hydrogel's walls. If the needle had been placed too close to the side walls, the hydrogel would have collapsed before reaching its total volume.

Understanding how substances are stored in hydrogels is crucial to predicting their release behavior over time [3]. This knowledge could help preserve cells encapsulated within the hydrogel by exchanging nutrients, but more reliable evidence is needed to confirm this [39].

2.4. Elongation at Breack

Table 4 displays the elongation at the break of PVA hydrogels with different C and MW. A total of 40 hydrogels was used, with 5 for each experiment. The hydrogel with MW2 (A3, A4 and B3, B4) exhibited a higher elongation at the break than those with MW1 (A1, A2 and B1, B2). This is because longer polymer chains can intertwine and form a more flexible and resistant network, allowing for greater deformation before breaking. In addition, the studied hydrogels have medium MWs, resulting in better overall mechanical properties characterized by high strength and toughness [40].

Table 4. Elongation at break of the hydrogel groups A and B.

Hydrogels (Group A)	**Elongation at Break (%)**	**Hydrogels (Group B)**	**Elongation at Break (%)**
A1	151 ± 17	B1	153 ± 21
A2	161 ± 5	B2	164 ± 8
A3	156 ± 4	B3	158 ± 10
A4	165 ± 7	B4	168 ± 18

Regarding the hydrogel concentration, the higher-concentration hydrogels (A2, A4, and B2, B4) exhibit a greater elongation at break compared to the lower-concentration hydrogels (A1, A3, and B1, B3). This is because a higher concentration of PVA generally leads to a denser and more cross-linked polymeric network, thereby increasing the mechanical strength of the hydrogel [40]. This is also evident in the standard deviation, where there is a broader scatter of data points in the lower-concentration hydrogels.

As for the dimensions of the hydrogels, the smaller hydrogels (group A) demonstrate a lower elongation at break than the longer hydrogels (group B) because they have less material to distribute the stress. However, this is also influenced by the composition of the hydrogel and its manufacturing process, both of which are consistent in this case.

Elongation at break is crucial in applications where the hydrogel must withstand mechanical stresses, such as in scaffolds for tissue regeneration and sustained drug release [40].

2.5. Scanning Electron Microscopy (SEM) and Porosity Distribution

The formulation process for group A and B hydrogels is identical; the only distinction lies in their length. Consequently, Figure 2 displays the most representative SEM images of group A hydrogels, with two resolutions, ×10,000 and ×20,000, and varying C and MW. These images provide information on the structure and pore distribution.

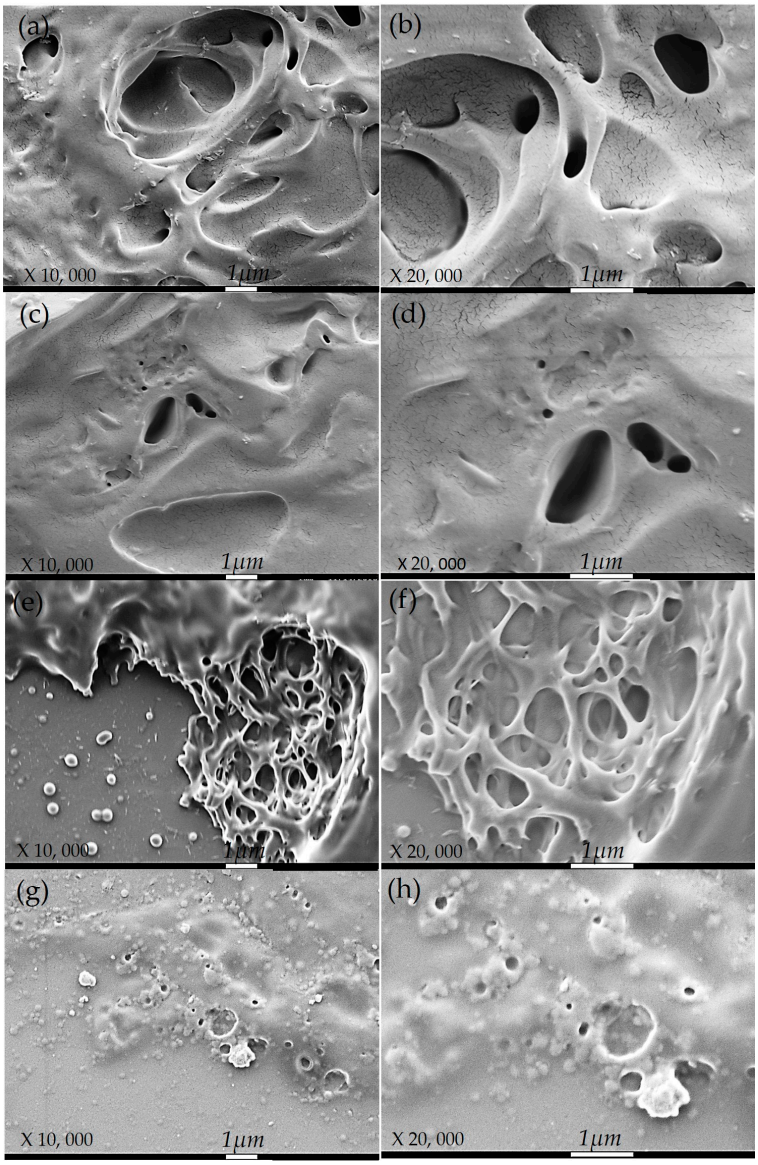

Figure 2. SEM images show more representatives of the group A hydrogels with resolutions ×10,000 and ×20,000, respectively: (A1) hydrogel (**a**,**b**), (A2) hydrogel (**c**,**d**), (A3) hydrogel (**e**,**f**), and (A4) hydrogel (**g**,**h**).

The hydrogels labeled A1, which have a low C and MW of PVA, display a porous structure characterized by larger and less dense pores. This is due to the low C and MW, leading to a less dense polymeric network, allowing larger pores to form (see Figure 2a,b). The hydrogel A2, with a high PVA concentration and low MW, exhibits a structure with smaller and denser pores. Despite the low MW, the high PVA concentration increases the polymeric network's density, reducing the pore size (Figure 2c,d). The A3 hydrogels with a low C and high MW exhibit a structure with intermediate-sized pores and a more uniform network. The high MW contributes to a better network formation. However, the low C limits the overall density (refer to Figure 2e,f). Finally, high-concentration and high MW hydrogels (A4) exhibit a very dense structure with small and uniform pores (Figure 2g,h). Due to their high C and MW, these hydrogels have a thick, uniform polymeric network with tiny, well-distributed pores. Some studies support this information [2,40].

Image analysis can enhance our comprehension of how PVA concentration and MW impact the structure and characteristics of hydrogels. Altering the PVA concentration and MW can also assist us in understanding the release of glucose through the porosity of hydrogels. Figure 3 displays the distribution of the porosity, which represents the number of pores based on their diameters for the hydrogels in groups A and B.

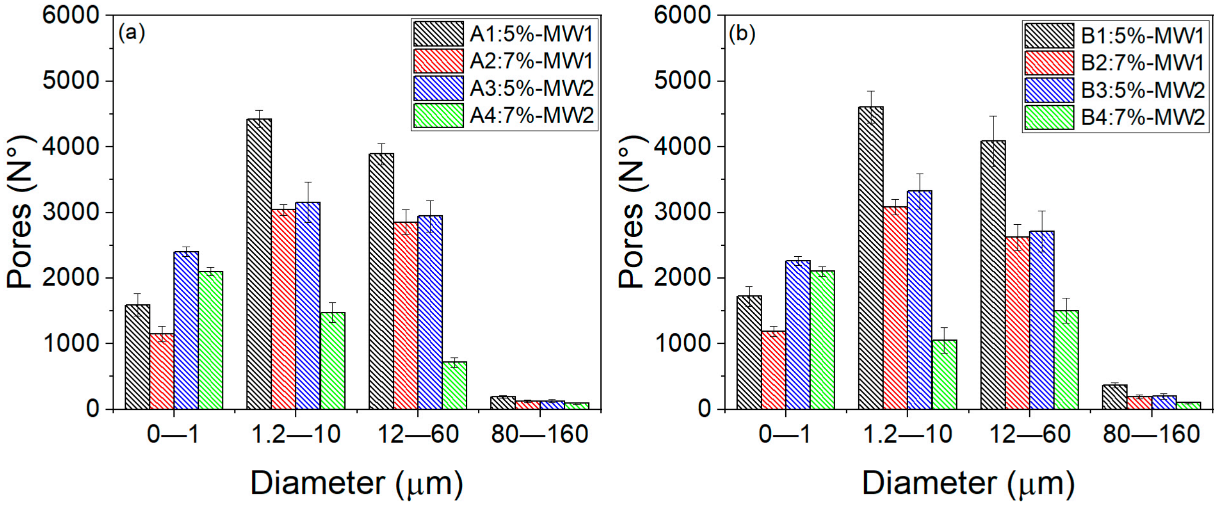

Figure 3. Histograms depict the porosity distribution (number of pores versus diameter) for the A1-A4 hydrogels (**a**) and B1-B4 hydrogels (**b**).

The porosity distribution of the hydrogels in group A is similar to that of group B, with minor differences. This is because both groups were prepared using the same formulation. That is, the same C and MW used in group A were also used in the hydrogels of group B. The only distinction between the groups is the size of the hydrogels in group B, which could impact the release of glucose depending on the storage capacity of the hydrogel.

The hydrogels with a higher MW (A3, A4, B3, B4) have more pores from 0 to 1 μm than those with a lower MW (A1, A2, B1 and B2). Additionally, the hydrogels with a lower C for both MW values have a greater porosity than those with a higher C. Specifically, A1 has a greater porosity than A2, and B1 has a greater porosity than B2; similarly, A3 has a greater porosity than A4, and B3 has a greater porosity than B4 in the same range from 0 to 1 μm.

For PVA hydrogels with diameters of 1.2–10 μm, 12–60 μm, and 80–160 μm, the higher C hydrogels with both MW values (A2, A4, B2, B4) exhibit a lower porosity compared to the lower C hydrogels and both MW values (A1, A3, B1, B3). It should be noted that, although the lower C and lower MW hydrogels have higher porosities at different diameters, their standard deviation is higher due to non-uniform porosity distribution, specifically the hydrogels A1 and B1.

According to the behavior of the porosity distribution by changing the C and MW of PVA mentioned in previous paragraphs, PVA hydrogels with a low C and low MW have a porous structure with larger and less dense pores, resulting in a less dense polymeric network that allows the formation of larger pores. On the other hand, hydrogels with a high C and high MW show a very dense structure with small and uniform pores, resulting in a thick and uniform polymeric network with tiny and well-distributed pores.

A standardized preparation method can maintain a hydrogel's porosity distribution, helping prevent significant variations in data, particularly in glucose release. However, the mechanical properties of an older hydrogel may change compared to a new one, leading to significant variability in the porosity distribution and glucose release behavior results [41].

2.6. Permeability Tests

This section illustrates the cumulative release, diffusion speed, and glucose flow from the inside to the outside of PVA hydrogel of all formulations for both A and B groups.

2.6.1. Glucose Release

The release of glucose through the pores of the hydrogels was analyzed using the Korsmeyer–Peppas model Equation (5), commonly used to describe drug release from PVA hydrogels. The fitted curve of the glucose release behavior shows a high coefficient of determination (R^2) in Figure 4.

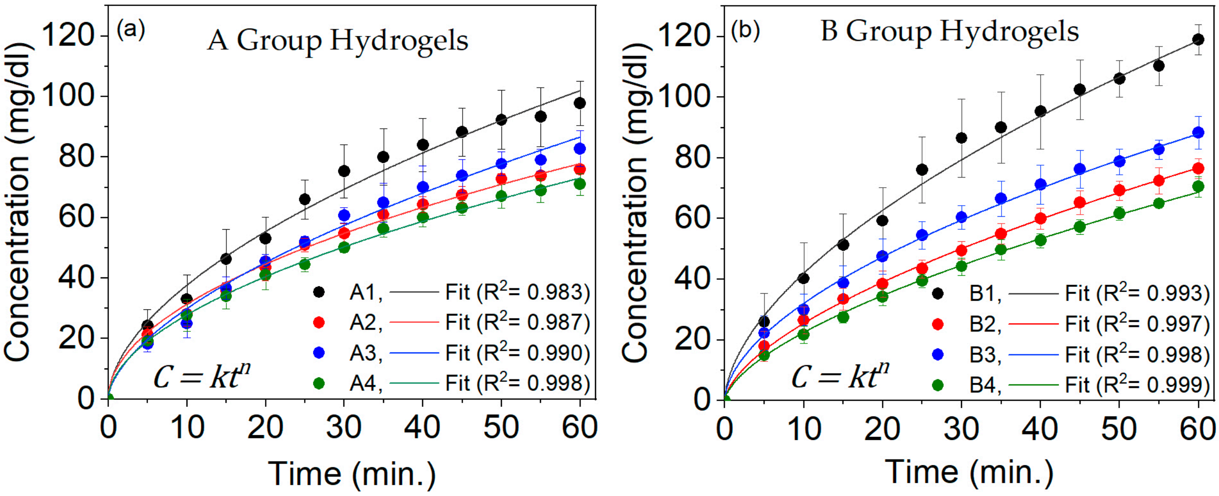

Figure 4. The curves showing the accumulation of glucose from inside to outside PVA hydrogels, presented as concentration versus time for group A (**a**) and group B (**b**) hydrogels.

The hydrogels in group A had an n value of 0.5, while those in group B had an n value of 0.6. This means that the glucose release mechanism for group A hydrogels follows Fickian diffusion, while for group B hydrogels, it involves Fickian diffusion and the relaxation phenomenon [8].

Glucose release from inside to outside of the hydrogel could last more than 60 min, especially for the longest hydrogel. However, we decided to monitor the release for 60 min because we noticed a slight slowdown. We considered that the hydrogel would reach equilibrium later, where the concentrations inside and outside the hydrogel would equalize, and the diffusion would significantly slow down.

Glucose release from group A and B hydrogels started to be measured at minute 5. From 5 to 20 min, no differences were observed in the hydrogels of group A. This could indicate that glucose may start to exit through the largest pores in the four types of hydrogels (80–160 um), as they all have similar numbers of pores with slight variations due to C and MW, as shown in Figure 3a. From 25 to 60 min, statistically significant differences (p-value < 0.05) were observed between hydrogels A1 and (A2, A3, and A4), and A3 and

A4. This difference is related to the distribution of porosity: at higher C and MW values, the structure is denser, resulting in smaller but more uniformly distributed pores.

In the comparison of hydrogels in group B, from 15 to 60 min, statistically significant differences (p-value < 0.05) were observed between B1 and (B2 and B4). Additionally, differences between B1 and B3 were observed from 25 to 60 min. Furthermore, from 45 to 60 min, differences were observed between B3 and (B2 and B4). As time progresses, differences between certain hydrogels become more apparent, which was initially obscured by the intersecting standard deviations of the hydrogels. The onset of glucose release from 0 to 10 min is linked to the larger pore distribution (80–160 µm) due to similar pore amounts with slight variations by C and MW, as depicted in Figure 3b.

The comparison between hydrogel groups A and B showed no differences between 5 and 10 min. However, statistically significant differences (p-value < 0.05) were observed between the following times:

- From 15 to 60 min between A1 and B4.
- From 20 to 60 min between A4 and B1.
- From 25 to 60 min between A2 and B1, A3 and B1, and A4 and B2.
- From 45 to 50 min between A3 and B4.

Furthermore, differences were observed between A1 and B1, as well as between A4 and B3, from 55 to 60 min. This glucose release behavior is related to the porosity distribution of each hydrogel type, as seen in Figure 3.

Although the glucose release behavior through the hydrogels of group B and group A is similar, differences in the release between the two groups are due to their length and the formation of the polymeric network along the material. These variations affect the hydrogel's swilling ratio, glucose storage capacity, and mechanical properties, as evidenced in Tables 2–4.

After analyzing the release curves of hydrogels from groups A and B, we found that the distribution of pores may have a greater impact on the initial release (from 0 to 20 min) for pore sizes of 80–160 µm, as the porosity levels are similar. However, from 25 to 60 min, the porosity distribution in the 0–1, 1.2–10, and 12–60 µm pore size ranges may have a more significant influence, as indicated in Figure 3 by the noticeable difference in porosity levels for each hydrogel.

Understanding the release behavior of glucose from capsule-shaped PVA hydrogel is essential for several reasons. It enables the design of controlled release systems, ensuring that glucose is released at the right place and time. We can only write these general statements based on glucose because every drug has a different structure. This understanding also helps fine-tune hydrogel properties such as porosity, C, and MW to achieve the desired release profile. Additionally, it reduces glucose wastage by allowing a better control over the amount released, thus avoiding overdoses or premature release. Furthermore, it ensures that the glucose remains stable and avoids degradation.

2.6.2. Diffusion Speed

Figure 5 shows the behavior of the diffusion speed (v_D) curves for glucose through the two groups of hydrogels, A and B. The v_D data are fitted to a power (allometric) equation with a high R^2 value. v_D decreases with the increase in the sampling time. This is because, as glucose diffuses, the concentration in the hydrogel decreases, reducing the concentration gradient that drives diffusion Equation (6).

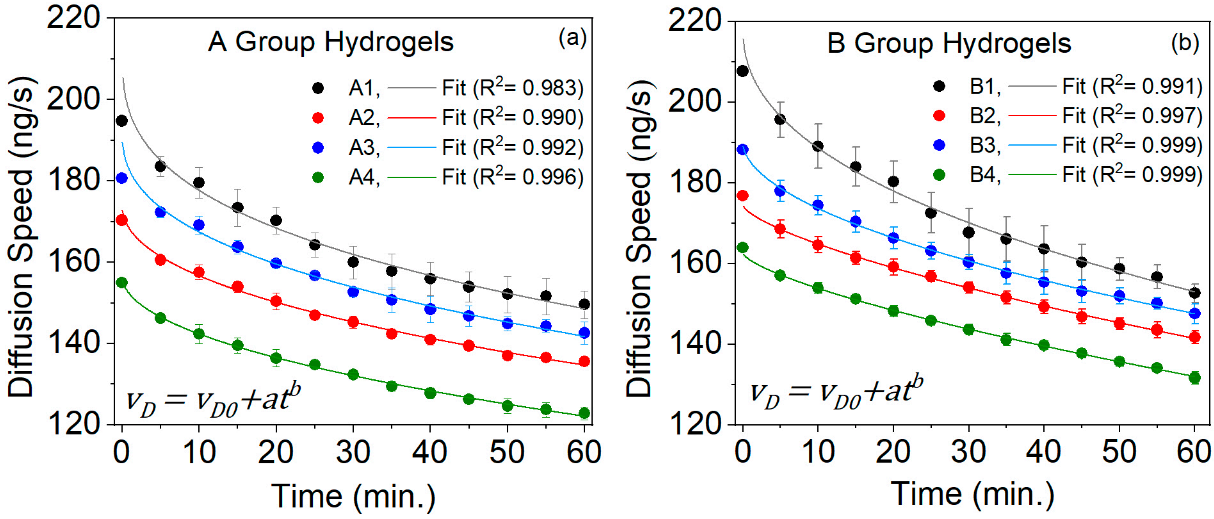

Figure 5. Diffusion speed (v_D) versus sampling time for the group A (**a**) and group B (**b**) PVA hydrogels.

The v_D of glucose through PVA hydrogels is the speed at which glucose molecules move through this matrix. When comparing the v_D between hydrogels in group A, we observed statistically significant differences (p-value < 0.05) from 0 to 60 min, except for the interval from 35 to 60 min for hydrogels A1 and A3, because their v_D values are closer, so their standard deviations intersect and follow the order of hydrogels from the highest to the lowest: A1 > A3 > A2 > A4. The decrease in v_D over longer intervals occurs as glucose diffuses out of the hydrogel, reducing the amount of glucose inside it. Several factors influenced these processes:

(a) Pore size: where larger pores (A1 > A3 > A2 > A4) allowed a faster diffusion (refer to Figure 3).
(b) Concentration gradient: the higher gradient generally resulted in a higher diffusion speed (A1 > A3 > A2 > A4); this is a consequence of item (a).
(c) Temperature: Higher temperatures cause molecules to move faster, increasing the diffusion speed. The hydrogels were exposed to 37 °C, allowing for a better glucose molecule diffusion.
(d) Molecule size: Smaller molecules diffuse through the hydrogels faster than larger ones. The glucose molecule is of the nanometric order (approximately 0.8 nm), which favors its diffusion.

There are significant statistical differences (p-value < 0.05) between the hydrogels of group B, except from 30 to 45 min of hydrogel B1 versus B3 due to their point spread. The v_D from the highest to the lowest for each hydrogel was B1 > B3 > B2 > B4. The same factors influence this sequence as those mentioned for the hydrogels of group A. However, these hydrogels are longer than group A, which might affect the v_D. Therefore, in the next paragraph, we compare the v_D for the two hydrogel groups, A and B.

When comparing the v_D between hydrogel groups A and B from 0 to 60 min, the following statistically significant (p-value < 0.05) differences were observed:

- A2 had differences compared to B1 and B2.
- A3 had differences compared to B1 and B2.
- A4 had differences compared to B1, B2, B3, and B4.

Furthermore, differences were observed between A1 and B1, B2, and B4 from 0 to 60 min, except from 30 to 50 min, due to the point dispersion, where standard deviations overlapped.

The hydrogels in group B are longer than those in group A, which enables them to support more glucose. This difference becomes significant in the v_D. It is theorized that, in longer hydrogels, the concentration gradient can decrease as the substance diffuses, slowing down the v_D in the more distant sections. However, despite this, hydrogels from group B exhibited a higher v_D. This could be attributed to the fact that glucose diffusion through these hydrogels occurred from the center to the outside because the concentration of glucose was higher in the center (the cylindrical shape of the hydrogel) than in the distant parts of the hydrogel (hemispherical ends of the hydrogel).

In conclusion, although the length of the hydrogel can impact the v_D, other factors, such as the concentration gradient, hydrogel structure, and chemical interactions, are equally important.

2.6.3. Diffusion Flow

The diffusion flux (J) is related to v_D, which represents the amount of glucose moving through the hydrogel per unit area and time, as shown in Equation (8). The negative sign in the J equation indicates that the substance moves in the direction that reduces the concentration gradient, ensuring that the flux is positive in that direction.

Figure 6 illustrates the J behavior of glucose through the PVA hydrogels of groups A and B. This behavior fits very well with a power (allometric) equation, showing a high R^2.

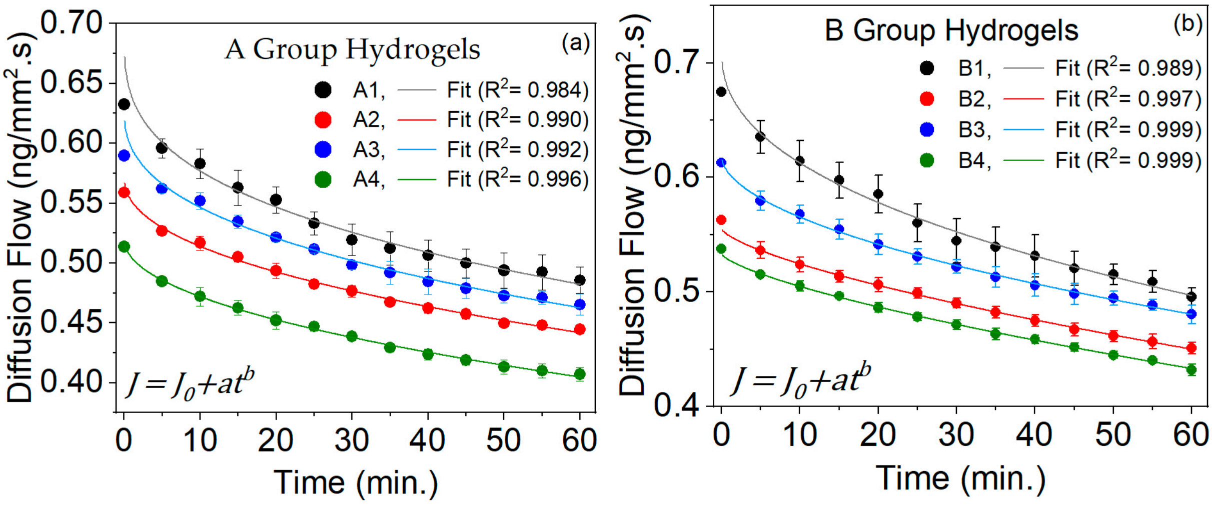

Figure 6. Diffusion flow versus sampling time for the group A (**a**) and group B (**b**) PVA hydrogels.

A statistically significant difference (p-value < 0.05) was observed between all hydrogels in group A when comparing them from 0 to 60 min, except from 35 to 60 min for hydrogels A1 and A3. This exception occurred because their J is closer, leading to their standard deviation crossing. Similarly, the hydrogels in group B also exhibited statistically significant differences (p-value < 0.05) when compared to each other, except from 35 to 60 min for hydrogels B1 and B3, due to the same reason that occurred between hydrogels A1 and A3.

When comparing the two groups of hydrogels A and B, we found statistically significant differences (p-value < 0.05), as follows:

- From 5 to 10 min, differences were observed between A3 and B2.
- From 5 to 25 min, differences were observed between A1 and B1.
- From 5 to 60 min, differences were observed between A1 and (A2 and A4), A3 and B1, A3 and B4, and A4 and (B1, B2, B3 and B4).

The distribution of porosity in PVA hydrogels plays a crucial role in facilitating the flow of glucose. Below are some key reasons that we believe are critical for achieving controlled dispersion in the results for each type of hydrogel:

(a) Using a standardized construction methodology (see Section 4.1), the pores of adequate size were uniformly distributed throughout each hydrogel depending on the C and MW, facilitating the movement of glucose molecules through the hydrogel. Larger and well-connected pores allow for a faster and more efficient diffusion.

(b) A reasonable amount of porosity was obtained, which increased the contact surface between the hydrogel and glucose, improving the interaction and, therefore, diffusion.
(c) The porosity distribution helped reduce the resistance to glucose flow, allowing for a less constrained and faster movement through the hydrogel.
(d) The porosity distribution obtained for each hydrogel allowed for balancing glucose retention and controlled release. It is worth mentioning that, in this study, the sampling time for glucose release was up to 60 min. However, a more extended release could be obtained until the maximum glucose release.

In summary, a well-designed porosity distribution according to the C and MW in PVA hydrogels is essential to optimize the diffusion of glucose or other substances, improving the process's efficiency and effectiveness.

2.7. Cell Proliferation

To confirm that the biomaterial did not inhibit cell proliferation or induce cell death, an experiment was conducted to determine its biocompatibility.

The cell line in direct contact with the 6 A1 hydrogels does not interfere with cell proliferation in culture ($p = 0.467$). The slight variations in the number of cells in each hydrogel could be attributed to differences in porosity distribution. The cell growth response and viability at 48 h in contact with the hydrogels was similar to that of the control (4.5×10^5 cells/mL, 98.5% vs. 4.8×10^5 cells/mL, 99.7% viability), thus demonstrating biocompatibility.

In Figure 7a, the graph columns represent cell proliferation at 0, 24, and 48 h, proving no inhibition in cell proliferation or death due to cell–hydrogel contact. Figure 7b corresponds to a cytospin that verifies the characteristic morphology of the cell line used (SUP-B15, ATCC CRL-1929, Manassas, VA, USA).

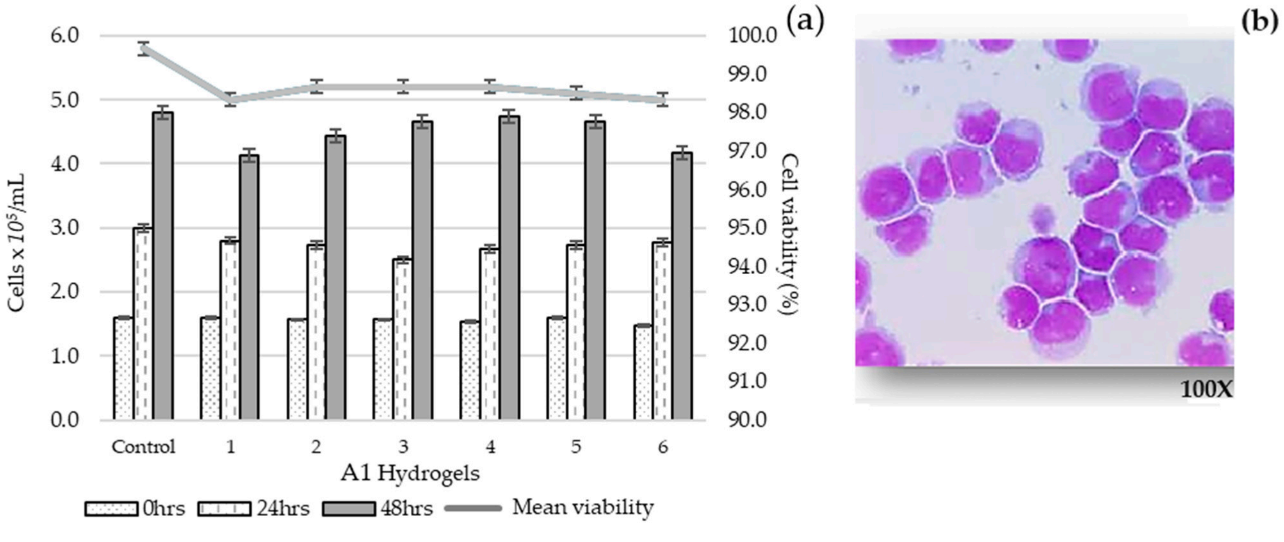

Figure 7. Cell proliferation and viability of the control sample (cell line in culture) and the cell line in contact with the 6 A1 hydrogels for 24 and 48 h with MTS Cell proliferation assay (**a**) and cell morphology (Wright stain) observed in cytospin (100×) (**b**). The cell count was performed in triplicate for each hydrogel.

Based on the standardized preparation and mechanical properties of hydrogels from groups A and B and the encouraging cell growth response, the project's next phase involves using various cell lines in direct contact with and within the hydrogels to assess their survival and proliferation rates.

3. Conclusions

The research found that low C and MW PVA capsule-shaped hydrogels have a wide range of porosity. Specifically, in the range of 0–1 µm, A1 > A2 and A3 > A4, and in the range of 1.2–160 µm, A1 > A3 > A2 > A4. This behavior is similar to the hydrogels of group B, with the only difference being their larger size. The porosity distribution of hydrogels A1 and B1 is wider. Still, these have a greater margin of error, and hydrogels with a higher C and MW have a more uniform porosity distribution, allowing for a more controlled release. Due to their wide porosity distribution, hydrogels A1 and B1 showed a greater glucose storage capacity, with B1 being greater than A1 due to its larger size. All hydrogels remained stable at 37 °C and under stirring at 500 rpm without degrading.

Statistically significant differences (p-value < 0.05) were found in the cumulative glucose concentration, diffusion speed, and diffusion flux between the hydrogels, particularly between A1 > A4, B1 > B4, and B1 > A1 over 60 min. Group B’s hydrogels were larger than group A’s, supporting a higher glucose content. The C and MW influenced the diffusion of glucose, allowing for a rapid or slow diffusion regardless of the size of the hydrogel, making them suitable for various applications such as releasing hydrophilic substances or preserving cells (e.g., SUP-B15 cell line) due to their biocompatibility.

The biocompatibility experiment results show that the contact between cells and the hydrogel did not have an anti-proliferative effect or impact cell viability.

4. Materials and Methods

4.1. Preparation of PVA Hydrogels

We followed a two-step process to prepare the capsule-shaped hydrogels of two sizes, two Cs and two MWs of PVA. Part of the methodology was adapted from a study [2].

Step 1: PVA gel

To prepare the gel, PVA powder with a 99% hydrolysis degree (Sigma Aldrich, Saint Louis, MO, USA) of MW1 = 85,000–124,000 and MW2 = 146,000–186,000, with concentrations of C1 = 5% and C2 = 7%, was used along with ultrapure water of MilliQ grade (Merck Millipore, Darmstadt, Germany). We used the following equation to achieve the desired PVA concentration:

$$W_{PVA}(\mathrm{g}) = [PVA\ concentration\ (\%) \times H_2O\ volume\ (\mathrm{mL})]/100\% \tag{1}$$

To prepare the gel for C1, MW1, and MW2 of PVA, 80 mL of ultrapure water and 4 g of PVA powder were mixed. For C2, MW1, and MW2 of PVA, a mixture of 80 mL of pure water and 5.6 g of PVA powder was used. The mixtures were heated from 20 °C to 85 °C for around 90 min while stirring with a magnetic bar to ensure a uniform solution. After heating, the gel was allowed to cool down to room temperature (20 °C) to remove any air bubbles.

Step 2: PVA cryogel

The gel obtained in the first step was poured into capsule-shaped molds of two sizes: L1 = 10 mm (300 µL PVA gel) and L2 = 20 mm (600 µL PVA gel), both with the same diameter of 6 mm, which had been previously sterilized. Subsequently, the molds filled with PVA gel were subjected to a freezing process at −80 °C using an ultra-freezer (Kaltis GV039M, Shanghai, China) for 20 min and then thawed at room temperature (20 °C) for 40 min in four cycles. Figure 8a shows the frozen hydrogels in the capsule molds after the fourth cycle. In contrast, Figure 8b displays the hydrogels removed from their molds four days after their preparation, which is why it is denser than the hydrogel in Figure 8c, which is the hydrogel thawed at room temperature after the fourth freezing cycle.

Figure 8. (**a**) PVA hydrogels in the capsule molds after the fourth frozen cycle, (**b**) PVA hydrogels immersed in ultrapure water four days after their preparation, and (**c**) PVA hydrogel at room temperature (20 °C) after the fourth freezing cycle.

Finally, 32 capsule-shaped hydrogels, consisting of 16 L1 hydrogels and 16 L2 hydrogels, were obtained. Table 5 displays the hydrogels labeled by concentration, molecular weight, and size.

Table 5. Formulations of PVA hydrogels using two concentrations (Cs) and two molecular weights (MWs). The number of hydrogels prepared is indicated in parentheses.

Group	Hydrogels (N°)	C	MW
A (L1 = 10 mm)	A1 (4)	C1 = 5%	MW1 = 85,000–124,000
	A2 (4)	C2 = 7%	MW1= 85,000–124,000
	A3 (4)	C1 = 5%	MW2 = 146,000–186,000
	A4 (4)	C2 = 7%	MW2 = 146,000–186,000
B (L2 = 20 mm)	B1 (4)	C1 = 5%	MW1 = 85,000–124,000
	B2 (4)	C2 = 7%	MW2 = 85,000–124,000
	B3(4)	C1 = 5%	MW1 = 146,000–186,000
	B4 (4)	C2 = 7%	MW2 = 146,000–186,000

The group A and B hydrogels are L1 = 10 mm and L2 = 20 mm long, respectively; four capsules were used for each C and MW. One side becomes more flattened after the hydrogels are removed from their molds, as depicted in Figure 8c. The hydrogels are placed in ultrapure water to maintain their viability for several days, as illustrated in Figure 8b.

The same methodology (standardization) was used to prepare PVA hydrogels for reproducibility and comparability.

(a) The Cs and MWs of PVA were carefully selected without using chemical cross-linking agents for biocompatibility testing.
(b) The PVA powder and ultrapure water were mixed according to a specific procedure, including heating and stirring.
(c) The optimal stirring temperature and frequency for gel formation were identified.
(d) The adequate temperature and timing of the freeze/thaw cycles were determined to achieve a homogeneous porosity distribution for each hydrogel formulation.
(e) The precise volume of PVA gel was poured into gelatin capsule molds corresponding to lengths of 10 and 20 mm.
(f) All steps were thoroughly documented for future reference.

The preparation of hydrogels can vary depending on the objective. This study was conducted to prepare hydrogels for controlled glucose release and cellular biocompatibility. Therefore, standardizing the methodology for each type of hydrogel helps minimize variations between hydrogel formulations and ensures consistent results, which are crucial for biomedical and tissue engineering applications.

4.2. Dehydration

A closed system at 20 °C containing silica gel granules and a device that the hydrogel released as a water filter was used for the controlled dehydration process. The function of the silica gel is to absorb the water in the hydrogel. With the help of this system, it was possible to monitor the hydrogel's dehydration by measuring their length and water mass loss every 15 min for 1 hour for group A and every hour for 24 h for group B group. This mechanism was used before hydrogels were filled with glucose to support a greater volume.

The following equation calculates the water mass loss in percentage (W_L) for all PVA hydrogel formulations.

$$W_L(\%) = \frac{W_1 - W_2}{W_1} \times 100\% \tag{2}$$

where W_1 and W_2 are the respective weights of the hydrogel before and after dehydration; each weight was measured four times to obtain an average value.

4.3. Swelling Ratio Determination

To determine the hydrogels' swelling ratio (W_s), we injected 150 µL of ultrapure water into the L1 hydrogels and 300 µL into the L2 hydrogels. We then wiped off any excess water before measuring their weight. After that, the samples were freeze-dried and incubated at room temperature (20 °C) and 50.4% relative humidity for 12 h for L1 hydrogels and 20 h for L2 hydrogels. Following incubation, their weight was measured again, and the swelling ratio was calculated using Equation (3).

$$W_s(\%) = \frac{W_3 - W_2}{W_2} \times 100\% \tag{3}$$

W_3 represents the sample weight in a swollen state, and W_2 represents the sample weight in a dry state. Each test was repeated four times to obtain an average value. This experiment was conducted according to M. Huang et al. and E. Rosa et al. [5,42].

4.4. Storage Capacity and Thermal Resistance

The PVA hydrogels were tested for storage capacity and thermal resistance using milk and green vegetable dye. This ensured the mixture filled the hydrogel and released it from the inside to the outside. Glucose was not used initially in this test due to its transparency; so, milk, with a molecule diameter similar to that of glucose, was used instead.

To test the storage capacity, an insulin syringe was used to inject a maximum volume of mixture into the center of the hydrogel (Figure 9a). The hydrogel was then sealed with a toothed clamp subjected to a force of 20 kg/cm^2 to prevent leakage (Figure 9b). The sealed hydrogel was then placed in 20 mL of saline solution at 37 °C and constantly stirred at 500 rpm to assess the release of the mixture for 60 min (Figure 9c).

Tests were only conducted on four A1-type and four B1-type hydrogels to ensure the proper filling and release of the mixture. This allowed for subsequent tests with greater reliability using glucose, the study's target substance, in all hydrogel formulations.

In the glucose filling tests for all PVA hydrogel formulations, the same procedure, including sealing the injection hole, was used for the milk and green vegetable dye mixture. A similar procedure was followed to test glucose release from inside to outside the hydrogel, but a glucometer was used to detect cumulative glucose release. This procedure is described in more detail in Section 4.6 on permeability tests.

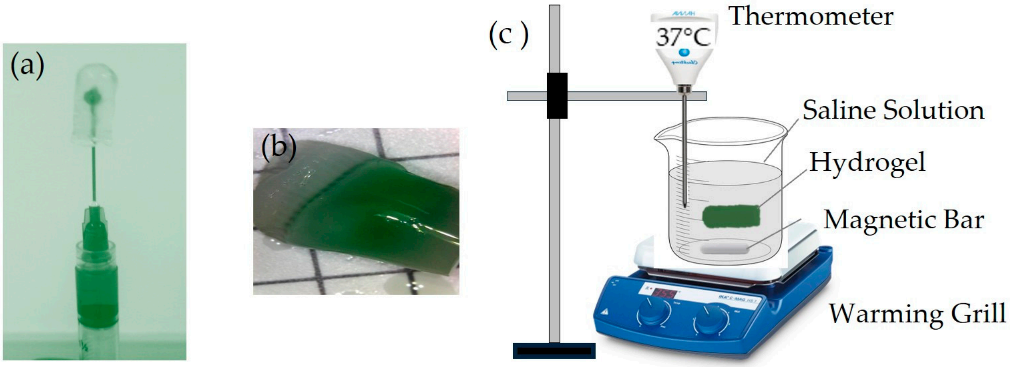

Figure 9. (**a**) Injection of the milk mixture with green vegetable dye into the PVA hydrogel using an insulin syringe, (**b**) PVA hydrogel sealed with a toothed clamp to prevent any leakage due injection of the mixture, and (**c**) proofs of PVA hydrogel degradation and release of the mixture in saline solution to 37 °C and constant stirring of 500 rpm.

4.5. Elongation at Break

Figure 10 shows that the PVA hydrogels underwent a tensile test using a system designed by the Research and Technological Development Unit (UIDT) of the General Hospital of Mexico "Dr. Eduardo Liceaga".

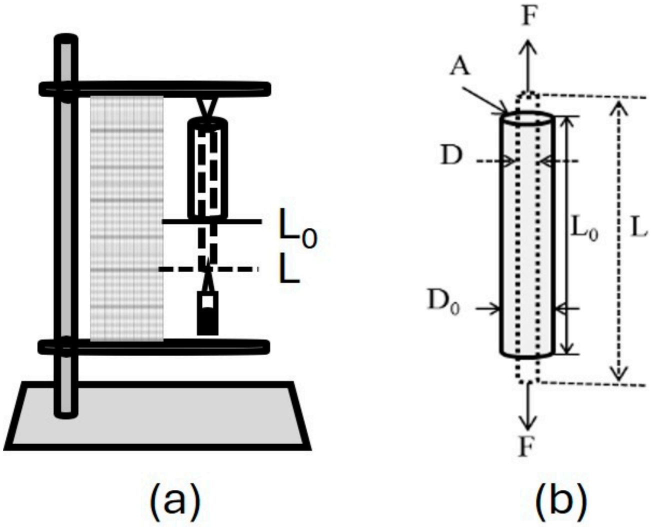

Figure 10. Schematic representation of the device used for uniaxial tensile testing of PVA hydrogels (**a**) and the uniaxial deformation of the PVA hydrogel under tensile forces (**b**).

The elongation at the break of PVA hydrogel measures the material's ability to stretch before it breaks. This property is determined using the elastic or Young's modulus equation, represented in Equation (4).

$$E = d\sigma / d\varepsilon \quad (4)$$

where $d\sigma$ is the longitudinal stress and $d\varepsilon$ is longitudinal deformation. This system was chosen because the samples are macro-sized, which helps to avoid significant errors. Four experiments were conducted for each hydrogel.

4.6. Scanning Electron Microscopy (SEM) and Porosity Distribution

The morphological nature of the PVA hydrogels in this study was identified by obtaining scanning electron microscopy (SEM) images using a (Quanta 3D FEG, Santa Clara, CA, USA) at an acceleration voltage of 2 kV. Before the SEM analysis, the samples were gold-coated and allowed to dry on filter paper at room temperature for 15 min.

Eight images of 50 μm thick slices were obtained from sections of four hydrogels of the same type to obtain a more robust porosity distribution.

The SEM images were converted to 8-bit format and then binarized using the ImageJ software to analyze the porosity distribution of PVA hydrogels. After binarization, the MATLAB R2021b-academic use software applied filters to the images to enhance the resolution.

4.7. Permeability Tests

Fifty units (ten units equals 100 μL) of (10% dextrose, Baxter, Mexico City, Mexico) glucose were injected into all the previously dehydrated PVA hydrogels [43]. The amount of glucose absorbed by each hydrogel depended on the C and MW [37]. These hydrogels were then immersed in 20 mL of saline solution (0.9% sodium chloride, Baxter, Mexico City, Mexico) and stirred continuously at 500 rpm at 37 °C. Using a glucometer (Accu-Chek, Mexico City, Mexico), the glucose concentration released into the saline solution was measured at 5 min intervals for one hour.

Glucose was selected due to its biocompatibility, non-toxic nature, and suitable molecular size for efficient diffusion through the PVA hydrogel matrix, allowing for controlled and sustained release. Specific sensors (glucometer) could also accurately monitor its concentration and release. Moreover, glucose is an essential energy source for the body's cells. It can have various medical applications, such as in diabetes treatment or as a nutrient exchange for cells within the hydrogel [19,20].

Saline solution was chosen as the medium for glucose release due to its pH, which is generally similar to that of the human body, making it compatible with body tissues and fluids.

Glucose Release Model

The nonlinear regression model Korsmeyer–Peppas was used to perform the curve fit of glucose release [44], since it is often used to describe the release of substances through PVA hydrogels. This is because of its versatility, simplicity, and ability to fit the data well, providing an accurate characterization. It helps generate useful parameters such as n and k to understand the release mechanisms and their applicability to a release system. When n equals 0.5, the substance release mechanism is Fickian diffusion. If n is between 0.5 and 1, it involves both Fickian diffusion and relaxation phenomenon [8].

$$C = M_t / M_\infty = k \cdot t^n \tag{5}$$

where M_t / M_∞ represents the fractional permeated glucose, t is the time, k is the transport constant (dimension of time^{-1}), and n is the transport exponent (dimensionless). The release constant k provides mostly information on the glucose formulation, whereas n is important since it relates to the glucose release mechanism.

4.8. Diffusion Speed

The hydrogels utilized in this study exhibit a non-stationary glucose release mechanism. Therefore, the speed of glucose diffusion is directly linked to the difference in concentration at any given moment and is not dependent on time. For this reason, Fick's second law is employed to calculate the glucose diffusion speed.

$$v_D = D \frac{A_h (C1 - C2)}{r} \tag{6}$$

where D is the glucose diffusion coefficient to 25 °C, which is 6.76×10^{-4} mm^{2}s^{-1} [45]; A_h is the surface area of the hydrogel; $C1$ is the highest concentration inside the hydrogel; $C2$ is the region (saline solution) of the lowest concentration; and r is the radius of the hydrogel, representing the path for glucose diffusion from the center to the outside.

Since the hydrogel has a capsule shape (spherocylinder), the following geometric equation was used to calculate its surface area.

$$A_h = A_c + A_{he} = 2\pi r h + 2\left(2\pi r^2\right) \tag{7}$$

where A_c is the cylinder's curved surface area, A_{he} is the hemisphere's curved surface area, and r is the radius of the hydrogel.

To determine the thickness of empty hydrogels and hydrogels filled with glucose, we utilized photographs of the hydrogels and the Adobe Photoshop Express 2022 photo editing tool. This method allowed us to achieve greater accuracy through the use of pixels. The dimensions of the hydrogels are shown in Table 6.

Table 6. Dimensions of the hydrogels. Each data point is an average of four hydrogels.

Hydrogels	**Length (mm) (Empty = Glucose)**	***d* (mm) (Empty/Glucose)**	**A_h (mm^2) (Empty/Glucose)**	**Volume (mm^3) (Empty/Glucose)**
A1	9.98 ± 0.15	5.99 ± 0.02/8.10 ± 0.16	187.87 ± 0.82/307.99 ± 10.03	225.02 ± 1.54/484.78 ± 24.35
A2	9.97 ± 0.04	5.96 ± 0.04/8.05 ± 0.13	186.24 ± 6.85/304.78 ± 8.21	225.02 ± 3.86/476.92 ± 17.04
A3	9.95 ± 0.09	5.98 ± 0.14/8.08 ± 0.11	187.80 ± 2.07/306.38 ± 7.06	222.00 ± 12.90/480.81 ± 19.84
A4	9.94 ± 0.04	5.95 ± 0.09/8.00 ± 0.10	186.01 ± 4.30/301.62 ± 6.28	221.61 ± 7.95/469.30 ± 15.08
B1	20.08 ± 0.19	6.00 ± 0.10/8.10 ± 0.10	188.43 ± 7.11/307.94 ± 6.35	226.21 ± 13.34/484.54 ± 15.40
B2	19.88 ± 0.13	5.98 ± 0.04/8.07 ± 0.09	187.25 ± 2.16/305.72 ± 5.90	223.87 ± 4.03/479.15 ± 14.28
B3	19.85 ± 0.11	5.98 ± 0.08/8.09 ± 0.15	187.26 ± 4.17/307.19 ± 9.62	223.93 ± 7.80/482.82 ± 23.34
B4	19.82 ± 0.11	5.96 ± 0.03/8.05 ± 0.09	186.37 ± 1.34/304.77 ± 5.89	222.22 ± 2.50/476.86 ± 14.16

The length of the hydrogel remains constant regardless of the amount of glucose present, as it is distributed more evenly in the central part of the capsule, which has a cylindrical shape. As a result, we present the diameter of the hydrogel (*d*), the surface area (A_h), and the volume with and without glucose for comparison.

4.9. Diffusion Flow

From the diffusion speed, we can calculate the diffusion flow (J):

$$J = -\frac{v_D}{A_h}. \tag{8}$$

J was calculated using the Section diffusion speed method, where A_h is the surface area of the hydrogel and v_D is the diffusion speed. The negative sign indicates that glucose diffuses towards a decreasing concentration gradient. This means that the glucose molecules move from a higher concentration (hydrogel) to a region of lower concentration (saline solution), and the concentration decreases in the direction of flow.

The analysis of J was plotted as a positive value to facilitate the interpretation of the data and comparison between the different experiments, i.e., between the various hydrogels. A positive J indicates the amount of glucose moving through the PVA hydrogel.

4.10. Sterilization Process

To ensure a sterile environment for preparing the PVA gel and hydrogel, we followed these steps:

(a) The material was sterilized using a Steri-Vac® 8XL sterilization chamber (3M Health Care, St. Paul, MN, USA).
(b) We kept the entire workspace clean with bleach.
(c) We cleaned the laminar flow hood (Biobase, BBS-SDC, Jinan, China) inside and out with benzalkonium chloride.
(d) We filled the laminar flow hood with equipment and materials needed to prepare the PVA hydrogel.

(e) We irradiated the interior of the laminar flow hood with UV rays for 15 min.
(f) We wore appropriate clothing and applied benzal to gloves to minimize contamination.
(g) We prepared the PVA gel and poured it into molds inside the laminar flow hood.
(h) We covered the molds with sterilized aluminum foil before transferring to the freezer.
(i) We used aerosols to eliminate viruses and bacteria in the path from the laminar flow hood to the freezer.
(j) We thawed and checked the hydrogel for sterility using a Falcon-type tube and microbiological growth juice.

These hydrogels can serve as suitable environments for optimal growth and development of cells within a living being without causing any adverse reactions or rejection.

4.11. Cell Proliferation Test

After the PVA hydrogels were sterilized, a cell proliferation test was conducted using the SUP-B15 (ATCC CRL-1929) cell line in an IMDM medium with 20% fetal bovine serum (FBS) [46] to assess cell proliferation and survival in direct contact with PVA hydrogels [47,48]. The SUP-B15 cell line was placed in direct contact with 6 A1 hydrogels evenly distributed in a multiwell dish, as illustrated in Figure 11. The multiwell dish was then incubated at 37 °C with 5% CO_2 for 24 and 48 h.

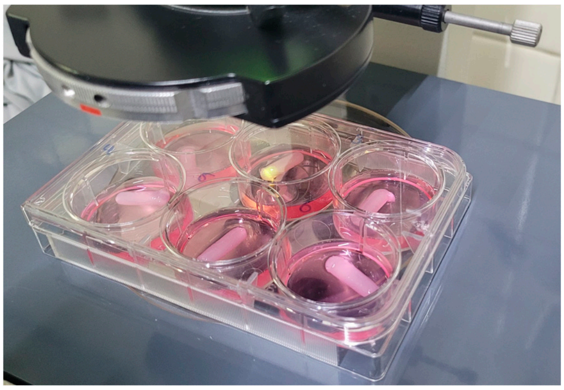

Figure 11. Microplate with A1 hydrogels and cell line SUP-B15 in IMDM medium with 20% BFS.

The hematological cell line SUP-B15, catalog number CRL-1929, was acquired directly from American Type Culture Collection (ATCC, Manassas, VA, USA) [46].

We utilized CellTiter 96® AQueous Non-Radioactive Cell Proliferation Assay (MTS) (PROMEGA, Madison, WI, USA) cell proliferation assay kit to measure viable cells, which is recognized for its precise quantification of viable cells [48].

To assess cell viability and proliferation, 100 µL of the cell suspension from each condition was mixed with 20 µL of a solution containing MTS and PMS in a 20:1 ratio. This mixture was placed in a 96-well plate (Corning, New York, NY, USA) and incubated for 2 h at 37 °C in a 5% CO_2 atmosphere to allow the production of Formazan. Cell viability was measured using an iMark Microplate Absorbance Reader (Bio-Rad, Lasec, Cape Town, South Africa) to assess the absorbance of Formazan at 490 nm, which is directly proportional to the number of living cells. All measurements were carried out in triplicate.

4.12. Statistical Tests

The estimated marginal means method was used with Bonferroni adjustment to compare Generalized Linear Models. The hydrogels of group A, group B, and both groups at different monitoring times (0, 5, 10, 15, 20, 25, 30, 35, 40, 45, 50, 55, and 60 min) were compared for glucose concentration, diffusion speed, and diffusion flow. The analysis showed statistically significant differences with a p-value < 0.05. We conducted this statistical analysis using SPSS version 25.

Author Contributions: Conceptualization, R.M.Q.-S. and J.C.L.-A.; methodology, O.I.M.-S., A.E.-T., A.M.-T., I.O.-C. and R.C.-M.; validation, R.M.Q.-S., O.I.M.-S., A.E.-T., A.M.-T. and I.O.-C.; formal analysis, R.M.Q.-S., A.M.-T., I.O.-C., R.C.-M., J.A.P.-P. and A.R.-B.; investigation, R.M.Q.-S., O.I.M.-S., A.E.-T., A.M-T. and I.O-C.; data curation, R.M.Q.-S. and J.A.P.-P.; writing—R.M.Q.-S.; writing—review and editing, R.M.Q.-S.; visualization, R.M.Q.-S.; supervision, R.M.Q.-S.; project administration, R.M.Q.-S., J.C.L.-A., A.M.-T. and I.O.-C. All authors have read and agreed to the published version of the manuscript.

Funding: The APC was funded by the Research Department of the General Hospital of Mexico "Dr. Eduardo Liceaga".

Institutional Review Board Statement: Not applicable.

Informed Consent Statement: Not applicable.

Data Availability Statement: The original contributions presented in the study are included in the article; further inquiries can be directed to the corresponding author.

Acknowledgments: This paper was supported by the General Hospital of Mexico "Dr. Eduardo Liceaga" (DI/12/111/04/17). We also want to acknowledge A. Durán Padilla and Alejandro K. Marquez Ramirez by providing us with the sections of PVA samples with the Leica Biosystems cryostat from Hospital General de México "Dr. Eduardo Liceaga", and Jocelin Correa Carranza for the porosity distribution of the hydrogels from SEM images.

Conflicts of Interest: The authors declare no conflicts of interest.

References

1. Boran, F. The Influence of Freeze-Thawing Conditions on Swelling and Long-Term Stability Properties of Poly (Vinyl Alcohol) Hydrogels for Controlled Drug Release. *Polym. Bull.* **2021**, *78*, 7369–7387. [CrossRef]
2. M-Chavarría, R.G.; Pérez-Pacheco, A.; Terán, E.; Quispe-Siccha, R.M. Study of Polyvinyl Alcohol Hydrogels Applying Physical-Mechanical Methods and Dynamic Models of Photoacoustic Signals. *Gels* **2023**, *9*, 727. [CrossRef] [PubMed]
3. Gupta, S.; Webster, T.J.; Sinha, A. Evolution of PVA Gels Prepared without Crosslinking Agents as a Cell Adhesive Surface. *J. Mater. Sci. Mater. Med.* **2011**, *22*, 1763–1772. [CrossRef] [PubMed]
4. Gao, T.; Jiang, M.; Liu, X.; You, G.; Wang, W.; Sun, Z.; Ma, A.; Chen, J. Patterned Polyvinyl Alcohol Hydrogel Dressings with Stem Cells Seeded for Wound Healing. *Polymers* **2019**, *11*, 171. [CrossRef]
5. Huang, M.; Hou, Y.; Li, Y.; Wang, D.; Zhang, L. High Performances of Dual Network PVA Hydrogel Modified by PVP Using Borax as the Structure-Forming Accelerator. *Des. Monomers Polym.* **2017**, *20*, 505–513. [CrossRef]
6. Galvis-García, E.S.; Sobrino-Cossío, S.; Reding-Bernal, A.; Contreras-Marín, Y.; Solórzano-Acevedo, K.; González-Zavala, P.; Quispe-Siccha, R.M. Experimental Model Standardizing Polyvinyl Alcohol Hydrogel to simulate Endoscopic Ultrasound and Endoscopic Ultrasoundelastography. *World J. Gastroenterol.* **2020**, *26*, 5169–5180. [CrossRef]
7. Asy-Syifa, N.; Kusjuriansah; Waresindo, W.X.; Edikresnha, D.; Suciati, T.; Khairurrijal, K. The Study of the Swelling Degree of the PVA Hydrogel with Varying Concentrations of PVA. *J. Phys. Conf. Ser.* **2022**, *2243*, 012053. [CrossRef]
8. Das, S.; Subuddhi, U. Controlled Delivery of Ibuprofen from Poly (Vinyl Alcohol)−poly (Ethylene Glycol) Interpenetrating Polymeric Network Hydrogels. *J. Pharm. Anal.* **2019**, *9*, 108–116. [CrossRef]
9. Massarelli, E.; Silva, D.; Pimenta, A.F.R.; Fernandes, A.I.; Mata, J.L.G.; Armês, H.; Salema-Oom, M.; Saramago, B.; Serro, A.P. Polyvinyl Alcohol/Chitosan Wound Dressings Loaded with Antiseptics. *Int. J. Pharm.* **2021**, *593*, 120110. [CrossRef]
10. Sánchez-Cardona, Y.; Echeverri-Cuartas, C.E.; López, M.E.L.; Moreno-Castellanos, N. Chitosan/Gelatin/Pva Scaffolds for Beta Pancreatic Cell Culture. *Polymers* **2021**, *13*, 2372. [CrossRef]
11. Li, R.; Lin, J.; Fang, Y.; Yu, C.; Zhang, J.; Xue, Y.; Liu, Z.; Zhang, J.; Tang, C.; Huang, Y. Porous Boron Nitride Nanofibers/PVA Hydrogels with Improved Mechanical Property and Thermal Stability. *Ceram. Int.* **2018**, *44*, 22439–22444. [CrossRef]
12. Rodríguez-Rodríguez, R.; García-Carvajal, Z.Y.; Jiménez-Palomar, I.; Jiménez-Avalos, J.A.; Espinosa-Andrews, H. Development of Gelatin/Chitosan/PVA Hydrogels: Thermal Stability, Water State, Viscoelasticity, and Cytotoxicity Assays. *J. Appl. Polym. Sci.* **2019**, *136*, 47149. [CrossRef]
13. Kanimozhi, K.; Khaleel Basha, S.; Sugantha Kumari, V. Processing and Characterization of Chitosan/PVA and Methylcellulose Porous Scaffolds for Tissue Engineering. *Mater. Sci. Eng. C* **2016**, *61*, 484–491. [CrossRef] [PubMed]
14. Popescu, I.; Constantin, M.; Solcan, G.; Ichim, D.L.; Rata, D.M.; Horodincu, L.; Solcan, C. Composite Hydrogels with Embedded Silver Nanoparticles and Ibuprofen as Wound Dressing. *Gels* **2023**, *9*, 654. [CrossRef]
15. Cascone, M.G.; Lazzeri, L.; Sparvoli, E.; Scatena, M.; Serino, L.P.; Danti, S. Morphological Evaluation of Bioartificial Hydrogels as Potential Tissue Engineering Scaffolds. *J. Mater. Sci. Mater. Med.* **2004**, *15*, 1309–1313. [CrossRef]
16. Zhang, G.; Ye, L. Toughening of Polyvinyl Alcohol Hydrogel Through Co-Crosslinking and Its Wastewater Treatment Performance by Immobilizing with Microorganism. *J. Polym. Environ.* **2017**, *25*, 229–240. [CrossRef]

17. Urushizaki, F.; Yamaguchi, H.; Nakamura, K.; Numajiri, S.; Sugibayashi, K.; Morimoto, Y. Swelling and Mechanical Properties of Poly (Vinyl Alcohol) Hydrogels. *Int. J. Pharm.* **1990**, *58*, 135–142.
18. Croitoru, C.; Roata, I.C.; Pascu, A.; Stanciu, E.M. Diffusion and Controlled Release in Physically Crosslinked Poly (Vinyl Alcohol)/Iota-Carrageenan Hydrogel Blends. *Polymers* **2020**, *12*, 1544. [CrossRef]
19. Qi, Z.; Yamamoto, C.; Imori, N.; Kinukawa, A.; Yang, K.C.; Yanai, G.; Ikenoue, E.; Shen, Y.; Shirouzu, Y.; Hiura, A.; et al. Immunoisolation Effect of Polyvinyl Alcohol (PVA) Macroencapsulated Islets in Type 1 Diabetes Therapy. *Cell Transpl.* **2012**, *21*, 525–534. [CrossRef]
20. Yoshimatsu, G.; Sakata, N.; Tsuchiya, H.; Ishida, M.; Motoi, F.; Egawa, S.; Sumi, S.; Goto, M.; Unno, M. Development of Polyvinyl Alcohol Bioartificial Pancreas with Rat Islets and Mesenchymal Stem Cells. *Transplant. Proc.* **2013**, *45*, 1875–1880. [CrossRef]
21. Karimi, A.; Navidbakhsh, M. Mechanical Properties of PVA Material for Tissue Engineering Applications. *Mater. Technol.* **2014**, *29*, 90–100. [CrossRef]
22. Kumar, A.; Han, S.S. PVA-Based Hydrogels for Tissue Engineering: A Review. *Int. J. Polym. Mater. Polym. Biomater.* **2017**, *66*, 159–182. [CrossRef]
23. Zhong, Y.; Lin, Q.; Yu, H.; Shao, L.; Cui, X.; Pang, Q.; Zhu, Y.; Hou, R. Construction Methods and Biomedical Applications of PVA-Based Hydrogels. *Front. Chem.* **2024**, *12*, 1376799. [CrossRef] [PubMed]
24. Song, S.; Liu, Z.; Abubaker, M.A.; Ding, L.; Zhang, J.; Yang, S.; Fan, Z. Antibacterial Polyvinyl Alcohol/Bacterial Cellulose/Nano-Silver Hydrogels That Effectively Promote Wound Healing. *Mater. Sci. Eng. C* **2021**, *126*, 112171. [CrossRef]
25. Thong Trinh, Q.; Gerlach, G.; Sorber, J.; Arndt, K.F. Hydrogel-Based Piezoresistive PH Sensors: Design, Simulation and Output Characteristics. *Sens. Actuators B Chem.* **2006**, *117*, 17–26. [CrossRef]
26. Vaddiraju, S.; Singh, H.; Burgess, D.J.; Jain, F.C.; Papadimitrakopoulos, F. Enhanced Glucose Sensor Linearity Using Poly (Vinyl Alcohol) Hydrogels. *J. Diabetes Sci. Technol.* **2009**, *3*, 863–874. [CrossRef]
27. Tavakoli, J.; Tang, Y. Hydrogel Based Sensors for Biomedical Applications: An Updated Review. *Polymers* **2017**, *9*, 364. [CrossRef]
28. Kobayashi, M.; Hyu, H.S. Development and Evaluation of Polyvinyl Alcohol-Hydrogels as an Artificial Atrticular Cartilage for Orthopedic Implants. *Materials* **2010**, *3*, 2753–2771. [CrossRef]
29. De Oliveira, P.P.M.; Bavaresco, V.P.; Silveira-Filho, L.M.; Schenka, A.A.; Vilarinho, K.A.D.S.; Barbosa De Oliveira Severino, E.S.; Petrucci, O. Use of a Novel Polyvinyl Alcohol Membrane as a Pericardial Substitute Reduces Adhesion Formation and Inflammatory Response after Cardiac Reoperation. *J. Thorac. Cardiovasc. Surg.* **2014**, *147*, 1405–1410. [CrossRef]
30. Sumi, S.; Yanai, G.; Qi, M.; Sakata, N.; Qi, Z.; Yang, K.; Shirouzu, Y.; Hiura, A.; Gu, Y.; Inoue, K. Review: Macro-Encapsulation of Islets in Polyvinyl Alcohol Hydrogel. *J. Med. Biol. Eng.* **2014**, *34*, 204–210. [CrossRef]
31. Kumar Parida, U.; Kumar Nayak, A.; Kumar Binhani, B.; Nayak, P.L. Synthesis and Characterization of Chitosan-Polyvinyl Alcohol Blended with Cloisite 30B for Controlled Release of the Anticancer Drug Curcumin. *J. Biomater. Nanobiotechnol.* **2011**, *2*, 414–425. [CrossRef]
32. Soto-Bustamante, F.; Bassu, G.; Fratini, E.; Laurati, M. Effect of Composition and Freeze-Thaw on the Network Structure, Porosity and Mechanical Properties of Polyvinyl-Alcohol/Chitosan Hydrogels. *Gels* **2023**, *9*, 396. [CrossRef] [PubMed]
33. Lungu, R.; Paun, M.A.; Peptanariu, D.; Ailincai, D.; Marin, L.; Nichita, M.V.; Paun, V.A.; Paun, V.P. Biocompatible Chitosan-Based Hydrogels for Bioabsorbable Wound Dressings. *Gels* **2022**, *8*, 107. [CrossRef] [PubMed]
34. Xu, Z.; Li, J.; Zhou, H.; Jiang, X.; Yang, C.; Wang, F.; Pan, Y.; Li, N.; Li, X.; Shi, L.; et al. Morphological and Swelling Behavior of Cellulose Nanofiber (CNF)/Poly (Vinyl Alcohol) (PVA) Hydrogels: Poly (Ethylene Glycol) (PEG) as Porogen. *RSC Adv.* **2016**, *6*, 43626–43633. [CrossRef]
35. Piacentini, E.; Bazzarelli, F.; Poerio, T.; Albisa, A.; Irusta, S.; Mendoza, G.; Sebastian, V.; Giorno, L. Encapsulation of Water-Soluble Drugs in Poly (Vinyl Alcohol) (PVA)- Microparticles via Membrane Emulsification: Influence of Process and Formulation Parameters on Structural and Functional Properties. *Mater. Today Commun.* **2020**, *24*, 100967. [CrossRef]
36. Santos, A.M.N.; Moreira, A.P.D.; Carvalho, C.W.P.; Luchese, R.; Ribeiro, E.; McGuinness, G.B.; Mendes, M.F.; Oliveira, R.N. Physically Cross-Linked Gels of PVA with Natural Polymers as Matrices for Manuka Honey Release in Wound-Care Applications. *Materials* **2019**, *12*, 559. [CrossRef]
37. Kudo, K.; Ishida, J.; Syuu, G.; Sekine, Y.; Ikeda-Fukazawa, T. Structural Changes of Water in Poly (Vinyl Alcohol) Hydrogel during Dehydration. *J. Chem. Phys.* **2014**, *140*, 044909. [CrossRef]
38. Meacham, R.; Liu, M.; Guo, J.; Zehnder, A.T.; Hui, C.Y. Effect of Hydration on Tensile Response of a Dual Cross-Linked PVA Hydrogel. *Exp. Mech.* **2020**, *60*, 1161–1165. [CrossRef]
39. Vrana, N.E.; O'Grady, A.; Kay, E.; Cahill, P.A.; McGuinness, G.B. Cell Encapsulation within PVA-Based Hydrogels via Freeze-Thawing: A One-Step Scaffold Formation and Cell Storage Technique. *J. Tissue Eng. Regen. Med.* **2009**, *3*, 567–572. [CrossRef]
40. Chen, Y.; Li, J.; Lu, J.; Ding, M.; Chen, Y. Strength and Toughness. *Polym. Test.* **2022**, *108*, 107516. [CrossRef]
41. Mandal, S.; Dasmahapatra, A.K. Effect of Aging on the Microstructure and Physical Properties of Poly (Vinyl Alcohol) Hydrogel. *J. Polym. Res.* **2021**, *28*, 269. [CrossRef]
42. Rosa, E.; Gallo, E.; Sibillano, T.; Giannini, C.; Rizzuti, S.; Gianolio, E.; Scognamiglio, P.L.; Morelli, G.; Accardo, A.; Diaferia, C. Incorporation of PEG Diacrylates (PEGDA) Generates Hybrid Fmoc-FF Hydrogel Matrices. *Gels* **2022**, *8*, 831. [CrossRef] [PubMed]
43. Ariga, O.; Kubo, T.; Sano, Y. Effective Diffusivity of Glucose in PVA Hydrogel. *J. Ferment. Bioeng.* **1994**, *78*, 200–201. [CrossRef]

44. Wu, I.Y.; Bala, S.; Škalko-Basnet, N.; di Cagno, M.P. Interpreting Non-Linear Drug Diffusion Data: Utilizing Korsmeyer-Peppas Model to Study Drug Release from Liposomes. *Eur. J. Pharm. Sci.* **2019**, *138*, 105026. [CrossRef] [PubMed]
45. Mogi, N.; Sugai, E.; Fuse, Y.; Funazukuri, T. Infinite Dilution Binary Diffusion Coefficients for Six Sugars at 0.1 MPa and Temperatures from (273.2 to 353.2) K. *J. Chem. Eng. Data* **2007**, *52*, 40–43. [CrossRef]
46. *ATCC SUP-B15 Intended Use*; ATCC: Manassas, VA, USA, 2022; pp. 1–6.
47. Mosmann, T. Rapid Colorimetric Assay for Cellular Growth and Survival: Application to Proliferation and Cytotoxicity Assays. *J. Immunol. Methods* **1983**, *65*, 55–63. [CrossRef]
48. Promega. CellTiter 96® Non-Radioactive Cell Proliferation Assay. In *Instructions for Use of Products G4000 and G4100*; Printed in USA. Revised 12/12 Part# TB112; Promega: Madison, WI, USA, 2012; pp. 1–19, ISBN 6082744330.

MDPI AG
Grosspeteranlage 5
4052 Basel
Switzerland
Tel.: +41 61 683 77 34

Gels Editorial Office
E-mail: gels@mdpi.com
www.mdpi.com/journal/gels

MDPI

Academic Open
Access Publishing

mdpi.com

ISBN 978-3-7258-4360-2